Relation between T_c and the defect structure of neodymium cerium cuprite $Nd_{2-x}Ce_xCuO_{4-y}$

V. I. Voronin, A. E. Kar'kin, and B. N. Goshchitskiĭ

Institute of Metal Physics, Ural Branch of the Russian Academy of Sciences, 620219 Ekaterinburg, Russia

A. Yu. Zuev, T. P. Rodionova, and A. N. Petrov

Urals State University, 620083 Ekaterinburg, Russia
(Submitted June 27, 1997)
Fiz. Tverd. Tela (St. Petersburg) **40**, 177–183 (February 1998)

Neutron powder diffraction has been used to study the defect structure of neodymium cerium cuprite $Nd_{2-x}Ce_xCuO_{4\pm y}$ ($x=0.15$). It has been shown that in addition to oxygen vacancies, O2 sites in superconducting samples may also contain a small quantity of implanted oxygen atoms positioned between copper ions and neodymium/cerium, which control the electrical charge in the Cu–O planes. The oxygen distribution among crystal lattice sites in $Nd_{2-x}Ce_xCuO_{4\pm y}$ ($x=0.15$) was determined, the average charge of the copper ions was calculated by the method of valence sums, and a correlation was established between the charge of the copper-oxygen plane and T_c. © *1998 American Institute of Physics.* [S1063-7834(98)00102-6]

Neodymium cerium cuprite, $Nd_{2-x}Ce_xCuO_{4\pm y}$, occupies a special position among the various copper-containing high-temperature superconductors (HTS) for various reasons. First, unlike other HTS cuprites, the charge carriers are electrons.[1–3] Second, superconductivity is observed in a fairly narrow range of Ce concentrations ($0.14<x<0.17$). Finally, even within this range of cerium concentrations, the superconduction transition temperature (T_c) is extremely sensitive to the oxygen stoichiometry. This compound has a tetragonal (T') crystal structure and the atomic configuration is similar to the $La_{2-x}Sr_xCuO_{4-y}$ ($x>0.10$) structure.[1] The T' structure of $Nd_{2-x}Ce_xCuO_{4-y}$ compounds (Fig. 1) consists of alternating copper-oxygen planes of CuO_2 in which the Cu ions have a square oxygen-ion neighborhood (O1 sites) and a ''sandwich'' formed by layers of oxygen ions (O2 sites) interspersed with neodymium-cerium ions.

Questions involving the relation between the superconducting transition temperature, the oxygen nonstoichiometry, and the structure of $Nd_{2-x}Ce_xCuO_{4\pm y}$ have attracted the attention of many researchers. However, information on the oxygen content as a function of the thermodynamic conditions in neodymium cerium cuprite, obtained by thermogravimetry and chemical analysis (iodometry) are contradictory. Some authors[4,5] assert that, even after treatment in pure oxygen, the oxygen index does not exceed four. Other authors[6–8] take the view that, after annealing in oxygen, samples contain excess oxygen in interstitial sites in the copper oxide structure. It is postulated that in a $Nd_{1.85}Ce_{0.15}CuO_{4-y}$ sample annealed in a rare gas atmosphere, the total oxygen content decreases ($y>0$), which leads to an additional increase in the charge carrier concentration in the lattice with the onset of superconductivity. Note that the optimum doping level cannot be achieved merely by varying the cerium concentration or merely by annealing in oxygen.[9]

However, thermogravimetry and iodometric titration can only provide data on the total oxygen content in samples, whereas neutron diffraction can be used to determine the distribution of oxygen and oxygen defects in the lattice. For instance, neutron powder diffraction was used to demonstrate the existence of oxygen vacancies in the lattice in superconducting and nonsuperconducting $Nd_{2-x}Ce_xCuO_{4-y}$ ($x=0.155$) samples.[10] However, it is unclear how the stoichiometrically excess oxygen, observed by thermogravimetric analysis[6,11] and by iodometric titration,[7] is distributed in the crystal lattice. The authors of Ref. 12 used neutron diffraction analysis to solve this problem for polycrystalline $Nd_{2-x}Ce_xCuO_{4-y}$ samples and showed that the oxygen atoms may be partially distributed at position O3 (Fig. 1), which is completely filled in the $La_{2-x}Sr_xCuO_{4-y}$ lattice by so-called ''apical'' oxygen (T-structure). These conclusions were then confirmed by neutron diffraction analyses for single crystals of pure Nd_2CuO_{4-y} (Ref. 13), cerium-doped $Nd_{1.85}Ce_{0.15}CuO_{4-y}$ (Ref. 14), and for $Nd_{1.9}Ce_{0.1}CuO_{4-y}$ polycrystals.[15] Studies have indicated that vacancies are present at the O1 and O2 sites together with a small quantity of apical oxygen at positions O3. The authors of Ref. 15 proposed a model for defect formation in $Nd_{1.9}Ce_{0.1}CuO_{4-y}$ which assumes that both oxygen vacancies and ''interstitial (O3) oxygen ions are present at crystallographic positions in the structure of neodymium cerium cuprite. Calculations of the cation valence state in $Nd_{1.9}Ce_{0.1}CuO_{4-y}$, using the method of valence sums from an analysis of cation-oxygen bond lengths,[16] provided further evidence to support the presence of both vacancies and interstitial oxygen in the lattice.

Thus, the properties of $Nd_{2-x}Ce_xCuO_{4-y}$, including su-

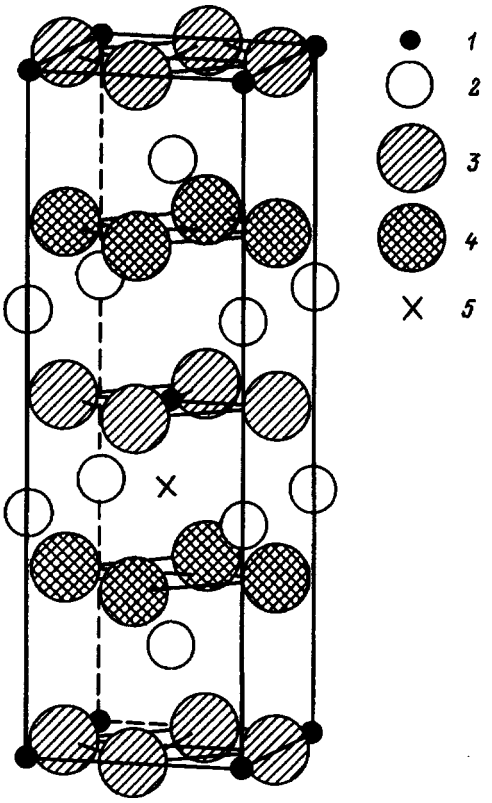

FIG. 1. T' crystal structure: *1*—Cu, *2*—Nd/Ce, *3*—O1, *4*—O2, and *5*—O3.

perconductivity, are determined by both the cerium and the oxygen content. Oxygen stoichiometry is established following synthesis of the compound by the sample annealing conditions; this is difficult to monitor, and frequently cannot be determined by the researchers. Unfortunately, very few systematic studies have been made of the distribution of oxygen ions in the $Nd_{2-x}Ce_xCuO_{4-y}$ defect lattice and its influence on the superconductivity of the samples.

The aim of the present study is to investigate the actual distribution of oxygen in the lattice of $Nd_{1.85}Ce_{0.15}CuO_{4-y}$ compounds having a fixed cerium content ($x=0.15$), which influences the valence of the copper, and to observe a correlation between the charge of the copper atoms and the superconducting transition temperature.

1. EXPERIMENTAL METHOD

The crystal structure was studied by x-ray diffraction (Dron-UMI1 diffractometer using copper radiation) and neutron diffraction ($\lambda=1.515$ Å). The neutron diffraction patterns at room temperature were obtained at the IVV-2M atomic reactor using a D7a diffractometer. A double monochromator: pyrolytic graphite (002 reflecting plane)–germanium (333), was used to improve the angular resolution ($\Delta d/d=0.3\%$). The structural parameters were refined by means of a Rietveld full-profile analysis using the ''Fullprof'' program.[17] The superconducting transition temperature was determined by the ac susceptibility method (frequency 1 kHz).

Neodymium cerium cuprite, $Nd_{1.85}Ce_{0.15}CuO_{4-y}$, was prepared using standard ceramic technology, in the temperature range 1223–1423 K. The process comprised three stages with intermediate grinding of the reaction mixture. The samples were preannealed at 1000 °C for 24 h under different oxygen pressures: $PO_2=0.0015$ (sample No. 1), 0.0026 (No. 2), 0.03 (No. 3), and 1 atm (No. 4), followed by rapid quenching.

2. RESULTS OF MEASUREMENTS

The x-ray diffraction analyses showed that all the $Nd_{1.85}Ce_{0.15}CuO_{4-y}$ samples are single-phase with a T' tetragonal crystal structure. The structural parameters (atomic coordinates, site occupation numbers, thermal vibration amplitudes, and static atomic displacements) were obtained from the neutron diffraction patterns by successive comparisons of the calculated and experimental data. A typical neutron diffraction pattern is shown in Fig. 2.

To a first approximation, we assumed that $Nd_{1.85}Ce_{0.15}CuO_{4-y}$ has a pure T' structure in which all the oxygen atoms are only occupy at O1 and O2 sites and the individual temperature factors for each atom are isotropic. In an earlier study[18] we showed that the incorporation of anisotropic thermal vibrations and static atomic displacements in calculations of $La_{2-x}Sr_xCuO_{4-y}$ improves the convergence with the experiment, reflecting an anisotropic variation in the crystal lattice parameters under strontium doping or fast neutron irradiation. Thus, we introduced anisotropic Debye–Waller factors for all the atoms to achieve further refinement. Finally, the best fit to the experiment (minimum values of the R factors) was achieved by introducing an additional oxygen position—''interstitial'' oxygen atoms in O3 positions (Fig. 1). Since there are a very small number of these positions, the occupation of the O3 positions $n(\mathrm{O3})$ and their position (z coordinate) were determined by successively fixing $n(\mathrm{O3})$ and z in small steps and then analyzing the convergence factors, to achieve their minimum values.

Similar procedures for refinement of the structure parameters of $Nd_{1.85}Ce_{0.15}CuO_{4-y}$ were performed for all the samples. These refined structure parameters are presented in Table I. The unit cell parameters for sample No. 4 differed fairly appreciably from those of the previous three. An accurate determination of the occupancy of the oxygen sites in the cell of this sample revealed that their occupancies differed from the first three, with position O2 being completely filled, whereas vacancies were identified at positions O1.

The values of T_c, determined from the onset of a superconducting transition, on the temperature dependences of the ac susceptibility are also presented in Table I.

We shall examine the structural characteristics of $Nd_{2-x}Ce_xCuO_{4-y}$ samples with different dopant concentrations. Published data[12,19,20] and our own data on the crystal lattice parameters of $Nd_{2-x}Ce_xCuO_{4-y}$ as a function of the cerium ion concentration, have shown that the reduction in the cell volume with increasing cerium concentration is mainly caused by a decrease in the parameter c from 12.15 ($x=0$) to 12.07 Å ($x=0.15$), whereas the parameter a remains unchanged to two decimal places (3.94 ± 0.01 Å). This behavior is attributable to characteristic features of the crystal structure, since it is well known that the symmetry, type, and dimensions of ionic compounds are determined to

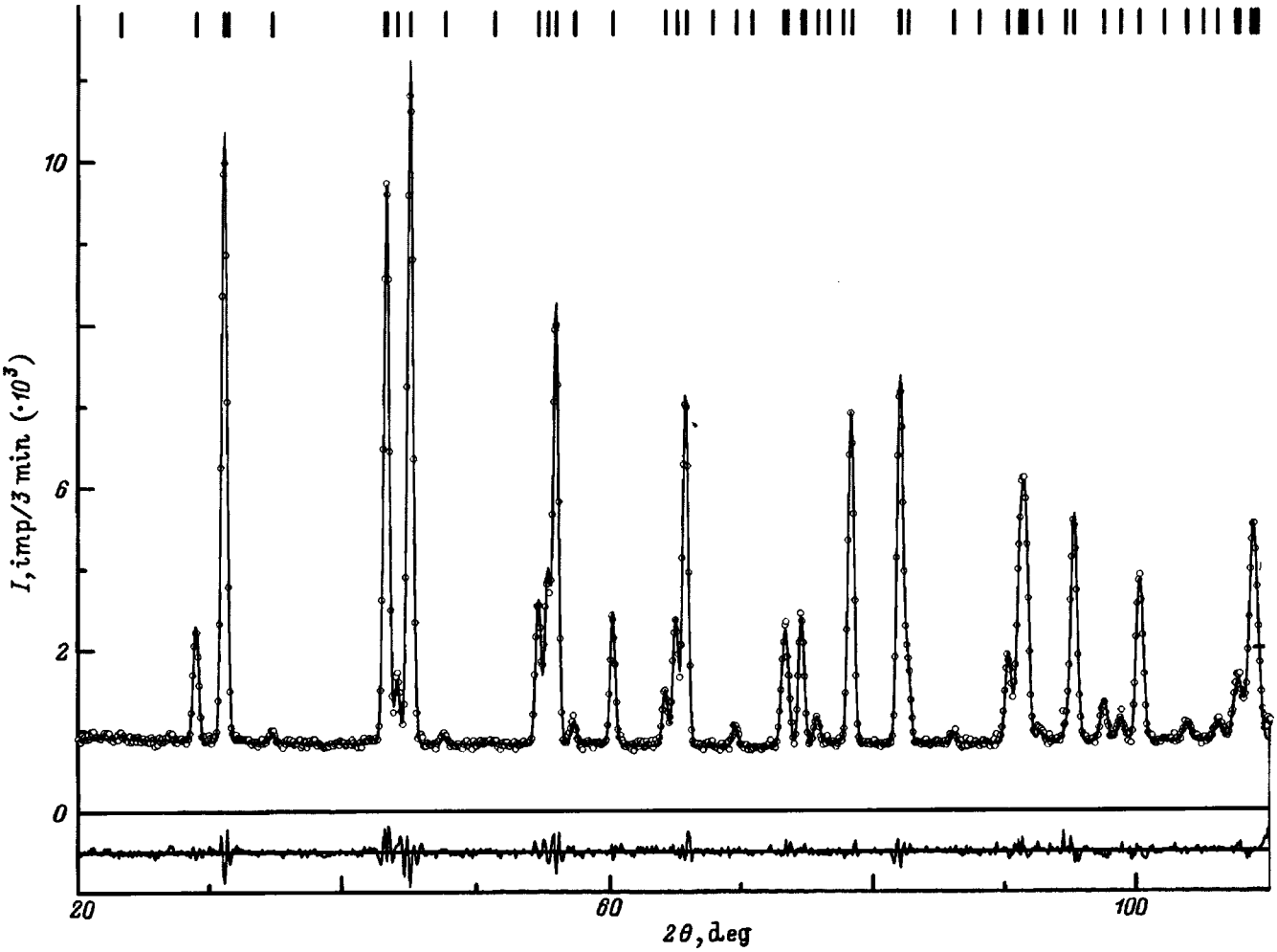

FIG. 2. Neutron diffraction pattern of $Nd_{1.85}Ce_{0.15}CuO_{4-y}$ No. 2. Circles—experiment, upper curve—calculations, and lower curve—difference between experiment and calculations.

a considerable extent by the relative dimensions of the ions whose radii depend on their nearest neighborhood.[21,22] In the T' structure the copper atoms (Fig. 1) have a square array of O1 oxygen ions in a plane (coordination number 4), and each O1 ion is surrounded by two copper and four neodymium atoms (coordination number 6). In the sandwich, the neodymium ions are adjacent to four oxygen ions in position O2 and, at a greater distance, four O1 ions located in the basal plane, whereas the nearest neighbors of the O2 ions are only four Nd cations. The ionic radii[21,22] are: $r(Cu^{2+})=0.57$ Å, $r(Cu^{1+})=0.60$ Å for coordination number 4, $r(O^{2-})=1.40$ Å for coordination number 6, and $r(O^{2-})=1.38$ Å for coordination number 4, and $r(Nd^{3+})=1.01$ Å for coordination number 8. It is known that when the ionic radii deviate from the ideal ratios, the lattice parameter in perovskite has one of three values: $2(r_A+r_O)$, $2\sqrt{2}(r_B+r_O)$, or $2\sqrt{2}r_O$ (Ref. 23). Using these values of the radii for $Nd_{2-x}Ce_xCuO_{4-y}$, we obtain the following relations: $2(r_A+r_O)<2\sqrt{2}(r_B+r_O)<2\sqrt{2}r_O$. We now consider the CuO_2 basal plane. The lattice parameter obtained from the oxygen–oxygen distance is greater ($a=2\sqrt{2}r(O^{2-})=3.96$ Å) than that obtained from the copper–oxygen distance ($2r(Cu^{2+}/Cu^{1+})+2r(O^{2-})=3.94$ Å). In the planes formed by O2 oxygen ions, the a parameter should be $2\sqrt{2}r(O^{2-})=3.903$ Å, since O2 is only surrounded by four Nd ions. Thus, the a parameter in $Nd_{2-x}Ce_xCuO_{4-y}$ compounds is controlled by the configuration of the oxygen ions in the CuO_2 plane.

The lower experimental values of the lattice parameters $a=3.94$ Å (samples No. 1–3) compared with the calculated values (3.96 Å) may be attributed to the large amplitudes of the O1 displacement and their anisotropy (Table I). This strong anisotropy of the O1 displacements may be caused by a change in the local neighborhood symmetry of the copper atoms, where this is reduced to orthorhombic. Such a reduction in symmetry from tetragonal ($I4/mmm$) to orthorhombic ($Cmca$) was observed when Nd ions were replaced by Tb (Ref. 19) or Gb ions[24] in $(Nd/Ln)_{1.85}Ce_{0.15}CuO_{4-y}$ compounds where Ln=Tb, Gb. Since we observed no additional reflections, we assumed that uncorrelated static displacements of O1 atoms were present together with the thermal vibrations. This assumption is based on the results of neutron-diffraction low-temperature measurements of $Nd_{18.5}Ce_{0.15}CuO_{4-y}$ single crystals, studied in Ref. 14, in which large anisotropic amplitudes of O1 displacements were observed at 11 K. We postulated that the oxygen ions were distributed statistically in a position having the coordi-

TABLE I. Structure parameters of $Nd_{1.85}Ce_{0.15}CuO_{4-y}$.

Parameters		Sample			
		No. 1	No. 2	No. 3	No. 4
a, Å		3.93956(15)	3.93889(15)	3.94628(12)	3.92806(17)
c, Å		12.06644(58)	12.06502(59)	12.08171(50)	12.02967(67)
c/a		3.0629	3.063	3.0615	3.0625
V, Å^3		187.273	187.187	188.150	185.613
T_c, K		20.4	18.3	16.5	–
Nd/Ce	z	0.35268(13)	0.35250(13)	0.35225(12)	0.35268(15)
	$\beta_{11}=\beta_{22}$	0.0068(9)	0.0061(9)	0.0035(8)	0.0100(11)
	β_{33}	0.0002(1)	0.0003(1)	0.0001(1)	0.0002(1)
Cu	$\beta_{11}=\beta_{22}$	0.0067(14)	0.0076(13)	0.0056(13)	0.0039(15)
	β_{33}	0.0010(1)	0.0012(1)	0.0010(1)	0.0008(1)
O1	β_{11}	0.0094(17)	0.0083(16)	0.0078(15)	0.0082(24)
	β_{22}	0.0219(19)	0.0216(19)	0.0118(16)	0.0024(21)
	β_{33}	0.0013(1)	0.0017(1)	0.0014(1)	0.0018(2)
	n	2	2	2	1.968(27)
O2, O3	$\beta_{11}=\beta_{22}$	0.0029(16)	0.0054(16)	0.0040(16)	0.016 8(17)
	β_{33}	0.0013(1)	0.0011(1)	0.0006(1)	0.0005(1)
	n	1.924(30)	1.941(29)	1.911(27)	2
O3	z	0.165(9)	0.165(9)	0.165(9)	0.165(9)
	n	0.023(10)	0.011(9)	0.041(9)	0.016(13)
n(O)		3.937(30)	3.952(30)	3.952(27)	3.984(13)
y		0.063(30)	0.048(30)	0.048(27)	0.016(13)
R_p		3.17	3.22	3.08	3.75
R_{wp}		4.15	4.25	4.10	4.93
R_B		2.62	2.61	2.29	3.26
R_f		2.52	2.81	2.72	3.16

Here a,c are the cell parameters, V is the volume, $\beta_{11},\beta_{22}=2\pi^2\langle u_{11}^2,u_{22}^2\rangle/a^2$, $\beta_{33}=2\pi^2\langle u_{33}^2\rangle/c^2$ are the anisotropic thermal parameters, n is the occupation of particular positions, n(O) is the total oxygen content in the cell, y is the oxygen deficit, R_p, R_{wp}, R_B, R_f are the convergence factors.[17] Space group $I4/mmm$: Cu($2a$)—0,0,0, Nd/Ce($4e$)—0,0,z, O1($4c$)—0.5,0,0, O2($4d$)—0,0.5,0.25, O3($4e$)—0,0,z.

nates $(0.5,0+y,0+z)$. The calculations yielded the following values of the O1 coordinates, for example, for sample No. 1: $y\sim0.024$ and $z\sim0.0053$, and all the amplitudes of the thermal vibrations $\langle\beta_{ii}\rangle$ were similar and close to those of the Nd/Ce and Cu vibrations. This effect was also observed for samples Nos. 2 and 3. Figure 3 gives the parameters a and c as a function of the amplitude of the displacement of the O1 atoms, which reveals a clear correlation between them. We draw attention to the fact that when the displacements of the O1 oxygen ions $\langle u_{ii}\rangle$ are taken into account, the Cu–O1 bond lengths are equal in all three superconducting compounds: $L(\text{Cu–O1})=1.9744\pm0.0006$ Å. We postulate that the square of oxygen ions rotates statistically about the copper atoms, as was observed in Refs. 19 and 20. The calculations indicate that the Nd–O2 bond is fairly rigid and thus $L(\text{Nd–O2})=2.3300\pm0.0003$ Å for all $Nd_{2-x}Ce_xCuO_{4-y}$ compounds. The Nd–O1 bonds are relatively weaker and the values of $L(\text{Nd–O1})$ are 2.676 ± 0.003 ($x=0$) and 2.656 ± 0.002 Å ($x=0.15$). As a result, substitution of trivalent Nd with tetravalent Ce, having a smaller ionic radius, appreciably shortens the lattice in the c direction.

The oxygen distribution pattern throughout the cell observed in the nonsuperconducting sample No. 4, annealed in a stream of pure oxygen, differs from that for the superconducting samples Nos. 1–3. First, the lattice parameters are considerably smaller. Second, the nonsuperconducting sample has vacancies at O1 and O2 sites and the displace-

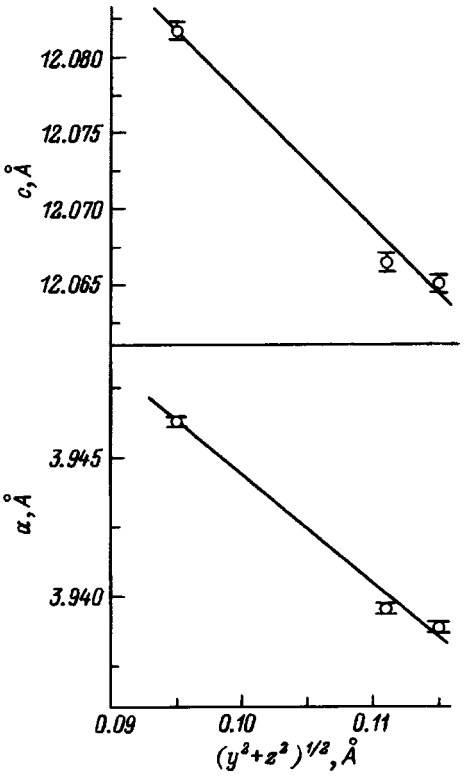

FIG. 3. Lattice parameters of $Nd_{1.85}Ce_{0.15}CuO_{4-y}$ with different oxygen contents as a function of the amplitude of static displacement of the oxygen atoms at position O1.

TABLE II. Cation–anion bond lengths (Å) in crystal cell of $Nd_{1.85}Ce_{0.15}CuO_{4-y}$ compounds.

	No. 1	No. 2	No. 3	No. 4
Nd–O1	2.6531(8)	2.6544(8)	2.6612(8)	2.6452(12)
Nd–O2	2.3272(6)	2.3255(6)	2.3276(6)	2.3203(12)
Nd–O3	2.265(3)	2.262(2)	2.265(2)	2.017(3)
Nd–O3	2.794(3)	2.793(2)	2.798(2)	2.814(3)
Cu–O1	1.9698(1)	1.9694(1)	1.9731(1)	1.9640(1)
Cu–O2	3.6028(1)	3.6023(1)	3.6078(1)	3.5919(1)
Cu–O3	1.991(3)	1.991(3)	1.994(3)	2.226(3)
⟨Cu–O1⟩	1.9742	1.9739	1.9748	–

⟨Cu–O1⟩ is the bond length allowing for the static displacement of the O1 oxygen atoms—(0.5, $0+y$, $0+z$).

ments of the O1 oxygen ions have a larger amplitude parallel to the Cu–O bond compared with that in the perpendicular direction. Third, the O2 vibrations are strongly anisotropic with a maximum displacement amplitude in the ab plane. Finally, the vibrations of the Nd/Ce atoms are also strongly anisotropic with a maximum displacement amplitude in the ab plane, the total oxygen content in the cell is close to four (Table I) and the convergence factors are higher than those of the superconducting samples Nos. 1–3. This not only indicates that the oxygen stoichiometry is impaired but also that vacancies appear in the Nd/Ce sublattice or their ratios change. This assumption leads to improved convergence, but gives a reduced oxygen concentration at O2. This model qualitatively explains the structural characteristics of this sample, especially the smaller lattice parameters, which are unusual for oxidized samples since the parameters are usually increased slightly by oxidation.[12–15] Since existing data cannot determine for certain whether vacancies are present in the Nd sublattice or whether the ratio of Nd/Ce ions in the site has changed, we did not attempt to refine the structure of this sample.

The existence of additional oxygen at O3 lattice sites remains an important issue. For our $Nd_{1.85}Ce_{0.15}CuO_{4-y}$ samples we used experimental values of the cation–oxygen bond length (Table II) for additional testing of the electrical neutrality of the crystal cell by the method of valence sums, as was performed in our previous study for $Nd_{1.9}Ce_{0.1}CuO_{4\pm y}$ (Ref. 15). It was found that electrical balance of the positive and negative charges in the crystal cell requires the introduction of additional apical oxygen at O3

TABLE III. Calculated percent content of Cu^{1+} and Cu^{2+} ions, charge state of copper sites V(Cu) and neodymium-cerium sites V(Nd/Ce), total positive (+) and negative (−) charge of cell, their difference Δ, and contribution to Cu valence made by apical oxygen δV(Cu-O3).

	No. 1	No. 2	No. 3	No. 4
Cu^{1+}, %	27.5	28.7	24.6	25.9
Cu^{2+}, %	72.5	71.3	75.4	74.1
V(Cu)	1.725	1.713	1.754	1.741
V(Nd/Ce)	3.079	3.086	3.075	3.199
(+)	7.882	7.884	7.904	8.133
(−)	7.894	7.900	7.920	7.960
Δ	0.012	0.016	0.016	0.179
δV(Cu–O3)	0.019	0.010	0.041	0.013

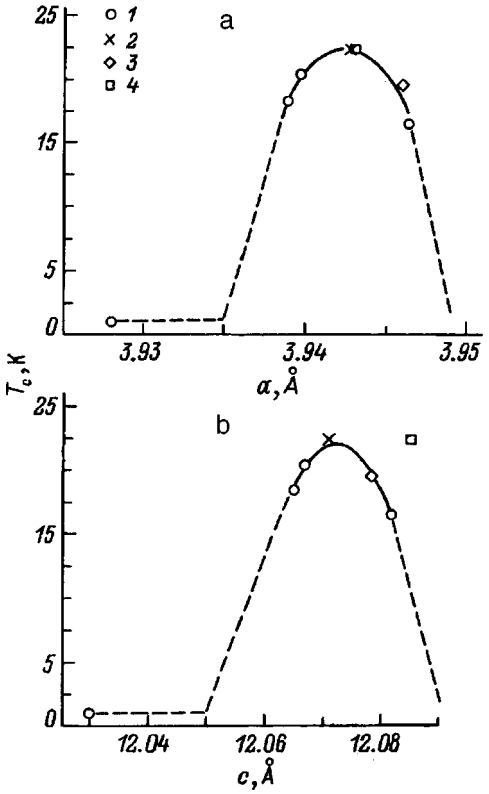

FIG. 4. Dependence of T_c on the lattice parameters: *1*—our results, *2*—Ref. 12, *3*—Ref. 19, and *4*—Ref. 25.

sites. The results are presented in Table III with allowance for the static displacements of O1 atoms. It can be seen that for samples Nos. 1–3, electrical neutrality of the cell is accurately (<0.02) conserved, whereas for sample No. 4 the difference between the positive and negative charges is very large. This difference is clearly attributable to the loss of oxygen and Nd/Ce stoichiometry during the annealing process, as has already been noted. Attention is drawn to the fact that the calculated valence of the Nd/Ce site (3.199) was considerably higher than the value of 3.075 typical of the composition 1.85Nd+0.15Ce. In our opinion, this result provides further confirmation of the validity of the method of valence sums to estimate the charge state of cations in ionic compounds.

Figure 4 gives T_c as a function of the lattice parameters of $Nd_{1.85}Ce_{0.15}CuO_{4-y}$. A clear correlation can be observed between T_c and the lattice parameters. The values of the parameters are determined by the specific position of the oxygen ions in the cell. The particular role of apical oxygen for the establishment of superconductivity in $La_{2-x}Sr_xCuO_{4-y}$ and $YBa_2Cu_3O_{7-y}$ compounds has been emphasized in many studies, including our own.[18,24] In $Nd_{1.85}Ce_{0.15}CuO_{4-y}$ the apical O3 oxygen promotes redistribution of charge between the O2-Nd/Ce-O2 sandwich and the Cu-O1 plane, thereby controlling the valence state of the copper ions. Figures 5a and 5b give T_c as a function of the copper ion charge and the concentration of apical oxygen in the lattice, respectively. Thus, in $Nd_{1.85}Ce_{0.15}CuO_{4-y}$ compounds an important role is played by the apical O3 oxygen which controls the effective charge in the CuO_2 plane, intro-

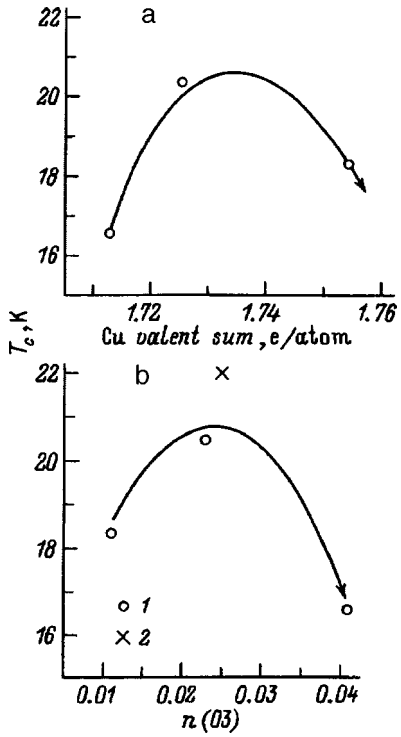

FIG. 5. Dependence of T_c on the valence state of the copper atoms (a) and on the filling numbers of the O3 position (apical oxygen) (b): *1*—our data and *2*—Ref. 12.

ducing distortions into the crystal lattice of neodymium cerium cuprite.

In this way, we have obtained the following main results.

Neutron diffraction was used to make a detailed study of the structural characteristics of the crystal lattice of neodymium cerium cuprite $Nd_{1.85}Ce_{0.15}CuO_{4-y}$ as a function of the oxygen stoichiometry. The oxygen content in the cell was determined and appreciable anisotropic displacements of oxygen atoms and their influence on the crystal lattice parameters were established. It was confirmed that superconductivity occurs in reduced samples having an oxygen deficiency. It was established that apical oxygen (O3 sites) exists in the lattice and this plays an important role in the formation of the charge state of the CuO_2 planes. It was demonstrated that the oxygen occupation of lattice sites may be additionally monitored by using the method of valence sums. We determined the dependence of T_c on the valence state of the copper atoms, which is governed not only by the oxygen concentration but also by its real distribution in the crystal cell.

This work was supported by the State Scientific-Technical Program ''Current Trends in Physics of the Condensed State,'' ''Neutron Research'' Trends (Projects Nos. 96-104 and 96-305), ''Superconductivity'' (Project No. 96-051), and by the Russian Fund for Fundamental Research (Grant No. 97-03-33632a).

[1] Y. Tokura, H. Takagi, and S. Uchida, Nature **337**, 345 (1989).
[2] H. Takagi, S. Uchida, and Y. Tokura, Phys. Rev. Lett. **62**, 1197 (1989).
[3] S. Uji and H. Aoki, Physica C **199**, 231 (1992).
[4] J. S. Kim and D. R. Gaskell, Physica C **209**, 381 (1993).
[5] K. Suzuki, K. Kishio, T. Hasegawa, and K. Kitazawa, Physica C **166**, 357 (1990).
[6] J. M. Tarascon, E. Wang, L. H. Greene, R. Ramesh, B. G. Bagley, G. W. Hull, C. Miceli, Z. Z. Wang, D. Brawner, and N. P. Ong, Physica C **162–164**, 258 (1989).
[7] E. Moran, A. I. Nazzal, T. C. Huang, and J. B. Torrance, Physica C **160**, 30 (1989).
[8] P. W. Klamut, J. Alloys Compd. **194**, L5 (1993).
[9] N. A. Fortune, K. Murata, Y. Yokoyama, M. Ishibashi, and Y. Nishinara, Physica C **178**, 437 (1991).
[10] F. Izumi, Y. Matsui, H. Takagi, Y. Tokura, and H. Asano, Physica C **158**, 433 (1989).
[11] E. Wang, J. M. Tarascon, L. H. Greene, and G. W. Hull, Phys. Rev. B **41**, 6582 (1990).
[12] I. Mangelschots, N. H. Anderson, B. Lebech, A. Wisnievski, and C. S. Jacobsen, Physica C **202**, 369 (1992).
[13] P. G. Radaelli, J. D. Jorgenson, A. J. Schultz, J. L. Peng, and R. L. Greene, Phys. Rev. B **49**, 15 322 (1994).
[14] A. J. Schultz, J. D. Jorgenson, J. L. Peng, and R. L. Greene, Phys. Rev. B **53**, 5157 (1996).
[15] A. N. Petrov, A. Yu. Zuev, T. P. Rodionova, and V. I. Voronin, J. Am. Ceram. Soc. (1997), in press.
[16] I. D. Brown and D. Altermatt, Acta Cryst. B **41**, 244 (1985).
[17] J. Rodriguez-Carjaval, Physica B **192**, 55 (1993).
[18] V. Voronin, A. Mirmelstein, V. Kozhevnikov, and B. Goshchitskii, Physica C **218**, 407 (1993).
[19] M. Braden, P. Aldermann, P. Schweiss, and T. Woisczyk, Phys. Rev. B **53**, R2975 (1996).
[20] P. Aldermann, R. Ahrens, G. Czjzek, G. Roth, and C. Steinleitner, Phys. Rev. B **46**, 3619 (1992).
[21] R. D. Shannon and C. T. Prewitt, Acta Cryst. B **25**, 925 (1969).
[22] S. S. Batsanov, Zh. Neorg. Khim. **36**, 3015 (1991).
[23] K. S. Aleksandrov, A. T. Anistratov, B. V. Beznosikov, and N. V. Fedoseeva, *Phase Transitions in Crystals of ABX_3 Halide Compounds* [in Russian], Nauka, Novosibirsk (1981).
[24] V. Voronin, A. Mirmelstein, A. Karkin, A. Tephykh, B. Goshchitskii, A. Ivanov, and L. Smirnov, High Press. Res. **14**, 139 (1995).
[25] Chang Fanggao, A. Al-Kheffaji, P. J. Ford, D. A. Ladds, J. Freestone, B. Chapman, Li Manosa, D. P. Almond, and G. A. Saunders, Supercond. Sci. Technol. **3**, 422 (1990).

Translated by R. M. Durham

Low-energy electron spectrum in copper oxides in the multiband $p-d$ model

V. A. Gavrichkov and S. G. Ovchinnikov

L. V. Kirenskiĭ Institute of Physics, Siberian Branch of the Russian Academy of Sciences, 660036 Krasnoyarsk, Russia

(Submitted March 25, 1997; resubmitted July 8, 1997)
Fiz. Tverd. Tela (St. Petersburg) **40**, 184–190 (February 1998)

An exact diagonalization of the Hamiltonian in the $p-d$ model of a CuO_6 cluster was used to obtain dependences on the model parameters of the lowest-energy two-hole terms: the energy difference between the $2p$ orbitals of planar and apical oxygen $\Delta(\text{apex})=\varepsilon(2p)-\varepsilon[2p(\text{apex})]$, the crystal field parameter $\Delta_d=\varepsilon_{3z^2-r^2}-\varepsilon_{x^2-y^2}$, and the ratio of the distances between the copper atom and the apical and planar oxygen atoms $d(\text{apex})/d(\text{pl})$. In the limit of large $d(\text{apex})/d(\text{pl})$ and Δ_d, our model is equivalent to the three-band $p-d$ model and, in this case, large singlet-triplet splitting $\Delta\varepsilon\geqslant 1$ eV is also observed. As the parameters decrease, a singlet-triplet crossover is observed. Two mechanisms are identified for stabilization of the triplet term $^3B_{1g}(0)$ as the ground state. It is shown that for realistic values of the parameters, reduction of the $p-d$ model to the three-band model is limited by the low energies of the current excitations because of the presence of the lower excited $^3B_{1g}$ and $^1A_{1g}$ cluster states. Intercluster hopping causes strong mixing of singlet and triplet states far from the Γ point. The results of the calculations are compared with data obtained by angle-resolved photoelectron emission in $Sr_2CuO_2Cl_2$. © *1998 American Institute of Physics.* [S1063-7834(98)00202-0]

The electronic structure of undoped and weakly-doped copper oxides does not lend itself to *ab initio* band calculations because of the difficulties involved in allowing for the strong electron correlations. The three-band $p-d$ model[1,2] is the simplest model for the energy structure of copper oxides which takes account of strong correlation effects at the Cu cation and the ionic nature of the chemical bond of the insulating ground state of undoped oxides having a semiconductor gap as a result of charge transport. It is currently assumed that holes induced by p-type doping or intrinsic nonstoichiometry are located on the oxygen and a ''hole on copper+ hole on oxygen'' pair is in the Zhang–Rice singlet state.[3] It is also assumed that the first excited state of a pair of holes is 2–3 eV higher and is unrelated to the low-energy dynamics of the current carriers. This is one reason for the appearance of numerous theoretical studies concerned with reducing the $p-d$ model to the single-band Hubbard model or the $t-J$ model.[4–6] Nevertheless, there is theoretical and experimental evidence to indicate the importance of other states, absent from the three-band $p-d$ model. For instance, polarized x-ray absorption spectroscopy (XAS)[7] and electron energy-loss spectroscopy (EELS)[8] show quite measurable filling of $d_{3z^2-r^2}$ orbitals in all the oxides studied. In order to give a three-band model in accordance with the observed states, its basis must also include the $d_{3z^2-r^2}$ copper state[9,10] and the $2p[2p(\text{apex})]$ state of planar (apical) oxygen, which transform by a similar irreducible a_{1g} representation. A study of the two-hole spectrum of a CuO_6 cluster using perturbation theory[11,12] for model parameters determined from CuO x-ray photoemission spectroscopy (XPS) reveals that the two-hole $^3B_{1g}$ level for La_2CuO_4 is 0.7 eV higher than the singlet $^1A_{1g}$ level. This value changes to zero or even becomes negative as a result of small variations in the parameters of the model. All these factors indicate the importance of $d_{3z^2-r^2}$ orbitals for the electronic structure.

Note also that *ab initio* calculations of the electronic structure of CuO_4 and CuO_6 clusters using the self-consistent field method with configurational interaction showed that a reduction in the distance from the apical oxygen leads to stabilization of the $^3B_{1g}$ triplet as the ground two-hole state rather than the $^1A_{1g}$ singlet.[13] The small energy spacing between these states produces changes in the low-energy part of the Fermi quasiparticle spectrum.[14] It was shown in Ref. 15 that strong mixing of singlet and triplet states takes place far from the Γ point.

Here we examine two problems. First, we make a multiband analysis of the validity of the three-band $p-d$ model. It was shown in similar studies[11,12] that between the Zhang–Rice singlet and its corresponding triplet $^3A_{1g}$ there are various two-hole states: $^3B_{1g}$, $^1A_{1g}$, $^1B_{1g}$, and others. Unlike the authors of Refs. 11 and 12, we examine in detail the dependence of these multielectron terms on the model parameters, which can reveal mechanisms for their possible stabilization as ground levels and can identify the range of validity of the three-band model. To this end, we studied the ground state of two holes in a CuO_6 cluster using the exact diagonalization method, we calculated the eigenvalues and eigenvectors as functions of the crystal field parameter $\Delta_d=\varepsilon(d_{3z^2-r^2})-\varepsilon(d_{x^2-y^2})$, the energy difference between the $2p$ orbitals of planar and apical oxygen $\Delta(\text{apex})=\varepsilon(2p)-\varepsilon(2p(\text{apex}))$, and the ratio of the distances between the copper atom and the apical and planar oxygen atoms $d(\text{apex})/d(\text{pl})$. In the limit of large $d(\text{apex})/d(\text{pl})$ and Δ_d values, our model is equivalent to the three-band $p-d$ model, and large singlet-triplet splitting $\Delta\varepsilon_2\geqslant 1$ eV is also observed, which agrees qualitatively with Ref. 3. By varying the values of the parameters, we observe

a reduction in the singlet-triplet splitting. For realistic parameters we find $-0.5<\Delta\varepsilon_2<0.5$. In practice, this implies that there is no good energy separation between the ground and first excited current states. This factor imposes some constraints on the reduction of the multiband model to the single-band Hubbard model or the $t-J$ model.

Second, we consider the influence of singlet-triplet mixing of states by intercluster hopping on the electron dispersion law near the top of the valence band. An intercluster hop is taken into account in perturbation theory by a method[14] wherein the zeroth approximation is the exact diagonalization of the clusters. The results of the calculations showed good agreement with data obtained by angle-resolved photoelectron spectroscopy (ARPES) for the antiferromagnetic dielectric $Sr_2CuO_2Cl_2$ (Ref. 16). In addition, singlet-triplet mixing by hopping indicates that a spin-exciton mechanism of superconductivity is possible.

1. EXACT DIAGONALIZATION OF A CuO_6 CLUSTER

We consider the Hamiltonian of the $2p$ electrons at oxygen and the $3d$ electrons at copper in the hole representation

$$H=H_d+H_p+H_{pd}+H_{pp}, \tag{1}$$

where

$$H_d=\sum_r H_d(\mathbf{r}),$$

$$H_d(\mathbf{r})=\sum_{\lambda\sigma}\left[(\varepsilon_{d\lambda}-\mu)d^+_{\mathbf{r}\lambda\sigma}d_{\mathbf{r}\lambda\sigma}+\frac{1}{2}U_d n^{\sigma}_{\mathbf{r}\lambda}n^{-\sigma}_{\mathbf{r}\lambda}\right]$$
$$+\sum_{\sigma\sigma'}(V_d n^{\sigma}_{\mathbf{r}1}n^{\sigma'}_{\mathbf{r}2}-J_d d^+_{\mathbf{r}1\sigma}d_{\mathbf{r}1\sigma}d^+_{\mathbf{r}2\sigma'}d_{\mathbf{r}2\sigma}),$$

$$H_p=\sum_i H_p(\mathbf{i}),$$

$$H_p(\mathbf{i})=\sum_{\alpha\sigma}\left[(\varepsilon_{p\alpha}-\mu)p^+_{\mathbf{i}\alpha\sigma}p_{\mathbf{i}\alpha\sigma}+\frac{1}{2}U_p n^{\sigma}_{\mathbf{i}\alpha\sigma}n^{-\sigma}_{\mathbf{i}\alpha\sigma}\right]$$
$$+\sum_{\sigma\sigma'}(V_p n^{\sigma}_{\mathbf{i}1}n^{\sigma'}_{\mathbf{i}2}-J_p p^+_{\mathbf{i}1\sigma}p_{\mathbf{i}1\sigma}p^+_{\mathbf{i}2\sigma'}p_{\mathbf{i}2\sigma}),$$

$$H_{pd}=\sum_{\langle\mathbf{i},\mathbf{r}\rangle}H_{pd}(\mathbf{i},\mathbf{r}),$$

$$H_{pd}(\mathbf{i},\mathbf{r})=\sum_{\alpha\lambda\sigma\sigma'}(T_{\lambda\alpha}p^+_{\mathbf{i}\alpha\sigma}d_{\mathbf{r}\lambda\sigma}+V_{\lambda\sigma}n^{\sigma}_{\mathbf{r}\lambda}n^{\sigma'}_{\mathbf{r}\lambda}$$
$$-J_{\alpha\lambda}d^+_{\mathbf{r}\lambda\sigma}d_{\mathbf{r}\lambda\sigma}p^+_{\mathbf{i}\alpha\sigma'}p_{\mathbf{i}\lambda\sigma}),$$

$$H_{pp}=\sum_{\langle\mathbf{i},\mathbf{J}\rangle}\sum_{\alpha\beta\sigma}(t_{\alpha\beta}p^+_{\mathbf{i}\alpha\sigma}p_{\mathbf{j}\beta\sigma}+\text{h.c.}).$$

Here the first two terms describe the intra-atomic energies at a copper (oxygen) site with Hubbard repulsion $U_d(U_p)$, interorbital intra-atomic Coulomb repulsion $V_d(V_p)$, and Hund exchange interaction $J_d(J_p)$. The indices λ and α correspond to different orbitals in the crystal field. The third term in Eq. (1) describes interatomic $p-d$ hopping, Coulomb V_{pd} and exchange J_{pd} interactions. The last term in Eq. (1) corresponds to a $p-p$ hop.

We shall consider the set of $d_{x^2-y^2}(\lambda=1)$ and $d_{3z^2-r^2}(\lambda=2)$ states of copper and p_x, p_y states of oxygen as being the most important to describe the low-energy spectrum of quasiparticles in the CuO_2 layer. We shall then use the following notation and relations between the model parameters: $\delta=\varepsilon(\sigma)-\varepsilon(d_{x^2-y^2})$, $T_{d_{x^2-y^2},\sigma}=T_{pd}$, $T_{d_{3z^2-r^2},\sigma(\text{apex})}=\sqrt{\frac{2}{3}}T_{pd}[d(\text{pl})/d(\text{apex})]^{3.5}$, $V_{x^2-y^2,\sigma[\sigma(\text{apex})]}\approx V_{d_{3z^2-r^2},\sigma[\sigma(\text{apex})]}=V_{pd}$, $J_{x^2-y^2,\sigma[\sigma(\text{apex})]}\approx J_{d_{3z^2-r^2},\sigma[\sigma(\text{apex})]}=J_{pd}$, and $t_{p_x,p_y}=t_{pp}$. The index $\sigma[\sigma(\text{apex})]$ refers to symmetrized combinations of $2p$ and $2p(\text{apex})$ oxygen orbitals which form σ bonds with $3d$ orbitals of copper. The electrically neutral compound $La^{3+}_{2-x}Sr^{2+}_x(CuO_4)^{-6+x}$ corresponds to $n_h=1+x$ holes per formula unit. Thus, for $x=0$ we have one hole per cluster and for $x\neq 0$, two-hole states make some contribution.

Exact diagonalization of the final clusters is a powerful method of studying systems with strong electron correlations and it is desirable to take a fairly large cluster to calculate the thermodynamic averages per site and the correlation functions.[17] We shall confine ourselves to the smallest possible CuO_2, CuO_4, and CuO_6 clusters since their exact diagonalization is required only to construct a local basis which is then used for approximate calculations of the electron Green functions of an infinite CuO_2 lattice. Diagonalization of the CuO_6 cluster is performed separately in different sectors of Hilbert space with the hole numbers $n=0,1,2$. The vacuum sector $n=0$ corresponds to the $3d^{10}$ configuration of copper and the $2p^6$ configuration of oxygen. In the one-hole sector, the eigenvectors are the molecular orbitals of oxygen hybridized with the $3d$ states of copper. All the basis states in the two-hole sector are different combinations of configurations of the two holes over oxygen and copper states. In our case, with one orbital per oxygen site and two orbitals per copper site, we have 28 triplet states: six $^3B_{1g}$, one $^3A_{2g}$, ten ^3E_u, four $^3A_{1g}$, two $^3B_{2u}$, three $^3A_{2u}$, two ^3E_g, and 36 singlet states: ten ^1E_u, eleven $^1A_{1g}$, seven $^1B_{1g}$, one $^1B_{2g}$, two $^1B_{2u}$, three $^1A_{2u}$, and two ^1E_g per cluster. In the following calculations only the three parameters indicated above were varied and the others were set as follows: $\delta=3.5$ eV, $T_{pd}=1.4$ eV, $V_d=9$ eV, $V_p=7$ eV, $J_d=1$ eV, $J_p=0.6$ eV, $V_{pd}=0.5$ eV, and $J_{pd}=0.2$ eV.

Figures 1a–1c give the lowest energies of the competing singlet $^1A_{1g}(i)$ and triplet $^3B_{1g}(i)$ states ($i=0$ for the ground state of this symmetry and $i=1$ for the excited state) as a function of the parameters $d(\text{apex})/d(\text{pl})$, Δ_d, and $\Delta(\text{apex})$. The fraction of states equivalent to the Zhang–Rice singlet is as high as 80% in $^1A_{1g}(0)$ and does not depend on the values of the above parameters. Thus, it is quite logical to identify this singlet as a Zhang–Rice singlet.[3] The remaining 20% are assigned to $^1A_{1g}$ symmetrized states of the $(d_{x^2-y^2})^2$ and $(2p)^2$ configurations. The contributions of the atomic orbitals to the other three states $^1A_{1g}(1)$ and $^3B_{1g}(i)$ vary substantially with the values of the parameters, so they cannot be identified with any specific molecular orbital having the same symmetry.

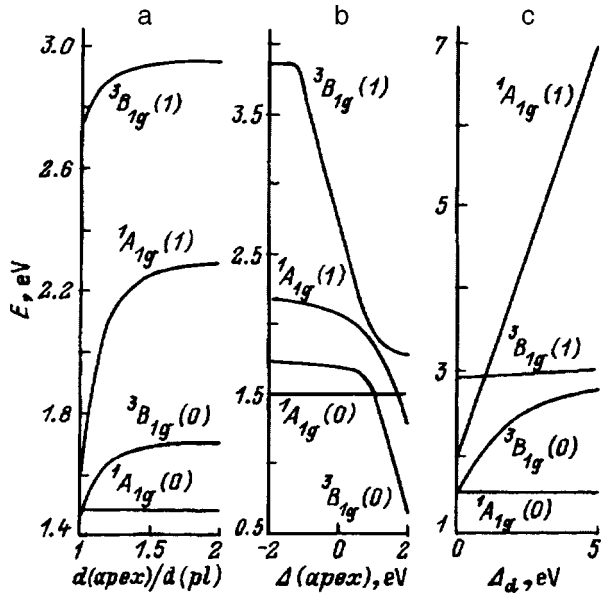

FIG. 1. Energies of the ${}^3B_{1g}(i)$ and ${}^1A_{1g}(i)$ terms as a function of the ratio of the distance between the copper atom and the apical and planar oxygen $d(\text{apex})/d(\text{pl})$ [$\Delta_d=0.3$ eV, $\Delta(\text{apex})=0.7$ eV] (a), the energy difference between the $2p$ orbitals of planar and apical oxygen $\Delta(\text{apex})=\varepsilon(2p)-\varepsilon[2p(\text{apex})]$($d(\text{apex})/d(\mathbf{pl})$]$=1.2$, $\Delta_d=0.3$ eV) (b), and the crystal field parameter $\Delta_d=\varepsilon(d_{3z^2-r^2})-\varepsilon(d_{x^2-y^2})$ [$d(\text{apex})/d(\text{pl})=1.2$, $\Delta(\text{apex})=0.7$ eV] (c).

The dependence of the level energy on $d(\text{apex})/d(\text{pl})$, plotted in Fig. 1a shows that for $d(\text{apex})/d(\text{pl})>1.05$ the Zhang–Rice singlet is the ground state of our cluster, which agrees well with Ref. 12, where the excited states ${}^1A_{1g}(1)$ and ${}^3B_{1g}(0)$ only extend by approximately ~ 0.2 eV above it for $d(\text{apex})/d(\text{pl})>1.3$. For $d(\text{apex})/d(\text{pl})<1.05$ the triplet ${}^3B_{1g}(0)$ becomes the ground two-hole state with the contribution made to it by the symmetrized configuration $d_{x^2-y^2}2p(\text{apex})$ increased from 10% [$d(\text{apex})/d(\text{pl})=2$] to 40% [$d(\text{apex})/d(\text{pl})=1$]. The contribution of the Hund state associated with the symmetrized configuration $d_{x^2-y^2}d_{3z^2-r^2}$ increases negligibly (to 10%).

As the energy of the $2p$(apex) orbitals of apical oxygen decreases, a crossover of the excited states and the Zhang–Rice singlet is observed (Fig. 1b). In the calculations the crossover point with the ${}^3B_{1g}$ level occurs at $\Delta(\text{apex})=1.2$ eV, which differs slightly from the 1.7 eV obtained in Ref. 11 and is attributable to differences in the calculation methods. As well as the tendency to crossover, it is observed that the fraction of the $d_{3x^2-r^2}2p(\text{apex})$ symmetrized configuration in ${}^1A_{1g}(1)$ increases from 5% [$\Delta(\text{apex})=0$] to 50% [$\Delta(\text{apex})=2$] and the fraction of the $d_{x^2-y^2}2p(\text{apex})$-symmetrized configuration in ${}^3B_{1g}(0)$ increases from 3% to 90%. It is important to note that this is only the first of the mechanisms for stabilization of the ${}^3B_{1g}(0)$ state as the ground state and, as we can see, the $d_{x^2-y^2}2p(\text{apex})$ symmetrized configuration makes a major contribution. An increase in this contribution is observed both for this dependence and for that plotted in Fig. 1a. In both cases, we are dealing with the same stabilization mechanism. However, whereas in the first case this stabilization is associated with a decrease in the energy of the $2p$(apex) orbitals, in the second case, it is associated with the dependence of the corresponding hopping integral on the distance from the apical oxygen. As in Ref. 18, a decrease in the energy of the $2p$(apex) orbitals effectively increases their contribution to the ground two-hole state.

The ${}^3B_{1g}(0)$ and ${}^1A_{1g}(0)$ states belong to different irreducible representations and nothing prevents their crossover, but the absence of effective repulsion of the ${}^1A_{1g}(0)$-and ${}^1A_{1g}(1)$ levels and the possible crossover of these levels appear to be a characteristic feature of our representation of the D_{4h} group. This feature is evidently closely related to the isolation of the Zhang–Rice singlet and its inability to hybridize with any states other than those of the $(d_{x^2-y^2})^2$- and $(2p)^2$ symmetrized configurations in the absence of interactions other than H_{pd}.

A decrease in the parameter Δ_d (Fig. 1c) leads to an appreciable increase in the fraction of the Hund state and ultimately leads to convergence of the ground ${}^1A_{1g}(0)$ Zhang–Rice singlet and the excited ${}^3B_{1g}(0)$ state, particularly in the range of real values $\Delta_d \leqslant 1$ eV. This is the second mechanism for stabilization of the ${}^3B_{1g}$ state as the ground state. Since this mechanism involves increased Hund interaction with an increasing contribution of the $d_{x^2-y^2}d_{3z^2-r^2}$ configuration, it is more efficient as the energy of the $2p$ orbitals of planar oxygen increases and the energy of the $d_{3z^2-r^2}$ orbitals decrease. In this method of stabilizing the ${}^3B_{1g}$ state, it is observed that the fraction of $2p$(apex) states decreases whereas the fraction of the Hund configuration $d_{x^2-y^2}d_{3z^2-r^2}$ via which filling of the $d_{3z^2-r^2}$ orbitals could be observed, remains small (around 10% for $\Delta_d=0$). A similar conclusion as to the stabilizing role of the Hund exchange interaction was reached in *ab initio* calculations.[13] It is interesting to note that a substantial decrease in the energy of the ${}^1A_{1g}(1)$ state with decreasing parameter Δ_d is associated with a negligible increase in the fraction of the $(d_{3z^2-r^2})^2$ configuration (from 5% to 15% for $\Delta_d=0$) with the major contribution being made by the $d_{3z^2-r^2}2p$ symmetrized configuration, remaining unchanged at 70%. In the ''dangerous'' vicinity of the ground state, we also observe the ${}^3B_{1g}(1)$ state which shows similar tendencies to converge as the parameters $d(\text{apex})/d(\text{pl})$, Δ_d, and the energy of the $2p$(apex) orbitals of apical oxygen decrease. However, because of the cluster symmetry, this level and the ${}^1B_{1g}(0)$ level repel and do not come closer than 1 eV to the ${}^1A_{1g}(0)$ level of the Zhang–Rice singlet.

2. DISCUSSION OF THE RESULTS OF THE EXACT DIAGONALIZATION

These results of the exact diagonalization of a cluster can be used to construct a local multielectron basis of states, between which hops in an infinite lattice lead to band formation. To discuss the reducibility of the p–d model to the single-band Hubbard model, we compare the more realistic local basis shown in Fig. 2a with the local basis of the Hubbard model (Fig. 2b), which consists of four states: the vacuum state $|0\rangle$, two single-particle states $|+\rangle=a_\uparrow^+|0\rangle$ and $|-\rangle=a_\downarrow^+|0\rangle$, and the two-particle state $|2\rangle=a_\uparrow^+a_\downarrow^+|0\rangle$. It can be seen from a comparison of Figs. 2a and 2b that in the energy range $E \ll \Delta\varepsilon_1$ and $E \ll \Delta\varepsilon_2$, where $\Delta\varepsilon_1$ and $\Delta\varepsilon_2$ are

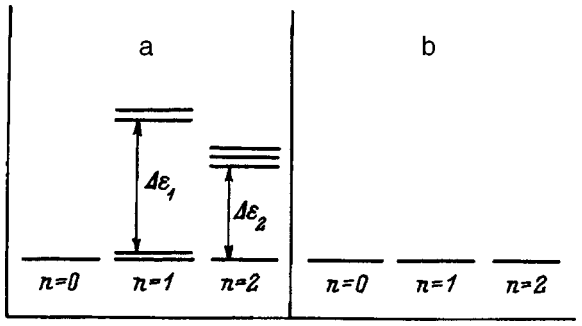

FIG. 2. Local bases of the multiband $p-d$ model (a) and the single-band Hubbard model (b). For the multiband $p-d$ model only the lowest excited terms in the single-particle and two-particle sectors of Hilbert space are shown.

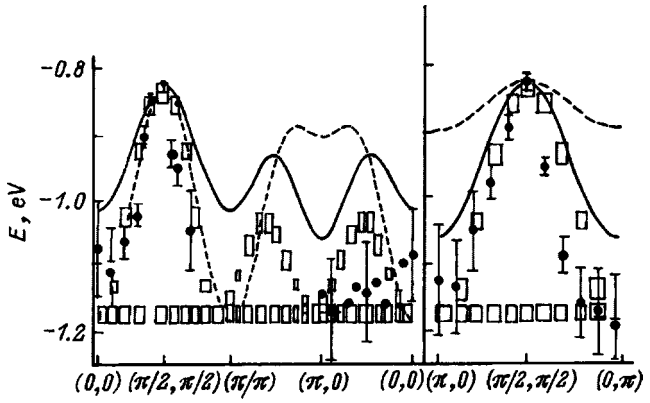

FIG. 3. Quasiparticle spectrum in $Sr_2CuO_2Cl_2$. The circles gives the ARPES data,[16] the dashed and solid curves give the results of calculations for the $t-J$ and $t-t'-J$ models.[20] The rectangles give the results of calculations using the multiband $p-d$ model.[23]

the energies of the local excitations (excitons) in the single-particle and two-particle sectors of Hilbert space, the difference between the bases of the $p-d$ model and the Hubbard model can be neglected and, in this sense, it is possible to make a low-energy reduction of the $p-d$ model to the single-band Hubbard model. The single-particle exciton energy $\Delta\varepsilon_1$ is determined by the excitations in the crystal field $d_{x^2-y^2}\rightarrow d_{3z^2-r^2}$ with the energy Δ_d; for typical parameters in copper oxides $\Delta\varepsilon_1 \geqslant 1$ eV. The energy of a two-particle exciton $\Delta\varepsilon_2$, associated with a hole-current carrier, depends very much on the choice of model. For instance, in the three-band $p-d$ model we find $\Delta\varepsilon_2 = 2-4$ eV and the excited triplet state can be neglected here. However, it can be seen from Figs. 1a and 1b that this situation changes in the more realistic multiband $p-d$ model where $\Delta\varepsilon_2 = E[^3B_{1g}(0)] - E[^1A_{1g}(0)]$ may be fairly small or even negative. For small $\Delta\varepsilon_2$, the range of possible reduction to the single-band model $E \ll \Delta\varepsilon_2$ becomes quite small, and for $\Delta\varepsilon_2 \leqslant 0$ no such range exists. Since the parameters on which $\Delta\varepsilon_2$ depends (the crystal field and the interatomic spacing) differ for different copper oxides and depend on the level of doping, it is possible to have a situation where singlet-triplet crossover takes place as the composition varies. This crossover was obtained in *ab initio* calculations[13] for $La_{2-x}Sr_xCuO_4$ with $x \approx 0.1$; for the superconducting phase in this system the lower two-hole term is a triplet. In another model copper oxide $Sr_2CuO_2Cl_2$, an octahedron of nearest neighbors incorporates two chlorine ions along the c axis; this increases the ionicity of the Cu–Cl bond compared with Cu–O and reduces the fraction of covalent mixing of chlorine p states in the a_{1g} molecular orbital which, according to Ref. 19, is less than 1% away from the top of the valence band. It has been noted that the occupancy of the Cl p states may vary widely, without influencing the low singlet-triplet splitting energy $\Delta\varepsilon_2$. In our opinion, the smallness of $\Delta\varepsilon_2$ shows up when the dispersion law in $Sr_2CuO_2Cl_2$ measured experimentally by the ARPES method[16] is compared with that calculated using the $t-J$ model.[20] Near the top of the valence band and in the energy range $E < 0.1$ eV, the agreement is fairly good but the differences increase for states deeper in the valence band (Fig. 3).

To calculate the dispersion law, we consider an infinite CuO_2 lattice with a unit cell in the form of an infinite cluster, for which an exact diagonalization of the initial Hamiltonian (1) has been performed. The results of the calculations are presented below.

3. DISPERSION OF ELECTRONS NEAR THE TOP OF THE VALENCE BAND

The following generalization of the strong coupling model[14] is proposed to allow for the strong electron correlations within the unit cell in the band calculations: the lattice is divided into nonintersecting cells (clusters), the intracell part of the Hamiltonian is exactly diagonalized, and the eigenvectors $|p\rangle = |n,\gamma\rangle$ and terms $E_{n,\gamma}$ are found for a cluster with n particles, where the index γ numbers all the other quantum numbers. The next stage involves constructing the Hubbard operators for this cell $\mathbf{f}$: $X_{\mathbf{f}}^{pp'} = |n,\gamma\rangle\langle n',\gamma'|$, in whose representation the intercell component of the Hamiltonian may be written exactly as a generalized multilevel Hubbard model. As a result, the initial Hamiltonian (1) is written exactly in the form $H = H_0 + H_1$,

$$H_0 = 7\sum_{\mathbf{f}n\gamma}(E_{n\gamma} - n\mu)X_{\mathbf{f}}^{\gamma\gamma},$$

$$H_1 = \sum_{(\mathbf{fg})}\sum_{\gamma\gamma'\Gamma\Gamma'}\Lambda_{\Gamma\Gamma'}^{\gamma\gamma'}(\mathbf{f},\mathbf{g})X_{\mathbf{f}}^{\gamma\gamma'}X_{\mathbf{g}}^{\Gamma'\Gamma}. \qquad (2)$$

The spectrum of single-particle hole excitations H_0 consists of a set of dispersion-free levels (''resonances'') $\Omega_m = E_{n+1,\gamma_1} - E_{n,\gamma_2}$, where the index m is the number of possible Fermi excitations between terms $|n+1,\gamma_1\rangle \rightarrow |n,\gamma_2\rangle$. Intercluster hops described by H_1 are taken into account in perturbation theory using the simplest ''Hubbard I'' approximation.[21] In the double-sublattice structure of the CuO_2 layer the dispersion equation has the form

$$\det\{\delta_{nm}\delta_{AB}(\omega - \Omega_m) - F_m\Lambda_{AB}^{mn}(\mathbf{k})\} = 0. \qquad (3)$$

Here A and B are the sublattice indices, $\Lambda(\mathbf{k})$ is the Fourier transform of the intercell interactions, and $F_m = \langle X_{\mathbf{f}}^{n+1,\gamma_1,n+1,\gamma_1}\rangle + \langle X_{\mathbf{f}}^{n,\gamma_2,n,\gamma_2}\rangle$ is the filling factor, which depends on the temperature and hole concentration.

The cell can be divided by various methods. The simplest case of a CuO_2 cell was used to calculate the hole spectrum in the paramagnetic[22] and antiferromagnetic phases.[23] However, the more symmetric clusters, CuO_4 or CuO_6, are more convenient because they correctly reflect the local symmetry of copper, but they cannot cover the entire lattice with nonintersecting clusters. Each in-plane oxygen ion belongs directly to two clusters and nonorthogonality of the Hubbard operators arises in neighboring cells. To solve this problem for the three-band $p-d$ model, it was suggested in Refs. 24 and 25 that Wannier functions should be constructed for each cell and then used to determine the X operators. After this procedure, the results of both approaches are almost the same. We shall subsequently use a simpler division into O–Cu–O clusters.

The results of the exact diagonalization of the CuO_6 or CuO_4Cl_2 clusters described above indicate that the singlet-triplet splitting $\Delta\varepsilon_2$ is small ($\Delta\varepsilon_2 < 0.5$ eV), and this will be used subsequently.

For the local basis shown in Fig. 2a, the top of the valence band is determined by three Fermi modes

$$X_\sigma^{\alpha_0} = |1,-\sigma\rangle\langle 2,0|, \quad X_\sigma^{\alpha_1} = |1,-\sigma\rangle\langle 2,1,0|,$$

$$X_\sigma^{\alpha_2} = |1,-\sigma\rangle\langle 2,1,2\sigma|, \tag{4}$$

where $|1,\sigma\rangle$ is the lowest molecular orbital in the single-hole sector, $|2,0\rangle$ is the Zhang–Rice singlet, and $|2,1,M\rangle$, $M=0,\pm 1$ are two-hole triplets. We shall adopt the Zaĭtsev notation[26] in which the initial and final states are replaced by a single root vector $X^{pq} \to X^{\alpha}$. The excitation energies (4) in the zeroth approximation are given by

$$\Omega_0 = E(2,0) - E(1,-\sigma), \quad \Omega_1 = E(2,1,0) - E(1,-\sigma),$$

$$\Omega_2 = E(2,1,2\sigma) - E(1,-\sigma).$$

We use a double-sublattice Fourier transformation to describe the antiferromagnetic phase. Assuming that $X_{\mathbf{k}}^{\alpha}$ and $Y_{\mathbf{k}}^{\alpha}$ denote the Fourier transforms of the Hubbard operator in sublattices 1 and 2, the Hamiltonian of an intercluster hop allowing for the Fermi modes (3) has the form

$$H_{pd} = \tilde{T}_{pd} \sum_{\mathbf{k}\sigma} \gamma(k) X_{\mathbf{k}\sigma}^{+\alpha_0} Y_{\mathbf{k}\sigma}^{\alpha_0} + 2i\sigma(\sin(k_x a) X_{\mathbf{k}\sigma}^{+\alpha_1} Y_{\mathbf{k}\sigma}^{\alpha_0} + \sin(k_y a) X_{\mathbf{k}\sigma}^{+\alpha_0} Y_{\mathbf{k}\sigma}^{\alpha_1}) + 2i\sigma\sqrt{2}(\sin(k_x a) X_{\mathbf{k}\sigma}^{+\alpha_2} Y_{\mathbf{k}\sigma}^{\alpha_0} + \sin(k_y a) X_{\mathbf{k}\sigma}^{+\alpha_0} Y_{\mathbf{k}\sigma}^{\alpha_2}) + \text{h.c.}, \tag{5}$$

where the following notation is introduced

$$\gamma(\mathbf{k}) = \cos(k_x a) + \cos(k_y a),$$

$$\tilde{T}_{pd} = -T_{pd}(uv_0 + u_0 v)vv_0/2,$$

$$u^2 = (1+\delta nu)/2, \quad v^2 = 1-u^2,$$

$$\delta = \varepsilon_p - \varepsilon_d, \quad \nu^2 = \delta^2 + 8T_{pd}^2,$$

$$u_0^2 = (1+\delta_0/\nu_0)/2, \quad v_0^2 = 1-u_0^2,$$

$$\delta_0 = \delta - V_{pd}, \quad v_0^2 = \delta_0^2 + 8T_{pd}^2.$$

For typical values of the parameters a renormalized hop is $\tilde{T}_{pd} \approx 0.1$ eV. The first term in Eq. (5) describes a quasiparticle (hole) hop with the excitation of a Zhang–Rice singlet while the second and third terms describe a hole hop with singlet-triplet mixing. The mixing vanishes at the Γ point. Details of calculations of the band structure in the antiferromagnetic phase are given in Ref. 23, and we used this procedure to calculate the hole dispersion law for undoped $Sr_2CuO_2Cl_2$ (Fig. 3). A comparison between our calculations and the ARPES data shows far better agreement than that obtained for calculations using the $t-J$ model.[20] Since the $t-J$ model can only be obtained with a local basis, as in Fig. 2b, where there are no triplet states and singlet-triplet mixing far from the Γ point, we conclude that allowance for the triplet states of two holes and its mixing with the Zhang-Rice singlet are important to describe the hole spectrum in the narrow energy range 0.1–0.5 eV below the top of the valence band, i.e., where high-temperature superconductivity is clearly an important effect.

4. INTERACTION OF HOLES WITH SPIN EXCITONS

Singlet-triplet mixing described by the last two terms in Eq. (5) may result in an additional mechanism of superconducting pairing. These terms resemble interband transitions which may well be a source of pairing.[27] These components of H_{pd} may also be explicitly written as Fermion-boson interaction using Hubbard operator algebra, whereby we have

$$X_{\mathbf{i}}^{|2,1,0\rangle\langle 1,-\sigma|} = X_{\mathbf{i}}^{|2,1,0\langle 2,0|} X_{\mathbf{i}}^{|2,0\langle 1,-\sigma|}. \tag{6}$$

This implies that the addition of a hole to the initial state $|1,-\sigma\rangle$ with the formation of a final triplet state (the process $|1,-\sigma\rangle \to |2,1,0\rangle$) is equivalent to the generation of a hole in the process $|1,-\sigma\rangle \to |2,0\rangle$ with the final state being a Zhang–Rice singlet, and the simultaneous generation of a spin exciton $|2,0\rangle \to |2,1,0\rangle$. It has been shown that the spin splitting energy $\Delta\varepsilon_2$ is small. Other exciton excitations from the singlet to higher two-hole terms are possible from the point of view of Hubbard operator algebra but are less effective because of the higher energy.

At the same time, the second term in Eq. (5) determines the exchange of spin excitons with $S_z = 0$ without hole spin flipping, which may lead to pairing, and the third term describes the emission and absorption of a spin exciton with $S_z = 1$, i.e., with spin flipping. This may give rise to pairing as in paramagnon exchange, and may also cause pair destruction as a result of hole spin flipping.

Note that this pairing mechanism may occur only in systems doped with holes with nonzero filling of two-hole states.

A multiband $p-d$ model allowing for the $d_{3z^2-r^2}$ orbitals of copper as well as $d_{x^2-y^2}$ orbitals was considered in Ref. 18, where it was shown that an increase in the population of the a_{1g} single-electron molecular orbitals reduces the population of the b_{1g} states and therefore lowers T_c. From our point of view (Figs. 1a and 1b), a substantial increase in the fraction of a_{1g} single-electron orbitals is clear evidence that singlet-triplet crossover may take place in these compounds. The need to allow for the $d_{3z^2-r^2}$ states to obtain an

adequate description of the low-energy part of the electron spectrum of $Sr_2CuO_2Cl_2$ is also noted in Ref. 28 using *ab initio* band calculations and comparing these with the strong coupling model.

We consider it meaningless to write the equations from the Bardeen–Cooper–Schrieffer theory in which the phonon parameters would be replaced by spin-exciton ones, since other mechanisms of superconductivity are also known in this model of the electronic structure: kinematic exchange,[29] caused by the first term in Eq. (5), exchange of excitons-crystal-lattice excitations, and paramagnon exchange (see a recent review presented in Ref. 30). In this study we wish to stress that the possibility of spin-exciton pairing in *p*-type copper oxides is caused by the specific characteristics of their electronic structure, specifically the proximity of singlet and triplet current two-hole states.

This work was carried out under the State Program ''Superconductivity'' (Project No. 93237) and was also supported by the Krasnoyarsk Region Science Foundation (Project No. 5F0009).

[1] V. J. Emery, Phys. Rev. Lett. **58**, 2794 (1987).
[2] C. M. Varma, S. Schmitt-Rink, and A. E. Ruchenstein, Solid State Commun. **62**, 681 (1987).
[3] F. C. Zhang and T. M. Rice, Phys. Rev. B **37**, 3759 (1988).
[4] E. Dagotto, Rev. Mod. Phys. **66**, 763 (1994).
[5] A. Kampf, Phys. Rep. **249**, 219 (1994).
[6] W. Brenig, Phys. Rep. **251**, 153 (1995).
[7] A. Biancomi *et al.*, Physica C **162–164**, 209 (1990).
[8] Y. Romberg *et al.*, Phys. Rev. B **41**, 2609 (1990).
[9] Yu. Gaididev and V. M. Loktev, Phys. Status Solidi B **147**, 307 (1988).
[10] W. Weber, Z. Phys. B **70**, 323 (1988).
[11] H. Eskes and G. A. Sawatzky, Phys. Rev. B **44**, 9556 (1991).
[12] H. Eskes, L. H. Tjeng, and G. A. Sawatzky, Phys. Rev. B **41**, 288 (1990).
[13] H. Kamimura and M. Eto, J. Phys. Soc. Jpn. **59**, 3053 (1990).
[14] S. G. Ovchinnikov and I. S. Sandalov, Physica C **198**, 607 (1989).
[15] V. J. Emery and G. Reiter, Phys. Rev. B **38**, 11 938 (1988); **41**, 7247 (1990).
[16] B. O. Wells *et al.*, Phys. Rev. Lett. **74**, 964 (1995).
[17] V. F. Elesin and V. A. Kashurnikov, Zh. Éksp. Teor. Fiz. **106**, 1773 (1994) [JETP **79**, 961 (1994)].
[18] M. Grilli, C. Castellani, and C. Di Castro, Phys. Rev. B **42**, 6233 (1990).
[19] A. Fujimori, Y. Tokura *et al.*, Phys. Rev. B **40**, 7303 (1989).
[20] A. Nazarenko, K. J. E. Vos, S. Haas *et al.*, J. Supercond. **8**, 671 (1995).
[21] J. C. Hubbard, Proc. Phys. Soc. London, Sect. A **276**, 238 (1963).
[22] S. G. Ovchinnikov, Zh. Eksp. Teor. Fiz. **102**, 127 (1992) [Sov. Phys. JETP **75**, 67 (1992)].
[23] S. G. Ovchinnikov, Zh. Éksp. Teor. Fiz. **107**, 726 (1995) [JETP **80**, 451 (1995)].
[24] S. V. Lovtsov and V. Yu. Yushankhai, Physica C **179**, 159 (1991).
[25] J. H. Jefferson, H. Eskes, and L. F. Feiner, Phys. Rev. B **45**, 7959 (1992).
[26] R. O. Zaĭtsev, Zh. Éksp. Teor. Fiz. **68**, 207 (1975) [Sov. Phys. JETP **41**, 100 (1975)].
[27] B. T. Geĭlikman, Usp. Fiz. Nauk. **109**, 65 (1973) [Sov. Phys. Usp. **16**, 17 (1973)].
[28] L. F. Mattheiss, Phys. Rev. B **42**, 354 (1990).
[29] R. O. Zaĭtsev and V. A. Ivanov, Fiz. Tverd. Tela (Leningrad) **29**, 2554 (1987) [Sov. Phys. Solid State **29**, 1475 (1987)].
[30] V. N. Loktev, Fiz. Nizk. Temp. **22**, 3 (1996) [Low Temp. Phys. **22**, 1 (1996)].

Translated by R. M. Durham

Response of a YBaCuO/MgO bolometer structure at high levels of laser excitation. Nonlinear model and experiment

A. Yu. Klokov, T. I. Galkina, and A. F. Plotnikov

P. N. Lebedev Physics Institute, Russian Academy of Sciences, 117924 Moscow, Russia
(Submitted July 11, 1997)
Fiz. Tverd. Tela (St. Petersburg) **40**, 191–194 (February 1998)

A nonlinear model is developed for the photoresponse of a bolometric structure taking into account the temperature dependences of the thermal constants of the YBaCuO/MgO structure and its boundary thermal resistance. The model also allows for the specific form of the current-voltage characteristic of YBaCuO and the heat release from the transport current flow. A comparison between the experimental data and the model showed that the nonlinear thermal model accurately describes the temporal characteristics of the photoresponse. © *1998 American Institute of Physics.* [S1063-7834(98)00302-5]

The phonon subsystem in Si/Ge heterostructures and superlattices in the temperature range between liquid helium and liquid nitrogen (and above) can be investigated using the thermal pulse method as described in Ref. 1, where the energy dissipation process in structures containing a GaAs/AlGaAs double barrier was studied by detecting nonequilibrium acoustic phonons. A high-temperature superconducting bolometer[2,3] is a natural choice as an acoustic phonon detector in this temperature range (4–90 K) and is undoubtedly of current interest.

However, for an accurate interpretation of the experimental data we require information on the temporal characteristics of such a bolometer, i.e., information on how accurately the bolometer can follow changes in the nonequilibrium phonon flux. In principle, this information can be obtained by investigating the temporal characteristics of the bolometer response to optical irradiation (and therefore heating) by a laser pulse, i.e., by measuring the photoresponse. However, there is some indication that in the region where the superconducting transition begins, the photoresponse is not only attributable to changes in the bolometer temperature (as a result of absorption of laser radiation) but is also (preferentially) caused by direct destruction of Cooper pairs by the incident radiation and thus by changes in the quasiparticle concentration.[4] In this case, the temporal characteristics of the photoresponse do not reflect the dynamics of the change in bolometer temperature and therefore cannot indicate its response time in the ''bolometer'' regime and thus its suitability for the detection of nonequilibrium acoustic phonons.

We need to investigate the photoresponse characteristics of a high-temperature superconducting bolometer and thus determine its response time in the bolometer regime, by comparing the experimentally measured photoresponse with that calculated using the nonlinear thermal model. An exceedingly thorough analysis of experimental data on the response to laser radiation was described in Ref. 5. Note that any attempt to model the thermal response requires quantitative data on the thermal contact between the film and the substrate. Such information is not generally available.

According to the acoustic mismatch model,[6] the heat flux across the boundary of two media is given by

$$W = B(T_0^4 - T_1^4), \tag{1}$$

where $T_{0,1}$ are the temperatures in media 0 and 1 at the interface, respectively, and B is a constant which depends on the properties of the adjacent media (the densities and velocities of sound).[6]

For small heat fluxes this relation is linearized

$$W = (T_0 - T_1)/R_{Bd}, \tag{2}$$

where $R_{Bd} = (4BT^3)^{-1}$ is the boundary thermal resistance.

The authors of Ref. 5 had no information on the boundary thermal resistance in a YBaCuO/MgO structure and therefore when modeling this using acoustic mismatch theory, took the value for a Rh:Fe/sapphire interface.[7] as the constant B in Eq. (1). The authors of Ref. 5 also neglected the heat released in the bolometer film from the current flow as well as the specific form of the YBaCuO current-voltage characteristic. This last factor may significantly alter the temporal characteristics of the bolometer response calculated near the superconducting transition.

We describe a nonlinear mathematical model of the response which does not have these shortcomings. The results of a numerical simulation of the photoresponse of a YBaCuO/MgO structure are compared with the experimental data. The boundary thermal resistance R_{Bd} used in the calculations was determined for this particular structure using a procedure developed in Ref. 8.

1. EXPERIMENTAL METHOD

A meander YBaCuO/MgO bolometric structure was prepared as in Ref. 9. The structure measured 3×4 mm, the ribbon width was 0.15 mm, and the YBaCuO film thickness 350 nm. Figure 1 gives the results of measuring a family of curves $R(T)$ for various bolometer currents which were used to determine the current-voltage characteristic of the YBaCuO film. The superconducting transition temperature T_c varied between $\simeq$86 and $\simeq$85 K, with the transition width $\Delta T \simeq 0.8$ K. The extremely high (for YBaCuO) temperature T_c and the narrow transition width ΔT, combined with the good stability of the parameters (no appreciable changes in T_c and ΔT were observed over a year) evidenced the high quality of the YBaCuO films.

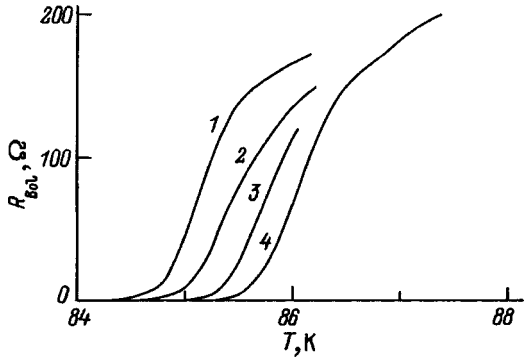

FIG. 1. Resistance of a YBaCuO bolometer R_{Bol} versus temperature for various transport currents through the bolometer: I_{Bol} (mA): *1*—10, *2*—5, *3*—1, and *4*—0.1.

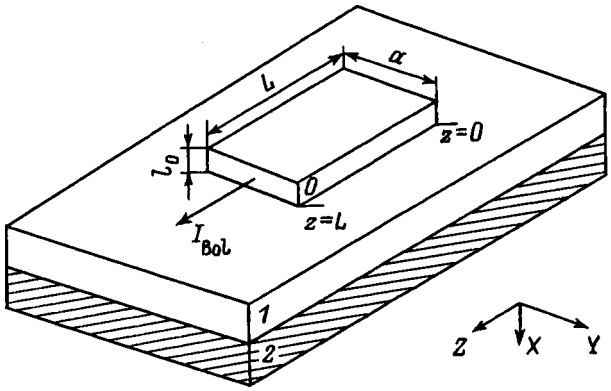

FIG. 3. Structure under study: *0*—YBaCuO film, *1*—MgO substrate, and *2*—cryostat cold sink at temperature T_B.

The source of photoexcitation was an LGI-21 nitrogen laser with a pulse length of $\simeq 10$ ns. The photoresponse was recorded with a V9-5 sampling voltage converter. Figure 2 gives results of measurements of the photoresponse near the beginning ($R_{\mathrm{Bol}}=0.015\ \Omega$, curve *1*) and middle ($R_{\mathrm{Bol}}=80\ \Omega$, curve *2*) of the superconducting to normal transition. The laser radiation flux was $P_0=5000$ W/cm^2 and the bolometer current $I_{\mathrm{Bol}}=10$ mA.

2. MATHEMATICAL MODEL

The structure under study is shown schematically in Fig. 3. The geometric and thermophysical parameters for the YBaCuO film and substrate are denoted by the indices 0 and 1, respectively. A current I_{Bol} flows along the YBaCuO film, creating a potential difference U between the $z=0$ and $z=L$ planes.

We shall assume that the current distribution in the film can be described by the function $J(U,T)$ (the current density, which depends on the voltage U and temperature T) so that

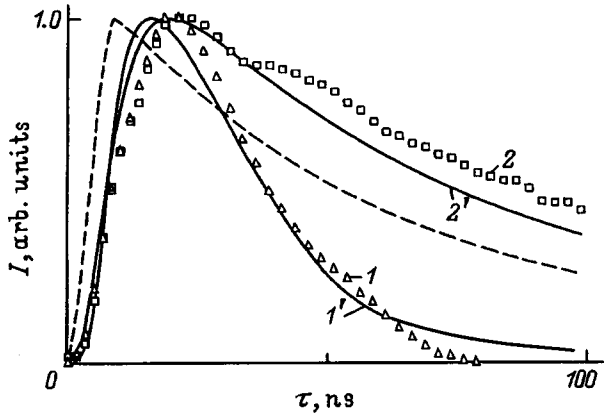

FIG. 2. Photoresponse I of YBaCuO bolometer to pulsed laser excitation: *1*—at the beginning of the transition $R_{\mathrm{Bol}}=0.015\ \Omega$ ($T_B=84.5$ K), *2*—at the center of the transition $R_{\mathrm{Bol}}=80\ \Omega$ ($T_B=85.1$ K); $P_0=5000$ W/cm^2. *1′*, *2′*—calculated values. For comparison the dashed curve gives the time dependence of the average overheating of the bolometer film (this is the same as the photoresponse at low levels of excitation), calculated at the center of the superconducting transition ($R_{\mathrm{Bol}}=80\ \Omega$, $T_B=85.1$ K).

$$a\int_0^{l_0} J(U,T)\,dx = I_{\mathrm{Bol}}. \tag{3}$$

This is a fairly safe assumption since it is known, for instance, that the current in granular films does not flow over the entire cross section but along a finite number of channels distributed randomly in the film (percolation conduction).[10] Nevertheless, we shall use this model representation, assuming that, in good-quality epitaxial films (of fairly large cross section), percolation effects should be very weak. Assuming that the absorption of incident radiation in the YBaCuO film obeys the Bouger–Lambert law [i.e., $\simeq 1-\exp(-\gamma x)$, where γ is the absorption constant], we write the heat conduction equations for the film and the substrate

$$\rho_0 c_0(T_0)\,\frac{\partial T_0}{\partial t} = \frac{\partial}{\partial x}\left(\varkappa_0(T_0)\,\frac{\partial T_0}{\partial x}\right) + \gamma\exp(-\gamma x)P_0(t) + Q, \tag{4}$$

$$\rho_1 c_1(T_1)\,\frac{\partial T_1}{\partial t} = \frac{\partial}{\partial x}\left(\varkappa_1(T_1)\,\frac{\partial T_1}{\partial x}\right), \tag{5}$$

$$Q = \frac{J(U(t),T)U(t)}{L}, \tag{6}$$

where $P_0(t)$ is the incident radiation flux, $U(t)$ is the potential difference between the $z=0$ and $z=L$ planes (Fig. 3), i.e., the response of the bolometric structure determined from condition (3), and $\rho_{0,1}$, $c_{0,1}$, and $\varkappa_{0,1}$ are the density, specific heat, and thermal conductivity of the film and substrate, respectively.

The boundary conditions have the form

$$\frac{\partial T_0}{\partial x}\Big|_{x=0} = 0, \tag{7}$$

$$-\varkappa_0(T_0)\,\frac{\partial T_0}{\partial x}\Big|_{x=l_0} - \varkappa_1(T_1)\,\frac{\partial T_1}{\partial x}\Big|_{x=0}, \tag{8}$$

$$-\varkappa_1(T_1)\,\frac{\partial T_1}{\partial x}\Big|_{x=0} = \frac{1}{4T_B^3 R_{Bd}}\left(T_0^4|_{x=l_0} - T_1^4|_{x=0}\right), \tag{9}$$

$$T_1|_{x=l_1} = T_B, \tag{10}$$

where T_B is the thermostat temperature.

The first boundary condition (7) corresponds to neglect of heat losses as a result of radiation from the surface of the film. The second condition (8) describes the continuity of the heat flux at the film/substrate interface. The third condition (9) describes the temperature jump at the film/substrate interface.[6] When the fourth powers of the temperatures are different, the coefficient is selected so that for a small heat flux and therefore a small temperature jump, the boundary thermal resistance is R_{Bd}. The value of R_{Bd} must be determined experimentally.

We write the initial conditions in the form

$$T_0(x,0)=T_0^s(x), \quad T_1(x,0)=T_1^s(x), \tag{11}$$

where the functions $T_0^s(x)$ and $T_1^s(x)$ may be determined by solving the system of equations obtained from Eqs. (3)–(10) if the time partial derivatives $\partial T_{0,1}/\partial t$ are assumed to be zero.

Note that the validity conditions of the heat conduction equation describing thermal processes[5] in this YBaCuO/MgO structure are strictly satisfied at liquid nitrogen temperature and above.

The system of equations (3)–(11) was solved numerically using an implicit scheme and the convergence was checked by the ''net accumulation point'' method.

3. DISCUSSION OF RESULTS

The photoresponse was calculated in the temperature range 84–88 K, i.e., in the transition range of the superconducting to normal state. The boundary thermal resistance $R_{Bd}=8\times10^{-4}$ K·cm^2/W used in the calculations was determined for this structure using a procedure developed in Ref. 8. The current density $J(U,T)$ was obtained by linear interpolation of the curves $R_{\mathrm{Bol}}(T)$ (Fig. 1). The curve $P_0(t)$, giving the time dependence of the laser radiation power, was approximated by a parabola.

The following should first be noted: the calculations showed that for the structure used experimentally, allowance for the Joule heat release from the flow of transport current was unimportant in the range of current densities up to 2×10^4 A/cm^2 (the maximum current density in our experiment) and only had a significant influence on the response at current densities higher than 10^5 A/cm^2).

1) The numerical simulation showed that at low incident radiation fluxes (<100 W/cm^2), the response profile is almost independent of the flux and thermostat temperature T_B in the entire temperature range 84–88 K. This is because (a) the maximum ''isothermicity'' of the bolometer is <20 mK (i.e., is much smaller than the width of the superconducting to normal transition $\simeq0.8$ K) and the response is proportional to the average overheating of the film;[8] and (b) the time dependence of the average overheating of the YBaCuO film in this temperature range ($\Delta T_B\simeq4$ K) is almost independent of the thermostat temperature, since the thermal constants of the YBaCuO/MgO structure vary negligibly.

2) When the incident radiation flux P_0 was increased to 10^3–10^4 W/cm^2, it was found that the temporal characteristics of the bolometer depend strongly on the thermostat temperature T_B and on P_0. For comparison with the experiment Fig. 2 gives the results of calculating the photoresponse (curves $1'$ and $2'$) under conditions corresponding to the experimental ones. An analysis of Fig. 2 reveals good agreement between the calculations and experiment for such parameters as the pulse full width at half maximum: the photoresponse at the beginning of the superconducting transition is appreciably shorter than that at the center. This variation in the duration of the calculated photoresponse for a given incident radiation flux (5×10^3 W/cm^2) is caused by the strong nonlinearity of the YBaCuO current-voltage characteristic near the superconducting transition and by the significant nonisothermicity of the YBaCuO film (of the order of $\simeq0.5$ K), which is comparable to the width of the superconducting transition. To illustrate this nonisothermicity, Fig. 4 gives the results of calculating the overheating distribution in a YBaCuO/MgO structure at the time corresponding to the maximum average film temperature (see dashed curve in Fig. 2). It is interesting to note that when the boundary thermal resistance is zero, the nonisothermicity of the bolometer film is even higher.

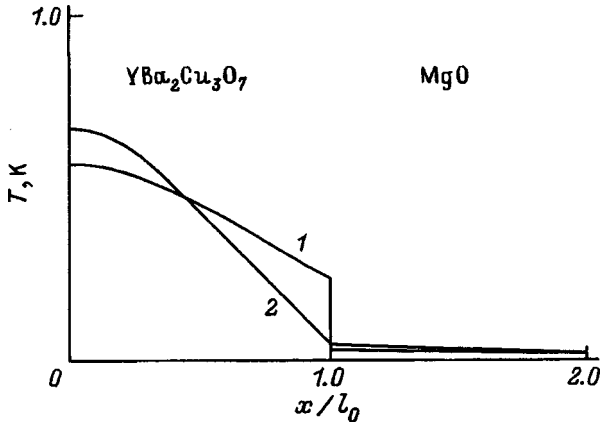

FIG. 4. Distribution of overheating in YBaCuO/MgO structure above bath temperature T_B (calculated), $P_0=5000$ W/cm^2. Curve *1*—$R_{Bd}=8\times10^{-4}$ K·cm^2/W. For illustration, curve *2* gives the hypothetical case of zero boundary thermal resistance at the YBaCuO/MgO interface. The coordinate is normalized to the thickness of the YBaCuO film.

To sum up, a comparison between the experimental results and the calculations has shown that this nonlinear thermal model accurately describes the time behavior of the photoresponse of this YBaCuO/MgO bolometer. The model can therefore be used to estimate the bolometer response time and can accurately take into account its response characteristics in proposed studies of the phonon subsystem in Si/Ge heterostructures and superlattices.

The authors would like to thank E. V. Pechen' for preparation of the YBaCuO films and A. I. Sharkov for useful advice and discussions.

This work was supported by the GNTP programs ''Superconductivity'' (Project No. 93190) and ''Promising Technologies and Devices in Micro- and Nanoelectronics'' (Project No. 130/57).

[1] M. Giltrow, A. Kozorezov, and M. Sahraoui-Tahar, Phys. Rev. Lett. **75**, 1827 (1995).
[2] M. Orby, J. Tate, P. Berberich, and H. Kinder, *Phonon-89*, *Proceedings of the Third International Conference on Phonon Physics*, edited by S. Hunklinger *et al.* (World Science, Singapore, 1990), Vol. 2, p. 328.
[3] M. M. Bonch-Osmolovskii, T. I. Galkina, A. Yu. Klokov, A. F. Plotnikov, Yu. Yu. Pokrovskii, and A. I. Sharkov, Solid State Commun. **92**, 203 (1994).
[4] A. D. Semenov, G. N. Gol'tsman, I. G. Gogidze, A. V. Sergeev, and E. M. Gershenzon, Appl. Phys. Lett. **60**, 903 (1992).
[5] M. I. Flik, P. E. Phelan, and C. L. Tien, Cryogenics **30**, 1118 (1990).
[6] W. A. Little, Can. J. Phys. **37**, 334 (1959).
[7] E. T. Shwartz and R. O. Pohl, Rev. Mod. Phys. **61**, 605 (1989).
[8] M. M. Bonch-Osmolovskiĭ, T. I. Galkina, A. Yu. Klokov, A. F. Plotnikov, and E. G. Romanov, Sverkhprovodimost' KIAE **5**, 2122 (1992).
[9] M. M. Bonch-Osmolovskiĭ, T. I. Galkina, A. Yu. Klokov, E. V. Pechen', O. B. Pokrovskiĭ, and D. O. Saks, Fiz. Nizk. Temp. **17**, 1470 (1991) [Sov. J. Low Temp. Phys. **17**, 799 (1991)].
[10] V. G. Gubankov, and Yu. Ya. Divin, Sverkhprovodimost' KIAE **3**, 2133 (1990).

Translated by R. M. Durham

Electronic structure and stability relations of CaF_2 and NaCl phases in a Ti-H system

I. A. Nechaev, V. I. Simakov, and V. S. Demidenko

Siberian Physicotechnical Institute at Tomsk State University, 634050 Tomsk, Russia
(Submitted February 13, 1997; resubmitted July 24, 1997)
Fiz. Tverd. Tela (St. Petersburg) **40**, 195–197 (February 1998)

Calculations are made of the electronic structures of $TiH_{0.73}$ and TiH hydrides having a NaCl crystal structure and $TiH_{1.5}$, $TiH_{0.73}$, and TiH having a CaF_2 structure. Estimates of their superconductivity temperature indicate that this should be significantly higher for the stoichiometric NaCl phase compared to nonstoichiometric phases. The results are compared with the characteristics of the χ phase of titanium hydride $TiH_{0.73}$ which undergoes a superconducting transition at 4.3 K. © *1998 American Institute of Physics.* [S1063-7834(98)00402-X]

A change in the crystal-structure type in compounds and solid solutions leads to changes in their physical properties. For instance, the superconducting transition temperatures T_c of NaCl-type implantation phases such as carbides, oxides, and nitrides of transition metals, have an abrupt maximum for stoichiometric compositions.[1] Superconducting PdH_x solid solutions with the same type of structure exhibit the same type of $T_c(x)/T_c^{\max}$ behavior[2] as in Ref. 1. However, a similar phase is not formed in a Pt-H system and interestingly, this does not exhibit superconductivity.[2] In a Ti-H system, hydrogen usually occupies tetrahedral interstitial sites and, at H concentrations higher than 50 at. %, the equilibrium type of crystal structure for this system is CaF_2. Despite this, the discussed law governing the correspondence between the distribution over octahedral interstitial sites of the implanted element and superconductivity for a Ti-H system is clearly confirmed in Ref. 3, where it is shown that the synthesized χ phase $TiH_{0.73}$, having an NaCl structure with a small ($c/a=0.95$) tetragonal distortion, has a fairly high temperature for hydrides $T_c \sim 4.3$ K. In view of these observations, it is relevant to identify the significance of the contribution of the electronic factor to the physical conditions prohibiting the existence of equilibrium titanium hydrides having an NaCl structure and to determine more precisely the characteristics of the T_c dependence of titanium hydrides on the composition and structural state.

To denote the type of crystal structure, we introduce the superscripts ''nc'' and ''cf'' to indicate NaCl and CaF_2, respectively. Figure 1 gives the density of electronic states of the hydride $Ti(H^{cf})_{1.5}$ calculated, as are all the following, using a modified scheme[7] compared with that used in Refs. 5 and 6. For the calculations we assumed the highest possible order for the given concentration in the unit cell of a face-centered cubic (fcc) lattice with the parameter $a=8.3224$ a.u. (Ref. 8). The good, detailed agreement with experiment in the vicinity of the Fermi level (inset to Fig. 1) indicates an ordered distribution of hydrogen in the tetrahedral interstitial sites of the fcc titanium lattice. The calculations showed that this state is energetically favored.

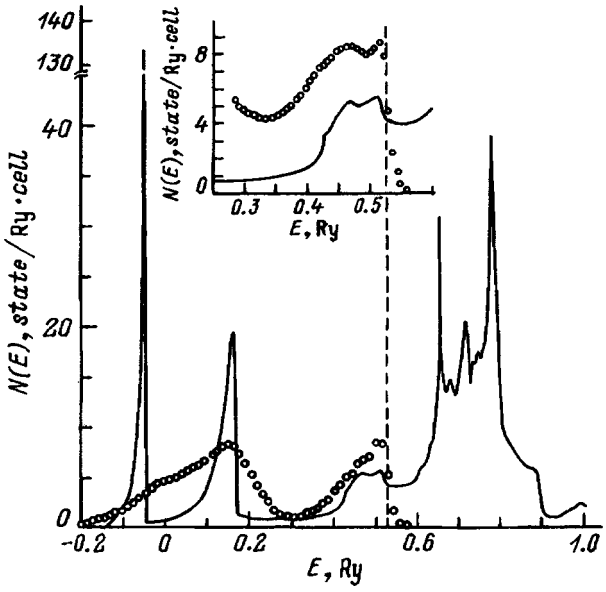

FIG. 1. Density of electronic states for the ordered hydride $Ti(H^{cf})_{1.5}$. Here and in Fig. 2 the vertical dashed line indicates the Fermi level. The open circles give the photoelectronic spectrum of $TiH_{1.5}$ from Ref. 4 with the photon energy $h\nu=21$ eV and the inset gives the spectrum for $h\nu=15$ eV.

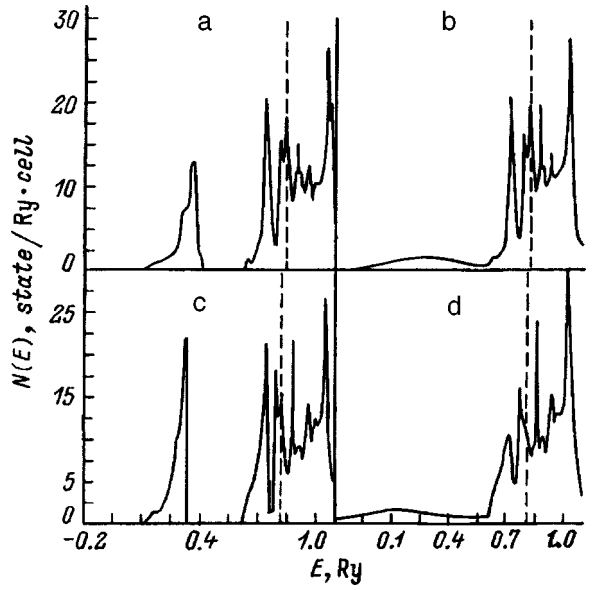

FIG. 2. Densities of electronic states for the hydrides $Ti(H^{nc})$ (a), $Ti(H^{nc})_{0.73}$ (b), $Ti(H^{cf})$ (c), and $Ti(H^{cf})_{0.73}$ (d).

TABLE I. Values of the parameter β (in Ry^{-1}) for the hydrides studied.

	$TiH_{1.5}$	TiH	$TiH_{0.73}$
NaCl	-	24.6	28.9
CaF_2	7.5	2.0	8.7

TABLE II. Calculated electron-phonon characteristics of the titanium hydrides studied.

Material	$N(E_f)$, state/Ry·atom	$M_H\langle\omega_D^2\rangle_H$, a.u.	θ_D, K	λ	λ_{Ti}	T_c, K
$Ti(H^{nc})_{0.73}$	8.73	0.038	282	0.67	0.40	3.9 4.3 (Ref. 3)
$Ti(D^{nc})_{0.73}$	8.73	0.032	280	0.72	0.40	4.9 5.0 (Ref. 3)
$Ti(H^{nc})$	9.30	0.031	290	0.98	0.43	10.2
$Ti(H^{cf})_{1.5}$	1.65	0.113	318	0.33	0.21	<0.1
Ti	-	-	380 (Ref. 13)	-	0.38 (Ref. 2)	0.27 0.39 (Ref. 2)

M_H is the hydrogen mass, $\langle\omega_D^2\rangle_H$ is the mean square of the Debye frequency of the hydrogen sublattice vibrations, θ_D is the Debye temperature; for all $M_{Ti}\langle\omega_D^2\rangle_H = 0.15$ a.u.

Figure 2 shows the densities of states of hypothetical cubic phases with H/Ti$\leqslant$1 with hydrogen obeying a probability distribution over octahedral interstitial sites, according to Ref. 3, and hydrogen having an ordered distribution over tetrahedral interstitial sites. The fcc lattice parameter $a=7.8462$ a.u. for these hydrides was obtained neglecting the tetragonality of the χ phase of $TiH_{0.73}$ and assuming volume invariance per atom. It can be seen that when both structures depart from stoichiometry, the band linking the *s* states of titanium and hydrogen becomes severely broadened whereas the *d*-band states below the Fermi level remain almost unchanged for NaCl-type fcc phases and are substantially transformed for CaF_2, promoting stability of the cubic lattice. Note that an analysis of the electronic energy spectrum of $Ti(H^{nc})$ and $Ti(H^{nc})_{0.73}$ showed that the experimentally observed[3] tetragonal distortion for the χ phase cannot be attributed here to the Jahn–Teller mechanism, as it was for TiH_2 (Ref. 9), although the Fermi energy E_f for these hydrides corresponds to the sharp density-of-states peak $N(E)$. In this case, the instability of the fcc lattice of titanium hydride to tetragonal distortion may be caused by the high value of $\beta = 1/N(E_f)\,(dN(E)/dE)|_{E_f}$ (Ref. 10). According to Ref. 10, taking account of Ref. 11, for this system where the contribution to the *d*-band binding energy $E_{bind}\sim 0.3$ Ry/atom depends weakly on the hydrogen concentration,[6] we have instability if $\beta>\beta_{cr}$, where $\beta_{cr}=14.7$ Ry^{-1}. The results of the calculations of β for all the systems studied are presented in Table I. It is easy to see that the theoretical model agrees with experiment,[12] isolates the NaCl structure as an uncharacteristic cubic phase for disordered titanium hydrides, having a tendency to lower the symmetry by means of a displacement type of transition. This may provide microscopic confirmation of the reasons for the experimental difficulties involved in obtaining a stoichiometric hydride with an NaCl structure.

The superconductivity characteristics of hydrides in different structural modifications should clearly differ substantially. Table II gives the results of calculations of the electron-phonon interaction constant λ and the superconducting transition temperature T_c. Standard approaches were used for the estimates.[14,15] The scattering phase for the hydrogen sublattice was taken as a ''weighted'' average of the scattering phases for an electron with the Fermi energy at the hydrogen potential and for a vacancy. The partial Debye frequencies in the hydrides were determined using the plasma jellium model[16] extended to a two-component system. Estimates of λ and T_c for $Ti(D^{nc})_{0.73}$ were made using the anharmonic relation.[14]

Table II shows that the strong influence of hydrogen in tetrahedral interstitial sites on the density of *d*-band electronic states has a negative influence on the superconducting properties of the system and reduces the electron-phonon interaction constant λ_{Ti} in the metal sublattice compared with its value in pure titanium, whereas hydrogen in octahedral interstitial sites alters negligibly this characteristic, i.e., the effective properties of hydrogen essentially differ in NaCl and CaF_2 structures. In the χ phase of $TiH_{0.73}$ (Ref. 3) a negative factor for the superconductivity is the presence of a fraction of vacancies in excess of stoichiometric. In fact, the complete absence of any negative contribution from vacancies in octahedral interstitial sites in the scattering of *s* and *p* electrons by the hydrogen sublattice gives a higher value of T_c for the stoichiometric hydride $Ti(H^{nc})$. Before experimental data are obtained, this factor may serve as an indication how realistic a general law for this type of structure is, such as that already identified for palladium nitrides and hydrides.

[1] R. White and G. Jebel, *Long-Range Order in Solids*, Moscow, 1985.
[2] P. V. Geld', R. A. Ryabov, and L. P. Mokhracheva, *Hydrogen and Physical Properties of Metals and Alloys* [in Russian], Moscow, (1985).
[3] I. O. Bashkin, A. I. Kolesnikov, E. G. Ponyatovskiĭ, A. M. Balagurov, and G. M. Mironova, Fiz. Tverd. Tela (St. Petersburg) **37**, 3744 (1995) [Phys. Solid State **37**, 2056 (1995)].
[4] J. H. Weaver, D. J. Peterman, D. T. Peterson, and A. Franciosi, Phys. Rev. B **23**, 1692 (1981).
[5] I. A. Nechaev, V. I. Simakov, and V. S. Demidenko, Izv. Vyssh. Uchebn. Zaved. Fiz. **10**, 57 (1995).
[6] I. A. Nechaev, V. I. Simakov, and V. S. Demidenko, Izv. Vyssh. Uchebn. Zaved. Fiz. **1**, 40 (1997).
[7] F. M. Mueller, J. W. Garland, M. H. Cohen, and K. H. Bennemann, Ann. Phys. **67**, 19 (1971).
[8] Z. M. Azarkh and P. I. Gavrilov, Kristallografiya, **15**, 275 (1970) [Sov. Phys. Crystallogr. **15**, 231 (1970)].
[9] M. Gupta, Solid State Commun. **29**, 47 (1979).
[10] U. M. Lomer, in *Phase Stability in Metals and Alloys* [in Russian], Moscow (1970).
[11] *Physical Metallurgy*, edited by R. W. Cahn and P. Haazen, [Moscow, 1987], Vol. 1.
[12] I. O. Bashkin, T. I. Dyuzheva, L. M. Lityagina, and V. Yu. Malyshev, Fiz. Tverd. Tela (St. Petersburg) **35**, 3104 (1993) [Phys. Solid State **35**, 1528 (1993)].
[13] N. W. Ashcroft and N. D. Mermin, *Solid State Physics* [Holt, Rinehart and Winston, New York, 1976; Mir, Moscow, 1979].
[14] D. A. Papaconstantopoulos, B. M. Klein, E. N. Economou, and L. L. Boyer, Phys. Rev. B **17**, 141 (1978).
[15] R. Evans, G. D. Gaspary, and B. L. Gyorffy, J. Phys. F: Metal Phys. **3**, 39 (1973).
[16] A. O. E. Animaly, Phys. Rev. B **8**, 3555 (1973).

Translated by R. M. Durham

Phonon-free mechanism of superconductivity in compounds containing quasi-two-dimensional NiB complexes

S. A. Karamov

Moscow Physicotechnical Institute, 141700 Dolgoprudnyĭ, Moscow Region, Russia
(Submitted April 28, 1997; resubmitted July 29, 1997)
Fiz. Tverd. Tela (St. Petersburg) **40**, 198–201 (February 1998)

A study is made of some characteristics of phonon-free pairing of hybridized p and d electrons in planar NiB complexes in the presence of strong short-range Hubbard repulsion. A generalized Hubbard model is used to calculate the superconductivity phase diagram as a function of the degree of underfilling of the $2p^6$ and $3d^{10}$ shells in NiB complexes. The phase region of states having the highest superconducting transition temperatures is established.
 [S1063-7834(98)00502-4]

Compounds such as $LuNi_2B_2C$ and $La_3NI_2B_2N_3$ (Refs. 1 and 2) containing a planar NiB structure have been studied. This structure is described assuming that it contains hole excitations of the type $3d(x^2-y^2)$ and $2p(x,y)$ in completely filled $3d^{10}$(Ni) and $2p^6(B^{5-})$ shells. In this case, $d(p)$ electrons tunnel through excited $p(d)$ states of boron (nickel—depending on the energy ratio of the single-particle $2p$ and $3d$ states). Possible atomic states are assumed to be: Ni—d^{10}, d^9, d^8 and B—p^6, p^5, p^4.

Strong internal correlations split the hole $3d(x^2-y^2)$ and $2p(x,y)$ levels into Hubbard sublevels (two d levels and four p levels according to the degrees of degeneracy of the single-particle atomic states) which correspond to certain single-particle energies ε_d and ε_p. Here an analysis is made of the limiting case of infinitely high Hubbard energies, when only one Hubbard p level and one d level are filled at the same time: $\varepsilon_p \sim \varepsilon_d$.

Allowance for tunneling interaction leads to hybridization and simultaneous filling of the Hubbard hole levels $\varepsilon_p, \varepsilon_d$. As a result, the levels are collectivized into Hubbard bands. Possible atomic ground states are: NiB^{5-}, Ni^+B^{5-}, NiB^{4-}, and Ni^+B^{4-}.

The energy shift $r=\varepsilon_p-\varepsilon_d$ of the anionic levels relative to the cationic ones is not calculated here: this is assumed to be a variable parameter which determines the phase properties of the compound.

1. GENERAL THEORY. EQUATIONS OF STATE AND SUPERCONDUCTIVITY CRITERION

The electronic structure of a NiB complex will be studied using the Emery model,[3–5] where the tunneling matrix elements $t_{p\lambda;d}$ are only taken into account between the p and d states of the nickel and boron atoms, which play a fundamental role in the formation of the elementary excitation spectrum. If the Coulomb interaction is neglected, assuming that this is strongly screened, this gives a generalized Hubbard model in the zeroth approximation of the average (self-consistent) field with the Hamiltonian[6]

$$\hat{H}=\sum \hat{N}_{\mathbf{r}n_p p}\varepsilon_p+\sum \hat{N}_{\mathbf{r}n_d d}\varepsilon_d+\hat{V}, \tag{1}$$

$$\hat{V}=\sum t_{p\lambda;d}(\mathbf{r}_1-\mathbf{r}_2)(\hat{p}^+_{\mathbf{r}_1\lambda}\hat{d}_{\mathbf{r}_2}+\hat{d}^+_{\mathbf{r}_2}\hat{p}_{\mathbf{r}_1\lambda}). \tag{2}$$

Here $\hat{p}^+$, $\hat{p}$, $\hat{d}^+$, and $\hat{d}$ are the creation and annihilation operators of the p- and d-hole states.

The following are selected as the basis of atomic hole states for changing to the Hubbard representation.

For the boron atom: The vacuum state B^{5-}, $2p^6$: $|0\rangle$, the single particle states B^{4-},$2p^5$: $p^+_{x\uparrow}|0\rangle$, $p^+_{y\uparrow}|0\rangle$, $p^+_{x\downarrow}|0\rangle$, $p^+_{y\downarrow}|0\rangle$ (quadruply degenerate level); and the two-particle states B^{3-},$2p^4$: $p^+_{x\uparrow}p^+_{y\uparrow}|0\rangle$, $p^+_{x\downarrow}p^+_{y\downarrow}|0\rangle$, $(p^+_{x\uparrow}p^+_{y\downarrow}|0\rangle+p^+_{x\downarrow}p^+_{y\uparrow}|0\rangle)/\sqrt{2}$ (triply degenerate level).

For the nickel atom: The Ni, vacuum state $3d^{10}$: $|0\rangle$, the single particle states Ni^+,$3d^9$: $d^+_\uparrow|0\rangle$,$d^+_\downarrow|0\rangle$ (doubly degenerate level), and the two-particle Ni^{2+},$3d^8$: $d^+_\uparrow d^+_\downarrow|0\rangle$ state.

Changing to the Hubbard representation reduces the Hamiltonian to the following form:

$$\hat{H}=\sum_{\mathbf{r}k}\varepsilon_k\hat{X}^{kk}_{\mathbf{r}}+\frac{1}{2}\sum_{\alpha\beta\mathbf{r}\mathbf{r}'}\hat{X}^{\alpha}_{\mathbf{r}}\hat{X}^{\beta}_{\mathbf{r}'}\hat{V}^{\alpha\beta}(\mathbf{r}-\mathbf{r}'), \tag{3}$$

where $\hat{X}^{\alpha}_{\mathbf{r}}$ are the Hubbard operators, α and β are the so-called root vectors which identify transitions between states of the cell.[7] This Hamiltonian corresponds to the following inverse, virtual, multicomponent, single-particle Green function of the loopless Hubbard approximation:[6]

$$[G_w^{-1}(\mathbf{p})]_{\alpha\beta}=[\{G_w^{(0)}(\mathbf{p})\}^{-1}]_{\alpha\beta}-f_\beta V_{\alpha\beta}(\mathbf{p}). \tag{4}$$

Here $G_w^{(0)}(\mathbf{p})$ is the diagonal atomic Green function.

Allowance for tunneling interaction is made in the nearest neighbor approximation; f_p and f_d are the so-called end factors which allow for the infinite Hubbard energy and are dependent on the average underfilling numbers n_p and n_d of the electronic $2p^6$ and $3d^{10}$ shells, respectively

$$f_p=\begin{cases}1-3n_p/4, & 0<n_p<1,\\ (n_p+2)/12, & 1<n_p<2,\end{cases} \tag{5}$$

$$f_d=\begin{cases}1-n_d/2, & 0<n_d<1,\\ n_d/2, & <n_d<2.\end{cases} \tag{6}$$

In addition to the noncollectivized p branches $E=\varepsilon_p$, the single-article Green function (4) gives two branches

$$E_{1,2}=-\mu\pm\sqrt{r^2/4+f_pf_d\tau^2}, \tag{7}$$

where

$$\tau^2/t^2=\begin{cases}4\left(\sin^2\{a(p_x+p_y)/2\}\right.\\ \quad\left.+\sin^2\{a(p_x-p_y)/2\}\right), & 0<n_p<1,\\ 6\left(\sin^2\{a(p_x+p_y)/2\}\right.\\ \quad\left.+\sin^2\{a(p_x-p_y)/2\}\right), & 1<n_p<2.\end{cases} \tag{8}$$

Here $\mu=-(\varepsilon_d+\varepsilon_p)/2$ is the chemical potential of the compound, $r=\varepsilon_p-\varepsilon_d$, t is the tunneling matrix element between states of the nearest Ni and B atoms, and a is the modulus of the vector of translational symmetry.

The average hole-state filling numbers n_p and n_d are expressed in terms of the matrix elements of the Green function

$$[D_w(\mathbf{p})]_{\alpha\beta}=[G_w(\mathbf{p})]_{\alpha\beta}f_\beta, \tag{9}$$

thereby determining the equations of state of the system

$$\sum_{\mathbf{p}j}B_jn_F(E_j)=\begin{cases}n_p/(2f_p)-n_F(\varepsilon_p), & 0<n_p<1,\\ 2(n_p-1)/3f_p-n_F(\varepsilon_p), & 1<n_p<2,\end{cases} \tag{10}$$

$$\sum_{\mathbf{p}j}A_jn_F(E_j)=\begin{cases}n_p/(2f_d), & 0<n_d<1,\\ (n_d-1)/f_d, & 1<n_d<2,\end{cases} \tag{11}$$

where

$$A_1=B_2=\frac{1}{2}\left[1-\frac{r}{\sqrt{r^2+4f_pf_d\tau^2}}\right],$$

$$A_2=B_1=\frac{1}{2}\left[1+\frac{r}{\sqrt{r^2+4f_pf_d\tau^2}}\right]. \tag{12}$$

The establishment of superconductivity in the system is determined by the presence of a negative scattering amplitude at the Fermi surface. The condition for the establishment of a superconducting state is the appearance of a singularity of the two-particle multicomponent vertex part $\Gamma_{\alpha\beta}(\mathbf{p})$ for zero total energy, momentum, and spin,[8] which in the empty lattice approximation (in the gas approximation) is given by the ladder series[9]

$$\Gamma_{\alpha\beta}(\mathbf{p})=\Gamma^{(0)}_{\alpha\beta}(\mathbf{p})-T\sum_{w\mathbf{p}'}\Gamma^{(0)}_{\alpha\beta\lambda\nu}(\mathbf{p},\mathbf{p}')G_w^{\lambda\lambda'}(\mathbf{p}')G_{-w}^{\nu\nu'}\times(-\mathbf{p}')\Gamma_{\lambda'\nu'}(\mathbf{p}'). \tag{13}$$

Here $\Gamma^{(0)}_{\alpha\beta\lambda\nu}(\mathbf{p})$ is the two-particle vertex part, irreducible over two lines in the same direction, which we find using the Dyson method.[10]

As a result, the superconductivity condition is expressed by the usual Bardeen–Cooper–Schrieffer (BCS) formula $\lambda>0$ with the effective constant λ

$$T_c\sim e^{-1/\lambda},\quad \lambda=gp. \tag{14}$$

Here $\rho=\Sigma_{\mathbf{p}}\delta(E(\mathbf{p}))$ is the energy density of states at the Fermi surface, g is the energy factor,

$$g=\frac{\varepsilon_d\varepsilon_p[C\varepsilon_pf_p+D\varepsilon_df_d]}{f_pf_d[\varepsilon_p+\varepsilon_d]^2}, \tag{15}$$

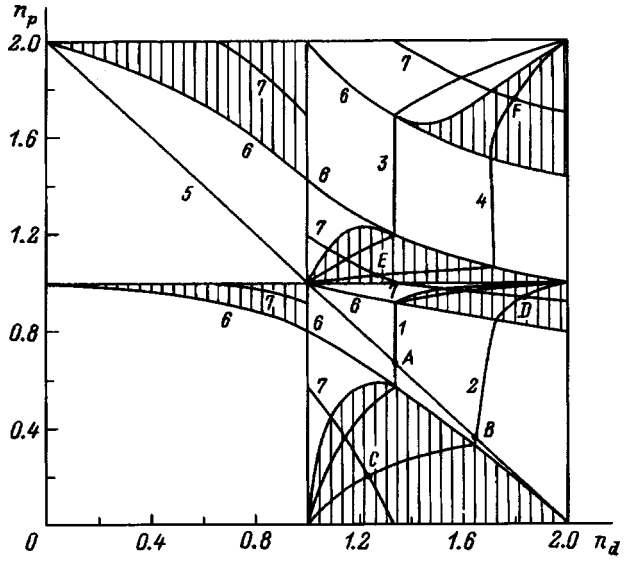

FIG. 1. Phase diagram of the superconductivity of an NiB complex in the square $0<n_p<2, 0<n_d<2$. The regions of superconductivity are shown hatched. C,D,E,F gives the approximate position of the points of maximum $T_c(n_p,n_d)$: *1, 3*—phase trajectories for $r/t=0$, *2, 4*—phase trajectories for $r/t=2$, *5*—electrical neutrality line (19) for $q=2$, *6*—curves bounding the regions of filling of localized p states, and *7*—curves of Van Hove singularities (K curve).

$$C=\begin{cases}-2, & 0<n_d<1,\\ 2, & 1<n_d<2,\end{cases} \tag{16}$$

$$D=\begin{cases}-1, & 0<n_p<1,\\ -1/3, & 1<n_p<2.\end{cases} \tag{17}$$

The density of states ρ is always positive so that the existence of superconductivity in the system is determined by the condition $g>0$.

2. OCCUPATION CHARACTERISTICS OF THE ELECTRONIC SPECTRUM

Each point in the phase plane (n_d,n_p) corresponds to some phase state which may be realized by various compounds of a particular type. Each phase state (n_d,n_p) has a one-to-one correspondence with the pair of values $(r/t,q)$, where $q=n_p+n_d$ is the total hole charge of the NiB complex. In other words, $(r/t,q)$ and (n_d,n_p) are alternative systems of phase coordinates. The value r/t is the parameter of the problem. It is subsequently assumed that $t=1$.

Taking the variable r as the parameter, the equations of state (10), (11) written in the form

$$\begin{cases}n_d=n_d(E_f,n_d,n_p),\\ n_p=n_p(E_f,n_d,n_p),\end{cases} \tag{18}$$

define parametrically in terms of the charge q in the coordinates (n_d,n_p) the family of phase trajectories $n_p=n_p(n_d)$ of the constant r, which are almost the same as the trajectories of motion of the phase-state points of the compounds during doping (curves *1–4* in Fig. 1).

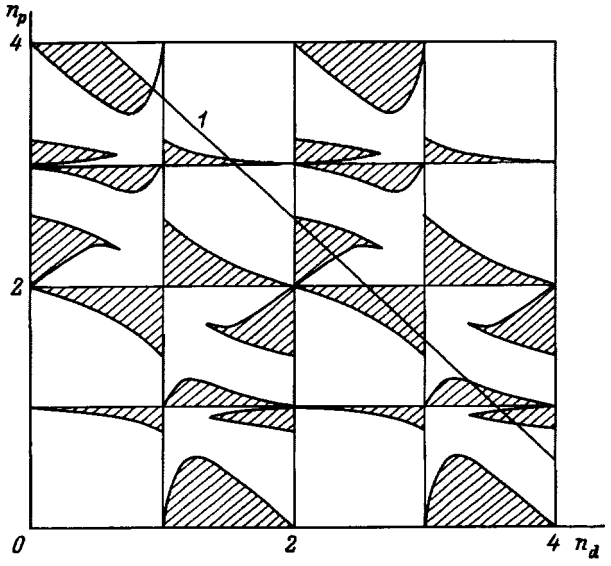

FIG. 2. Phase diagram of the superconductivity of the NiB complex in the square $0<n_p<4{,}0<n_d<4$. The regions of existence of superconductivity are shown hatched: *1*—line of electrical neutrality for $La_3Ni_2B_2N_{2,7}$ ($q=4.55$).

The parameter q is determined by the condition of electrical neutrality of the compound. A set of phase states (r,q) with the same q value forms a line of electrical neutrality (line *5* in Fig. 1) in the phase plane (n_d,n_p)

$$n_p=q-n_d. \tag{19}$$

Thus, the position of the phase state (r,q) in the coordinates (n_d,n_p) is determined by the point of intersection of the phase trajectory of the corresponding r and the line of electrical neutrality of the corresponding q (points A and B in Fig. 1).

3. PHASE DIAGRAM

Under conditions of strong Hubbard repulsion, the existence of superconductivity is determined by the sign and magnitude of the $d-d$ and $p-p$ scattering amplitudes. The superconductivity phase region is now sought. The superconductivity condition has the form $\lambda=g\rho>0$. A numerical solution of the problem is plotted in Fig. 1 (the regions of existence of the superconducting state are shown hatched and the curves *6* delimit the regions of filling of localized p states).

Thus, the phase diagram is constructed in the square $0<n_p<2{,}0<n_d<2$. This problem is symmetric relative to the partial hole transformation $n_p\to 4-n_p, n_d\to 2-n_d$, so that the phase diagram in the square $2<n_p<4{,}0<n_d<2$ is the square $0<n_p<2{,}0<n_d<2$, turned through 180° about the center. For the region $0<n_p<4{,}2<n_d<4$, which corresponds to hybridization of hole excitations of the type $3d(3z^2-r^2)$ and $2p(x,y)$, the theory gives the same results as for the region $0<n_p<4{,}0<n_d<2$ (Fig. 2).

4. PHASE RELIEF OF T_c

It has been noted that each point (n_d,n_p) in the phase plane corresponds to some phase state which may be realized by various high-temperature superconducting compounds with the same T_c corresponding to the given phase state. Thus, the dependence of T_c on the parameters n_d and n_p forms a certain relief which is of major interest because it can be used to determine the phase states and the compounds giving the highest T_c values.

The relief of $T_c(n_d,n_p)$, to within a preexponential factor of the order of magnitude of t, is the exponential relief of the function $-\lambda^{-1}(n_d,n_d)$, determined by relations (14) and (15). Thus, we investigate the function $\lambda(n_d,n_p)$.

For each subband $E(\mathbf{p})$ and each value of r, there is a charge q for which the state (r,q) corresponds to the Fermi level which passes through the saddle points of the spectral surface $E(\mathbf{p})$. Then, the energy density of the electronic states on the Fermi surface for these phase states has a clearly defined van Hove singularity, i.e., an extremum for given r. The set of these points for all possible values of r form parametrically defined curves in terms of r (curves *7* in Fig. 1) which will be arbitrarily called K curves.[11,12] All the points on this line correspond to states for which the Fermi surface passes through van Hove singularities. It follows from Eq. (14) that these states correspond to maxima of T_c for $\lambda>0$ and $T_c=0$ for $\lambda<0$ in the dependence $T_c(q)$ for constant r which describes the change in T_c along the corresponding phase trajectory of constant r. For each subband, the set of these states for different r forms a K curve in the phase plane which on the relief $T_c(n_d,n_p)$ corresponds to a ''ridge''—a line of T_c peaks for constant r. Each phase trajectory of constant r intersects the K curve at the phase point of the maximum $\rho(q)$ and $\lambda(q)$ for this value of r. If the point of intersection corresponds to $g>0$, this point lies in the region of superconductivity. It was shown in Refs. 11 and 12 that for each subband the maximum of $T_c(n_d,n_p)$ corresponds to the point of intersection of the phase trajectory $r\sim t$ with the corresponding K curve (points C, D, E, and F in Fig. 1).

5. COMPARISON WITH THE EXPERIMENT

It was assumed here that, in the compounds being studied, the electron-phonon interaction is negligible compared with the kinematic electron-electron interaction. Numerous experiments confirm that the superconductivity in these compounds cannot be described by the BCS model. For instance, experimental data are given in Ref. 1 for $La_3Ni_2B_2N_3$ (1) and LaNiBN (2). In accordance with the BCS model, T_c is given by the expression $T_c\sim M^{-1/2}\exp(-1/\lambda)$, where M is the mass of a unit cell and λ is the BCS constant. It is known[13,14] that at temperatures above the Debye temperature, the temperature derivative ρ_T' of the electrical resistivity of a compound is proportional to the BCS constant λ for this compound. Results of resistivity measurements[1] can be used to determine the ratio of the parameters λ_1 and λ_2 for these compounds: $\lambda_1/\lambda_2\approx 30$. In this case we find $M_2<M_1$. Thus, in accordance with the BCS theory $T_{c2}>T_{c1}$ should be found. In practice compound (2) is not a superconductor which sharply contradicts this theory.

Generally, calculations for high-temperature superconducting compounds allowing only for kinematic interaction of the electrons (including the Emery model[11,12]) describe the behavior of T_c as a function of the carrier concentration consistent with that observed experimentally[15,16] although this dependence cannot be described in terms of the BCS model.

The electrical neutrality condition for these compounds has the form (19). A superconducting transition was observed in various $La_3^{3+}Ni_2B_2N_{3-\delta}^{3-}$ compounds, particularly for $\delta=0.3$ (Ref. 1). The corresponding electrical neutrality line ($q=4.55$) is shown in Fig. 2 (line *1*). The position of the phase-state point of the compound on this line is determined by its parameter r. This point is clearly located in the region of superconductivity, in the square $3<n_p<4,1<n_d<2$.

To conclude, the author would like to than R. O. Zaĭtsev for extremely valuable recommendations and comments on this work.

This work is supported by the State Program on High-Temperature Superconductors under the ''Extend II'' Project No. 94011.

[1] R. J. Cava, H. W. Zandbergen, B. Batlogg *et al.*, Nature (London) **372**, 245 (1994).
[2] W. E. Pickett and D. J. Singh, Phys. Rev. Lett. **72**, 3702 (1994).
[3] V. J. Emery, Phys. Rev. Lett. **58**, 2794 (1987).
[4] R. O. Zaĭtsev, Fiz. Tverd. Tela (Leningrad) **33**, 3183 (1991) [Sov. Phys. Solid State **33**, 1789 (1991)].
[5] R. O. Zaĭtsev and Yu. V. Mikhaĭlova, Fiz. Tverd. Tela (Leningrad) **34**, 2521 (1992) [Sov. Phys. Solid State **34**, 1352 (1992)].
[6] J. C. Hubbard, Proc. R. Soc. London, Ser. A **276**, 238 (1963).
[7] R. O. Zaĭtsev, Zh. Éksp. Teor. Fiz. **70**, 1100 (1976) [Sov. Phys. JETP **43**, 574 (1976)].
[8] L. P. Gor'kov, Zh. Éksp. Teor. Fiz. **34**, 735 (1958) [Sov. Phys. JETP **34**, 505 (1958)].
[9] R. O. Zaitsev. Phys. Rev. Lett. **134**, 199 (1988).
[10] F. Dyson, Phys. Rev. B **102**, 1217 (1956).
[11] R. O. Zaĭtsev and S. A. Karamov, Sverkhprovodimost' KIAE **8**, 583 (1995).
[12] R. O. Zaitsev and S. A. Karamov, Functional Materials **3**, 259 (1996).
[13] A. Sommerfeld and H. A. Bethe, *Elektronentheorie der Metalle*, in *Handbuch der Physik*, edited by H. Geiger and K. Scheel, Vol. 24, Part 2 [Springer-Verlag, Berlin (1933); ONTI, NKTL, Leningrad (1938)].
[14] J. M. Ziman, *Electrons and Phonons* [Clarendon Press, Oxford, 1960; IL, Moscow, 1962].
[15] C. C. Tsuei *et al.*, Phys. Rev. Lett. **65**, 2724 (1990).
[16] J. B. Torance *et al.*, Physica C **162–164**, 241 (1990).

Translated by R. M. Durham

Current-voltage characteristics of $YBa_2Cu_3O_{7-x}$ single crystals and Kosterlitz–Thouless transition

N. D. Kuz'michev and M. A. Vasyutin

N. P. Ogarev Mordovian State University, 430000 Saransk, Russia
(Submitted September 16, 1997)
Fiz. Tverd. Tela (St. Petersburg) **40**, 202–204 (February 1998)

The nonlinear $I-V$ characteristic ($V(I)$) of $YBa_2Cu_3O_{7-x}$ single crystal was investigated near the transition from the resistive to the superconducting state in the absence of a magnetic field. A modulation Fourier analysis at temperature T^* (the maximum of the amplitudes of the higher ($n>1$) harmonics of the response voltage) was used to determine an analytic dependence $V(I)$ which accurately describes the experimental results (direct measurements and harmonics) in the range of currents $I<30$ mA ($j<310$ A/cm^2). It is shown that at T^* the power approximation of the $I-V$ characteristic $V\sim I^3$ is only found in the low current density limit ($j\ll j_0=140$ A/cm^2). The results are interpreted in terms of the Kosterlitz–Thouless (KT) transition model. It is established that T^* corresponds to the temperature of the KT transition T_{KT}, which means that T_{KT} can be determined directly. The deviation of $V(I)$ from a power dependence is caused by the nonlogarithmic variation of the vortex interaction energy as a function of the distance between them. [S1063-7834(98)00602-9]

Studies of the $I-V$ characteristics ($V(I)$) of single crystals and high-quality, high-temperature superconducting films are an important and topical issue which has been addressed by numerous authors (see, for instance, Refs. 1–12). However, the properties of $YBa_2Cu_3O_{7-x}$ single crystals have not been sufficiently well studied.

In the vast majority of the studies known to us, the authors only investigated the dependence $U(I_d)$ which was described over a wide range of current using the power function

$$V\sim I^{a(T)}, \tag{1}$$

where $a(T)$ is an exponent which depends on the temperature T.

In Refs. 11 and 12 we reported strong nonlinearity of the $I-V$ characteristics of $YBa_2Cu_3O_{7-x}$ single crystals, observed near T_c. Here we analyze these results using a method of modulation Fourier analysis which can be used to investigate the $I-V$ characteristics of high-temperature superconductors.

This method involves studying a large number of harmonics $U_k(I_d)$ (U_k is the kth harmonic voltage) of the sample response signal and using these to determine $V(I)$ and its derivatives. The following notation is adopted: U are experimental values and V are calculated values. The current I is taken to be the total current $I=I_d+I_a\cos(\omega t)$, where I_a is the amplitude of the ac current, $\omega=2\pi\nu$, and ν is the frequency, i.e., $V(I)=V(I_d)$ for $I_a=0$.

An analysis of studies of the $I-V$ characteristics shows that the function (1) cannot describe the harmonics of the response signal $U_k(I_a,I_d)$ (Refs. 11 and 12).

1. EXPERIMENTAL METHOD

A modulation technique (low modulation amplitudes) is used to study the current-voltage characteristics of tunnel junctions.[13]

A modulation method for arbitrary modulation amplitudes (modulation Fourier analysis) was developed in Refs. 11, 12, 14, and 15.

When the function $V(I)$ is expanded as a Fourier series in terms of the argument ωt, in the absence of hysteresis we have $V(I)=V_0(I_d,I_a)/2+\Sigma V_k(I_d,I_a)\cos(k\omega t)$. The coefficients $V_k(I_d,I_a)$ (the amplitudes of the harmonics) are determined using formulas for the Fourier coefficients[16] or using the formula[14,15]

$$V_k(I_d,I_a)=2\sum_{m=0}^{\infty}\frac{1}{m!(m+k)!}\left(\frac{I_a}{2}\right)^{2m+k}V^{(2m+k)}(I_d), \tag{2}$$

where $k=0,1,2,3,\ldots$ is the number of the harmonic, $V^{(p)}\times(I_d)$ is the p-order derivative of $V(I)$ with respect to I taken at $I=I_d$. Formula (2) is more convenient for moderately small amplitudes I_a when few harmonics are observed ($k\simeq 5$) which causes rapid convergence of the series in formula (2).

The experimental curves $U_k(I_a,I_d)$ for fixed I_a and $U(I_d)$ measured directly using direct current are used to determine $V(I)$. First, the function $V_k(I_a,I_d)$ is selected for specific I_a which approximately describes $U_k(I_a,I_d)$ (here we assumed $k=2$) and then, by integrating (taking into account the boundary conditions, existing physical models, and the identified properties of $U_k(I_a,I_d)$) this function is used to determine a proposed $V(T)$ (i.e., in the zeroth approximation it is assumed that $V_k(I_a,I_d)$ is proportional to the derivative d^kV/dI^k). Various modifications of this function $V(I)$ are then analyzed to determine the condition for minimum rms deviation of $V_k(I_a,I_d)$ from $U_k(I_a,I_d)$.

2. EXPERIMENT

The $I-V$ characteristics of high-temperature superconducting $YBa_2Cu_3O_{7-x}$ single crystals were studied, using both modulation Fourier analysis and direct current, in the

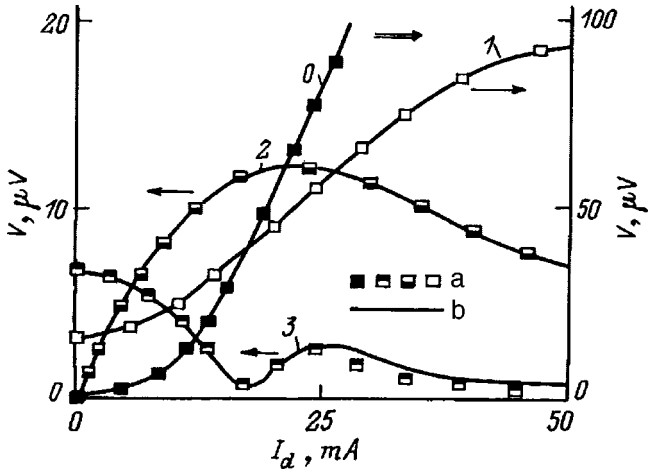

FIG. 1. $I-V$ characteristic (*0*) and current dependences of the first U_1 (*1*), second U_2 (*2*), and third harmonic voltage U_3 (*3*) of the response signal at temperature $T=T^*=92.0$ K, $I_a=27$ MA, $\nu=1$ kHz: a—experiment, b—calculations using equation (3).

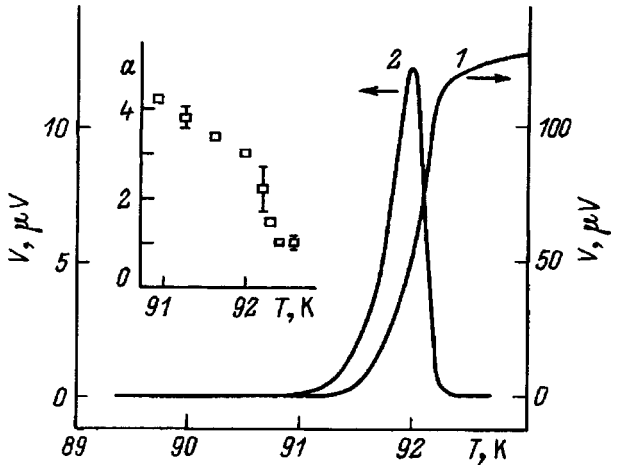

FIG. 2. Temperature dependences of the first U_1 (*1*) and second U_2 ($I_d=20$ mA) (*2*) harmonic voltages of the response signal for $I_a=27$ mA and $\nu=27$ kHz. Inset—temperature dependence of the exponent $a(T)$ ($a(T^*)=3$).

temperature range $83<T<94$ K. The direct current was between 0 and 50 mA, the amplitude of the ac current varied in the range $0<I_a<27$ mA, and the frequency was in the range 40 Hz$\leqslant\nu\leqslant$10 kHz.

The $I-V$ characteristics and the harmonic voltage of $YBa_2Cu_3O_{7-x}$ single crystals were investigated by a four-contact method. The resistance of the contacts was less than 0.3 Ω. Technical aspects and characterization of the samples were examined in greater detail in Ref. 12.

From the results, we found (Fig. 1) that the $I-V$ characteristic of the single crystals at $T=T^*=92.0\pm0.2$ K (T^* is the position of $\max|U_k(T)|$) may be approximated by the analytic function[1)]

$$V(I)=R_0[I-I_0\arctan(I/I_0)]=(R_0I_0/3)[(I/I_0)^3-(3/5)\times(I/I_0)^5+\ldots], \tag{3}$$

where $R_0=5.4\pm0.1$ mΩ ($\rho_0=7.6\times10^{-5}$ Ω·cm), $I_0=13.5\pm0.1$ mA ($j_0=1.4\times10^2$ A/cm^2) are temperature-dependent parameters.

Figure 2 gives the temperature dependences $U_1(T)$, $U_2(T)$, and $a(T)$ (inset). The curve $a(T)$ was obtained by approximating the initial region of $U(I_d)$ by the function (1) at different temperatures.

3. KOSTERLITZ-THOULESS TRANSITION IN $YBa_2Cu_3O_{7-x}$ SINGLE CRYSTALS

At low currents ($I\ll I_0$, $j<30-50$ A/cm^2) assuming that $\arctan(I/I_0)\approx(I/I_0)-(1/3)(I/I_0)^3$, we obtain for function (3)

$$V(I)\approx MI^3, \tag{4}$$

where $M=R_0/(3I_0^2)\approx10$ Ω/A^2 is the coefficient of nonlinearity of $V(I)$ for single crystals.

To explain equation (4), we use the concept of a two-dimensional Kosterlitz-Thouless (KT) transition,[1–5] caused by appreciable anisotropy of the resistance, the critical magnetic field H_{c2}, and the coherence length ξ of this material. ''Soliton'' objects participate in a KT transition, comprising vortices coupled in ''vortex-antivortex'' pairs. Their interaction energy is proportional to the logarithm of the distance between them.[1–5,17] Assuming weak pinning of vortices at inhomogeneities in the sample, the resistance R is proportional to the density of free vortices N_F (Ref. 17): $R\sim N_F\sim(I/I_0)^{q/2k_BT}$, where $q=(\pi n_s h^2/2m)^{1/2}$ is the effective charge of a vortex, $n_s=n_s^{2D}=n_s^{3D}d_0$ is the 2D electron density, d_0 is the thickness of the superconducting layer, h is Planck's constant, m is the electron mass, and k_B is the Boltzmann constant. The $I-V$ characteristic has the form $V\sim I^{a(T)}$, where $a(T)=1+q^2/(2k_BT)$.

The curve $a(T)$ changes abruptly at $T=T_{KT}$ (Nelson–Kosterlitz jump) from three to one (Fig. 2). The temperature T_{KT} coincides with the temperature of the maximum of the highest harmonics T^*, i.e., $T_{KT}=T^*=92.0$ K and $a(T_{KT}=T^*)=3$ (Fig. 2). The maximum of $U_k(T)$ should be observed at that temperature at which the maximum number of free vortices are created, i.e., at T_{KT}. This may be explained as follows. According to the KT model (see Ref. 17), the sample resistance R $T\leqslant T_{KT}$ is $R=2\pi\xi^2R_NN_F$, where ξ is the Ginzburg-Landau coherence length, and R_N is the normal-state resistance of the sample. The concentration of free vortices is given by the expression $N_F(T\leqslant T_{KT})\sim(j/j_0)^2\sim j^2(\xi/n_s)^2$. According to the Ginzburg-Landau and BCS models,[18] we have $\xi\sim(1-T/T_c)^{-1/2}$ and $n_s\sim1-T/T_c$.

From this we obtain the dependence $R(T)$

$$R\sim(1-T/T_c)^{-4}. \tag{5}$$

Equation (5) is meaningful up to temperatures $T=T_{KT}$. Above T_{KT} annihilation of vortices leads to a sharp drop in R and a rapid decrease in the nonlinearity caused by the motion of ''KT vortices'' so that R has a maximum at $T=T_{KT}$ and $U_k(T)$ ($k>1$) should have a peak at T_{KT} since $U_k\sim R$.

The similarity between T_{KT} and T_c in $YBa_2Cu_3O_{7-x}$ single crystals leads to a high value of $R(T_{KT})$ (see equation (5)), which is easy to observe experimentally from observations of higher harmonics.

Our results show that in the range of currents $I<30$ mA ($j<310$ A/cm^2) the $I-V$ characteristics are accurately de-

scribed by the dependence (3), which is not a power law and hence casts doubts on the validity of the KT model. According to Ref. 17, there are several reasons for the nonpower behavior of $V(I)$ in a KT transition, such as screening of intervortex interaction, the domain structure of the $YBa_2Cu_3O_{7-x}$ single crystal, and other factors. This produces a nonlogarithmic dependence of the interaction energy on the distance between the vortices. In the low current limit, where the number of paired vortices is negligible, we find $V(I\rightarrow 0)\sim I^3$ [see Eq. (4)]. From Eq. (4) we can obtain $n_s(T_{KT})\approx 1.3\times 10^{21}$ cm^{-3} and $\xi_{ab}(T_{KT})=5.4$ nm.

Since the distance between the CuO planes in $YBa_2Cu_3O_{7-x}$ is an order of magnitude smaller than the vortex dimensions ($\sim\xi_{ab}$), these may form normal three-dimensional Abrikosov vortices but then a KT transition would be impossible. Thus, the authors of Ref. 1 suggested that the objects involved in the KT transition are normal-state excitations which form pairs at K_{KT} in the form of quasitwo-dimensional condensates. Genenko *et al.*[19,20] assume that the magnetic flux transported by a vortex is very small ($\Phi\ll\Phi_0$) and two-dimensional superconductivity is possible. As was found qualitatively and by numerical simulation in Refs. 21 and 22, Josephson interaction between layers in $YBa_2Cu_3O_{7-x}$ is screened in the KT transition regime.

To sum up, we have determined the analytic $I-V$ characteristic of $YBa_2Cu_3O_{7-x}$ single crystals whose harmonics $[V_k(I_a,I_d)]$ accurately describe the experimental curves $U_k(I_a,I_d)$, and we have also identified the range of validity of the function (1) to describe the $I-V$ characteristics of this material. It has also been established that the maximum temperature of the dependences of the amplitudes of the higher harmonics of the response voltage $U_k(T)$ ($k>1$) is the Kosterlitz-Thouless temperature (T_{KT}), which may serve as a new method of determining T_{KT}.

[1)]The temperature T^* was determined by averaging over the temperatures of the maxima of all the harmonics studied.

[1] P. C. E. Stamp, L. Forro, and C. Ayache, Phys. Rev. B **38**, 2847 (1988).
[2] N.-C. Yeh and C. C. Tsuei, Phys. Rev. B **39**, 9708 (1989).
[3] S. Martin, A. T. Fiory, R. M. Fleming *et al.*, Phys. Rev. Lett. **62**, 677 (1989).
[4] S. N. Artemenko, I. G. Gorlova, and Yu. I. Latyshev, Phys. Lett. A **138**, 428 (1989).
[5] H. Teshima, K. Nakao, H. Izumi *et al.*, Physica C **199**, 149 (1992).
[6] C. Y. Chang, Lue Chin-Shan, and Y. C. Chou, Phys. Rev. B **49**, 1488 (1994).
[7] S. N. Gordeev, W. Jahn, A. A. Zhukov *et al.*, Phys. Rev. B **49**, 15420 (1994).
[8] Chen Jun, Tan Jian, Li Juangui *et al.*, Chin. J. Temp. Phys. **16**, 21 (1994).
[9] B. I. Smirnov, Yu. M. Baĭkov, A. N. Kudymov, T. S. Orlova, and Yu. P. Stepanov, Fiz. Tverd. Tela (St. Petersburg) **37**, 1794 (1995) [Phys. Solid State **37**, 977 (1995)].
[10] B. I. Smirnov, T. S. Orlova, A. N. Kudymov, M. T. Lanagan, N. Chen, and K. K. Goretta, Fiz. Tverd. Tela (St. Petersburg) **38**, 2931 (1996) [Phys. Solid State **38**, 1603 (1996)].
[11] M. A. Vasyutin and N. D. Kuz'michev, Pis'ma Zh. Tekh. Fiz. **18**(23), 5 (1992) [Sov. Phys. Tech. Phys. **18**, 764 (1992)].
[12] N. D. Kuz'michev, M. A. Vasyutin, A. I. Golovashkin, and I. S. Levchenko, Fiz. Tverd. Tela (St. Petersburg) **37**, 2070 (1995) [Phys. Solid State **37**, 1121 (1995)].
[13] A. Barone and G. Paterno, *Physics and Applications of the Josephson Effect* [Wiley, New York, 1982; Mir, Moscow, 1984].
[14] N. D. Kuz'michev, Pis'ma Zh. Tekh. Fiz. **17**, 56 (1991) [*sic*].
[15] N. D. Kuz'michev, Zh. Tekh. Fiz. **64**, 63 (1994) [Tech. Phys. **39**, 1236 (1994)].
[16] I. N. Bronshteĭn and K. A. Semendyaev, *Mathematics Handbook* [in Russian], Moscow (1961).
[17] A. M. Kadin, K. Epstein, and A. M. Goldman, Phys. Rev. B **27**, 691 (1983).
[18] V. V. Shmidt, *Introduction to the Physics of Superconductors* [in Russian], Moscow (1982).
[19] Yu. A. Genenko and Yu. V. Medvedev, Sverkhprovodimost' KIAE **5**, 46 (1992).
[20] Yu. A. Genenko, Sverkhprovodimost' KIAE **5**, 1402 (1992).
[21] V. Cataudella and P. Minnhagen, Physica C **166**, 442 (1990).
[22] H. Weber and H. J. Jensen, Phys. Rev. B **44**, 454 (1991).

Translated by R. M. Durham

$YBa_2Cu_3O_{7-\delta}/CeO_2$ heterostructures on sapphire *R*-plane

Yu. A. Boĭkov

A. F. Ioffe Physicotechnical Institute, Russian Academy of Sciences, 194021 St. Petersburg, Russia

T. Claeson

Physics Department, Chalmers Institute of Technology, S-41296, Göteborg, Sweden

D. Érts

Institute of Chemical Physics, Latvia University, 1586 Riga, Latvia

(Submitted June 13, 1997)
Fiz. Tverd. Tela (St. Petersburg) **40**, 205–208 (February 1998)

$(001)YBa_2Cu_3O_{7-\delta}$ epitaxial films were prepared by laser ablation on $(1\bar{1}02)Al_2O_3$ surface. A thin $(001)CeO_2$ or $(111)CeO_2$ buffer layer was deposited between the substrate and the superconductor film to reduce their chemical interaction. In the initial stages of CeO_2 buffer formation, its orientation depended strongly on the intensity of cerium ion interaction with oxygen. Epitaxial growth of $(001)YBa_2Cu_3O_{7-\delta}$ films was achieved both on $(001)CeO_2//(1\bar{1}02)Al_2O_3$ and $(111)CeO_2//(1\bar{1}02)Al_2O_3$. The T_c temperature of epitaxial $(001)YBa_2Cu_3O_{7-\delta}$ films was within 88–90 K, and the current J_c at 77 K was in excess of 10^6 A/cm^{-2}. © *1998 American Institute of Physics.* [S1063-7834(98)00702-3]

The low values of dielectric permittivity ε and of losses $\tan\delta$ characteristic of sapphire make it a promising substrate material for thin high-T_c superconducting films for use in microwave technology (filters, resonators, etc.). Preparation of perfect epitaxial $(001)YBa_2Cu_3O_{7-\delta}$ (YBCO) films on sapphire, however, is complicated by the considerable difference in lattice parameters and by chemical interaction of the growing layer with the substrate at temperatures of 700–800 °C (Ref. 1).

Thin CeO_2 (CeO) layers were used successfully[2–4] as buffers in growing epitaxial YBCO films on $(1\bar{1}02)Al_2O_3$ (AO). The CeO layer exhibits a preferred orientation relationship with sapphire *R*-plane both azimuthally and with respect to the substrate normal, $(001)[110]CeO||(1\bar{1}02)[2\bar{2}01]AO$ (Ref. 3), despite the significant lattice mismatch $[\Delta a=2(a_1-a_2)/(a_1+a_2)\approx 10\%$, where a_1 and a_2 are the lattice constants of the substrate and film material, respectively]. (111)-oriented CeO grains are usually present in the bulk of cerium dioxide. The volume fraction of (111)-oriented CeO grains in the buffer can be reduced by subjecting it to a thermal treatment in oxygen at $T\approx 950$ °C (Ref. 4).

The available literature on chemical inertness of YBCO to CeO in film heterostructures is contradictory. It was proposed[2] to use a thin CeO buffer to produce a tunneling barrier between YBCO electrodes, since the insolubility of Ce in YBCO permits one to achieve an atomically smooth interface. On the other hand, YBCO was observed to interact strongly with the epitaxial CeO buffer at $T=790$ °C.[5] Among the main products of interaction is $BaCeO_3$.

This work considers some features in the epitaxial growth of CeO buffer on sapphire and studies the effect of its structure on the parameters of YBCO films.

1. EXPERIMENT

Laser ablation (KrF, $\lambda=248$ nm, $\tau=30$ ns) was used for deposition of a thin (50 nm) CeO buffer layer on $(1\bar{1}02)$AO, followed by growing on it a 200-nm thick epitaxial YBCO film.

The starting targets were wafers prepared by standard ceramic technology. During the CeO layer deposition, the oxygen pressure P_0 in the growth chamber was varied within $1\times10^{-3}-4\times10^{-1}$ mbar. The YBCO film was grown with T_s varied in the 740–785 °C interval and with P_O fixed at 0.4 mbar. The CeO layer was grown at $T_s=750$ °C. The YBCO target was ablated at a laser radiation density $Q=2$ J/cm^{-2}. CeO was evaporated with Q varied within 0.8–2.5 J/cm^{-2}.

The phase composition and structure of the grown layers were characterized using Philips PW 1710 ($\theta/2\theta$) and Siemens D 5000 (ϕ scanning) diffractometers.

The morphology of the YBCO film surface was studied with an atomic-force microscope.

The superconducting transition temperature T_c of the YBCO films was determined from the temperature dependence of resistivity ρ and effective magnetic susceptibility χ ($f=30$ kHz). The critical current density was derived from *I-V* curves measured on YBCO microbridges 4–8 μm wide and 50 μm long. The microbridges were patterned by photolithography and Ar ion milling (500 V).

2. EXPERIMENTAL RESULTS

The structure of the CeO layer depended substantially on Q and P_0 during their growth. Growth under $Q<1$ J/cm^{-2} and $P_0>0.1$ mbar produced azimuthally oriented (001)CeO layers (Figs. 1a and 2a). X-ray diffraction data indicate absence of (111)-oriented CeO grains in the buffer layer.

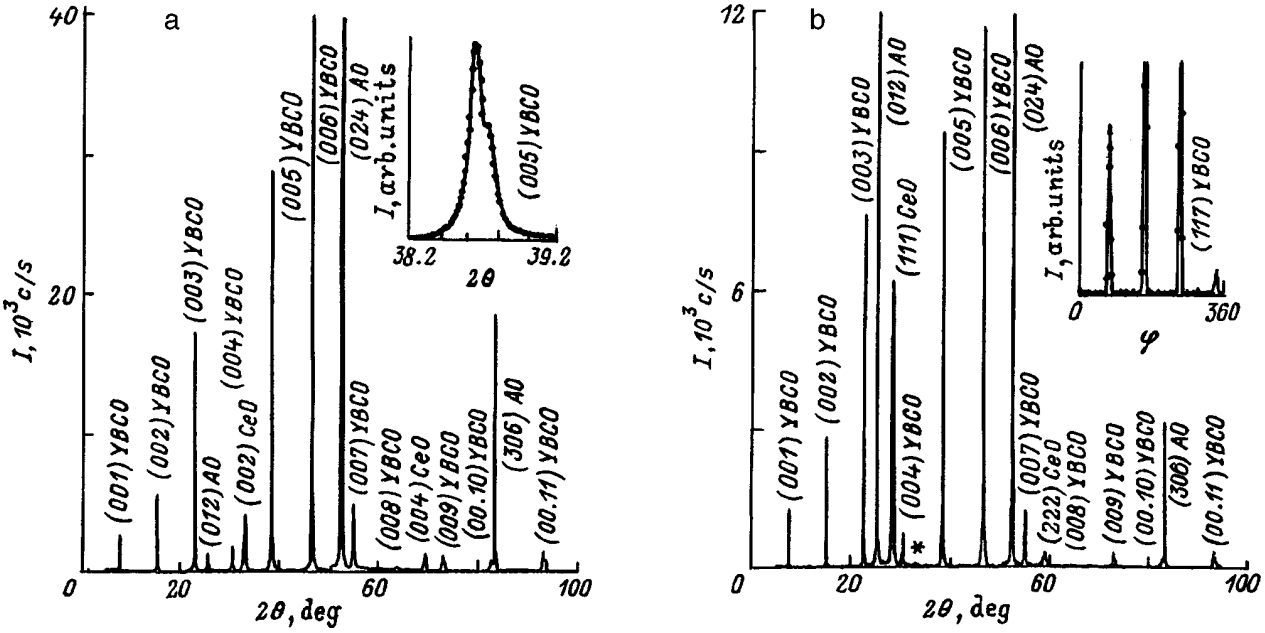

FIG. 1. $\theta/2\theta$ diffractograms obtained with Cu $K\alpha$ source on (a) (001)YBCO//(001)CeO and (b) (001)YBCO//(111)CeO heterostructures grown on $(1\bar{1}02)$AO. The Cu $K\alpha$ doublet is shown resolved in the (005)YBCO diffraction peak for (001)YBCO//(001)CeO (inset in panel a). Panel b shows a ϕ scan for (117)YBCO. In inset, star identifies the (002)CeO diffraction peak.

When grown under $Q>1.5$ J cm^{-2} and $P_0<10^{-2}$ mbar, the (111)CeO//$(1\bar{1}02)$AO orientation became dominant (see Fig. 1b). The weak reflection at $2\theta\approx33°$ (inset in Fig. 1b) implies the presence of (001)-oriented CeO grains in the (111)CeO buffer layer. For intermediate values of Q and P_O, the CeO layer had polycrystalline structure with two clearly pronounced preferential grain orientations, (001)CeO$\|(1\bar{1}02)$AO and (111)CeO$\|(1\bar{1}02)$AO.

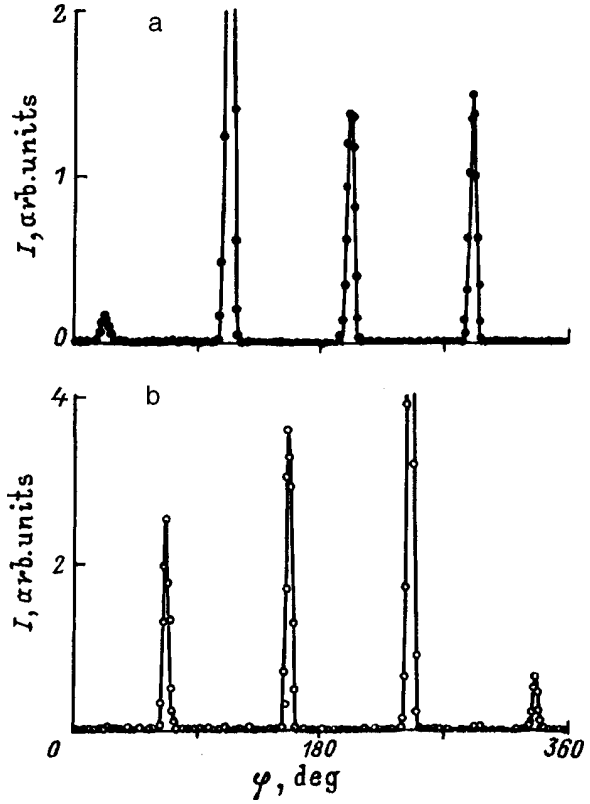

FIG. 2. X-ray φ scans (Cu $K\alpha$) of (a) (113)CeO and (b) (117)YBCO for a (001)YBCO$\|$(001)CeO epitaxial heterostructure grown on $(1\bar{1}02)$AO at $T_s=750$ °C.

For $T_s=750$ °C, the (001)YBCO film grew epitaxially both on (001)CeO$\|(1\bar{1}02)$AO and on (111)CeO$\|(1\bar{1}02)$AO (Figs. 1 and 2). The Cu K_α doublet was actually resolvable for the (005)YBCO peak in the (001)YBCO$\|$(001)CeO case. The FWHM of the (005)YBCO peak for Cu $K_{\alpha1}$ was 0.09°. The parameter $c=11.67$ Å for the YBCO cell was calculated using the value of 2θ for the (00.11)YBCO peak. The (005)YBCO x-ray peak measured on (001)YBCO$\|$(111)CeO was 20–40% broader, and the lattice parameter was $c=11.65$ Å.

YBCO films grown on (001) and (111) buffer layers at $T_s=750$ °C did not reveal any significant differences in surface morphology. The films had a smooth surface, with the density of a-oriented particles (the c axis was parallel to the substrate plane) not exceeding 10^6 cm^{-2}. No growth spirals whose core contains screw dislocations were observed. The surface of (001)YBCO films grown at $T_s>780$ °C was not smooth and exhibited a large number of pinholes (Fig. 3).

The values of T_c for YBCO films grown on both (001) and (111)CeO buffers were within 88–90 °C (Fig. 4). The values of T_c found from the $\rho(T)$ relation were in good agreement with data on the temperature dependence of χ (see inset to Fig. 4). The current J_c for YBCO films prepared on (001) and (111)CeO buffers was in excess of 10^6 A/cm^{-2} at 77 K.

3. DISCUSSION

The mechanisms responsible for the formation of preferentially (001)-oriented CeO layers on a substrate with a large

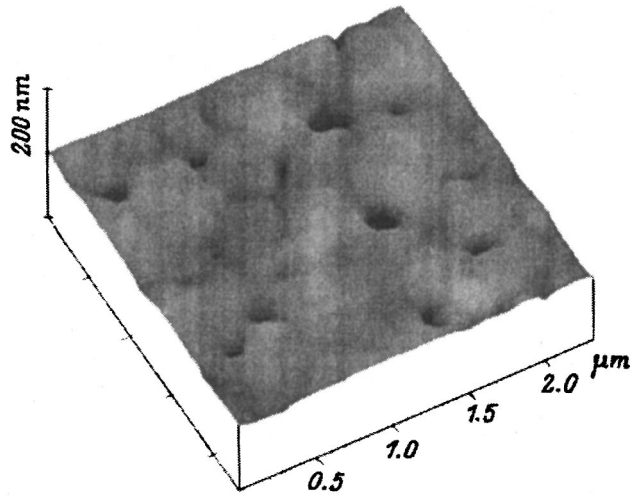

FIG. 3. Photomicrograph of the surface of an YBCO film grown at $T_s = 785$ °C was obtained with an atomic-force microscope.

lattice mismatch, as is the case, for example, with $(1\bar{1}02)$AO, are still not fully clear. The process of CeO nucleation is apparently affected to a considerable extent by the character of the oxygen environment around the Ce ions. The CeO complexes forming on the sapphire substrate may be different, depending on the oxygen pressure in the growth chamber and cerium atom (ion) concentration in the adsorbed phase. The valence state of Ce in compounds with oxygen may be either $4+$ (CeO_2) or $3+$ (Ce_2O_3) (Ref. 6). CeO_2 has a cubic fluorite unit cell ($a = 5.411$ Å), with each cerium ion sitting at the center of an oxygen cube. Ce_2O_3 has a hexagonal cell ($a = 3.888$ Å), $c = 6.096$ Å (Ref. 6), with

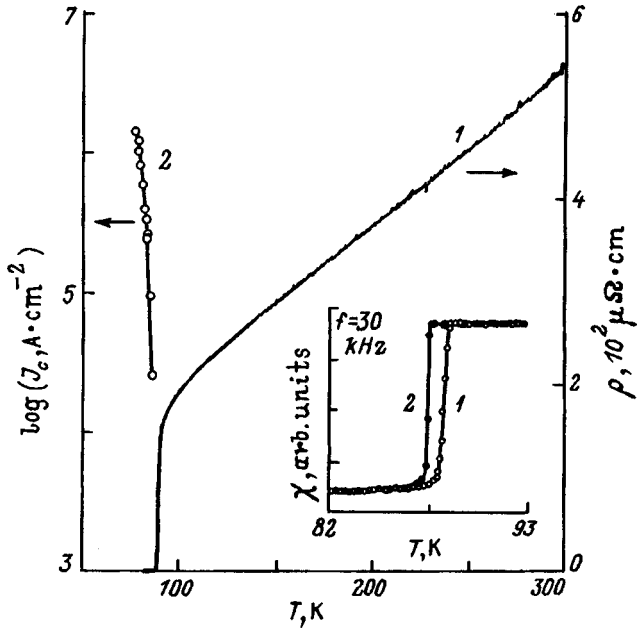

FIG. 4. Temperature dependence of (*1*) resistivity ρ and (*2*) critical current density J_c for an (001)YBCO film grown on (001)CeO$\|(1\bar{1}02)$AO at $T_s = 750$ °C. The inset shows effective magnetic susceptibility χ vs temperature for (001)YBCO films grown at $T_s = 750$ °C on (*1*) (001)CeO$\|(1\bar{1}02)$AO and (*2*) (111)CeO$\|(1\bar{1}02)$AO.

the seven nearest-neighbor oxygen ions occupying positions at two substantially different distances from the cerium ions.

In the conditions of oxygen deficiency ($P_0 < 10^{-2}$ mbar, $Q > 1.5$ J cm^{-2}), Ce_2O_3 nuclei are the first to become stable in the initial stage of the CeO film formation. The $(0001)Ce_2O_3$ plane has a minimum surface energy, and therefore the nuclei are oriented in such a way as to make the c axis in Ce_2O_3 perpendicular to the substrate plane. The lattice mismatch between CeO_2 and $(0001)Ce_2O_3$ is the lowest for $(111)CeO_2 \| (0001)Ce_2O_3$, and it is this that determines the CeO layer orientation in its subsequent growth (Fig. 1b).

In the case of a high oxygen-adatom concentration on the substrate ($P_0 > 0.1$ mbar and $Q < 1$ J cm^{-2}), $(001)CeO_2$ nuclei become stable from the very beginning of CeO layer growth, and this predetermines the orientation of an epitaxial CeO film with respect to the substrate normal (Fig. 1a). Minimization of the elastic strain energy in the nucleus-substrate system governs the predominant azimuthal orientation of the nuclei.

The mechanisms favoring formation of an (001)YBCO film on a substrate with a small lattice mismatch were considered by the present authors elsewhere.[7] (001)YBCO achieves a good lattice match to (001)CeO (with $\Delta a \approx 1\%$) when the corresponding oxygen sublattices are rotated azimuthally by 45° for a YBCO film grown on a (001)CeO buffer, as derived from x-ray characterization (Figs. 1a, 2a, and 2b), is (001)[010]YBCO$\|$(001)[110]CeO.

One of the causes of reduction of the c parameter in YBCO films grown on sapphire compared to $SrTiO_3$ or $NdGaO_3$ substrates[7] is the high level of tensile stresses in the axb plane due to the significant thermal-expansion mismatch between YBCO and AO.

A (001)YBCO film was grown epitaxially on a sapphire substrate also with a (111)CeO buffer (Fig. 1b). A ϕ scan shows clearly the four diffraction peaks due to reflection from the (117)YBCO crystallographic planes (inset in Fig. 1a). The azimuthal orientation of the YBCO film on the (111)CeO buffer is governed apparently by YBCO nuclei formed on (001)CeO grains (see inset in Fig. 1b). The lower intensity of formation of stable YBCO nuclei on the surface of (111)-oriented CeO grains compared to that on (001)CeO may be the result of (a) the relatively high level of mechanical stress in the YBCO nucleus-(111)CeO system because of a larger effective lattice mismatch and (b) the presence of microinclusions of secondary phases (primarily of $BaCeO_3$) formed in chemical interaction between (111)CeO and atoms (ions) of Ba in the vapor phase which are produced in the laser ablation of the starting YBCO target. The high density of noncompleted unit cells of cerium dioxide on (111)CeO surface should stimulate more active reaction of Ce with particles adsorbed from the vapor phase compared to (001)CeO.

The high density of pinholes on the free surface of YBCO films grown at $T_s > 780$ °C (Fig. 3) is a consequence of a reaction between the superconductor film and the CeO layer, which becomes intense at high T_s. The main products of the reaction between the CeO buffer and the phase adsorbing on it in laser ablation of an YBCO target are Y_2BaCuO_5, $BaCeO_3$, and CuO (Ref. 5). The presence of $BaCeO_3$ micro-

inclusions in multilayered (001)YBCO||(001)CeO heterostructures grown at $T_s = 750$ °C was established by the present authors in x-ray diffraction studies[8]. $BaCeO_3$ has a perovskite structure [$a = 4.397$ Å (Ref. 6)]. The formation of stable YBCO nuclei on the surface of $BaCeO_3$ microinclusions, as well as intergrowth of $BaCeO_3$ precipitates into the superconductor layer, is suppressed by the significant lattice mismatch. Particles adsorbed on $BaCeO_3$ surface diffuse to YBCO growth ledges or reevaporate. As a rule, $BaCeO_3$ inclusions cluster close to the superconductor/CeO-buffer interface.[3,4]

(001)YBCO films grown on (001)CeO||$(1\bar{1}02)$AO and (11)CeO||$(1\bar{1}02)$AO at $T_s = 750$ °C had close values of $T_c = 88-90$ K and $J_c > 10^6$ A/cm^{-2} at 77 K (see Fig. 4). The drop in χ at the superconducting transition temperature attests to the absence of microinclusions of an YBCO phase with a lower T_c in the YBCO films thus grown.

To conclude, the structure of the CeO buffer layer grown by laser ablation on the $(1\bar{1}02)$AO surface is strongly dependent on the intensity of Ce–O chemical interaction in the initial stages of the layer formation. Epitaxial (001)YBCO films can be grown both on (111)CeO||$(1\bar{1}02)$AO and on (001)CeO||$(1\bar{1}02)$AO. One of the main reasons for formation of a large number of pinholes in YBCO films grown at $T_s > 780$ °C is precipitation of microinclusions of secondary phases at the interface. The values of T_c for the epitaxial (001)YBCO films produced lie within 88–90 K, with $J_c > 10^6$ A/cm^{-2} at 77 K.

Support of the Russian Fund for Fundamental Research (Grants 95-02-04186-a and 96-02-17848) is gratefully acknowledged.

[1] C. T. Cheung and E. Ruckenstein, J. Mater. Res. **4**, 1 (1989).
[2] M. W. Denhott and J. P. McCaffrey, J. Appl. Phys. **70**, 3986 (1991).
[3] W. L. Holstein, L. A. Parisi, D. W. Face, X. D. Wu, S. R. Foltyn, and R. E. Muenchausen, Appl. Phys. Lett. **61**, 982 (1992).
[4] A. P. Bramley, S. M. Morley, S. R. M. Grovenor, and B. Pecz, Appl. Phys. Lett. **66**, 517 (1995).
[5] G. L. Skofronik, A. H. Carim, S. R. Folyn, and R. E. Muenchausen, J. Mater. Res. **8**, 2785 (1993).
[6] R. W. G. Wyckoff, *Crystal Structure* (Interscience Publishers, New York, 1964), Vols. 1 and 2, pp. 3 and 241.
[7] Yu. A. Boikov, Z. G. Ivanov, E. Olsson, V. A. Danilov, T. Claeson, M. Shcheglov, and D. Érts, Fiz. Tverd. Tela (St. Petersburg) **37**, 880 (1995) [Phys. Solid State **37**, 478 (1995)].
[8] Yu. A. Boikov, T. Claeson, and D. Érts, J. Appl. Phys. (to be published).

Translated by G. Skrebtsov

Investigation of laser-induced defect formation in CdTe crystals by Rutherford backscattering

L. A. Golovan', P. K. Kashkarov, Yu. N. Sosnovskikh, V. Yu. Timoshenko, and N. G. Chechenin

M. V. Lomonosov State University, 119899 Moscow, Russia

V. M. Lakeenkov

State Institute of Rare Metals, 109017 Moscow, Russia

(Submitted June 25, 1997)
Fiz. Tverd. Tela (St. Petersburg) **40**, 209–211 (February 1998)

Rutherford backscattering has been used to study defect formation processes in a CdTe surface layer exposed to pulsed laser radiation. It was established that scattering centers are formed only at laser pulse energies exceeding the melting threshold of the surface. The spatial distributions of Cd and Te and of structural defects in the irradiated layer were determined. The data are interpreted assuming intensive evaporation of one of the components (Cd). © *1998 American Institute of Physics.* [S1063-7834(98)00802-8]

Cadmium telluride is an important material in modern optoelectronics that can be used to fabricate solar cells, electrooptical modulators, hard radiation detectors, and also as a substrate for growing layers of $Cd_xHg_{1-x}Te$ solid solution. Characteristics of this material include comparatively low thermal conductivity and specific heat, as well as highly volatile components.[1] A promising method for specific modification of the electrical and recombination properties of binary compounds is pulsed laser irradiation, characterized by local, short-lived action on the semiconductor.[2,3] Pulsed laser irradiation of CdTe and the induced modification of the properties of this semiconductor has only been examined in a few studies.[4–10] Most attention was paid to the laser-induced modification of the composition of the surface layers. For instance, Te enrichment of the surface layer and Cd depletion are reported in Refs. 4–7. However, the data on the changes in composition and defect formation presented in Refs. 4–8 do not allow us to draw any definitive conclusion on the laser-induced modification mechanisms. This is so because the authors made no distinction between the case where pulsed laser irradiation causes a melting phase transition at the surface and the case of laser irradiation at energies below the melting threshold. Also, the formation of defects was inferred by studying the electronic properties of the irradiated materials, for example, using photoluminescence and photoconductivity methods.[5–10] One method for direct determination of the concentration and distribution of defects in the surface region is Rutherford backscattering (RBS).[11] Here, this method is used for the first time to study the laser-induced modification of the surface layer of CdTe. Note that the melting threshold W_m of CdTe was calculated by us in Ref. 9 and determined experimentally in Ref. 10. On exposure to nanosecond ruby laser pulses, the threshold W_m was 40 mJ/cm^2, which is several times lower than the melting thresholds for most IV and III-V semiconductors.[3]

1. EXPERIMENTAL METHOD

The measurements were made using (111) oriented CdTe single crystals. The RBS spectra were recorded using a system built on a Van de Graaff accelerator at the Scientific-Research Institute of Nuclear Physics at Moscow State University using a 1.4 MeV He^+ ion beam. Single pulses from an OGM-20 ruby laser ($\lambda = 694$ nm, $\tau = 20$ ns) were used for the pulsed laser irradiation. A homogenizer was used to obtain unpolarized spatially homogeneous radiation.[3] The samples were irradiated in vacuum at $T = 300$ K and the RBS spectra were recorded in situ immediately after the laser irradiation. A detailed description of the apparatus is given in Ref. 12. The RBS spectra were measured for randomly and axially incident ion beams. The distribution of the components was determined by a computer analysis of the spectral profile using the RUMP program.[13]

It is known that RBS spectra in the channeling mode contain information on the defect concentration and distribution. The depth distribution profile of the relative concentration of point defects may be obtained from the relation[11]

$$n_d(z) = \frac{N_d(z)}{N} = \frac{\chi_d(z) - \chi_r(z)}{1 - \chi_r(z)}, \tag{1}$$

where N_d and N are the concentrations of defects and regular atoms in the appropriate sublattice, χ_d is the RBS yield for oriented incidence of the ion beam from the irradiated crystal, normalized to the yield for random incidence, $\chi_r(z) = \chi_v(z) + F(z)$ is the contribution of the unchanneled ion component propagating in the irradiated crystal, $\chi_v(z)$ is the normalized RBS yield for the unirradiated crystal with oriented incidence of the ion beam. The dechanneling function $F(z)$ was calculated using the single scattering approximation, whose validity was confirmed by a later check (see Ref. 11).

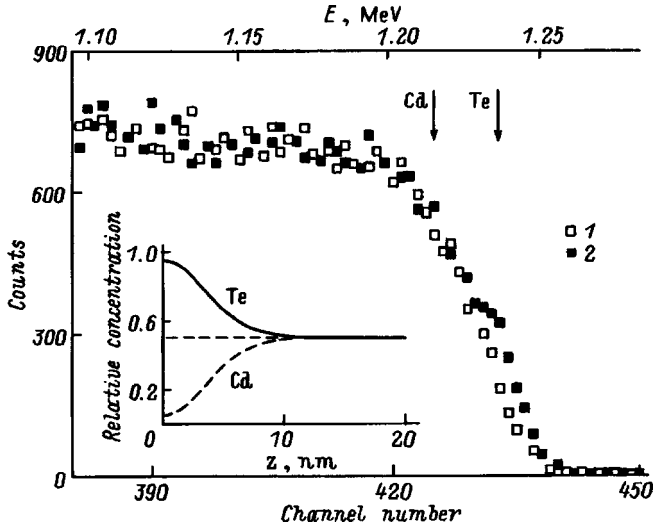

FIG. 1. Rutherford backscattering spectra with unoriented ion beam incidence for unirradiated (*1*) and irradiated CdTe (*2*) with $W=120$ mJ/cm^2. The inset shows the concentration distribution profile of the CdTe components after irradiation at $W=120$ mJ/cm^2 (solid curve—Te, dashed curve—Cd).

2. EXPERIMENTAL RESULTS

We shall first consider the change in the composition of the CdTe surface layers which is observed as variations in the RBS spectra obtained for randomly incident ions. Changes in the profile of these spectra were identified experimentally for $W\geqslant 100$ mJ/cm^2. The RBS spectra for the initial sample and for a sample irradiated at the energy density $W=120$ mJ/cm^2, obtained for unoriented ion beam incidence, are shown in Fig. 1. In view of the similarity between the masses of Cd and Te, the contributions of these components to the RBS spectra of the unirradiated crystal were almost impossible to resolve. As a result of the pulsed laser irradiation, the surface layers of the sample became appreciably enriched in tellurium and depleted in cadmium. This result is extremely logical if we bear in mind that the vapor pressure of cadmium at the melting point is appreciably higher than the vapor pressure of tellurium at the same temperature (7 and 0.2 atm, respectively[1]) and thus, Cd is preferentially evaporated from the melt under pulsed laser irradiation. The distribution of the relative concentrations of the components obtained from the analysis is shown in the inset to Fig. 1. It can be seen that with increasing depth z, the relative Te concentration in the irradiated crystal decreases and the relative Cd concentration increases, becoming constant at the levels of the corresponding concentrations of the components in the unirradiated CdTe crystal. Thus, the thickness of the CdTe surface layer with laser-induced modified composition is ≈ 10 nm.

The RBS spectra of CdTe in the channeling mode are shown in Fig. 2. It can be seen that the action of a laser pulse with $W\approx W_m$ caused no changes. Modification of the channeling spectra was initiated at $W\geqslant 50$ mJ/cm^2. The axial RBS yield increased with increasing energy density of the laser pulse.

An analysis of the variations in the RBS spectra in the ion channeling mode revealed that defect formation in the surface region is satisfactorily described assuming that point scattering centers are formed as a result of the laser irradiation. Calculated defect distribution profiles for various energy densities are shown in Fig. 3. It can be seen that at $W=80$ mJ/cm^2 the damage to the surface layer is very appreciable: approximately 30% of the atoms are displaced from their regular positions and the thickness of the defect layer is ≈ 70 nm. As W increases further, the defect zone

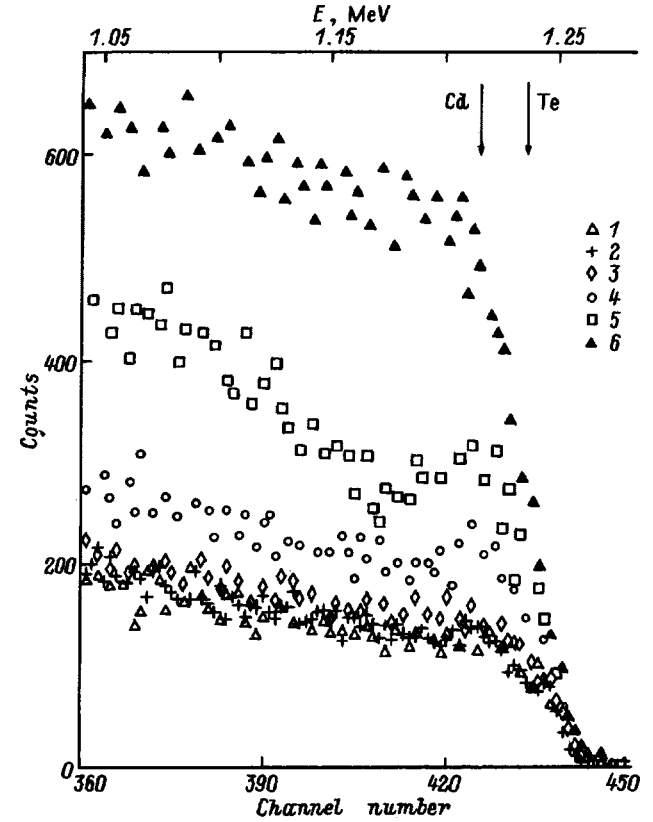

FIG. 2. Axial RBS spectra of CdTe before (*1*) and after pulsed laser irradiation with $W=40$ (*2*), 50 (*3*), 103 (*4*), and 143 mJ/cm^2 (*5*). The random RBS yield of CdTe is shown by the filled triangles (*6*).

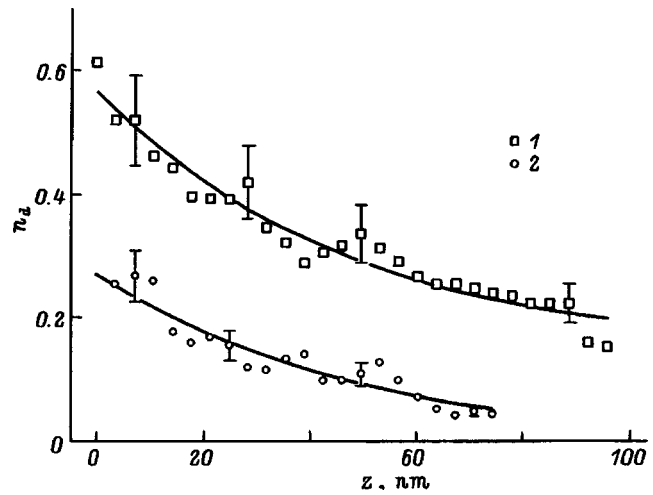

FIG. 3. Concentration profile of point defects in CdTe after pulsed laser irradiation at $W=82$ (*1*) and 143 mJ/cm^2 (*2*).

becomes broader (to ≈ 100 nm at $W = 143$ mJ/cm^2) and the defect concentration corresponds to amorphization of the surface.

3. DISCUSSION OF RESULTS

In our experiments, Rutherford backscattering has been used for the first time to record changes in the composition of a CdTe surface layer induced by laser irradiation. Changes in the composition are observed as a result of laser irradiation at $W > 120$ mJ/cm^2 which causes efficient evaporation of the highly volatile cadmium component from the melt. This is evidenced by a layer depleted in Cd and enriched in Te, ≈ 10 nm thick, which is appreciably less than the thickness of the molten layer (≈ 400 nm, according to our calculations).

The experiments showed that defect formation in CdTe is an above-threshold process: the formation of defects—point scattering centers—at laser pulse energy densities $W \geqslant 50$ mJ/cm^2 is recorded by RBS. As the pulse energy increases, the defect concentration and the thickness of the defect layer increase. Note that the thickness of the defect layer l_d is several times less than the thickness of the molten layer d. For instance at $W = 80$ mJ/cm^2, we find $l_d \approx 70$ nm whereas, according to our calculations,[8] the thickness d for the same pulse energy density was 235 nm.

Possible causes of this laser-induced defect formation include the high rate of solidification of the melt and intensive evaporation. This latter process was recorded optically at $W \geqslant 100$ mJ/cm^2 (Ref. 14). Intensive evaporation may produce defects as a result of the formation of a nonstoichiometric layer, or as a result of an increased rate of solidification caused by the outflux of heat accompanying evaporation. It is known that for III-V compounds this last process may cause nonepitaxial solidification of the melt from the surface which then gives rise to surface layer defects.[15] Since it has been noted that CdTe components are highly volatile, it may be postulated that, for this material, defect formation is attributable to this mechanism. The assumption that the surface layer becomes amorphized as a result of intensive evaporation from the surface is also consistent with the observation that the thickness of the defect layer is appreciably greater than the thickness of the modified layer. As a result of evaporation, the material loses the energy λm_v (where λ is the specific heat of evaporation and m_v is the mass of evaporated material), which may lead to crystallization of a certain layer whose mass m_c is determined from the simple relation[15]

$$\lambda m_v = L m_c, \tag{2}$$

where L is the specific heat of crystallization, which is $L = 209$ J/g for CdTe (Ref. 1). Since it has been shown that cadmium evaporates preferentially from the melt, λ should be determined by the heat of evaporation of Cd (888 J/g (Ref. 16)). Thus, the evaporation of Cd from a layer 15 nm thick assures crystallization of a CdTe layer ≈ 30 nm thick. This factor clearly plays an increasing role in defect formation with increasing W.

To conclude, we note that RBS has been used for the first time to study laser-induced defect formation and compositional changes in CdTe. It was observed that pulsed laser irradiation at energy densities above the melting threshold induces defects, predominantly point scattering centers. Defect formation is caused by intensive evaporation of one of the components.

[1] K. Zanio, *Cadmium Telluride, Semiconductors and Semimetals Vol. 13* (New York, 1978)
[2] A. V. Dvurechenskiĭ, G. A. Kachurin, E. V. Nidaev, and L. S. Smirnov, *Pulsed Annealing of Semiconductor Materials* [in Russian], Moscow (1982).
[3] P. K. Kashkarov and V. Yu. Timoshenko, Poverkhnost' Fiz. Khim. Mekh. No. 6, 5 (1995).
[4] P. D. Brewer, J. J. Zinck, and G. L. Olson, Appl. Phys. Lett. **57**, 2526 (1990).
[5] V. N. Babentsov, A. Baĭdullaeva, A. I. Vlasenko, S. I. Gorban', B. K. Dauletmuratov, and P. E. Mozol', Fiz. Tekh. Poluprovodn. **27**, 1617 (1993) [Semiconductors **27**, 894 (1993)].
[6] V. N. Babentsov, A. Baĭdullaeva, B. M. Bulakh, S. I. Gorban', and P. E. Mozol', Poverkhnost' Fiz. Khim. Mekh. No. 12, 144 (1988).
[7] V. V. Artamonov, M. Ya. Valakh, A. P. Litvinchuk, and V. V. Strel'chuk, Poverkhnost' Fiz. Khim. Mekh. No. 1, 46 (1989).
[8] F. X. Wagner, K. Dhese, P. H. Key, D. Sands, S. R. Jackson, R. Kirbitson, and J. E. Nicholls, Appl. Surf. Sci. **86**, 364 (1995).
[9] I. Yu. Viskovatykh, V. M. Lakeenkov, P. K. Kashkarov, V. I. Petrov, V. Yu. Timoshenko, and F. I. Khilinskiĭ, Izv. Ross. Akad. Nauk, Ser. Fiz. **57**(9), 12 (1993).
[10] L. A. Golovan', V. Yu. Timoshenko,and P. K. Kashkarov, Poverkhnost' Fiz. Khim. Mekh. No. 10, 65 (1995).
[11] F. F. Komarov, M. A. Kumakhov, and I. S. Tashlykov, *Nondestructive Ion-Beam Analysis of Solid Surfaces* [in Russian], Minsk (1987).
[12] N. G. Chechenin, E. V. Monakhov, and K. K. Burdel', Prib. Tekh. Éksp. **3**, 142 (1994).
[13] L. R. Doolitle, Nucl. Instrum. Methods Phys. Res. B **9**, 344 (1985).
[14] L. A. Golovan', P. K. Kashkarov, and V. Yu. Timoshenko, Pis'ma Zh. Tekh. Fiz. **21**(23), 26 (1995) [Tech Phys. Lett. **21**, 960 (1995)].
[15] P. K. Kashkarov, V. Yu. Timoshenko, N. G. Chechenin, and A. N. Obraztsov, Laser Phys. **2**, 790 (1992).
[16] *Handbook of Physical Quantities*, edited by I. K. Kikoin [in Russian], Atomizdat, Moscow (1976).

Translated by R. M. Durham

Optoelectronic effects in p-$CdGeAs_2$ single crystals and structures based on them

B. Kh. Baĭramov, I. K. Polushina, and Yu. V. Rud'

A. F. Ioffe Physicotechnical Institute, Russian Academy of Sciences, 194021 St. Petersburg, Russia

V. Yu. Rud'

State Technical University, 195251 St. Petersburg, Russia

P. G. Schunemann

Lockheed Sanders Inc., Nashua, NH, USA

M. C. Ohmer and N. C. Fernelius

AFWL, Wright Lab., Wright Patterson AFB, OH, USA

G. Irmer and J. Monecke

Bergakademie Freiberg, Institut für Theoretische Physik, D-09596, Freiberg, Germany
(Submitted July 8, 1997)
Fiz. Tverd. Tela (St. Petersburg) **40**, 212–216 (February 1998)

Spectra of inelastic light scattering by optical phonons in p-$CdGeAs_2$ single crystals were obtained for the first time. The observed clear polarization dependence and the absence of any appreciable dependence of the intensity and frequency of the observed lines when the sample is swept in ≈ 300 μm steps indicates these $CdGeAs_2$ single crystals grown by directional crystallization from a near-stoichiometric flux, are of high quality and homogeneous. The type of symmetry of the observed phonon lines is interpreted and it is shown that the force constants in $CdGeAs_2$ and $CdSnP_2$ crystals differ slightly. Temperature dependences of the electrical conductivity and the Hall constant were studied in oriented homogeneous p-$CdGeAs_2$ single crystals. It was established that the conductivity of these crystals is determined by the deep acceptor level $E_A = 0.175$ eV and has the degree of compensation 0.5–0.6. The temperature dependence of the Hall mobility reflects the competition between impurity and lattice mechanisms of hole scattering. The photosensitivity of In/$CdGeAs_2$ surface barrier structures reaches 20 μA/W at $T = 300$ K and remains at this level within the fundamental absorption of $CdGeAs_2$. It is concluded that these structures may be used as wide-band photoconverters for natural light and as selective photoanalyzers for linearly polarized radiation. [S1063-7834(98)00902-2]

Cadmium germanium diarsenide $CdGeAs_2$ is a direct-gap semiconductor ($E_G = 0.57$ eV at $T = 300$ K) and may be obtained as n or p type by doping or by controlling the deviations of the flux composition from stoichiometry.[1] The development of the basic principles of the growth technology for $CdGeAs_2$ single crystals having a chalcopyrite lattice and the observation of the highest coefficients of nonlinear susceptibility among known nonlinear optical materials[1–5] have been responsible for the unique applications of this material as high-efficiency laser radiation converters. The extensive application of $CdGeAs_2$ in radiation converters is limited by the significant level of optical absorption in the region of transparency which can be attributed to a high concentration of lattice defects of various types.[1,6] Recently, intensive physicotechnological studies of growth processes for high-optical-quality $CdGeAs_2$ single crystals have been initiated in leading scientific centers throughout the world.[7] As for well-studied phases of variable composition — II-VI compounds — it is vitally important to carry out technological studies in different laboratories and then compare the main physical properties of the materials to establish a correlation between the physical properties of $CdGeAs_2$ and the growth conditions. This may provide the clarity required to understand the problems involved in improving the quality of complex semiconductor materials. In the present paper, which takes a step in this direction, we report results of the first studies of inelastic light scattering and the electrical properties of electrically homogeneous $CdGeAs_2$ single crystals grown by Lockheed using a technique[4] developed at the A. F. Ioffe Physicotechnical Institute. The development of photosensitive structures using these materials is also examined.

EXPERIMENTAL RESULTS AND DISCUSSION

1) Preparation of single crystals. Single crystals of $CdGeAs_2$ were grown by directional crystallization of a near-stoichiometric flux of the ternary compound in a horizontal crucible in a low and constant temperature gradient.[6]

2) Raman light scattering. Chalcopyrite $CdGeAs_2$ crystals possess a tetrahedral atomic coordination and are an isoelectronic analog of III-V crystals having a zinc blende structure. Mixing of two cationic sublattices leads to ordering and also changes the $T_d^2(F43m)$ space group typical of zinc blende to the $D_{2d}^{12}(I42d)$ group typical of chalcopyrite. Since

the sphalerite unit cell is doubled in this case, the ratio 4:1 is obtained for the volume of the corresponding Brillouin zones and the points $\Gamma(000)$, $X(0,0,2\pi/a)$ and $W(2\pi/a,0,\pi/a)$ in the Brillouin zone of zinc blende are transformed into the Γ point in the Brillouin zone of chalcopyrite. Thus, phonons at points Γ, X, and W in the sphalerite structure correspond to phonons at the center of the Brillouin zone of the chalcopyrite structure. Consequently, the phonons corresponding to the boundary of the Brillouin zone in the sphalerite structure may be recorded in first-order light scattering.

Thus, the primitive $CdGeAs_2$ cell contains eight atoms (two formula units) and the spectrum of lattice vibrations consists of 21 optical and three acoustic branches. According to a group-theoretical analysis, the long-wavelength normal vibrations (at point Γ) are transformed as follows in terms of symmetry type:

$$1\Gamma_1+2\Gamma_2+3\Gamma_3+4\Gamma_4+7\Gamma_5, \tag{1}$$

where all the Γ_5 vibrational modes are doubly degenerate. Vibrations having the symmetry Γ_1, Γ_3, Γ_4, and Γ_5 are active in the Raman scattering spectrum while Γ_4 and Γ_5 are active in the infrared absorption spectrum. The vibrations having Γ_2 symmetry are not active in scattering processes or in infrared absorption.

This analysis neglects the internal electric field in polar crystals. Allowance for long-range Coulomb interaction caused by the macroscopic electrostatic field coupled with optical polar lattice vibrations of Γ_4 and Γ_5 symmetry, leads to splitting into longitudinal and transverse vibrations $(3\Gamma_4+6\Gamma_5)$. Thus, 22 optical vibration modes may be predicted experimentally in the first-order light scattering process:

$$1\Gamma_1+3\Gamma_3+3\Gamma_4(LO)+6\Gamma_5(LO)+6\Gamma_5(TO). \tag{2}$$

The Raman scattering spectra were measured for $CdGeAs_2$ crystals at room temperature using two argon laser lines at 488.0 and 514.5 nm. A backscattering geometry was used. The focused laser beam was directed perpendicular to the (112) crystallographic plane. The angle between the direction of phonon propagation and the **c** tetragonal axis of the crystal was 54.7°. The polarization vectors of the incident and scattered light were directed along [110](⊥) and [112](∥) in the (⊥⊥) or (⊥∥) configuration. The scattered light was analyzed with a double diffraction spectrometer with a spectral resolution of 4 cm^{-1}.

Typical Stokes components of the light scattering spectra observed for the 514.5 nm line are shown in Figs. 1 and 2 for parallel (⊥⊥) and crossed polarizations (⊥∥) of the incident and scattered light, respectively. Similar spectra were obtained using the 488.0 nm radiation. Corresponding spectra were also obtained for the anti-Stokes components of these spectra. This indicates that all the observed spectral lines (Figs. 1 and 2) are caused by first-order Raman light scattering by optical phonons corresponding to the center of the Brillouin zone of the $CdGeAs_2$ lattice. These spectra demonstrate a clear polarization dependence and indicate that the vibrational modes are anisotropic.

The general law governing the behavior of chalcopyrite crystals involves a relatively weak dependence of the vibrational spectra for the optical phonons on the direction of the wave vector of phonon propagation relative to the crystallographic axes.[8,9] This characteristic indicates that the dispersion of the optical phonons corresponding to the center of the Brillouin zone is low.

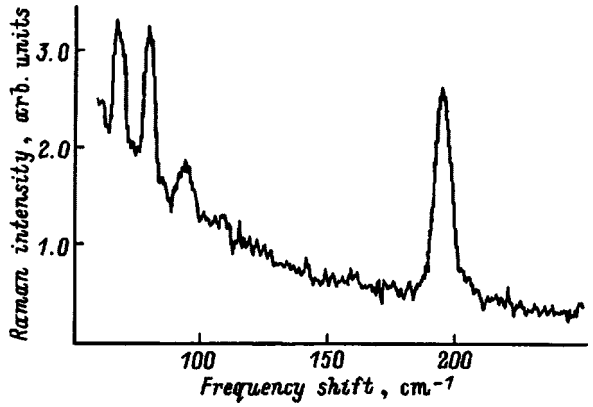

FIG. 1. Raman scattering spectrum of a p-$CdGeAs_2$ single crystal obtained using 514.5 nm Ar^+ laser radiation with backscattering from the (112) plane, for parallel polarized incident and scattered light (⊥⊥) at $T=300$ K. Slit width $R=1.3$ cm^{-1}.

In the first-order light scattering process phonons of symmetry Γ_1-, $\Gamma_4(TO)$- and $\Gamma_5(TO)$ are active for parallel polarized incident and scattered light (⊥⊥) while those of Γ_3- and $\Gamma_5(LO)$ symmetry are active for crossed polarizations (⊥∥). To identify the observed phonon lines it is also useful to compare the light scattering spectra of $CdGeAs_2$ crystals and another member of this class—$CdSnP_2$, which also has a chalcopyrite structure.[8]

The measured frequencies together with the results of our interpretation of the phonon line symmetry are presented in Table I. A comparison with the structure of zinc blende indicates that the $\Gamma_5(TO)$-, $\Gamma_4(TO)$-, and $\Gamma_5(LO)$ phonons with frequencies of 66, 78, and 94 cm^{-1}, respectively, originate from acoustic phonon branches. These phonons may be represented as the result of folding of the appropriate acous-

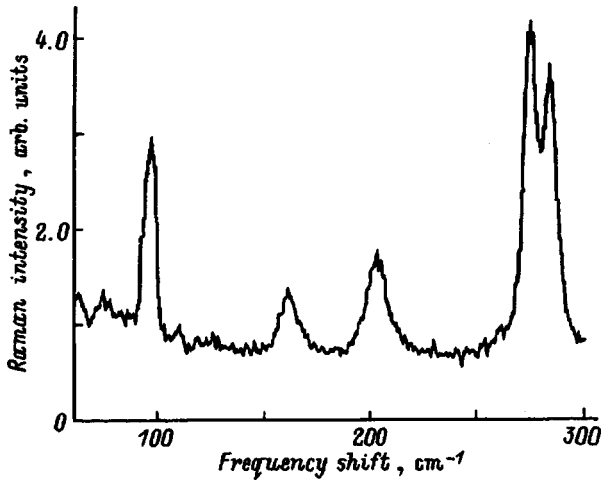

FIG. 2. Raman scattering spectrum of a p-$CdGeAs_2$ single crystal obtained using 514.5 nm Ar^+ laser radiation with backscattering from the (112) plane, for crossed polarizations of the incident and scattered light (⊥∥) at $T=300$ K. Slit width $R=1.3$ cm^{-1}.

TABLE I. Measured frequencies and interpretation of the type of phonon symmetry in a $CdGeAs_2$ crystal.

Frequency, cm^{-1}	Type of symmetry
66	$\Gamma_5(TO)$
78	$\Gamma_4(TO)$
94	$\Gamma_4(LO)$
161	$\Gamma_5(LO)$
193	Γ_1
202	$\Gamma_5(LO)$
273	$\Gamma_5(LO)$
283	$\Gamma_5(LO)$

tic branches toward the center of the Brillouin zone of $CdGeAs_2$. The observation of a clearly defined polarization dependence for the spectra as well as the absence of any appreciable dependence of the intensity and frequency of the observed lines (see Table I) when the sample is swept in $\approx 300\mu$ m steps over an area of $\approx 3\times 3$ mm indicates these crystals are high-quality and homogeneous.

For $ZnSiP_2$ crystals, which also have a chalcopyrite structure, it was shown that the main contribution to the Γ_1 phonons is preferentially attributable to anion vibrations, while the cation atoms may be considered to be in a state of rest.[8] Assuming that this relation is also satisfied for other chalcopyrite crystals, the difference in the frequencies of the Γ_1 phonons in the Keating model[10] for a $CdSnP_2$ crystal, for which we found 193 cm^{-1}, is only $\sim 1\%$ if we take into account the difference in the atomic masses of P and As. This then indicates a small difference between the force constants in $CdGeAs_2$ and $CdSnP_2$ crystals.

3) Carrier transport effects. The tensors of the electrical conductivity σ and the Hall coefficient R were investigated for (001) oriented samples with average dimensions of $1\times 2\times 15$ mm, which allowed us to measure the following tensor components: $\sigma^{\perp}$ and $R^{\perp}$. The kinetic coefficients were measured using a four-probe compensation method in the temperature range 80–400 K in weak static electric and magnetic fields. After mechanical polishing, the surface of the samples was usually treated with a polishing etchant (3 parts HNO_3:1 partHF:3 parts H_2O) at $T=300$ K for approximately 1 min. Current and potential contacts were prepared by deposition of copper from an aqueous solution of $CuSO_4$ at appropriate points on the samples. The relative measurement error for σ and R did not exceed 3% and 5%, respectively.

The measurements show that this method can produce a p-type material with a free hole concentration $p\approx 1.5\times 10^{15}$ cm^{-3} at $T=300$ K, which corresponds to the lowest p values published in Refs. 11 and 12. The main feature of the crystals used is their high electrical homogeneity. The spread of $\sigma^{\perp}$ and $R^{\perp}$ values in measurements of the voltage drop at different pairs of probes did not exceed 1% at $T=300$ K and when the surface of the samples was probed with an optical probe (~ 0.2 mm in diameter), the photovoltage typical of all previously studied p-$CdGeAs_2$ samples was not observed.

Typical temperature curves $\sigma^{\perp}(T)$ and $R^{\perp}(T)$ for current transport in a $\mathbf{i}\perp\mathbf{c}$ geometry, where $\mathbf{c}$ is the unit vector

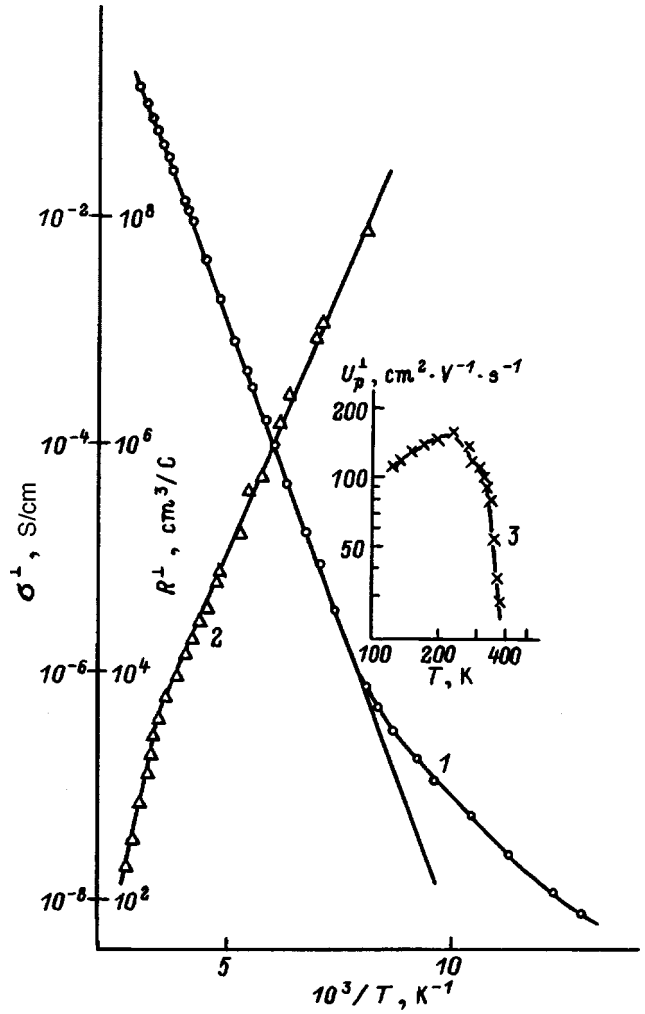

FIG. 3. Temperature dependences of the electrical conductivity $\sigma^{\perp}$ (*1*), the Hall constant $R^{\perp}$ (*2*), and the Hall mobility of the holes $U_p^{\perp}$ (*3*) for a p-$CdGeAs_2$ single crystal.

along the tetragonal axis are plotted in Fig. 3 (curves *1* and *2*). These curves are similar to those plotted in Refs. 11 and 12 and show that below 300 K, p-type hole impurity conductivity is observed in these crystals and the faster drop in $R^{\perp}$ at $T>300$ K is caused by the onset of mixed conduction. The exponential decrease in conductivity and increase in the Hall coefficient when the samples are cooled to $\approx 120-130$ K reveal a similar slope and may be attributed to thermalization of electrons at the acceptor level. Figure 3 shows that $\lg R^{-1}\sim T^{-1}$. Since the level of the growth technology for $CdGeAs_2$ crystals does not provide the basis for assessing the degree of compensation beforehand, this behavior of $R^{\perp}(T)$ may suggest that in these crystals in the temperature range 140–300 K the free hole concentration remains below the concentration of acceptors and compensating donors ($p\ll N_A<N_D$). For a nondegenerate hole gas and a single acceptor level, neglecting the influence of excited states, the following expression[13] can be used to analyze the curves $p(T)$

$$p=[(N_A-N_D)/N_A](N_v/g)\ \exp(-E_A/kT). \tag{3}$$

An analysis of the experimental curves $p(T)$ using this ex-

pression yielded the acceptor level activation energy $E_A = 0.175$ eV and their degree of compensation by donors $K \approx 0.5-0.6$. For calculations of the effective density of states in the valence band N_v the effective hole mass was taken to be $m_1 \approx 0.3m_0$ (Ref. 14). It should be noted that this acceptor activation energy falls within the range of known E_A values for $CdGeAs_2$ (Ref. 1). Deviations from the exponential behavior of $\sigma^{\perp}(T)$ at $T < 120$ K may be caused by a transition to conduction via localized states.

The dependence behavior of the Hall mobility tensor $U_p^{\perp}(T)$ on the holes in these crystals (curve *3* in Fig. 3) was similar to that observed earlier for $CdGeAs_2$ crystals[11,12,14] and may be interpreted as the result of competition between two scattering mechanisms: impurity ions and lattice vibrations. The sharp drop in $U_p^{\perp}$, like the decay of the Hall constant at $T > 300$ K, may be caused by the participation of two kinds of charge carriers in the transport process. Assuming that the coefficient of anisotropy of the Hall mobility of the holes is $K = U_p^{\parallel}/U_p^{\perp}$, according to Ref. 11, we can estimate the maximum Hall mobility of the holes as $U_p^{\parallel} \approx 500$ cm^2/V·s for this material, near the temperature $T^m \approx 220$ K at which the mobility passes through a maximum as a result of the impurity mechanism being replaced by the lattice one. We stress that the estimated $U_p^{\parallel}$ value is slightly lower than that in Ref. 11. This may indicate a higher acceptor concentration compared with the samples used in Ref. 11. Thus, the lower $U_p^{\parallel}$ values obtained for our samples compared with Ref. 11 may be caused by the higher acceptor compensation.

4) Photosensitivity of In/p-CdGeAs$_2$ structures. A semitransparent layer of indium was deposited on the $CdGeAs_2$ plane parallel to the tetragonal **c** axis by thermal deposition in vacuum. This contact exhibits a photovoltaic effect whose polarity corresponds to the negative polarity at the barrier contact and did not depend on the incident photon energy or on the localization of the light probe on the surface of the structures. These In/p-$CdGeAs_2$ surface barrier structures exhibited the maximum current photosensitivity when they were illuminated on the barrier contact side $S_i \approx 20\mu$ A/W and $S_U \approx 2$ V/W at $T = 300$ K. The photosensitivity increased by two to three orders of magnitude when the temperature was reduced to ≈ 80 K.

Typical spectral dependences of the short-circuit photocurrent for one of these structures are plotted in Fig. 4. The energy position of the long-wavelength edge of the photocurrent for these structures with its distinct step corresponds to interband A-transitions in $CdGeAs_2$ (Ref. 15). Above the energy of the A-transitions, the photocurrent of surface-barrier structures typically continues to increase and reaches a maximum near the energy of the B transitions.[15] It can be seen from Fig. 4 that the photocurrent remains high over a wide spectral range within the fundamental absorption of $CdGeAs_2$, which indicates that the efficiency of photogenerated pair collection is sufficient to suppress surface recombination. It can be seen from Fig. 4 (curve *2*) that a decrease in temperature is accompanied by broadening of the long-wavelength photocurrent edge as a result of enhanced photoactive absorption involving defect levels. The long-wavelength photosensitivity peak at $\hbar\omega_D \approx 0.48$ eV may be

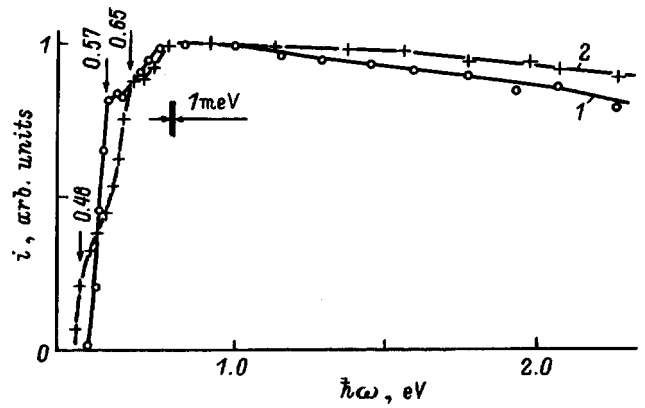

FIG. 4. Spectral dependences of the photocurrent i normalized to the same number of incident photons, for an In/$CdGeAs_2$ structure using natural radiation: $T(K)$: *1*—300, *2*—77.

attributed to transitions of electrons to the conduction band from the level $E_V + 0.17$ eV, which is observed in the temperature dependences of the kinetic coefficients of these crystals (Fig. 3).

When the plane of the In/$CdGeAs_2$ structures parallel to the **c** axis is illuminated by linearly polarized radiation, the photocurrent along the normal to it exhibits a periodic dependence on the azimuthal angle φ between the electric vector of the light wave **E** and **c**, as for $CdGeAs_2$ homojunctions, which is typical of uniaxial crystals.[14] The polarization difference of the photocurrent $\Delta i = i^{\parallel} - i^{\perp}$ (curve *1* in Fig. 5) is positive in accordance with the selection rules for interband A transitions in $CdGeAs_2$ (Ref. 14) and has a maximum near the A-transition energy. Unlike homojunctions, for which the influence of absorption in the layer adjacent to the active region of the structures changes the sign of Δi to

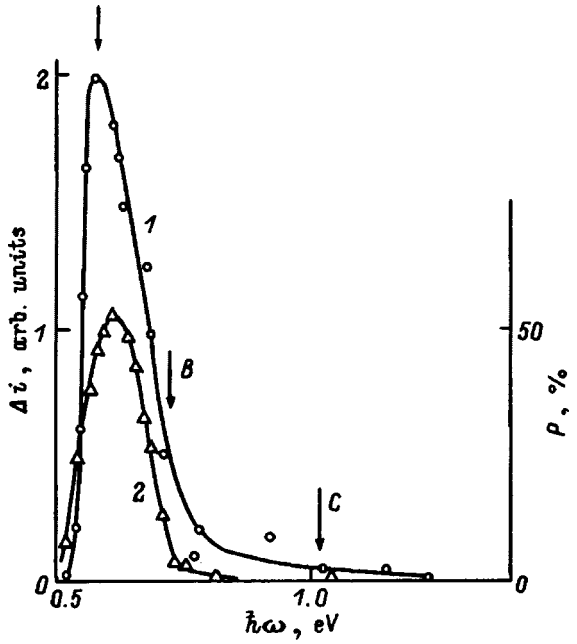

FIG. 5. Spectral dependences of the photocurrent polarization difference Δi (*1*) and the coefficient of natural photopleochroism P (*2*) for an In/$CdGeAs_2$ structure at $T = 300$ K.

negative,[14] in In/$CdGeAs_2$ structures we find $\Delta i > 0$ over the entire range of polarization photosensitivity. The short-wavelength drop in Δi is caused by the onset of B transitions, which dominate for $\mathbf{E} \perp \mathbf{c}$. The coefficient of natural photopleochroism[15] of p-$CdGeAs_2$ single-crystal surface-barrier structures is also positive and dominates near the A-transition energy (curve *2* in Fig. 5), as for other direct-gap II-IV-V_2 chalcopyrite crystals.

To sum up, this method of directional crystallization of $CdGeAs_2$ from a near-stoichiometric flux can reproducibly give single crystals with a fairly low hole concentration and high electrical homogeneity. The clear polarization dependence of the spectra of inelastic light scattering by optical phonons combined with the absence of any local dependence of the intensity and frequency of the observed lines provides evidence of the high quality and homogeneity of these single crystals. Surface-barrier structures using these single crystals may be used as wide-band detectors for natural light, and selective photoanalyzers for linearly polarized radiation.

[1] V. D. Prochukan and Yu. V. Rud', Fiz. Tekh. Poluprovodn. **12**, 209 (1978) [*sic*].
[2] N. A. Goryunova, F. P. Kesamanly, É. O. Osmanov, and Yu. V. Rud', Izv. Akad. Nauk SSSR, Neorg. Mater. **1**, 885 (1965).
[3] R. F. Mekhtiev, É. O. Osmanov, and Yu. V. Rud', Prib. Tekh. Eksp. **2**, 179 (1964).
[4] Yu. V. Rud', Author's Abstract of Thesis for Candidate's Degree [in Russian], A. F. Ioffe Physicotechnical Institute, Leningrad (1965).
[5] N. A. Goryunova, A. A Grinberg, S. M. Ryvkin, I, M, Fishman, G. P. Shpen'kov, and I. D. Yaroshetskiĭ, Fiz. Tekh. Poluprovodn. **2**, 1525 (1968) [Sov. Phys. Semicond. **2**, 1272 (1968)].
[6] J. L. Shay and J. H. Wernick, *Ternary Chalcopyrite Semiconductors. Growth, Electronic Properties, and Applications* (Pergamon Press, Oxford, 1975).
[7] P. G. Shunemann and T. M. Pollak, *Abstracts of 1996 ICEM Fall Meeting of the MRS*, Boston (1996), p. 371.
[8] G. Irmer, A. Heinrich, and J. Monecke, Phys. Status Solidi B **132**, 93 (1985).
[9] I. P. Kaminov, E. Buehler, and J. H. Wernick, Phys. Rev. B **2**, 960 (1970).
[10] P. N. Keating, Phys. Rev. B **145**, 637 (1966).
[11] V. Yu. Rud' and Yu. V. Rud', Fiz. Tekh. Poluprovodn. **24**, 2181 (1990) [Sov. Phys. Semicond. **24**, 1352 (1990)].
[12] V. Yu. Rud' and Yu. V. Rud', Jpn. J. Appl. Phys. **32**, 672 (1993).
[13] J. S. Blakemore. *Semiconductor Statistics* [Pergamon Press, Oxford, 1962; Mir, Moscow, 1964].
[14] A. S. Borshchevskiĭ, N. E. Dagina, A. A. Lebedev, K. Ovezov, I. K. Polushina, and Yu. V. Rud', Fiz. Tekh. Poluprovodn. **10**, 1905 (1976) [Sov. Phys. Semicond. **10**, 593 (1976)].
[15] F. P. Kesamanly, V. Yu. Rud', and Yu. V. Rud', Fiz. Tekh. Poluprovodn. **30**, 1921 (1996) [Sov. Phys. Semicond. **30**, 1001 (1996)].

Translated by R. M. Durham

Depth distribution of point defects in Si bombarded by high-energy N^{5+} and Si^{5+} ions

A. V. Dvurechenskiĭ and A. A. Karanovich

Institute of Semiconductor Physics, Siberian Branch of the Russian Academy of Sciences, 630090 Novosibirsk, Russia

R. Grötzschel, F. Herrmann, and R. Kegler

Rossendorf Scientific-Research Center, D-01314 Dresden, Germany

A. V. Rybin

Mordovian State Pedagogical Institute, 430007 Saransk, Russia

(Submitted September 2, 1997)
Fiz. Tverd. Tela (St. Petersburg) **40**, 217–222 (February 1998)

Electron spin resonance has been used to study the depth distribution of point defects in Si samples bombarded by N^{5+} ($E=16$ MeV) and Si^{5+} ($E=26.8$ MeV) ions at 175 and 300 K in the dose range $(4-8)\times10^{15}$ cm^{-2}. It was established that unlike the implantation of moderate-energy Si ions ($E\sim100$ keV), the depth distributions of planar tetravacancies in samples bombarded by ions at 300 K under these conditions have two maxima. The experimental results indicate that the tetravacancy density maximum closer to the surface is formed as a result of secondary defect formation processes. No continuous amorphous layer was observed in the bulk of any of the Si samples. This experimental observation is evidence of defect annealing which takes place when high-energy ions are implanted in Si. © *1998 American Institute of Physics.* [S1063-7834(98)01002-8]

Ion implantation with $E\sim1$ MeV/ion is beginning to be used successfully for the production of integrated circuits and microelectronics devices with an increased density of active and passive elements.[1,2] Clearly, in the future the energy which will be used in implantation to fabricate integrated circuits will be ~1 MeV/a.m.u.. Although the main laws governing defect formation processes in Si bombarded by $E\sim10$ keV/a.m.u. ions have been fairly well studied, those for Si bombarded by $E\sim1$ MeV/a.m.u. ions have been little studied, even though the first publications on this topic appeared more than twenty years ago.[3] Note that at present, there are very few reported investigations of the depth distributions of point defects in Si irradiated by $E\sim1$ MeV/a.m.u. ions as a function of the sample temperature under irradiation.

Here ESR was used to investigate the structure and depth distribution of point defects in Si bombarded by ~1 MeV/a.m.u. N^{5+} and Si^{5+} ions at temperatures of 175 and 300 K in the dose range $D=(4-8)\times10^{15}$ cm^{-2}.

1. EXPERIMENTAL METHOD AND TECHNIQUE

For the experiments we used commercial, zone-refined Si doped with boron ($\rho\approx1$ k$\Omega\cdot$cm). The samples measured $10\times5\times0.3$ mm.

The samples were bombarded with ions at the Rossendorf Scientific Center (Germany) using the TANDEM ion accelerator. The implantation parameters are given in Table I. To prevent heating, an indium-gallium paste was deposited on the unirradiated part of the samples which were then rigidly attached to a steel microscope stage which was mounted in a chamber with automatic temperature control over the range 175–500 K.

The ESR spectra were recorded using a Varian spectrometer in the microwave X range (9 GHz) at room temperature. The depth distribution profile of the concentration of paramagnetic defects was constructed by varying the intensity of the ESR signal while gradually removing Si layers from the irradiated side. The material was removed layer by layer by mechanical polishing using diamond paste (grain size ~1 μm). The thickness of the removed layer was determined by weighing the sample before and after polishing using analytic weights with an accuracy of 10^{-7} g. The absolute error in the determination of the thickness of the removed layer did not exceed 0.1 μm.

2. EXPERIMENTAL RESULTS AND DISCUSSION

1) *Atomic configuration of paramagnetic defects.* For Si samples irradiated under these conditions the ESR spectrum consists of two superposed components: a broad intense line with an isotropic g factor and a series of narrow lines whose position depends on the orientation of the magnetic field.

The first component has the same g factor as VV centers[4,5] (a VV center is a broken bond in an amorphous region, $g=2.0055$, $H_{pp}=(5-7)\times10^{-4}$ T, where H_{pp} is the line width of the ESR spectrum).

TABLE I. Implantation parameters.

Ion	E, MeV	D, Ion/cm^2	j, nA/cm^2	T, K
Si^{5+}	26.8	8×10^{15}	150	300
Si^{5+}	26.8	4×10^{15}	150	175
N^{5+}	16	6×10^{15}	30	300
N^{5+}	16	6×10^{15}	30	175

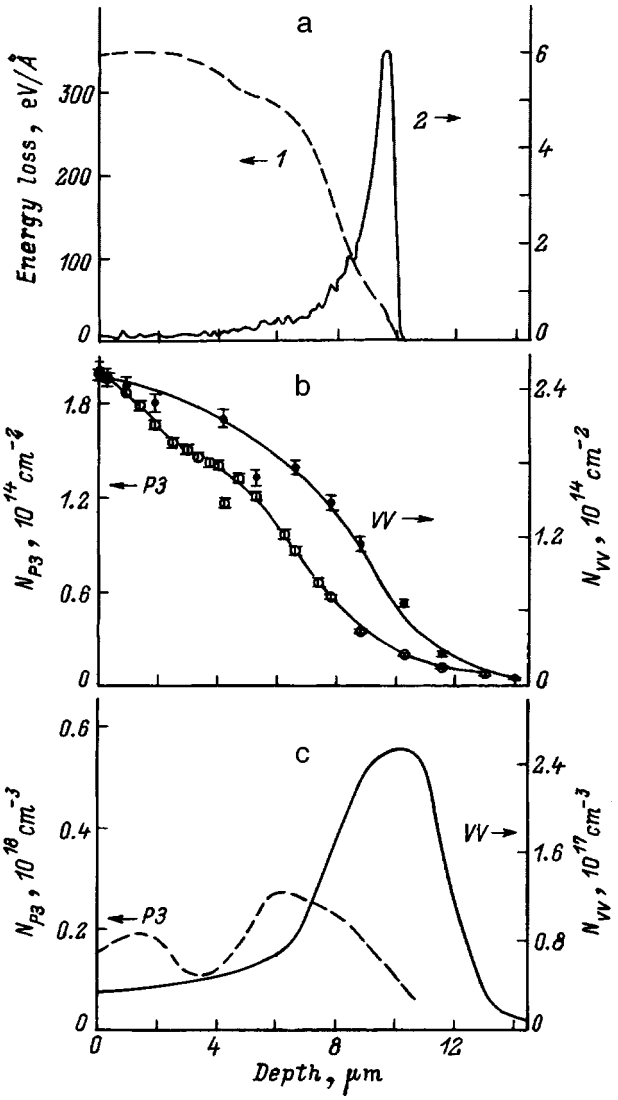

FIG. 1. Depth distribution of inelastic (*1*) and elastic (*2*) energy losses of implanted 26 MeV Si ions in Si (Ref. 8) (a), integrated depth distribution of layer concentration of planar tetravacancies ($P3$ center) and VV centers in Si bombarded with 26 MeV Si^{5+} ions (b), and differential depth distribution of bulk concentration of planar tetravacancies ($P3$ centers) and VV centers (c): $T=300$ K and $D=8\times10^{15}$ cm^{-2}.

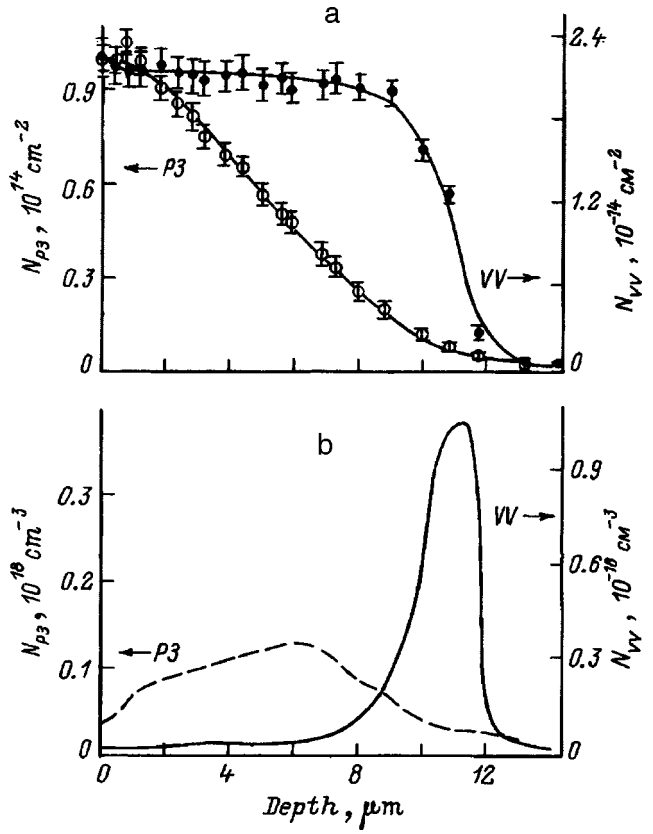

FIG. 2. Integrated depth distribution of layer concentration of planar tetravacancies ($P3$ centers) and VV centers in Si bombarded with Si^{5+} ions (a) and differential depth distribution of bulk concentration of planar tetravacancies ($P3$ centers) and VV centers in Si bombarded with Si^{5+} ions (b): $E=26.8$ MeV, $T=175$ K, and $D=4\times10^{15}$ cm^{-2}.

An analysis of the positions of the lines of the second component in the ESR spectrum for various magnetic field orientations identified this as the $P3$ spectrum[6,7] produced by planar tetravacancies.

2) *Depth distribution of VV centers.* The depth distributions in the irradiated samples have a single peak near the end of the path. The density of VV centers in Si samples bombarded by Si^{5+} ions at 300 and 175 K (Figs. 1c and 2b) and by N^{5+} ions at 300 K (Fig. 3b) show a slight increase in the initial sections of the range whereas for the samples bombarded by N^{5+} ions at 175 K the concentration of VV centers is below the sensitivity limit of the technique for most of the range (Fig. 3c).

We shall analyze the experimentally determined depth distributions of VV centers using known amorphization mechanisms, especially those studied by Gibbons.[9]

The distribution of VV centers in Si samples bombarded by Si^{5+} ions at 175 K correlates reasonably well with the distribution of primary radiation defects (Figs. 1a and 2b). In addition, the ratio of the concentration at the elastic ion stopping peak to the concentration at the beginning of the range is approximately the same for primary defects and for VV centers (≈60 for implantation of Si^{5+} ions in Si). This implies that the number of amorphous inclusions formed by ion stopping per unit path length is approximately proportional to the number of primary displacements. Thus, in this case, the amorphous phase is formed as a result of the overlap of subcascades in the track of a single ion.

The distributions of VV centers in samples bombarded by Si^{5+} ions at 300 K and in those bombarded by N^{5+} ions are broadened appreciably in both the directions toward and away from the surface. For these samples the ratio of the concentration of primary defects at the elastic ion stopping peak to this concentration at the beginning of the range is several times greater than the ratio of the concentration of VV centers at the distribution peak to its concentration at the beginning of the range (Figs. 1a and 1c, 3a and 3b). Thus, the formation of the depth distribution profiles of VV centers in this case is appreciably influenced by secondary defect formation processes such as the diffusion of Frenkel-pair components toward the surface and in the depth direction, and their interaction with each other and with defect complexes.

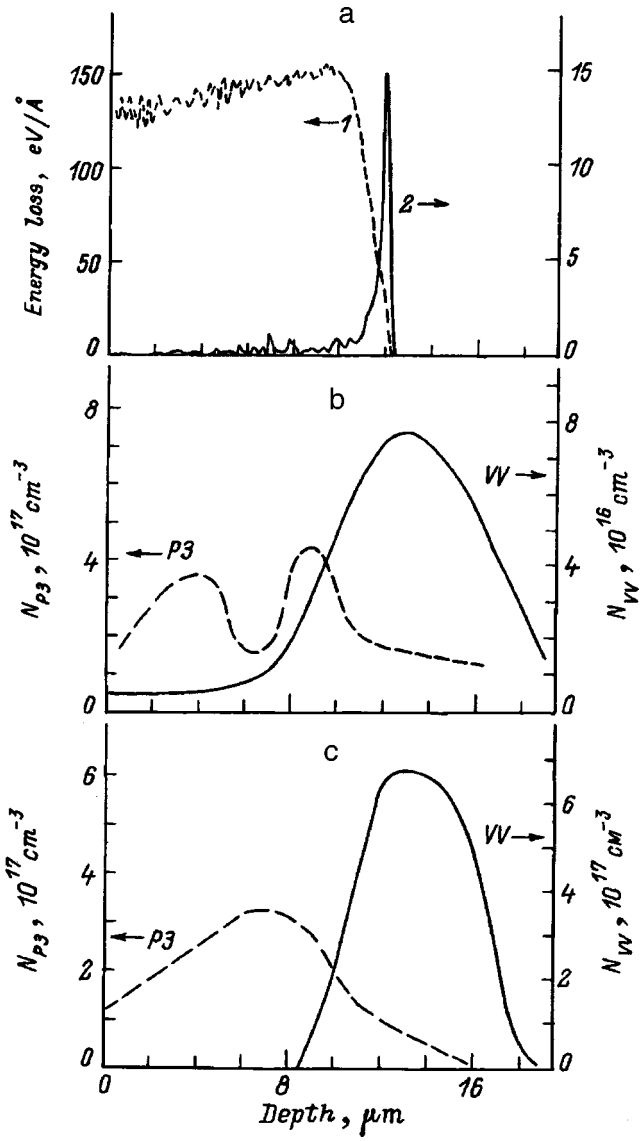

FIG. 3. Depth distribution of inelastic (*1*) and elastic (*2*) energy losses of 16 MeV N ions implanted in Si (Ref. 8) (a) and differential depth distribution of bulk concentration of planar tetravacancies ($P3$ centers) and VV centers in Si bombarded with 16 MeV N^{5+} ions at 300 (b) and 175 K (c): $D=6\times10^{15}$ cm^{-2}.

The concentration of VV centers in samples bombarded by 16 MeV N^{5+} ions at 175 K in the depth range $0<x<(2/3)R_p$ is below the sensitivity limit of the method (i.e., the intensity of the ESR line caused by the paramagnetism of the VV centers does not vary in this depth range) whereas near the average projected range R_p the distribution of VV centers has a broad maximum (Fig. 3c). Since the full-width at half maximum of the VV centers is approximately ten times that for the corresponding maximum of the primary Frenkel pairs (Figs. 3c and 2a), it may be concluded that the depth distribution of VV centers in these samples is mainly formed by overlap of disordered regions created by different ions and partly as a result of interaction between primary radiation defects and disordered regions.

3) *Absence of a continuous amorphous layer within the bulk of the implanted silicon.* As a result of these investigations, it was also observed that no continuous amorphous layer was formed in the bulk of any of the irradiated Si samples. This is evidenced by the low concentrations of VV centers at the elastic stopping peak ($N_{VV}<10^{18}$ cm^{-3}), which is between two and three orders of magnitude lower than the concentration typical of a continuous amorphous layer ($N_{VV}\sim10^{20}$ cm^{-3} (Refs. 4 and 5). In addition, the concentration of tetravacancies at any point in the range is 10^{16}–10^{17} cm^{-3} (note that a tetravacancy, like all other defects, excepting VV centers, can only exist in the crystal phase of Si). Nevertheless, it is well known[9,10] that the implantation of $\sim$10 eV/a.m.u. Si ions under the same implantation conditions as those used in our experiments, leads to complete amorphization of the implanted layer. Note that, using positron annihilation, the authors of Ref. 11 observed the formation of a continuous amorphous layer near R_p in Si samples bombarded by Si ions at $T\approx300$ K with $E\approx12$ MeV and $D=10^{16}$ cm^{-2}.

Thus, doses appreciably higher (more than an order of magnitude higher) than the critical amorphization doses characteristic of moderate-energy implantation (under otherwise the same irradiation conditions) are required for the formation of a continuous amorphized layer at the end of the range under bombardment by $\sim$1 MeV/a.m.u. Si ions.

For all implantation conditions used in these experiments, the calculated energy density released by the high-energy ions at the elastic stopping peak is 10^{24}–10^{25} cm^3 and is sufficient to form a continuous amorphous layer in Si bombarded by moderate-energy ions under otherwise the same irradiation conditions.[12,13]

Thus, the absence of a continuous amorphous layer in the bulk of these Si samples may be caused by the following factors: 1) implantation of $\sim$1 MeV/a.m.u. ions in Si is accompanied by partial annealing of defects, which, as has been indicated in various studies, is possible if the inelastic energy loss of the implanted ions exceed $\approx$100 eV/Å (Refs. 14 and 16); 2) near R_p the implanted ions create mobile and fixed defects, whose interaction has the result that the number of fixed defect complexes per unit volume does not exceed the critical concentration needed to form a continuous amorphous layer.[13,17] Mobile and fixed defects are formed near R_p because the energy dispersion of implanted ions with energy $E\approx1$ MeV/a.m.u. in a solid near the end of the range is $\sim$1 MeV (Ref. 8). Thus, ions whose energy near R_p is $\approx$10 keV will create predominantly fixed defects since ion-atom collisions take place with a small impact parameter. Ions whose energy at the end of the range is $\approx$1 MeV will create predominantly vacancies and interstitial atoms since in this case, ion-atom collisions take place with a large impact parameter. Thus, in high-energy implantation ($E\sim1$ MeV/a.m.u.) the formation of a continuous amorphous layer may be impeded by the interaction between mobile and fixed defects.[13,17]

4) *Depth distribution of planar tetravacancies.* In samples irradiated at 175 K the tetravacancy density increases monotonically from the surface and reaches a maximum at a certain depth ($x<R_p$) after which it decreases monotonically (Figs. 2b and 3c) as a result of a decrease in the fraction of the volume occupied by the crystalline phase.[16] The range distributions of the tetravacancy densities

in samples bombarded by ions at $T=300$ K (Figs. 1c and 3b) do not correlate with the distribution of the elastic and inelastic energy losses of the implanted ions (Figs. 1a and 3a) and are characterized by two peaks in the Si bulk. One of these peaks is closer to R_p and the other is 2–3 μm from the surface. It should be noted that in the depth range $0<x<4$ μm the layer concentration of tetravacancies in Si samples bombarded by N^{5+} ions at 300 K ($E=16$ MeV, $D=6\times10^{15}$ cm^{-2}) is almost twice this concentration in samples bombarded by N^{5+} ions at 175 K ($E=16$ MeV, $D=6\times10^{15}$ cm^{-2}). This drop in the tetravacancy density near the end of the range is evidently attributable to the reduced volume of the crystalline phase for irradiation at 175 K. Note that the maximum density of defects (divacancies, tetravacancies, A and E centers) in Si samples bombarded by high-energy ions ($E\sim1$ MeV/a.m.u.) at room temperature was observed by the authors of Refs. 14, 18–21 at the depth $x\sim(0.2-0.5)R_p$ using ESR, Rutherford backscattering, infrared spectroscopy, positron annihilation, and capacitive deep-level transient spectroscopy.

In our view, the formation of the defect-density maximum close to the surface cannot be explained qualitatively by denser cascades of recoil atoms in the initial sections of the high-energy ion range[18] because our experimental results indicate that the formation of a tetravacancy density maximum close to the surface depends on the sample temperature under irradiation. The authors of Ref. 14 suggested that the defect density maximum close to the surface is formed as a result of the interaction of vacancies which diffuse toward the surface from the region of maximum elastic energy losses. However, this interpretation is also purely qualitative and incomplete, since it neglects the diffusion of interstitial atoms toward the surface and their annihilation by vacancies, as well as interactions of primary radiation defects with various defect complexes.

Our experimentally determined temperature dependences of the tetravacancy range distributions indicate that the tetravacancy density maximum close to the surface is formed as a result of secondary defect formation processes, probably as a result of the interaction of vacancies among themselves and/or with vacancy complexes.

3. NUMERICAL SIMULATION

One of the most likely reasons for the formation of a tetravacancy density maximum near the surface is that the steady-state depth distribution of vacancies under ion bombardment of Si may also have a maximum in the initial sections of the range. Interaction of these vacancies among themselves and/or with vacancy complexes may lead to the formation of a tetravacancy maximum. The possible existence of this vacancy density maximum derives from the following reasoning.

Ion bombardment of Si is inevitably accompanied by spatial redistribution of Frenkel pair components[22] since the diffusion coefficient of interstitial atoms is considerably greater than that of vacancies. Consequently, in the steady state the ratio of the concentration of interstitial atoms to that of vacancies varies substantially over the range. It is known that the surface is a powerful sink for vacancies and interstitial atoms. Thus, in the immediate vicinity of the surface, even if defect interaction is neglected, the concentration of interstitial atoms may be lower than the concentration of vacancies since in the diffusion approximation, the coefficients of the quasichemical reactions which determine the interaction between components of Frenkel pairs and sinks, are directly proportional to their diffusion coefficients.[10] If the diffusion of interstitial atoms and vacancies from their generation site to the surface is considered as fluxes of noninteracting particles, in certain parts of the range some distance from the surface, the concentrations of interstitial atoms and vacancies will clearly be comparable whereas in the region of maximum generation, the vacancy concentration will substantially exceed the concentration of interstitial atoms. Thus, quasichemical reactions, especially annihilation of interstitial atoms with vacancies, a sink for vacancies and interstitial atoms at the surface, and also interaction between components of Frenkel pairs and various defect complexes, may have the result that, in addition to concentration maxima near R_p, the steady-state depth distribution of vacancies will also have another maximum closer to the surface.

To check this hypothesis, we carried out a numerical simulation, which involved calculating the steady-state depth distribution of the densities of vacancies and interstitial atoms for the implantation of Si with high-energy ($E\sim1$ MeV/a.m.u.) and moderate-energy ($E\sim10$ keV/a.m.u.) ions. The following assumptions were made.

1) The steady-state depth distributions of vacancies and interstitial atoms may be determined by solving a system of nonlinear differential equations written in the diffusion approximation[10]

$$D_V d^2V/dx^2=\beta_{IV}IV+\beta_{VV}V^2+\beta_V V+g_V(x),$$

$$D_I d^2I/dx^2=\beta_{IV}IV+\beta_{II}I^2+\beta_I I+g_I(x). \quad (1)$$

Here V and I are functions describing the range distributions of the densities of vacancies and interstitial atoms, D_I and D_V are the diffusion coefficients of interstitial atoms and vacancies, respectively, $g_I(x)$ and $g_V(x)$ are the generation terms describing the depth distributions of the densities of interstitial atoms and vacancies formed by elastic stopping of a given ion flux ($g(x)$ was calculated using the TRIM-94 program[8] where $g_I(x)$ and $g_V(x)$ were assumed to be equal), β_{IV}, β_{VV}, and β_{II} are the quasichemical reaction constants which determine the interaction between vacancies and an interstitial atom, between two vacancies, and between two interstitial atoms, respectively, and β_I and β_V are the quasichemical reaction constants which determine the interaction between sinks and components of Frenkel pairs.

2) The sink distribution was assumed to be directly proportional to the distribution of elastic energy losses.

3) The system (1) was solved for the following boundary conditions: a) the irradiated surface of the sample was assumed to be an ideal sink for vacancies and interstitial atoms, i.e., the trapping coefficient of interstitial atoms and vacancies, which determines their interaction with the surface, was assumed to be infinite; b) the unirradiated surface of the

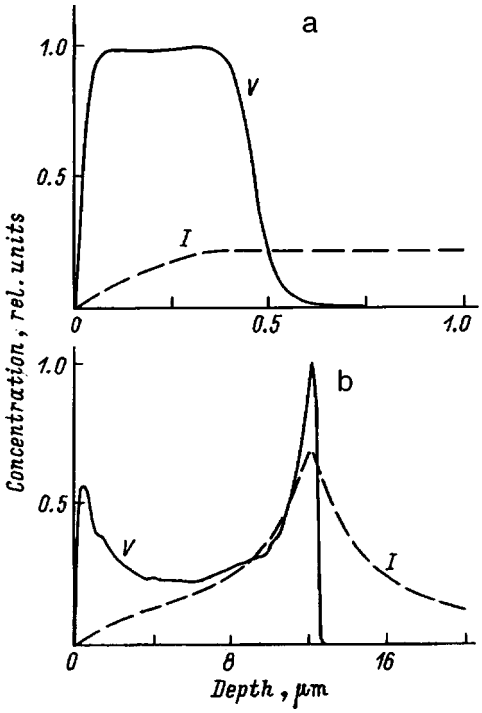

FIG. 4. Calculated steady-state depth distribution of the bulk concentration of vacancies V and interstitial atoms I in Si bombarded with 200 keV (a) and 16 MeV (b) N ions. In the calculations D_V and D_I were taken as 2×10^{-7} and 5×10^{-5} cm^2/s, respectively.

sample was assumed to be a reflecting face, i.e., the trapping coefficient of interstitial atoms and vacancies, which determines their interaction with the surface, was assumed to be zero (the thickness of the samples was taken as 300 μm).

The system (1) was solved by an iterative method described in Ref. 23. The diffusion coefficients of the vacancies and interstitial atoms were assumed to be free parameters.

An analysis of the solutions of system (1) revealed the following:

1) The steady-state depth distribution of the vacancy density, having two maxima—the second positioned at the end of the range and the first closer to the surface—may be obtained by solving system (1) for reasonable values of the free parameters: $D_V \leqslant 3\times10^{-7}$ cm^2/s and $D_I \geqslant 5\times10^{-5}$ cm^2/s.

According to the published data, the diffusion coefficients of vacancies and interstitial atoms at room temperature are $\sim10^{-8}$ and $\sim10^{-5}$ cm^2/s, respectively.[10]

2) A bimodal vacancy distribution cannot be obtained by solving system (1) for any values of the free parameters if the term $\beta_{IV}IV$ responsible for the annihilation of Frenkel pair components is eliminated from system (1). However, if the terms responsible for interaction between vacancies and interstitial atoms ($\beta_{II}I^2, \beta_{VV}V^2$), and for their interaction with sinks ($\beta_I I, \beta_V V$) are alternately eliminated from the system, a bimodal vacancy distribution may be obtained by solving system (1) for values of the free parameters in the range indicated above.

Figure 4 shows calculated depth distributions of vacancies and interstitial atoms in Si samples bombarded by 16 MeV and 20 keV N^{5+} ions (the free parameters used to solve system (1) were the same in both cases). The density maxima for the calculated depth distributions of the vacancy concentrations are poorly resolved for moderate-energy ion implantation of Si (Fig. 4a) and well resolved for high-energy ion implantation (Fig. 4b). The reason for this is obvious: when Si is bombarded by moderate-energy ions, the region of maximum Frenkel pair generation is situated in the immediate vicinity of the surface whereas for high-energy ion implantation this region is some distance from the surface. To conclude, the results of this numerical simulation indicate that the formation of a tetravacancy density maximum close to the surface when $E\sim1$ MeV/a.m.u. ions are implanted in Si at 300 K, may be caused by the spatial redistribution of vacancies and interstitial atoms and their interaction with the surface, between themselves, and with various defect complexes.

[1] J. Ogawa and R. Koelsch, Solid State Technol. **11**, 28 (1993).
[2] A. La Ferla, E. Rimini, A. Garnero, and A. Golanski, Nucl. Instrum. Methods Phys. Res. **55**, 561 (1991).
[3] R. L. Fleischer, P. B. Price, and R. M. Walker, *Nuclear Tracks in Solids. Principles and Application* (University of California Press, Berkeley, 1975).
[4] N. N. Gerasimenko, A. V. Dvurechenskiĭ, and L. S. Smirnov, Fiz. Tekh. Poluprovodn. **5**, 1700 (1971) [Sov. Phys. Semicond. **5**, 1487 (1971)].
[5] N. N. Gerasimenko, A. V. Dvurechenskiĭ, and L. S. Smirnov, Fiz. Tekh. Poluprovodn. **6**, 1111 (1972) [Sov. Phys. Semicond. **6**, 965 (1972)].
[6] K. L. Brower and W. J. Beezhold, Appl. Phys. **43**, 3499 (1972).
[7] W. Jung and G. S. Newel, Phys. Rev. **132**, 648 (1979).
[8] J. F. Ziegler, J. P. Biersack, and U. Littmark, *Stopping and Ranges of Ions in Matter* (Pergamon Press, New York, 1985).
[9] J. F. Gibbons, Proc. IEEE **60**, 1062 (1972).
[10] *Problems in Semiconductor Radiation Technology*, edited by L. S. Smirnov [in Russian], Nauka, Moscow (1980).
[11] J. Makinen, E. Punkka, A. Vehanen, and E. Arevatanen, J. Appl. Phys. **67**, 990 (1990).
[12] F. F. Komarov, A. P. Novikov, V. S. Solov'ev, and S. Yu. Shiryaev, *Structural Defects in Ion-Implanted Silicon* [in Russian], Minsk (1990).
[13] V. S. Vavilov, V. F. Kiselev, and B. N. Mukashev, *Defects in Silicon and on its Surface* [in Russian], Nauka, Moscow (1989).
[14] T. A. Belykh, A. L. Gorodishchensky, L. A. Kazak, and A. R. Urmanov, Nucl. Instrum. Methods Phys. Res. B **51**, 242 (1990).
[15] M. Takahashi, J. Nakata, and K. Kajjyama, Jpn. J. Appl. Phys. **20**, 2211 (1981).
[16] Y. Yajima, N. Natsuaki, K. Yokogawa, and S. Nishimatsu, Nucl. Instrum. Methods Phys. Res. B **55**, 607 (1991).
[17] O. W. Holland, Appl. Phys. Lett. **54**, 320 (1989).
[18] A. V. Dvurechenskii, A. A. Karanovich, A. V. Rybin, and R. Grötzschel, Nucl. Instrum. Methods Phys. Res. B **80/81**, 620 (1991).
[19] B. Nielson, O. W. Holland, T. C. Leung, and K. G. Lynn, J. Appl. Phys. **74**, 1636 (1993).
[20] F. Al'-Bauur, A. Yu. Didyk, I. P. Kozlov, N. M. Penina, and A. M. Zaĭtsev, Fiz. Tekh. Poluprovodn. **25**, 1841 (1991) [Sov. Phys. Semicond. **25**, 1109 (1991)].
[21] I. V. Antonova, A. V. Dvurechenskii, A. A. Karanovich, A. V. Rubin, S. S. Shaimeev, and H. Klose, Phys. Status Solidi A **147**, K1 (1995).
[22] N. B. Pridachin and L. S. Smirnov, Fiz. Tekh. Poluprovodn. **5**, 166 (1972) [Sov. Phys. Semicond. **5**, 135 (1972)].
[23] N. S. Bakhvalov, N. P. Zhidkov, and G. M. Kobel'kov, *Numerical Methods* [in Russian], Nauka, Moscow (1987).

Translated by R. M. Durham

Strontium diffusion in $Sr_{3-3x}La_{2x}\square_x(VO_4)_2$ solid solutions

O. N. Leonidova and I. A. Leonidov

Institute of Solid-State Chemistry, Ural Branch of the Russian Academy of Sciences, 620219 Ekaterinburg, Russia

G. I. Dontsov and A. S. Zhukovskaya

Urals State Technical University, 620002 Ekaterinburg, Russia

(Submitted February 27, 1997)
Fiz. Tverd. Tela (St. Petersburg) **40**, 223–226 (February 1998)

Layer-by-layer radiometric analysis in the temperature range 800–950 °C was used to measure the diffusion coefficients of ^{90}Sr, ^{45}Ca, ^{133}Ba radionuclides in $Sr_{3-3x}La_{2x}\square_x(VO_4)_2$ ($x=0,0.1,0.15,0.2,0.25$) solid solutions. It was established that $D^*_{Ca}>D^*_{Sr}>D^*_{Ba}$. An increase in the concentrations of vacancies ($\square$) in the strontium sublattice leads to increased coefficients of diffusion of rare-earth metal cations. The activation energies for radionuclide diffusion were determined. It was shown that M^{2+} cations migrate via Sr(2) positions. © *1998 American Institute of Physics.* [S1063-7834(98)01102-2]

The presence of structural defects in inorganic compounds in many respects determines their transport characteristics. The formation of a $Sr_{3-3x}La_{2x}\square_x(VO_4)_2$ solid solution, where $0\leqslant x\leqslant 0.33$, was identified in a $Sr_3(VO_4)_2$–$LaVO_4$ system.[1] When lanthanum orthovanadate $LaVO_4$ is added to strontium orthovanadate $Sr_3(VO_4)_2$, La^+ ions are incorporated into the sublattice of the strontium ions. However, with two VO_4^{3-} groups, only two La^{3+} ions are incorporated instead of the three replaceable strontium ions with the result that vacancies appear in the strontium sublattice. These compounds are attracting attention because high ionic conductivity has been observed with Sr^{2+} ions as current carriers.[2] On the basis of the results of studies of the electrophysical properties (electrical conductivity, transport numbers), it was postulated that a vacancy mechanism is responsible for the transport of strontium ions. Here we investigate the diffusion of Ca^{2+}, Sr^{2+}, and Ba^{2+} cations in $Sr_{3-3x}La_{2x}\square_x(VO_4)_2$ ceramic samples and we determine the diffusion parameters as a function of temperature and dopant concentration.

1. EXPERIMENTAL METHOD

Samples synthesized as described in Ref. 2 were pressed into disks $\simeq$10 mm in diameter, sintered at 1200 °C, and then annealed at the experimental temperature. The open porosity of the ceramic was close to zero and the density, measured by hydrostatic weighing, was $\simeq$90–92% of the x-ray density. The diffusion of rare-earth metal cations in $Sr_{3-3x}La_{2x}\square_x(VO_4)_2$ was studied by systematically removing layers and measuring the residual integrated activity (I) (Ref. 3). The radionuclides ^{90}Sr, ^{45}Ca, and ^{133}Ba were used as labels.

The source of diffusion on the surface of the sample was a thin layer of the material enriched in the appropriate radionuclide. Diffusion annealing was carried out for 11 h at 800–950 °C. The radionuclide distribution over the depth (l) of the ceramic was determined by removing parallel layers 10–20 μm thick by polishing. The residual integrated activity of the ^{133}Ba γ radiation was measured using a BDBSZ-1 eM system complete with a PSO-2-4 scaler. The ^{45}Ca and ^{90}Sr β radiation was measured with an RKB-4-1 eM radiometer. The diffusion coefficients of ^{90}Sr, ^{45}Ca, and ^{133}Ba were calculated using standard solutions of the Fick equation. The diffusion parameters were determined by approximating the experimental points with the calculated curves $I(l)$ and finding the minimum variance between the experimental and calculated values of the residual integrated activities.[4] The relative measurement error for the diffusion coefficient was less than 30% at the 0.95 confidence level.

2. RESULTS AND DISCUSSION

Figure 1 shows typical experimental curves of the relative integrated activity of ^{45}Ca, ^{90}Sr, ^{133}Ba (I/I_0) as a function of the depth of penetration in $Sr_{3-3x}La_{2x}\square_x(VO_4)_2$ ceramic samples, where I_0 is the integrated activity at zero penetration depth. The diffusion coefficients of the radionuclides in $Sr_{2.4}La_{0.4}\square_{0.2}(VO_4)_2$, calculated from these diffusion profiles, at 900 °C are 11.7×10^{-9}, 11.0×10^{-9}, and 6.8×10^{-9} cm^2/s for calcium, strontium, and barium, respectively. The relation $D^*_{Ba}<D^*_{Sr}<D^*_{Ca}$ may be attributed to the size factor.

The experimental curves of the radionuclide diffusion coefficients are satisfactorily described by the Arrhenius equation

$$D^*_M=D^{*0}_M\exp(-U_d/kT). \tag{1}$$

The temperature dependences of D^*_M in $Sr_{3-3x}La_{2x}\square_x(VO_4)_2$ ($x=0.1,0.15,0.2,0.25$) solid solutions were used to determine the diffusion activation energies (U_d) for ^{45}Ca, ^{90}Sr, and ^{133}Ba, which were similar, $\approx$1 eV.

In a previous study[2] the Tubandt method was used to show that the Sr^{2+} ions are responsible for the electrical transport, and the temperature dependence of the ionic con-

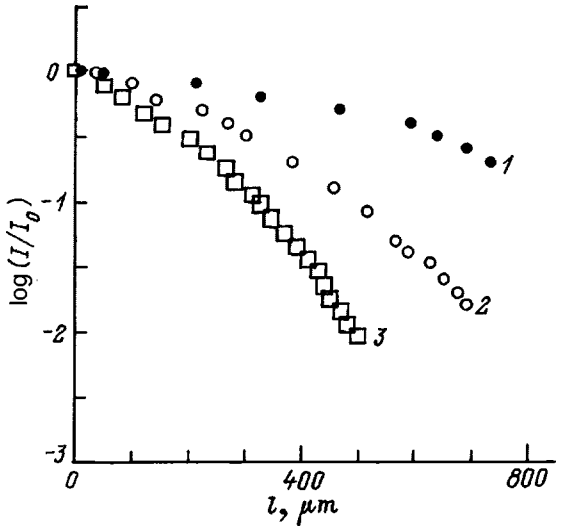

FIG. 1. Relative residual integrated activity of ^{45}Ca(*1*), ^{90}Sr(*2*), and ^{133}Ba(*3*) radionuclides for $Sr_{2.4}La_{0.4}\square_{0.2}(VO_4)_2$ as a function of depth at an annealing temperature of 900 °C.

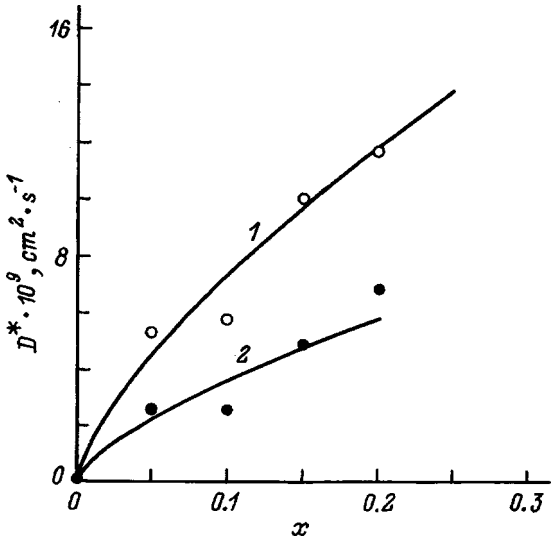

FIG. 3. Diffusion coefficients of ^{45}Ca(*1*) and ^{133}Ba(*2*) in $Sr_{2.4}La_{0.4}\square_{0.2}(VO_4)_2$ as a function of the lanthanum concentration x at 900 °C.

ductivity ($\varkappa$) of strontium and barium orthovanadate solid solutions $M_{3-3x}La_{2x}\square_x(VO_4)_2$, where M=Sr,Ba, $x \leqslant x < 0.33$, is described by

$$\varkappa T = \varkappa^0 \exp(-U/kT). \tag{2}$$

The activation energy (U) for ionic conduction in $Sr_{3-3x}La_{2x}\square_x(VO_4)_2$ is 0.77 eV and does not depend on the concentration of strontium vacancies in the structure. Note that the activation energies for ^{90}Sr diffusion in these compounds, around 1 eV, are slightly higher than the activation energy for ionic conduction.

Figure 2 gives the ^{90}Sr diffusion coefficients as a function of the composition of the $Sr_{3-3x}La_{2x}\square_x(VO_4)_2$ solid solution for T=const. The diffusion coefficients of divalent metal radionuclides in undoped $Sr_3(VO_4)_2$ are lower than those in the solid solutions under study because they contain small quantities of strontium vacancies.[5] At 800 °C, 850 °C, and 900 °C, D^*_{Sr} in strontium orthovanadate is 1.1×10^{-10} cm^2/s, 1.5×10^{-10} cm^2/s, and 2.3×10^{-10} cm^2/s, respectively

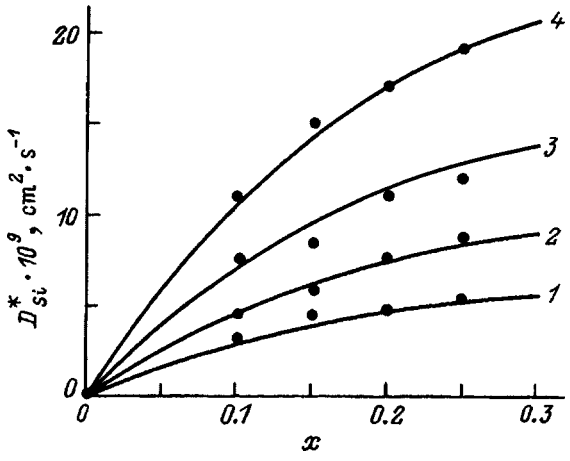

FIG. 2. Coefficients of diffusion of ^{90}Sr in $Sr_{3-3x}La_{2x}\square_x(VO_4)_2$ as a function of the lanthanum concentration x at various temperatures: T(°C): *1*—800, *2*—850, *3*—900, and *4*—950.

The changes in D^*_{Sr} as a function of x in $Sr_{3-3x}La_{2x}\square_x(VO_4)_2$ may be described for small x by the well-known expression[6] for the vacancy transport mechanism

$$D^*_{Sr} = f\nu r^2[V_{Sr}]\exp(-U_d/kt), \tag{3}$$

where f is the correlation factor, ν is the frequency of hopping attempts, r is the hopping length, and $[V_{Sr}]$ is the vacancy concentration in the strontium sublattice. According to Eq. (3), the dependences of the radionuclide diffusion coefficients on the vacancy concentration x for constant T and f should be nearly linear. However, it can be seen from Fig. 2 that the dependences $D^*(x)$ deviate substantially from straight lines. Similar curves were obtained for ^{45}Ca and ^{133}Ba radionuclides (Fig. 3). Of the parameters appearing in expression (3), the correlation factor may undergo the largest variation as a function of x. It may be supposed that its value is mainly influenced by the deformation of the crystal lattice caused by doping.

In order to compare the radionuclide diffusion coefficients and the coefficients of random diffusion of strontium ions calculated using the Nernst–Einstein equation using ionic conductivity data

$$D_{Sr} = kT\varkappa/q^2_{Sr}n_{Sr}, \tag{4}$$

we need to determine the concentration of strontium ions n_{Sr} involved in the charge transport. Figure 4 gives the preexponential factor of the ionic conductivity $\varkappa^0$ as a function of x. These values are accurately described by

$$\varkappa^0 = \varkappa'(2-3x)x, \tag{5}$$

where $\varkappa' = 26.6\times10^3$ S·cm^{-1}·K. The factor $(2-3x)$ is proportional to the carrier concentration in

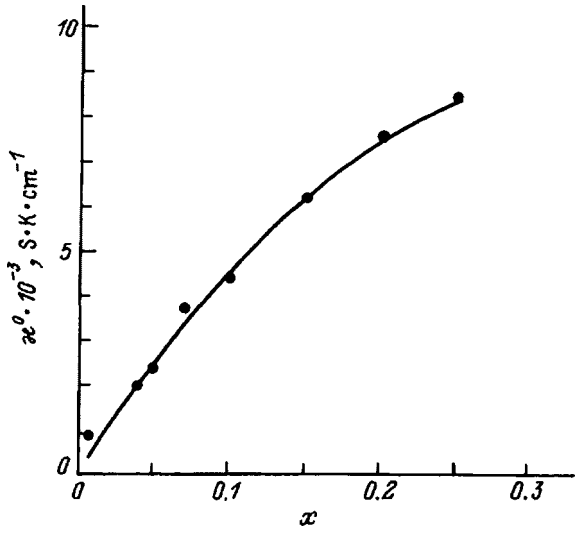

FIG. 4. Preexponential factor of ionic conductivity versus lanthanum concentration. The curve was calculated using Eq. (5).

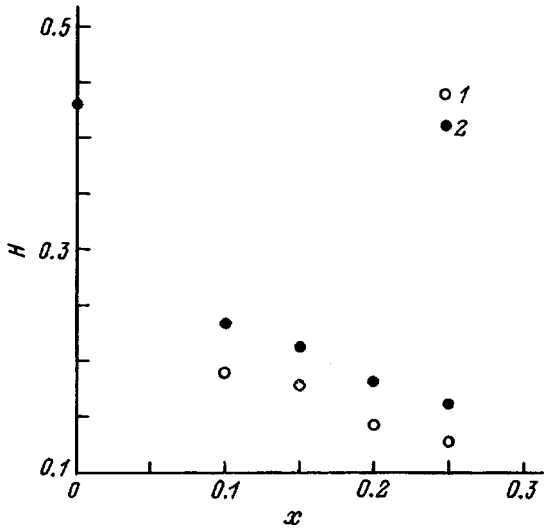

FIG. 5. Haven ratio H in $Sr_{3-3x}La_{2x}\square_x(VO_4)_2$ for various x. T(°C): *1*—800, *2*—950.

$Sr_{3-3x}La_{2x}\square_x(VO_4)_2$ and shows that the maximum number of strontium ions involved in the transport is close to two per formula unit.

The structure of $Sr_3(VO_4)_2$ has not been determined to within interatomic distances but it has been shown that this compound has the same structure as barium orthovanadate.[7] An analysis of the structure of $Ba_3(VO_4)_2$ also indicates that two barium ions, Ba($2a$) and Ba($2b$), situated in a ten-oxygen neighborhood and positioned perpendicular to the a_H axis, may participate in the transport process. This statement is also supported first, by the longer bond lengths between positions Ba($2a$), Ba($2b$) and position Ba(1), in a six-oxygen neighborhood (Ba($2a$)–Ba(1)—4.37 Å and Ba($2b$)–Ba(1)—4.30 Å), compared to the Ba($2a$)–Ba($2b$) bond length of 3.71 Å (Ref. 8). Second, the sizes of the necks linking the free and filled positions are $\simeq$1.6 Å between positions Ba($2a$) and Ba($2b$) whereas between Ba(1) and Ba($2a$) and between Ba(1) and Ba($2b$), they are 0.6 and 1 Å, respectively. These small necks impede the diffusion of rare-earth metal cations along the c_H axis. Assuming that the structure is the same, it may be postulated that in $Sr_3(VO_4)_2$ the Sr^{2+} ions migrate via Sr(2) positions in the plane perpendicular to the c_H axis. The value $3x$ shows that the La^{3+} ions and strontium vacancies are in the same position. The concentration of mobile ions is then $n_{Sr}=z(2-3x)/V$ ($z=3$ is the number of formula units).

These dependences of the coefficients of random diffusion in $Sr_{3-3x}La_{2x}\square_x(VO_4)_2$ on temperature and donor concentration are described by:

$$D=D_0x\ \exp(-U/kT). \tag{6}$$

The difference between the activation energies U and U_d is $\simeq$0.2 eV, which may be attributed to the temperature dependence of the correlation factor f. Since no detailed information is currently available on the structure of $Sr_3(VO_4)_2$ or solid solutions based on this, we used the Haven ratio ($H=D^*/D$) to compare the experimental isotope diffusion coefficients (D^*) and the random diffusion coefficients (D), assuming that the parameters H and f are interrelated.

Figure 5 gives the Haven ratio H at 800 and 950 °C. It can be seen that H depends on T and x and is less than 0.5 of the correlation factor calculated in the first approximation using the Manning formula ($f=(1-P)/(1+P)$, where $P=1/m$, m is the number of nearest neighbors, which is three for the Sr(2) sublattice). More accurate values of f may be obtained using the relation

$$f=\frac{1+\langle\cos\ \theta\rangle}{1-\langle\cos\ \theta\rangle}, \tag{7}$$

where $\langle\cos\ \theta\rangle$ is the average cosine of the angle between the directions of a pair of successive hops used to calculate the correlation factors for the simplest structures with a unit hopping frequency in all directions.[9] Assuming that strontium ions migrate predominantly via Sr(2) positions in $Sr_{3-3x}La_{2x}\square_x(VO_4)_2$, the closest structure to these compounds is a honeycomb structure for which $f=0.33$ ($\theta=120°$). Since in real structures there is a difference in positions along the c_H axis between neighboring Sr($2a$) and Sr($2b$) ions (corrugated honeycomb structure), in an undistorted solid-solution structure where $x\rightarrow0$ we find the angle $\theta<120°$ and $f>0.33$. The value of H in $Sr_3(VO_4)_2$ is $\approx$0.43. This value may be reduced substantially for at least two reasons. For example, it has been shown for anisotropic structures[10] that if the hopping frequencies along the z axis (ν_z) and in the xy plane (ν_x) are taken into account, for large ratios ν_x/ν_z the correlation factor describing the diffusion process at the frequency ν_x decreases. Moreover, when some of the strontium ions in positions Sr(2) are replaced by lanthanum ions, accompanied by the formation of vacancies in this sublattice, the Sr($2a$)–Sr($2b$), Sr(2)–La(2), and Sr(2)–□(2) bond lengths may vary appreciably. As a result of this local distortion of the structure, the angle θ increase

and in accordance with Eq. (7), f decreases. Thus, as the temperature increases, the distortions of the crystal lattice decrease, the angle θ should decrease and f increases. It has been found that the Haven ratio increases with temperature.

To conclude, as a result of studying the transport characteristics of $Sr_{3-3x}La_{2x}\square_x(VO_4)_2$, it has been observed that the distribution of impurity centers (lanthanum ions and strontium vacancies) and the transport of strontium cations is strongly anisotropic. Defects distort the structure in the Sr(2) plane, which substantially influences the correlation factor for the diffusion of radionuclide.

The authors are grateful to the Soros International Science Foundation and the Russian Fund for Fundamental Research for supporting this work.

[1] G. le Flem and P. C. Easstman, Bull. Soc. Chem. France **7**, 2769 (1968).
[2] I. A. Leonidov, O. N. Leonidova, and A. A. Fotiev, Élektrokhimiya **28**, 1515 (1992).
[3] B. S. Bokshteĭn, *Diffusion in Metals* [in Russian], Moscow (1978).
[4] G. I. Dontsov and M. V. Slinkina, *Interuniversity Collection of Scientific Papers* [in Russian], Sverdlovsk (1988), p. 61.
[5] O. N. Leonidova, A. A. Fotiev, and I. A. Leonidov, Élektrokhimiya **32**, 518 (1996).
[6] V. N. Chebotin, *Physical Chemistry of Solids* [in Russian], Khimiya, Moscow (1982).
[7] A. A. Fotiev, B. V. Slobodin, and M. Ya. Khodos, *Vanadates: Composition, Structure, and Properties* [in Russian], Moscow (1988).
[8] R. Susse and M. J. Buerger, Z. Kristallogr. **6**, 161 (1970).
[9] K. Compaan and Y. Haven, Trans. Faraday Soc. **52**, 786 (1956).
[10] *Physics of Electrolytes*, edited by Dzh. Khladik [in Russian], Moscow (1978).

Translated by R. M. Durham

Entropy of crystallization of materials from a ''molten'' sublattice of superionic conductors

M. A. Korzhuev

A. A. Baĭkov Institute of Metallurgy, Russian Academy of Sciences, 117911 Moscow, Russia
(Submitted March 17, 1997; resubmitted May 28, 1997)
Fiz. Tverd. Tela (St. Petersburg) **40**, 227–228 (February 1998)

It is shown that the entropy of crystallization of materials (such as Cu, Ag, Au, and Li) in a ''molten'' sublattice of superionic conductors→crystal system may substantially exceed the entropy of crystallization of the same materials from a melt. The observed behavior explains the known tendency of various superionic conductors to form filamentary crystals (whiskers) in the solid phase, together with the completely different structure of these whiskers.
 [S1063-7834(98)01202-7]

The crystal structure of superionic conductors (SICs) may be represented as the superposition of a ''molten'' sublattice of mobile ions (Cu^{1+}, Ag^{1+}, Li^{1+}, H^{1+}, F^{1-}, $C1^{1-}$, and so on) and a hard ''core'' which conserves the properties of the solid up to the melting point of the compound (T_m). ''Melting'' of the sublattice of mobile ions generally occurs at the temperature of the superionic phase transition $T_c \sim 0.3-0.4T_m$ when some of the SIC ions are excited in interstitial sites (Frenkel defects), where they are distributed over many vacancies (order–disorder phase transition). The order–disorder transition makes the major contribution (up to 90%) to the total entropy of the superionic transition $\alpha_c = \Delta S_c / R_0$ (R_0 is the universal gas constant), with deformation of the core accounting for the remaining 10%. On the whole, α_c can have a fairly high value in superionic conductors (up to one or higher).[1–3] Thus, the entropy of melting/crystallization of SIC samples at $T = T_m$ decreases appreciably[4,5] ($\alpha'_m \sim \alpha_m - \alpha_c$, where $\alpha_m = \Delta S_m / R_0$ is the reduced entropy of melting of an ordered material) (curves *2* and *3* in Fig. 1), like the tendency of ingots to faceting[6] (this tendency usually shows up clearly for $\alpha_m > 4-6$) (Ref. 7).

The process of crystallization in superionic conductors can also take place in the solid state by a ''molten'' SIC sublattice→crystal system (growth of whiskers, ribbons, and dendrites using Cu, Ag, Na, and so on).[8–11] For Cu, Ag, and Na we have $\alpha_m = 1.12$, 1.17, and 0.85, respectively,[12] which presupposes samples with a polycrystalline structure and a rounded surface when these crystallize from a melt.[7] However, whiskers and ribbons[8–11] typically have a single-crystal structure and partial faceting which indicates a possible disparity between the values of α_m and α''_m (here $\alpha''_m = \Delta S''_m / R$ is the reduced entropy of crystallization of materials from a molten SIC sublattice). The value of α''_m for SICs has not been estimated separately before.

Here it is shown that the value of α''_m for SICs may substantially exceed the entropy of crystallization α_m of the same materials from a melt.

The change in the configurational component of the entropy accompanying melting of the sublattice of mobile ions in an SIC is described by the expression

$$\Delta S_i^{\text{conf}} = k_0(\ln W_{T>T_c} - \ln W_{T<T_c}). \tag{1}$$

Here $k_0 = R_0 / N_0$ is the Boltzmann constant, N_0 is Avogadro's number, $W = C_a^b = (b!)/[(b-a)!a!]$ is the statistical weight of the appropriate states, C_a^b is the number of ways of distributing a mobile ions a in b vacancies in the crystal.[3,13,14]

Assuming in expression (1) $a = b = nN_0 (T < T_c)$ and $a = nN_0$, $b = NN_0 (T > T_c)$ (n and N are the number of mobile ions and vacancies per formula unit of the compound), we obtain using the Stirling formula $\ln(y!) \simeq y(\ln(y) - 1)$ for $N \gg n \sim 1$

$$\alpha_i^{\text{conf}} = \Delta S_i^{\text{conf}} R_0 = \left(N \ln \frac{N}{N-n} + n \ln \frac{N-n}{n} \right) \sim \ln N. \tag{2}$$

Figure 2 gives the curves $\alpha_i^{\text{conf}} = f(n)$, calculated using Eq. (2) for various values of the parameter N (curves *1–3*). Also plotted are the values of the configurational component of

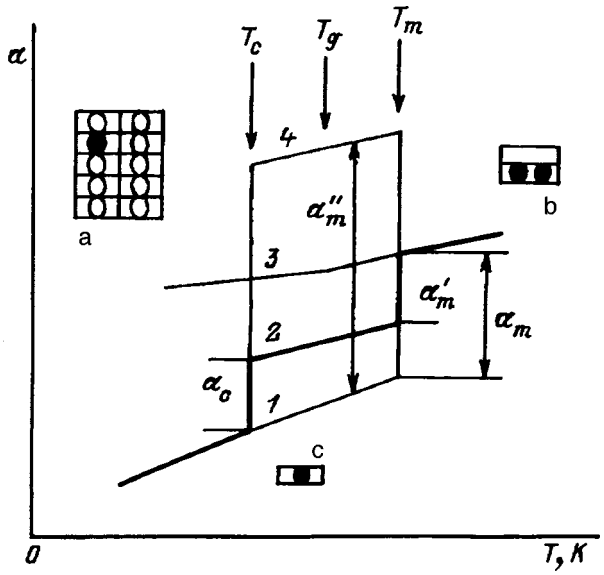

FIG. 1. Typical temperature dependences of the reduced entropy $\alpha = S/R_0$ for ordered materials (*1*), SICs (*2*), amorphous materials (*3*), and a molten sublattice of mobile ions in a SIC (*4*): T_c, T_g, and T_m are the superionic transition temperature, the glass-transition temperature of amorphous materials, and the crystal melting point. Configurational space: a—SIC ($N = 10$, $Cu_{2-x}Se$) (Refs. 1 and 2), b—liquid ($N = 2$, cellular model[15,16]), and c—ordered solid phase ($N = 1$).

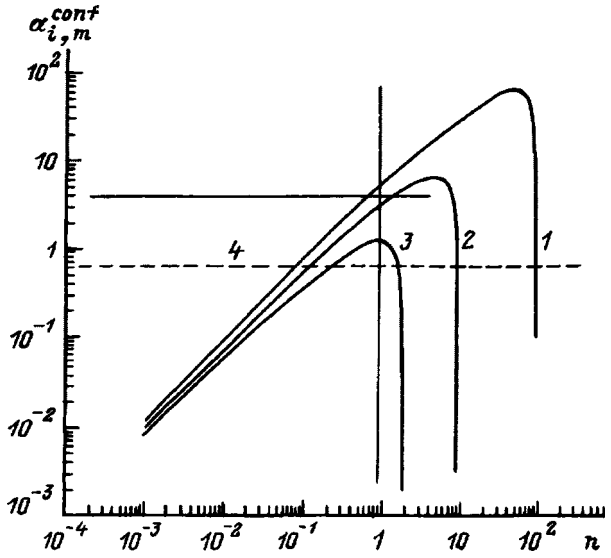

FIG. 2. Configurational component α_i^{conf} of the reduced entropy of disordering of mobile ions versus the atomic fraction n of mobile ions for a superionic phase transition in a SIC (*1–3*). The disorder parameter N is: *1*—100, *2*—10 ($Cu_{2-x}Se$), *3*—2; *4*—$\alpha_m^{\text{conf}}=\ln 2$.

the enthalpy of melting for the cellular model of a liquid $\alpha_m^{\text{conf}}=\ln 2$ (curve *4*) (Refs. 15 and 16) which makes the main contribution (up to 70–80%) to the total entropy of melting of Cu, Ag, Au, Li, and Na (Ref. 12).

It can be seen from Fig. 2 that for $N>2$ and $n>0.1$, it is possible to have $\alpha_m''\sim\alpha_i^{\text{conf}}\sim\alpha_c M/M_i>\alpha_m^{\text{conf}}\sim\alpha_m$ in a SIC (M_i is the atomic weight of the mobile ions excited in interstitial sites and M is the molecular weight of the SIC), because the ions in a ''distributed'' SIC sublattice have a higher degree of disorder than those in a liquid. This is possible because of the hard SIC core which increases the dimensionality of the configuration space for possible disordering of ions when $I>I_c$ (Fig. 1) (Ref. 17).

Thus, for $N>2$ and $n>0.1$ mobile ions in the molten SIC sublattice may possess the excess entropy $(\alpha_m''-\alpha_m)\sim\ln(N/2)$ in relation to ordinary melting (curve *4* in Fig. 1). Thus, crystallization of mobile ions by a molten SIC sublattice→crystal system corresponds to a change in entropy $\alpha'\sim\alpha_i^{\text{conf}}$ which exceeds the entropy of crystallization α_m of the same materials from a melt (curve *4*→curve *1* in Fig. 1).

For copper selenide $Cu_{2-x}Se$ (fluorite structure, $N=10$, $n\sim1$, around half the copper melts)[8,17] when mobile copper crystallizes from the molten sublattice, we have $\alpha_m''\sim3.25$ (curve *2* in Fig. 2), which explains in terms of the empirical relations[7] the high rate of copper whisker generation in $Cu_{2-x}Se$, their perfect crystal structure, the growth anisotropy, and partial faceting.[8,9]

The highest values of the parameters N and n in known inorganic SICs are $N=21$ for AgI and $n\sim2$ for Ag_2HgI_4 and $(Na_2O)_x(Li_2O)_y(Al_2O_3)_{11}$ (two sublattices of the compounds melt)[1,2] from which the maximum entropy is estimated as $\alpha_m''\sim5-6$ (Fig. 2). Even higher values of α_m'' may be observed in more complex organic SICs and in biological objects as a result of an increase in the parameters N and/or n. This high value of α_m'' may be responsible for the increased tendency of this group of materials to grow new formations.[18] Studies of the physical properties and phase transitions of these materials may be especially interesting.

[1] *Physics of Superionic Conductors*, edited by M. B. Salamon [Springer-Verlag, New York, 1979; Zinatne, Riga, 1982].
[2] Yu. Ya. Gurevich and Yu. I. Kharkats, *Superionic Conductors* [in Russian], Nauka, Moscow (1992).
[3] M. J. Rice, S. Strassler, and G. A. Toombs, Phys. Rev. Lett. **32**, 596 (1974).
[4] A. F. Polishchuk, T. A. Tishura, and A. N. Budarina, Ukr. Fiz. Zh. **40**, 120 (1974).
[5] M. A. Korzhuev, Rasplavy, No. 6, 105 (1991).
[6] M. A. Korzhuev, Phys. Status Solidi **121**, K7 (1991).
[7] K. A. Jackson, in *Crystal Growth*, edited by S. Peiser (Pergamon Press, Oxford, 1967), p. 13.
[8] M. A. Korzhuev, V. F. Bankina, N. Kh. Abrikosov, A. V. Arakcheeva, and M. A. Lobzov, Zh. Tekh. Fiz. **56**, 797 (1986) [*sic*].
[9] M. A. Korzhuev, Fiz. Khim. Obrat. Mater No. 5, 153 (1993).
[10] V. V. Vol'skiĭ, G. L. Koshel', and N. V. Makukin, *Abstracts of Papers presented at Seventh All-Union Conference on Physics, Chemistry, and Electrochemistry of Ionic Melts and Solid Electrolytes*, Vol. 3 [in Russian], Nauka, Leningrad (1983), p. 39.
[11] Yu. M. Gerbshteĭn, E. I. Nikulin, and F. A. Chudnovskiĭ, *ibid.*, p. 43.
[12] V. M. Glazov and A. A. Aĭvazov, *Entropy of Melting of Metals and Semiconductors* [in Russian], Metallurgiya, Moscow (1980).
[13] L. Zhirifal'ko, *Statistical Physics of Solids* [Mir, Moscow, 1975].
[14] T. Tanaka, S. Miyazima, T. Kakiuchi, and Y. Ota, Prog. Theor. Phys. Suppl. **115**, 185 (1994).
[15] S. M. Stishov, Usp. Fiz. Nauk **144**, 3 (1974) [*sic*].
[16] V. S. Vorob'ev, Zh. Éksp. Teor. Fiz. **110**, 683 (1996) [JETP **83**, 368 (1996)].
[17] M. A. Korzhuev, V. V. Baranchikov, N. K. Abrikosov, and V. F. Bankina, Fiz. Tverd. Tela (Leningrad) **26**, 2209 (1984) [Sov. Phys. Solid State **26**, 1341 (1984)].
[18] M. A. Korzhuev, JETP Lett. **64**, 105 (1996).

Translated by R. M. Durham

Interactive process in the mechanism of thermostimulated luminescence in anion-defect α-Al_2O_3 crystals

I. I. Mil'man, V. S. Kortov, and S. V. Nikiforov

Ural State Technical University, 620002 Ekaterinburg, Russia
(Submitted June 30, 1997)
Fiz. Tverd. Tela (St. Petersburg) **40**, 229–234 (February 1998)

A study of the role of deep traps in the specific features of the thermoluminescence (TL) of anion-defect α-Al_2O_3 single crystals is reported. The existence of deep traps is proven by direct observation of the associated TL peaks. Experimental support for the effect of deep-trap filling on the main characteristics of the main TL peak at 450 K is presented. A model involving trap interaction is proposed, which differs radically from the others described in the literature by taking into account the temperature dependence of the carrier capture probability by deep traps. This model was used to calculate the dependences on heating rate and deep-trap filling of the main parameters of the main TL peak for the crystals under study (TL yield, glow-curve shape, and sensitivity to the stored light sum), which were found to be close to those observed experimentally. © *1998 American Institute of Physics.* [S1063-7834(98)01302-1]

Interest in investigation of the luminescence properties of anion-defect α-Al_2O_3 crystals stems from their use for development of high-sensitivity detectors for ionizing radiation.[1] Experimental investigation of thermoluminescence (TL) of nominally pure anion-defect α-Al_2O_3 single-crystals reveals several features which are not accounted for by the available models of TL kinetics in solids. The most essential of them are the substantial drop of the average activation energy $[\langle E\rangle(T)]$ within the main (dosimetric) peak at 450 K, which is demonstrated by the fractional glow technique,[2] and the dependence of the TL yield on crystal heating rate.[3,4] The reliability of the experimental observations is not subject to doubt, since during the recent years they have been confirmed more than once in independent measurements.[5–8]

Investigation of the temperature behavior of radiation-induced and photoluminescence within the main crystal luminescence band (410 nm) permitted one to relate the observed features of the TL to thermal quenching, which is most efficient around the main peak.[2,4] Establishment of this relation made possible formal description of the dependence of TL yield on heating rate and of the anomalous behavior of $\langle E\rangle(T)$ by a kinetic equation with a modified Mott factor, which takes into account the thermal quenching. The mechanism of the observed TL features at the microscale remained, however, unclear, and the observation that they became manifest in the same way in other characteristic luminescence bands as well (330 and 690 nm)[9] did not find adequate interpretation. In this connection it appeared reasonable to analyze the role played by other processes capable of affecting strongly the kinetics of luminescence and, in particular, of carrier capture by deep traps. Because direct measurements met with difficulties, the presence of deep traps in nominally pure anion-defect corundum crystals has so far been revealed from indirect evidence. In particular, it is with their competition in carrier trapping that one associated the change in dosimetric sensitivity observed in crystals subjected to high-dose irradiation. TL of the same crystals irradiated with visible or UV light was explained as due to redistribution of charge from deep to shallower traps, which are responsible for the 450-K peak.[10]

The objective of this work was experimental detection of the deep traps and establishment of their role in the above features of TL in anion-defect α-Al_2O_3 single crystals.

1. SAMPLES AND EXPERIMENTAL TECHNIQUE

We studied samples of nominally pure α-Al_2O_3 single crystals grown by directed crystallization in strongly reducing conditions provided by the presence of graphite (thermochemical coloring). The oxygen vacancy (F center) concentration in the samples, as derived from the optical absorption spectra, was about 10^{17} cm^{-3}. The main TL peak at 450 K (heating rate $\beta = 2\ K\cdot s^{-1}$) was excited by $^{90}Sr/^{90}Y$ β radiation. TL measurements in the linear or fractional heating regime were made using a computerized setup described in detail elsewhere.[11] A distinctive experimental feature of this work was the possibility of selectively filling the deep traps at different crystal temperatures. To reduce the sample exposure time under excitation, we used nonselective UV radiation capable of efficiently populating deep traps. The radiator lamp was DRT-240 mercury-vapor quartz type with a focusing attachment. The TL was measured in the 300–1100-K range with a PM tube whose spectral sensitivity excluded recording thermal radiation.

2. RESULTS AND DISCUSSION

Our studies demonstrate the possibility of detecting deep traps by direct observation of the TL they are responsible for. Figure 1 presents glow curves of anion-defect α-Al_2O_3 crystals excited by UV light at 500 K (curve *1*) and 620 K (curve *2*). Besides the conventional TL features, namely, the main peak A ($T_m = 450$ K) and peak B ($T_m = 570$ K), which is associated with Cr^{3+} ions, we readily see the appearance in the glow curves, of new maxima, C and D ($T_m = 740$ and

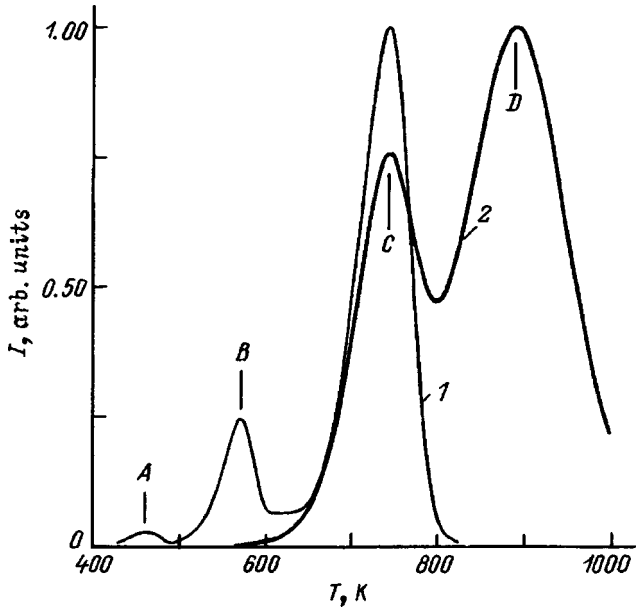

FIG. 1. Glow curves of UV-excited anion-defect α-Al_2O_3 crystals obtained at a heating rate of 2 $K \cdot s^{-1}$. Excitation temperature T(K): *1*—500, *2*—620.

890 K, respectively). The TL peaks *A*, *B*, *C*, and *D* are identical in spectral composition, and their spectra contain bands characteristic of F and F^+ centers.

We see also from Fig. 1 that the relative TL yield in peaks *C* and *D* depends noticeably on the temperature at which the samples were excited. The same is true for peaks *A* and *B* too. For instance, when TL was excited at room temperature, the main peak *A* dominated in yield, with peaks *B*, *C*, and *D* becoming practically undetectable.

One of the main results demonstrated by Fig. 1 is the possibility of selectively populating the deep traps responsible for the TL peaks *C* and *D* by properly varying the illumination temperature, with the traps associated with peak

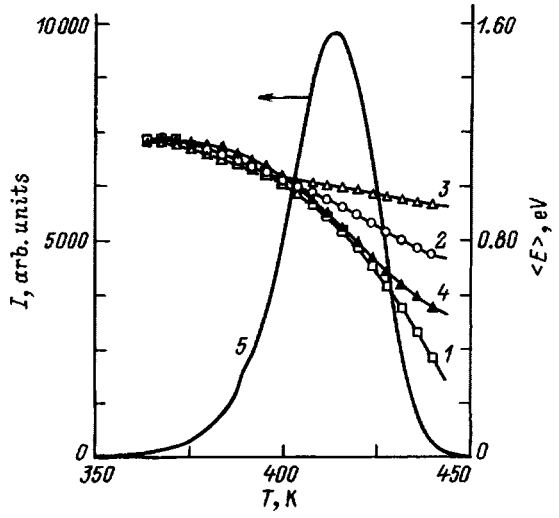

FIG. 2. (*1–4*) Temperature dependences of average activation energy for four deep-trap states and (*5*) glow curve for the main TL peak of anion-defect α-Al_2O_3 crystals excited at room temperature by $^{90}Sr/^{90}Y$ radiation. *1*—deep traps not filled on purpose, *2*—the deepest trap filled at 825 K, *3*—both traps filled at 620 K, *4*—both deep traps depleted by annealing at 1220 K for 15 min.

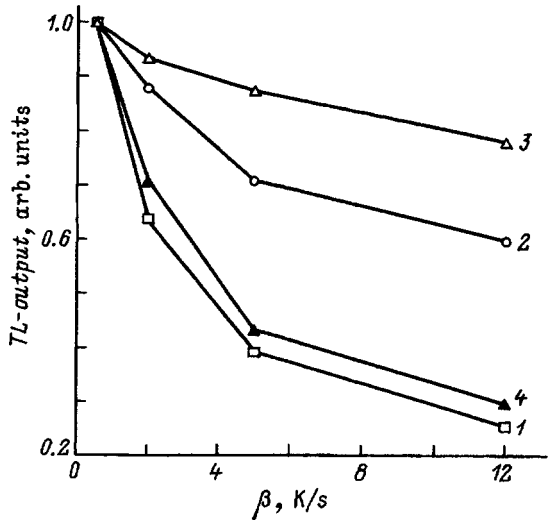

FIG. 3. Light sum emitted in the main TL peak as a function of heating rate of anion-defect α-Al_2O_3 crystals for the same deep states as in Fig. 2. The notation is the same.

A left empty. This makes possible investigation of the dependence of the kinetics of the peak *A* thermoluminescence on the deep-trap filling when the crystal is subsequently illuminated at room temperature. Figure 2 shows the $\langle E \rangle(T)$ relation for peak *A* obtained for four deep-trap states, namely, when the deep traps were not populated on purpose (initial state *1*), when only the deepest trap was filled (state *2*), when both deep traps were populated (state *3*), and when both deep traps after filling were emptied by heating the sample at 1220 K for 15 min (state *4*).

Shown in Fig. 3 are the results of a study of the peak *A* TL yield as a function of the heating rate of excited crystals, made for the deep-trap states similar to those described in discussion of Fig. 2, with the notation left unchanged. Table I illustrates the dynamics of variation in shape of the glow curve, which was estimated from its halfwidth at peak *A*, under variation of the heating rate and for the same changes of deep-trap state. As seen from Table I, the emptying of deep traps results in a stronger dependence of the glow curve halfwidth on heating rate.

An analysis of the experimental data presented in Figs. 2 and 3 and Table I shows convincingly that the TL parameters of peak *A* depend on carrier filling of the deep traps. The most essential point is, however, that the above features of the main-peak TL also are directly related to the deep-trap state. By varying properly their population, one can control the temperature dependence of the average activation energy

TABLE I. Glow-curve halfwidth of anion-defect α-Al_2O_3 crystals vs heating rate and deep-trap state.

Deep-trap state	Halfwidth, K			
	$\beta = 0.5\ K \cdot s^{-1}$	$\beta = 2\ K \cdot s^{-1}$	$\beta = 5\ K \cdot s^{-1}$	$\beta = 12\ K \cdot s^{-1}$
1	33	42	47	56
2	32	38	39	41
3	29	32	34	37
4	33	40	45	54

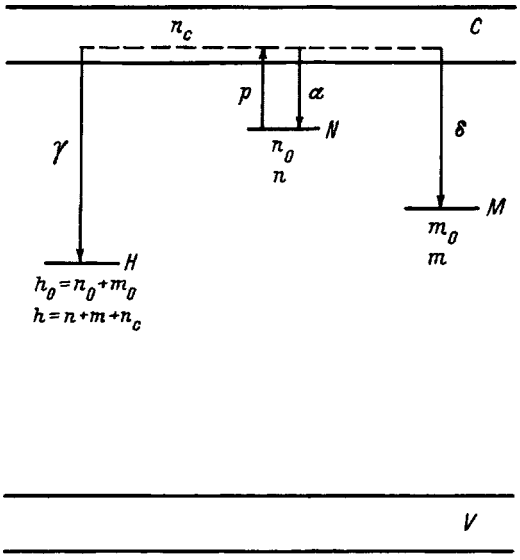

FIG. 4. Band diagram of the interactive trap system. N—TL-active trap, M—deep trap, H—luminescence center. Transitions: γ—radiative recombination at luminescence center H, δ—capture by deep traps M, α—capture by traps N, p—thermal depletion of shallow TL-active traps. See text for other symbols.

(Fig. 2) and the drop in TL yield with increasing crystal heating rate (Fig. 3). As evident from the above results, annealing of the crystals at 1220 K for 15 min resulted in emptying of the deep traps and recovery of the anomalous TL features of peak A.

The studies associated with the population of the deep traps revealed that the probability of their filling grows with temperature. This begins to be seen in the temperature region characteristic of the TL peak A. This observation led to accepting as a working hypothesis the assumption that the TL mechanism in anion-defect α-Al_2O_3 crystals involves an interactive process. This process consists essentially in competing capture by the deep traps of the carriers released in readout of the main TL peak.[12–14]

The simplest band diagram for the interaction of shallow TL-active traps with deep traps (an interactive trap system) is shown in Fig. 4. Here H,N,M (cm^{-3}) are the total concentrations of the luminescence centers, shallow, and deep traps, respectively; h,n,m (cm^{-3}) are the concentrations of the filled H, N, and M levels; α, δ, and γ ($\mathrm{cm}^{-3}\,\mathrm{s}^{-1}$) are the carrier trapping coefficients; p is the thermal ionization probability for the shallow TL-active traps; and n_c (cm^{-3}) is the free-carrier concentration in conduction band C. The zero index refers to the initial filling of the levels after excitation.

Excitation at room temperature fills levels N, M, and H by carriers. It is assumed that during this process and for some time after the start of the heating electric neutrality persists: $h=n+m+n_c$, where $n_c=0$ before heating. Thermal activation ejects electrons from the filled active traps N into the conduction band C. There are three possible paths by which the electrons can relax from their excited states: (1) radiative recombination at the luminescence center H; (2) capture by deep traps M; and (3) retrapping by levels N. It is also assumed that levels H and M are thermally stable within the temperature interval of TL measurement.

This model involving an interactive trap system can be described by the following coupled equations[12,13]

$$\frac{dn}{dt} = -pn + \alpha(N-n)n_c, \tag{1}$$

$$\frac{dm}{dt} = \delta(M-m)n_c, \tag{2}$$

$$\frac{dn_c}{dt} = pn - \alpha(N-n)n_c - \delta(M-m)n_c - \gamma(n+m+n_c)n_c, \tag{3}$$

$$I(t) = -\frac{dh}{dt} = \gamma(n+m+n_c)n_c, \tag{4}$$

where $I(t)$ is the TL intensity at the instant t. The probability for an electron to be ejected into the conduction band by thermal ionization of the traps is described by the expression $p=S\,\exp(-E/kT)$, where E is the activation energy, S is the frequency factor for this process, T is the absolute temperature, and k is the Boltzmann constant. The meaning of the other parameters was explained before.

Equations (1)–(4) were solved numerically by the fourth-order Runge–Kutta method. The equations modeled the interaction of the shallow and deep traps under linear heating. The solution was presented in the form of a glow curve, with both the filling of traps N and M and the heating rate being variable parameters.

Having assumed an interactive process, the dependence of TL yield on the heating rate was studied theoretically for two scenarios. In the first of them, the probability of carrier trapping at deep levels, $\delta(T)$, was made temperature-independent,[12,13] whereas in the second it was prescribed on purpose, since we observed it to exist in experimentally. The analytical form of the $\delta(T)$ relation was based on our knowledge of the luminescence quenching parameters, which provided earlier a good agreement of the $\langle E\rangle(T)$ curves and of the drop of the TL yield with increasing heating rate between model and actual experiments.[2] In this work we limited ourselves to considering only two processes involved in the main TL peak, namely, radiative recombination with a probability η and trapping of the released carriers at deep levels with a probability $1-\eta$. In this case the $\delta(T)$ relation can be presented in the following analytical form:

$$\delta(T) = \delta_0(1-\eta) = \delta_0\left(1 - \frac{1}{1 + C\,\exp(-W/kT)}\right) = \delta_0\frac{C\,\exp(-W/kT)}{1 + C\,\exp(-W/kT)}, \tag{5}$$

where δ_0 is a temperature-independent factor.

The quenching activation energy W and constant C entering Eq. (5) were estimated using the data obtained[2] in modeling the TL features with inclusion only of the thermal quenching characteristics. Application of the best-fit criterion to experimental data yielded[2] also the values for E and S. Thus there were grounds to use as input in the numerical solution of Eqs. (1)–(4) the parameters already substantiated

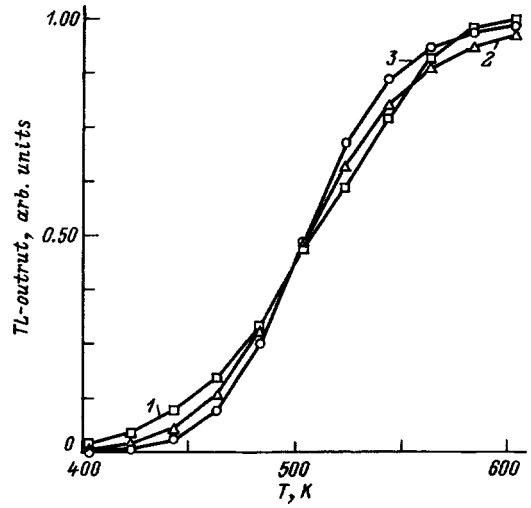

FIG. 5. (*1*) Experimental and (*2,3*) calculated TL yield for the 740-K peak vs excitation temperature. W(eV) and C: *2*—0.88 and 6×10^{8}, *3*—1.1 and 10^{11}.

earlier[2]: $E=1.31$ eV, $S=10^{13}$ s^{-1}, $W=0.97$ eV, and $C=10^{11}$. The applicability of the values of W and C to description of the $\delta(T)$ relation was verified by comparing the corresponding measurements with the figures calculated from the analytical expression (5). The deep trap responsible for the TL peak at 740 K is best suited for experimental control of its population. Therefore in this stage the experimental values of $\delta(T)$ were determined from measurements of the TL yield for the 740-K peak as a function of the crystal excitation temperature. Initially the deepest trap was completely filled.

The results of the comparison are shown in Fig. 5. Curves *2* and *3* are plots of Eq. (5) with parameters W and C varied. Taking into account the good qualitative agreement between the theoretical and experimental $\delta(T)$ relations, the values $W=1.1$ eV and $C=10^{11}$ were subsequently used in the numerical solution of Eqs. (1)–(4). The other parameters were chosen based on the criterion that the solution should provide a qualitatively close description of the experimentally obtained dependence of the main-peak TL under variation of the heating rate and deep-trap filling, whose characteristics are displayed in Fig. 3 and Table I.

TABLE II. Calculated dependence of the halfwidth of the main TL peak on heating rate and deep-trap filling.

	Halfwidth, K			
m_0/M	$\beta=0.5$ K·s^{-1}	$\beta=2$ K·s^{-1}	$\beta=5$ K·s^{-1}	$\beta=12$ K·s^{-1}
1	34	36	38	38
0.01	34	38	42	45
0.001	34	42	49	53
0.0001	38	41	53	58

The calculated effect of deep-trap population simultaneously on the TL yield at the main peak and on its shape under heating-rate variation is presented in Fig. 6 and Table II. The data listed in Table II show the dependence of the glow-curve halfwidth on heating rate decreasing with increasing deep-trap filling. A comparison of the results presented in Figs. 3 and 6 and in Tables I and II shows them to be in sufficiently good qualitative agreement.

The results of the TL modeling by means of Eqs. (1)–(4), which are illustrated in Fig. 6 and Table II, were obtained with $\alpha_0=10^{-14}$ cm^{-3} s^{-1}, $\delta_0=10^{-12}$ cm^{-3} s^{-1}, $\gamma_0=10^{-11}$ cm^{-3} s^{-1}, $W=1.1$ eV, $C=10^{11}$, $E=1.31$ eV, $S=10^{13}$ s^{-1}, $N=10^{13}$ cm^{-3}, $M=10^{14}$ cm^{-3}, $n_0=10^{11}$ cm^{-3}, and $n_c=10^{6}$ cm^{-3}. The variable parameters were the deep-trap filling m_0/M and the crystal heating rate β.

An experimental study of the effect of deep-trap filling on the TL properties of anion-defect corundum revealed one more feature. It was found that the TL sensitivity at the main peak is also connected to the deep-trap states, namely, it increased to saturation with their filling and could be returned to the initial level by annealing at 1220 K for 15 min. This observation is depicted by curve *1* in Fig. 7. The data

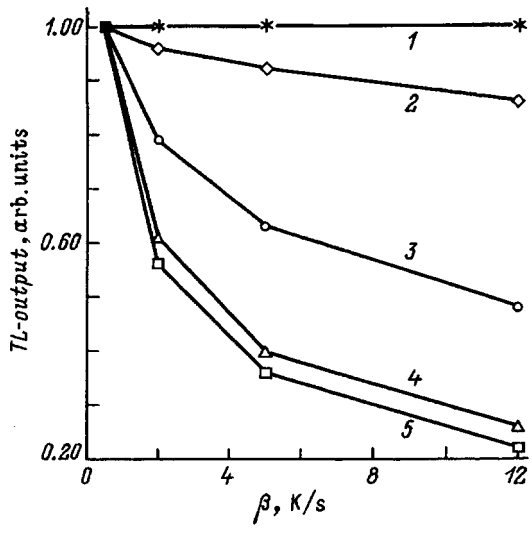

FIG. 6. Calculated main-peak TL vs heating rate and filling of deep traps M (m_0/M): *1*—1, *2*—0.1, *3*—0.01, *4*—0.001, *5*—0.0001.

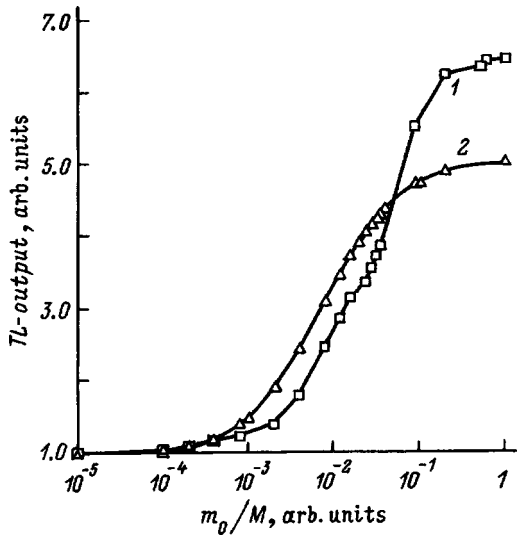

FIG. 7. Main-peak TL yield vs deep-trap filling. *1*—experiment, *2*—calculation.

for this graph were obtained by measuring the main-peak TL under gradual filling of the trap responsible for the TL peak at 740 K (Fig. 1). The excitation dose at which the TL sensitivity at the main peak and the TL yield at peak *C* were observed to saturate was accepted to correspond to $m_0/M=1$. Curve *2* in Fig. 7 shows the calculated change in TL sensitivity at the main peak as a function of deep-trap filling. Eqs. (1)–(4) were solved with the parameters used to obtain the data of Fig. 6 and Table II. As seen from Fig. 7, curves *1* and *2* are qualitatively similar. When considered together with the other results, this observation argues for the adequacy of our trap interaction model, which determines the main features and characteristics of the TL of anion-defect corundum crystals.

Thus this work demonstrates the existence of deep traps in anion-defect corundum by direct TL observation. The spectral composition of the glow at the peaks associated with these traps and their kinetic parameters were determined. Convincing experimental data are presented for the effect of deep-trap filling on all features of the main TL peak. The experimentally observed relations were used to develop an interaction model of the relatively shallow active traps responsible for the 450-K TL peak with thermally stable deep traps. This model differs radically from others described in the literature in its inclusion of a temperature dependence of the trapping probability of the carriers released in TL readout by the deep traps within the temperature interval 300–600 K. The calculations based on this model support simultaneous dependence on the heating rate and deep-trap filling of the main TL parameters of the crystals under study, namely, the main-peak TL yield, the glow curve shape, and the sensitivity to stored light sum, which are found to be close to those observed experimentally. The model involving an interactive process in the TL mechanism for anion-defect corundum crystals provides an explanation of the totality of experimental observations within a common frame. In this model, thermal quenching of luminescence is considered as a direct consequence of an interaction of shallow and deep traps in the crystal. This accounts for the success of our earlier attempt at the description of their TL features both based on the thermal quenching concept and by taking into consideration the temperature dependence of the probability of carrier capture by deep traps.

[1] V. S. Kortov, I. I. Milman, V. I. Kirpa, and Ja. Lesz, Radiat. Prot. Dosim. **65**, 255 (1996).
[2] I. I. Mil'man, V. S. Kortov, and V. I. Kirpa, Fiz. Tverd. Tela (St. Petersburg) **37**, 1149 (1995) [Phys. Solid State **37**, 625 (1995)].
[3] V. S. Kortov, I. I. Milman, V. I. Kirpa, and Ja. Lesz, Radiat. Prot. Dosim. **55**, 279 (1994).
[4] V. S. Kortov and I. I. Mil'man, Izv. Vuzov, Fizika **39**, No. 11, 145 (1996).
[5] T. I. Gimadova, T. S. Bessonova, I. A. Tale, L. A. Avvakumova, and S. V. Bodyachevsky, Radiat. Prot. Dosim. **33**, 47 (1991).
[6] T. S. Bessonova, T. I. Gimadova, I. A. Tale, L. A. Avvakumova, and L. A. Litvinov, Zh. Prikl. Spektrosk. **54**, 433 (1991).
[7] T. S. Bessonova, L. A. Avvakumova, T. I. Gimadova, and I. A. Tale, Zh. Prikl. Spektrosk. **54**, 258 (1991).
[8] A. S. Pradhan, Radiat. Prot. Dosim. **65**, 73 (1996).
[9] S. V. Nikiforov, I. I. Milman, and V. S. Kortov, *Abstracts of 9th Intern. Conf. Radiation Physics and Chemistry of Inorganic Materials*, Tomsk (1996), p. 296.
[10] M. S. Akselrod and E. A. Gorelova, Nucl. Tracks Radiat. Meas. **21**, 143 (1993).
[11] S. V. Nikiforov, A. K. Kil'metov, I. I. Mil'man, and V. S. Kortov, Available from VINITI, 1996, No. 2054-B96.
[12] C. M. Sunta, R. N. Kulkarni, E. M. Yoshimura, A. W. Mol, T. M. Piters, and E. Okuno, Phys. Status Solidi B **186**, 199 (1994).
[13] C. M. Sunta, E. M. Yoshimura, and E. Okuno, J. Phys. D **27**, 852, 2636 (1994).
[14] R. Chen, G. Fogel, and C. K. Lee, Radiat. Prot. Dosim. **65**, 63 (1996).

Translated by G. Skrebtsov

Electronic structure of lead (II) fluoride and lead (II) chloride crystals

I. V. Murin, A. V. Petrov, I. I. Tupitsyn, and R. A. Évarestov

Scientific-Research Institute of Chemistry at St. Petersburg State University, 199034 St. Petersburg, Russia
(Submitted June 6, 1997)
Fiz. Tverd. Tela (St. Petersburg) **40**, 235–236 (February 1998)

The method of complete neglect of differential overlap was used to calculate the electronic structure of α PbF_2, β PbF_2, and $PbCl_2$ crystals which form the basic matrices for the synthesis of new superionic conductors. It was shown that the electronic subsystem is fairly stable on transition from the high-symmetry β PbF_2 crystal to the low-symmetry α PbF_2. The electronic structure of the cotunnite crystal $PbCl_2$ was calculated for the first time. © *1998 American Institute of Physics.* [S1063-7834(98)01402-6]

Lead halide compounds form the basis for the synthesis of a broad class of superionic compounds.[1,2] However, the nature of the anomalously high mobility of fluorides or chlorides has not yet been sufficiently explained in physicochemical studies of these compounds. As a first step toward understanding the essence of the ionic conduction process, we attempt to calculate the electronic structure of the lead halides PbF_2 and $PbCl_2$.

It is known that lead fluoride crystallizes in two modifications: cubic (space group $Fm3m$)[3] and orthorhombic ($Pnma$).[4] The cubic crystal is stable at high temperatures. In order to search for promising new compounds, it is important to determine the differences in the electronic structure of these two PbF_2 modifications which have the same overall composition but different spatial configurations of the atoms.

The superionic state of the crystal is characterized by structural disordering of the fluorine sublattice in lead fluoride. It may be postulated that the fluorine ions in tetragonal lead fluoride, which possesses lower local symmetry, are in a state closer to disordered.

We are not aware of any calculated data on the electronic structure of lead fluoride in the orthorhombic modification so that it is interesting to make a theoretical study of the electronic structure and charge state of the ions in this crystal. This information will also be useful for spectroscopic investigations of this crystal.

The lead chloride crystal has the same spatial characteristics as tetragonal lead fluoride and is known as cotunnite.[5] We are also unaware of any calculations of the electronic structure of cotunnite.

The electronic structure of lead fluoride and lead chloride crystals was calculated using the method of crystal orbitals—linear combination of atomic orbitals (CO LCOA) in the complete neglect of differential overlap (CNDO) approximation.[6] This method can be used to calculate the band structure of a fairly complex crystal, having a large number of atoms per unit cell and low space group symmetry.

If cyclic boundary conditions are imposed on the main region of the crystal, the wave vector $\mathbf{k}$ has N different values which corresponds to N primitive cells numbered by the position vector $\mathbf{R}_n$. Since a considerable number of integrals are not calculated in the CNDO approximation, the expressions for the matrix elements of the single-electron Hamiltonian and the Hartree-Fock operator in the crystal have the following form:

$$H_{pp}(\mathbf{k}) = U_{pp} + Z_A \gamma_{AA}^{00} - \sum_C \sum_{n=0}^{N-1} Z_C \gamma_{AC}^{0n} + \sum_{n=1}^{N-1} \beta_{AA}^0 S_{pp}^{0n} \exp(i\mathbf{k}\mathbf{R}_n), \tag{1}$$

$$H_{pq}(\mathbf{k}) = \sum_{n=0}^{N-1} \beta_{AB}^0 S_{pq}^{0n} \exp(i\mathbf{k}\mathbf{R}_n), \tag{2}$$

$$F_{pp}(\mathbf{k}) = H_{pp}(\mathbf{k}) + \frac{1}{N} \sum_C \sum_{n=0}^{N-1} \sum_{k'} P_{rr}(\mathbf{k}') \gamma_{AC}^{0n} - \frac{1}{2N} \sum_{n=0}^{N-1} \sum_{k'} P_{pp}^*(\mathbf{k}') \gamma_{AA}^{0n} \exp(i(\mathbf{k}-\mathbf{k}')\mathbf{R}_n), \tag{3}$$

$$F_{pq}(\mathbf{k}) = H_{pq}(\mathbf{k}) - \frac{1}{2N} \sum_{n=0}^{N-1} \sum_{k'} P_{pq}^*(\mathbf{k}') \gamma_{AB}^{0n} \times \exp(i(\mathbf{k}-\mathbf{k}')\mathbf{R}_n). \tag{4}$$

Calculation of the $\mathbf{k}$-dependent density matrix

$$P_{pq}(\mathbf{k}) = 2 \sum_i^{\text{occ.}} C_{ip}^*(\mathbf{k}) C_{iq}(\mathbf{k}), \tag{5}$$

involves summation over all occupied crystal orbitals (i) which are linear combinations of atomic orbitals. In expressions (1)–(4), S_{pq}^{0n} and γ_{AB}^{0n} are the overlap and Coulomb integrals, respectively, for the p orbital of atom A in primitive cell 0 and the q atomic orbital of atom B in cell n, U_{pp} describes the interaction between an electron and the atomic core of atom A, and the core charge Z_A is equal to the number of valence electrons of atom A.

A characteristic feature of the CNDO method is that it has variable (fitting) parameters, which makes computer calculations considerably easier. Experimental data for well studied crystals were used to make an accurate choice of parameters, especially the so-called resonant integrals β. Thus, the parameters of fluorine and chlorine were chosen on the basis of calculations on CaF_2 and KCl crystals, respectively. The parameters of lead were refined for the cubic

TABLE I. Parameters of the electronic structure of lead (II) fluorides and chloride (in eV).

Parameter	Crystal		
	α PbF_2	β PbF_2	$PbCl_2$
Bottom of conduction band	1.247	1.227	5.151
Top of upper valence band	−4.558	−4.510	−3.748
Band gap	5.805	5.737	8.899
Bottom of upper valence band	−14.816	−15.113	−14.527
Width of upper valence band	10.258	10.604	10.779

modification, it being the most studied. Finally, it was assumed that the parameters of a given type of atom were transferrable from one crystal to another.

The calculations showed (see Table I) that when a PbF_2 crystal is converted from the β phase (fluorite structure) to the α phase (cotunnite structure), the change in the electronic structure is very small. The band gap, the width of the upper valence band, and the atomic charges vary negligibly. In both cases, the top of the upper valence band consists of *s* states of lead while the bottom of the conduction band is formed by *p* states of lead. The existence of a fairly wide energy gap (5.8 and 5.7 eV for α and β PbF_2, respectively) means that these crystals can be reliably classified as insulators. The calculated charges at the fluorine atoms are $-0.94e$ which is consistent with the experimentally observed high ionic conductivity for fluorine.

One can distinguish conditionally two contributions to the electrical conductivity associated with the ionic and electronic subsystems. The electronic subsystem determines the type of chemical bond and the electron density distribution in the crystal. The ionic subsystem determines the characteristics of these crystals from the point of view of the ion as the smallest particle involved in charge transport. In this approach, the calculated data on the electronic structure of the crystal ''fit in'' with the general picture of the ionic transport process. In this particular case, a comparison between the electronic structure of two crystals having the same overall composition but different spatial configurations of the atoms indicates that the electronic subsystem is fairly stable on transition from the high-symmetry to the low-symmetry crystal. This is consistent with the fact that fluoride compounds of lead are conductors with high ionic conductivity because of the characteristic features of the fluorite and cotunnite crystal structures.

We calculated for the first time the electronic structure of a cotunnite $PbCl_2$ crystal. Our calculations give a band gap of 8.9 eV which indicates that this crystal has dielectric properties. The width of the upper valence band is 10.7 eV, i.e., is similar to that for lead fluorides. The structure of the upper valence band is similar to that for fluorides: the top of the band is determined by the *s* states of lead while the bottom of the conduction band of PbF_2 is formed by the *s* states of lead. The charges at the chlorine atoms are $-0.96e$, which also shows the high degree of ionicity of the bond in the crystal.

Some researchers have already attempted to explain the nature of the ionic transport in cationic-conducting solid electrolytes,[7,8] by attributing the cationic conductivity to characteristics of the electronic structure (in particular, the appearance of local levels in the conduction band and an appreciable change in the band gap). For anionic-conducting solid electrolytes, the electronic pattern before and after transition of the crystal to the superionic phase most likely varies negligibly. This implies that the nature of the anionic disorder in these crystals has qualitatively different characteristics.

When a fluorine atom leaves its regular site in the lattice (0_h symmetry for a fluorine atom in a fluorite crystal), it moves via positions which are known to be less symmetric. However, in the α phase of lead fluoride (cotunnite structure) the regular position already has fairly low symmetry, but this does not cause appreciable changes in the electronic structure compared with the β phase of lead fluoride (fluorite structure).

This work was supported by the Russian Fund for Fundamental Research (Grant 96-03-33134).

[1] I. V. Murin, O. V. Glumov, and A. M. Andreev, in *Proceedings of the Thirteenth International Symposium on Reactivity of Solids*, Hamburg, Germany (1996), Paper 3PO-196.
[2] I. V. Murin, A. M. Andreev, and H. Elgandoz, in *Proceedings of the Seventh Europhysics Conference on Defects in Insulating Materials*, Lyon, France (1994), p. 138.
[3] H. Koto, H. Schulz, and R. A. Huggins, Solid State Ionics **1**, 355 (1980).
[4] P. Boldrini and B. O. Loopstra, Acta Crystallogr. **22**, 744 (1967).
[5] Yu. Z. Nozik, L. E. Fykin, and L. A. Muradyan, Kristallografiya **21**, 76 (1976) [Sov. Phys. Crystallogr. **21**, 38 (1976)].
[6] R. A. Evarestov and V. A. Veryazov, Rev. Solid State Sci. **5**, 415 (1991).
[7] A. Hasegava, Solid State Ionics **15**, 81 (1985).
[8] N. N. Kristofel', Fiz. Tverd. Tela (Leningrad) **27**, 2001 (1985) [Sov. Phys. Solid State **27**, 1202 (1985)].

Translated by R. M. Durham

Study of crystals in medium- and long-wavelength IR ranges by surface-electromagnetic-wave spectroscopy

E. V. Alieva, G. N. Zhizhin, L. A. Kuzik, and V. A. Yakovlev

Institute of Spectroscopy, Russian Academy of Sciences, 142092 Troitsk, Moscow District, Russia
(Submitted July 23, 1997)
Fiz. Tverd. Tela (St. Petersburg) **40**, 237–241 (February 1998)

First observation of excitation of surface electromagnetic waves (SEW) is reported in the reststrahlen region in for biaxial crystal $KTiOPO_4$ (KTP) using a tunable CO_2 laser around 10 μm, and for CaF_2, BaF_2, MgO (cubic crystals), and $LiNbO_3$ (uniaxial crystal) in the far IR using ith a free-electron laser. The parameters of SEW propagation in these crystals have been obtained by the interference method of SEW phase spectroscopy, and the possibility of determining the complex dielectric permittivity of crystals from the SEW propagation parameters demonstrated in the range of SEW existence. © *1998 American Institute of Physics.*
[S1063-7834(98)01502-0]

Spectral studies of thin films on crystal surfaces require the knowledge of optical constants of the substrate in the frequency region of interest. For this purpose one customarily uses reflectance spectra with their subsequent treatment by dispersion analysis[1] or Kramers–Kronig transformation procedure.[1] In the reststrahlen region, however, the desired accuracy cannot be achieved, because in dispersion analysis fitting the calculated to experimental spectra is quite frequently impossible because of the anharmonicity in the region of the absorption bands, and the dielectric permittivity calculated by the Kramers–Kronig method depends on extrapolation beyond the measured spectrum and is sensitive to the accuracy with which the absolute value of the reflectance was determined, particularly in regions with a small reflectance. All these difficulties can be avoided by using phase-sensitive reflectance measurement methods, for instance, IR ellipsometry[2] and dispersive Fourier spectroscopy.[3] In this work we also employed a phase-sensitive method of determining the optical constants of crystals, namely, phase spectroscopy of surface electromagnetic waves (SEW), which permits unambiguous calculation of the complex dielectric permittivity from the SEW propagation parameters. Moreover, the presence of a thin (about a few nm thick) insulating film on the crystal surface, which does not affect the crystal reflectance spectrum within measurement accuracy, results in a noticeable change of the SEW propagation parameters for the crystal with a film, thus permitting one to find the dielectric permittivity not only of the bulk crystal but of the thin film as well.[4]

SEW are a TM mode and, thus, exist at the interface between media one of which is surface active, which means that the real parts of the dielectric permittivities ε of these media must have opposite signs.[5] The SEW electric field is maximum at the interface, thus making these waves highly sensitive to the state of the surface and to thin films. The wave vector of SEW is larger than that of the bulk wave, and, as a result, SEW is a nonradiative mode. To convert the bulk wave to SEW and back, one has to have a device capable of wave-vector matching, for instance, a diffraction grating, an impedance step etc. SEW spectroscopy permits direct determination of both the imaginary and the real part of the dielectric permittivity of the medium along which the SEW propagate. This was used to advantage in determining the optical constants of metals,[6] for which the conditions of SEW existence are met throughout the IR region up to the visible. On the surface of insulator crystals, SEW can exist only within narrow spectral intervals corresponding to reststrahlen bands, within which crystals are surface active ($\mathrm{Re}\,\varepsilon<0$). Crystal studies by SEW spectroscopy meet with difficulties associated with the fact that the SEW damping coefficient by crystals is several orders of magnitude larger than that by metals, which calls for miniaturization of the experiment. Earlier studies determined the SEW propagation parameters and the dielectric permittivity of crystalline quartz[7] and of sodium chlorate[8] with a CO_2 tunable laser near 1000 cm^{-1}. Surface electromagnetic waves were found to propagate over $SrTiO_3$ at several methanol-laser frequencies near 100 cm^{-1}.

In this work, SEW spectroscopy has been tried on a number of crystals popular in various areas of optics and electronics. Besides the CO_2 laser, we used also a FELIX free-electron laser, which is continually tunable from 100 to 2000 cm^{-1} and which permitted investigation over a broad IR range, including the long-wavelength domain that has been practically inaccessible until now.

1. EXPERIMENT

The optical arrangement used in SEW phase spectroscopy is presented schematically in Fig. 1. Fixed-frequency laser radiation was focused by a parabolic mirror onto a slit between a metal screen and the sample surface and diffracted from it. Part of the diffracted radiation acquired a wave vector equal to that of the surface wave. It transformed into a SEW, which propagated along the surface of the sample under study up to the edge and diffracted from it to become again a bulk wave. Interference of these two bulk waves produced, at a certain distance from the sample, a field distribution which was measured either by a receiver moving along the Z axis or by an array of pyrolitic detectors oriented along the Z axis (256 devices on a strip 25.4 mm long). The

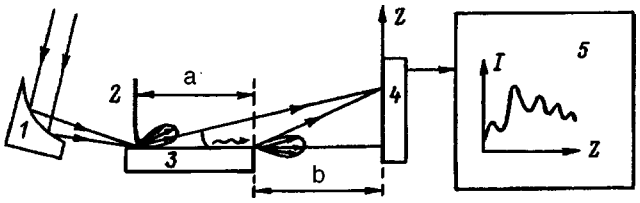

FIG. 1. Optical arrangement for a SEW phase spectroscopy experiment. *1*—parabolic mirror, *2*—metal screen, *3*—sample under study, *4*—IR radiation receiver or pyrolitic detector array, *5*—digital oscillograph.

Z scan of the SEW interference pattern was read out from the detectors and fed into a digital oscillograph to be stored later in the data file.

The SEW interference pattern contains information on SEW phase and amplitude at the edge of the sample. The coordinates of the extrema z_m can be written

$$\mathrm{Re}(n_{\mathrm{eff}})a+(b^2+z_m^2)^{1/2}-[(a+b)^2+z_m^2]^{1/2} =(m+\Delta m)/2\nu, \quad (1)$$

where ν is the laser radiation frequency, n_{eff} is the effective SEW refractive index, a is the distance from the SEW excitation slit to sample edge, b is the minimum distance from sample edge to the receiver or detector array, m is the extremum number (even for maxima, and odd for minima), and Δm is the SEW phase advance depending on the surface properties. It can be considered constant for a fixed slit width within a certain interval of a and ν variation.

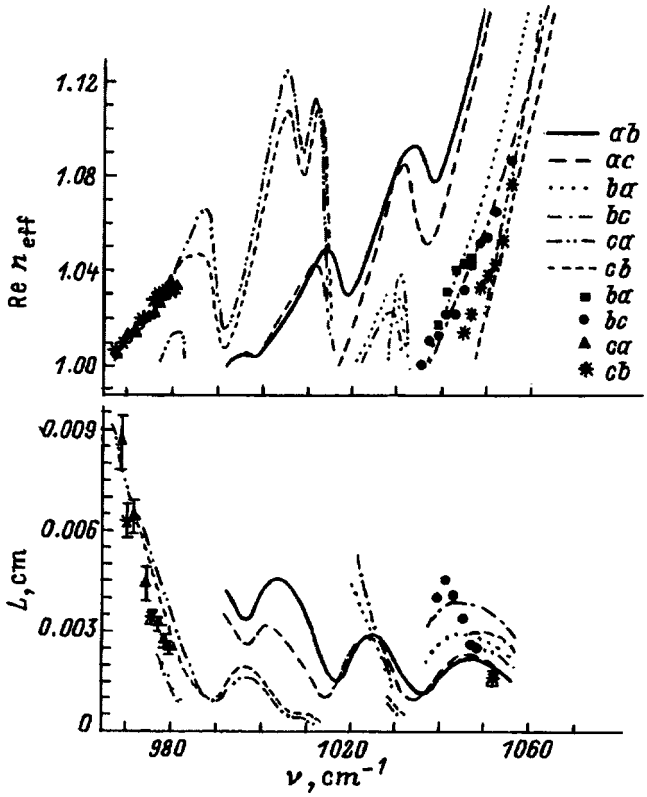

FIG. 2. Frequency dependence of SEW parameters for different directions of propagation over the KTP crystal.

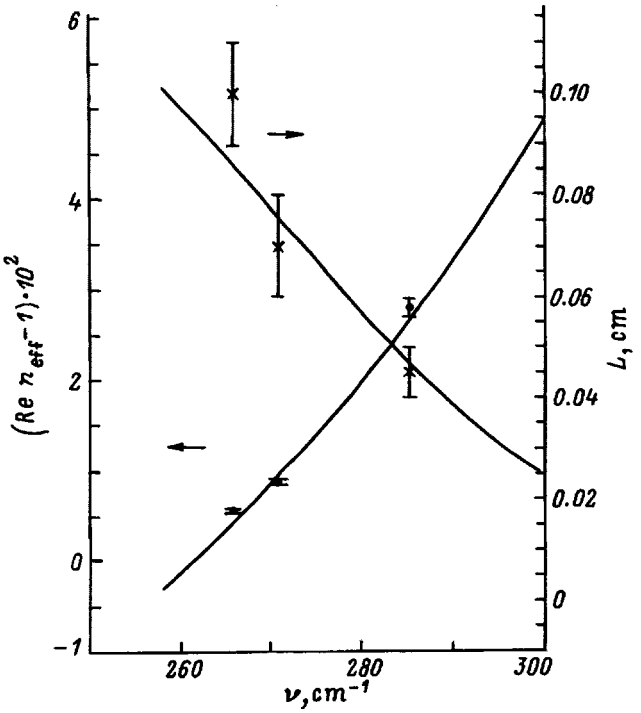

FIG. 3. Frequency dependence of SEW propagation parameters over the CaF_2 crystal.

The positions of the extrema obtained for several distances a can be used to derive from Eq. (1) the absolute value of the real part of the SEW effective refractive index, $\mathrm{Re}\, n_{\mathrm{eff}}$, for the given frequency.[10] To reduce the time required for measurement of the frequency dependence of SEW dispersion, one can fix all geometric parameters entering Eq. (1) and measure the relative change in the interfer-

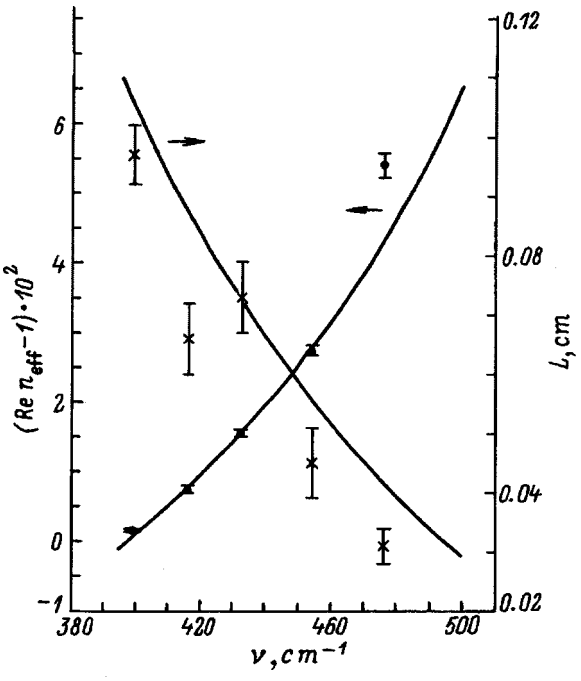

FIG. 4. Frequency dependence of SEW propagation parameters over the MgO crystal.

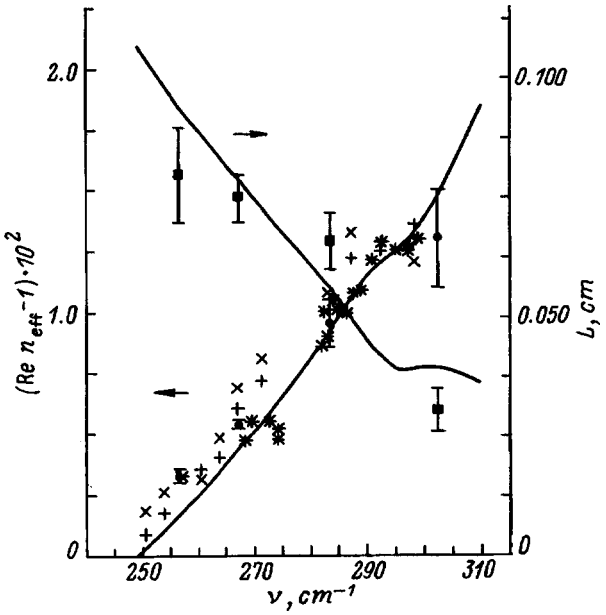

FIG. 5. Frequency dependence of SEW parameters for propagation along the $LiNbO_3$ crystal axis. The various symbols refer to different series of relative measurements of SEW dispersion. Filled circles and squares correspond to absolute values of SEW propagation parameters.

ence pattern by properly sweeping the laser frequency. Having treated a series of interferograms obtained in this way, one can calculate the relative values of $\mathrm{Re}\, n_{\mathrm{eff}}$ (SEW dispersion).[8]

From the modulation of the interference pattern one can estimate the SEW absorption by calculating the SEW free path L (the distance in which the SEW intensity decreases e times) using the relation[11]

$$a/L = 2\ln[(\sqrt{I_{\max}} - \sqrt{I_{\min}})/(\sqrt{I_{\max}} + \sqrt{I_{\min}})] + A, \qquad (2)$$

where $I_{\max}$ and $I_{\min}$ are the maximum and minimum values of the interferogram envelopes taken at a coordinate z, and A is a constant depending on SEW excitation efficiency.

Since the bulk to SEW wave conversion efficiency is small, it is desirable to use in SEW spectroscopy high-intensity coherent collimated radiation sources, i.e. lasers. In this work, investigation of SEW propagation over the KTP crystal was made with a tunable CO_2 laser ($930-1080\ \mathrm{cm}^{-1}$). For a large number of crystals, however, the absorption bands lie below $900\ \mathrm{cm}^{-1}$, and these crystals became accessible for SEW studies only with the advent of free-electron lasers, which have broadened substantially the possibilities of SEW spectroscopy.[12] For instance, SEW propagation over CaF_2, BaF_2, MgO, and $LiNbO_3$ crystals in the far IR region was studied with a FELIX pulsed free-electron laser having unique characteristics.[13]

2. RESULTS

Figure 2 shows frequency dependences of the quantities $\Delta n = (\mathrm{Re}\, n_{\mathrm{eff}} - 1)$ and L for a biaxial KTP crystal obtained for several directions of SEW propagation. The letters specify the direction of SEW propagation with respect to the a, b, and c axes of the KTP crystal, namely, the first letter identifies the SEW propagation axis, and the second, the axis normal to the crystal surface. The points refer to the SEW parameters (SEW dispersion and free path) extracted from the interference patterns, and the lines, to SEW parameters calculated from the dielectric permittivity ε of the crystal by combined use of dispersion and Kramers–Kronig analysis of the reflectance spectrum. Figures 3–5 display theoretical (calculated by dispersion analysis) and experimental SEW parameters for CaF_2 and MgO (cubic crystals) and $LiNbO_3$ (uniaxial crystal) for the case of SEW propagation along the crystal axis. The data presented in Figs. 3–5 demonstrate a good agreement of calculated SEW propagation parameters with experiment. Table I sums up the experimental SEW characteristics for all the crystals studied by us, namely, the spectral regions covered, free-path variation ranges, and dispersion of the surface waves. The SEW propagation parameters can be used to calculate the complex dielectric permittivity of the crystal ε for the region where these waves exist. Table II lists the real and imaginary parts of ε for MgO, which were derived from the values of Δn and L obtained from the experimental SEW propagation parameters, and the reflectance calculated from them for several frequencies. Also presented for comparison are data obtained from a dispersion analysis of the reflectance spectrum of MgO and the experimentally measured reflectance. All the data are seen to be in good agreement.

The above studies have demonstrated the possibility of determining optical constants of crystals in the reststrahlen region by SEW spectroscopy.

TABLE I. Parameters of SEW propagation over crystals.

Crystal and orientation	Frequency range ν, cm^{-1}	Real part of SEW effective refractive index n_{eff}	SEW free path L, mm
BaF_2	186–193	1.002–1.0096	1.1–0.9
CaF_2	265–293	1.0056–1.042	1.0–0.4
MgO	399–476	1.0016–1.053	0.97–0.31
$LiNbO_3$, SEW	263–281	1.0046–1.016	0.6–0.2
Perpendicular to crystal axis	175–180	1.012–1.0186	0.8–0.38
$LiNbO_3$, SEW parallel to crystal axis	256–302	1.0033–1.013	0.8–0.3
KTP (ba)	1039.4–1046.8	1.017–1.045	
KTP (bc)	1035.5–1055.6	1.0006–1.086	0.04–0.025
KTP (ca)	967.7–981.0	1.005–1.033	00.86 (969 cm^{-1})–0.025 (980 cm^{-1})
KTP (cb)	967.7–979.7	1.002–1.027	0.063 (970.5 cm^{-1})–0.034 (976 cm^{-1})
KTP (cb)	1045–1055.6	1.014–1.077	0.016 (1052 cm^{-1})

TABLE II. Comparison of complex dielectric permittivities ε and reflectances R (s polarized radiation, angle of incidence 10°) calculated from SEW propagation parameters and by dispersion analysis (DA) of the reflectance spectrum for a MgO crystal.

	SEW					DA			
ν, cm^{-1}	n'_{eff}	L, μm	ε'	ε''	R_{calc}	ε'	ε''	R_{calc}	R_{exp}
416.15	1.00705± 0.00005	660±60	−62±2	25±2	91.2±0.9	−61.4	17.4	93.5	92.6
432.9	1.0155±0.0003	730±60	−32.2±0.7	5.1±0.5	94.9±0.4	−31.9	5.1	94.8	94.2
454.5	1.0274±0.0004	450±30	−18.6±0.3	2.5±0.3	94.3±0.4	−18.4	2.0	95.4	95.7
476.19	1.054±0.002	310±30	−9.9±0.4	0.9±0.2	94.9±0.6	−12.2	1.06	95.6	95.4

The authors are grateful to Stichting voor Fundamenteel Onderzoek der Materie (FOM, Netherlands) for the possibility to use the free-electron laser FELIX, and to the personnel of FELIX, particularly to A. F. G. van der Meer, for assistance.

The reflectance measurements and the calculation of optical constants from them were carried out in collaboration with G. Mattei (IMAI, CNR, Italy).

The work was supported by a NATO Grant (NATO Guest Fellowships, Program 1995 N 005335). Partial support of the Russian Fund for Fundamental Research (Grants (95-02-04194 and 95-02-04195) is gratefully acknowledged.

[1] G. Andermann and L. R. Brantley, J. Phys. Chem. Solids **34**, 661 (1973).
[2] A. Röseler and E. H. Korte, J. Mol. Struct. **349**, 321 (1995).
[3] J. R. Birch and T. J. Parker, Infrared and Millimeter Waves **2**, 137 (1979).
[4] E. V. Alieva, L. A. Kuzik, F. A. Pudonin, and V. A. Yakovlev, Fiz. Tverd. Tela (Leningrad) **32**, 3550 (1990) [Sov. Phys. Solid State **32**, 2059 (1990)].
[5] *Surface Polaritons* [in Russian], edited by V. M. Agranovich and D. L. Mills, Nauka, Moscow, 1985.
[6] V. I. Silin, S. A. Voronov, V. A. Yakovlev, and G. N. Zhizhin, Int. J. Infrared Millim. Waves **10**, 101 (1989).
[7] E. V. Alieva, L. A. Kuzik, F. A. Pudonin, and V. A. Yakovlev, Fiz. Tverd. Tela (Leningrad) **34**, 3233 (1992) [Sov. Phys. Solid State **34**, 1874 (1992)].
[8] E. V. Alieva, L. A. Kuzik, V. A. Yakovlev, G. Mattei, and M. Pagannone, J. Electron Spectrosc. Relat. Phenom. **64/65**, 733 (1993).
[9] R. Miller, D. L. Begley, G. A. Ward, R. W. Alexander, and R. J. Bell, Surf. Sci. **71**, 491 (1978).
[10] A. F. Goncharov, G. N. Zhizhin, S. A. Kiselev, L. A. Kuzik, and V. A. Yakovlev, Phys. Lett. A **133**, 163 (1988).
[11] S. A. Voronov, G. N. Zhizhin, S. A. Kiselev, L. A. Kuzik, and V. A. Yakovlev, Komp. Optika No. 4, 66 (1989).
[12] V. A. Yakovlev, G. N. Zhizhin, E. V. Alieva, L. A. Kuzik, A. F. G. van der Meer, and M. J. van der Wiel, Laser Phys. **7**, 239 (1997).
[13] D. Oepts, A. F. G. van der Meer, and P. W. Amersford, Infrared Phys. Technol. **36**, 297 (1995).

Translated by G. Skrebtsov

Dufour effect in superionic copper selenide

M. A. Korzhuev

A. A. Baĭkov Institute of Metallurgy, Russian Academy of Sciences, 117911 Moscow, Russia
(Submitted August 5, 1997)
Fiz. Tverd. Tela (St. Petersburg) **40**, 242–244 (February 1998)

The Dufour effect has been observed in the superionic conductor copper selenide, $Cu_{2-x}Se$. This effect is the opposite of the Soret thermal diffusion effect which was previously only observed in gaseous and liquid systems.
[S1063-7834(98)01602-5]

The Dufour effect, which is the opposite of the Soret thermal diffusion effect, involves the establishment of a heat flux J_q and a temperature gradient ∇T during the interdiffusion of components of a binary system under the action of a concentration gradient ∇C_1 of one of the components.[1] In the linear approximation for the generalized forces, the fluxes of heat J_q and mass J_1 in a binary system with interdiffusing components may be expressed in the form

$$J_q = -\varkappa \nabla T - \rho_1 T \mu_{11}^C D'' \nabla C_1, \tag{1}$$

$$J_1 = -\rho C_1 C_2 D' \nabla T - \rho D \nabla C_1, \tag{2}$$

where $\varkappa$ is the thermal conductivity, T is the average absolute temperature, $\mu_{11}^C = (\delta\mu_1/\delta C_1)_T$, μ_1 is the chemical potential of the first component, D'', D', and D are the Dufour, Soret, and interdiffusion coefficients, ρ_1 and ρ_2 are the densities, and $C_{1,2}$ are the concentrations of the components.[1,2]

For the steady state ($J_q = J_1 = 0$) expressions (1) and (2) give

$$D' = -D\nabla C_1/(C_1 C_2 \nabla T), \tag{3}$$

$$D'' = \lambda \nabla T/(T\rho_1 \mu_{P11}^C \nabla C), \tag{4}$$

which, assuming the Onsager reciprocity relation $D' = D''$ (Refs. 1 and 2), yields the following expression for the temperature difference in the Dufour effect

$$\Delta T = \Delta C (T\rho_1 \mu_{11}^C D/(\lambda C_1 C_2))^{1/2}, \tag{5}$$

where $\Delta T = \nabla T h$ and $\Delta C = \nabla C h$ are the temperature and concentration gradients in the sample, and h is the height of the sample. It follows from expression (5) that the magnitude of the Dufour effect ΔT is mainly limited by the diffusion coefficients D of the system components.

At near-room temperature, the diffusion coefficients of atoms and ions in gases, liquids, and solids are $D \sim 10^{-1}$ cm^2/s, $\sim 10^{-5}$ cm^2/s, and $\sim 10^{-10} - 10^{-19}$ cm^2/s, respectively.[3–5] Thus, the best conditions for observing the Dufour effect are found in gases. The measured values of ΔT for gases are a few degrees, in liquids these ΔT values are $\sim 10^4$ times smaller, and in normal solids the Dufour effect is negligible.[2]

In superionic conductors (solid electrolytes) the diffusion coefficients of mobile ions may be similar to those of ions in liquids and gases.[5] This situation is observed in mixed electronic-ionic conductors where the ions are accelerated by more mobile electrons as they undergo combined ''chemical'' diffusion in samples.[5–9]

So far the highest ''chemical'' diffusion coefficients $\tilde{D}$ (up to 10^{-1} cm^2/s) have been observed in I-VI semiconductors having the formula $A^{I}_{2-x}B^{VI}$ (A=Cu, Ag, Au and B=S, Se, Te).[6] In nonstoichiometric copper selenide p-$Cu_{2-x}Se$ ($x = 0.01-0.3$) approximately one third of the copper ions are mobile [$\tilde{D} \sim 10^{-2}$ cm^2/s is found at room temperature and $D \sim 10^{-2}$ cm^2/s at $T > T_c = 413$ K, where T_c is the superionic phase transition temperature (Fig. 1)], and these ions are readily displaced in the sample under the action of concentration, temperature, pressure, and other force gradients.[7,10,11] The possibility of a large Dufour effect in $Cu_{2-x}Se$ was indicated by the anomalously high values of the inverse Soret effect which were observed earlier.[12]

Here, in order to observe the Dufour effect, concentration gradients ($\Delta x \sim 0.04-0.3$, $\Delta C_{Cu} \sim 10^{21} - 10^{22}$ cm^{-3}) were established in the material by bringing two $Cu_{2-x}Se$ samples of different composition in mechanical contact and then homogenizing them (Fig. 2) (Ref. 13). The Dufour effect $\Delta T \sim 1$ K caused by diffusion fluxes of mobile copper in the sample was observed during the homogenization process.

1. EXPERIMENT

Polycrystalline $Cu_{2-x}Se$ alloys of varying composition ($x = 0.01-0.1$) were prepared by ampoule synthesis.[10] The measurements were made using cylindrical samples (6 mm diameter, $h = 16$ mm) of varying composition ($x_1 < x_2$). The sample compositions ($x_1 = 0.01$ and $x_2 = 0.05$ and 0.1) were selected within the homogeneous range of the compound (Fig. 1) so that the homogenization process was not accompanied by phase transitions to the solid state. Copper-constantan thermocouples (0.1 mm diameter, differential thermo-emf $\alpha = 40$ μV/K) were attached to the ends of the samples and were used to measure T and ΔT (Fig. 2). The samples were held in a thermostat (± 0.01 K) for an hour and were then compressed at a pressure of 0.01 GPa.

The compression process produced a composite inhomogeneous sample where the mobile copper diffused from one part (x_1) to the other (x_2) (Fig. 2) (Ref. 13). The homogenization process was monitored by measuring the thermo-emf α (Ref. 13). Homogenization was accompanied by the Dufour effect—by a temperature variation in different parts of the composite sample. These Dufour temperature gradients ΔT were identified using an N-309 automatic plotter (sensitivity 25 μV/cm) controlled by a Shch-301 digital voltmeter (sensitivity 0.1 μV). The measurements were made in the

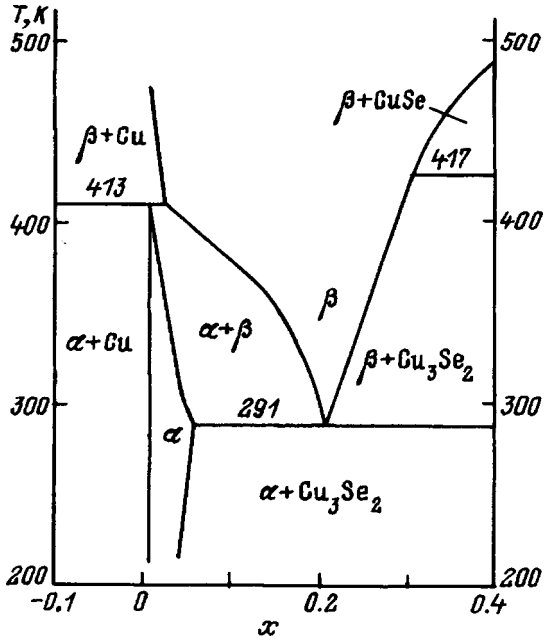

FIG. 1. Part of $T-x$ phase diagram of Cu-Se system near the compound $Cu_{2-x}Se$. Polymorphic modifications: α—Cm, β—$F\bar{4}3m$ (Ref. 10).

temperature range $T=300-430$ K, covering the stability regions of the low-temperature α phase and the high-temperature β phase of the compound (Fig. 1). Compression of the samples, which were separated by an antidiffusion layer (Al foil, $h=0.05$ mm), showed that the plastic deformation accompanying the compression causes negligible heating of the composite sample near the x_1/x_2 phase boundary ($\Delta T \leqslant +0.01-0.02$ K).

2. EXPERIMENTAL RESULTS AND DISCUSSION

Figure 2 shows the Dufour temperature gradients ΔT (curves *1–3*) observed for a composite $Cu_{2-x_1}Se/Cu_{2-x_2}Se$ sample ($x_1=0.01$, $x_2=0.05$ and 0.1). The sign of the observed effect corresponded to heating of the material with decreasing x and cooling with increasing x during the diffusion process ($\nabla T \parallel J_{Cu}$, J_{Cu} is the mobile copper flux in the sample).

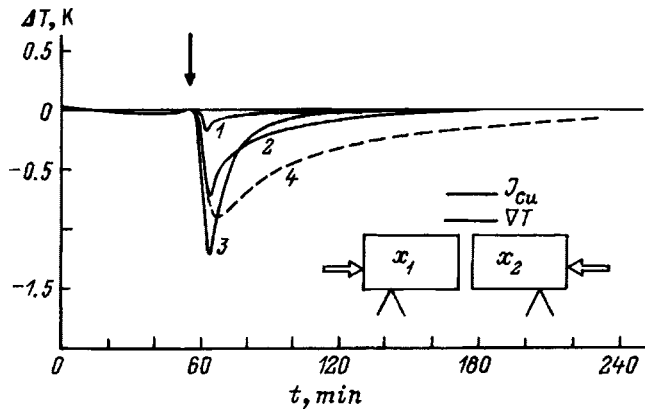

FIG. 2. Dufour temperature difference ΔT (*1–3*) established in composite $Cu_{2-x_1}Se/Cu_{2-x_2}Se$ sample by diffusion of copper. The time of contact between the samples is indicated by the arrow: $x_1=0.01$; x_2: *1, 2*—0.05, *3*—0.1. T (K): *1, 4*—300, *2*—340, *3*—420, *4*—nitric acid was used as the copper acceptor.[11]

It can be seen from Fig. 2 that at room temperature the Dufour effect in $Cu_{2-x}Se$ samples is fairly small (ΔT up to 0.2 K) (curve *1*), the effect increases with temperature, reaching a maximum (ΔT up to 1.2 K) in the high-temperature β phase of the compound (curves *2* and *3*). The kinetics of the Dufour effect (curves *1–3* in Fig. 2) was completely determined by the homogenization kinetics of the composite sample.[13] At $T=340-430$ K the composite sample homogenized completely within $t\sim 1-3$ h ($\bar{x}\sim 0.03$, (Ref. 13)). In this case, the Dufour effect reached a maximum (ΔT up to 1.2 K), and then decreased monotonically to zero for $J_{Cu}\rightarrow 0$ (curves *2* and *3* in Fig. 2). At room temperature the homogenization process was considerably slower and did go to completion because of the difficulties involved in relaxation of the mechanical stresses created in the sample as a result of the Kirkendall effect,[12,13] and the Dufour effect therefore decreased ($\Delta T\sim 0.2$ K) (curve *1* in Fig. 2).

The Dufour effect at room temperature was increased (ΔT to 0.7 K) (curve *4* in Fig. 2) by using a more efficient method of extracting the mobile copper from the donor sample with 10% nitric acid [by the chemical reaction $Cu_{2-x}Se + HNO_3 \rightarrow Cu_{2-(x+\Delta x)}Se + Cu(NO_3)_2 + NO(NO_2)\uparrow + H_2O$] (Ref. 11). For this purpose one end of the sample (x_1) in the thermostat was brought in contact with the acid and the temperature gradient ΔT along the sample was measured.

The observed increase in ΔT (curve *4* in Fig. 2) may be attributed to an increase in the concentration gradient Δx acting along the sample to ~ 0.3. Some contribution may also be made by endothermic phase transitions in the solid state accompanying the change in the composition of the samples $x=0.01\rightarrow 0.3$ (Fig. 1) and the extraction process itself.[11] Thus, curve *4* (Fig. 2) gives the Dufour effect observed in the material under conditions of so-called ''reactive'' ''chemical'' diffusion.[4,5]

Thus, the Dufour effect (Fig. 2), previously only observed in gaseous and liquid systems,[1,2] has now been detected in the superionic conductor copper selenide $Cu_{2-x}Se$. The relatively strong Dufour effect in $Cu_{2-x}Se$ (Fig. 2) is determined by the following factors: 1) the superionic nature of the compound, which gives high copper diffusion coefficients in the samples (up to 10^{-2} cm^2/s); 2) the large composition gradients Δx and mobile copper concentration gradients ΔC_{Cu} established in the samples achieved as a result of the wide region of homogeneity of the compound (Fig. 1); 3) the high μ_{11}^C values and low thermal conductivity $\varkappa=4.2\times 10^{-3}$ J/(cm·s·K). For this reason $Cu_{2-x}Se$ has a high thermoelectric efficiency $Z=\alpha^2/\delta\varkappa$, where δ is the electrical conductivity.

The high chemical potential $\mu_{11}^C=(\delta\mu_1/\delta C_1)_T$ can be attributed to the x-dependence of the free energy of nonstoichiometric $Cu_{2-x}Se$. The standard heat of formation of the compound is $\Delta H_f^0(298.15)=-65.5$ kJ/mol for $x=0$ and -416.4 kJ/mol for $x=0.18$ (Ref. 14). Thus, for complete homogenization of an inhomogeneous sample $x_1=0.01/x_2=0.05(0.1)\rightarrow\bar{x}\sim 0.025(0.045)$ under

adiabatic conditions, the temperature of the donor (acceptor) sample should decrease (increase) by $\Delta T \sim [\Delta H_f^0(x=0.01) - \Delta H_f^0(x=0.05)]/(MC) \sim 1-3$ K ($M = 206$ g is the molecular weight and $C = 88.2$ J/(g·K) is the specific heat of the compound), which explains both the magnitude and the sign of the observed effect (Fig. 2).

Thus, the Dufour effect may also be observed in other nonstoichiometric superionic conductors possessing a wide region of homogeneity and mixed electronic and ionic conductivity. Of particular interest for research purposes may be the alloys $Cu_{0.93}Ag_{0.07+x}Se$ and $Cu_{0.8775}Ag_{0.125}Se$, which undergo an electronic p-n transition where the chemical diffusion coefficients of mobile copper and silver ions attain record levels for solids ($D \sim 10^{-1}$ cm^2/s) (Ref. 15).

The author would like to thank V. F. Bankina and N. N. Filipovich for growing the crystals for the measurements.

[1] S. Groot and P. Mazur, *Nonequilibrium Thermodynamics* [in Russian], Moscow (1964).
[2] *Physics Encyclopedia*, Vol. 2 [in Russian], Sovetskaya Entsiklopediya, Moscow (1990).
[3] *Handbook of Physical Quantities*, edited by I. S. Grigor'ev and E. Z. Meĭlikov, [in Russian], Atomizdat, Moscow (1991).
[4] J. R. Manning, *Diffusion Kinetics for Atoms in Crystals* [Van Nostrand, New York, 1968; Mir. Moscow, 1971].
[5] V. N. Chebotin, *Chemical Diffusion in Solids* [in Russian], Nauka, Moscow (1989).
[6] V. L. Bonch-Bruevich and S. G. Kalashnikov, *Physics of Semiconductors* [in Russian], Nauka, Moscow (1977).
[7] M. A. Korzhuev, Fiz. Tverd. Tela (Leningrad) **31**, 25 (1989) [Sov. Phys. Solid State **31**, 1666 (1989)].
[8] M. A. Korzhuev, Fiz. Tverd. Tela (Leningrad) **34**, 1209 (1992) [Sov. Phys. Solid State **34**, 639 (1992)].
[9] M. A. Korzhuev, Pis'ma Zh. Tekh. Fiz. **64**, 107 (1996) [*sic*].
[10] M. A. Korzhuev, V. V. Baranchikov, N. Kh. Abrikosov, and V. F. Bankina, Fiz. Tverd. Tela (Leningrad) **26**, 2209 (1984) [Sov. Phys. Solid State **26**, 1341 (1984)].
[11] M. A. Korzhuev, Fiz. Tverd. Tela (Leningrad) **31**, 25 (1989) [Sov. Phys. Solid State **31**, 1666 (1989)].
[12] M. A. Korzhuev, Fiz. Khim. Obrab. Mater. **1**, 92 (1989).
[13] M. A. Korzhuev, A. V. Laptev, and N. Kh. Abrikosov, Fiz. Tverd. Tela (Leningrad) **29**, 1543 (1987) [Sov. Phys. Solid State **29**, 885 (1987)]; Fiz. Khim. Obrab. Mater. **5**, 132 (1987).
[14] *Handbook of Physicochemical Properties of Semiconductor Materials*, edited by A. V. Novoselova [in Russian], Nauka, Moscow (1979).
[15] R. A. Yakshibaev and M. Kh. Balapanov, Fiz. Tverd. Tela (Leningrad) **29**, 2819 (1987) [Sov. Phys. Solid State **29**, 1620 (1987)].

Translated by R. M. Durham

Excess space charge in strontium titanate

A. I. Dedyk and L. T. Ter-Martirosyan

St. Petersburg State Electrical Engineering University, 197376 St. Petersburg, Russia
(Submitted September 9, 1997)
Fiz. Tverd. Tela (St. Petersburg) **40**, 245–247 (February 1998)

An analysis is made of mechanisms of the formation and redistribution of space charge which influence the dielectric hysteresis in $SrTiO_3$. The excess space charge density in $SrTiO_3$ at 4.2 K is estimated by comparing calculated and experimental dependences of the initial capacitance and the dielectric hysteresis parameter $\Delta C/C_0$ as a function of the crystal thickness.
 [S1063-7834(98)01702-X]

The nonlinear dielectric strontium titanate $SrTiO_3$ (STO) has recently attracted increasing interest among developers of new electronic devices.[1–3] These devices are based on a capacitor structure with a STO dielectric and the electrodes are made of metal or the high-temperature superconductor $YBa_2Cu_3O_{7-\delta}$ (YBCO).

However, a STO-based capacitor structure almost always has an excess negative[4] space charge localized at the acceptors.[5,6] This excess space charge is caused by effects at the STO-electrode contact and possibly also by the technological processes involved in the fabrication of the structure. When the dc voltage applied to the capacitor structure is increased, the space charge may increase substantially as a result of the injection of electrons from the negative electrode (cathode).[6] After fabrication, the capacitor structure is usually stored at 300 K with short-circuited electrodes and the space charge is distributed uniformly in the STO bulk with a time constant of $\sim$30 s. After the structure has been cooled to the working temperature (78 K or lower), this space charge distribution is conserved until an external electric field is applied to the STO. The applied static field redistributes the space charge and after the external field has been switched off, a new, nonuniform space charge distribution is conserved. In this case, the initial capacitance of the structure is higher than that for a uniform distribution and this increase in the initial capacitance may be described as ''positive'' hysteresis.[6]

When the external dc voltage applied to the structure is increased further, the negative space charge injected from the negative electrode into the STO crystal begins to predominate and the initial (with the external voltage switched off) capacitance of the structure decreases. This reduction in the initial capacitance may be described as ''negative'' hysteresis.[6] In this reasoning it is assumed that when an external dc voltage is applied to the capacitor structure, the space charge does not drift to the electrode because of hole barriers at the STO-metal contacts.[7]

Dielectric hysteresis, i.e., a multivalued capacitance-voltage characteristic, significantly impedes the development of electronic devices using STO.

Here we make a quantitative estimate of the excess space charge density (neglecting the injected space charge) based on experimental data obtained at 4.2 K (Ref. 6).

We consider a nonlinear capacitor with uniformly distributed excess space charge at 4.2 K, using the relations obtained in Ref. 8. The reciprocal initial specific capacitance of this capacitor may be written in the form

$$\frac{S}{C_0}=\frac{2E_H z_0}{\sigma}L, \tag{1}$$

where E_H is the normalization constant, $z_0=E(0)/E_H$ is the normalized electric field strength at the crystal–electrode interface ($x=0$), L is the thickness of the STO crystal, and σ is the excess space charge per unit area of the electrode.

The value z_0 is the root of the equation[8]

$$K\ \arctan(z_0)+z_0=\frac{\sigma}{2\varepsilon_0\varepsilon_{\min}E_H}, \tag{2}$$

where $K=(\varepsilon_{\max}/\varepsilon_{\min})-1$, and $\varepsilon_{\max}$ and $\varepsilon_{\min}$ are the permittivities of STO in the absence of an external static electric field and in an infinitely strong field, respectively.

Assuming different values of the space charge density σ, we can find z_0 using Eq. (2) and then, using formula (1), we can determine the thickness dependence of the reciprocal specific capacitance for a uniform space charge distribution in the crystal. We also need to know the values of the parameters $\varepsilon_{\min}$, K, and E_H for STO single crystals for which the experimental data used for comparison were obtained.

On the basis of known experimental data for STO single crystals at 4.2 K (Refs. 6 and 8), we can take $\varepsilon_{\max}\simeq(36-40)\times10^3$, $\varepsilon_{\min}\simeq2\times10^3$, and $E_H\simeq0.8\times10^5$ V/m. Taking different values of σ, we can then use Eqs. (1) and (2) to find the corresponding thickness dependences of the specific reciprocal capacitance.

The calculated curves are plotted in Fig. 1 together with the experimental data obtained on samples with metal electrodes before the voltage is first applied.[6]

Satisfactory agreement between the calculated and experimental dependences is obtained for $\sigma\sim5\times10^{-2}$ S/m^2, where $(S/C_0)\simeq3.75\times10^6$ m^2/F. Note that, in the absence of space charge, the specific reciprocal initial capacitance is $(S/C_0)=L/\varepsilon_0\varepsilon_{\max}\simeq2.98\times10^6$ m^2/F.

Thus, a comparison between the calculated and experimental data shows that, after fabrication of the capacitor structure, the STO crystal contains space charge with a surface (per unit electrode area) density $\sigma=\sim0.05$ S/m^2. We stress that this estimate does not include the injected space charge since we used experimental data obtained before the voltage is first applied.

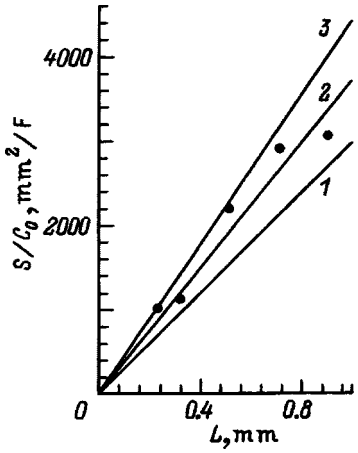

FIG. 1. Reciprocal specific capacitance versus crystal thickness at $T=4.2$ K: *1–3*—calculated curves for $\sigma=0$, 0.05, and 0.06 $\mathrm{S\cdot m^{-2}}$, respectively. The filled circles give the experimental data.

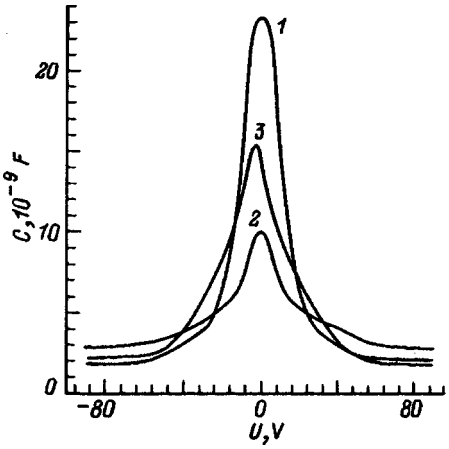

FIG. 3. Calculated capacitance-voltage characteristics for various space charge distributions in a strontium titanate crystal at $T=4.2$ K: $\rho(z)\times(\mathrm{S\cdot m^{-3}})$: *1*—0, *2*—10, and *3*—100 ($\rho_{\max}$, Gauss law).

Attention should be drawn to the fact that the slope of the thickness dependence of the specific reciprocal capacitance is determined by the total excess space charge in the STO per unit electrode area and does not depend on the crystal thickness.

It should also be borne in mind that, according to our estimates, the maximum concentration of charged acceptors is $N_A\simeq 5\times 10^{21}$ $\mathrm{m^{-3}}$ (Ref. 8) so that an excess space charge with the surface density $\sigma\simeq 0.05$ $\mathrm{S/m^2}$ can exist only for the crystal thickness $L_{\min}\geqslant\sigma/|e|N_A\simeq 70$ μm. If the crystal thickness is $L\leqslant L_{\min}$, the space charge distribution clearly cannot vary under the action of an external bias voltage (we assume here that the external field strength is insufficient to redistribute the space charge as a result of electron injection from the cathode) since N_A is the highest possible concentration of charged acceptors. Thus, for $L\leqslant L_{\min}$, it is impossible to have positive hysteresis. This conclusion is quite consistent with the experimental data:[6] Extrapolating (dashed curve) the experimental dependence (filled circles) of the dielectric hysteresis parameter $\Delta C/C_0$ on the STO crystal thickness, plotted in Fig. 2, gives $\Delta C/C_0=0$ $L\simeq 70-100$ μm. This may be regarded as indirect evidence that the above estimates are valid.

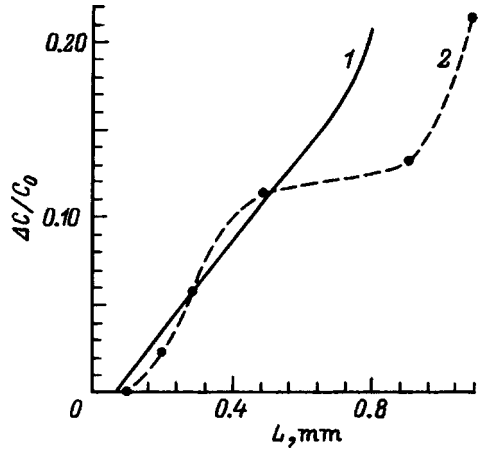

FIG. 2. Calculated (*1*) and experimental (*2*) dependences of the dielectric hysteresis on the crystal thickness at $T=4.2$ K.

As an additional check on the validity of these conclusions, we can compare this experimental thickness dependence of the dielectric hysteresis parameter $\Delta C/C_0$ for metal electrodes[6] with the corresponding calculated thickness dependence.

To obtain this calculated dependence, we first note that for $L=L_{\min}\simeq 70$ μm the specific reciprocal capacitance of a capacitor structure with space charge depends on the crystal thickness L as $S/C_0=3.75\times 10^6 L$, and the concentration of charged acceptors has a maximum over the entire crystal so that no positive hysteresis occurs $\Delta C/C_0=0$.

For $L>L_{\min}$ the space charge becomes redistributed under the influence of the external electric field, being located at the positive electrode (anode).

Figure 3 (curves *1–3*) gives the capacitance-voltage characteristics obtained by solving numerically the equations describing a nonlinear capacitor with space charge (*1*—without excess space charge, *2*—for a uniform space charge distribution with the density $\rho_0=10$ $\mathrm{S/m^3}$, and *3*—for a Gaussian space charge distribution with the maximum density $\rho_{\max}=10\rho_0$ at one electrode[9]). It can be seen that preferential distribution of space charge at one electrode leads to an increased specific initial capacitance compared with a uniform space charge distribution (when the total space charge is the same). This increased capacitance which is conserved when the external field is switched off, is positive hysteresis.

To simplify the calculations, we assume that as a result of the action of an external field, the excess space charge fills acceptors at the anode to the maximum concentration $N_A\simeq 5\times 10^{21}$ $\mathrm{m^{-3}}$ (in a layer of thickness $L_{\min}$), whereas no excess space charge is found in the rest of the crystal. In this case, the influence of the space charge on the capacitance of the structure will decrease as the thickness L increases. For $L=L_{\min}$ the thickness dependence of the specific reciprocal capacitance of the structure should be almost the same as that in the absence of space charge, i.e., $(S/C_0)=2.98\times 10^6 L$. We assume that this agreement is found for $L\geqslant 1$ mm.

Thus, the angular coefficient α of the thickness depen-

dence of the reciprocal specific capacitance $(S/C)=\alpha L$ of a capacitor structure exposed to the action of an external voltage varies between 3.75×10^6 for $L=L_{\min}\simeq70$ μm and 2.98×10^6 for $L\simeq1$ mm. We assume that the angular coefficient $\alpha(L)$ varies linearly in the thickness range from 70 μm to 1 mm, for which we obtain $\alpha=3.81\times10^6-0.828\times10^6L$.

The dielectric hysteresis is usually characterized by the parameter $\Delta C/C_0=[C(0)-C_0]/C_0$ (Ref. 6). Here C_0 is the capacitance before the primary application of voltage and $C(0)$ is the capacitance after voltage has been applied. In our case, this expression is conveniently given in the form

$$\frac{\Delta C}{C_0}=\frac{C(0)}{C_0}-1=\frac{S/C_0}{S/C(0)}-1, \tag{3}$$

where, in accordance with the above $(S/C_0)\simeq3.75\times10^6L$ and $[S/C(0)]\simeq(3.81\times10^6-0.828\times10^6L)L$ for $0.07\leqslant L\leqslant1$ mm. Substituting these thickness dependences into expression (3), we find the thickness dependence of the dielectric hysteresis parameter $\Delta C/C_0$, which is given by the solid curve in Fig. 2. It can be seen that the agreement between the calculated and experimental dependences for $L\leqslant0.6$ mm is extremely good. This condition indirectly confirms the assumptions and estimates made above.

For $L\geqslant0.6$ mm, the experimental values of the dielectric hysteresis parameter are considerably lower than the calculated ones. This may be because a fairly high voltage is applied to the capacitor structure, at large thicknesses, which leads to appreciable injection of electrons from the cathode into the STO crystal because of the electric field inhomogeneity around the cathode and thus reduces the influence of the space charge redistribution, i.e., decreases the dielectric hysteresis parameter.

Thus, a comparison between the experimental and calculated data yields the following conclusions with a high degree of reliability.

1) During the fabrication of a metal-STO-metal capacitor structure an excess space charge is found in the dielectric whose density, according to our estimates for these STO crystals, is $\sigma\simeq0.05$ S/m^2.

2) When the capacitor structure is fabricated using thin ($L\leqslant100$ μm) STO layers, the entire bulk of the crystal is completely filled with space charge having a maximum concentration of charged acceptors ($N_A\simeq5\times10^{21}$ m^{-3}). In this case, the application of an external voltage to the capacitor structure cannot cause redistribution of the space charge so that no positive hysteresis should occur in such a structure.

The authors would like to thank O. G. Vendik for useful discussions.

This work was carried out as part of the State Program ''High-Temperature Superconductivity''; (Project No. 94051).

[1] T. Uchihashi, T. Okusako, T. Tsujuguchi, Y. Sagawara, M. Igarashi, R. Kaneko, and S. Morita, Jpn. J. Appl. Phys. **33**, Pt 1, 5573 (1994).
[2] T. Fujii, K. Sakuta, T. Awaji, K. Matsui, T. Hirano, Y. Ogawa, and T. Kobajashi, Jpn. J. Appl. Phys. **31**, Pt 2, L612 (1992).
[3] O. G. Bendik, L. T. Ter-Martirosyan, A. I. Dedyk, S. F. Karmanenko, and R. A. Chakalov, Ferroelectrics **144**, 33 (1993).
[4] O. G. Vendik, A. I. Dedyk, R. V. Dmitrieva, A. Ya. Zaĭonchkovskiĭ, Yu. V. Likholetov, and A. S. Ruban, Fiz. Tverd. Tela (Leningrad) **26**, 684 (1984) [Sov. Phys. Solid State **26**, 412 (1984)].
[5] K. E. Borisovskiĭ, A. I. Dedyk, N. V. Plotkina, and L. T. Ter-Martirosyan, Sverkhprovodimost' KIAE **5**, 762 (1992).
[6] A. I. Dedyk, S. F. Karmanenko, M. N. Malyshev, and L. T. Ter-Martirosyan, Fiz. Tverd. Tela (St. Petersburg) **37**, 3470 (1995) [Phys. Solid State **37**, 1906 (1995)].
[7] A. L. Kholkin, Yu. I. Sezonov, V. A. Trepakov, and Yu. V. Likholetov, Fiz. Tverd. Tela (Leningrad) **29**, 1252 (1987) [Sov. Phys. Solid State **29**, 717 (1987)].
[8] A. I. Dedyk and L. T. Ter-Martirosyan, Zh. Tekh. Fiz. **64**(3), 51 (1994) [Tech. Phys. **39**, 250 (1994)].
[9] O. G. Vendik, A. I. Dedyk, A. Ya. Zaĭonchkovskiĭ, and N. A. Smurova, Izv. Vyssh. Uchebn. Zaved. Fiz. No. **3**, 68 (1982).

Translated by R. M. Durham

Studies of the structure of defects in In_4Se_3 crystals by small-angle neutron scattering

V. M. Garamus

Joint Institute for Nuclear Research, 141980 Dubna, Moscow Region, Moscow;
I. Ya. Franko State University, 290000 Lvov, Ukraine

A. Kh. Islamov

Joint Institute for Nuclear Research, 141980 Dubna, Moscow Region, Moscow

Ya. P. Pilat and V. P. Savchin

I. Ya. Franko State University, 290000 Lvov, Ukraine

(Submitted June 23, 1997)
Fiz. Tverd. Tela (St. Petersburg) **40**, 248–250 (February 1998)

Small-angle neutron scattering is used to study the layered semiconductor In_4Se_3. It is observed that the samples contain inhomogeneities of colloidal dimensions, which are attributed to the precipitation of indium. Annealing reduces the concentration of inhomogeneities. Modeling the system using an ensemble of primary spherical inhomogeneities showed that a single cluster of a rectangular superlattice (2–2–6) contains 24 primary inhomogeneities of radius $13.5 \pm 1{,}5$ Å and the distance between them is 70.9 ± 1.5 Å. © *1998 American Institute of Physics.* [S1063-7834(98)01802-4]

1. Indium selenide In_4Se_3 is a layered semiconductor ($a = 15.296$ Å, $b = 12.308$ Å, $c = 4.0806$ Å, space group $Pnnm$) which has various characteristic features compared with other layered crystals. The most important characteristic is the experimentally proven one-dimensional disorder which may be established by the superposition of some pseudostructure on the main lattice structure.[1,2]

The characteristics of the crystal structure and its capacity for disorder show up in the anisotropy of the kinetic, optical, and photoelectronic properties over a wide temperature range. A broad spectrum of localized states is observed, whose existence is attributed to structural defects and dynamic disorder.

Appreciable concentrations of defects may strongly influence the phonon and electron spectra of semiconductors. An analysis of the mobility dynamics for indium-doped In_4Se_3 single crystals after annealing[3,4] indicated that cylindrical defects oriented along the c axis may be formed. It is assumed that these defects form as a result of a decrease in the maximum solubility of indium and its precipitation at structural lattice defects and between In_4Se_3 layers. The anisotropy of the internal field in the In_4Se_3 crystal lattice may lead to characteristic features in the distribution of structural defects.[5,6] If the growth conditions are not optimum, n-In_4Se_3 exhibits implantation regions whose number is reduced after annealing in vacuum. Crystals of p-In_4Se_3 typically have a block structure which is not changed by annealing. However, the density of extended defects in p-In_4Se_3 is considerably lower than that in n-type crystals.

Here we use small-angle neutron scattering to study the structure of defects in In_4Se_3 samples as well as the distribution of these defects.

2. It is known[7] that the presence of isolated point defects in a single-crystal matrix makes no contribution to small-angle scattering. When the defect concentration is large, fluctuations in the defect density may be recorded by means of its contrast to the crystal matrix. The existence of small-angle scattering provides evidence that the sample contains colloidal inhomogeneities and means that the inhomogeneity scales can be estimated without using model representations.

We measured the small-angle neutron scattering spectra for single-crystal In_4Se_3 samples and also for finely dispersed powder. The In_4Se_3 single crystals were grown by the Czochralski method. Single-crystal samples were prepared by cleaving thin wafers of varying thickness (0.5–2.0 mm) along the (100) natural cleavage plane. These crystals are n-type with a carrier concentration of 5×10^{15} cm^{-3}.

The measurements were made using the YuMO small-angle neutron-scattering spectrometer in the IBR-2 pulsed reactor at the I. M. Frank Neutron Physics Laboratory of the Joint Institute for Nuclear Research (Dubna, Russia). The range of neutron wavelengths used was between 0.7 and 4 Å so that neutron scattering cross sections could be recorded in the range of scattering vectors between 0.01 and 0.3 Å^{-3}. The absolute values of the scattering cross sections were determined using a standard metallic vanadium scatterer. The measurement error for the differential neutron scattering cross sections did not exceed 5% (Ref. 8).

Small-angle neutron scattering was observed for all the samples. The presence of a minimum ($q \approx 0.05$ Å^{-1}) indicates a narrow inhomogeneity size distribution (Fig. 1). Using the relation[7]

$$q_{\min} R = \pi, \tag{1}$$

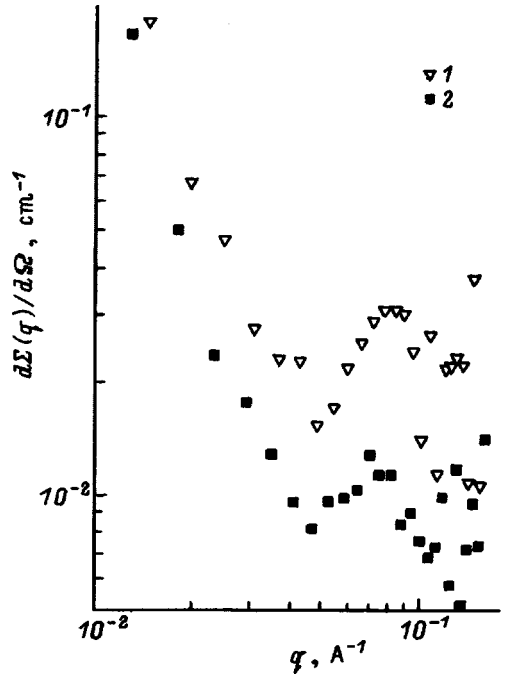

FIG. 1. Differential neutron scattering cross section for In_4Se_3 semiconductors versus scattering vector: *1*—initial crystal state, *2*—after heat treatment.

we obtain $R=120$ Å. Here R is the inhomogeneity radius, $q=4\pi \sin\theta/\lambda$ is the scattering vector, 2θ is the scattering angle, and λ is the neutron wavelength.

The maximum on the scattering curve may be interpreted as interference between the scattering of isolated inhomogeneities. In this case, an accumulation of point defects (clusters) should be considered. The authors of Refs. 3 and 4 put forward the hypothesis that indium may be precipitated in the interlayer region and at structural lattice defects. At present, no other explanation has been put forward for the physical nature of these defects.

After the samples had been annealed in vacuum at 350 °C for 12 h, the character of the scattering curves changed negligibly with only an appreciable drop in the scattering intensity (Fig. 1). These data indicate that the concentration of the defects decreases while their average sizes increase slightly. An estimate of the scattering intensity for samples with and without annealing gives a decrease in the concentration of defect clusters by a factor of approximately 2.5. These results agree with the results of electrophysical investigations which showed a substantial decrease in the carrier concentration and the concentration of localized states.[6]

The general form of the neutron scattering curve for In_4Se_3 powder reflects the characteristic features for the In_4Se_3 single-crystal sample (Fig. 2), although the minimum and maximum are less well-defined. A Guinier approximation[7] to the differential neutron scattering cross section $d\Sigma(q)/d\Omega$ was made for the initial section of the scattering curve

$$d\Sigma(q)/d\Omega = d\Sigma(0)/d\Omega \exp(-q^2R_g^2/3), \tag{2}$$

where R_g is the radius of inertia of the scattering particle density (radius of gyration)

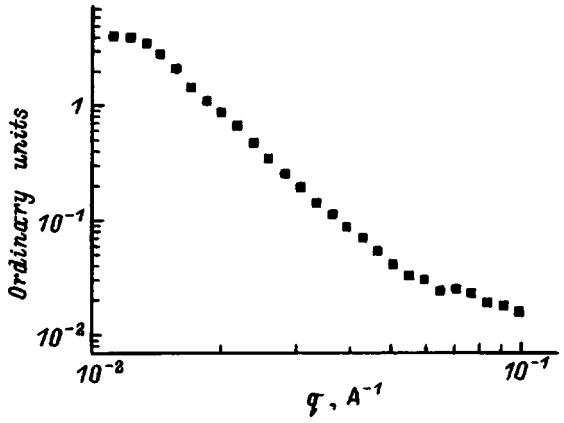

FIG. 2. Differential neutron scattering cross section for In_4Se_3 powder versus scattering vector.

$$R_g^2 = \int_V [\rho(r)-\rho_s]r^2 dv \Big/ \int_V [\rho(r)-\rho_s]dv. \tag{3}$$

where $\rho(r)$ is the neutron scattering density distribution in the particle, ρ_s is the average scattering density of the solvent (in this case, the crystal matrix), $d\Sigma(0)/d\Omega$ is the zero-angle scattering,

$$d\Sigma(0)/d\Omega = n(\rho-\rho_s)^2V^2, \tag{4}$$

n is the inhomogeneity concentration and V is the inhomogeneity volume. The value obtained for the radius of inertia is 100 Å with a systematic error of 15% (Ref. 7).

It should be noted that measurements of the small-angle neutron scattering spectra for powder samples yield information averaged over all orientations of the crystallites whereas for crystal samples, it is possible to observe a scattering curve which is only averaged in the plane perpendicular to the beam. A comparison between the scattering curves for the powder and crystal samples may provide information on the anisotropy of the orientation of the defect clusters in crystalline In_4Se_3. It can be confirmed that single-crystal In_4Se_3 has some pseudostructure formed by defect clusters, as was noted in Ref. 3.

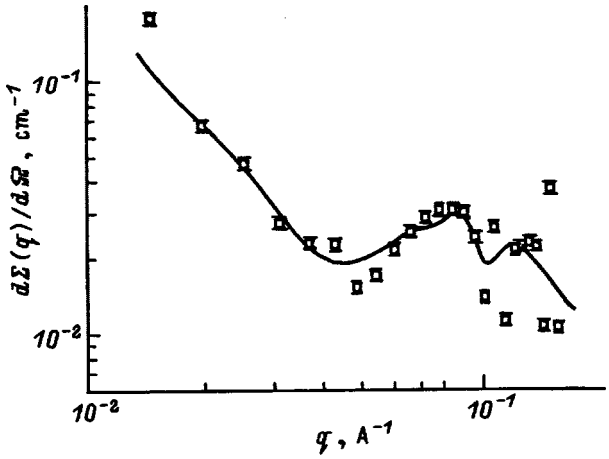

FIG. 3. Modeling of neutron scattering by In_4Se_3 sample using a rectangular superlattice of primary inhomogeneities (continuous curve).

Assuming that indium may be precipitated in the interplanar region in In_4Se_3 samples and also assuming that there is a maximum which can be interpreted as interference in the scattering of inhomogeneities, we modeled this system with an ensemble of primary spherical inhomogeneities forming a superlattice. The scattering intensity was calculated using the Debye formula, which is written as follows for a system of spheres having the same radius R (Ref. 9):

$$d\Sigma(q)/d\Omega = nF^2(qR)\left[1+\frac{2}{n}\sum_{j=i+1}^{n}\frac{\sin qr_{ij}}{qr_{ij}}\right], \qquad (5)$$

where $F^2(qR)$ is the scattering by a homogeneous sphere of radius R, n is the number of spheres, and r_{ij} is the distance between the centers of two spheres.

The best agreement (Fig. 3) was obtained by the least squares method for the following parameters: 2–2–6 lattice, radius of primary inhomogeneities 13.5 ± 1.5 Å, and distance between them 70.0 ± 1.5 Å. Thus, according to our data, a single superlattice cluster contains 24 primary inhomogeneities. The normalized χ^2 value is 1.1 and the radius of inertia of the model structure is 110 Å.

In sum, we have obtained the following results:

Small-angle neutron scattering in In_4Se_3 crystals has revealed defect clusters having a narrow size distribution.

Annealing the samples in vacuum at 350 °C for 12 h reduces the defect concentrations approximately 2.5 times while the size of the defect clusters changes negligibly.

By modeling the system with an ensemble of primary spherical inhomogeneities, we established that a single cluster of a rectangular superlattice (2–2–6) contains 24 primary inhomogeneities of radius 13.5 ± 1.5 Å and the distance between them is 70.9 ± 1.5 Å.

The results of these small-angle investigations indicate that the position of the defect clusters in crystalline In_4Se_3 exhibits long-range order, i.e., a certain pseudostructure exists which could form the subject of a further investigation.

[1] U. Schwarz and H. Hillebrecht, Z. Kristallogr. **210**, 342 (1995).
[2] O. I. Bodak, Yu. M. Orishchin, V. P. Savich, and I. M. Stakhira, Kristallografiya **25**, 628 (1980) [Sov. Phys. Crystallogr. **25**, 363 (1980)].
[3] I. M. Stakhira and P. G. Ks'ondzik, Ukr. Fiz. Zh. **26**, 762 (1981).
[4] D. M. Bercha, O. B. Mitin, L. Yu. Kharkhalis, and A. I. Bercha, Fiz. Tverd. Tela (St. Petersburg) **37**, 3233 (1995) [Phys. Solid State **37**, 1778 (1995)].
[5] V. Ya. Kuryachiĭ, G. Yu. Bogachev, V. P. Mikhal'chenko, and I. M. Stakhira, Deposited Paper No. 14.14k-84 [in Russian], Ukr. NIINTI, Chernovtsy (1984).
[6] Ya. S. Umanskiĭ, Yu. A. Skakov, and A. N. Ivanov, *Crystallography, X-Ray Diffraction Analysis, and Electron Microscopy* [in Russian], Nauka, Moscow (1982).
[7] D. I. Svergun and L. A. Feĭgin, *X-Ray and Neutron Small-Angle Scattering* [in Russian], Moscow (1986).
[8] Yu. M. Ostanevich, Makromol. Chem., Macromol. Symp. **15**, 91 (1988).
[9] Yu. A. Rol'bin, R. L. Kayushina, L. A. Feĭgin, and B. M. Shchedrin, Kristallografiya **18**, 701 (1973) [Sov. Phys. Crystallogr. **18**, 442 (1973)].

Translated by R. M. Durham

Kinetics of impurity segregation at grain boundaries in polycrystals. II. Concentrated solution

V. V. Slezov, L. N. Davydov, and V. V. Rogozhkin

Khar'kov Physico-Technical Institute, 310108 Khar'kov, Ukraine
(Submitted August 8, 1997)
Fiz. Tverd. Tela (St. Petersburg) **40**, 251–253 (February 1998)

The isothermal impurity segregation from a finite-size grain into an intergrain boundary region or at an external free surface is investigated when the impurity concentration in the boundary region is not small. Simple algebraic equations are obtained that describe the impurity concentration for the case of several competing and interacting impurities. The process of segregation of two impurities is discussed in detail, and it is shown that the concentration of one of them can have a maximum as a function of time. © *1998 American Institute of Physics.* [S1063-7834(98)01902-9]

In Ref. 1 we presented the first analytical investigation of impurity segregation from a finite-size grain which allowed us to describe correctly the process of impurity segregation in the intergrain boundary region in polycrystalline materials.

Our theory in Ref. 1 involved a relatively simple situation, however, where only one type of impurity was present whose concentrations in the grain and in the boundary region were small. As the concentration of impurities in the boundary region increases in the course of the segregation and becomes large, the exodus of impurities into the boundary region can slow down (for example, due to a decrease in the number of free sites at the boundary). In addition to this ''local'' interaction, in a concentrated solution the direct (''nonlocal'') interaction between neighboring impurity atoms becomes important. When the segregation involves several different impurities at the same time, the competition for space and interaction between neighboring atoms can lead, as shown in Ref. 2, to a nonmonotonic change in the concentration of one of the impurities with time. Since the grain size was infinitely large in Ref. 2, the question of how this process takes place in a real finite-size grain remains to be addressed. In this paper we investigate the segregation of several (or one) types of impurity simultaneously into the boundary region from a finite-size grain when the impurity concentration in the boundary region happens to be large.

As we showed in Ref. 1, the equation that describes the change in the impurity concentration $c^b(t)$ with time t in a boundary region of thickness $2d$ has the form

$$\frac{d}{l}[c^b(t)-c^b(0)]=(c_0-\lambda(t))S(t), \tag{1}$$

where $2l$ is the thickness of the planar grain, c_0 is the initial impurity concentration in the grain, $c(x=\pm l,t)\equiv\lambda(t)$ is the impurity concentration in the grain near the boundary, and $S(t)$ is a known function of time[1] given by the following interpolation formula

$$S(t)=1-\exp\left(-\frac{2}{\sqrt{\pi}}\sqrt{\frac{Dt}{l^2}}\right), \tag{2}$$

where D is the diffusion coefficient of the impurity.

Let us assume the concentration of impurities within the grain is small ($c(x,t)\ll 1$) but that its value in the boundary region can be arbitrary ($0\leqslant c^b(t)\leqslant 1$). The corresponding condition at the boundary has the form of a Langmuir isotherm[3]

$$\frac{c^b(t)}{1-c^b(t)}=\alpha(T)\lambda(t), \tag{3}$$

where α is referred to as the redistribution coefficient which, for small $c^b(t)$, should depend on concentration

$$\alpha=\exp\frac{E+E'c^b(t)}{T}. \tag{4}$$

Here T is the temperature and E, E' are energy parameters that describe the difference in solution energies of the impurity in the grain and in the boundary region. The function $\alpha(c^b)$ describes the interaction of closely spaced impurity atoms (on neighboring sites): attraction (for $E'>0$) or repulsion (for $E'<0$). Another kind of interaction (single-site or local interaction), which is expressed mathematically by allowing the denominator on the left side of Eq. (3) to be different from unity, arises from a competition for space, i.e., from the impossibility of placing more than one impurity atom at the same site. In contrast to the local interaction between impurity atoms, which is specified by the parameter E', we customarily refer to this new interaction as ''nonlocal''. When $c^b\ll 1$, Eq. (3) becomes the Henry isotherm $c^b(t)=\alpha\lambda(t)$ with $\alpha=\exp(E/T)$. In this case the segregation is similar to that discussed in Ref. 1.

If there are different kinds of impurity atoms present in the solid solution able to segregate simultaneously into the grain boundary region, interacting with one another as they do, the situation becomes much more complicated. Since Eq. (1) does not depend on the choice of equilibrium conditions at the boundary (2), in the multicomponent case these relations take the forms

$$\frac{d}{l}[c_i^b(t)-c_i^b(0)]=(c_{0i}-\lambda_i(t))S_i(t), \tag{5}$$

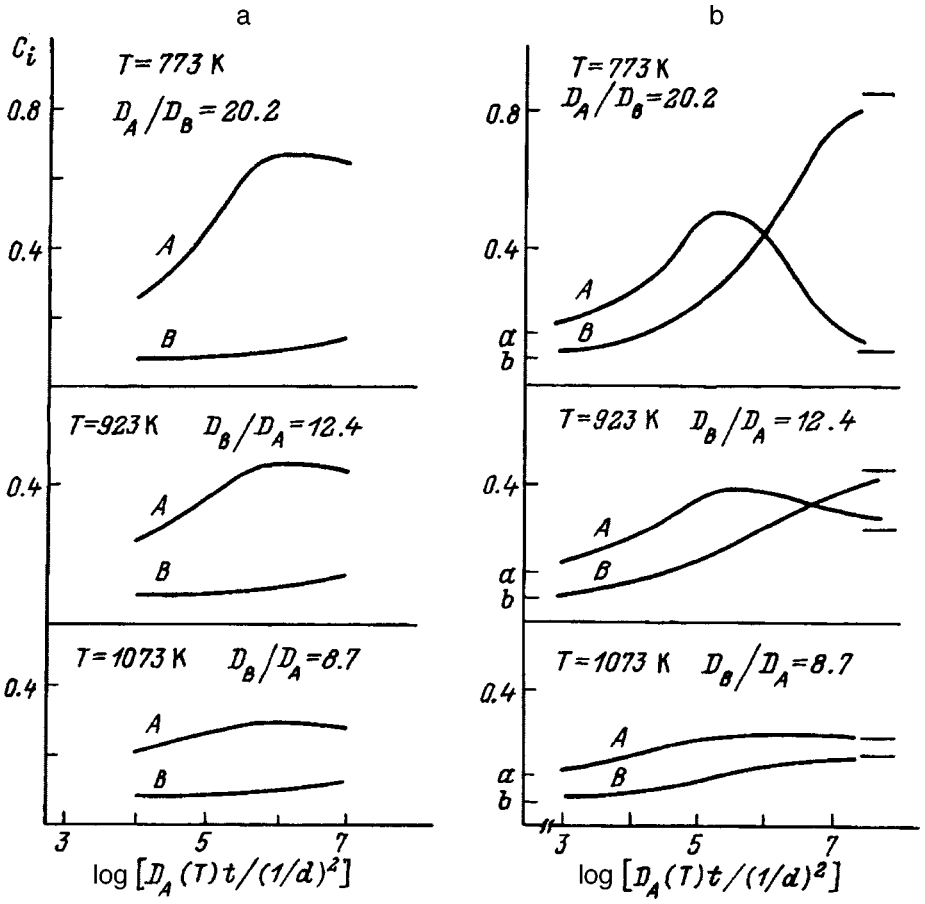

FIG. 1. Time dependence of the concentration of two impurities segregating out of (a) a finite-sized grain ($l=10^{-6}$ m) and (b) an infinitely large grain ($l=\infty$, see Ref. 2) under various isothermal conditions.

$$\frac{c_i^b(t)}{1-\Sigma_k^N c_k^b(t)}=\alpha_i(c^b,T)\lambda_i(t), \tag{6}$$

where $i=1, 2...,N$ labels the impurity, N is the number of these impurities, and

$$\alpha_i(c^b,T)=\exp\frac{1}{T}\left(E_i+\sum_j^N E_{ij}c_j^b(t)\right). \tag{7}$$

Note that Eq. (5) is valid for any interaction of the impurities at the boundary.

Let us consider the simultaneous segregation of several different impurities in more detail for the example of a two-component solution ($i=1,2$). It is not difficult to show that when $\alpha_1<\alpha_2$ and $D_1>D_2$ the time dependence of the impurity concentration in the boundary region can be nonmonotonic. The time dependences of the impurity concentrations c_1^b and c_2^b for this case are shown in Fig. 1a (under various isothermal conditions). In this case we have used the same values of parameters as in Ref. 2 (see the Table). In Fig. 1b we show the results of Ref. 2 for comparison.

TABLE I. Parameters for segregation process used to solve Eqs. (5)–(7) and make the plots shown in Fig. 1 (see Ref. 2).

$E_1=0.6$ eV	$E_{12}=E_{21}=-0.13$ eV
$E_2=0.8$ eV	$E_{11}=E_{22}=0$
$c_1^b(0)=0.15$	$c_{01}=10^{-3}$
$c_2^b(0)=0.08$	$c_{02}=10^{-4}$
$D_1=D_{0i}\exp(-Q_i/T)$	$D_{01}=D_{02}=10^{-4}$ m^2/s
$Q_1=2.2$ eV	$Q_2=2.4$ eV

Thus, it is clear that the approach used in Ref. 1, which leads to simple algebraic expressions for the time-dependent change in the concentration of impurities segregating out of a finite-size grain into the boundary region, can be used for a concentrated solution of impurities in the boundary region as well. The condition for equilibrium at the surface separating the boundary and grain is, in this case, the Langmuir isotherm.[3]

If the impurity concentration is not small, it is necessary to include interactions between impurity atoms. The local interaction or competition for space, i.e., the impossibility of placing more than one impurity atom on a given site, is explicitly taken into account by the Langmuir isotherm. The dependence of the redistribution coefficient α on the concentration c^b takes into account the nonlocal interaction of neighboring atoms. Both forms of interaction have a significant effect on the segregation process; whereas competition for space decreases the segregation, the nonlocal interaction can either facilitate the segregation (when the impurity atoms attract) or limit it (when they repel).

If two (or several) kinds of impurity are segregating into the boundary region, it can happen that one of the impurities precipitates out predominantly in the boundary. However, another scenario is also possible, in which an impurity that diffuses more slowly but dissolves better in the boundary region will in due time begin to displace a rapidly diffusing impurity that has already arrived there from the boundary region. Once this process begins, the concentration of the

latter will begin to decrease. In a finite-size grain, the maximum concentration of this impurity, and also the relative changes in the concentrations, are not as marked as they are for an infinitely large grain. This is natural because the smaller strength of a finite grain as an impurity source will limit the segregation.

Finally, it is worth noting that once the solubility of the impurities in the boundary is known, Eqs. (5) and (6) immediately tell us what the maximum initial concentration of impurities in a grain c_0 or (and) the size of a grain l should be in order that no new phase separation with this impurity take place at the boundary, or (for prespecified c_0, $c^b(0)$, l) the time at which its precipitation begins. Generally speaking, Eqs. (5) and (6) allow us to find the time it takes for the impurity concentration at the boundary to reach some preset limit imposed, e.g., by some applications-related criterion. For times greater than this, we can reverse the segregation process by increasing the sample temperature for a certain time and thereby preventing a portion of the impurity from re-dissolving into the grain. Because this resegregation, as before, is described by Eqs. (5) and (6) (with new initial conditions), we now can find the time required to establish a given low level of impunity concentration in the boundary. These facts must be taken into account when a method is chosen for thermal processing of a polycrystalline material.

This work was partially supported financially by the government of Ukraine and the International Science Fund (ISF) (grant U2Y200), the German Federal Ministry of Research and Technology (BMBF) (Grant ROS-1995B6) and the International Soros Support for Education Program (ISSEP) (Grant ISSEPSPU 042062).

[1] V. V. Slezov, L. N. Davydov, and V. V. Rogozhkin, Fiz. Tverd. Tela (St. Petersburg) **37**, 3565 (1995) [Phys. Solid State **37**, 1964 (1995)].
[2] M. Militzer and J. Wieting, Acta. Metall. **34**, 1229 (1986).
[3] B. S. Bokshteĭn, Ch. V. Kopetskiĭ, and L. S. Shvinderman, *Thermodynamics and Kinetics of Grain Boundaries in Metals* (Metallurgiya, Moscow, 1986) [in Russian].

Translated by Frank J. Crowne

Anomalous absorption of thermal neutrons in copper in the presence of strong mechanical stresses

A. G. Lipson, I. I. Bardyeshev, V. A. Kuznetsov, and B. F. Lyakhov

Institute of Physical Chemistry, Russian Academy of Sciences, 117915 Moscow, Russia
(Submitted July 11, 1997)
Fiz. Tverd. Tela (St. Petersburg) **40**, 254–259 (February 1998)

A study has been made of the interaction between an ultraweak flux of thermal neutrons ($I_n = 20$ n/s·cm^2) and a copper cathode during electrolysis in a 1M solution of KOH in H_2O. An effect involving the generation of appreciable elastic and plastic deformations, revealed as transverse bending of the copper plate and damage to its surface, was observed in the copper. It was shown that the average cross section for absorption of thermal neutrons in the copper is increased approximately twenty times compared with its equilibrium value. © *1998 American Institute of Physics.* [S1063-7834(98)02002-4]

It was established in Refs. 1 and 2 that in nonequilibrium ferroelectrics in a state of ferroelectric–paraelectric phase transition under the action of an ultraweak thermal neutron flux ($0.1-100.0$ n/s·cm^2), appreciable mechanical stresses are generated, leading to defect formation and the appearance of microcracks, as well as anomalous absorption of thermal neutrons. The consequences of the action of ultraweak thermal neutron fluxes (suppression of spontaneous deformation and a shift of the Curie point T_C by 3–4 K toward low temperatures) are equivalent to irradiating the crystals with a 5 Mrad γ-radiation dose.[3] It was postulated[1] that such effective interaction between thermal neutrons and a crystal involves inelastic scattering of neutrons by nonequilibrium phonons generated in the phase transition process resulting from the extremely efficient conversion of the elastic energy stored by the lattice into plastic deformation energy. Thus, the presence of a second-order phase transition or strong mechanical stresses in a crystal irradiated by thermal neutrons is a necessary condition for the excitation of nonequilibrium phonons whose energy is transformed by an inelastic mechanism in the neutron diffusion process.

Similar effects could be observed in crystals by creating highly nonequilibrium conditions, for example, by introducing mechanical stresses during the hydrogenation of metals which do not dissolve hydrogen, by simultaneously exposing them to an ultraweak flux of thermal neutrons. In this case, as a result of the shallow depth of hydrogen penetration and the high rate of surface defect generation under irradiation,[4] the mechanical stresses will be created in a thin surface layer, so that they are concentrated in a small volume.

In particular, the interaction between hydrogen and copper can take place by substitution only in a thin surface layer $\leqslant 10$ nm thick (Refs. 5 and 6). Hydrogen atoms accumulate preferentially within pile-ups of point defects and dislocations and also near twin boundaries. The hydrogen implantation process in copper (by analogy with the injection of low-energy argon ions[6]) should result in the formation of dislocation pile-ups in parallel rows at the crystal surface. This gives rise to the creation of strong lateral compressive stresses in bands oriented in the {112} and {110} directions. It will be shown subsequently that the surface stresses during the electrolysis of copper may reach values comparable with its bulk modulus.[7] Note that the creation of such appreciable mechanical stresses for long time intervals by any other method (apart from electrolysis) would present problems. In addition, the presence of dynamic stresses whose magnitude is of the order of the bulk modulus is a necessary condition for the generation of the strongly nonequilibrium optical phonon branch in a crystal since, under the action of these stresses, the entire spectrum of normal modes is excited to the Debye frequency. However, it is known[8] that, when the optical phonon mode is introduced in a crystal, the cross section for capture of thermal neutrons may be increased compared to crystals containing only the acoustic phonon branch. However, the current view is that the action of electromagnetic vibrations of a lattice in equilibrium with a medium cannot significantly (severalfold) increase the cross section for absorption of thermal neutrons in this medium.[9]

However, we show here that under highly nonequilibrium conditions of interaction between hydrogen and copper (in the presence of an ultraweak thermal neutron flux), accompanied by strong mechanical stresses in the surface layer of the sample, the average cross section for capture of thermal neutrons by Cu^{63} and Cu^{65} nuclei in a crystal environment may be increased twenty times.

1. EXPERIMENTAL METHOD

In order to create strong mechanical stresses, hydrogen was introduced into the surface layer of copper by means of electrolysis. The hydrogen was introduced into the copper by an electrochemical method using samples of electrolytic, cold-rolled, technical-grade copper, having an area $S = 6$ cm^2 and thickness $d = 2\times10^{-2}$ cm. The results of a x-ray microprobe analysis indicate that the main impurity in the samples is silicon (2.5×10^{-1} mol %), which is introduced to improve the elastic properties.

The electrolysis was carried out in a 100 ml glass cell filled with a 1M solution of KOH in H_2O. The copper samples were the cathodes and the anodes were made of platinum. The process used a dc current $j = 40$ mA/cm^2 at room temperature. The duration τ of one electrolysis cycle was $\tau = 2000-10\,000$ s. After each cycle, the copper

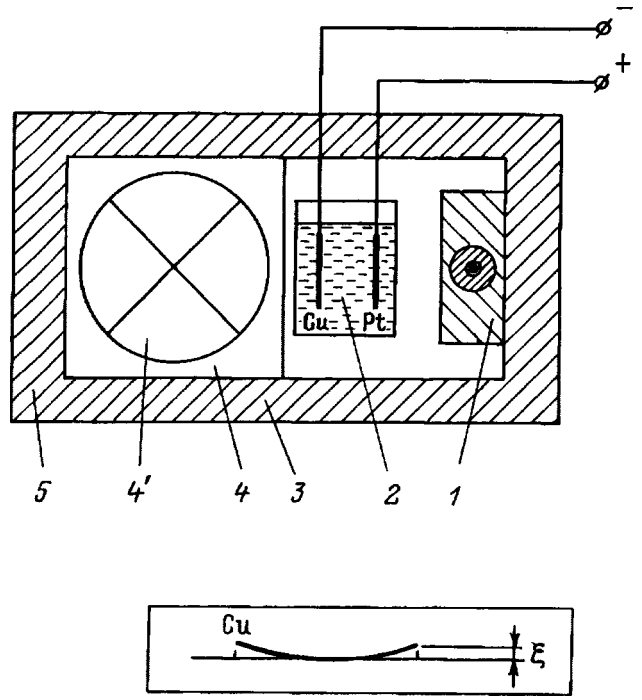

FIG. 1. Arrangement of apparatus: *1*—lead capsule containing Cf^{252} neutron source, *2*—electrolytic cell, *3*—Cu(Pd) cathode, *4*—neutron detector (in series No. 1), *4′*—γ detector (in series No. 2), and *5*—passive polyethylene (Co) shield. Inset—profile of Cu cathode after electrolysis for $\tau = 10\,000$ s; ξ—transverse deflection of cathode.

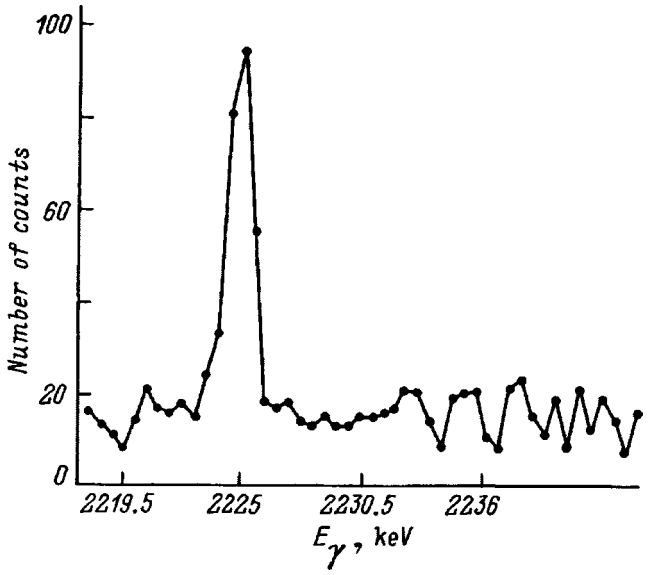

FIG. 2. Complete γ-radiation spectrum formed by capture of thermalized neutrons from source in the hydrogen-containing materials (Fig. 1). Exposure time $\tau = 10\,000$ s.

samples were degreased. The hydrogen concentration in the copper after electrolysis was measured by thermal diffusion in vacuum.[10]

The cell was placed inside a passive shield made of 6 cm thick Neutrostop polyethylene blocks. The volume of the shield including the free internal space was $V = 0.4$ m^3. A Cf^{252} neutron source ($I_n = 200$ n/s in the solid angle 4π), contained in a lead capsule with a 2.5 cm thick protective polyethylene casing, was positioned inside the shield at the distance $r = 8$ cm from the Cu cathode. In order to record changes in the neutron flux and/or γ-quantum flux inside the system (Fig. 1), in the immediate vicinity of the cell we positioned a neutron detector comprising an array of seven NWI-62 proportional neutron counters coated with cadmium sheet[1,2] or a low-background GEM-20180P γ detector (extrapure germanium in a supersensitive γ spectrometer) made by EG&G Ortec.[11] From calibration measurements using a Cf^{252} source, the efficiency of the neutron detector (for neutrons with $E_n > 0.1$ eV) in this measurement geometry was $\varepsilon_n = 2.0 \times 10^{-2}$. The γ recording efficiency, according to calibration measurements using a Na^{22} γ source, was $\varepsilon_\gamma = 1.5 \times 10^{-3}$ with an intrinsic γ detector efficiency of 24.1%. A comparison between the effect and the background for the γ spectral measurements and an analysis of the γ peaks were made using the MAESTRO-1 program and an SIG multifunctional system designed to use digital information (program package by Soft Service Ltd).

The thermal neutron flux intersecting the Cu cathode was monitored by measuring the integral intensity of the γ peak at $E_\gamma = 2225$ keV (Fig. 2) observed by recording the capture γ radiation in the reaction $p + n \rightarrow d + \gamma$ (2.22 MeV), which takes place when thermal neutrons are captured in the polyethylene shield and the electrolyte. The thermal neutron flux inside the system was determined using relation[9]

$$I_n = \frac{\Delta N_\gamma \, v_t}{3 \varepsilon_\gamma \, [1 - \exp(-N_H \sigma_H L] V}, \tag{1}$$

where ΔN_γ is the total number of counts at the peak $E_\gamma = 2225$ keV with the continuous background subtracted, including the Compton scattering background, ε_γ is the efficiency of the γ detector with allowance for the measurement geometry, v_t is the thermal neutron velocity, n_H is the hydrogen concentration in the polyethylene shield, σ_H is the cross section of the $n(p,d)\gamma$ reaction for the thermal neutrons, L is the thickness of the shield, and V is the volume of the system enclosed by the polyethylene shield. Experiments using the γ detector showed that in this system the average thermal neutron flux (for $I_n = 200$ n/s in 4π) per unit area of the cathode is $I_n = 20.0 \pm 1$ n/s·cm^2.

In all the series of tests we used the following control experiments: a) experiments at $j = 40$ mA/cm^2 in the absence of a neutron source (under conditions of cosmic thermal neutron background, i.e., $I_n < 0.1$ n/cm^2); b) experiments at $I_n = 20$ n/s·cm^2 but without an electrolysis current, i.e., $j = 0$; c) experiments at $j = 40$ mA/cm^2 and $I_n = 20$ n/s·cm^2 using a palladium plate as the cathode ($S = 4$ cm^2, $d = 50$ μm). The series c) control experiments were carried out to demonstrate the preferential activity of the cathode compared with the other materials exposed to the electrolytic action at $I_n = 20$ n/s·cm^2 (such as the electrolyte, anode, cell material, and so on).

2. EXPERIMENTAL RESULTS

The experiments showed that during electrolysis in the presence of an ultraweak flux of thermal neutrons $I_n = 20$ n/s·cm^2 for 10 000 s ($j = 40$ A/cm^2[21]), a vigorous damage process takes place at the surface of the copper ca-

thode. The surface of the copper sample becomes black and the electrolyte solution becomes blue because of the crumbling of the copper (after a few hours, a deposit of highly disperse copper forms at the bottom of the cell). In addition, after electrolysis has ended, the sample is laterally deformed (curved). The transverse deflection is $\xi = 1$ mm (Fig. 1). At the same time, under the conditions of cosmic thermal neutron background $I_n = 0.1$ n/s·cm^2 (in the absence of the Cf^{252} neutron source), electrolysis at $j = 40$ mF/cm^2 and $\tau = 10\,000$ s reveals no visible changes at the cathode. The experiments showed that the hydrogen concentration in the samples after electrolysis ($\tau = 10\,000$ s) is $n_H \simeq 10^{-3}$ cm^3/g copper. Bearing in mind the maximum depth of penetration of hydrogen in copper ($H = 10^{-6}$ cm), we can conclude that a compound of the type CuH_x, where $x \simeq 0.1$, forms at the surface layer of the cathode.

Thus, as a result of the irradiation of a copper cathode by thermal neutrons $I_n = 20$ n/s·cm^2 during electrolysis, elastic and plastic deformation energy is stored in the cathode, which is observed as transverse deflection and surface damage to the sample. This indicates that powerful elastic stresses act in the surface layer of the cathode (into which hydrogen penetrates). It will be shown subsequently that these mechanical stresses are capable of generating nonequilibrium optical phonons, whose presence could alter the absorption cross section of thermal neutrons in the cathode.

The experiments showed that in almost all of the twenty 1 h intervals in which the intensities of the neutron or γ-quantum capture fluxes were measured, the number of background counts is higher than the values obtained in measurements during electrolysis with a Cu cathode (curves *1* and *2* in Fig. 3). However, during similar electrolysis in the same cell using a Pd cathode, no changes in the intensity of the thermal neutron flux were recorded. Data giving changes in the intensity of the thermal neutron flux for the electrolysis of Cu and Pd are summarized in Table I. Note that in order to improve the accuracy of the analysis, the γ lines ($E_\gamma = 2225$ keV) in the effect and the background were compared after subtracting the continuous background (including the Compton scattering background) from the spectral range 2220–2230 keV, which corresponds to the γ peak formed by proton capture of a neutron. It can be seen from Table I that the copper electrolysis process reduces the count rate for $E_n > 0.2$ eV neutrons by approximately 2.5%. At the same time, the thermal neutron count rate ($E_n \sim kT$) is reduced by approximately 12% compared with the background value. Since while γ radiation is recorded, γ quanta with $E_\gamma = 2.225$ MeV are formed exclusively by capture of thermal neutrons by the hydrogen surrounding the detector, the deficiency of these γ quanta during electrolysis (compared with the background) can be uniquely attributed to the absorption of $\sim 12\%$ thermal neutrons in the cathode material (Cu), i.e., it can be attributed to capture rather than inelastic scattering processes with increasing neutron energy. This last case would inevitably involve slowing and subsequent capture of neutrons in the polyethylene. As a result, the intensity of the peak $E_\gamma = 2225$ keV would be the same in the effect and in the background. The fact that the relative change in counts $\Delta N/\langle N_b \rangle$ for the recording of neutrons ($E_n > 0.2$ eV)

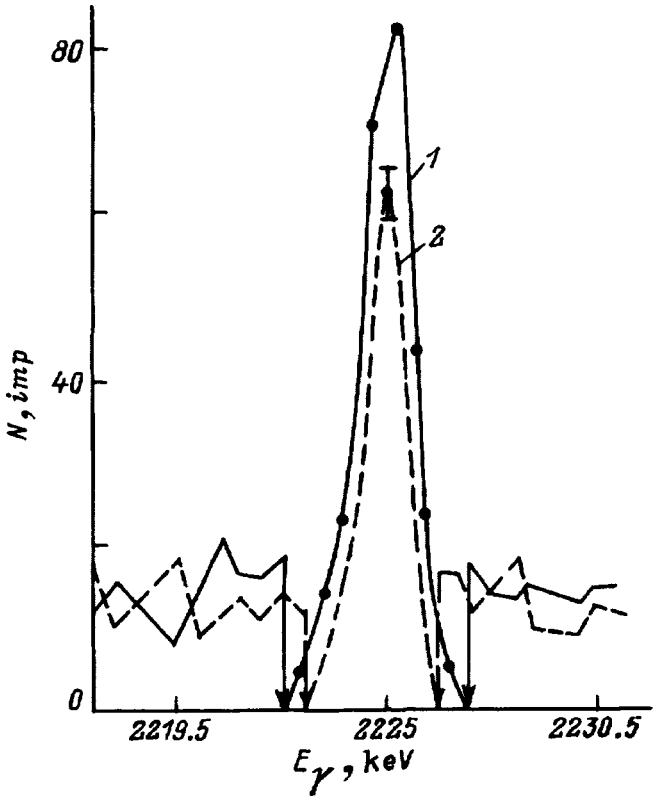

FIG. 3. γ peaks (with continuous background subtracted, including Compton scattering background), formed by capture of thermalized neutrons by hydrogen in material: *1*—without electrolysis (exposure time $\tau = 8000$ s), *2*—with electrolysis ($j = 40$ mA/cm^2) for $\tau = 8000$ s. The measurement geometry for exposures 1 and 2 is the same. The arrows delimit the region of the γ spectra in which the continuous background is subtracted.

is lower than the ratio for γ quanta (see Table I) indicates that only approximately one fifth of the thermalized neutrons can have energies higher than cadmium. This is because the neutron distribution inside the polyethylene shield is close to Maxwellian.[8] Thus, to obtain a more accurate estimate of the cross section (σ) for absorption of thermal neutrons in the copper cathode, it is better to use the γ-quantum data because these directly correspond to the change in the thermal neutron flux inside the polyethylene shield. The cross section for possible absorption of thermal neutrons, averaged over the volume of the copper sample used in the electrolysis process, is given by[1]

$$\sigma = \frac{1}{nd} \ln\left(\frac{\langle N_b \rangle}{\langle N_{eb} \rangle} \right), \tag{2}$$

where n is the concentration of copper nuclei, d is the cathode thickness, $\langle N_b \rangle$ is the average γ count rate in the background, and $\langle N_{eb} \rangle$ is the average γ count rate in the electrolysis process (see Table I). Using the data given in Table I, we then have $\sigma = 71.5$ b. This value of σ is almost twenty times higher than the known cross section for capture of thermal neutrons in a stoichiometric isotopic Cu mixture.

If the capture of thermal neutrons by Cu^{63} and Cu^{65} nuclei is a radiative process, the observed γ spectrum should contain a hard component which corresponds to the neutron binding energy in the Cu^{64} (7.91 MeV) and Cu^{66} (7.060 MeV) nuclei. In order to check this assumption, we studied

TABLE I. Variation of count rates ΔN for neutrons with $E_n > 0.2$ eV and γ quanta at the peak $E_\gamma = 2.225$ MeV during electrolysis with copper and palladium cathodes ($j = 40$ mA/cm^2) compared with background measurements ($j = 0$).

Type of measurement	$\langle N_b \rangle$, counts/s	$\langle N_{eb} \rangle$, counts/s	ΔN, counts/s	Δn, neutr.(γ)/s
Neutrons ($E_n > 0.2$ eV, Cu cathode	1.402 ± 0.006	1.370 ± 0.007	$-(3.2 \pm 0.9) \times 10^{-2}$	$-(2.5 \pm 0.5)$
γ quanta ($E_\gamma > 2.225$ MeV, Cu cathode)	$(2.41 \pm 0.03) \times 10^{-2}$	$(2.10 \pm 0.04) \times 10^{-2}$	$-(3.1 \pm 0.5) \times 10^{-3}$	$-(3.0 \pm 0.5)$
Neutrons (Pd cathode)	1.328 ± 0.005	1.330 ± 0.006	$+(2.0 \pm 7.0) \times 10^{-3}$	-
γ quanta (Pd cathode)	$(2.45 \pm 0.04) \times 10^{-2}$	$(2.46 \pm 0.05) \times 10^{-2}$	$+(1.0 \pm 6.0) \times 10^{-3}$	-

Note: $\langle N_b \rangle$ is the average count rate in the background ($j = 0$) with the continuous spectrum subtracted, $\langle N_{eb} \rangle$ is the average count rate in the ''effect'' ($j = 40$ mA/cm^2) with the continuous spectrum subtracted, and $\Delta N = \langle N_{eb} \rangle - \langle N_b \rangle$, $\Delta n = \Delta N / \varepsilon$, where ε is the detector efficiency.

the hard part of the γ spectrum ($2.4 < E_\gamma < 8.5$ MeV) and compared this with the background measurements. However, the results showed that, within measurement error, the intensity of the spectra during electrolysis of Cu and the background show no difference in this range. This indicates that the capture of neutrons by copper nuclei is not a radiative process and is evidently similar to the Mössbauer effect, i.e., the neutron binding energy in the Cu^{64} and Cu^{66} nuclei is preferentially transferred to the copper lattice in the form of phonons and/or the generation of structural defects.[12,13]

Thus, it has been established by two independent methods that in a highly nonequilibrium copper cathode during electrolysis (i.e., in the presence of appreciable elastic deformations intensified by the action of an ultraweak thermal neutron flux), the cross section for absorption of thermal neutrons is increased approximately twenty times.

3. DISCUSSION OF RESULTS

The measurable transverse deflection of the copper plate ($\xi = 1$ mm) observed during the electrolysis process in the presence of an ultraweak thermal neutron flux ($I_n = 20$ n/s·cm^2) can be used to calculate the mechanical stresses acting in the surface layer of the sample (cathode) during hydrogenation. We showed in Ref. 10 that the free energy of the elastic deformations stored in the sample during hydrogenation may be estimated approximately using relation[14]

$$W_F = Ed(\xi/l)^4 S, \tag{3}$$

where E is Young's modulus of the copper plate, d is the thickness of the sample, l is its length, which is equal to its width under conditions of transverse deflection, and S is the area of the Cu cathode. Thus, per unit length of the cathode we have $W_F = 2 \times 10^{-2}$ J/cm^2. Then, the efficiency of conversion of the energy supplied during electrolysis $W_{\text{el}} = jU\tau$ (where $U \simeq 2$ V is the cell voltage) to elastic energy stored in the sample is $\beta = W_F / jU\tau = 2.5 \times 10^{-5}$. The rest of the supplied energy is expended mainly in plastic deformations and damage to the surface layer of the cathode (crumbling of the copper in the electrolyte solution), and is also expended in electrochemical dissociation of water molecules.

In order to estimate the stresses acting in the sample, we need to estimate the volume into which hydrogen penetrates during electrolysis. Taking the depth of penetration of hydrogen in the cathode to be $H = 10^{-7} - 10^{-6}$ cm (Ref. 6), we obtain mechanical stresses of $\sim 10^{10} - 10^{11}$ Pa, which is similar to the bulk modulus of copper.[15] These stresses are dynamic as a result of the simultaneous absorption and desorption of hydrogen in the surface layer of the sample. Thus, intensive generation of nonequilibrium optical phonons and coherent multiphonon excitations[16,17] should be expected in a copper cathode during electrolysis in the presence of an ultraweak thermal neutron flux. In fact, the equilibrium bulk modulus (B) may be expressed in terms of the energy of the phonon subsystem (W) of the crystal and the volume (V) occupied by the excited vibrations in k space, as $B = 10W/9V$ (Ref. 18). In this case, the energy W per unit fcc cell is written as $W = 3k\hbar\omega_D$ (where k is the number of atoms per unit cell, $\hbar$ is Planck's constant, and ω_D is the Debye frequency of copper). This energy corresponds to the volume $V = r_0^3$, where r_0 is the distance between the nearest neighbors in the lattice. This gives

$$B = \frac{10}{3} \frac{k\hbar\omega_D}{r_0^3}. \tag{4}$$

The value of B for copper obtained from Eq. (4) agrees satisfactorily with the published data.[15] Thus, it follows from expression (4) that a necessary condition for the generation of a nonequilibrium optical phonon branch is the creation of mechanical stresses comparable to B, since only in this case is the entire spectrum of normal modes with the cutoff frequency ω_D excited in the crystal. Conversely, it is also clear from (4) that, when the mechanical stresses in the crystal are much smaller than B, the probability of generating nonequilibrium modes with the frequency ω_D is negligible.

However, an abrupt increase in the intensity of the optical phonon mode in the crystal can increase the cross section for absorption of thermal neutrons.[8,9] For instance, the author of Ref. 13 described the generation and concentration (summation over amplitudes) of nonequilibrium optical phonons and coherent multiphonon excitations when various metals were saturated with hydrogen. It was shown that under highly nonequilibrium conditions (similar to those created in the surface layer of a copper cathode during electrolysis and exposure to thermal neutrons), the energy of a ''collection'' of optical phonons (coherent multiphonon excitations) may be comparable with the neutron binding energy in the nucleus.[19] This type of process can realistically increase the capture cross section of thermal neutrons, especially in regions with a high concentration of elastic energy, and specifically in the surface layer of a copper cathode. No anomalous absorption of thermal neutrons is observed in a Pd cathode because of the fairly uniform distribution of hydrogen in the sample as a result of its high solubility in

palladium.[20] This distribution makes it highly unlikely that regions of high elastic energy density will form in a Pd cathode and thus does not result in the generation of an intense optical mode.[17]

In sum, we have studied the electrochemical hydrogenation of copper in the presence of an ultraweak thermal neutron flux ($I_n = 20$ n/cm$^2\cdot$s). It has been shown that under these conditions, appreciable mechanical stresses, up to 10^{11} Pa, are created in a thin surface layer of the copper cathode, causing bending and damage to the surface of the sample. In the absence of irradiation by an ultraweak thermal neutron flux, no measurable bending or surface damage are detected. At present, the mechanism for the stimulation of plastic deformation processes by an ultraweak thermal neutron flux is not understood. However, it may be hypothesized that the thermal neutron flux diffuses into the copper cathode where it interacts with nonequilibrium phonons generated in the crystal as a result of the hydrogenation of the surface layer. In this case, the energy of the nonequilibrium phonons, i.e., the elastic energy of the cathode, should be very efficiently converted into plastic deformation energy as a result of inelastic scattering of neutrons, which have acquired energy from nonequilibrium phonons, at imperfections in the copper crystal lattice. This process gives rise to strong plastic deformations and damage to the cathode surface which is not observed under normal conditions of cosmic neutron background. Such appreciable deformations of the copper cathode give rise to an anomalous increase in the absorption cross section of incident thermal neutrons which is clearly attributable to the generation of nonequilibrium optical phonons and multiphonon excitations.[1] In this case, the anomalous increase in the absorption cross section prevents further damage to the surface of the sample by regulating (reducing) this thermal neutron flux (''negative feedback'').

The authors would like to thank A. V. Strelkov and V. B. Belyaev (Joint Institute for Nuclear Research, Dubna) for their interest in this work and for useful discussions.

This work was supported by Grants from the Russian Fund for Fundamental Research Nos. 94–02–04895 and 95–03–08014.

[1] A. G. Lipson, D. M. Sakov, and E. I. Saunin, JETP Lett. **62**, 828 (1995).
[2] A. G. Lipson, D. M. Sakov, and E. I. Saunin, Pis'ma Zh. Tekh. Fiz. **22**(2), 8 (1996) [Tech. Phys. Lett. **22**, 49 (1996)].
[3] T. R. Volk, I. Rakhimov, V. M. Sarnatskiĭ *et al.*, Fiz. Tverd. Tela (Leningrad) **27**, 3613 (1985) [Sov. Phys. Solid State **27**, 2176 (1985)].
[4] A. G. Lipson, B. F. Lyakhov, E. I. Saunin *et al.*, Pis'ma Zh. Tekh. Fiz. **22**(15), 42 (1996) [Tech. Phys. Lett. **22**, 618 (1996)].
[5] M. W. Thompson, *Defects and Radiation Damage in Metals* [Cambridge University Press, Cambridge, 1969; Mir, Moscow, 1971].
[6] L. N. Begrambekov and A. A. Pustobaev, Izv. Ross. Akad. Nauk, Ser. Fiz. **60**(4), 218 (1996).
[7] M. I. Molotskiĭ. Fiz. Tverd. Tela (Leningrad) **20**, 1651 (1978) [Sov. Phys. Solid State **20**, 956 (1978)].
[8] I. I. Gurevich and L. V. Tarasov, *Low-Energy Neutron Physics* [North-Holland, Amsterdam, 1968; Nauka, Moscow, 1965].
[9] Neutron Physics. Springer Tract. Mod. Phys. Springer-Verlag, Berlin (1977). V. 80. N 1.
[10] A. G. Lipson, B. F. Lyakhov, V. A. Kuznetsov *et al.*, Zh. Fiz. Khim. **69**, 1989 (1995).
[11] A. G. Lipson, I. I. Bardyshev, D. M. Sakov, Pis'ma Zh. Tekh. Fiz. **20**(23), 53 (1994) [Tech. Phys. Lett. **20**, 957 (1994)].
[12] H. Kozima, Nuovo Cimento A **27**, 1781 (1994).
[13] P. L. Hagelstein, Trans. Fusion Tech. **26**, No. 4T, 461 (1994).
[14] L. D. Landau and E. M. Lifshitz, *Theory of Elasticity*, 2nd. ed. [Pergamon Press, Oxford, 1965; Nauka, Moscow, 1965].
[15] *Handbook of Physical Quantities*, edited by I. S. Grigor'ev and E. Z. Maĭlikhov [in Russian], Energoatomizdat, Moscow (1981).
[16] J. Harris, Surf. Sci. **221**, 335 (1989).
[17] P. L. Hagelstein, Bull. APS **40**, 808 (1995).
[18] N. W. Ashcroft and N. D. Mermin, *Solid State Physics* [Holt, Rinehart and Winston, New York, 1976; Mir, Moscow, 1979].
[19] J. Schwinger, Prog. Theor. Phys. **85**, 711 (1991).
[20] A. G. Lipson, B. F. Lyakhov, D. M. Sakov, and V. A. Kuznetsov, Fiz. Tverd. Tela (St. Petersburg) **38**, 1657 (1996) [Phys. Solid State **38**, 915 (1996)].

Translated by R. M. Durham

Influence of the sign of the load on deformation instability and fracture of aluminum and its alloys at liquid-helium temperatures

V. V. Shpeĭzman and V. I. Nikolaev

A. F. Ioffe Physicotechnical Institute, Russian Academy of Sciences, 194021 St. Petersburg, Russia
(Submitted July 16, 1997)
Fiz. Tverd. Tela (St. Petersburg) **40**, 260–263 (February 1998)

An analysis is made of the influence of impurity content and of the sign and variation of the load on the stress-strain curves of aluminum at liquid helium temperatures. It is shown that the deformation instability, observed as jumps in the diagrams, depends on all these factors. When the sign of the load is reversed, the amplitude of the deformation jumps increases, which leads to the appearance of macrocracks, even under compression. The temperature-strain rate region of unstable deformation was determined for the alloy D16T. © *1998 American Institute of Physics.* [S1063-7834(98)02102-9]

It is known that impurities strongly influence macroscopic plastic deformation instability at liquid-helium temperatures.[1] For instance, for pure aluminum jumps on the tensile stress-strain diagram are observed at temperatures below 1.6 K (Ref. 2) whereas for technical-grade aluminum containing impurities, these jumps are observed at temperatures of 4.2 K and above.[1,3] This behavior is usually attributed to the increased flow stresses in impure crystals and to their strong temperature dependences, which is an important factor in models of thermal deformation instability.[4] For this reason, jumps are sometimes observed in pure metals at the end of the stress-strain diagram, i.e., after appreciable plastic deformation whereas, in impure metals and alloys, they are observed almost immediately beyond the yield point.[3] Compared with their influence on deformation, impurities can have an even greater influence on fracture. The most typical example of this is the low-temperature embrittlement, known as cold shortness, which is in many cases attributed to impurities.[5] However, even at liquid-helium temperatures the material retains its plasticity, although this is generally lower for impure crystals compared with pure ones.[2]

In addition to analyzing the influence of impurity content on abrupt deformation and fracture, we also investigate the part played by the sign of the deformation and its variation during the loading process (i.e., we studied the Bauschinger effect in the region of deformation instability). It was assumed that since a plastic material does not fracture under compression, this can explain, first, how instability develops at high strains and, second, how fracture occurs under tension at the instant of a deformation jump.

1. EXPERIMENTAL METHOD

Uniaxial tension and compression testing was carried out using cylindrical samples of AD1 aluminum and its alloys V95 and D16T. The diameter of the tensile samples was 4 mm and the length of the working section was 30 mm, for the compression samples these values were 3–4 and 7–10 mm, respectively. New samples were prepared from the working section of some samples fractured under tension, and these were then used for compression tests.

The testing was carried out in an Oxford helium cryostat using an Instron 1342 universal testing machine. Liquid nitrogen was used for precooling and liquid helium was fed into the cryostat using two pumps which created a weak vacuum in the cryostat.

The test temperature was varied over the range 4.2–20 K.

2. EXPERIMENTAL RESULTS AND DISCUSSION

Figure 1 gives the tensile and compressive stress-strain diagrams of the initial samples while Fig. 2 gives the compressive stress-strain diagrams of previously tensile-tested samples, plotted using the coordinates: stress $\sigma = P/F_0$ (where P is the load, F_0 is the initial cross-sectional area) versus strain $\varepsilon = (\Delta l + M)/l_0$ (where Δl is the change in the sample length, l_0 is the initial sample length, and the value of M is determined by the rigidity of the machine, and in our case at maximum loads its contribution to the deformation of the sample did not exceed 1.5%). When analyzing the data plotted in Fig. 2, the preliminary deformation was taken into account in the strain calculations but its sign was neglected. This may be justified by the results of Ref. 6 where it was shown that the dislocation density ρ in LiF single crystals increases under each new load regardless of the sign of the deformation and ρ was proportional to the algebraic sum of the deformations for each load.

Note that if the tension and compression curves drawn through the tops of the jumps (upper envelopes) are compared, in true coordinates where F_0 is replaced by the instantaneous area $F_0/(1+\varepsilon)$, and ε is replaced by $\ln(1+\varepsilon)$, the compression and tension curves for AD1 and D16T are almost the same, which indicates that there is no anisotropy in relation to the sign of the load. For the V95 alloy the tension curve is lower than the compression curve and ends rapidly with rupture of the sample.

This abrupt deformation develops differently in the materials studied. It can be seen from Fig. 1a that for AD1 aluminum, jumps under tension appear at the end of a section of uniform deformation (near the maximum of the diagram the strain is approximately 20%) and have immediately a fairly large amplitude, which varies little until the instant of

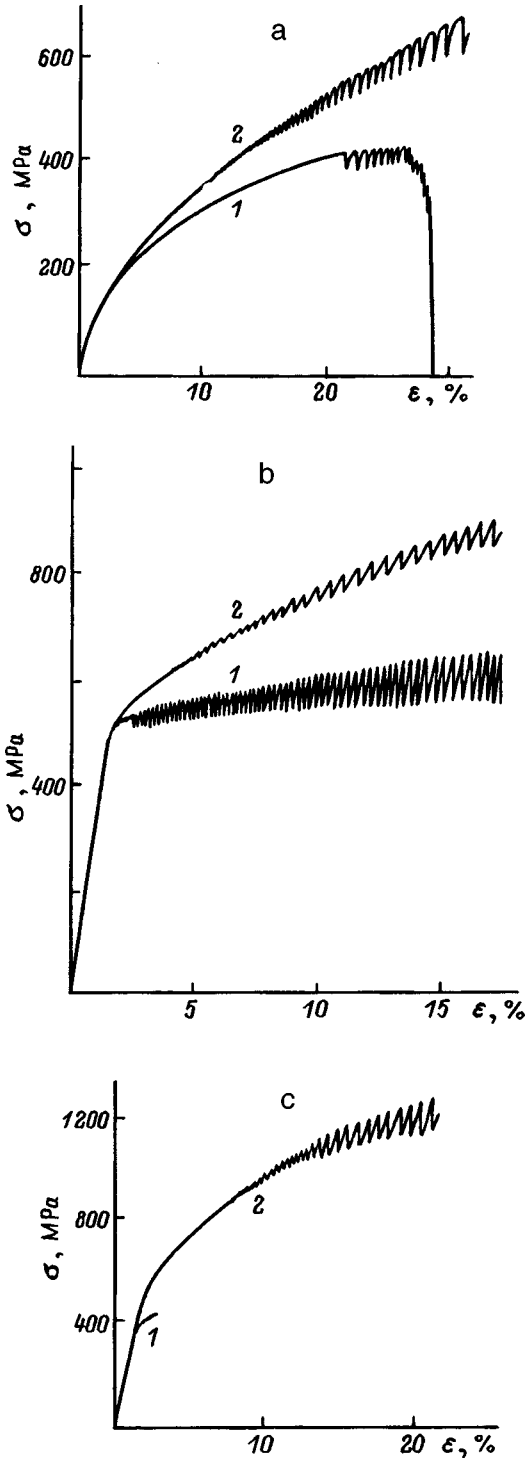

FIG. 1. Tension (*1*) and compression (*2*) stress-strain diagrams for AD1 aluminum (a), and aluminum alloys D16T (b) and V95 (c) at 4.2 K.

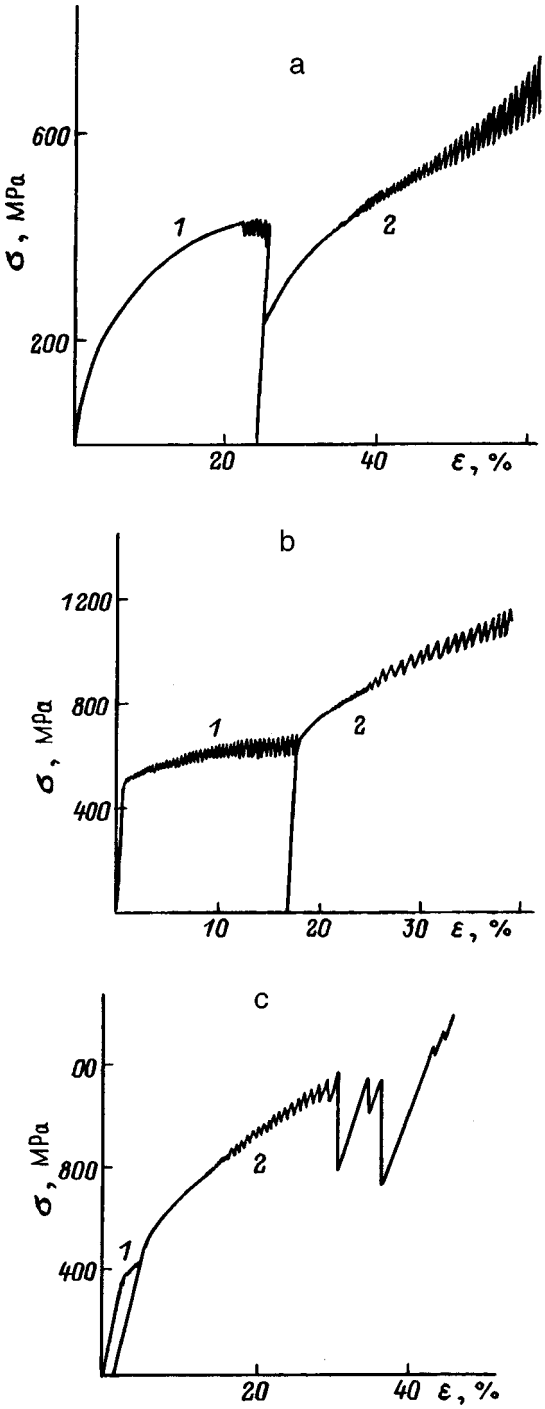

FIG. 2. Compression stress-strain diagram (*2*) after tensile-testing (*1*) of AD1 aluminum (a) and alloys D16T (b) and V95 (c) at 4.2 K.

fracture. On the compression diagram jumps of very small amplitude are initiated beyond the yield point at approximately 8% strain and the curve then becomes a pulsating line with jumps of continuously increasing amplitude.

Thus, the first jumps under compression are initiated earlier in terms of strain and have a smaller amplitude than those under tension but then as the strain increases, the amplitude of these jumps increases and if they are compared for the same strain, the jumps under compression are found to be larger than those under tension. For a sample subjected to compression after tension, the plastic deformation is initiated at stresses lower than those at the instant of unloading (more precisely, at the point of the maximum averaged over the jumps on the diagram, i.e., at the instant where uniform deformation is converted to localized deformation in a neck).[1)] The difference in the flow stresses (the Bauschinger effect) is $\Delta B = 110$ MPa. The jumps are initiated almost immediately after reaching the stresses at which the uniform deformation under tension ended. Compared with compression of the initial sample under repeated loading, more intensive hardening

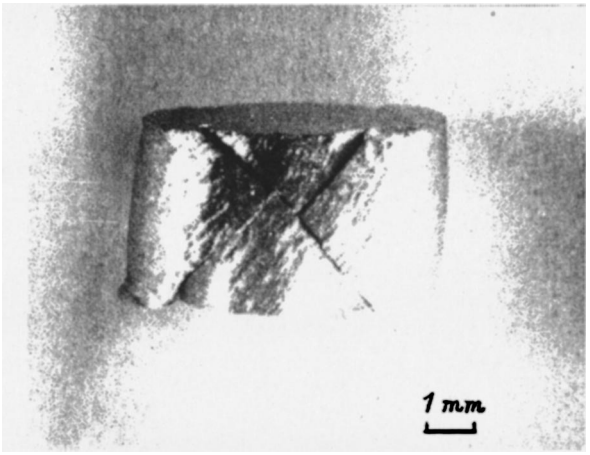

FIG. 3. Formation of cracks along inclined fault bands during compression of tensile-tested V95 alloy sample at $T=4.2$ K.

and a larger increase in the amplitude of the jumps are observed with increasing deformation.

For alloy D16T (Fig. 1b) the jumps under compression and tension begin immediately beyond the yield point. Under tension they rapidly attain a large amplitude (~ 50 MPa) which increases with deformation and reaches ~ 100 MPa at the instant of rupture. Thus, the behavior of alloy D16T under tension differs from the behavior of aluminum described above. Under compression the diagrams for AD1 and D16T are externally similar, only the scale of the stresses show any difference.

It can be seen from Fig. 2b that the Bauschinger effect for alloy D16T is extremely small and the compression diagram of the previously tensile-tested samples is similar to that of the initial samples, even though the preliminary strain was 17%. One reason why aluminum and its alloy exhibit such different behavior may be because the deformation hardening values (i.e., the difference between the flow stresses at $\varepsilon=10-20\%$, σ_ε, and the yield point, σ_s) differ

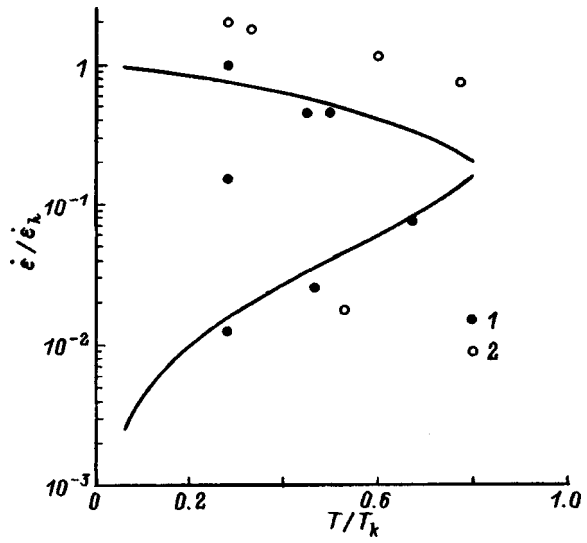

FIG. 4. Calculated curves showing the boundaries of the region of unstable deformation.[8] The experimental points for D16T alloy correspond to tension curves with deformation jumps (*1*) and smooth deformation curves (*2*).

substantially: the yield point is appreciably higher and the deformation hardening lower for the alloy. If the Bauschinger effect is compared with the relative deformation hardening, the stress jump when the sign of the load is reversed is approximately half the difference between σ_ε and σ_s for both aluminum and D16T. The strain dependence of the jump amplitude under repeated loading with reversal of the sign of the load can then be understood: this is determined in any case only by the deformation under the last load, i.e., the jumps do not ''remember'' the previous deformation of opposite sign. It should also be noted that a ''memory'' for deformation of the same sign undoubtedly exists: when compression or tension is interrupted, after removal of the load and application of a new load, the diagram almost returns to the unloading point and the jumps are restored with their former amplitude.

Since a sample of alloy V95 fractured under tension at very low strain (around 3%), the compression diagrams of the initial sample and that cut from the tensile-tested sample are almost the same (as can be seen from Fig. 2c). However, this is only valid up to $\sim 25\%$ strain. When the tensile-tested sample undergoes further compression, two deep drops in load (by $\sim 30\%$) can be identified on the diagram. This appreciable localization of the deformation leads to the formation of inclined fault bands with macrocracks along these bands (Fig. 3), which is typical of the compression of low-plasticity materials (such as marble[7]) but is by no means typical of aluminum and its alloys. Unlike the other materials studied here, at liquid-helium temperature the alloy V95 tends to exhibit highly localized deformation and ensuing fracture, as is also evidenced by the low limiting deformation of this alloy under low-temperature tension.[2)]

It has already been noted that the abrupt deformation of aluminum has been studied by many authors. The author of Ref. 8 attempted to determine theoretically the temperature-strain rate boundaries of the region of unstable deformation. For technically pure aluminum (99.5%) the normalization parameters determining these boundaries were: $T_k=6.6$ K and $\varepsilon=10^{-1}$ s^{-1}. Here we determined the range of temperature and strain rates for the stretching of D16T aluminum in which deformation jumps are observed (Fig. 4). One parameter is $\varepsilon_h=2.5\times 10^{-2}$ s^{-1} and the other $T_k=15$ K. A comparison between the region of unstable deformation for aluminum and its alloy shows that for the alloy this region is shifted toward higher temperatures and lower strain rates.

In sum, we have shown that deformation instability at liquid-helium temperatures cannot produce large macrodeformations. Its increased localization leads to the formation of macrocracks, which reaffirms the importance of strain localization in the fracture process.

The authors would like to thank G. A. Malygin and B. I. Smirnov for discussions of the results.

[1)]Note that in this case, the juxtaposition of uniform and localized deformation is not completely correct since the deformation was localized before the maximum of the averaged diagram.

[2)]It is also possible that fracture may occur without reversal of the load under compression if the sample is subjected to high stress rates.

[1] V. I. Startsev and V. V. Pustovalov, *Plasticity and Strength of Materials at Low Temperatures* [in Russian], Metallurgiya, Moscow (1975).
[2] O. V. Klyavin and A. V. Stepanov, Fiz. Met. Metalloved. **8**, 274 (1959); Fiz. Tverd. Tela (Leningrad) **1**, 956 (1959).
[3] V. I. Nikolaev and V. V. Shpeĭzman, Fiz. Tverd. Tela (St. Petersburg) **39**, 647 (1997) [Phys. Solid State **39**, 565 (1997)].
[4] G. A. Malygin, Fiz. Met. Metalloved. **81**(3), 5 (1996).
[5] D. A. Wigley, *Mechanical Properties of Materials at Low Temperatures* (Plenum Press, New York, 1977).
[6] T. S. Orlova, B. I. Smirnov, and V. V. Shpeĭzman, Fiz. Tverd. Tela (Leningrad) **23** 1981 (1981) [Sov. Phys. Solid State **23**, 1157 (1981)].
[7] A. Nadai, *Theory of Flow and Fracture of Solids*, Vol. 1 (McGraw–Hill, New York 1950).
[8] G. A. Malygin, Fiz. Nizk. Temp. **12**, 849 (1986) [Sov. J. Low Temp. Phys. **12**, 481 (1986)].

Translated by R. M. Durham

Study of the local defect structure of CdTe-Ge crystals by microindentation

L. S. Fomenko and S. V. Lubetnets

Low-Temperature Physico-Technical Institute, Ukrainian Academy of Sciences, 310164 Khar'kov, Ukraine

P. I. Feĭchuk and L. P. Shcherbak

Chernovytsy State University, 274012 Chernovytsy, Ukraine

(submitted June 30, 1997; resubmitted September 23, 1997)
Fiz. Tverd. Tela (St. Petersburg) **40**, 264–268 (February 1998)

This paper demonstrates the effectiveness of the microindentation method as a way to monitor the quality of cadmium telluride crystals. Measurements of microhardness and the length of dislocation rays from the rosette around the indentation pit can clearly identify nonuniform distributions of structural defects, both along the direction of growth and along a diameter of a CdTe boule. The mobility of α dislocations is more sensitive to nonuniformities in the structure than the mobility of β dislocations and the microhardness. A qualitative correspondence is established between the microplasticity characteristics of CdTe:Ge and its germanium content: the hardness of the crystal is insensitive to changes in the Ge content in the range from 3×10^{16} to 1×10^{17} at/cm^3, but increases sharply beginning at a concentration of $\sim1\times10^{17}$ at/cm^3. The correlation between the value of the microhardness and the length of the dislocation rays from the rosette around the imprint of the indentor are analyzed. An estimate is obtained for the hardness of pure CdTe. © *1998 American Institute of Physics.* [S1063-7834(98)02202-3]

Imperfections in semiconducting crystals, e.g., impurities, intrinsic nonstoichiometric defects, and dislocations, have a very strong effect on those properties of the crystals that are important for applications.[1,2] The structure and properties of a grown crystal are often found to be variable both over its cross section and along its length, which for semiconducting materials is undesirable. Therefore, it is important to study the defect structure and degree of uniformity of these crystals in order to optimize their growth regimes.

It has been established that the mechanical, electrical, and optical properties of undoped crystals of cadmium telluride are all interrelated.[3,4] One way to monitor the mechanical strength and plasticity of materials is the method of microindentation, which is distinguished by simplicity and ease of use. Other advantages of the method are the nondestructive and local character of its sampling, and also, what is particularly important for our purposes, its sensitivity to the presence of structural defects.

In this work we have measured the microhardness and the length of rays from the dislocation rosette in the vicinity of the indentor imprint to study the effect of germanium impurities on the micromechanical characteristics of cadmium telluride. By doping CdTe crystals with microadmixtures of germanium we obtain a high-resistance material whose properties are close to those of intrinsic CdTe,[15] which makes it a promising candidate for use in fabricating detectors of ionizing radiation[6] and in optoelectronics.[7]

1. EXPERIMENTAL METHOD

A boule of CdTe doped with germanium with a mass of 600 g was grown by the vertical Bridgman method in an evacuated graphitized ampoule with an inner diameter of 35 mm. The rate of crystallization was 3 mm/h, the gradient at the crystallization front was 6–7 K/cm. The initial concentration of impurities introduced into the melt was $c_0=1.6\times10^{19}$ at./cm^3.

The distribution of impurities dissolved in the crystal was monitored by using a germanium source tagged with the radioisotope Ge^{71} (K capture, $T_{1/2}=7$ days) and subsequent radiometric analysis of a 3-mm-thick plate cut from the boule parallel to the growth axis.

In order to study the micromechanical properties, a 4-mm-thick plate oriented in the (111) plane was cut from the boule with a tungsten wire 1 mm in diameter and a suspension of abrasive powders with particle diameters 3–5 μm in kerosene. The angle between the plate surface and the growth axis of the boule was 60°. The shapes of the plate and the sample are shown in Fig. 1. After being abraded on glass, the film surface was twice treated with polishing etch E[8] of composition $K_2Cr_2O_7+HNO_3+H_2O$ (4 g: 10 ml: 25 ml), first to a depth of ~20 μm and then, after indenting the sample, to a depth of ~500 μm.

The sample was indented on the $(\overline{111})$Te plane using a PMT-3 device with a standard Vickers pyramid at a load of $P=0.1$ N at the indentor. The value of microhardness H_V was determined from the expression

$$H_V=1.854P/(2a)^2,$$

where $2a$ is the length of the diagonal of the indentor pit. The error in measuring the microhardness was $\sim3\%$.

The dislocation structure was revealed by selective chemical etching in a solution of HF(concentrated)+50% solution of CrO_3 in water (2:3).[9] The average density of grown-in dislocations in our sample was $\sim2\times10^5$ cm^{-2}. In the ''background'' region (see Fig. 1) we observed a high density of flat-bottomed etch pits which usually form at point-defect sites. Since the structure of the dislocation en-

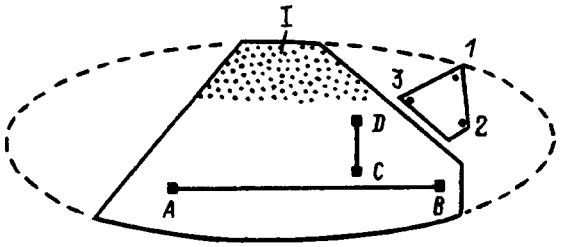

FIG. 1. Shape of sample cut from a cylindrical boule of CdTe:Ge (outlined by the solid lines). *AB* (projection of the growth direction from left to right) and *CD* are lines along which the indentations are made; to the left of the sample is another orientation that has been cleaved off, to the right a chip on which the germanium concentration was measured at points 1, 2, and 3. *I* is the ''background'' region.

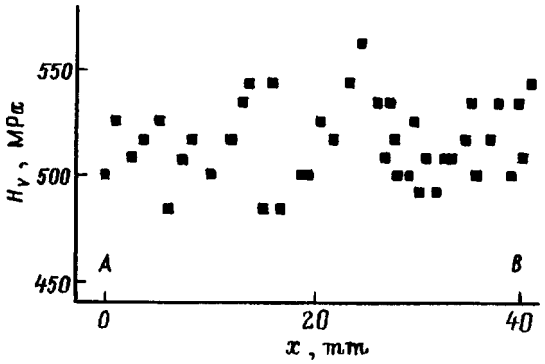

FIG. 3. Measurement of bulk microhardness along segment *AB*.

semble around the imprint of the indentor is not in equilibrium, the dislocation rays from the rosette around the indentor pit spontaneously get longer with time.[10] For this reason, the indented sample was kept at room temperature for 24 hours before etching in order to relax the stresses in the dislocation system.

Figure 2 shows a dislocation rosette containing six double rays having the direction ⟨110⟩. The authors of Ref. 11 state that the rays are made up of 60° α dislocations (the long rays) and 60° β dislocations (the short rays). Note that the diameter of the etch figure for β dislocations is 1.4 times larger than for α dislocations. This difference allows us to identify the types of dislocations to some extent. In this work we measured average values of the lengths of α and β radials in each rosette as a function of the coordinates of the indentation on the sample surface.

2. RESULTS AND DISCUSSION

Our studies were carried out on the single-crystal portion of the film, which is identified in Fig. 1 by the solid lines. Extrapolation from data from the radiometric analysis indicated that the concentration of germanium along the axial direction (segment *AB*) varied from 3×10^{16} to 2×10^{17} at./cm^3. On segment *CD*, i.e., in the radial direction, the impurity content can be assumed constant, and the same extrapolation procedure gives a value of $(1-1.5)\times10^{17}$ at./cm^3 for it. This prediction is in good agreement with studies of the germanium concentration in a chip from the sample at points *1–3* using an EMAL-2 laser mass spectrometer. According to our measurements, $c_1=3.6\times10^{-4}$, $c_2=4.7\times10^{-4}$, and $c_3=9.7\times10^{-4}$ at. % Ge, that is, 5.3×10^{16}, 7.0×10^{16} and 1.4×10^{17} at./cm^3 respectively.

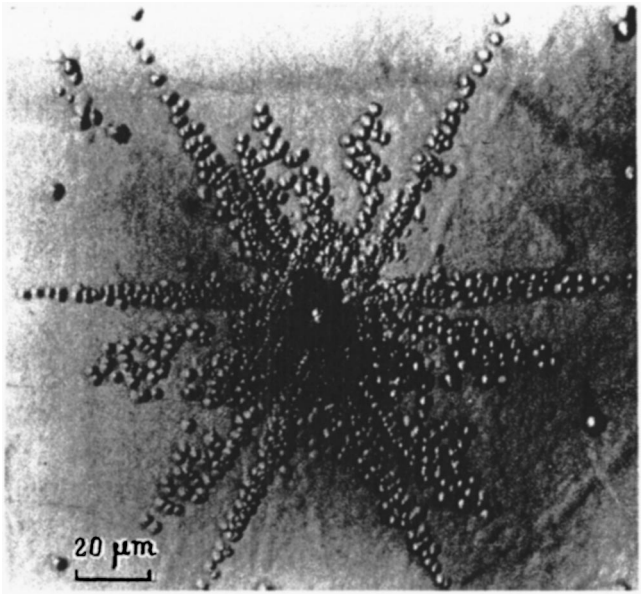

FIG. 2. Dislocation rosette near the imprint of the indentor in a CdTe+Ge crystal.

Figure 3 shows how the microhardness H_V varies in the direction of the *x* axis along segment *AB* (which is the projection of the direction of growth onto the surface of the film, see Fig. 1) on the sample after removal of the damaged surface layer to a depth of $\sim$500 μm. It is clear that the function $H_V(x)$ does not exhibit any marked regularity. The microhardness exhibits a narrow peak in the interval $20<x<30$ mm against a background of non-systematic changes, and a certain tendency to increase after the point *B*. The maximum and minimum values $H_{V_{\max}}=585$ MPa and $H_{V_{\min}}=485$ MPa differ by only 17%. Measurements of microhardness along the line *CD* located roughly in the center part of the film and perpendicular to the direction of growth show that the quantity H_V changes from 530 MPa at point *C* to 610 MPa at point *D*, i.e., by roughly 13%. Although these differences are not large, they exceed the measurement errors. This implies that our data are reflecting a structural nonuniformity in the plane of the cut plate that arises during crystallization of the boule.

The lengths $l_{\alpha,\beta}$ of the rosette rays, which characterize the mobility of α and β dislocations, are considerably more sensitive to nonuniformities in the structure than the microhardness or size of the indentor imprint. Whereas the diagonal of the imprint varies by no more than a factor of 1.07 as a function of its location on the sample surface, and the microhardness by only a factor of 1.2, the length of the rosette rays changes by almost a factor of 2.

Data from our measurements of $l_{\alpha,\beta}$ along the lines *AB* and *CD* are shown in Fig. 4. For the direction *x* the dependence of the length of the rosette rays on the coordinates of the indentation is characteristically nonmonotonic (Fig. 4a). The function $l_\alpha(x)$ exhibits a dip in the range

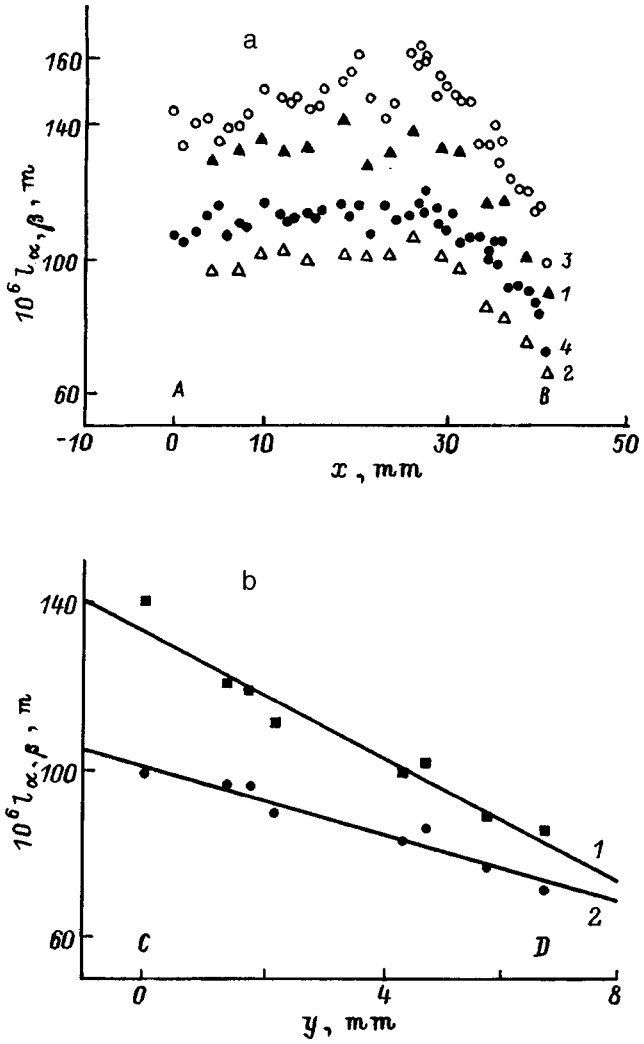

FIG. 4. Measurement of the length of rosette rays from indentor pits on segments *AB* (a) and *CD* (b). (a) l_α (*1*) and l_β (*2*) are at the surface of a sample polished after cutting to a depth of ~ 20 μm, l_α (*3*) and l_β (*4*) are after removal of a surface layer to a depth of ~ 500 μm. (b) l_α (*1*) and l_β (*2*) are for the surface of a sample polished after cutting to a depth of ~ 20 μm.

$20 < x < 30$ mm, which corresponds to the microhardness peak in Fig. 3, and less obvious dips near $x \simeq 5$ and 15 mm, along with a rather abrupt decrease in the length l_α of the α rays at the end of the sample. This wave-like variation of $l_\alpha(x)$ is obviously associated with the periodic incorporation into the solid phase of impurities that are forced back into the melt at the crystallization front. These features, which reflect the nonuniformity of the sample structure, are not nearly so evident in the function $l_\beta(x)$ and, when the film is indented after being polished to a small depth, they cannot be found at all, as is clear from the figure. This is probably due to the presence of residual internal strains in a near-surface layer that has been hardened during the cutting process, since these strains limit the development of the dislocation structure under the indentor. In the hardened layer, the rays of the rosettes from the indentor pit are 25–30% shorter than in the bulk. This observation correlates with the data of Refs. 12, 13. In Ref. 13 it was shown that as the damaged layer is removed the microhardness of an undoped CdTe crystal changes by a factor of 1.5 from 450 to 300–320 MPa after polishing to a depth of 40–50 μm.

Qualitatively, the data set shown in Fig. 4a can be approximated by two line segments. In the range of values $x < 20$ mm corresponding to a germanium content from 3×10^{16} to 1×10^{17} at./cm^3, the length of the dislocation rays, i.e., the plasticity of the material, changes very little. As the concentration of Ge is increased further, there is a marked decrease in the quantities $l_{\alpha,\beta}$ both in the hardened layer and in the bulk. This type of concentration dependence of $l_{\alpha,\beta}$ correlates with the data of Ref. 14, which indicate a change in the way that germanium incorporates into the lattice of Bridgman-grown CdTe+Ge crystals when $c = 1\times10^{17}$ at./cm^3. According to the model, at low concentrations the impurity occupies a Cd position forming a singly ionized $Ge^{\cdot}_{Cd}$ center. Electrical neutrality of the crystal in this case is ensured by twice as many doubly charged acceptors, provided by cadmium vacancies V''_{Cd}. At higher concentrations the impurity dissolves both in the form of isolated centers $Ge^{\cdot}_{Cd}$ and in the form of associates $(Ge_{Cd}V_{Cd})'$. In this range of germanium concentrations the cadmium telluride lattice is hardened. Evidence for this is the decrease we observe in the length of dislocation rays and the slight increase in the microhardness (Fig. 3 and Fig. 4a).

The linear decrease in $l_{\alpha,\beta}$ along the line segment *CD* (Fig. 4b) is evidence that the hardness of the material increases as we approach the ''background'' region of the sample, which enriched by point defects that probably are complexes of vacancies and vacancy disks. The character of the function $l_{\alpha,\beta}(y)$ is unchanged by removal of the hardened surface layer.

It is interesting to compare the results given here with the data available in the literature on mechanical properties of CdTe crystals with impurities and intrinsic defects. High-resistance undoped stoichiometric crystals exhibit the smallest yield stress. However, the yield stress increases by almost a factor of 2 as the concentration of electrons or holes increases (due to interstitial $Cd_i^{\cdot\cdot}$ ions or vacant cadmium sites).[3] The introduction of isovalent (Zn)[15,16] or donor (In)[17] impurities into the CdTe crystal also leads to an increase in the yield stress[15,16] and microhardness,[17] the more so the higher the impurity concentration. Wth regard to the value of their hardness, our CdTe+Ge samples lie between very soft samples of CdTe reported in the literature, with a value of $H_V = 300$ MPa,[13] and very hard samples with a value of $H_V = 670$ MPa (for CdTe+1.2×10^{17} In/cm^3), see Ref. 17 (heavily doped CdTe+2×10^{18} In/cm^3 possesses the maximum hardness $H_V = 1.4$ GPa; see Ref. 17). However, it would be rash to assume that the hardness is associated with germanium atoms alone. Rather, it arises from the combined influence of growth dislocations, impurities, vacancies, and interstitial atoms on the micromechanism for the hardness characteristics.

In conclusion, let us discuss the relation between the measured values of H_V and $l_{\alpha,\beta}$. In the theory of Gridneva *et al.*,[18] which treats the evolution of dislocation structures in a semiconducting crystal near an indentor pit, the following relation is obtained:

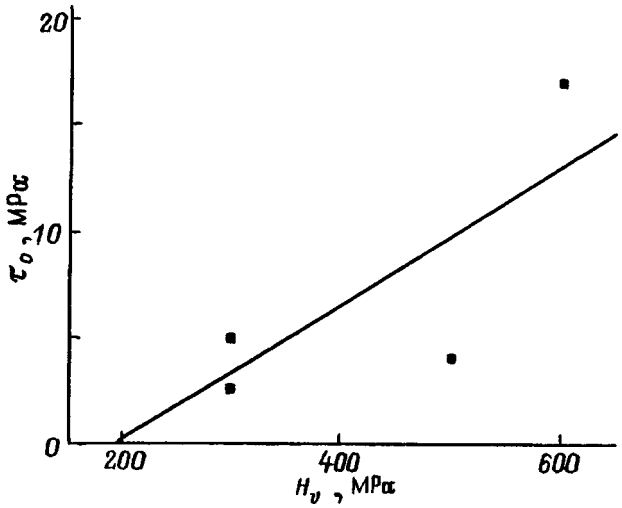

FIG. 5. A $\tau_0 - H_V$ plot made using data from measurements of the yield stress τ_0 and microhardness H_V of CdTe crystals with various hardness and impurity content obtained in Refs. 10, 11, and 18–21.

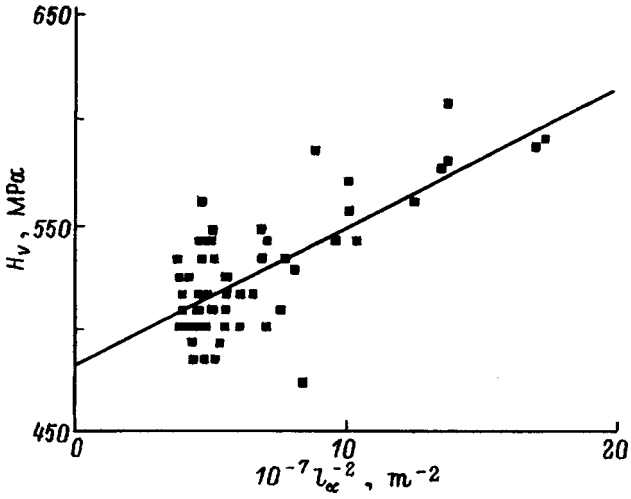

FIG. 6. Relation between microhardness H_V and the length l_α of α-dislocation rays from rosettes measured along segments AB and CD (see Fig. 1).

$$l_0 = \left(\frac{ANP}{\tau_T}\right)^{1/2},$$

where l_0 is the steady-state length of a ray from the rosette, $A = (1-2\nu)/\pi\sqrt{\sigma}$, $N = 1 + \frac{3}{4}\beta(\cos\alpha + \sin\alpha/1-\nu)$, ν is the Poisson coefficient, the constant $\beta > 1$, $\alpha = 60°$ is the angle between dislocation lines and the Burgers vector, P is the load on the indentor, and τ_T is the long-range component of the yield stress τ_0, i.e., the starting stress for the motion of a dislocation. There is a definite relation between the yield stress τ_0 and the microhardness H_V. For brittle and strongly strain-hardened materials this relation is simple: $\tau_0 \simeq H_V/3$; see Ref. 19; for plastic materials it must be found by a special investigation. For a number of alkali-halides it has been shown that $\tau_0 = C(H_V - H_{V0})$ over a wide range of impurity concentrations; see Ref. 20, where $C = \text{const}$, and H_{V0} is the hardness of a pure crystal. The available unrelated data sets on the yield stress and microhardness,[12,13,15–17,21–23] along with the measurements in this work, serve only to establish the fact that this latter relation between τ_0 and H_V is qualitatively satisfied for cadmium telluride crystals of various hardness.

By making a $\tau_0 - H_V$ plot (Fig. 5) on which the minimum (known) values $\tau_0 = 5 \pm 2$,[21] 2.5,[22,23] and 4.8 ± 0.5 MPa[24] are assigned to the minimum value of the hardness $H_V = 300$ MPa,[13] while the values $\tau_0 = 4$ MPa[25] for CdTe and $\tau_0 = 17$ MPa[15] for CdZnTe are assigned to the value of the hardness $H_V = 500$ and 600 MPa that we measure, we obtain the approximate dependence $\tau_0 = C(H_V - H_{V0})$, where $C = 0.03$. Then the value $H_{V0} = 190$ MPa should correspond to the value of hardness for a pure CdTe crystal. If so, the relation given above between l_0 and τ_T should be replaced by a relation between l_0 and the microhardness in the form

$$(H_V - H_V^*) - H_{V0} = a l_0^{-2},$$

where $H_V - H_V^* = H_{VT}$, H_V^* is the component of the hardness that depends on temperature, while H_{VT} is the athermal component of the hardness (analogous to τ_T), and $a = ANP/C \simeq 0.5$ N (here we take $\nu = 0.3$, $\beta = 1.5$).

Our experimental conditions ensured that the measured lengths $l_{\alpha,\beta}$ of the rosette rays correspond to steady-state values, since we allowed the dislocation structure around the imprint of the indentor to stabilize after 24 hours of relaxation at room temperature. The time dependence $l_{\alpha,\beta}(t)$ reaches saturation after 1–2 h.[10] Preliminary studies show that the dependence $H_V(T)$ is still strong at room temperature and far from athermal, at which point the condition $H_V(T) = H_{VT} = \text{const}$ should hold.

Figure 6 shows the relation between microhardness and the lengths of dislocation rays l_α corresponding to a given imprint of the indentor for measurements along the directions AD and CD. For β dislocation rays the dependence is analogous. The slopes of the straight lines computed by the method of least squares have the following values: 0.66 N for α dislocation rays and 0.46 N for β dislocation rays, i.e., in rather good order-of-magnitude agreement with the value $a = 0.5$ N calculated from the theory of Ref. 18. The range of values that defines the segment of the H_V axis corresponds to the total value $H_V^* + H_{V0}$.

We can conclude that there is a qualitative correlation between the length of the dislocation rays and the value of the microhardness. However, the lengths of the rays, which characterize the mobility of dislocations in the crystal, are more sensitive to structural imperfections. The hardness is a more complicated characteristic determined not only by the resistance of a dislocation to motion but also by processes of re-creation and multiplication of dislocations in the material under the indentor, which are difficult to take into account theoretically. Therefore, we can hardly expect complete agreement between $l_{\alpha,\beta}$ and H_V without taking into account the local properties of the material.

With regard to the value $H_{V0} = 190$ MPa obtained from Fig. 5, which should indicate the hardness of pure cadmium telluride, let us say the following. Previously it has been reported that the empirical relation $H_{V0} \simeq 2 \times 10^{-3} E$ is well satisfied for polycrystalline metals with cubic symmetry,[26]

while for a number of alkali-halide crystals $H_{V0} \simeq 5 \times 10^{-3} E_{111}$,[27] where E is Young's modulus of the polycrystal and E_{111} is Young's modulus of the crystal along [111]. Let us use these relations to estimate the hardness of pure cadmium telluride, with the understanding that the first case will be an underestimate and the second case an overestimate, in light of the difference in nature of the interatomic bond forces for the respective solids. Note that a high degree of bond ionicity is characteristic for CdTe.[28] By computing the moduli $E = 5.34 \times 10^{10}$ N/m^2 and $E_{111} = 5.23 \times 10^{10}$ N/m^2 at $T = 300$ K, using the stiffness constants c_{ij} for CdTe crystals measured in Refs. 29, 30, we obtain for H_{V0} the values 106.8 and 261.5 MPa. The quantity H_{V0} taken from the abscissa intersection in Fig. 5 is between these computed values. Thus, although the approach taken here is obviously approximate, we nevertheless find that the estimate obtained for the hardness of pure cadmium telluride of 190 MPa is entirely reasonable.

Authors L. Fomenko and S. Lubenets are grateful to V. D. Natsik and V. P. Soldatov for useful discussions and critical reading of the manuscript.

[1] F. A. Kroeger, *The Chemistry of Imperfect Crystals* [North-Holland Publ. Corp., Amsterdam, 1964; Mir, Moscow, 1969].
[2] Yu. A. Osip'yan, V. F. Petrenko, A. V. Zaretskii, and R. W. Whitworth, Adv. Phys. **35**, 115 (1986).
[3] L. Carlsson and C. N. Ahlquist, J. Appl. Phys. **43**, 2529 (1972).
[4] F. Buch and C. N. Ahlquist, J. Appl. Phys. **45**, 1756 (1974).
[5] L. P. Shcherbak, E. S. Nikonyuk, O. E. Panchuk, A. V. Savistskiĭ, P. I. Feĭchuk, and V. V. Matlak, Bull. Acad. Sci. USSR, Ser. Inorg. Mater. **13**, 415 (1977) [in Russian].
[6] P. Feichuk. L. Shcherbak, D. Pljuta, P. Moravec, S. Franc, E. Belas, and P. Hoeshl, *Abstr. Int. Conf. ''Material science and Material Properties for Infrared Optoelectronics.''* Uzhgorod, Ukraine (30 Sept–2 Oct. 1996), p. 17.
[7] K. Shcherbin, A. Shumeljuk, S. Odoulov, P. Feichuk, and G. Brost, Proc. SPIE **2797/237**, 236 (1996).
[8] M. Inoue, I. Teramoto, S. Takayanagi, J. Appl. Phys. **33**, 2578 (1962).
[9] G. V. Indenbaum, R. P. Bouleonenkova, and N. M. Boĭnik, Physics and Chemistry of Processed Materials **2**, 91 (1971) [in Russian].
[10] S. V. Lubenets, P. I. Feĭchuk, L. S. Fomenko, and L. P. Shcherbak, Fiz. Tverd. Tela (Leningrad) **31**, 246 (1989) [Sov. Phys. Solid State **31**, 1239 (1989)].
[11] C. Braun, H. W. Helberg, and A. George, Philos. Mag. A **53**, 277 (1986).
[12] N. Ya. Gorid'ko, N. N. Novikov, and V. S. Vlasov, Ukr. Fiz. Zh. **33**(1), 78 (1988) [in Russian].
[13] S. A. Medvedev, S. N. Maksimovskiĭ, Yu. V. Klevkov, and P. V. Shapkin, Bull. Acad. Sci. USSR, Ser. Inorg. Mater. **4**(7), 1179 (1968) [in Russian].
[14] O. É. Panchuk, L. P. Shcherbak, and E. S. Nikonyuk, Bull. Acad. Sci. USSR, Ser. Inorg. Mater. **16**(4), 638 (1980) [in Russian].
[15] S. V. Lubenets and L. S. Fomenko, Fiz. Tverd. Tela (Leningrad) **31**, 145 (1989) [Sov. Phys. Solid State **31**, 256 (1989)].
[16] D. Imhoff, A. Zozime, and R. Triboulet, J. Phys. III (France) **1**, 1841 (1991).
[17] V. Swaminathan, F. A. Selim, and F. A. Kroeger, Phys. Status Solidi A **30**(2), 721 (1975).
[18] I. V. Gridneva, Yu. V. Milman, V. I. Trafilov, and S. I. Chugunova, Phys. Status Solidi A **54**(1), 195 (1979).
[19] D. Tabor, *The Hardness of Metals* (Clarendon Press, Oxford, 1951).
[20] G. Y. Chin, L. G. van Uitert, M. L. Green, G. J. Zidzik, and T. Y. Kometani, J. Am. Ceram. Soc. **56**(7), 369 (1973).
[21] K. Maeda, K. Nakagawa, and S. Takeuchi, Phys. Status Solidi A **48**(2), 586 (1978).
[22] E. Y. Gutmanas, N. Travitsky, U. Plitt, and P. Haasen, Scr. Metall. **13**(4), 293 (1979).
[23] E. Y. Gutmanas and P. Haasen, Phys. Status Solidi A **63**(1), 193 (1981).
[24] R. Balasubramanian and W. R. Wilcox, Mater. Sci. Eng. B **16**, 1 (1993).
[25] S. V. Lubevicher, V. G. Lirtsman, V. D. Natsik, L. S. Fomenko, Fiz. Nizk. Temp. **18**, 904 (1992) [Sov. J. Low Temp. Phys. **18**, 636 (1992)]; V. G. Lirtsman, S. V. Lubenets, V. D. Natsik, L. S. Fomenko, Mater. Sci. Eng. **A164**, *1-2*, 367 (1993).
[26] E. R. Petty and H. O'Neill, Metallurg'a (Jan. 1961), p. 25 (cited in[23].)
[27] G. Y. Chin, L. G. van Uitert, M. L. Green, and G. Zydzik, Scr. Metall. **6**(6), 475 (1972).
[28] J. C. Phillips, Rev. Mod. Phys. **42**, 317 (1970).
[29] Yu. Kh. Verikov and A. P. Rusanov, Fiz. Tverd. Tela (Leningrad) **13**, 1157 (1971) [Sov. Phys. Solid State **13**, 956 (1971)].
[30] R. D. Greenough and S. B. Palmer, J. Phys. D **6**(5), 587 (1973).

Translated by Frank J. Crowne

Static and dynamic properties of an isolated strip domain in a thin ferromagnetic film

Yu. I. Gorobets and Yu. I. Dzherzherya

Institute of Magnetism, Ukrainian Academy of Sciences, 252680 Kiev, Ukraine
(Submitted April 22, 1997)
Fiz. Tverd. Tela (St. Petersburg) **40**, 269–273 (February 1998)

A perturbation theory is developed for the integrodifferential Landau–Lifshits equation that describes the state of 2π-domain walls in ferromagnetic films. The static and dynamic parameters of a 2π-domain wall are determined, taking into account its micromagnetic structure. The limits of applicability of geometric domain wall models are indicated. © *1998 American Institute of Physics.* [S1063-7834(98)02302-8]

The theory of the nonlinear Landau–Lifshits equations has been studied in considerable detail, especially for one-dimensional systems.[1–3] However, in certain applications-related problems that involve properties of nonlinear domain-wall-like structures in ferromagnetic systems, the structure of these equations can become much more complicated. Thus, in finite-size samples magnetostatic contributions lead to the appearance of integrodifferential terms in the Landau–Lifshits equations. Solution of the resulting equations requires the use of direct methods, including representation of domain walls by geometric boundaries and conversion to simplified equations of the type used by Slonczewsky *et al.* to describe the dynamics of the magnetization. Like all direct methods, these procedures are not without well-known flaws, the most important of which is the possibility of introducing uncontrolled errors. Perturbation theory is free of these difficulties when it is developed in the neighborhood of exact solutions whose results are asymptotically exact. However, it should be understood that their are special problems with perturbation theory for nonlinear systems, in that the neglect of terms with small parameters can qualitatively change the type of solution.

In this paper we develop a perturbation theory for the one-dimensional integrodifferential Landau–Lifshits equation that describes the state of a 2π-domain wall in a thin ferromagnetic film, which will lead to relations that refine the structure and parameters of a 2π-domain wall.[1,4] This theory, which incorporates the internal structure of the domain wall, predicts a value of the collapse field of a 2π-domain wall that differs considerably from results obtained within the framework of a geometric domain wall model; it also indicates the limits of applicability of the latter model.

The characteristics of the system discussed in this paper are given by the energy density

$$w=M_0^2\left\{\frac{\alpha}{2}\left(\frac{\partial m}{\partial x}\right)^2+\frac{\beta}{2}(1-m_z^2)-h_z m_z-\frac{1}{2}mh_m\right\}, \quad (1)$$

where $m=M/M_0$ is a unit magnetization vector, α, β are the exchange interaction constant and uniaxial anisotropy constant respectively, $h_z=H_z/M_0$ is the reduced magnetic field parallel to the easy-magnetization axis and orthogonal to the plane of the film, and $\mathbf{h}_m$ is the intrinsic magnetostatic field of the ferromagnet determined by the relation

$$\mathbf{h}_m=\nabla\int dr'\,\frac{\operatorname{div}\mathbf{m}(\mathbf{r}')}{|\mathbf{r}-\mathbf{r}'|}. \quad (2)$$

In studying the structure of a 2π-domain wall it is convenient to use the variables φ, $q=\cos\theta$, where φ, θ are azimuthal and polar angles in a coordinate system whose polar axis OX is orthogonal to the plane of the 2π-domain wall. In this case the components of the magnetization vector are given in terms of the new variables by the relations

$$\mathbf{m}=(q,\sqrt{1+q^2}\,\sin\,\varphi,\sqrt{1+q^2}\,\cos\,\varphi)\,\theta(z)\,\theta(z-\delta),$$
$$\theta(z)=\begin{cases}0, & z<0,\\ 1, & z>0.\end{cases} \quad (3)$$

In the approximation of an infinite ferromagnet, a 2π-domain wall has a Bloch structure characterized by rotation of the magnetization in the plane of the domain wall.[5] This model is useful for investigating ferromagnetic materials whose thickness greatly exceeds the characteristic magnetic length ($\Lambda=\sqrt{\alpha/4\pi}$). For finite samples we must take into account the effect of surface nonuniformity of the magnetization, however, which leads to the appearance of regions with Néel structure near the surface and to warping of the surface of the 2π-domain wall. For films whose thickness is close to Λ, the strong exchange interaction suppresses this effect, and the domain wall may be considered uniform in thickness.[1]

Thus, within the thin-film model we assume that the 2π-domain wall has a Bloch structure. In this case $q=m_x$, which describes the departure of the magnetization vector from the plane of the wall, is a small quantity, i.e., $q\ll 1$.

In the new variables, the Landau–Lifshits equations are Hamiltonian in form:

$$-\varepsilon\frac{\partial q}{\partial\tau}=\frac{1}{\beta M^2}\frac{\delta W}{\delta\varphi}, \quad (4a)$$

$$\varepsilon\,\frac{\partial\varphi}{\partial\tau}=\frac{1}{\beta M^2}\frac{\delta W}{\delta q}, \quad (4b)$$

where $\varepsilon=1/\beta\ll 1$, $\tau=\omega_0 t$, $\omega_0=2\mu_B M_0/\hbar$, and μ_B is the Bohr magneton.

In light of what was said above, we will retain nonleading terms in q in these equations, and write the value of φ in the form

$$\varphi=\varphi_0(x)+\varphi_1(x,y,\tau), \quad |\varphi_1/\varphi_0|\ll 1. \tag{5}$$

The function $\varphi_0(x)$ describes the equilibrium distribution of magnetization of the 2π-domain wall. Its value is determined by the integrodifferential equation

$$-l^2\frac{\partial^2\varphi_0}{\partial x^2}+\sin\varphi_0\cos\varphi_0+\varepsilon(h_z+h_{0z}^m(x))\sin\varphi_0=0,$$

$$h_{0m}=\frac{1}{\delta}\int dx' J(x-x')\cos\varphi_0,$$

$$J(x-x')=2\ln\frac{(x-x')^2}{(x-x')^2+\delta^2}, \tag{6}$$

where δ is the thickness of the ferromagnetic film in units of $l=\sqrt{\alpha/\beta}$.

Perturbations of the equilibrium structure are in this case determined by the system of linear integrodifferential equations

$$\begin{pmatrix} L_1(\varphi_0) & 0 \\ 0 & L_2(\varphi_0)\end{pmatrix}\begin{pmatrix}\varphi_1\\ q\end{pmatrix}+\varepsilon\begin{pmatrix} L_{11}^m & L_{12}^m \\ L_{21}^m & L_{22}^m\end{pmatrix}\begin{pmatrix}\varphi_1\\ q\end{pmatrix}=0, \tag{7}$$

where

$$L_1(\varphi_0)=-l^2\frac{\partial^2}{\partial x^2}+\cos 2\varphi_0+\varepsilon(h_z+h_{0z}^m)\cos\varphi_0,$$

$$L_2(\varphi_0)=L_1(\varphi_0)+\sin^2\varphi_0-l^2\left(\frac{\partial\varphi_0}{\partial z}\right)^2. \tag{8}$$

The first term in Eq. (7) is the zero-approximation operator, while the second term contains the small parameter ε and will be treated as a perturbation in what follows. In it we include corrections that describe slow dynamic and surface perturbations of exchange and magnetostatic origin. The components of this operator have the form

$$L_{11}(\varphi_1)=-\frac{1}{\delta}\int d\rho' I_1(\rho-\rho')\sin\varphi_0(x')(\varphi_1(\rho')-\varphi_1(\rho))$$
$$-l^2\frac{\partial^2\varphi_1(\rho)}{\partial y^2}-\frac{1}{\delta}\frac{\partial^2}{\partial y^2}$$
$$\times\int d\rho' I_2(\rho'-\rho)\cos\varphi_0(x)\cos\varphi_0(x')\varphi_1(\rho'),$$

$$L_{12}(q)=\frac{\partial q}{\partial\tau}-\frac{1}{\delta}\frac{\partial}{\partial y}\int d\rho' I_2(\rho-\rho')\cos\varphi_0(x)\frac{\partial q}{\partial x'},$$

$$L_{21}(\varphi_1)=-\frac{\partial\varphi_1}{\partial\tau}-\frac{1}{\delta}\frac{\partial}{\partial y}$$
$$\times\int d\rho' I_2(\rho-\rho')\frac{\partial}{\partial x'}\cos\varphi_0(x')\varphi_1(\rho'),$$

$$L_{22}(q)=4\pi q+\frac{1}{\delta}\int d\rho' I_1(\rho-\rho')q(\rho')$$
$$+\frac{1}{\delta}\frac{\partial^2}{\partial y^2}\int d\rho' I_2(\rho-\rho')q(\rho')-l^2\frac{\partial^2 q}{\partial y^2}, \tag{9}$$

$$I_1(\rho-\rho')=-\int_0^\delta dz\int_0^\delta dz'\frac{\partial^2}{\partial z\partial z'}\frac{1}{|r-r'|},$$

$$I_2(\rho-\rho')=\int_0^\delta dz\int_0^\delta dz'\frac{1}{|r-r'|},$$

$$\rho=e_x x+e_y y. \tag{10}$$

Since solutions to Eq. (6) are only extrema of the energy functional of the ferromagnetic system, the physical states described by them must be tested for stability. The most complete information about the stability and character of possible transformations of a 2π-domain wall can be obtained by analyzing the dispersion relations for bending and pulsating perturbations of its equilibrium structure.

At this stage of the investigation we should examine the properties of solutions to Eq. (6) in general form. This will make it possible to treat not only an isolated domain wall but also a periodic domain structure in what follows.

As a result of integrating Eq. (6) we obtain

$$l^2\left(\frac{\partial\varphi_0}{\partial x}\right)^2=\sin^2\varphi_0+2\varepsilon h_z(C-\cos\varphi_0)$$
$$+2\varepsilon\int_{-\infty}^{x}dx' h_{0m}(x')\frac{\partial}{\partial x'}\cos\varphi_0(x'), \tag{11}$$

where C is a constant of integration whose value is determined by the state of the system. In particular, for a 2π domain wall its value equals unity. From Eq. (11) it follows that the zero-approximation operators L_1 and L_2 coincide to zero order in ε; consequently, their eigenfunctions differ only by a small quantity.

After differentiating Eq. (6) with respect to the variable x, we find

$$L_1(\varphi_0)\varphi_0'=-\varepsilon\sin\varphi_0(x)\frac{\partial}{\partial x}h_{0m}(x). \tag{12}$$

It is not difficult to confirm that

$$L_2(\varphi_0)\sin\varphi_0(x)=0. \tag{13}$$

Thus, $\psi_1(x)=\varphi_0'(x)$, $\psi_2(x)=\sin\varphi_0'(x)$ are eigenfunctions of the zero-approximation operator. They are orthogonal, possess different symmetries, and correspond to two closely-spaced levels. The solution to Eq. (7) can be written in the form of an expansion

$$\varphi_1(\rho,\tau)=(C_1(k,\omega)\psi_1(x)+C_3(k,\omega)\psi_2(x))e^{i(ky-\omega t)},$$
$$q(\rho,\tau)=(C_4(k,\omega)\psi_1(x)+C_2(k,\omega)\psi_2(x))e^{i(ky-\omega t)}. \tag{14}$$

Substituting Eq. (14) into Eq. (7) and scalar-multiplying with the corresponding eigenfunctions, we obtain a system of algebraic equations

$$A_{ij}(\omega,k)C_j(\omega,k)=0. \tag{15}$$

At this stage it is necessary to specify the value of the function that describes the ground state $\varphi_0(x)$, which is a

solution to the nonlinear integrodifferential Eq. (6). The presence of the small parameter ε allows us to use perturbation theory modified to take into account the nonlinearity of the equation. The magnetostatic interaction has a long-range character and over a scale of magnetic uniformity l it changes very little. This makes it possible to formally introduce the parameter h into the discussion, whose value is the effective superposition of intrinsic magnetostatic and external magnetic fields. In this case we can write the equation of state in the form

$$-l^2\frac{\partial^2\varphi_0}{\partial x^2}+\sin\ \varphi_0\ \cos\ \varphi_0+\varepsilon h\ \sin\ \varphi_0$$
$$=\varepsilon(h-h_z-h_{0m})\sin\ \varphi_0. \tag{16}$$

The right side is now treated as a perturbation, and the solution is determined by perturbation theory

$$\varphi_0(x)=\Phi(x)+\delta\Phi(x), \tag{17}$$

where

$$\Phi(x)=\pi+2\ \arctan\left\{\sqrt{\frac{\varepsilon h}{1+\varepsilon h}}\ \sinh(\sqrt{1+\varepsilon h}(x/l))\right\}$$

is the solution to the unperturbed Eq. (16) that describes an isolated 2π-domain wall, whose properties are well known,[5,6] while $\delta\Phi(x)$ is a correction whose values are determined by the equation

$$L_1(\varphi_0)\,\delta\Phi=\varepsilon\ \sin\ \varphi_0(h-h_z-h_{0m}). \tag{18}$$

Although the value of the correction proportional to ε is insignificant, the condition of solvability of Eq. (18) determines the unknown parameter $h=H/M_0$. The solutions to the uniform equation in zero approximation are known, see Eqs. (12) and (13).

In the case where $\delta\gg 1$, computations lead to the result

$$\frac{H_z-H}{4\pi M_0}=\frac{1}{\pi}\left\{2\ \arctan\left(\frac{1}{a}\right)-a\ \ln(1+a^{-2})\right\},$$
$$H=4\beta M_0 e^{-d},\quad a=d/\delta. \tag{19}$$

Equation (19) relates d (the width of the 2π-domain wall in units of l) to the external magnetic field. In small fields, where the wall width is considerable, the quantity H is negligibly small and Eq. (19) reverts to the well-known form given in Ref. 2 The exponential correction derived in this paper comes from exchange, and is important near the collapse field. In Fig. 1 we compare how the width of a 2π-domain wall depends on the external magnetic field for a film thickness $\delta=10l$, taking into account the exchange interaction (solid curve) and without it (dashed curve).

Analysis of the function Eq. (19) shows that near the collapse field ($H_z\approx 4\pi M_0$) the width of the wall is mainly determined by the value of the exchange interaction and magnetic anisotropy.

Using the solution we have found for the ground state to calculate the coefficients of Eq. (15) in the long-wavelength approximation ($\varkappa^2=(k\delta)^2\ll 1$), we derive

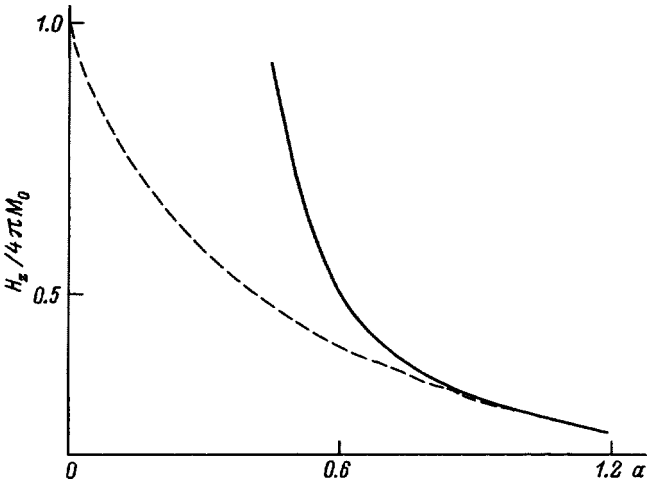

FIG. 1. Functional dependence of H_z on a from Eq. (19).

$$A_{11}=\varkappa^2\varepsilon\lambda(\lambda-g_1(a)),$$
$$A_{22}=G_1(\lambda,a)+\varkappa^2\varepsilon\lambda(\lambda+g_2(a)),$$
$$A_{33}=G_2(\lambda,a)+\varkappa^2\varepsilon\lambda\left(\lambda+g_1(a)+4\left(\ln\frac{\gamma\varkappa}{2}-1\right)\right),$$
$$A_{44}=(G_1(\lambda,a)-2h)+\varkappa^2\varepsilon\lambda$$
$$\times\left(\lambda-\pi^2-g_2(a)+\pi^2\left(\ln\frac{\gamma\varkappa}{2}-1\right)\right),$$
$$A_{14}=A_{41}^*=A_{32}=A_{23}^*=i\omega/\omega_0,$$
$$A_{12}^*=A_{21}=A_{34}=A_{43}^*=4\pi i\varepsilon\lambda\varkappa,$$
$$A_{13}=A_{31}=A_{24}=A_{42}=0,$$
$$\lambda=l/\varepsilon\delta,\quad \gamma=e^{0.577\ldots},$$
$$G_1=4\pi\left(1-\varepsilon\lambda\ \frac{\pi}{4}[\ln((\lambda/\varepsilon)^2)-\ln(1+1/a^2)]\right),$$
$$G_2=2h+8\varepsilon\lambda\ \ln(1+1/a^2),$$
$$g_2(a)=\left(\frac{\pi}{2}\right)^2(3a^2\ \ln(1+1/a^2)$$
$$-8a\ \arctan(1/a)-\ln(1+a^2),$$
$$g_1(a)=-a^2\ \ln\ a^2+(1+a^2)\ln(1+a^2). \tag{20}$$

The constant $\lambda=1/\varepsilon\delta=\sqrt{\alpha\beta}/\Delta$ introduced into Eq. (20) (where $\Delta=l\delta$ is the width of the ferromagnetic film) is a combination of fundamental characteristics of magnetic films and completely determines their properties. It is obvious that a sample may be considered thin when $\lambda\gg 1$.

Spin-wave perturbations of a 2π-domain wall have two dispersion branches $\omega_1(\varkappa),\omega_2(\varkappa)$, which correspond to bending and pulsating vibrations. Their asymptotic behaviors, calculated using Eq. (20) along with the condition that $\varepsilon\lambda\ll 1$, have the following forms in the long-wavelength limit:

$$\omega_1(\varkappa)=\sqrt{A_{11}A_{44}},$$
$$\omega_2(\varkappa)=\sqrt{A_{22}A_{33}}. \tag{21}$$

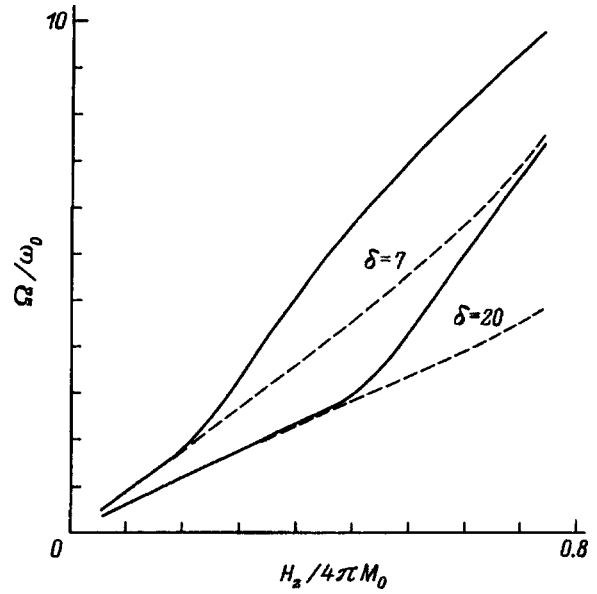

FIG. 2. Dependence of Ω on external magnetic field.

Since we used an expansion in powers of $\varkappa$ to determine the coefficients in Eq. (20), we are guaranteed accuracy of the expressions in Eq. (21) under the square root only up to terms that are quadratic in the wave vectors.

The branch $\omega_2(\varkappa)$ corresponds to pulsating perturbations of a 2π-domain wall, and has a gap $\Omega(h_z)$, whose value depends on the external magnetic field:

$$\frac{\Omega(h_z)}{\omega_0}=\left\{4\pi\left(1-\frac{\pi}{4\delta}\left[\ln\,\delta^2-\ln\left(1+\frac{1}{a^2}\right)\right]\right)\times\left[2h+\frac{8}{\delta}\ln\left(1+\frac{1}{a^2}\right)\right]\right\}^{1/2}.$$

In Fig. 2 we compare our results (the solid curve) for how the value of the gap depends on film thickness with results obtained from a geometric domain wall model (the dashed curve) for a typical material[7,8] with an anisotropy constant $\beta=100$.

Obviously, the internal structure of a 2π-domain wall is strongly affected by the dynamic properties of the ferromagnetic system in magnetic fields for which $H_z\approx 4\pi M_0$.

Our expressions for the dispersion relations can be used to investigate in detail the existence region of a strip domain structure. The ground state is stable if the spectrum of spin-wave perturbations is real and positive definite, while at critical points the spectrum reduces to zero. Analysis of Eq. (21) shows that the structure of a 2π-domain wall is most sensitive to bending distortions, because the branch $\omega_1(\varkappa)$, which corresponds to bending distortions, reduces to zero first. The condition $\omega_1(\varkappa)\geqslant 0$ breaks into two inequalities that determine the region of existence of the strip structure:

$$A_{11},A_{44}\geqslant 0. \tag{22}$$

The first inequality has the form

$$\frac{1}{\varepsilon\delta}\geqslant -a^2\,\ln\,a^2+(1+a^2)\ln(1+a^2). \tag{23}$$

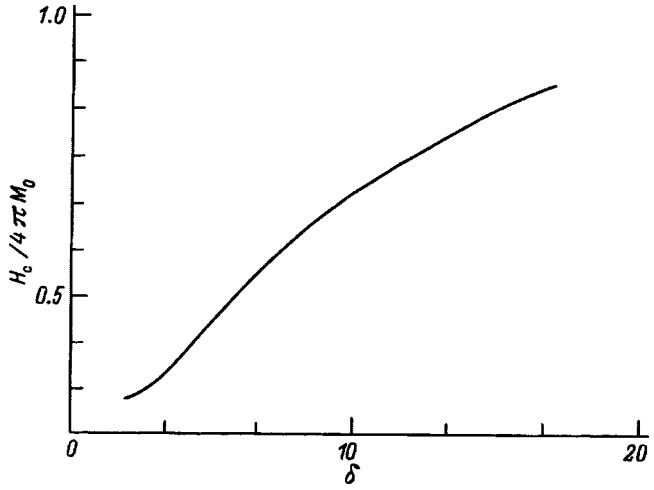

FIG. 3. Dependence of H_c on δ.

Combined with Eq. (19), Eq. (23) determines the lower stability boundary for the 2π-domain wall. Expression (23) is in complete agreement with the results of Ref. 9 obtained from a model of geometric domain boundaries, which in turn is evidence of the magnetostatic nature of the bending instability.

In this investigation, the second inequality Eq. (22) is of great interest, because it reveals how the structure of the magnetization distribution affects the stability of a 2π-domain wall. Combined with Eq. (19) it determines the upper boundary of stability (the collapse field) and has the form

$$\frac{H_z}{M_0}\leqslant 2\pi\left(1-\frac{\pi}{4\delta}[2\,\ln\,\delta-\ln(1+a^{-2})]\right)-4\beta\,\exp(-\alpha\delta)+O(\delta^{-2}).$$

Analysis of the solution to Eq. (20) indicates that the structure of a 2π-domain wall becomes unstable against es-

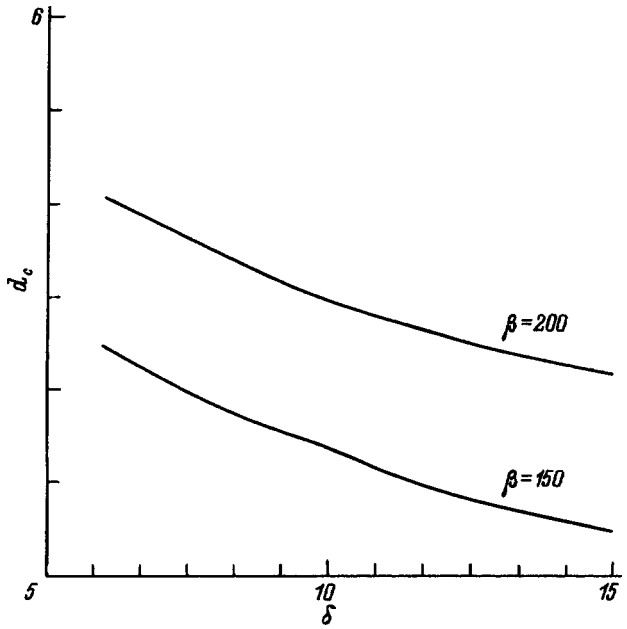

FIG. 4. Dependence of d_c on δ.

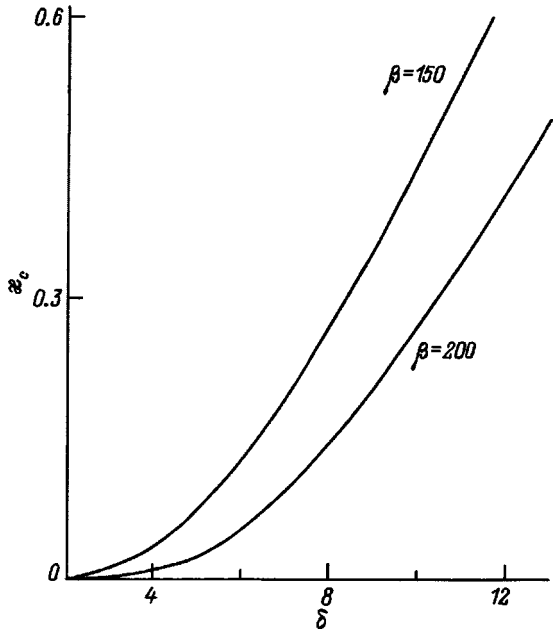

FIG. 5. Dependence of $\varkappa_c$ on δ.

cape of the magnetization vector from the plane of the domain wall. Obviously the collapse will be accompanied by an ''uncoiling'' of the magnetization in the plane of the film with the formation of segments of a bound state of two oppositely-polarized domain walls, which are topological instabilities, leading to destruction of the 2π-domain wall. This assertion is confirmed by experimental studies.[10]

Figures 3 and 4 show the dependence of the collapse field H_c and critical width d_c of a 2π-domain wall on the film thickness obtained from the theory developed here.

These results cannot be obtained from a model of geometric domain walls, which indicates that these models are unsuitable for investigating the properties of 2π-domain walls in magnetic fields close to critical values. Thus, in a geometric model collapse is identical with the width of the wall reducing to zero, whereas the exact theory predicts a finite value of the critical width of a 2π-domain wall which greatly exceeds the parameter l for the width of a Bloch domain wall. Thus, our theory quantitatively determines the limits of applicability of geometric models of domain structures, along with the properties of the latter in this field range. Analysis of A_{44} reveals that during collapse of a 2π-domain wall the mathematical representations are periodic in character, with a finite wave vector $\varkappa_c$. The dependence of this wave vector on film thickness is shown in Fig. 5.

Although the representation of the coefficient A_{44} in the form of an asymptotic expansion in powers of $\varkappa^2$ somewhat limits the applicability of these results, the theory developed in this paper is applicable for highly anisotropic materials, for which $\beta > 100$, which corresponds to a rather wide class of orthoferrites and epitaxial ferrite-garnet films. In order to use the theory in more general cases, we must relax the requirement that an asymptotic expansion in $\varkappa^2$ be used in Eq. (20).

[1] A. P. Malozemoff and J. C. Slonczewski, *Magnetic Domain Walls in Bubble Materials* [Academic Press, New York, 1979; Mir, Moscow, 1982].
[2] D. MacLaughlin and E. Scott, *Solitons in Action*, p. 210, K. Longren and E. Scott, Eds. [Mir, Moscow, 1981].
[3] A. M. Kosevich, B. A. Ivanov, and A. S. Kovalev, *Nonlinear Magnetization Waves: Dynamic and Topological Solitons* (Naukova Dumka, Kiev, 1983) [in Russian].
[4] A. H. Bobeck, Bell Syst. Tech. J. **46**, 1901 (1967).
[5] M. Ya. Shirobokov, Zh. Éksp. Teor. Fiz. **15**, 57 (1945).
[6] Yu. I. Dzherzhya, Fiz. Tverd. Tela (St. Petersburg) **35**, 2270 (1993) [Phys. Solid State **35**, 1128 (1993)].
[7] E. V. Liverts, Fiz. Tverd. Tela (St. Petersburg) **24**, 3526 (1982) [Sov. Phys. Solid State **24**, 2009 (1982)].
[8] V. G. Bar'yakhtar, Yu. I. Gorobets, and S. I. Denisov, Ukr. Fiz. Zh. **28**, 3, 436 (1983) [in Russian].
[9] F. L. Vaĭsman, Yu. I. Gorobets, and S. I. Denisov, Ukr. Fiz. Zh. **31**, 8, 1234 (1986) [in Russian].
[10] V. G. Bar'yakhtar and Yu. I. Gorobets, *Magnetic Bubbles and their Arrays* (Naukova Dumka, Kiev, 1988).

Translated by Frank J. Crowne

Effect of thermal broadening on the paramagnetic susceptibility of the Invar alloys $Fe_{65}Ni_{35}$ and $Fe_{72}Pt_{28}$

V. M. Zverev

P. N. Lebedev Institute of Physics, Russian Academy of Sciences, 117924 Moscow, Russia
(Submitted June 4, 1997)
Fiz. Tverd. Tela (St. Petersburg) **40**, 274–275 (February 1998)

Experimental data is used to show that bulk thermal broadening makes a considerable contribution to the Curie constants of the Invar alloys $Fe_{65}Ni_{35}$ and $Fe_{72}Pt_{28}$. [S1063-7834(98)02402-2]

Many theoretical approaches have been used to discuss the temperature dependence of magnetic susceptibilities of metals and alloys in the literature (see, e.g., Ref. 1), among them the traditional approach of Ref. 2 in which the temperature dependence of the magnetic susceptibility αT^2 is determined by Stoner excitations. Another important cause of temperature dependence of the magnetic susceptibility is spin fluctuations (see, e.g., Refs. 3–5), which when the real band structures of metals and alloys are taken into account gives a temperature dependence close to the Curie-Weiss law.

In Ref. 6 Zverev and Silin proposed yet another possible mechanism for temperature dependence of the magnetic susceptibility of metals and alloys—a contribution to the Curie constant from thermal acoustic phonons due to magnetoelasticity. After a detailed analysis of the experimental data on magnetoelasticity, these authors[6] concluded that such a contribution should be important for the Invar alloys Fe–Ni, Fe–Ni–Mn, and Fe–Pt, with various compositions and degrees of alloy ordering.

In order to compare these theoretical approaches with experimental data obtained at constant pressure, it is important to identify the role played by thermal expansion of the bulk solid in generating the temperature dependence of the magnetic susceptibility. Thermal expansion enters into the magnetic properties of metals and alloys via the well-known magnetostriction effect (see Refs. 7–10). In this case, Zverev and Silin[8] used experimental data on paramagnetostriction and thermal expansion of the bulk to demonstrate that a significant role is played by thermal expansion in the temperature dependence of the magnetic susceptibility in metals such as platinum, rhodium, molybdenum, and iridium.

In this paper it is shown for the example of the ferromagnetic Invar alloys $Fe_{65}Ni_{35}$ and $Fe_{72}Pt_{28}$ that thermal expansion is indeed important in discussing the temperature dependence of the paramagnetic susceptibility of these alloys. The alloys $Fe_{65}Ni_{35}$ and $Fe_{72}Pt_{28}$ are chosen primarily because they are characterized by anomalously large magnetostriction (see, e.g., Refs. 11 and 12). This suggests that the effect of thermal expansion on the temperature dependence of the paramagnetic susceptibility of these alloys should be considerable. Furthermore, the thermal expansion of these alloys is determined primarily by the lattice at high temperatures (above the Curie temperature) (c.f., Refs. 13 and 14). Because this is yet another example of how thermal phonons affect the magnetic properties of metals and alloys, which differ from discussion in Ref. 6, it is interesting to compare the contributions from thermal phonons to the temperature dependence of the paramagnetic susceptibility of the Invar alloys $Fe_{65}Ni_{35}$ and $Fe_{72}Pt_{28}$ arising from two different effects: magnetostriction and magnetoelasticity.

Let us start from the well-known thermodynamic relation for paramagnetic susceptibilities defined at constant pressure $\chi_P(P,T)$ and constant volume $\chi_V(V,T)$ (see, e.g., Ref. 1):

$$\chi_P(P,T)=\chi_V(V,T) \tag{1}$$

and take into account the increase in the volume of the solid due to thermal expansion explicitly:

$$V(P,T)=V_c(P)+\Delta V(P,T). \tag{2}$$

Here $V_c(P)=V(P,T_c)$ is the volume of the solid at the Curie temperature T_c and pressure P, while $\Delta V(P,T)$ is the change in volume caused by the difference between the temperature T and T_c. Since the paramagnetic temperature range $T>T_c$ in Invar alloys $Fe_{65}Ni_{35}$ and $Fe_{72}Pt_{28}$ corresponds to a range of temperatures above the Debye temperature,[13,14] for thermal expansion of the volume we can use the approximation $\Delta V(T)/V_c=3\beta(T_c)(T-T_c)$, where $\beta(T_c)$ is the linear coefficient of thermal expansion of the paramagnetic state at the Curie temperature. What we have said above allows us to write the following simple expansion:

$$\chi_P(P,T)=\chi_V(V_c,T)\left[1+3\beta(T_c)(T-T_c)\left(\frac{\partial \ln \chi_V}{\partial \ln V_c}\right)_T\right], \tag{3}$$

which takes into account the contribution of thermal expansion to the temperature dependence of the paramagnetic susceptibility. Above the Curie temperature we can use expressions that correspond to the Curie-Weiss law for the magnetic susceptibilities Eq. (1):

$$\chi_P(P,T)=\frac{C(P)}{T-T_c(P)}, \quad \chi_V(V,T)=\frac{C(V)}{T-T_c(V)}, \tag{4}$$

where C is the Curie constant. Expressions (3) and (4) allow us to find the following relations:

$$T_c(P)=T_c(V_c) \tag{5}$$

$$\left(\frac{\Delta C}{C}\right)_{MV}=\frac{C(P)-C(V_c)}{C(V_c)}=-3\beta(T_c)K(T_c)\,\frac{dT_c}{dP}. \quad (6)$$

Here $C(V_c)$ is the Curie constant when the thermal expansion of the volume is neglected, and $K(T_c)$ is the modulus of hydrostatic compression of the paramagnetic state at the Curie temperature. Equation (6) assumes that the condition $|d\ \ln T_c/dP| \gg |d\ \ln C/dP|[(T-T_c)/T_c]$ is satisfied, which is true for these Invar alloys over a wide range of temperatures due to the large absolute value of the baric derivative of the Curie temperature.

Since the ferromagnetic transition in Invar alloys $Fe_{65}Ni_{35}$ and $Fe_{72}Pt_{28}$ is ''washed out'' with respect to temperature, in order to estimate Eq. (6) we will use two values for the thermal expansion coefficient $\beta(T_c)$ and hydrostatic compression modulus $K(T_c)$, the larger of which corresponds to a value extrapolated from the high-temperature region down to the Curie temperature, while the smaller is measured experimentally at $T=T_c$.

We can use Fig. 1 of Ref. 13 to find the thermal expansion coefficient of the Invar alloy $Fe_{65}Ni_{35}$, which gives the value $\beta(T_c)=(1.5-1.0)\times 10^{-5}$ K^{-1}. Analogously, using Fig. 6 of Ref. 15 we find for the modulus of hydrostatic compression the two values $K(T_c)=(15.0-11.8)\times 10^2$ kbar.

For the baric derivative of the Curie temperature we use data from Table I of Ref. 11, according to which $dT_c/dP=-(3.9-3.6)$ K/kbar. Then Eq. (6) leads to the following very remarkable estimate for the contribution of thermal expansion to the Curie constant: $(\Delta C/C)_{MV}=0.13-0.26$. This contribution coincides in sign with the contribution to the Curie constant from thermal phonons resulting from magnetoelasticity, for which we obtain the estimate $(\Delta C/C)_{ME}=0.14-0.18$ for this Invar alloy from Table 2 of Ref. 6. Therefore, the total contribution of thermal phonons to the Curie constant of the Invar alloy $Fe_{65}Ni_{35}$ when both the magnetostrictive effect and the magnetoelastic effect are simultaneously included turns out to be the comparatively large value $\Delta C/C=(\Delta C/C)_{MV}+(\Delta C/C)_{ME}=0.27-0.44$.

For the disordered Invar alloy $Fe_{72}Pt_{28}$ we used Fig. 4b of Ref. 14 to find the thermal expansion coefficient, obtaining a value $\beta(T_c)=1.1\times 10^{-5}$ K^{-1}, which corresponds to the lattice contribution extrapolated down to the Curie temperature; the experimentally measured value $\beta(T_c)\simeq 0$. Data on the modulus of hydrostatic compression $K(T_c)=(15.8-12.1)\times 10^2$ kbar was obtained from Fig. 4 of Ref. 15. The value of the baric derivative of the Curie temperature $dT_c/dP=-(4.0-3.2)$ K/kbar was taken from Ref. 12. Then Eq. (6) allows us to obtain the following upper estimate for the contribution of thermal expansion to the Curie constant: $(\Delta C/C)_{MV}=0.13-0.21$, which turns out to be roughly the same as that of the Invar alloy $Fe_{65}Ni_{35}$. If we then use Table 2 of Ref. 6 to estimate the contribution of thermal phonons to the Curie constant due to the magnetoelasticity effect $(\Delta C/C)_{ME}=0.37-0.41$ for the disordered Invar alloy $Fe_{72}Pt_{28}$, we find for the total contribution the anomalously large value $\Delta C/C=(\Delta C/C)_{MV}+(\Delta C/C)_{ME}=0.50-0.62$.

Thus, using experimental data we have shown that bulk thermal expansion is important in discussing the temperature dependence of the paramagnetic susceptibility of Invar alloys $Fe_{65}Ni_{35}$ and $Fe_{72}Pt_{28}$, and that the total contribution of thermal phonons to the Curie constant of these alloys when the effects of magnetostriction and magnetoelasticity are combined turns out to be anomalously large.

In conclusion I would like to thank V. P. Silin for directing my attention to the question discussed here.

This work was carried out within the framework of Project 96-02-17318-*a* of the Russian Fund for Fundamental Research.

[1] M. Shimizu, Rep. Prog. Phys. **44**, 329 (1981).
[2] D. M. Edwards and E. P. Wohlfarth, Proc. Roy. Soc. A **303**, *1427*, 127 (1968).
[3] I. E. Dzyaloshinskiĭ and P. S. Kondratenko, Zh. Éksp. Teor. Fiz. **70**, 1987 (1976) [Sov. Phys. JETP **43**, 1036 (1976)].
[4] T. Moriya, *Spin Fluctuations in Magnets with Collectivized Electrons* (Mir, Moscow, 1988).
[5] M. Shimizu, Physica B **159**, 26 (1989).
[6] V. M. Zverev and V. P. Silin, JETP Lett. **64**, 33 (1996).
[7] K. Sumiyama, M. Shiga, and Y. Nakamura, J. Phys. Soc. Jpn. **40**, 996 (1976).
[8] V. M. Zverev and V. P. Silin, JETP Lett. **43**, 579 (1986).
[9] V. M. Zverev and V. P. Silin, Short Commun. in Physics, FIAN *11*, 35 (1986) [in Russian].
[10] F. I. Dolinin, V. M. Zverev, E. A. Pamyatnykh, and V. P. Silin, Fiz. Met. Metalloved. **63**, 876 (1987).
[11] G. Hausch, Phys. Status Solidi A **16**, 371 (1973).
[12] G. Oomi and N. Mōri, J. Phys. Soc. Jpn. **50**, 2924 (1981).
[13] S. Chikazumi, J. Magn. Magn. Mater. **10**, 2–3, 113 (1979).
[14] B. Rellinghaus, J. Kästner, T. Schneider, E. F. Wassermann, and P. Mohn, Phys. Rev. B **51**, 2983 (1995).
[15] M. Shiga, K. Makita, K. Uematsu, Y. Muraoka, and Y. Nakamura, J. Phys.: Condens. Matter **2**, 1239 (1990).
[16] G. Hausch, J. Phys. Soc. Jpn. **37**, 819 (1974).

Translated by Frank J. Crowne

Ferromagnetism and the metal-insulator transition in the magnetic semiconductor system $Fe_xMn_{1-x}S$

G. V. Loseva, L. I. Ryabinkina, and A. D. Balaev

L. V. Kirensky Institute of Physics, Russian Academy of Sciences (Siberian Department), 660036 Krasnoyarsk, Russia

(Submitted June 2, 1997)
Fiz. Tverd. Tela (St. Petersburg) **40**, 276–277 (February 1998)

The results of investigations of the structure, electrical, and magnetic properties in the system of antiferromagnetic semiconductors $Fe_xMn_{1-x}S$ ($0<x\leqslant 0.5$) are described. It is established that metal-insulator transitions with respect to concentration and temperature are connected with changes in the magnetic properties of the system.
[S1063-7834(98)02502-7]

It has been observed previously[1,2] that the electric and magnetic state of the system of antiferromagnetic semiconductors $Fe_xMn_{1-x}S$ changes as the concentration of iron x increases until a concentration-induced metal-insulator transition occurs. Studies of systems of magnetic semiconductors based on two monosulfides from the $3d$ series containing magnetoactive cations such as MnS–CrS, MnS–FeS, FeS–CrS, CoS–CrS have shown[3] that cation replacement in the solid solutions is one effective method that can be used not only to regulate the parameters of the metal-insulator transition in these materials but also to significantly change their magnetic characteristics, and also create new magnetic materials with metal-insulator transitions.

In this paper we report the results of studies of the structure, electrical, and magnetic properties of the system of antiferromagnetic semiconductors $Fe_xMn_{1-x}S$ undergoing a metal-insulator transition and the interrelation between the metal-insulator transition with respect to concentration and temperature and changes in the magnetic properties.

Samples of the $Fe_xMn_{1-x}S$ system ($0<x\leqslant 0.5$) were obtained by heating vacuum quartz ampoules containing electrolytic Mn, reduced Fe, and sulphur with a purity of 99.999%, at 1233 K for a week to induce cation replacement. A compound with $x\sim 0.3$ having special electrical and magnetic properties[2] was synthesized several times using the same fabrication technology.

According to x-ray structure analysis, all the compounds investigated with $0<x\leqslant 0.5$ in the temperature range 80–300 K were solid solutions with the FCC lattice of α MnS.

The electrical resistivity ρ measured by a four-probe potentiometer at constant current showed that, as x increases, a metal-insulator transition takes place with respect to concentration when $x_c\sim 0.4$.[1] It is clear from Fig. 1 that, as the temperature increases, the composition with $x\sim 0.3$ exhibits a smooth change in the type of conductivity from semiconducting to semimetallic at $T>700$ K (a metal-insulator transition with respect to temperature) with a change in activation energy from 0.18 to 0.03 eV.

As the iron concentration x increases, ferromagnetism appears in the collinear antiferromagnetic host α MnS (type II) when $x_{cr}\sim 0.3$. The following experimental effects confirm the appearance of ferromagnetism and coexistence of antiferromagnetism and ferromagnetism in these compounds: the appearance of a hysteresis loop for the spontaneous moment, the presence of a Curie temperature, and a deviation from linear behavior for the field dependence of the magnetization at 300 K. The existence of ferromagnetic exchange in this system is confirmed by constructing the magnetic phase diagram based on magnetic measurements and Monte Carlo calculations.[2]

Magnetic measurements show that as x increases from 0 to 0.2 the temperature behavior of the magnetic susceptibility (the curve $1/\chi(t)$) corresponds to antiferromagnetism in the temperature range 80–700 K. However, the low-temperature measurements of magnetization indicate nucleation of ferromagnetism at sufficiently low concentrations of x, for example $x\sim 0.05$. Figure 2 shows the temperature dependence of the magnetization for the composition $x\sim 0.3$. Measurements were made using an automated magnetometer with a superconducting solenoid in the temperature range 4.2–300 K in a field of 700 Oe. The curve $\sigma(T)$ has a low-temperature anomaly in the range $35<T<40$ K. A similar high-temperature anomaly was observed at ~ 45 K in the system of antiferromagnetic semiconductors $Li_xMn_{1-x}Se$, which is isostructural with the $Fe_xMn_{1-x}S$ system.[4] Measurements of the magnetic properties and neutron-scattering investigations of the system $Li_xMn_{1-x}Se$ lead these authors to conclude that this low-temperature anomaly is connected with the formation of a canted antiferromagnetic structure and the appea rance of a magnetic moment. However, whereas increasing x and T in the system $Li_xMn_{1-x}Se$ leads to a change from antiferromagnetic ordering to ferromag-

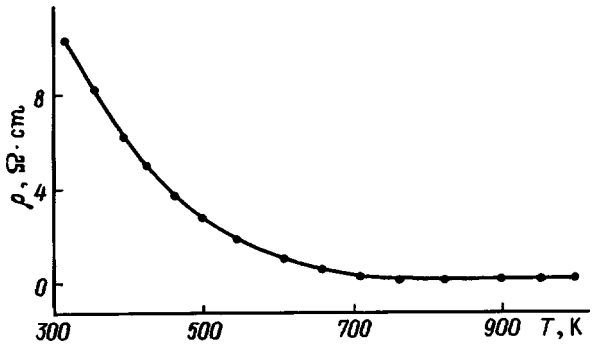

FIG. 1. Temperature dependence of the resistivity of $Fe_{0.3}Mn_{0.7}S$.

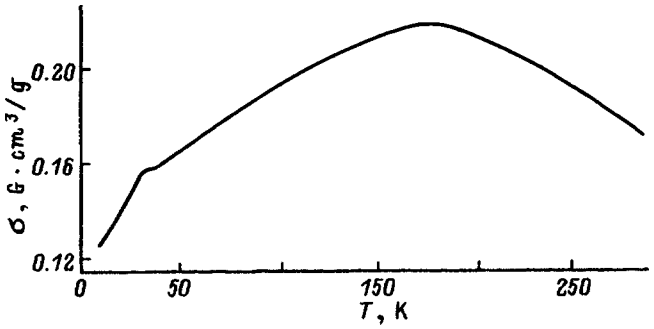

FIG. 2. Temperature dependence of the magnetization of $Fe_{0.3}Mn_{0.7}S$ in a magnetic field of 700 Oe.

netic, with simultaneous replacement of semiconductor conductivity by metallic conductivity, in the system $Fe_xMn_{1-x}S$ the change in electrical and magnetic properties has its own peculiarities: 1) compositions with $0<x\leqslant 0.3$ are impurity semiconductors with nucleated ferromagnetism; 2) compositions with $0.3\leqslant x\leqslant 0.4$ are ferromagnetic semiconductors in which a smooth high-temperature transition takes place with increasing temperatures from semiconductor to semimetal in the temperature range $\sim 700-1000$ K; 3) compositions with $0.4\leqslant x\leqslant 0.5$ are ferromagnetic semimetals with a Curie temperature $T_c\sim 780$ K which become metallic at $T\sim 1000$ K, i.e., they enter the paramagnetic phase.

Thus, the system $Fe_xMn_{1-x}S$ for $0<x\leqslant 0.5$ exhibits a metal-insulator transition with respect to concentration x and temperature T, which are connected with changes in the magnetic properties. In this system the concentration-induced metal-insulator transition occurs at $x_c\sim 0.4$, so that the magnetic AFM→FM transition at $x_{cr}\sim 0.3$ precedes the metal-insulator transition. As for the temperature transition, with increasing x and T the conductivity type is smoothly replaced in the system, accompanied by the magnetic transformation AFM→FM→PM and coexistence of antiferromagnetism and ferromagnetism.

The author is grateful to G. A. Petrakovskiĭ and S. S. Aplesnin for discussing this work.

[1] G. V. Loseva, L. I. Ryabinkina, S. G. Ovchinnikov, and O. A. Bayukov, Fiz. Tverd. Tela (Leningrad) **25**, 3717 (1983) [Sov. Phys. Solid State **25**, 2142 (1983)].
[2] G. A. Petrakovskiĭ, S. S. Aplesnin, G. V. Loseva, L. I. Ryabinkina, and K. I. Yanushkevich, Fiz. Tverd. Tela (Leningrad) **33**, 406 (1991) [Sov. Phys. Solid State **33**, 233 (1991)].
[3] G. V. Loseva, S. G. Ovchinnikov, and G. A. Petrakovskiĭ, *Metal-Insulator Transitions in 3d–Metal Sulfides* (Nauka, Novosibirsk, 1983) [in Russian].
[4] R. R. Heikes, T. R. McGuire, and R. J. Happel Jr., Phys. Rev. **121**, 703 (1961).

Translated by Frank J. Crowne

The antiferromagnetic-ferromagnetic transition in the system $Zn_{1-x}Cu_xCr_2S_4$

R. Z. Sadykhov, D. A. Guseĭnov, and A. I. Akhmedov

Institute of Physics, Azerbaijani Academy of Sciences, 370143 Baku, Azerbaijan
(Submitted June 11, 1997)
Fiz. Tverd. Tela (St. Petersburg) **40**, 278–279 (February 1998)

The magnetization and paramagnetic susceptibility of the system of compounds $Zn_{1-x}Cu_xCr_2S_4$ ($0<x\leqslant 1$) are investigated at low temperatures. It is shown that as the content of Cu increases the system exhibits a transition from an antiferromagnetic to a ferromagnetic state.
 [S1063-7834(98)02602-1]

In Refs. 1 and 2 we investigated the low-temperature magnetic properties of the system of compounds $Zn_{1-x}Me_xCr_2S_4$ (where Me=Fe, Co). We associated the observed deviations from linearity in the concentration dependence of the magnetic moment at 4.2 K in both systems with re-orientation of the spin magnetic moments of Cr ions in an octahedral sublattice, resulting in a concentration-induced magnetic phase transition from antiferromagnetism to ferromagnetism.

The goal of this paper is to continue investigating how the occupancy of the $3d$ shell of the ion being replaced affects the magnetic properties of such compounds. To accomplish this, we have studied the magnetization and paramagnetic susceptibility of the system $Zn_{1-x}Cu_xCr_2S_4$. Our interest in this system stems from the fact that it allows us to trace the dynamics of a transition from an antiferromagnetic ($ZnCr_2S_4$) to a ferromagnetic state ($CuCr_2S_4$) as Zn ions are progressively replaced by Cu ions.

The samples we investigated were obtained by direct solid-phase reaction of the high-purity starting components in quartz ampoules. The synthesis took place at 850 °C over a period of 10 days. The powered samples obtained as a result of this synthesis were again pulverized, pressed into shapes under high pressure, and annealed in vacuum for a period of 7 days. X-ray analysis allows us to verify the single-phase character of the samples and determine their crystal lattice parameters. We found that all the compounds crystallize in a cubic lattice, like the end-point compounds,[3] with lattice parameters 0.9976($x=0.1$), 0.9942($x=0.3$), 0.9910($x=0.5$), 0.9878($x=0.7$), 0.9849($x=0.9$), and 0.9820 nm($x=1.0$), which satisfies Vegard's law.

The magnetization σ was measured with a Domenicalli pendulum magnetometer, and the magnetic susceptibility χ was measured by Faraday's method with magnetoelectric weights. The spontaneous magnetization at a given temperature was determined by extrapolating the magnetization measured at various magnetic fields down to zero field.

Figure 1 shows the dependence of the specific magnetization of compounds $Zn_{1-x}Cu_xCr_2S_4$ with $x\geqslant 0.3$ on magnetic field at 4.2 K. It is clear that the function $\sigma(H)$ has the ferromagnetic shape. The rather wide range of technical magnetization of the sample with $x=0.3$ decreases with increasing Cu content, with the process of technical magnetization completed essentially by rotation of the magnetic moments.

For the composition with $x=0.1$ the function $\sigma(H)$ is linear in character, which is a sign of antiferromagnetism. Evidence for antiferromagnetic ordering in this compound is the temperature dependence of the magnetic susceptibility (see the inset to Fig. 2). It is clear from this figure that, as the temperature increases from 4.2 K, the susceptibility increases up to a certain maximum value in the range $T=25$ K, after which it falls off linearly.

The temperature 25 K at which the susceptibility $\chi(T)$ reaches its maximum value corresponds to the Néel temperature of the composition with $x=0.1$. Note that the Néel temperature of the original compound $ZnCr_2S_4$ is 18 K.[4]

By processing the experimental temperature dependence of the magnetization (Fig. 2) in the region of magnetic transformation by the method of thermodynamic coefficients we determine the Curie temperature of the compounds being used, which turned out to equal 325 ($x=0.3$), 371 ($x=0.5$), 380 ($x=0.7$), 390 ($x=0.9$) and 420 K ($x=1.0$). The high value of the Curie temperature even at $x=0.3$ is probably a result of the exchange interaction mediated by charge carriers that appear once a certain concentration of Cu ions has been reached.

The calculated experimental values of the magnetic moment n at 4.2 K for compounds with $0.3\leqslant x\leqslant 1$ were: 0.7 ($x=0.3$), 1.9 ($x=0.5$), 3.0 ($x=0.7$), 4.1 ($x=0.9$) and 4.6 μ_B($x=1.0$).

The concentration dependence of the Curie temperature and magnetic moment are shown in Fig. 3. It is clear from this figure that the concentration dependence of the magnetic

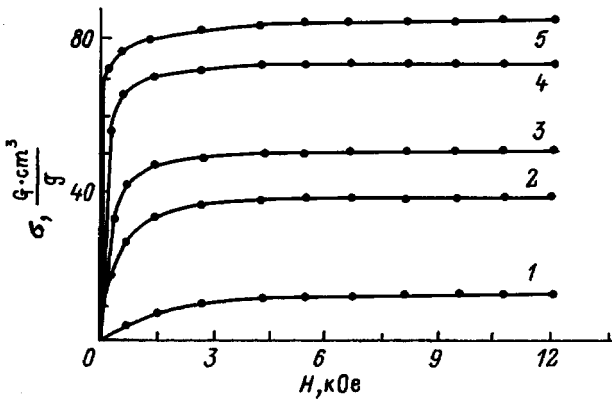

FIG. 1. Plots of the specific magnetization of compounds of the system $Zn_{1-x}Cu_xCr_2S_4$ versus magnetic field at 4.2 K. x: *1*—0.3, *2*—0.5, *3*—0.7, *4*—0.9, *5*—1.0.

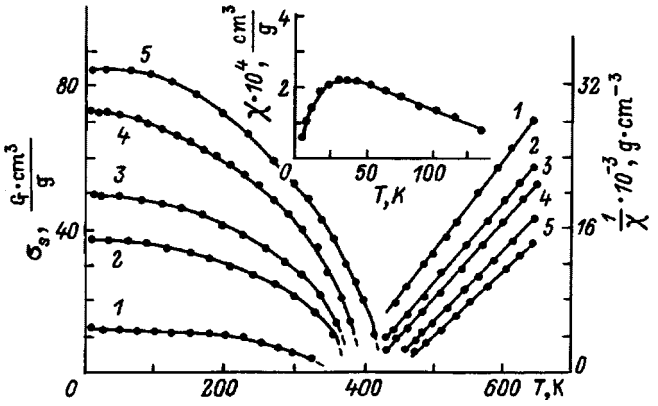

FIG. 2. Temperature dependence of the spontaneous magnetization and inverse paramagnetic susceptibility of the compounds $Zn_{1-x}Cu_xCr_2S_4$. x: *1*—0.3, *2*—0.5, *3*—0.7, *4*—0.9, *5*—1.0. The inset shows the temperature dependence of magnetic susceptibility of $Zn_{0.9}Cu_{0.1}Cr_2S_4$.

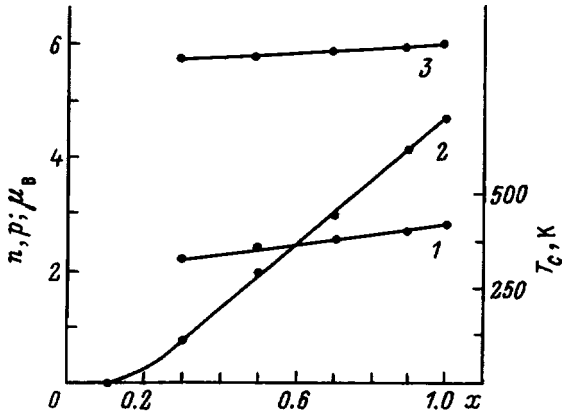

FIG. 3. Concentration dependence of the Curie temperature (*1*), the magnetic moment at 4.2 K (*2*), and the effective magnetic moment (*3*) of compounds from the system $Zn_{1-x}Cu_xCr_2S_4$.

moment is essentially made up of three segments, each of which is characterized by a different type of magnetic ordering: 1) a segment where the ordering is antiferromagnetic ($0 \leqslant x \leqslant 0.1$); 2) a transition region ($0.1 < x < 0.3$), where it is most likely that antiferromagnetic and ferromagnetic ordering coexist; and 3) a segment where the ordering is ferromagnetic ($0.3 \leqslant x \leqslant 1$).

For samples with $0.3 \leqslant x \leqslant 1$ (Fig. 2), the temperature dependence of the inverse paramagnetic susceptibility has the typical ferromagnetic shape. Knowing the function $1/\chi(T)$ allows us to calculate the following effective magnetic moments p: 5.7 ($x=0.3$), 5.75 ($x=0.5$), 5.8 ($x=0.7$), 5.9 ($x=0.9$), and $6\mu_B$($x=1.0$).

The concentration dependence of the effective magnetic moment p is plotted in Fig. 3. It is clear that as the Cu content increases there is a definite increase in the effective magnetic moment. This dependence of the effective magnetic moment on the concentration of Cu, and also its numerical value, are in satisfactory agreement with calculations that use pure spin values of the magnetic moments of trivalent Cr^{3+} and divalent Cu^{2+}. Thus, for these states of the Cr and Cu ions, the value of effective magnetic moment expected from such calculations increase from 5.55 ($x=0.3$) to $5.75\mu_B$($x=1.0$).

Thus, replacement of Zn ions by Cu ions in the system $Zn_{1-x}Cu_xCr_2S_4$ leads to a transition from an antiferromagnetic to a ferromagnetic state: up to $x=0.1$ the state antiferromagnetic, in the region $0.1<x<0.3$ antiferromagnetic ordering coexists with ferromagnetic, and for $x \geqslant 0.3$ the compounds are all ferromagnetic in structure.

[1] R. Z. Sadykhov, L. M. Valiev, D. A. Guseĭnov, and A. O. Ismailov, Fiz. Tverd. Tela (Leningrad) **26**, 1206 (1984) [Sov. Phys. Solid State **26**, 732 (1984)].
[2] R. Z. Sadykhov and A. D. Namazov, Fiz. Tverd. Tela (Leningrad) **31**, 314 (1989) [Sov. Phys. Solid State **31**, 175 (1989)].
[3] S. Methfessel and D. C. Mattis, in *Handbuch der Physik*, V. 18, Part 1, H. P. J. Wijn (Ed.), Springer-Verlag, Berlin (1968); Mir, Moscow, (1972).
[4] E. Agostinelli, P. Filaci, D. Fiorani, and E. Paparazzo, Solid State Commun. **56**, 541 (1985).

Translated by Frank J. Crowne

Magnetic phase diagrams of ferrimagnets having two magnetically unstable subsystems

N. P. Kolmakova and M. Yu. Nekrasova

Bryansk State Technical University, 241035 Bryansk, Russia

R. Z. Levitin and A. S. Markosyan

M. V. Lomonosov State University at Moscow, 119899 Moscow, Russia

(Submitted June 14, 1997)
Fiz. Tverd. Tela (St. Petersburg) **40**, 280–284 (February 1998)

The molecular field approximation is used to construct magnetic phase diagrams along with magnetization curves for ferrimagnets having two magnetically unstable subsystems. Diverse sequences of phase transitions of various kinds—first order (metamagnetic) and second order (via a noncollinear phase)—are realized in the course of magnetizing such ferrimagnets. Analysis reveals how the magnetization curves depend on the relative values of parameters of the two subsystems, e.g., sublattice magnetizations in weak and strong states, critical fields, and values of the exchange interaction between sublattices. © *1998 American Institute of Physics.* [S1063-7834(98)02702-6]

In a two-sublattice ferrimagnet with stable sublattices, an external magnetic field induces a transition from a ferrimagnetic state with antiparallel magnetic moments to a ferromagnetic state with parallel magnetic moments via two second-order phase transitions through a noncollinear phase (see, e.g., Ref. 1). If one of the magnetic subsystems (sublattices) of the ferrimagnetic exhibits magnetic instability, i.e., it undergoes a metamagnetic transition from a weak to a strong magnetic state when a magnetic field is applied, various sequences of metamagnetic transitions and noncollinear phases can also occur. Magnetic phase diagrams for such ferrimagnets were discussed theoretically in Ref. 2. In this paper, the analysis centered on how the magnetization process depends on the system parameters: the magnetizations of the stable and unstable sublattices (in strong and weak states), the field for the metamagnetic transition, and the value of the intersublattice exchange interaction. Magnetization curves of this kind were observed experimentally in Refs. 3 and 4 for $4f-3d$ intermetallic compounds of type $Y_{1-t}R_t(Co_{1-x}Al_x)_2$, where R is a heavy ''rare earth.'' In these compounds the d-band subsystem is unstable, and thus is subject to metamagnetic transitions in a magnetic field from a weakly magnetic state to a strongly magnetic state, while the rare-earth subsystem is considered to be stable. A number of these compounds have been observed to have two metamagnetic transitions with a noncollinear phase between them,[3,4] in agreement with the theory developed in Ref. 2.

Recently, however, a number of more complicated systems have been discovered in which the second magnetic subsystem is magnetically unstable as well. Thus, for example, recent studies of the magnetic properties of the intermetallic compound $TmCo_2$ show that, along with the Co subsystem, the Tm subsystem is also magnetically unstable in this compound, and that various magnetic states of this subsystem are possible depending on stoichiometry.[5] The nature of this instability is unclear at the present time. In particular, it could arise from the phenomenon of crossover in the Tm subsystem, which is often observed in compounds with rare-earth ions (see, for example, Ref. 6). Ferrimagnets in which magnetic instability is manifested by both sublattices are a new class of magnetic materials in which magnetization curves and magnetic phase diagrams are still more complicated than those discussed in Ref. 2. Although there is no information available from experimental studies of ferrimagnets having two unstable subsystems, such compounds could be exist among the $f-d$ intermetallics, in which the d-band subsystem is metamagnetic while the rare-earth subsystem exhibits the phenomenon of crossover. Moreover, such ferrimagnets could be found among the $d-d$ intermetallics, in which two magnetically unstable sublattices are present with negative interlattice exchange interactions.

In this paper we discuss theoretically the magnetic phase diagrams and magnetization curves of a two-sublattice ferrimagnet with two magnetically unstable sublattices in which a first-order transition takes place from the weakly magnetic to the strongly magnetic state. The discussion is based on the effective field model in the exchange approximation; for simplicity it is assumed that there is no susceptibility, and that the magnetizations of both subsystems change discontinuously at the metamagnetic transition fields.

1. MODEL

Let us consider a two-sublattice ferrimagnet, both of whose magnetic sublattices ($i=1,2$) are magnetically unstable, i.e., at a critical value of the magnetic field H_i the lattice transforms from a weakly magnetic (w) state with magnetization m_i to a strongly magnetic (s) state with magnetization M_i:

$$M_i=m_i, \quad H<H_i; \quad M_i=M_i, \quad H\geqslant H_i. \tag{1}$$

Let us consider the magnetic phase diagrams and magnetization curves of such ferrimagnets in the molecular field approximation, in which magnetic moments of the sublattices in a state of thermodynamic equilibrium are assumed to be directed along the effective fields that act on them. We will analyze the signs and magnitudes of these effective fields

and choose the state corresponding to a minimum value of the thermodynamic potential for a given value of the external magnetic field.

In the simplest model, the thermodynamic potential of a ferrimagnet with a negative exchange interaction between sublattices with magnetic moments $\mathbf{M}_1$ and $\mathbf{M}_2$ is characterized by the exchange parameter λ_{12}, and can be written in the form

$$G(\mathbf{H},T)=F_1+F_2-\mathbf{H}(\mathbf{M}_1+\mathbf{M}_2)+\lambda\mathbf{M}_1\mathbf{M}_2,$$
$$\lambda=|\lambda_{12}|(\lambda_{12}<0). \tag{2}$$

Here F_i $(i=1,2)$ is the thermodynamic potential of the i-th unstable subsystem, which is different for the strong and weak magnetic states. In this simple model, the connection between F_i in the s and w states can be determined by the relation

$$F_{is}=F_{iw}+(M_i-m_i)H_i. \tag{3}$$

In these calculations we will be interested only in the difference in values of thermodynamic potentials for the two states of each unstable subsystem.

Let us introduce the following nomenclature for denoting phases that occur in this ferrimagnet. The possible phases in the usual two-sublattice ferrimagnet differ by the mutual orientation of magnetic moments of the sublattices. Let usw label them in the following fashion: a ferrimagnetic phase (with antiparallel orientation of the magnetic moments) by A, a ferromagnetic phase by F, and a noncollinear phase by N. Because of the existence of weak and strong magnetic states for each of the sublattices in this ferrimagnet, the number of phases increases by a factor of 4, and we will denote them by adding W to the phase notation if both subsystems are in the weakly magnetic state; W_i $(i=1,2)$ if one of the i-th subsystems is in the weakly magnetic state, and S if both subsystems are in the strongly magnetic state. Thus, for example, it $AW1$ corresponds to a ferrimagnetic phase with the first subsystem in the weakly magnetic state, while the second is in the strongly magnetic state.

Depending on the value of the intersublattice exchange interaction and the relation between parameters of the subsystem, the original state at $H=0$ will be one of four possible ferrimagnetic states: AW, $AW1$, $AW2$, AS. Let us introduce characteristic values of the exchange parameter λ which separate the regions of various original states:

$$\lambda_i=\frac{(M_1-m_1)H_1+(M_2-m_2)H_2}{M_1M_2-m_1m_2},$$
$$\lambda_2=\frac{H_2}{m_1},\quad \lambda_3=\frac{H_1}{m_2},\quad \lambda_4=\frac{H_1}{M_2},\quad \lambda_5=\frac{H_2}{M_1}. \tag{4}$$

In what follows we will write out conditions for the existence of each of the ferrimagnetic states at $H=0$ obtained by using Eqs. (1) and (3).

For AW

$$\lambda<\lambda_1,\quad \text{if } \lambda_1<\lambda_2,\lambda_3,$$
$$\lambda<\lambda_2,\quad \text{if } \lambda_2<\lambda_1,\lambda_3,$$
$$\lambda<\lambda_3,\quad \text{if } \lambda_3<\lambda_1,\lambda_2, \tag{5a}$$

for $AW1$

$$\lambda_2<\lambda<\lambda_4, \tag{5b}$$

for $AW2$

$$\lambda_3<\lambda<\lambda_5, \tag{5c}$$

for AS

$$\lambda>\lambda_1,\quad \text{if } \lambda_1<\lambda_2,\lambda_3,$$
$$\lambda>\lambda_4,\quad \text{if } \lambda_2<\lambda_1,\lambda_3,$$
$$\lambda>\lambda_5,\quad \text{if } \lambda_3<\lambda_1,\lambda_2. \tag{5d}$$

The process of magnetizing a ferrimagnet from any of these original states can take place in various ways depending on the specific relation of parameters of both subsystems. Among these we can have a magnetic phase diagram that includes the sequence of all twelve possible phases listed above.[7] This interesting case we will treat in the following section: here, however, we discuss only certain general features that are characteristic of the magnetization processes.

Phase transitions between possible states of the system can be both type I (metamagnetic transitions) and type II (transitions to a noncollinear phase). The critical fields at which the magnetic state of the system changes correspond to setting the thermodynamic potentials of the phases equal. In the simplest model we will discuss, analytic expressions can be obtained rather simply for all the critical fields at which the magnetic state of the system changes, and for this reason we will list only a few of them in this article. By choosing $m_2>m_1$ for definiteness and without loss of generality, and varying the relation between the remaining parameters, we can derive 32 different phase transitions in all. For first-order phase transitions between noncollinear phases the critical fields are linear in the exchange parameter λ. For example, the phase transition $FW2\leftrightarrow AS$ gives

$$H_{FW2\leftrightarrow AS}=\frac{(M_2-m_2)H_2-\lambda M_1(M_2+m_2)}{|M_1-M_2|-M_1-m_2}. \tag{6}$$

The critical fields for first-order phase transitions between a noncollinear phase and a ferrimagnetic phase (or ferromagnetic phase) are nonlinear functions of λ. For example,

$$H_{NW2\leftrightarrow AW}=\lambda(m_2-m_1)-\{\lambda(M_1-m_1)[2H_1-\lambda M_1 -\lambda m_1]\}^{1/2}. \tag{7}$$

Noteworthy is the fact that second-order phase transitions occur only between noncollinear and ferromagnetic (or ferrimagnetic) phases, and occur without a change in the state of either of the subsystems. The critical fields equal

$$H_{Ai\leftrightarrow Ni}=\lambda|M_{2i}-M_{1i}|,\quad H_{Ni\leftrightarrow Fi}=\lambda(M_{1i}+M_{2i}),$$
$$i=W,\ W1,\ W2,\ S,$$
$$M_i=m_i,\quad i=W;\quad M_i=M_i,\quad i=W1,\ W2,\ S. \tag{8}$$

2. THE CASE OF A MAXIMUM NUMBER OF PHASE TRANSITIONS

If the magnetic moments of the second subsystem in both states are so large that the condition

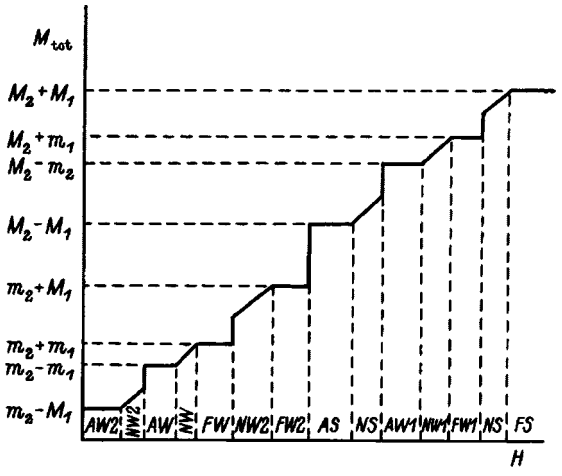

FIG. 1. Schematic magnetization curve for a ferrimagnet with two magnetically unstable subsystems satisfying conditions (9) and (10) for $\lambda_6<\lambda<\lambda_7$.

$$m_2>M_1, \quad M_2>m_2+2M_1, \tag{9}$$

is satisfied, and furthermore if

$$H_2>H_1+\lambda(m_2-m_1), \tag{10}$$

for values of the exchange parameter λ that satisfy condition (5c) for the existence of the original state $AW2$ (i.e., the first subsystem in the strongly magnetic state, the second in the weakly magnetic state), very curious magnetization curves can occur, in which magnetization reversal of the first unstable system can take place twice: the first time when the role of a stable subsystem is played by the second subsystem with magnetization m_2, and the second time when the role of the stable subsystem is again played by the same subsystem, but now with a magnetization M_2.

For values of λ that satisfy the condition

$$\lambda_6>\lambda>\lambda_7, \quad \lambda_6=H_1/M_1, \quad \lambda_7=2H_1/(M_1+m_1), \tag{11}$$

the magnetization curve is shown in Fig. 1. It is clear that it is exhibits five first-order phase transitions and six noncollinear phases. Magnetization up to state $FW2$ takes place according to the scenario $AW2\rightarrow NW2\rightarrow AW\rightarrow NW\rightarrow FW\rightarrow NW2\rightarrow FW2$. Then, via a first-order phase transition the system arrives at the state AS, and once more magnetization reversal of the first subsystem takes place according to the scenario $AS\rightarrow NS\rightarrow AW1\rightarrow NW1\rightarrow FW1\rightarrow NS\rightarrow FS$ up to a second stable subsystem with magnetization M_2, and finally to the last state FS. A characteristic feature of this magnetization curve is its ''detours'' from the noncollinear phases $NW2$ and NS into ''strange'' ferrimagnetic phases. In this case, the configurations of magnetic moments are determined by well-known expressions for the angles (see, e.g., Ref. 8) in fields that make the thermodynamic potentials equal one another.

If the values of the exchange parameter λ satisfy the following condition instead of condition (11):

$$\lambda_3<\lambda<\lambda_6, \tag{12}$$

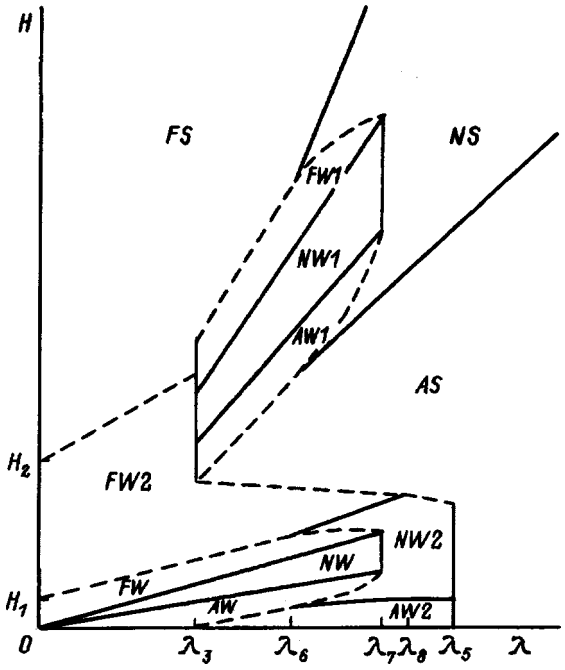

FIG. 2. Magnetic phase diagram for a ferrimagnet with two magnetically unstable subsystems satisfying conditions (9) and (10). Phase transitions of first and second kind are shown by dashed and solid curves respectively.

then the magnetization curve differs from that shown in Fig. 1 by the appearance of not six but only two noncollinear phases: NW and $NW1$.

Fig. 2 shows the full magnetic phase diagram in coordinates (H,λ) when the original magnetization curve of the second subsystem is characterized by a larger value of the magnetization and critical field than the first subsystem (see Eqs. (9) and (10)). Note that the phase transition field $H_{FW2\leftrightarrow AS}$ is a linearly decreasing function of λ (see Eq. (6)). Depending on the specific relation between parameters of the subsystems, the value of the exchange parameter λ_8

$$\lambda_8=\frac{(M_2-m_2)H_2}{2M_1(M_2-M_1-m_2)+m_2(M_2-m_2)}, \tag{13}$$

for which $H_{FW2\leftrightarrow AS}=H_{NW2\leftrightarrow FW2}$ can be larger (as in Fig. 2) or smaller than λ_7. If $\lambda_8<\lambda_7$, then in the range of values of the exchange parameter $\lambda_8<\lambda<\lambda_7$ the magnetization curve will differ from that shown in Fig. 2 by the absence of a phase $FW2$ and the presence of a first-order phase transition $NW2\leftrightarrow AS$. From Fig. 2 it is clear that small ($\lambda<\lambda_3$) and large ($\lambda>\lambda_7$) values of the exchange parameter λ correspond to a situation with a considerably simpler sequence of magnetic system states.

3. ANOTHER EXAMPLE OF A MAGNETIC PHASE DIAGRAM

When conditions (9) and (10) for the subsystem parameters are not satisfied, the magnetic phase diagrams are simpler. When the relations between parameters are much less strict than (9) and (10), for example

$$M_2>M_1, \quad H_2<H_1, \quad \lambda_2<\lambda_4 \tag{14}$$

(recall that for definiteness we set $m_2>m_1$), the magnetic phase diagram is shown in Fig. 3. Magnetization curves for

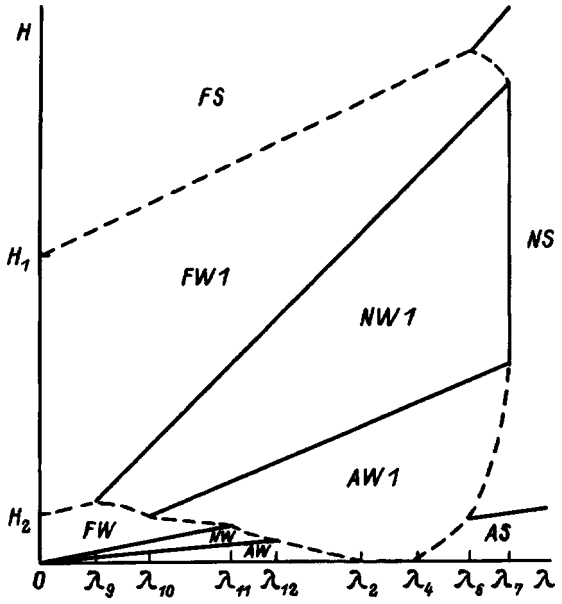

FIG. 3. The same as in Fig. 2 for case (14). $\lambda_9 = H_2/M_2$, $\lambda_{10} = (M_2 - m_2)H_2/(M_2 - m_2)(M_2 - 2m_1) + 2m_1^2$, $\lambda_{11} = (M_2 - m_2)H_2/(M_2 - m_2)(2m_1 + m_2) - 2m_1^2$, $\lambda_{12} = H_2/m_2$.

compounds with a magnetic phase diagram of this kind will be much simpler than those shown in Fig. 1. However, it is clear from Fig. 3 that different values of the exchange parameter λ correspond to various sequences of phase transitions that differ in their characteristics. For example, the noncollinear phase can be followed by two first-order phase transitions, or it may be located between the first-order phase transitions. Thus, by analyzing the magnetization curves we can estimate the value of the exchange interaction between subsystems of the ferrimagnet.

Once we have considered the various relations between the subsystem parameters (m_i, M_i and H_i), including those that do not satisfy conditions (9), (10), and (14), we can construct all possible magnetic phase diagrams. In coordinates (H,λ) they number twelve. These magnetic phase diagrams allow us to construct magnetization curves which have different forms and various intervals of values of the exchange parameter λ for a given magnetic phase diagram, as was shown in Figs. 2 and 3.

Thus, in this paper we have discussed magnetic phase diagrams within the effective-field model for a ferrimagnet having two magnetically unstable sublattices. Use of the simplest model allowed us to sort out the possible topologies for the phase diagrams and their dependences on fundamental subsystem parameters, and also to identify the situation with the largest number of phase transitions. In order to refine this theoretical approach it is necessary to include the magnetic susceptibility, washing-out of the metamagnetic transitions with respect to field, the influence of anisotropy, temperature effects, etc., which we also propose to do in the future. The question of what specific sequence of phase transitions and in what real systems they can be observed requires a special study. As we have already noted, certain Laves phases based on $TmCo_2$ could be ferrimagnets of the kind discussed above if the rare-earth subsystem can exhibit crossover. In future papers we shall address the question of whether it is possible for low-lying energy levels of the thulium ion to intersect when the latter is present in compounds of the type RCo_2 in positions with cubic symmetry, and we shall also discuss the jumps in the magnetization that accompany such crossing. Once we have derived the parameters of the thulium subsystem, it will be clear which of the phase diagrams we have discussed is the actual diagram. We should also look for other compounds which could be ferrimagnets having two magnetically unstable subsystems, in particular among ternary rare-earth intermetallics with transition metals or in certain intermetallics with manganese.

This work was carried out with the support of the Russian Fund for Fundamental Research (Project 96-02-16373) and INTAS—RFFI (Project 96-IN-RU-641).

[1] S. V. Tyablikov, *Methods in the Quantum Theory of Magnetism* [Wiley, New York, 1967; 2nd ed., Nauka, Moscow, 1975], p. 196.
[2] I. S. Dubenko, N. P. Kolmakova, R. Z. Levitin, A. S. Markosyan, and A. K. Zvezdin, J. Magn. Magn. Mater. **153**, 207 (1996).
[3] P. E. Brommer, I. S. Dubenko, J. J. M. Franse, F. Kayzel, N. P. Kolmakova, R. Z. Levitin, A. S. Markosyan, and A. Yu. Sokolov, Phys. Lett. A **189**, 253 (1994).
[4] P. E. Brommer, I. S. Dubenko, J. J. M. Franse, F. Kayzel, N. P. Kolmakova, R. Z. Levitin, A. S. Markosyan, and A. Yu. Sokolov, Physica B **211**, 155 (1995).
[5] I. S. Dubenko, I. V. Golosovsky, E. Gratz, R. Z. Levitin, A. S. Markosyan, and I. Mirebeau, J. Magn. Magn. Mater. **150**, 304 (1995).
[6] P. E. Brommer, I. S. Dubenko, J. J. M. Franse, R. Z. Levitin, A. S. Markosyan, and A. Yu. Sokolov, Physica B **183**, 363 (1993).
[7] N. P. Kolmakova and R. Z. Levitin, in *Abstracts of MM-M'96*, Atlanta (1996), P. BU-11.
[8] K. P. Belov, A. K. Zvezdin, A. M. Kadomtseva, and R. Z. Levitin, *Orientational Phase Transtions in Rare-Earth Magnets* (Nauka, Moscow, 1979) [in Russian], p. 211.

Translated by Frank J. Crowne

Magnetic anisotropy of $YFe_{11}Ti$ and its hydride

S. A. Nikitin, I. S. Tereshina, V. N. Verbetskiĭ, and A. A. Salamova

Moscow State University, 119899 Moscow, Russia
(Submitted June 14, 1997)
Fiz. Tverd. Tela (St. Petersburg) **40**, 285–289 (February 1998)

A study of the magnetic anisotropy of single-crystal $YFe_{11}Ti$ and of its hydride is reported. The measurements were performed on a vibrating-sample and a torsion magnetometer on field-oriented single-crystal and powder samples. The temperature dependence of the magnetic anisotropy constants K_1 and K_2 was determined by a mathematical treatment of experimental torque curves and by applying the Sucksmith-Thompson technique to magnetization data. It is shown that the temperature dependence of the magnetic anisotropy constants of $YFe_{11}Ti$ and of its hydride does not follow the prediction of the single-ion exchange model. It is found that hydrogenenation results in a growth of the magnetic anisotropy constant, which can be explained by an electron-density redistribution near the lattice positions occupied by iron atoms. © *1998 American Institute of Physics.* [S1063-7834(98)02802-0]

$RFe_{11}Ti$ compounds, which have the $ThMn_{12}$ structure, are currently studied in a number of laboratories.[1–4] Due to the specific features of their crystal and magnetic structure, these alloys are convenient subjects for investigation of fundamental problems in the physics of magnetic phenomena.

$RFe_{11}Ti$ compounds may be considered as a two-sublattice magnet.[2] The rare-earth (RE) metal and iron sublattices contribute both to the resultant magnetization and to the overall anisotropy. For light rare earths, the magnetic moments on both sublattices order ferromagnetically and, for heavy ones, ferrimagnetically. At low temperatures the dominant contribution to the overall anisotropy comes from the RE sublattice, while in the high-temperature domain the iron sublattice contribution prevails. Compensation of the anisotropy contributions due to the two sublattices gives rise in some compounds, such as $TbFe_{11}Ti$ and $DyFe_{11}Ti$ (Refs. 2–4), to spin-reorientation transitions under temperature variation.

To obtain information about the properties of the iron sublattice, we studied compounds with rare earths having not a localized magnetic moment, such as Y and Lu.[5,6] The $YFe_{11}Ti$ composition was studied by various methods, including measurement of magnetic properties,[7] neutron diffraction,[8] and Mössbauer spectroscopy.[9] As for the magnetic anisotropy of single-crystal $YFe_{11}Ti$ and its hydride, it has received inadequate attention; indeed, data on the magnitude and temperature dependence of the anisotropy field H_a of $YFe_{11}Ti$ are contradictory. Estimates of H_a scatter over a wide range, from $H_a = 21-48$ kOe at $T = 300$ K to 35–60 kOe at 77 K,[10] the constant K_1 has not been determined to a sufficiency accuracy within a broad temperature range from 4.2 K to the Curie point, the anisotropy constant was derived indirectly from the magnetization curve obtained for oriented powder samples, and there are no data on the second magnetic-anisotropy constant K_2. The magnetic anisotropy constants of the hydride of this compound also require refinement.

The objective of the present work was a comprehensive study of magnetocrystalline anisotropy of $YFe_{11}Ti$ and $YFe_{11}TiH$. For the first time torque measurements were carried out on single-crystal $YFe_{11}Ti$ and field-oriented hydride samples, thus offering direct determination of the magnetic anisotropy constants of these compounds.

1. SAMPLE PREPARATION TECHNOLOGY AND MEASUREMENT TECHNIQUE

The technology of preparation and quality control of $YFe_{11}Ti$ samples are similar to those used earlier.[11] The samples for magnetic measurements were single-crystal blocks with misorientation within 1–2°. The crystal quality was estimated from Laue x-ray diffraction patterns. The samples intended for torque measurements were discs ~ 4 mm in diameter and $\sim 0.3-0.4$ mm thick. The disc plane contained either the (110) or (001) crystallographic plane. The samples for magnetization measurements were spheres ~ 2 mm in diameter.

The hydrogen used for hydrogenation was obtained by decomposing $LaNi_5H_{6+x}$ hydride containing $10^{-3}-10^{-4}$% impurities. The interaction of the starting material with hydrogen was studied at pressures of up to 20 atm in a temperature range 293–593 K, with the amount of reacted hydrogen derived volumetrically. The H/Me ratio (the number of gram-atoms of hydrogen per one gram-atom of the intermetallic compound) was calculated using the van der Waals equation. The composition of the hydrides thus prepared was checked by high-temperature hydrogen extraction.

At room temperature, the intermetallic compound under study did not react with hydrogen. The reaction started with a slight delay after the temperature was raised to 573 K and ended in about an hour.

X-ray diffraction analysis of the hydride was performed on a Dron-2 diffractometer (Cu $K\alpha$ radiation) using powder samples. The analysis showed the samples to be single phase and crystallize in $ThMn_{12}$ structure, with lattice constants agreeing with literature data. The only reflections present in the diffraction patterns correspond to this structure. No reflections of α iron, which is found almost inevitably in iron-rich cast alloys, were observed in the diffraction patterns.

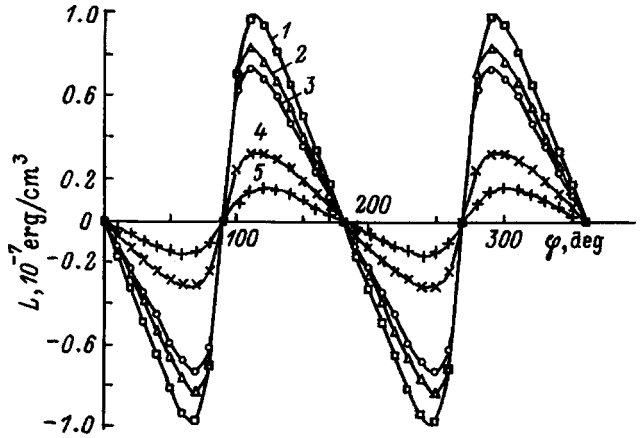

FIG. 1. Experimental torque (L) curves for single-crystal $YFe_{11}Ti$ measured in (110) plane in a field $H=13$ kOe at different temperatures $T(K)$: *1*—78, *2*—200, *3*—300, *4*—400, *5*—480.

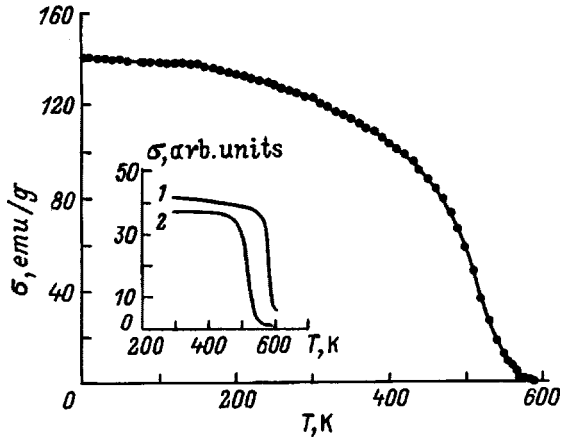

FIG. 2. Temperature dependence of saturation magnetization σ_s of single-crystal $YFe_{11}Ti$. Inset: temperature dependence of magnetization σ measured in a field $H=2$ kOe. *1*—$YFe_{11}TiH$, *2*—$YFe_{11}Ti$.

Magnetic measurements of $YFe_{11}TiH$ were made on free powder placed in a ceramic vial, as well as on powder grains oriented in a static magnetic field of ~ 7 kOe and fixed in this position with epoxy resin. The samples were shaped as discs and spheres, thus ensuring correct consideration of the demagnetizing factor.

Experimental torque curves were obtained on a torque magnetometer within at temperature range of 77–700 K and in magnetic fields of up to 13 kOe. The torque was measured in 2° steps of single-crystal sample rotation relative to the magnetic field.

The magnetic anisotropy constants were derived from the torque dependence on the angle of turn by separating the harmonics successively for external magnetic fields H in excess of the magnetic anisotropy field H_a. For fields below H_a, the processing of experimental curves required preliminary correction by least-squares.[12] The relative error in determination of constant K_1 by this method did not exceed 3%, and that of constant K_2, 10%.

Sample magnetization in static magnetic fields of up to 13 kOe was measured along different crystallographic directions by means of a vibrating-sample magnetometer within a 77–700-K range. To determine the magnetic anisotropy, magnetization was measured in pulsed magnetic fields up to 120 kOe and temperatures ranging from 4.2 to 300 K.

When working in the low-temperature domain, the magnetic anisotropy constants were determined also by the method of Sucksmith-Thompson,[13] which consists in a special mathematical treatment of the magnetization curves measured along the easy and hard directions. The relative error of K_1 and K_2 determination by this method did not exceed 9%. The magnetic anisotropy constants thus obtained were used in checking the main aspects of the theoretical model underlying investigation of $RFe_{11}Ti$-type compounds.

2. RESULTS OF MEASUREMENTS AND DISCUSSION

The experimental torque curves, $L(\varphi)$, for the $YFe_{11}Ti$ compound measured in a field of 13 kOe for the (110) plane as a function of the angle φ the field **H** makes with the tetragonal axis **c** are presented in Fig. 1 for different temperatures (without preliminary correction). This shape of the curves, with a repetition period of 180°, is typical of uniaxial magnets, with the [001] direction being the easy axis, and [110], the hard magnetization axis. As seen from Fig. 1, the torque curve amplitude decreases monotonically with increasing temperature. The measurements performed on a disc in the (001) plane did not reveal any anisotropy in the basal plane of the sample.

The torque acting on a ferromagnetic single crystal is related in a straightforward way to the derivative of the magnetic anisotropy energy $F_a(\theta)$ through[14]

$$L(\theta) = -\partial F_a / \partial \theta,$$

where θ is the angle between the spontaneous-magnetization vector $\mathbf{M}_s$ and the tetragonal **c**.

The conversion of $L(\varphi)$ to $L(\theta)$ curves required to take into account the difference between the angles φ and θ is described in detail in Ref. 14. In this way one corrects for differences in the orientation of vectors $\mathbf{M}_s$ and **H**.

Figure 2 displays the temperature dependence of saturation magnetization σ_s for single-crystal $YFe_{11}Ti$, which was measured on the sample used to obtain torque curves in a magnetic field of 13 kOe. This dependence follows a typical ferromagnetic pattern with a monotonic decrease of magnetization as the sample temperature increases from 4.2 K to the Curie point. The temperature dependence of the curve is well fitted by Stoner's relation.[7] For the (110) crystallographic plane, the angular dependences of the torque can be specified in the form[14]

$$L_{110}(\theta) = -2K_1 \sin\theta \cos\theta - 4K_2 \sin^3\theta \cos\theta. \qquad (2)$$

Least-squares fitting of the $L(\theta)$ curves yielded the temperature dependence of the magnetic anisotropy constants K_1 and K_2 (filled circles in Fig. 3) within the temperature range 77–600 K. To determine the constants K_1 and K_2 in the low-temperature domain, magnetization curves were obtained along the easy and hard directions in magnetic fields of up to 120 kOe, well in excess of the magnetic anisotropy

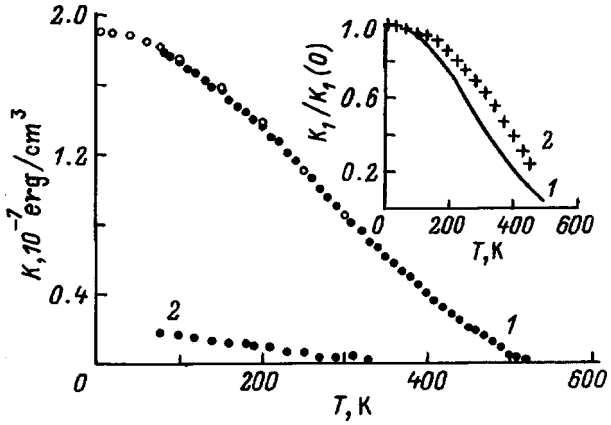

FIG. 3. Temperature dependence of magnetic anisotropy constant for single-crystal $YFe_{11}Ti$: *1*—K_1, *2*—K_2 (filled circles—torque method, open circles—Sucksmith-Thompson method). Inset: temperature dependence of reduced magnetic anisotropy constant $K_1/K_1(0)$; *1*—experiment, *2*—calculation.

field. The magnetic anisotropy constants were found by plotting H/M vs M^2 by the method of Sucksmith-Thompson (open circles in Fig. 3).

The temperature dependence of K_1 and K_2 presented in Fig. 3 exhibits a monotonic decrease of the constants with increasing temperature as one approaches the Curie point. The values of the magnetic anisotropy constant K_1 determined by the two methods coincided with a fairly good accuracy within the 77–300 K range. It was found that $K_1=(0.85\pm0.031)\times10^7$ erg/cm^3 at $T=300$ K and $K_1=(1.89\pm0.06)\times10^7$ erg/cm^3 at $T=77$ K. As for constant K_2, in the first case (torque measurements) it was an order of magnitude smaller than K_1, namely, $K_2=(0.032\pm0.003)\times10^7$ erg/cm^3 for $T=300$ K and $K_2=(0.17\pm0.02)\times10^7$ erg/cm^3 for $T=77$ K (see Fig. 3). The calculations made by the Sucksmith-Thompson method yielded still smaller values: $K_2=(0.014\pm0.001)\times10^7$ erg/cm^3 for $T=300$ K and $K_2=(0.095\pm0.009)\cdot10^7$ erg/cm^3 for $T=77$ K.

The high magnetocrystalline anisotropy of the $YFe_{11}Ti$ compound is a consequence of a partial ''unfreezing'' of the orbital moment L of Fe ions in the anisotropic local crystal field, which differs strongly for different crystallographic positions. This small ''unfrozen'' moment (a component of the orbital moment L) aligns with the easy magnetization axis to affect, in its turn, the orientation of the total spin moment via spin-orbit coupling.

The inset to Fig. 3 compares the experimental $K_1(T)/K_1(0)$ curve with the theoretical relation[15] for the case of a localized magnetic moment in terms of the single-ion exchange model, which takes into account the interaction of the orbital moment with the crystal field:

$$K_1(T)/K_1(0)=[M_s(T)/M_s(0)]^3, \tag{3}$$

where $K_1(0)$ and $M_s(0)$ are the magnetic anisotropy constant and the saturation magnetic moment at $T=0$ K, respectively. The discrepancy between the experimental and theoretical data may be attributed to the magnetic moment of the $3d$ sublattice and the magnetic anisotropy obtaining a certain contribution from the itinerant electrons, a point disregarded by the theory of Ref. 15.

TABLE I. Lattice parameters a and c, unit cell volume V, magnetic anisotropy constant K_1, and saturation magnetization σ_s for the $YFe_{11}Ti$ compound and its hydride.

Compound	a, Å	c, Å	V, Å^3	c/a	$K_1\cdot10^7$, erg/cm^3	σ_s, emu/g
$YFe_{11}Ti$	8.509	4.783	346.6	0.56211	0.85	120
$YFe_{11}TiH$	8.547	4.786	349.6	0.55996	1.25	138

The above conclusion on the nature of magnetocrystalline anisotropy is in agreement with neutron diffraction data,[8] which showed that the magnetic moments localized on Fe atoms in $YFe_{11}Ti$ in the three nonequivalent positions $8i$, $8j$, and $8f$ of $ThMn_{12}$ [the iron magnetic moments, μ_{Fe}, are (in μ_B): 1.92, 2.28, 1.8 for the $8i$, $8j$, and $8f$ positions, respectively] differ strongly in magnitude from those on the di- and trivalent iron ions (4 and $5\mu_B$, respectively). It thus follows that the magnetism of the iron sublattice is to a certain extent itinerant.

We consider now the effect of hydrogenation on the magnetic properties of $YFe_{11}Ti$. Hydrogenation is known[16,17] to increase the interatomic distances and the unit cell volume. In some compounds (R_2Fe_{17} and others) the increase of atomic volume results in a large increase in the Curie temperature.

The Curie temperature of $YFe_{11}Ti$ is dominated by exchange interactions between iron atoms. We determined T_c as the temperature corresponding to the steepest drop of magnetization in the transition of ferromagnetic to paramagnetic state in a weak magnetic field (see inset in Fig. 2). We found $T_c=538$ K for $YFe_{11}Ti$, which is less by far than that for metallic iron. Our calculation[8] showed the shortest distances between iron atoms in $YFe_{11}Ti$ to be those in the $8f$-$8f$ and $8i$-$8i$ pairs (2.3818 and 2.3900 Å, respectively). Such small Fe-Fe distances make possible negative exchange interactions. Hydrogenation of $YFe_{11}Ti$ increases noticeably the lattice constant a and the unit cell volume V (by $\sim0.95\%$), while only weakly affecting the constant c (Table I).

The Curie point of the hydride $YFe_{11}TiH$ is substantially, almost by 60 K, higher (see inset Fig. 2). The increase of T_c can be attributed to the exchange energy increasing with increasing Fe-Fe separation and atomic volume.[16,18]

The rising Curie temperature induced by interstitial elements brings about also a substantial increase of such a technically important characteristic as the saturation magnetization ($\sigma_s=120$ G·cm^3/g for $YFe_{11}Ti$ and $\sigma_s=138$ G·cm^3/g for $YFe_{11}TiH$ at $T=300$ K). The $\sigma_s(T)$ dependence for $YFe_{11}TiH$ has a typically ferromagnetic character, similar to the starting compound, with a monotonic decrease of σ with heating.

It appeared of interest to obtain information on the character of the effects responsible for the change in magnetic anisotropy induced by hydrogenation.

The magnetic anisotropy constants of $YFe_{11}TiH$ were

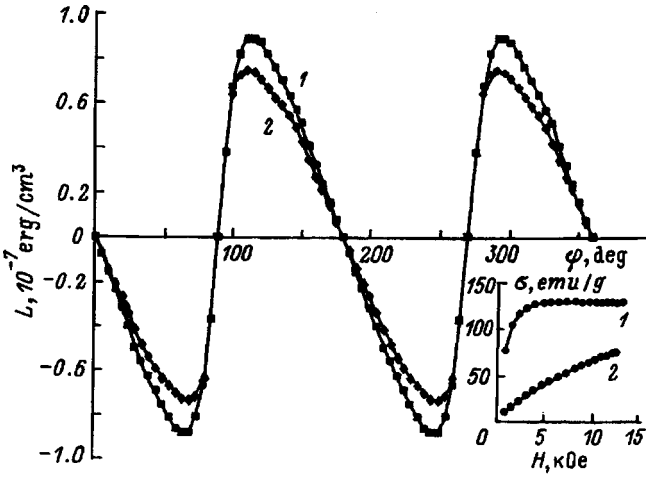

FIG. 4. Experimental torque (L) curves for an oriented $YFe_{11}TiH$ powder sample measured in a field $H=13$ kOe at different temperatures $T(K)$: *1*—77, *2*—300. Inset: magnetization σ vs magnetic field plot obtained at $T=300$ K on an oriented $YFe_{11}TiH$ sample along (1) easy and (2) hard directions.

obtained by the above two techniques. Figure 4 shows torque curves measured on oriented powder samples in a magnetic field of 13 kOe at $T=77$ and 330 K. The inset to Fig. 4 presents magnetization curves for the hydride taken on oriented powder samples along the easy and hard directions at $T=300$ K. We see that the magnetic anisotropy of the hydride is also uniaxial, since the $L(\varphi)$ curves repeat with a 180° period. The anisotropy field of the hydride $H_a=30$ kOe at $T=300$ K, exceeds that of the starting compound $YFe_{11}Ti$ ($H_a=20$ kOe).

The dependence of the first magnetic anisotropy constant of the intermetallic compound $YFe_{11}Ti$ and of its hydride $YFe_{11}TiH$ on reduced temperature T/T_c is shown in Fig. 5 for field-oriented powder samples of both compositions. The first anisotropy constant for the interstitial compound $YFe_{11}TiH$ is larger than that for the starting intermetallic, namely, by about 40% at $T=300$ K (after the hydrogenation K_2 also increases). This behavior of magnetocrystalline anisotropy of the hydride $YFe_{11}TiH$ cannot be due to size effects only.

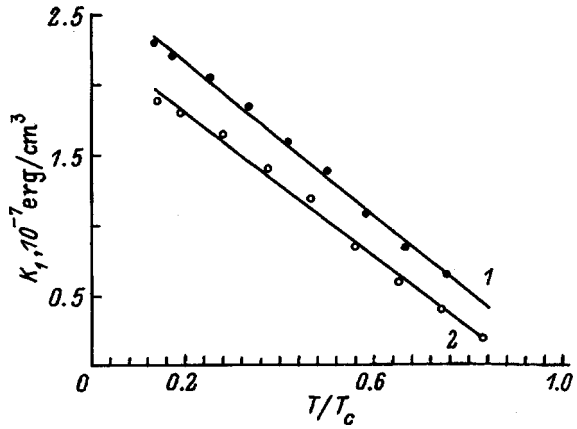

FIG. 5. Dependence of the magnetic anisotropy constant K_1 on reduced temperature T/T_c for: *1*—$YFe_{11}TiH$, and *2*—$YFe_{11}Ti$.

It is known that single-ion exchange theory for localized moments yields the following expression for the magnetic anisotropy constant K_1 (Ref. 19):

$$K_1 \sim M_s^3[1-(c/a)^2]. \tag{4}$$

Estimation of the variation of K_1 due to the hydrogenation-induced change in magnetization and of the axial ratio $\eta=c/a$ from this expression does not, however, yield satisfactory results. Indeed, Table I and the above relation predict a change of K_1 approximately by 6%, whereas the experimental value of the change in K_1 is larger by an order of magnitude.

One may thus conclude that the theory of magnetic anisotropy based on the single-ion exchange model is inadequate in our case. Hydrogenation not only affects the crystal fields generated by ionic charges in the nearest-neighbor environment but gives rise to larger effects of another origin as well.

Hydrogen atoms incorporating into $YFe_{11}Ti$ during hydrogenation occupy tetrahedral interstices.[17] Experimental data (see Table I) suggest that hydrogenation changes the lattice parameters and unit-cell volume. This results in a narrowing of the itinerant $3d$ electron band.[18] The nearest-neighbor environment of Fe atoms changed by incorporation of hydrogen atoms stretches the Fe-Fe valence bond, which results in a redistribution of the valence-electron density.[20] It is these effects that apparently account for the considerable increase of the magnetic anisotropy constant of $YFe_{11}TiH$ observed in this work.

In conclusion, the authors express gratitude to O. A. Zolotukhin and K. A. Skokov for supplying the single-crystal samples of the compounds, and to I. V. Telegina for assistance in sample characterization.

Support of the Russian Fund for Fundamental Research (Grants 96-02-18271 and 3/97-52) is gratefully acknowledged.

[1] K. Yu. Guslienko, X. C. Kou, and R. Grossinger, J. Magn. Magn. Mater. **150**, 383 (1995).
[2] B.-P. Hu, H.-S. Li, J. M. D. Coey, and J. P. Gavigan, Phys. Rev. B **41**, 2221 (1990).
[3] A. A. Kazakov, N. V. Kudrevatykh, and P. E. Markin, J. Magn. Magn. Mater. **146**, 208 (1995).
[4] A. V. Andreev, N. V. Kudrevatykh, S. M. Razgonyaev, and E. N. Tarasov, Physica B **183**, 379 (1993).
[5] B.-P. Hu, H.-S. Li, J. P. Gavigan, and J. M. D. Coey, J. Phys.: Condens. Matter **1**, 755 (1989).
[6] B.-P. Hu, H.-S. Li, and J. M. D. Coey, J. Appl. Phys. **67**, 4838 (1990).
[7] N. V. Kudrevatykh, M. I. Bartashevich, V. A. Reĭmer, S. S. Sigaev, and E. N. Tarasov, Fiz. Met. Metalloved. **69**, No. 11, 53 (1990).
[8] Y.-C. Yang, H. Sun, L.-S. Kong, J.-L. Yang, Y.-F. Ding, B.-S. Zhang, C.-T. Ye, L. Jin, and H.-M. Zhou, J. Appl. Phys. **64**, 5968 (1988).
[9] Z. W. Li, X. Z. Zhou, A. H. Morrish, and Y. C. Yang, J. Phys.: Condens. Matter **2**, 4253 (1990).
[10] L. Schultz and M. Katter, in *NATO Advanced Study Institute, Ser. C: Mathematic and Physical Sciences*, Vol. 331, ed. by G. J. Long and F. Grandjean (Kluwer Academic, Dordrecht, 1991), p. 227.
[11] O. A. Zolotukhin, V. V. Zubenko, T. I. Ivanova, S. A. Nikitin, V. V. Sergeev, I. V. Telegina, and I. S. Tereshina, Vestn. Mosk. Univ. Fiz. Astron. **34**, No. 5, 80 (1993).
[12] F. Ono, Y. Ohtsu, and O. Yamada, J. Phys. Soc. Jpn. **55**, 4014 (1986).

[13] W. Sucsmith and J. E. Thompson, Proc. R. Soc. London, Ser. A **225**, 362 (1954).
[14] S. A. Nikitin, T. I. Ivanova, V. V. Zubenko, I. V. Telegina, and I. S. Tereshina, Fiz. Tverd. Tela (St. Petersburg) **37**, 561 (1995) [Phys. Solid State **37**, 306 (1995)].
[15] E. Callen and H. B. Callen, J. Phys. Chem. Solids **16**, 310 (1960).
[16] J. M. D. Coey, H. Sun, and D. P. F. Hurley, J. Magn. Magn. Mater. **101**, 310 (1991).
[17] D. Fruchart and S. Miraglia, J. Appl. Phys. **69**, 5578 (1991).
[18] J. Yang, S. Dong, W. Mao, P. Xuan, and Y. Yang, Physica B **205**, 341 (1991).
[19] F. Bolzony, J. P. Gavigan, D. Givord, H. S. Li, O. Moze, and L. Pareti, J. Magn. Magn. Mater. **66**, 158 (1987).
[20] R. Coehoorn and K. H. J. Buschow, J. Appl. Phys. **69**, 5590 (1991).

Translated by G. Skrebtsov

Magnetic, electrical, and crystallographic properties of thin $La_{1-x}Sr_xMnO_3$ films

O. Yu. Gorbenko, R. V. Demin, A. R. Kaul', and L. I. Koroleva

Moscow State University, 119899 Moscow, Russia

R. Szymczak

Institute of Physics, Polish Academy of Sciences, 02-668 Warsaw, Poland
(Submitted July 16, 1997)
Fiz. Tverd. Tela (St. Petersburg) **40**, 290–294 (February 1998)

A study is reported of the magnetic, electrical, and crystallographic properties of $La_{1-x}Sr_xMnO_3$ ($0.15 \leqslant x \leqslant 0.23$) epitaxial films grown on single-crystal substrates of $(001)ZrO_2(Y_2O_3)$ having the fluorite structure and $(001)LaAlO_3$ having the perovskite structure. It was found that films with close compositions for $x=0.15$ and 0.16, grown on different substrates, have different properties, namely, the film on a fluorite substrate is semiconducting and has a coercive strength 30 times that of the film on a perovskite substrate; the temperature dependence of electrical resistance of the latter film has a maximum around the Curie point T_C and follows metallic behavior for $T<T_C$. These differences are explained as due to different structures of the films. The $x=0.23$ film on the perovskite substrate has been found to exhibit a combination of giant magnetoresistance at room temperature with a resistance of $\approx 300\ \Omega$ which is useful for applications. The maxima in resistance and absolute value of negative magnetoresistance are accounted for by the existence of two-phase magnetic states in these films. © *1998 American Institute of Physics.* [S1063-7834(98)02902-5]

Studies of rare-earth manganites having the perovskite structure have recently been attracting considerable interest due to the giant magnetoresistance (MR) which some of them exhibit at room temperature.[1] The temperature dependence of the MR of these materials, similar to other magnetic semiconductors,[2] has a maximum in absolute magnitude about the Curie point T_C, and it is only in this temperature region that a giant MR is observed. In this class of magnetic semiconductors, $La_{1-x}Sr_xMnO_3$ compounds with $0.3 \leqslant x \leqslant 0.4$ have the highest Curie temperatures, ~ 370 K.[3,4] The Curie temperatures of compositions with $0.175 \leqslant x \leqslant 0.3$ also lie around 300 K.[3] In these compositions with $T_C > 300$ K, however, the resistivity ρ of bulk single crystals is of the order of $10^{-2}-10^{-3}\ \Omega \cdot$cm.[3] Such a small magnitude of ρ makes bulk crystals inconvenient for applications, although they exhibit giant MR around T_C. More suitable for applications are thin films, whose resistivity is several orders of magnitude larger than that of bulk samples.

The objective of this work was to prepare $La_{1-x}Sr_xMnO_3$ epitaxial films with $0.15 \leqslant x \leqslant 0.23$ on different substrates and to study their physical properties and the effect of substrate structure on their magnetic and electrical characteristics, as well as to grow films with giant MR around 300 K and an electrical resistance suitable for applications.

1. THIN-FILM PREPARATION AND EXPERIMENTAL METHOD

The films were grown by MOCVD using a vapor aerosol source of metallo-organic compounds (La, Sr, and Mn dipivaloyl methanates).[5] 1-mm thick single-crystal $(001)ZrO_2(Y_2O_3)$ and $(001)LaAlO_3$ plates were used as substrates. The films were deposited in a vertical reactor on an inductively heated substrate. After deposition, the films were additionally annealed in oxygen at the deposition temperature (750 °C) for 0.5 h. X-ray characterization of the films, including determination of the phase composition, orientation, and lattice parameters, was made with a four-circle Siemens D5000 diffractometer with a secondary graphite monochromator (Cu $K\alpha$ radiation). The film composition was determined by x-ray microprobe analysis (by means of a CAMSCAN scanning electron microscope equipped with an EDAX system). The magnetization of the thin films was measured with a SQUID magnetometer, and electrical resistance, by the four-probe technique.

2. EXPERIMENTAL RESULTS AND DISCUSSION

A. Crystallographic properties

As follows from x-ray diffraction measurements, the $LaAlO_3$ perovskite substrate (the parameter of pseudocubic perovskite cell $a=0.3792$ nm) permits one to grow (001) oriented $La_{1-x}Sr_xMnO_3$ films (Fig. 1a). φ scanning shows the perovskite lattices of the film to be in epitaxial relation with the substrate. The rocking-curve width measured at half maximum (FWHM) for the (002) and (004) reflections was typically 0.17–0.25°. The mosaic structure of the substrate did not permit one to reach a higher perfection in film orientation.

$ZrO_2(Y_2O_3)$ ($a=0.514$ nm) has the fluorite structure. Thin $La_{1-x}Sr_xMnO_3$ films grown on this substrate had (110) orientation (Fig. 1b) with a FWHM of the rocking curve for (111) and (222) reflections of 0.25–0.3°. The choice of this orientation was motivated by the fact that the $(Zr)^{4+}(O_2)^{4-}(LaMnO)^{4+}(O_2)^{4-}$ atomic layer sequence is energetically preferable to $(Zr)^{4+}(O_2)^{4-}(LaO)^{+}(MnO_2)^{-}$ for the (001) orientation. In the case of the (110) film orienta-

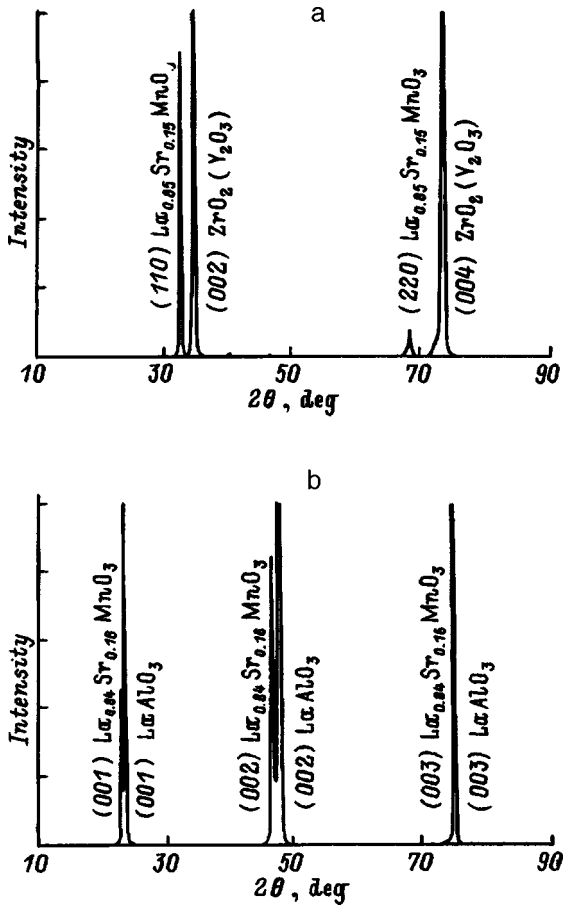

FIG. 1. X-ray diffraction patterns of thin films: (a) $La_{0.85}Sr_{0.15}MnO_3$ on $ZrO_2(Y_2O_3)$ and (b) $La_{0.84}Sr_{0.16}MnO_3$ on $LaAlO_3$.

tion, the fluorite lattice of the substrate possesses excess symmetry elements in the interface plane, which gives rise to equivalent structural arrangements in the film. The φ scanning technique established coexistence in the film of the following possible orientations in the interface plane:

(1) $[1\bar{1}1]_f//[110]_s$, $[\bar{1}12]_f//[\bar{1}10]_s$;

(2) $[1\bar{1}1]_f//[110]_s$, $[\bar{1}12]_f//[1\bar{1}0]_s$;

(3) $[1\bar{1}1]_f//[\bar{1}10]_s$, $[\bar{1}12]_f//[110]_s$;

(4) $[1\bar{1}1]_f//[\bar{1}10]_s$, $[\bar{1}12]_f//[\bar{1}\bar{1}0]_s$;

where indices f and s refer to the film and substrate, respectively. The orientation of the body diagonal of the perovskite cell along the diagonal of the fluorite cell face is common for all possible variants (Fig. 2), with high-angle boundaries (19.5, 70.5, and 90°) forming in the film plane.

B. Magnetic properties

Film magnetization was measured in a magnetic field applied parallel to the film plane, with the results being corrected for the substrate magnetization. Figure 3 presents magnetization M vs magnetic field H plots obtained at $T=5$ K, and Fig. 4, an $M(T)$ dependence obtained at 30 kOe for all the films studied. We readily see that the compositions with $x=0.16$ and 0.23 exhibit a strong rise of M with decreasing temperature starting from $T=50$ K. As evident from Fig. 3, the $M(T)$ curves for these compositions taken at $T=5$ K are far from saturation up to 30 kOe, the maximum fields at which the measurements were performed. A similar phenomenon was observed earlier for bulk samples,[6] with no explanation given. It should be pointed out that, as seen from Fig. 3, for compositions $x=0.23$ for $T<50$ K, and $x=0.16$ for $T<185$ K the magnetization M is in excess of the values due to the spin only, which on the average are 660 G for compositions $0.15\leqslant x\leqslant 0.23$. By contrast, for the $x=0.15$ composition the magnetization M is lower than the above theoretical value. This may be due to errors in determination of the film thickness, which was derived only from the deposition time, and could be as high as 30%. In this case the deviations of the experimental values of magnetization lie within the error limits.

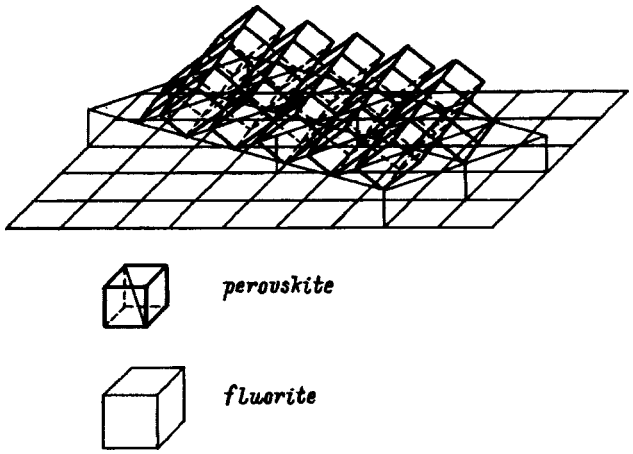

FIG. 2. Orientation of a thin $La_{1-x}Sr_xMnO_3$ film on $ZrO_2(Y_2O_3)$ substrate having the fluorite structure. Shown is one of four equivalent orientations in the interface plane.

As seen from Fig. 4, determination of T_C from the $M(T)$ curves [for instance, by extrapolating the steepest part of the

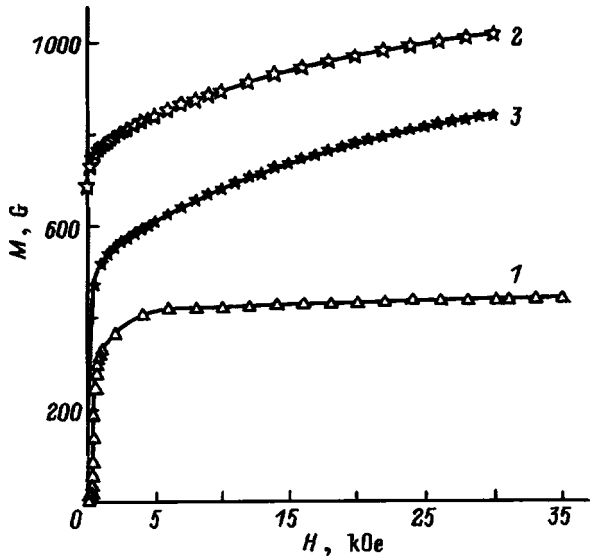

FIG. 3. 5-K magnetization isotherms of thin $La_{1-x}Sr_xMnO_3$ films with x: *1*—0.15, *2*—0.16, *3*—0.23.

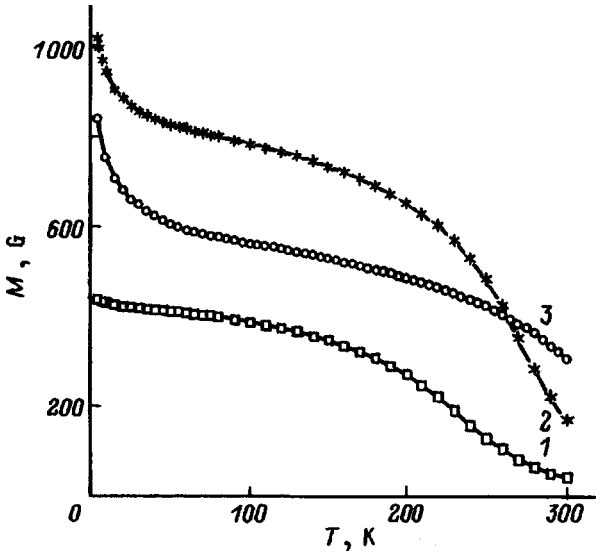

FIG. 4. Temperature dependence of magnetization in a magnetic field of 30 kOe obtained on $La_{1-x}Sr_xMnO_3$ films with x: *1*—0.15, *2*—0.16, *3*—0.23.

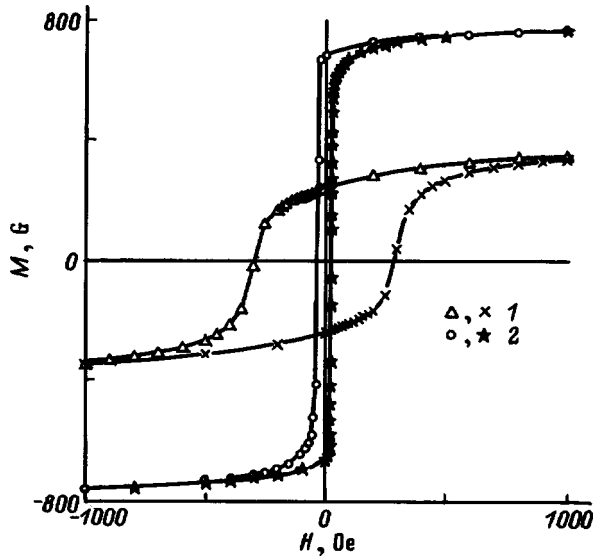

FIG. 6. Hysteresis loops of thin $La_{1-x}Sr_xMnO_3$ films with x: *1*—0.15 and *2*—0.16.

$M(T)$ curve to the temperature axis] would be fairly difficult because of the slow falloff of magnetization in the vicinity of T_C. The Belov–Arrott plots also turned out to be inapplicable because of the absence of linear parts in the $M^2/(H/M)$ relations in the strong-field domain. Therefore we used for determination of T_C the $M(T)$ curves measured in weak fields (Fig. 5). For compositions with $x=0.15$ and 0.16, the magnetization was obtained by cooling the sample in a field $H=20$ Oe, and for the $x=0.23$ composition the sample was cooled down to $T=5$ K with no field applied, after which the magnetization was measured at 20 Oe during heating. For the first two above compositions, T_C was obtained by extrapolating the steepest part of the $M(T)$ curve to the temperature axis (yielding 220 and 265 K, respectively), and for the latter composition, from the maximum in the $M(T)$ relation (272 K). Figure 6 displays hysteresis loops for all the films studied; we see that the loop for the $x=0.15$ sample is substantially broader, and the coercive force is about 30 times that for the other two compositions.

C. Electrical properties

Figure 7 presents the temperature dependence of electrical resistance R of all compositions studied, and Fig. 8, that of magnetoresistance of the $x=0.23$ composition. We see in Fig. 7 that the $R(T)$ relation for the $x=0.15$ composition follows semiconducting behavior, whereas for the film with a close composition, $x=0.16$, but grown on another substrate, this relation is not monotonic. Indeed, in the low-temperature domain, R of the latter composition increases weakly with temperature, which is characteristic of metallic conduction, and, starting from $T\approx 230$ K, exhibits a steep growth to reach a maximum near T_C. The $R(T)$ relation of the $x=0.23$ composition has a metallic character with a strong growth of

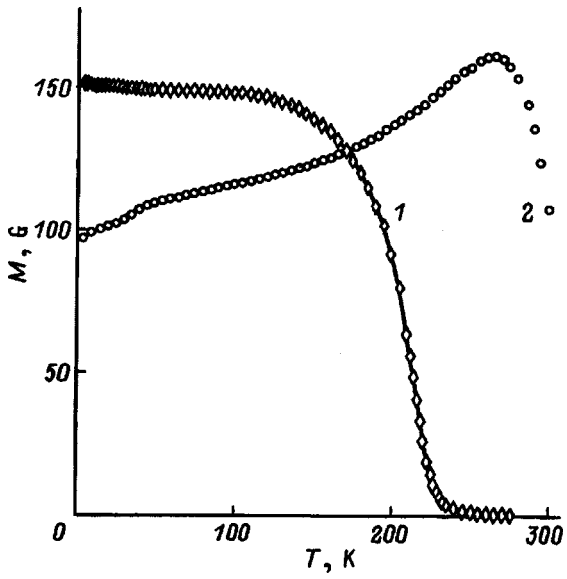

FIG. 5. Temperature dependence of magnetization in a magnetic field of 20 Oe obtained on $La_{1-x}Sr_xMnO_3$ films with (*1*) $x=0.15$ (the magnetization was measured with the film cooled in this field down to 5 K) and (*2*) $x=0.23$ (the film was zero-field-cooled down to 5 K, after which its magnetization was measured during heating).

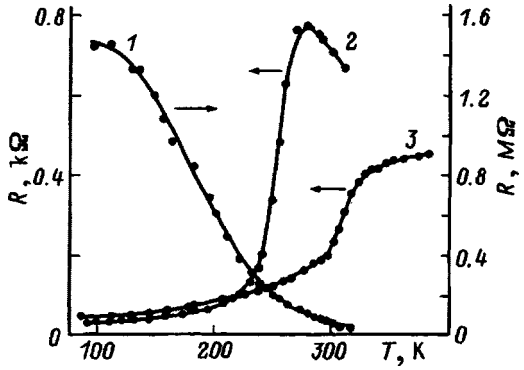

FIG. 7. Temperature dependence of the resistance of thin $La_{1-x}Sr_xMnO_3$ films with x: *1*—0.15, *2*—0.16, and *3*—0.23.

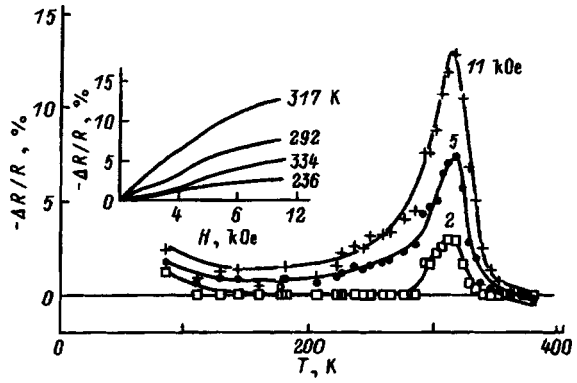

FIG. 8. Temperature dependences of magnetoresistance of a $La_{1-x}Sr_xMnO_3$ film with $x=0.23$ measured in different magnetic fields H. Inset: magnetoresistance isotherms of this film.

R slightly above T_C; indeed, within the region $280 \leqslant T \leqslant 330$ K the resistance increases approximately by a factor three.

The magnetoresistance $\Delta R/R$ ($\Delta R = R_H - R_{H=0}$) of all three compositions is negative and isotropic in the film plane (no MR measurements with the field perpendicular to the film plane were performed). As seen from Fig. 8, the $|\Delta R/R|(T)$ relations measured for the $x=0.23$ composition in various magnetic fields pass through a maximum around 310 K, i.e. slightly above T_C. At the maximum this quantity reaches a giant magnitude, $|\Delta R/R| \sim 13\%$ in a field of 11 kOe. This film is very suitable for applications, since its resistance, at the temperature where $|\Delta R/R|$ has a maximum, is $\sim 400\ \Omega$, i.e., it lies in the range convenient for $|\Delta R/R|$ measurements. The magnetoresistance of the other two compositions behaves in a pattern similar to that shown in Fig. 8, namely, $|\Delta R/R|$ reaches a maximum near T_C, and its magnitude at the maximum is larger than that for the $x=0.23$ composition. For instance, for $x=0.15$ it is 20%, and for $x=0.16$, 35% in a field of 11 kOe. These giant magnetoresistances are observed, however, below room temperature, and therefore these compositions are less attractive from the standpoint of applications than the $x=0.23$ composition. Note that, as seen from the inset to Fig. 8, the MR isotherms are far from saturation at 11 kOe, the maximum field in which measurements were made.

D. Effect of substrate crystal structure on the magnetic and electrical properties

As seen from Subsections A–C, films with close compositions, $x=0.15$ and 0.16, but grown on different substrates differ substantially in their magnetic and electrical properties. Indeed, Fig. 6 demonstrates that the hysteresis loop of the film grown on the fluorite substrate is noticeably wider than that of the film on the perovskite substrate. This may be explained in the following way. In the latter case the easy magnetization axes of different parts of the film are parallel to one another, and therefore magnetic domains with 180° walls should occupy most of the film area. Domain walls can move here even in a weak field. By contrast, in films on the fluorite substrate there are four different crystallographic orientations listed in Subsect. A, and this accounts for coexistence of magnetic domains with at least four different easy-axis directions, whose walls make different angles with the domain magnetizations. In such a film, magnetization by domain-wall motion requires stronger magnetic fields than that in the case of 180° domain walls, and therefore the hysteresis loop of the film on a fluorite substrate is wider than that for the film grown on a perovskite substrate.

As seen from Fig. 7, the resistance of the $x=0.15$ film on the fluorite substrate is two to three orders of magnitude larger than that of the $x=0.16$ film on the perovskite substrate. Moreover, the latter film has metallic conduction, and the maximum in its $R(T)$ relation lies slightly above T_C, whereas the former has semiconducting behavior. As mentioned in Subsect. A, the O-Mn-O bonds in the structure of the fluorite-based film make angles of 19.5, 70.5, and 90°, which makes Zener double exchange in it impossible. By contrast, the O-Mn-O bond angles in perovskite-based films are always close to 180°, thus creating favorable conditions for the Zener double exchange and, hence, for metallic conduction.

E. Two-phase magnetic states as the main cause of the maxima in electrical resistance and magnetoresistance near the Curie point

Calculations[7,8] show that Zener double exchange alone cannot account for the features observed experimentally in rare-earth–doped manganites, for instance, the large values of ρ above T_C and the jump in ρ in the vicinity of T_C. Besides, it predicts a weak dependence of ρ on the amount of doping, and magnetic-field and temperature dependences of ρ below T_C which are not observed in experiment.[7] It was proposed[8,9] to explain the anomalies in ρ and the colossal MR in these compounds as due to Zener double exchange combined with dynamic Jahn-Teller effect. In this way one can associate the metal-semiconductor crossover near T_C with a transition from the polaron-type conduction above T_C to the hopping regime below T_C. This assumption, however, is not capable of explaining the fact that the temperatures of the metal-semiconductor transition and of the maximum in MR are very close to the Curie point.

We are proposing another mechanism to account for the features observed in electrical resistance and magnetoresistance in these materials, namely, the existence of a two-phase magnetic state, which is characteristic of magnetic semiconductors.[1,2] It is known that the conduction-electron energy in magnetic semiconductors is the lowest at complete ferromagnetic (FM) ordering in the crystal. In a nondegenerate antiferromagnetic (AFM) semiconductor, however, the electron concentration is too small to change the state of the whole crystal. At the same time FM microregions can form in an AFM semiconductor through the gain in electron s-d exchange energy, and electrons stabilize them by self-trapping. As the impurity concentration increases, these FM drops in the AFM insulating matrix grow in size, which may result in percolation if the amount of doping is high enough. Thus we come to another two-phase magnetic state, with insulating AFM regions incorporated in a conducting FM matrix.

$La_{1-x}Sr_xMnO_3$ is a Sr-doped $LaMnO_3$ AFM semiconductor. The $x=0.15$ film with semiconducting behavior may be considered as being in a two-phase magnetic state of the first type, in which FM drops occluding charge carriers are distributed throughout an insulating AFM matrix. Application of an external magnetic field destroys the FM drops and releases the carriers trapped in them earlier, as a result of which the sample resistance drops abruptly, and one observes giant magnetoresistance. Above T_C, this two-phase magnetic state is thermally destroyed, and therefore there is no giant MR in this temperature region. It was shown[2] that the radius of FM drops is maximal near T_C, and this is why magnetoresistance reaches a maximum in absolute magnitude at these temperatures.

In films with $x=0.16$ and 0.23, where the conduction is metallic, one may expect the two-phase magnetic state of the second type to set in, in which insulating AFM microregions form in a conducting FM matrix. It was shown[10] that when in this type of state impurity-induced magnetic interaction can act on resistance by two mechanisms, namely, through scattering of carriers which reduces their mobility, and through formation of a band tail consisting of localized states. It was shown[10] that the mobility of the carriers decreases sharply in the vicinity of T_C, and they localize partially in the band tail. These phenomena result in an abrupt increase of resistance near T_C, which is observed in films with $x=0.16$ and 0.23. Application of an external magnetic field brings about delocalization of carriers from the band tails and an increase of their mobility,[10] which manifests itself in the onset of giant negative MR. Above T_C, this two-phase magnetic state is thermally destroyed, as a result of which magnetoresistance passes through a maximum in absolute magnitude near T_C.

Partial support of the Russian Fund for Fundamental Research (Grant 97-03-32979a) is gratefully acknowledged.

[1] É. L. Nagaev, Usp. Fiz. Nauk **166**, 833 (1996).
[2] É. L. Nagaev, *Physics of Magnetic Semiconductors* [in Russian] (Nauka, Moscow, 1979).
[3] A. Urushibara, Y. Moritomo, T. Aruma, A. Asamitsu, G. Kido, and Y. Tokura, Phys. Rev. B **51**, 14103 (1995).
[4] L. I. Koroleva, R. V. Demin, and A. M. Balbashov, JETP Lett. **65**, 474 (1997).
[5] O. Yu. Gorbenko, A. R. Kaul, N. A. Babushkina, and L. M. Belova, J. Mater. Chem. **7**, 747 (1997).
[6] A. Anane, C. Dupas, K. le Dang, J. P. Renard, P. Veillet, A. M. Guevara, F. Millot, L. Pinsard, and A. Revclevschi, J. Phys.: Condens. Matter **7**, 7015 (1995).
[7] A. J. Millis, P. B. Littlewood, and B. I. Shraiman, Phys. Rev. Lett. **74**, 5144 (1995).
[8] A. G. Millis, B. I. Shraiman, and R. Mueller, Phys. Rev. Lett. **77**, 175 (1996).
[9] A. J. Millis, Phys. Rev. B **53**, 8434 (1996).
[10] É. L. Nagaev, Phys. Lett. A **211**, 313 (1996).

Translated by G. Skrebtsov

Paramagnetism in copper monoxide systems

A. A. Samokhvalov, T. I. Arbusova, N. A. Viglin, S. V. Naumov, V. R. Galakhov, D. A. Zatsepin, Yu. A. Kotov, O. M. Samatov, and D. G. Kleshchev

Institute of Metal Physics, Russian Academy of Sciences (Ural Department), 620219 Ekaterinburg, Russia
(Submitted June 21, 1997)
Fiz. Tverd. Tela (St. Petersburg) **40**, 295–298 (February 1998)

This paper describes the problem of high-temperature superconductivity related to investigations of the magnetic susceptibility, electron paramagnetic resonance, and O $K\alpha$ x-ray emission spectra of samples from the following systems based on copper monoxide: CuO–Cu, CuO–Cu_2O and CuO–MgO. In all these systems, thermal processing results in a paramagnetism which is not observed in the individual components of these systems before they are processed. O $K\alpha$ spectra of the interface of a Cu–single-crystal CuO film structure indicate the presence of not only Cu^{2+} but also Cu^{1+} ions in the layer of CuO in close contact with Cu. Possible reasons for the appearance of paramagnetism in these systems are discussed. It is proposed that a paramagnetic layer at the contact between the antiferromagnetic copper monoxide and the other copper-oxide phases or with copper could be the cause of the impurity metastability observed previously in the high-T_c superconducting phase. © *1998 American Institute of Physics.* [S1063-7834(98)03002-0]

In Ref. 1 we showed that regions of a localized superconducting phase (seeds or fragments) with a critical temperature of 200–300 K form in specially prepared samples of copper monoxide. Unfortunately, the small content of this phase, equal to 2-3% by volume, prevents it to be identified by x-ray diffraction. However, information about this phase can be obtained by studying its properties. To this end, we have prepared several heterophase systems based on copper monoxide that imitate the specially treated samples of CuO, i.e., consisting of CuO, Cu and Cu_2O, and the system CuO–MgO. We also have investigated their magnetic properties, electron paramagnetic resonance, and O $K\alpha$ x-ray spectra, which allows us to determine the valence state of the copper ions. The samples underwent x-ray structure and x-ray phase analysis.

1. SAMPLES AND MEASUREMENT METHOD

Several series of samples based on CuO (CuO–Cu, CuO–Cu_2O and CuO–MgO) were prepared from reactants with the trademark OSC.

Samples of the CuO–Cu system were prepared from mixtures of CuO-Cu powders by stirring, pressing, and annealing in air at 600–650 °C for 1–3 min. X-ray phase analysis showed that the samples primarily contained the original phases CuO and Cu, but with a rather small admixture of Cu_2O (3%) formed by partial oxidation of copper when the mixture is heated in air. The samples used for investigating the O $K\alpha$ x-ray spectra were CuO–Cu heterostructures consisting of single-crystal CuO with a film of copper on the (110) plane. These heterostructure were identical to the heterostructure in which we observed a Meissner effect at $T=300$ K.[1]

Samples of the CuO–Cu_2O–Cu system were prepared by explosively atomizing a copper wire by passing a high-power current pulse through it in an air atmosphere. The samples consisted of a mixture of phases of CuO and Cu_2O in equal amounts with an admixture of 3–5 mol. % Cu in the form of finely dispersed powders.

Samples of the system CuO–Cu_2O were prepared hydrothermally at 160–170 °C over a period of 5 h from a suspension of $Cu(OH)_2$ and Cu_2O in a Na_2SO_4 solution.

Samples of the system CuO–MgO were prepared by annealing a pressed mixture of CuO and MgO powders in air at 300 °C for 40 h, i.e., under conditions in which the solid solution $Mg_{(1-x)}Cu_xO$ cannot form. The resulting samples consisted of a mixture of particles of MgO coated by a fine layer of CuO. In essence, this was an imitation of the thin-film state of CuO on an MgO substrate. X-ray phase analysis clearly showed only two phases: CuO and MgO.

In order to evaluate the role of a free surface (as opposed to bulk) in the magnetism of CuO, we prepared fine crystalline powders (with an average particle size of 10μm) of mono- and polycrystalline CuO. The resulting powders have a surface area that is several orders of magnitude larger than the bulk sample.

Thus, these samples were heterophase systems made up of CuO phases with Cu, Cu_2O or MgO. Since CuO is an antiferromagnet while Cu, Cu_2O and MgO are diamagnets, samples of these systems show no EPR signal before thermal processing, and their magnetic susceptibilities will not have any paramagnetic temperature dependence $\chi(T)$ (i.e., C/T). In this case $\chi(T)$ is determined by the additive sum of χ for CuO and the diamagnetic components. Thermal processing changes the magnetic properties of the samples considerably.

The magnetic susceptibility was measured in the temperature range from 70 to 500 K using magnetic Faraday weights with a sensitivity of 5×10^{-8} cm^3/g for $H=15$ kOe. The electron paramagnetic resonance was studied with an ERS-231 EPR spectrometer in X-band. The O $K\alpha$ x-ray emission spectra of the Cu–CuO interface were investigated with a JCXA-733 electron microprobe analyzer at 5 kV and 100 nA having an aperture width of 0.5 eV.

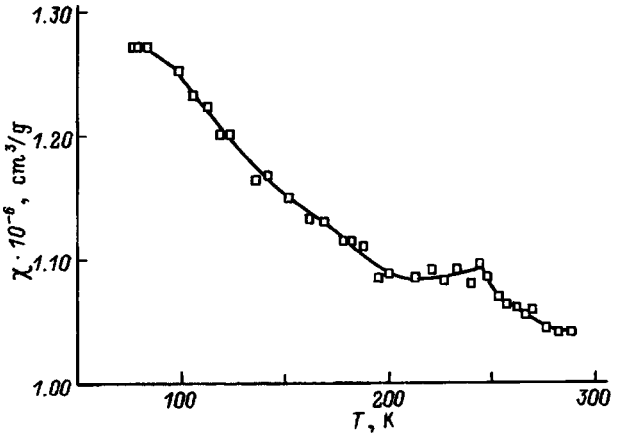

FIG. 1. Temperature dependence of the magnetic susceptibility of sample 0.79CuO+0.21Cu

2. RESULTS

1) *The CuO–Cu System.* Figure 1 shows the typical temperature dependence of the magnetic susceptibility $\chi(T)$ for samples with the composition 0.79CuO–0.21Cu by mole. It is clear that the function $\chi = C/T$, i.e., it is paramagnetic in character with a negative temperature coefficient that is opposite what it should be if $\chi(T)$ were determined only by the susceptibility of CuO (see Ref. 2). It is also clear that below 240 K $\chi(T)$ exhibits an anomaly against the background of overall paramagnetic dependence whose character is ''diamagnetic,'' i.e., whose contribution decreases the paramagnetic $\chi(T)$ (see Ref. 1).

2) *The $CuO-Cu_2O$ System.* Figure 2 shows the function $\chi(T)$ for two samples of the system $x\mathrm{CuO}+(1-x)\mathrm{Cu_2O}$ where $x=0.4$ and 0.5. These functions $\chi(T)$ are primarily paramagnetic in character, i.e., $\chi = C/T$; the paramagnetic contribution increases with increasing fraction of Cu_2O in the sample. As the fraction of CuO increases, $\chi(T)$ acquires an opposite dependence that is characteristic of CuO with a positive temperature coefficient.

3) *The CuO–MgO System.* Figure 3 shows the function $\chi(T)$ for samples of $x\mathrm{CuO}+(1-x)\mathrm{MgO}$ where $x=0.1$ and 0.2. Since MgO usually contains uncontrolled amounts of paramagnetic impurities, Fig. 3 also shows the function $\chi(T)$ for MgO and the difference $\Delta\chi = \chi_s - \chi_{\mathrm{CuO}} - \chi_{\mathrm{MgO}}$ (where χ_s is the magnetic susceptibility of the sample). By plotting this difference we eliminate the impurity paramagnetism of MgO from our results. It is clear that $\Delta\chi(T)$ has the same character as for the system $CuO–Cu_2O$ with increasing fraction of CuO.

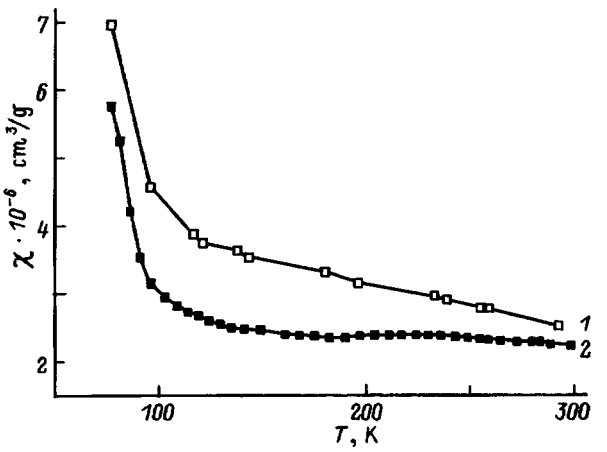

FIG. 2. Temperature dependences of the magnetic susceptibility of samples $0.4\mathrm{CuO}+0.6\mathrm{Cu_2O}$ (*1*) and $0.5\mathrm{CuO}+0.5\mathrm{Cu_2O}$ (*2*)

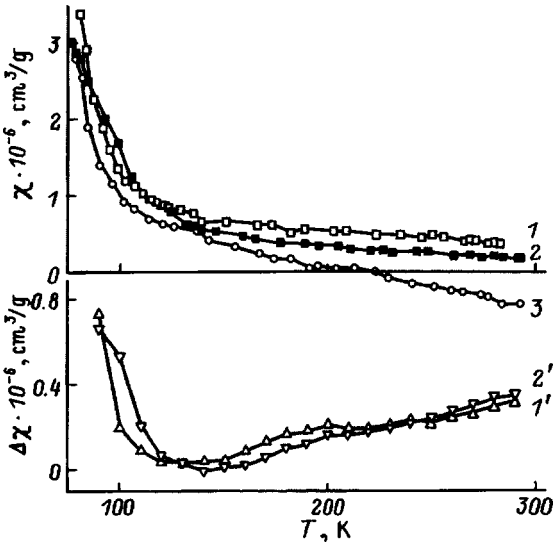

FIG. 3. Temperature dependences of the magnetic susceptibility of samples 0.2CuO+0.8MgO (1), 0.1CuO+0.9MgO (2), and MgO (3), and the difference $\Delta\chi = \chi_s - \chi_{\mathrm{CuO}} - \chi_{\mathrm{MgO}}$ for sample *1* (*1′*) and sample 2 (*2′*)

Comparative measurements of $\chi(T)$ for bulk and fine-powder samples of CuO show the same results within measurement error. This indicates that the free surface of CuO plays only a small role in creating the magnetic properties of copper monoxide.

EPR measurements show that whereas initial system impurities (before thermal processing) give rise to no EPR signal, samples of all the systems that showed a paramagnetic $\chi(T)$ have an easily measured EPR signal after thermal processing. Typical values of the EPR linewidth were in the range 100–1100 Oe for a g-factor equal to 2.00–2.20. For example, at 293 K for the CuO–MgO system, the 0.05CuO+0.95MgO sample had $\Delta H = 258 + 5$ Oe and $g = 2.182 \pm 0.005$, the $0.10\mathrm{CuO}\pm0.90\mathrm{MgO}$ sample had $\Delta H = 420 \pm 10$ Oe and $g = 2.164 \pm 0.005$, and the $0.20\mathrm{CuO}\pm0.80\mathrm{MgO}$ sample had $\Delta H = 570 \pm 20$ Oe and $g = 2.14 \pm 0.01$. Similar values of ΔH and the g-factor were obtained for the other systems as well.

The results of investigating the O $K\alpha$ x-ray emission spectra of the Cu–CuO interface are shown in Fig. 4. On this plot, we also show the CuO and Cu_2O spectra for comparison. It is clear that the Cu–CuO interface in the region of CuO in close contact with Cu contains not only Cu^{2+} but also Cu^{1+} ions.

3. DISCUSSION OF RESULTS

The results of these studies of the magnetic susceptibility and EPR of heterophase systems consisting of antiferromagnetic CuO and diamagnetic Cu, Cu_2O or MgO show that in all these systems thermal processing gives rise to a paramag-

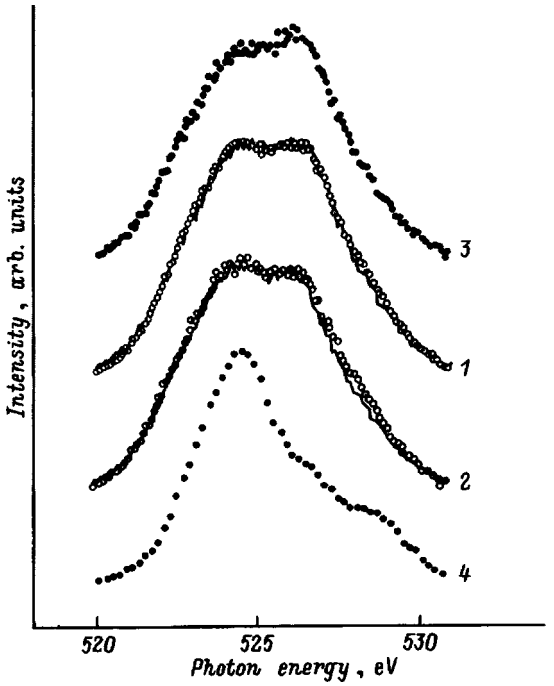

FIG. 4. O $K\alpha$ *x*-ray emission spectra for the Cu–CuO interface (*1*,*2*), CuO (*3*), and Cu_2O (*4*). The solid curves show fitted spectra for the Cu–CuO interface obtained by adding the CuO and Cu_2O spectra in the corresponding proportions (1—$0.95CuO+0.05Cu_2O$, 2—$0.79CuO+0.21Cu_2O$)

netic phase along with the antiferromagnetic CuO phase. The Cu, Cu_2O or MgO phases present in the samples have practically no effect on the magnetism of the system due to their small amounts and the weak temperature dependence of their diamagnetic susceptibilities.

The CuO–Cu system exhibits a ''diamagnetic'' anomaly against a background function $\chi(T)$ that is paramagnetic in character, due to the appearance of impurities (fragments) of a localized superconducting phase with a critical temperature of 240 K (see Ref. 1). Above 240 K, $\chi(T)$ is purely paramagnetic in character. We used the function $\chi(T)$ measured in this temperature range, taking into account the phase content of the sample (for a concentration of 2% of the paramagnetic phase; see Ref. 1), to make a best-guest estimate of the extrapolated Curie temperature, which turns out to be close to 0 K for an effective magnetic moment of $1.73\mu_B$, assuming a spin $S=1/2$ for the Cu^{2+} ions.

A similar picture of the appearance of paramagnetism applies also to the systems CuO–Cu_2O and CuO–MgO. For the system CuO–MgO the paramagnetism may be associated either with the thin film of CuO on the MgO grains or, as in the other systems, with CuO–MgO interfaces.

The observation of paramagnetism in the temperature dependence of the magnetic susceptibility is confirmed by the appearance of clear EPR signals in these systems. The observed dependence of the EPR linewidth on the composition of the CuO–Cu_2O system can be explained by exchange narrowing of the paramagnetic resonance linewidth. The values of ΔH and the g factor for this system are close to observed values for the specially prepared samples of CuO.[3]

Thus, systems based on copper monoxide exhibit a paramagnetism that is absent before thermal processing. In light of the small role played by the free surface in creating magnetism in CuO, we can assume that the physical reason for this paramagnetism in CuO is the defective nature of the surface layer of the CuO phase, which enhances contact with the other (diamagnetic) phases. This defective nature in turn leads to destruction of the antiferromagnetic exchange bonds in the near-contact CuO layer and conversion of a portion of the Cu^{2+} ions to the free magnetically-disordered (paramagnetic) state. In this case the possibility of antiferromagnetic ordering of this phase at low temperatures cannot be ruled out. It is well known that the presence of such a magnetically ordered state in low-dimensional cuprate compounds is one of the conditions for occurrence of high-temperature superconductivity. Another necessary condition for high-temperature superconductivity is metallic conductivity. In the copper monoxide based systems we have studied, and in the specially prepared samples of CuO, this metallic conductivity comes either from the metastable oxides Cu_4O, Cu_8O (see Refs. 4, 5) or the copper film. We can assume that in CuO–Cu systems, e. g., in polycrystalline mixtures of CuO–Cu phases or in heterostructure CuO single-crystal—Cu films as in the specially prepared samples of CuO, multiple interfaces (contacts) create a near-contact paramagnetic layer of copper–copper monoxide. This CuO–Cu interface could be the cause of the magnetic and electric anomalies we observed previously in Ref. 1, which we explained by an impurity superconducting phase with a high critical temperature. At this time it is difficult to say anything definite regarding the structure of this interface; however, several assertions can be made. Thus, the O $K\alpha$ spectra of the CuO–Cu interface imply that this interface contains both Cu^{2+} ions and Cu^{1+}, suggesting that the interface can contain the oxide CuO with the NaCl structure or the oxide Cu_4O_3, which favor the appearance of superconductivity (see Ref. 1). We also cannot exclude the possibility that seeds of polar Jahn-Teller centers form in the interface layer, or that phase separation occurs (see Ref. 1). Both these possibilities could also mediate the creation of an impurity superconducting phase at the CuO–Cu interface.

We may add that the assumption of paramagnetism localized in the CuO–MgO interface (and other interfaces based on CuO) agrees with the results of Ref. 6 with regard to multilayer CuO–MgO films. In this paper it was shown that paramagnetism in such films is localized to the CuO–MgO interface layer. As the thickness of the CuO layer decreases, i.e., as the role of the interface increases and the role of the bulk decreases, the Néel temperature of the film decreases and the film exhibits an overall paramagnetic temperature dependence for the magnetic susceptibility.

Thus, we can claim that heterophase systems based on copper monoxide exhibit a paramagnetism after thermal processing that is localized at interphase boundaries. The presence in these systems of other copper-oxide phases in addition to copper monoxide with metallic conductivity or copper in contact with a paramagnetic layer of copper monoxide could be the origin of the impurity metastable high-T_c superconducting phase observed previously.[1]

This work was carried out within the framework of the federal program ''Surface Atomic Structures'' (Project No 95-210).

[1] A. A. Samokhvalov, T. I. Arbusova, V. V. Osipov, N. A. Viglin, S. V. Naumov, N. I. Solin, B. A. Gizhevskiĭ, I. B. Smolyak, V. A. Teplov, V. P. Pilyugin, Fiz. Tverd. Tela (St. Petersburg) **38**, 3277 (1996) [Phys. Solid State **38**, 1788 (1996)].
[2] T. I. Arbuzova, A. A. Samokhvalov, I. B. Smolyak, B. V. Karpenko, N. M. Chebotaev, and S. V. Naumov. J. Magn. Magn. Mater. **95**, 168 (1991).
[3] N. A. Viglin, S. V. Naumov, and. A. Samokhvalov, Fiz. Tverd. Tela (St. Petersburg) **38**, *4*, 1277 (1996) [Phys. Solid State **38**, 706 (1996)].
[4] R. Guan, H. Hoshimoto, and T. Yoshida, Acta Cryst. B **40**, *6*, 109 (1984).
[5] R. Guan, H. Hoshimoto, and K. H. Kuo, Acta Cryst. B **40**, *6*, 560 (1984).
[6] M. Sohma, K. Kawaguchi, and Y. Fujii, J. Appl. Phys. **77**, 1189 (1995).

Translated by Frank J. Crowne

Exchange mechanism for localization of phonons near the surface of a magnetically ordered crystal

S. V. Tarasenko

Donetsk Physico-Technical Institute, Ukrainian Academy of Sciences, 340114 Donetsk, Ukraine
(Submitted June 21, 1997)
Fiz. Tverd. Tela (St. Petersburg) **40**, 299–304 (February 1998)

It is shown that first-principles inclusion of nonuniform exchange interaction leads to the creation of a new type of generalized shear acoustic wave propagating near the mechanically free surface of a magnet. Criteria are formulated that can be used to specify conditions under which an ''exchange'' type of surface acoustic wave can exist at the boundary between a magnetic and a nonmagnetic medium once the spectrum of magnetoelastic oscillations of the unbounded magnetic crystal is known. © *1998 American Institute of Physics.* [S1063-7834(98)03102-5]

It is well known from the acoustics of anisotropic media that surface acoustic waves can propagate without attenuation along a mechanically free crystal surface only when their velocities are below a certain limiting velocity. If this condition is not fulfilled, only traveling pseudosurface (leaky) elastic waves can exist, which generate bulk elastic oscillations and consequently decay in the direction of propagation. However, a qualitatively different situation arises when the propagation of an elastic wave along a mechanically free sample surface is collinear with one of the high-symmetry directions of the crystal. In this case, surface Rayleigh waves and the so-called limiting bulk waves can propagate simultaneously and independently. The latter, referred to as bulk elastic waves of shear type, have a wave displacement lying in the plane parallel to the free surface of the crystal. It is not difficult to show that such an acoustic wave simultaneously satisfies both the equation of motion of the elastic medium and the boundary conditions. When the velocity of propagation of the Rayleigh wave in this high-symmetry direction exceeds the velocity of the limiting bulk wave, small departures from the symmetry direction cause the solution for the bulk limiting wave to disappear, and instead it becomes possible to create an elastic surface quasibulk wave.[1–4] However, the conditions for localization of a limiting bulk wave turn out to be sensitive not only to the choice of propagation directions of the wave but also to changes in the character of the boundary conditions, even when a wave of this type propagates along a high-symmetry direction. This fact leads to the possibility of creating surface acoustic waves of shear type when piezoelectric[5,6] (piezomagnetic[7,8]) effects are present. The surface acoustic wave types listed above that propagate near a mechanically free surface (Rayleigh, quasibulk, and Gulyaev-Bleustein waves) can all exist not only in nonmagnetic but also in magnetic crystals. In this case the presence of a macroscopic ferromagnetic (antiferromagnetic) moment when $T<T_c$ (where T_c is the Curie temperature) in magnetic crystals (both exchange-collinear and exchange-noncollinear) can lead to additional mechanisms for piezomagnetic (piezoelectric) effects.[9] There are also other ways to generate shear surface acoustic waves near the surface of a magnetically ordered crystal. The presence of additional mechanisms for generating surface acoustic waves of shear type can be understood in light of the fact that there is a complete analogy between the generation of s-type magnetic polaritons and shear surface acoustic waves when the surface of the magnetic crystal is in continuous acoustic contact with a nonmagnetic insulating medium. This problem is greatly clarified by using Green's functions to eliminate the magnetic subsystem from consideration, When this is done, the magnetoelastic dynamics of the crystal can be described by using effective elastic moduli that now possess temporal dispersion. In analyzing the conditions for creation and propagation of shear surface acoustic waves with a given polarization, the role of the magnetic susceptibility tensor is played by a set of corresponding components of the effective elastic moduli of the crystal. Following the terminology introduced to analyze conditions for generation of surface polaritons,[10] we can speak of a type-I shear surface acoustic wave, which exists when a principal value of the effective elastic moduli tensor has a negative sign, and a type-II shear surface acoustic wave, which can exist for any sign of the effective elastic moduli. It should be noted that type-I shear surface acoustic waves also exists in situations where the effective acoustic retardation can be ignored (the elastostatic approximation; see Ref. 11). In this case these waves become elastostatic spin waves,[12] in complete agreement with the situation where surface magnetic polaritons (TE wave) become surface magnetostatic spin waves when the effects of electromagnetic retardation are ignored. As for type-II shear surface acoustic waves, they cannot exist without including the effect of acoustic retardation, and their spectrum ends at a point for which $k\neq 0$, i.e., they also can be referred to as ''virtual'' shear surface acoustic waves by analogy with type-II surface polaritons.[13] Finally, one more type of shear surface acoustic wave can exist in a magnetically ordered crystal when the spontaneous nonzero magnetization of the latter (for $T<T_c$) points along the normal to the propagation plane of the limiting bulk wave ($T>T_c$), or, when the spontaneous magnetization equals zero, the equilibrium antiferromagnetism and external magnetic-field vectors point along this direction. In terms of the matrix of effective elastic moduli this corresponds to a magnet with acoustic activity. However, despite intense studies of various aspects of the creation and propagation of surface acoustic waves in magnetically ordered crystals, the corresponding calculations tra-

ditionally neglect the nonuniform spin-spin interaction (''the exchangeless approximation''). In the few papers devoted to studying the effect of nonuniform spin-spin exchange on the conditions for localization and propagation of surface acoustic waves, the role played by nonlocality of the Heisenberg spin-spin exchange in the phonon dynamics of the crystal is reduced to converting surface acoustic waves into pseudosurface (leaky) acoustic waves, i.e., to delocalization of the latter.[14] The question of whether the exchange mechanism can localize phonons near the surface of a magnetically ordered crystal has yet to be addressed.

This latter fact provides the motivation for this paper, in which we determine the necessary conditions under which a new type of shear surface acoustic wave can exist near the mechanically free surface of a semi-infinite magnet, whose localization is determined by the nonlocality of the Heisenberg mechanism for spin-spin interaction, i.e., without taking into account the magnetic-dipole interaction.

The structure of the paper involves several sections. In the first section, general boundary conditions are formulated for a two-sublattice model of a rhombic antiferromagnet based on first-principles with inclusion of magnetoelasticity and nonuniform exchange interactions, assuming that the antiferromagnet occupies a space whose surface is free from elastic stresses and the spins are completely unpinned. In the second section, the possible types of shear acoustic oscillations propagating along a high-symmetry direction are classified with respect to the character of their localization near the boundary of the magnetic medium. In the third section, a solution to the boundary problem formulated above is found that is localized near the surface of the magnet, and its dispersion relation is investigated for a generalized shear surface acoustic wave traveling along the surface separating the media. In a separate (fourth) section we investigate how surface magnetic anisotropy affects the character of spatial localization of this type of surface acoustic wave. In the fifth section of the paper, based on results obtained in the previous sections, criteria are proposed for the existence of this type of surface acoustic wave at a free surface of a magnetic half-space with free spins in the presence of nonuniform spin-spin exchange. These criteria can be used to identify sufficient conditions under which generalized shear surface acoustic waves of exchange type can exist at the surface of a magnet with completely unpinned spins once the structure of the spectrum of normal magnetoelastic oscillations of the unbounded magnet is known. In the last section of the paper we state the conclusions that follow from these results.

1. BASIC RELATIONS

It is well known that exchange simultaneously enhances magnetoelastic effects and weakens magnetic-dipole effects in ferromagnets.[15] As an example of this, consider the magnetoelastic dynamics of a two-sublattice model (here $\mathbf{M}_{1,2}$ are the magnetizations of the sublattices and $|\mathbf{M}_1|=|\mathbf{M}_2|=M_0$) of a rhombic antiferromagnet. If we introduce the ferro- and antiferromagnetic vectors ($\mathbf{m}$ and $\mathbf{l}$), then for a sufficiently weak magnetic field H (compared to the exchange field) the following approximation holds with good accuracy:

$$|\mathbf{m}|\ll|\mathbf{l}|, \quad \mathbf{m}=\frac{\mathbf{M}_1+\mathbf{M}_2}{2M_0}, \quad \mathbf{l}=\frac{\mathbf{M}_1-\mathbf{M}_2}{2M_0}. \tag{1}$$

Taking this circumstance into account, we can write the energy density W of a rhombic antiferromagnet that includes the interaction of the magnetic and elastic subsystems of the crystal in the form[16]

$$W=W_m+W_{me}+W_e, \tag{2}$$

$$W_m=M_0^2\left\{\frac{\delta}{2}\mathbf{m}^2+\frac{\alpha}{2}(\nabla\mathbf{l})^2+\frac{\beta_z}{2}l_z^2+\frac{\beta_y}{2}l_y^2\right\},$$

$$W_{me}=\gamma M_0^2 l_1 l_k u_{1k}, \tag{3}$$

$$W_e=\frac{\lambda}{2}u_{11}^2+\mu u_{1k}^2, \tag{4}$$

where

$$u_{1k}=\frac{1}{2}\left(\frac{\partial u_1}{\partial x_k}+\frac{\partial u_k}{\partial x_1}\right)$$

is the strain tensor, λ, μ, and γ are the Lamé coefficient, the shear modulus, and the magnetoelastic interaction constant respectively, $\beta_{u,z}$ is the magnetic anisotropy constant, and δ and α are the uniform and nonuniform exchange constants respectively. In what follows, we shall assume without loss of generality that the following relation holds between the magnetic anisotropy constants ($\beta_{y,z}$) calculated with magnetostrictive strain included (in the ground state):

$$\beta_z\geqslant\beta_y>0. \tag{5}$$

This corresponds to equilibrium orientation of the antiferromagnetism vector along the OX axis. It is well known that the dynamics of this model are described by a closed system of equations consisting of the Landau-Lifshits equations for the sublattice magnetizations and the basic equation for the displacement vector $\mathbf{u}$ from the theory of elasticity. If the magnetic medium occupies a half-space with a mechanically free surface at which the spins are entirely unpinned, then the system of boundary conditions that determines the linear surface magnetoelastic dynamics for this model of the magnet (we assume that the normal to the magnet surface $\mathbf{n}$ coincides with one of the Cartesian axes of the coordinate system introduced above) can be cast in the form

$$\frac{\partial\tilde{\mathbf{l}}_{y,z}}{\partial\xi}=0, \quad \sigma_{1k}n_k=0, \quad \xi=0,d,$$

$$\tilde{\mathbf{l}}_{y,z}\to 0, \quad \xi\to-\infty, \tag{6}$$

where $\tilde{\mathbf{l}}$ describes the amplitude of small oscillations of the antiferromagnetism vector $\mathbf{l}$ near the equilibrium direction ($\mathbf{l}\parallel 0X$), ξ is the coordinate along the direction $\mathbf{n}$, and σ_{1k} is the elastic stress tensor.

Following the standard method for solving boundary value problems, we look for a solution to this dynamic system of equations, for instance for $\tilde{l}$, that is localized near the free surface of the magnet, i.e., in the form

$$\tilde{l}\approx\sum_j^N A_j\,\exp(i\omega t-q_j\xi-1k_\perp r_\perp), \tag{7}$$

where A_j are arbitrary constants. The quantities q_j^2 ($q^2 \equiv -(kn)^2$, $1 \leqslant j \leqslant N$), which are roots of the dispersion (characteristic) equation, determine the spectrum of magnetoelastic oscillations of the magnet without taking into account the boundary conditions; $k_\perp$ and $r_\perp$ are respectively the projections of the wave vector and running coordinate along the propagation direction of the magnetoelastic oscillations in the plane of the boundary. For our model, the dispersion equation is a fifth-order polynomial ($N=5$) in q^2. As a result, the corresponding dispersion equation will be very awkward in general, and its solution will be possible only by numerical methods. Therefore, in what follows we limit ourselves to considering only shear acoustic oscillations propagating along high-symmetry directions of the crystal (i.e., in planes normal to a Cartesian coordinate axis). Moreover, by virtue of Eq. (5) we need consider only the interaction of elastic oscillations with the low-frequency magnon mode of the spectrum of an unbounded antiferromagnet Eq. (2). As an example, let us consider the case $\mathbf{n} \parallel 0X$, $\mathbf{k} \in XZ$. Calculations show that the characteristic equation for the magnetoelastic boundary value problem under discussion is a reduced biquadratic equation in q whose coefficients are functions of two external parameters specified by experiment: the oscillation frequency ω and the component perpendicular to $\mathbf{n}$ of the wave vector of the magnetostatic oscillations $k_\perp$:

$$q^4 - P_1 q^2 + P_2 = 0, \quad P_1 = \frac{\omega_0^2 + 2c^2 k_\perp^2 - \omega^2(1 - c^2/s^2)}{c^2},$$

$$P_2 = \frac{\omega_0^2 + c^2 k_\perp^2 + \omega_{me}^2 - \omega^2}{c^2}(k_\perp^2 - \omega^2/s^2). \tag{8}$$

Here $c^2 = g^2 \alpha \delta M_0^2/2$ and s is the velocity of the propagating spin and shear elastic waves in an unbounded magnet Eq. (2), g is the gyromagnetic ratio, and ω_0 and ω_{me} are respectively the activation and magnetoelastic gaps for that mode of the spectrum of normal spin waves of an unbounded magnet Eq. (2) for which $\tilde{\mathbf{l}} \parallel 0Y$ when $\mathbf{k} \in XZ$.

Using Eqs. (7), (8), we can classify the possible types of propagating magnetoelastic oscillations based on the character of their spatial localization near the magnet surface.

2. CLASSIFICATION OF POSSIBLE TYPES OF MAGNETOELASTIC EXCITATIONS

Analysis of Eqs. (7) and (8) shows that depending on the magnitudes of the frequency ω and the wave vector projection $k_\perp$ of $\mathbf{k}$ onto the plane of the film, four fundamentally different types of propagating two-component magnetoelastic normal oscillations are possible, which differ in the character of their spatial localization along the normal to the magnet surface ($q_{1,2}$ are roots of Eq. (8), and $\omega_\pm^2(k_\perp)$ are the roots of the equation $P_1^2 = 4P_2$, which is quadratic in ω^2).

A. Type-I bulk magnetoelastic waves ($q_1^2 < 0$, $q_2^2 < 0$):

$$k_\perp < k_2, \quad \omega_0^2 + \omega_{me}^2 + c^2 k_\perp^2 < 2,$$

$$k_2 < k_\perp, \quad \omega^2 > s^2 k_\perp^2,$$

$$k_1 < k_\perp < k_2, \quad \omega_+^2(k_\perp) < \omega^2 < s^2 k_\perp^2,$$

$$k_2 < k_\perp < k_3, \quad \omega_+^2(k_\perp) < \omega^2 < \omega_0^2 + \omega_0^2 + \omega_{me}^2 + c^2 k_\perp^2. \tag{9}$$

B. Surface magnetoelastic waves ($q_1^2 > 0$, $q_2^2 > 0$):

$$k_3 < k_\perp, \quad \omega_+^2(k_\perp) < \omega^2 < \omega_0^2 + \omega_{me}^2 + c^2 k_\perp^2,$$

$$0 < k_\perp < k_1, \quad \omega^2 < s^2 k_\perp^2,$$

$$k_1 < k_\perp < k_4, \quad \omega^2 < \omega^2(k_\perp). \tag{10}$$

C. Quasisurface magnetoelastic waves ($\mathrm{Re}\, q_{1,2}^2 \neq 0$; $\mathrm{Im}^2\, q_{1,2} \neq 0$):

$$k_1 < k_\perp, \quad \omega_-^2(k_\perp) < \omega_1^2 < \omega_+^2(k_\perp). \tag{11}$$

D. Type-II bulk magnetoelastic waves ($q_1^2 > 0$, $q_2^2 < 0$):

$$k_2 < k_\perp, \quad \omega_0^2 + \omega_{me}^2 + c^2 k_\perp^2 < \omega^2 < s^2 k_\perp^2,$$

$$k_\perp < k_2, \quad s^2 k_\perp^2 < \omega^2 < \omega_0^2 + \omega_{me}^2 + c^2 k_\perp^2. \tag{12}$$

Here $\omega_0^2 = g^2 c^2 \beta_y / \alpha$, $\omega_{me}^2 = g^2 c^2 \gamma^2 M_0^2/(\mu\alpha)$ for $\mathbf{k} \in XZ$ ($\mathbf{u} \parallel 0Y$) and

$$k_1^2 = \omega_0^2/(s^2 - c^2), \quad k_2^2 = (\omega_0^2 + \omega_{me}^2)/(s^2 - c^2),$$

$$k_3^2 = (\omega_0^2 + \omega_{me}^2)(1 + s^2/c^2)/(s^2 - c^2), \quad \omega_-^2(k_4) = 0.$$

Analysis of Eqs. (9)–(12) in the geometry under discussion reveals one particular characteristic feature of the spectrum of bound magnon-phonon oscillations induced by the simultaneous inclusion of nonuniform exchange and acoustic retardation: the presence at the surface of ''high-'' and ''low-frequency'' bands of parameters ω and $k_\perp$ in which surface magnetoelastic waves can coexist with both type-I and type-II bulk magnetoelastic waves.

3. GENERALIZED SHEAR SURFACE ACOUSTIC WAVES OF EXCHANGE TYPE

Using Eqs. (6)–(12), we now can turn to a more detailed investigation of surface linear magnetoelastic dynamics of a semi-infinite rhombic antiferromagnet. The corresponding dispersion equation can be written in the form

$$q_1^2 + q_2^2 + q_1 q_2 - (k_\perp^2 - \omega^2/s^2) = 0,$$

$$q_{1,2}^2 = \frac{P_1}{2} \pm \left[\left(\frac{P_1}{2} \right)^2 - P_2 \right]^{1/2}. \tag{13}$$

Analysis shows that Eq. (13) describes a two-component shear surface acoustic wave of exchange type, whose dispersion law can be found from Eq. (13) in explicit form for arbitrary $k_\perp$ ($k_\perp a \gg 1$, where a is the lattice constant):

$$\omega^2 = \frac{N_1}{2} + \left[\left(\frac{N_1}{2} \right)^2 - N_2 \right]^{1/2},$$

$$N_1 = \frac{2\omega_0^2 + c^2 k_\perp^2 - c^2(\omega_0^2 + \omega_{me}^2 + c^2 k_\perp^2)/s^2}{1 - c^2/s^2},$$

$$N_2 = \frac{(\omega_0^2 + c^2 k_\perp^2)^2 - c^2 k_\perp^2(\omega_0^2 + \omega_{me}^2)}{1 - c^2/s^2}. \tag{14}$$

The appearance of this type of surface magnetoelastic wave at the boundary between a magnetic and nonmagnetic media is a consequence of the influence of nonuniform ex-

change on the interaction of bulk elastic and low-frequency bulk spin modes of an unbounded magnet. In this case, both the elastic displacement vector $\tilde{u}$ and the amplitude of oscillations of the antiferromagnetism vector $\tilde{l}$ are polarized linearly and directed along the normal to the sagittal plane of the surface acoustic wave.

Comparison of Eqs. (13) and (14) with Eqs. (9)–(12) shows that this type of surface acoustic wave is delocalized when $k_\perp = k_\perp \neq 0$ and transforms into a bulk elastic wave. However, if $k_0 < k_\perp < k_*$ (where $k_* = 6\omega_{me}/5c$), the shear surface acoustic wave under study is a two-component generalized surface elastic wave whose dispersion curve for $k_\perp = k_*$ becomes a two-component surface elastic wave (in Eq. (7) we have $q_{1,2}^2 > 0$). It is simple to show that this type of localized magnetoelastic excitation cannot occur without including the nonuniform exchange interaction ($\alpha \to 0$).

4. EFFECT OF SURFACE MAGNETIC ANISOTROPY

The dispersion characteristics of the traditional types of shear surface acoustic waves are practically independent of the character of the surface magnetic anisotropy; however, analysis shows that this is by no means true for the shear surface acoustic wave of exchange type discussed in this paper. To illustrate this statement, let us assume as before that the surface of the magnetic half-space is mechanically free, but that the spins are partially pinned at the surface (here b is the constant for uniaxial surface magnetic anisotropy). In this case, the system of boundary conditions that determines the linear surface magnetoelastic dynamics for this model of the magnet takes the following form in place of Eq. (6):

$$\frac{\partial \tilde{l}_{y,z}}{\partial \xi} + b\,\tilde{l}_{y,z} = 0, \quad \sigma_{1k} n_k = 0, \quad \xi = 0, d,$$

$$\tilde{l}_{y,z} \to 0, \quad \xi \to -\infty. \tag{15}$$

Calculations show that when the surface magnetic anisotropy is included, the dispersion relation for surface magnetoelastic oscillations in this model of an antiferromagnet can be written in the form

$$q_1^2 + q_2^2 + q_1 q_2 - (k_\perp^2 - \omega^2/s^2) = b(q_1 + q_2). \tag{16}$$

If the spins are partially pinned, then it is not possible to find an exact solution to the dispersion Eq. (9) in explicit form. However, we can investigate the main consequences of allowing the surface magnetic anisotropy to influence the localization of this type of surface acoustic wave near a mechanically free magnet surface by considering the point at which this surface acoustic wave transforms into a bulk elastic wave in the case of easy-plane surface magnetic anisotropy ($b < 0$):

$$k_1^2(b) = \frac{\omega_0^2 - c^2 b^2}{s^2 - c^2}. \tag{17}$$

Comparison of Eq. (17) and Eqs. (9)–(12) shows that easy-plane surface magnetic anisotropy ($b < 0$) leads to abrupt (compared to Eq. (13)) localization of the traveling spin wave near the surface in the region of relatively small $k_\perp$. In this case the spin wave becomes a pure surface wave ($q_{1,2}^2 > 0$), which agrees with Eqs. (9)–(12) for the low-frequency band of surface magnetoelastic excitations. If, however, the surface magnetic anisotropy is the easy-axis type ($b > 0$), it follows from Eq. (16) that for small $k_\perp$ there is no localization at all of magnetoelastic excitations of this type near the magnet surface. However, with increasing $k_\perp$ the influence of pinning of the magnetic moments on the character of the dispersion curves Eq. (16) is gradually weakened until for $k_\perp = k_{*1}(b)$ the surface acoustic waves, both for this and the previous case, smoothly pass into the regime of quasisurface (generalized) magnetoelastic waves. As $k_\perp$ continues to increase, the localized surface acoustic wave determined by Eq. (16) smoothly passes into the regime of ''high-frequency'' surface magnetoelastic waves Eq. (9)–(12) when $k_\perp = k_{*2}(b)$. Analysis of Eqs. (16) and (17) shows that the value of the easy-plane anisotropy constant cannot be higher than a certain critical value, otherwise the directions of the equilibrium magnetization will be different in the bulk and near the surface of the magnet.[17]

5. CRITERIA FOR GENERATING GENERALIZED SHEAR SURFACE ACOUSTIC WAVES OF EXCHANGE TYPE

In order to observe this type of magnetoelastic surface acoustic wave experimentally, it is clearly vital to find criteria based on analysis of the spectrum of magnetoelastic oscillations of an unbounded magnet [in this case Eq. (8)] that indicate what relative orientations of the vectors l, n and $k_\perp$ allow the exchange type of shear magnetoelastic surface acoustic waves to exist along the mechanically free surface of the magnet. To find these criteria, it is above all necessary to note that [as follows from Eq. (14)] the corresponding antiferromagnet should be, according to the terminology of Ref. 18, a low-temperature antiferromagnet, i.e., $T_N > T_D$ [where $T_N(T_D)$ is the Néel (Debye) temperature]. Even if this condition is fulfilled, however, it follows from Eq. (8) that the new type of shear surface acoustic wave found in this paper will propagate in this high-symmetry direction only if the direction along which conditions are realized for strong magnetoelastic coupling in the unbounded antiferromagnetic crystal[14] coincides with the direction n normal to the boundary between the magnetic and nonmagnetic media for the semi-infinite magnet. Our confidence in the correctness of this criterion is based on solutions for the boundary value problem Eq. (6) for propagation of magnetoelastic oscillations in planes other than those associated with Eqs. (8)–(17). Calculation shows that analogous types of magnetoelastic shear surface acoustic waves arise from the model Eqs. (2)–(6) when $\mathbf{n} \parallel 0Y$ and $\mathbf{k} \in YZ$ ($\tilde{l} = \tilde{l}_z$) as well.

It is noteworthy that this type of magnetoelastic shear surface acoustic wave can be viewed as intermediate in nature between the first and second kinds of magnetoelastic surface acoustic waves, since, like the first kind of magnetoelastic shear surface acoustic wave, it can also exist without inclusion of acoustic retardation, but its existence does not require that the effective elastic modulus simultaneously have a negative sign, as is the case for ''virtual'' magnetoelastic surface acoustic waves.

Thus, from the results obtained above it follows that 1) first-principles incorporation of nonlocal Heisenberg exchange effects into the interaction of spin and elastic subsystems in a bounded magnet can lead to localization of phonons near the surface of a magnetically ordered crystal and the generation of a new type of surface magnetoelastic oscillation—the shear surface acoustic wave of exchange type; 2) the character of localization of this type of surface acoustic wave near the surface of a magnetically ordered crystal depends considerably on the character of the surface magnetic anisotropy, in which case the character of the spatial localization of this type of magnetoelastic oscillation depends significantly on the value of the wave number; 3) a necessary condition for the existence of this type of surface magnetoelastic excitation in the case of a semi-infinite low-temperature antiferromagnet is that the direction of the normal to the boundary between the magnetic and nonmagnetic medium coincide with the direction along which conditions for strong magnetoelastic coupling hold in the unbounded model of the antiferromagnet.

As a result, when first-principles magnetoelastic and nonuniform exchange interactions are included in the description of a magnetically ordered crystal, the crystal can support a Rayleigh type of surface elastic wave propagating along a high-symmetry direction in addition to surface acoustic waves, even in the absence of magnetic-dipole interactions—a shear magnetoelastic surface acoustic wave of exchange type.

In conclusion, the author expresses his deep gratitude to A. N. Bogdanov and T. N. Tarasenko for support of the idea of this paper and for fruitful discussions.

[1] V. N. Lyubimov and D. G. Sannikov, Fiz. Tverd. Tela (Leningrad) **15**, 1851 (1973) [Sov. Phys. Solid State **15**, 1234 (1973;)].
[2] V. N. Lyubimov and D. G. Sannikov, Fiz. Tverd. Tela (Leningrad) **17**, 478 (1975) [Sov. Phys. Solid State **17**, 300 (1975)].
[3] E. Lote and V. I Al'shits, Kristallografiya **22**, *5*, 906 (1977) [Sov. Phys. Crystallogr. **22**, 519 (1977)].
[4] V. I. Al'shits and E. Lote, Kristallografiya **23**, *5*, 901 (1978) [Sov. Phys. Crystallogr. **23**, 509 (1978)].
[5] Yu. V. Gulyaev, JETP Lett. **9**, 40 (1969).
[6] J. L. Bleustein, Appl. Phys. Lett. **13**, 412 (1968).
[7] Yu. V. Gulyaev, Yu. A. Kuzavko, I. N. Oleĭnik, and V. G. Shavrov, Zh. Éksp. Teor. Fiz. **87**, *8*, 674 (1984) [Sov. Phys. JETP **60**, 386 (1984)].
[8] M. I. Kaganov and Yu. A. Kosevich, Surfaces **5**, *3*, 148 (1986) [in Russian].
[9] Yu. V. Gulyaev, I. E. Dikshteĭn, and V. G. Shavrov, Usp. Fiz. Nauk **147**, 429 (1997).
[10] N. D. Dmitruk, V. G. Litochenko, and V. L. Strizhevskiĭ, *Surface Polaritons in Semiconductors and Dielectrics* (Naukova Dumka, Kiev 1989) [in Russian].
[11] Yu. I. Sirotin and M. P. Shaskol'skaya, *Principles of Crystallography* (Nauka, Moscow, 1979) [in Russian].
[12] S. V. Tarasenko, Zh. Éksp. Teor. Fiz. **110**, 1411 (1996) [Sov. Phys. JETP **83**, 778 (1996)].
[13] V. M. Agranovich and V. L. Ginzburg, Crystal Optics with Spatial Dispersion, and Excitons, 2nd ed. (Springer-Verlag, New York, 1984) [Russ. original 2nd ed., Nauka, Moscow, 1979].
[14] R. E. Camley and R. Q. Scott, Phys. Rev. B **11**, 4327 (1978).
[15] E. A. Turov and V. G. Shavrov, Usp. Fiz. Nauk **140**, 429 (1983) [Sov. Phys. Usp. **26**, 593 (1983)].
[16] A. L. Sukstanskiĭ and S. V. Tarasenko, Zh. Éksp. Teor. Fiz. **105**, 928 (1994) [Sov. Phys. JETP **78**, 498 (1994)].
[17] M. I. Kaganov and A. V. Chubukov, *Magnetic Properties of Crystalline and Amorphous Media* (Nauka, Novosibirsk, 1989).
[18] V. I. Ozhogin and V. L. Preobrazhenskiĭ, Usp. Fiz. Nauk **155**, *4*, 593 (1988) [Sov. Phys. Usp. **31**, 713 (1988)].

Translated by Frank J. Crowne

Pulsed magnetization reversal of single-crystal iron borate in the presence of a transverse magnetic field

O. S. Kolotov, A. P. Krasnozhon, and V. A. Pogozhev

M. V. Lomonosov State University at Moscow, 119899 Moscow, Russia
(Submitted 24 July, 1997)
Fiz. Tverd. Tela (St. Petersburg) **40**, 305–309 (February 1998)

This paper describes the first investigations of the process of pulsed 180° magnetization reversal in iron borate in the presence of a transverse magnetic field. How the intensity of magnetoelastic oscillations depends on the amplitude of the magnetization reversal field and the duration of the primary period of the transient process is studied, and also the analysis of hodographs of the magnetization vector, which show that the primary reason why the pulsed magnetization reversal curve exhibits a kink is a decrease in the energy lost to excitation of magnetoelastic oscillations, caused by lagging of the elastic subsystem of the crystal behind the magnetic subsystem for magnetization reversal times less than 13–16 ns. © *1998 American Institute of Physics.* [S1063-7834(98)03202-X]

The study of transient processes in single crystals of $FeBO_3$ (iron borate) is of special interest since this magnet exhibits an interaction between the elastic and magnetic subsystems of the crystal in a way that is most remarkable and accessible to investigation.[1–3] It has now been established[2–4] that the magnetoelastic interaction can have a strong effect on the form of the primary pulsed integral characteristics, i.e., the pulsed magnetization reversal curve, in which the inverse duration of the transient process τ^{-1} is plotted versus the amplitude of the magnetization reversal field H_s. It is observed that the ''freezing'' of the crystal lattice previously seen in ferro- and antiferromagnetic resonance experiments at frequencies of $\sim 10^3-10^4$ MHz,[5,6] really begins to appear at magnetization reversal times $\leqslant 13-16$ ns. However, only one transient process has been investigated in detail—that of pulsed 180° magnetization reversal (at zero transverse field). In order to obtain a deeper understanding of the peculiarities of magnetic interactions and their influence on the transient processes that occur, it is desirable to broaden the range of processes under study. Thus, the study of 90° pulsed magnetization could reveal the reason for the kink we discovered in the curve $\tau^{-1}(H_s)$.[7] Analysis of the hodograph of the magnetization vector has shown that throughout the range of fields H_s studied to date the magnetization of single crystals of $FeBO_3$ takes place via a quasi-uniform rotation of the magnetization vector. Thus it is unambiguously established that the shape of the curve $\tau^{-1}(H_s)$ is entirely determined by the character of energy loss to pulsed excitation of magnetoelastic oscillations.

In this paper we describe the first studies of pulsed 180° magnetization reversal of single crystals of $FeBO_3$ in the presence of a transverse magnetic field $H_\perp$. Based on studies of Fe–Ni films,[8,9] we might expect that, for a sufficiently large value of the field $H_\perp$, magnetization reversal of iron borate will take place by a quasi-uniform rotation of the magnetization. In itself, confirmation of the validity of this assertion would be of great value to the evolving understanding of the physics of transient processes, since it would imply an additional way to directly confirm that equations of motion for the magnetization can be used to describe pulsed magnetization reversal. Up to now detailed confirmation that this is true has been obtained only for Fe–Ni films (for example, in Ref. 8). However, since these films are polycrystalline in structure, it is not possible to study them with sufficient theoretical precision. Our interest lies in the possibility of obtaining unequivocal indications that magnetoelastic oscillations can affect the shape of the pulsed magnetization reversal curve.

1. EXPERIMENTAL METHOD

We studied six single crystals of $FeBO_3$, with thicknesses ranging from 24 to 110 μm and irregular polygonal shapes with transverse dimensions 3–8 mm. In the absence of external fields, the total magnetic moment of each single crystal was close to zero. The minimum DC magnetic field intensity H_{sat} that produces technical saturation in any direction in the plane of the sample (perpendicular to the c axis) was in the range 1.4–2.5 Oe for various samples. Our results are illustrated by a sample with the following parameters: thickness of 45 μm, saturation field $H_{sat}=1.4$ Oe, and period of magnetoelastic oscillations of 22 ns.

Our investigations were carried out in an induction apparatus similar to the one used to study pulsed properties of Fe–Ni films.[10] The samples were placed in a magnetization reversal apparatus consisting of a short-circuited segment of stripline. The amplitude of the magnetization reversal pulses reached 12 Oe, with a duration of the leading edge τ_f that did not exceed 1 ns.[14]

In order to construct the hodograph of the magnetization vector **M** we analyzed its components M_x and M_y collinear and perpendicular to the pulse field $\mathbf{H}_s$ respectively. Their changes were recorded by longitudinal and transverse removable coils.[8–10] A signal induced in one of these was sent to a stroboscopic converter, then processed by a device that automaticaly subtracts out noise, then sent through a low-frequency RC filter to a plotter. Graphical integration of the plotter signals yields instantaneous relative values of the components $m_x=M_x(t)/M_s$ and $m_y=M_y(t)/M_s$, where M_s is the saturation magnetization.

The initial saturated state of the sample is set by an adjustable DC magnetic field $H_0 \approx (1.25-1.5)H_{sat}$ and a transverse magnetic field $H_\perp \approx 0.4-0.6$ Oe. The field H_0 is directed antiparallel to the pulse field H_p that drives the process under study, and the field $H_\perp$ is perpendicular to the latter. In what follows, we will understand the quantity $H_s = H_p - H_0$ to be the amplitude of the magnetization reversal field. Since there is practically no anisotropy in the plane of the sample,[6,11] we can assume that in the original state ($t \leqslant 0$)

$$m_{0x} = \frac{H_0}{\sqrt{H_0^2 + H_\perp^2}}, \quad m_{0y} = \frac{H_\perp}{\sqrt{H_0^2 + H_\perp^2}}, \tag{1a}$$

while in the final state ($t \to \infty$)

$$m_{lx} = \frac{H_s}{\sqrt{H_s^2 + H_\perp^2}}, \quad m_{ly} = \frac{H_\perp}{\sqrt{H_s^2 + H_\perp^2}}. \tag{1b}$$

In our arrangement we used auxiliary magnetic field pulses of durations ~ 100 μs, which are suppressed for 60 μs before the start of the process under study and repeated with a frequency that is half the frequency of the H_p pulses.[10] Their purpose is to saturate the sample (in the direction of the field $\mathbf{H}_s$) before the arrival of every other H_p pulse and in this way ensure conditions for separating the signal from noise. In order that the accuracy of this operation not depend on the transverse field, the latter is chosen to be a pulsed field as well. Pulses of this field (with duration ~ 100 μs) arrive at the sample under study at a rate that is half the repetition rate of the H_p field pulses, but within the period in which the saturating pulses are suppressed.

As in previous studies of transient processes, we are interested in the correlation between the duration of the ''primary period'' of magnetization reversal and the intensity of the magnetoelastic oscillations. The duration of the primary period τ_e is taken to be the interval between times t_i and t_f at which the longitudinal signal voltage is 0.1 of its amplitude A_m. Following this primary period we observe decaying signal oscillations which, as we showed previously,[1–4] are signs of pulse-induced magnetoelastic oscillations. As a measure of the intensity of the latter, the amplitude A_1 of oscillations in the longitudinal signal voltage (measured during the first oscillation period immediately after the end of the primary period) is used. Since in the majority of cases $A_1 < 0.1A_m$, our definition of the duration coincides with the definition of magnetization reversal time most widely used in the literature.[10,12] As the field intensity H_s increases, from ~ 85 to $\sim 96\%$ of the total change in magnetization takes place during the primary period, i.e., within τ_e. Therefore, we will consider the quantity τ_e to be the magnetization reversal time, and refer to the curve $\tau_e^{-1}(H_s)$ as the pulsed magnetization reversal curve.

2. RESULTS AND DISCUSSION OF THEM

In this work, as in our previous studies of transient processes,[2–4,7] the most significant result is that the process under discussion here leads to a pulsed magnetization reversal curve with two well-defined segments. Figure 1 shows as an example the pulsed magnetization reversal curve obtained in fields $H_0 = 2$ Oe and $H_\perp = 0.5$ Oe. This curve exhibits a kint at a field $H_s = H_{br} = 3.7$ *Oe*, accompanied by an abrupt increase in the magnetization reversal rate. We also found that for transverse field intensities exceeding 0.4–0.6 Oe (depending on the sample), magnetization reversal of an iron borate crystal actually takes place by quasiuniform rotation of the magnetization over the entire range of fields H_s investigated. In order to confirm this, we show magnetization hodographs in Figs. 2 and 3, obtained in fields that were smaller ($H_s = 2.7$ Oe) and larger ($H_s = 7$ Oe) than the kink field H_{br}. At each experimental point, which shows the position of the end of the normalized magnetization vector $\mathbf{m} = \mathbf{M}/M_s$, we show the time at which it was obtained measured from the beginning of the pulse field H_p. We also mark the times t_i and t_f corresponding to the beginning and end of the primary period of magnetization reversal, along with the initial $\mathbf{m}_0$ and final $\mathbf{m}_l$ positions of the magnetization vector determined by Eqs. (1a) and (1b).

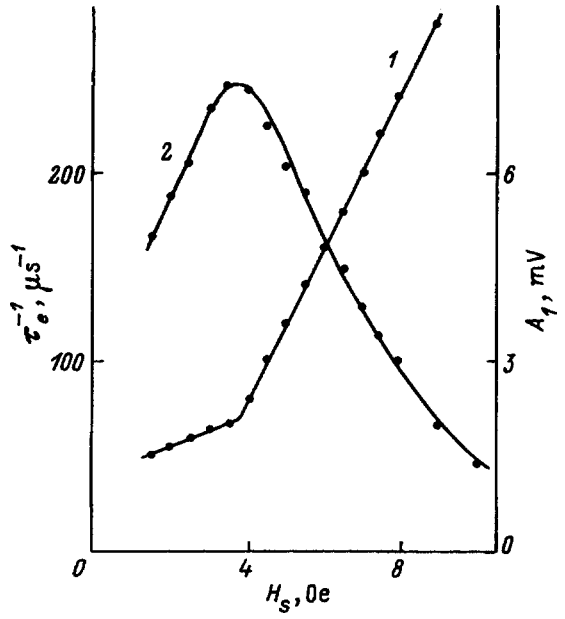

FIG. 1. Plot of inverse duration of the transient process τ_e^{-1} (for $H_\perp = 0.5$ Oe) (pulsed magnetization reversal curve) (*1*) and the amplitude of the signal oscillation (*2*) versus magnetization reversal field intensity H_s.

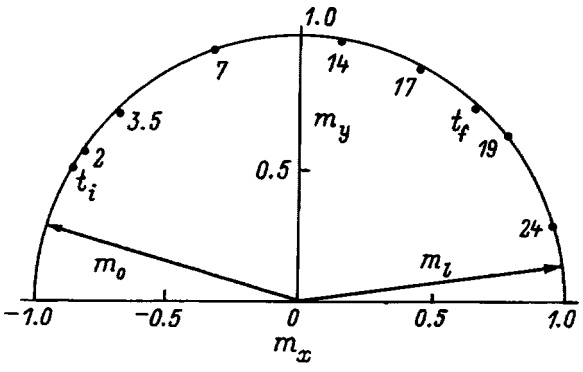

FIG. 2. Hodograph of magnetization vector obtained for $H_s = 2.7$ Oe and $H_\perp = 0.5$ Oe.

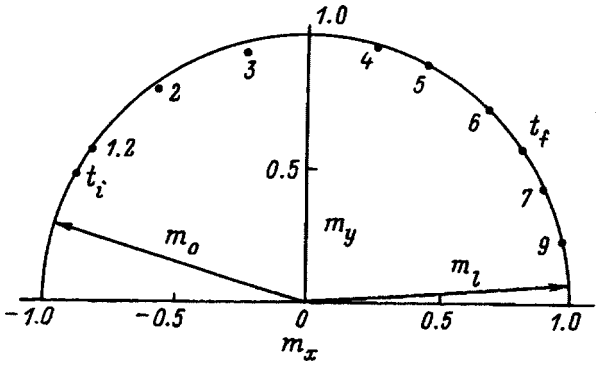

FIG. 3. Hodograph of magnetization vector obtained for $H_s=7$ Oe and $H_\perp=0.5$ Oe.

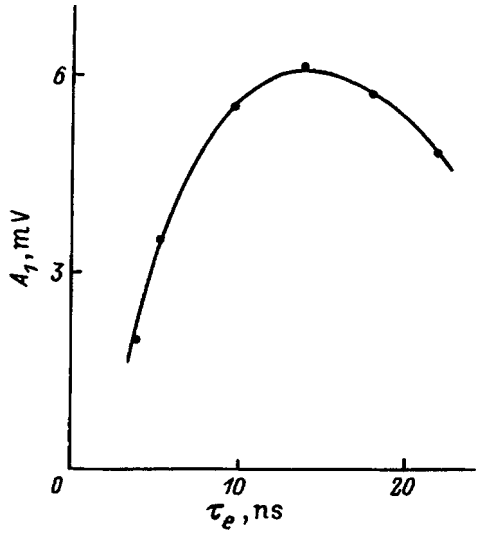

FIG. 4. Plot of oscillation amplitude of the signal A_1 versus duration of the primary period ($H_0=2$ Oe, $H_s=9$ Oe and $H_\perp=0.5$ Oe).

It is significant that the experimental points shown in Figs. 2 and 3 measured within the primary period of magnetization reversal practically lie on the arc of a circle with a radius equal to unity. From this follows that the magnetization reversal of single-crystal iron borate is accomplished by a quasiuniform rotation of the magnetization, whether the field is smaller ($H_s<H_{\rm br}$) or larger ($H_s>H_{\rm br}$) than the kink field. Thus, the kink in the pulsed magnetization reversal curve is not associated with any fundamental change in the magnetization reversal mechanism. This in turn implies that for the regime under study here we can unambiguously investigate the question of how the intensity of magnetoelastic oscillations affects the kink in the curve $\tau_e^{-1}(H_s)$.

The results of these investigations are shown in Fig. 1, where the function $A_1(H_s)$ is plotted along with the curve $\tau_e^{-1}(H_s)$. As we found in our previous investigations of 180° magnetization reversal (at $H_\perp=0$) and 90° magnetization, the intensity of magnetoelastic oscillations clearly increases with increasing field H_s, and then, having reached a maximum, begins a rather abrupt decrease. The maximum of the curve $A_1(H_s)$ coincides with the kink in the pulsed magnetization reversal curve. All these results taken together imply unambiguously that the kink in the pulsed magnetization reversal curve of single-crystal iron borate actually is not caused by a change in the magnetization reversal mechanism but rather by a decrease in the fraction of energy of the spin subsystem of the crystal expended on exciting the magnetoelastic oscillations.

Table I shows the times for 90° magnetization τ_m^*, 180° magnetization reversal at $H_\perp=0$ τ_s^*, 180° magnetization reversal for $H_\perp\neq 0$ $\tau_{s\perp}^*$, and the period of magnetoelastic oscillations T^*, measured at the points where kinks appear in the pulsed magnetization curves and magnetization reversal curves in samples with different thickness D. It follows from this table that the duration of the primary period of the transient process, during which the intensity of magnetoelastic oscillations begins to decrease significantly, is practically independent of the frequency of the magnetoelastic oscillations, i.e., the resonance properties of the crystal. It also depends only slightly on the character of the transient process. In Ref. 2 we claimed that for magnetization reversal times $\tau_s\sim 13-16$ ns there is a significant lag between the elastic subsystem of the crystal and the magnetic subsystem. This assertion was then confirmed by experiments in which the amplitude of the magnetization reversal pulse was fixed while the duration of its front was varied, which varied the duration of the primary period as well.[3]

TABLE I. Temporal parameters of samples with various thicknesses.

D, μm	τ_m^*, ns	τ_s^*, ns	$\tau_{s\perp}^*$, ns	T^*, ns
24	13±1	13±1	13±1	13±1
45	15±1	15±1	14±1	22±1
48	14±1	15±1	16±1	23±1
80	15±1	15±1	16±1	40±2
90	15±1	15±1	15±1	48±2
110	14±1	16±1	16±1	56±2

Similar studies were made in this work. In Fig. 4 we plot the intensity of magnetoelastic oscillations obtained for $H_0=2$ Oe, $H_\perp=0.5$ Oe and $H_s=9$ Oe. The left-hand portion of this function is especially interesting. The first point on it corresponds to $\tau_f\approx 1$ ns and $\tau_e\approx 3.5$ ns. It is clear that when the duration of the primary period increases to 12–14 ns, which is accomplished by increasing the duration of the front τ_f of the pulse to 14–16 ns, the intensity of the oscillations grows by a factor of 3, despite the fact that as τ_f increases the magnetization reversal takes place primarily at the pulse front, which naturally is accompanied by a considerable decrease in energy deposited in the magnetic subsystem of the crystal by the external field. In short, for large τ_f (and τ_e) this factor acts to decrease the intensity of the magnetoelastic oscillations.

However, the left-hand portion of this curve clearly illustrates the ''thawing-out'' effect of the crystal lattice, in that the rate of magnetization reversal decreases within the primary period of the transient process under study. In its turn, this result shows decisively that the decrease in intensity of the magnetoelastic oscillations for magnetization reversal times smaller than 13–16 ns is caused by the elastic subsystem of the crystal lagging behind the magnetic subsystem.

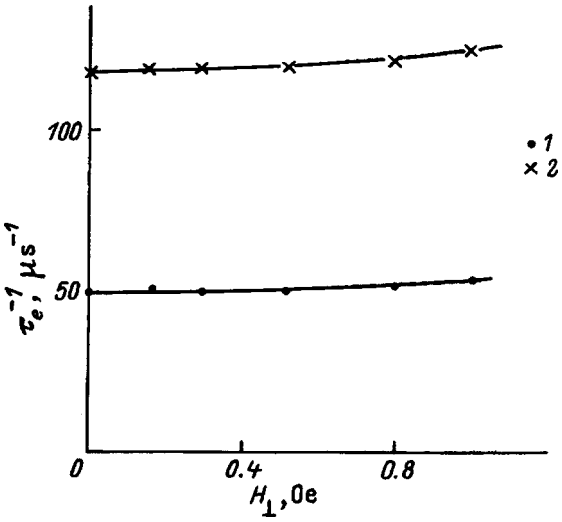

FIG. 5. Plot of inverse magnetization reversal time versus transverse field intensity. H_s (Oe): *1*—2.5, *2*—5.8. $H_0=2$ Oe.

It is obvious that the study of this transient process would be incomplete without investigating the dependence of the magnetization reversal rate on the transverse field intensity. However, it turns out that the magnetization- reversal rate of single crystals of iron borate is practically independent of the field intensity $H_\perp$. In order to confirm this, we show in Fig. 5 the function $\tau_e^{-1}(H_\perp)$ for two values of the magnetization-reversal-field intensity H_s: 2.5 and 5.8 Oe. It is clear that the rate of magnetization reversal increases by no more than 5% as the transverse field intensity varies from zero to 1 Oe.

As for other magnets, the influence of the transverse field on the rate of magnetization reversal has been studied in detail only for Fe–Ni films.[13–15] Recall that when the field $H_\perp$ varies within the limits specified above, the rate of magnetization reversal of permalloy films increases by more than two orders of magnitude, and several characteristic segments can be identified on the curve representing the function $\tau_e^{-1}(H_\perp)$.

Unfortunately, realistic mechanisms for pulsed magnetization reversal of Fe–Ni films when $H_\perp \neq 0$ have been insufficiently investigated, and the data obtained cannot be compared to the function $\tau_e^{-1}(H_\perp)$ obtained here.[16,17] Nevertheless, the difference in behavior of Fe–Ni films and single-crystal iron borate can be explained in the following way. In this and in other cases, when $H_\perp=0$ the magnetization reversal is associated with free rotation of the magnetization.[4,18] However, whereas a mechanism for ''true'' free rotation acts in iron borate single crystals, which is unimpeded by any slower processes, in Fe–Ni films where the magnetization is two orders of magnitude larger, the influence of the magnetostatic interaction is large, and therefore the initial rotation is rapidly braked by the dispersion field. Furthermore, in this material magnetization reversal takes place by the formation and subsequent destruction of strip blocking domains.[18]

In the presence of the transverse field, and as it increases, both materials exhibit a transition to quasiuniform rotation of the magnetization. In Fe–Ni films there are certain intermediate values of $H_\perp$ at which abrupt changes take place in the behavior of the magnetization, connected, for example, with a change in the behavior of the strip domains: for small $H_\perp$ we observe the destruction of domain boundaries, while for rather large $H_\perp$ their motion is accompanied by rotation of the magnetization within the domains, etc.[17] As a result, segments appear on the curves $\tau_e^{-1}(H_\perp)$ with abruptly different slopes.

However, there are no domain structures in single crystals of iron borate like the blocking domains mentioned above, obviously due to the small value of the magnetostatic interaction, and so the nature of the magnetization rotation itself (two-sided, one-sided, or quasiuniform when $H_\perp \geqslant 0.3-0.6$ Oe, depending on the sample) is not found to affect the rate of the transient process significantly. Naturally, in this case we assume that local regions of the single crystal with strongly differing directions of the magnetization are quite large in size, so that exchange interaction forces do not have much effect.

Thus, we see that, for a sufficiently large value of the transverse field, the magnetization reversal of single-crystal iron borate in fields $H_s > H_{\text{sat}}$ takes place by quasiuniform rotation of the magnetization. We have established that the kink in the pulsed magnetization reversal curve is caused not by changes in the pulsed magnetization reversal mechanism but rather is due to a decrease in the energy loss to excitation of magnetoelastic oscillations. We have shown that, as in transient processes investigated previously, the decrease in intensity of magnetoelastic oscillations during pulsed magnetization reversal in the presence of a transverse field is caused by lagging of the phonon subsystem of the crystal behind the magnon system.

The authors are grateful to G. V. Smirnov and Yu. V. Shvydko for valuable discussions.

The authors also thank the International Science Fund and the Russian government for material support for this work (Grants NCT 000 and NCT 300).

[1] O. S. Kolotov, V. A. Pogozhev, G. V. Smirnov, and Yu. V. Shvyd'ko, Fiz. Tverd. Tela (Leningrad) **29**, 8, 254 (1987) [*sic*].
[2] O. S. Kolotov, Kim En Hen, A. P. Krasnozhon, and V. A. Pogozhev, JETP Lett. **58**, 53 (1993).
[3] O. S. Kolotov, Kim En Hen, A. P. Krasnozhon, and V. A. Pogozhev, Fiz. Tverd. Tela (Leningrad) **36**, 231 (1994) [Sov. Phys. Solid State **36**, 127 (1994)].
[4] O. S. Kolotov, Kim En Hen, and V. A. Pogozhev, Bull. Moscow State University, Ser. 3: Physics and Astronomy *6*, 57 (1996) [in Russian].
[5] E. A. Turov and V. G. Shavrov, Usp. Fiz. Nauk **140**, 429 (1983) [Sov. Phys. Usp. **26**, 593 (1983)].
[6] R. Diehl, W. Jantz, B. I. Nolang, and W. Wettling, Curr. Top. Mater. Sci. **11**, 1, 241 (1984).
[7] O. S. Kolotov, A. P. Krasnozhon, and V. A. Pogozhev, Fiz. Tverd. Tela (St. Petersburg) **38**, 1017 (1996) [Phys. Solid State **38**, 565 (1996)].
[8] K. U. Z. Stein, Angew. Phys. **18**, 529 (1965) [in German].
[9] V. I. Ivashkin, G. I. Rudenko, K. M. Polivanov, and A. L. Frumkin, *Physics of Magnetic Films* (1968), [in Russian], p. 350.
[10] O. S. Kolotov, V. A. Pogozhev, and R. V. Telesnin, *Methods and Apparatus for Investigating the Pulsed Properties of Thin Magnetic Films* (Moscow, 1970) [in Russian].
[11] V. D. Doroshev, N. M. Krygin, S. M. Lukin, A. M. Molchalov, A. D. Prokhorov, V. V. Rudenko, and V. V. Seleznev, JETP Lett. **29**, 257 (1979).

[12] F. B. Humphrey and E. M. Gyorgy, J. Appl. Phys. **30**, 935 (1959).
[13] R. V. Telesnin, O. S. Kolotov, and V. A. Pogozhev, Fiz. Met. Metalloved. **19**, 52 (1965).
[14] F. B. Hagedorn, IEEE Trans. Magn. Mag. **4**, 41 (1968).
[15] J. K. Watson, IEEE Trans. Magn. Mag. **4**, 722 (1968).
[16] M. H. Kryder and F. B. Humphrey, J. Appl. Phys. **40**, 2469 (1969).
[17] Yu. A. Durasova, O. S. Kolotov, T. N. Letova, and R. V. Telesnin, Fiz. Met. Metalloved. **42**, 882 (1976).
[18] O. S. Kolotov, V. A. Pogozhev, and R. V. Telesnin, Usp. Fiz. Nauk **113**, 569 (1973) [Sov. Phys. Usp. **17**, 528 (1973)].

Translated by Frank J. Crowne

Magnetopolaron states of a spin-correlated antiferromagnet in the neighborhood of the spin-glass transition

V. V. Val'kov and D. M. Dzebisashvili

L. V. Kirensky Institute of Physics, Siberian Branch of the Russian Academy of Sciences, 660036 Krasnoyarsk, Russia; Krasnoyarsk State University, 660000 Krasnoyarsk, Russia; Krasnoyarsk State Technical University, 660036 Krasnoyarsk, Russia

(Submitted September 4, 1997)
Fiz. Tverd. Tela (St. Petersburg) **40**, 310–314 (February 1998)

The problem of the spectrum of magnetopolaron states of a strongly correlated conducting canted antiferromagnet is solved. The approach used to study the spectrum is based on an atomic representation and a diagram technique for Hubbard operators. This approach makes it possible to include strong intra-ion interactions in a first-principles way, and to obtain the dispersion equation for the magnetopolaron spectrum for arbitrary values of the magnitude of the spin, temperature, and magnetic field. In the vicinity of the spin-flip transition an analytic expression is obtained for the spectrum of magnetopolaron states that goes beyond the framework of the quasiclassical approximation. © *1998 American Institute of Physics.*
[S1063-7834(98)03302-4]

In the course of their experimental studies of the de Haas-van Alphen effect in the heavy-fermion compound $CeCu_2Si_2$, Hunt *et al.*[1] observed an abrupt change in the frequency of de Haas-van Alphen oscillations as they scanned through the spin-flip point. In its normal phase, $CeCu_2Si_2$ has antiferromagnetic order with a low value of the Néel temperature. Therefore, in the range of strong magnetic fields and low temperatures, the de Haas-van Alphen effect will coexist with a spin-flip phase transition.

The role of antiferromagnetic order in the de Haas-van Alphen-effect was discussed in Refs. 2 and 3. However, these papers do not predict any change in the period of the oscillations. In Ref. 4 we used a simple model that included $s-d(f)$-exchange coupling between spin moments of the collectivized and localized electrons to demonstrate that the frequency of de Haas-van Alphen oscillations in a conducting antiferromagnet could be different on different sides of the spin-flip point. The results of Refs. 2–4 show that it is important to take into account both antiferromagnetism and the exchange coupling between collectivized and localized subsystems when attempting to understand experimental de Haas-van Alphen-oscillation data from first principles.

The latter is also important for strongly correlated systems having low concentrations of current carriers. Examples of systems that belong to this new class of strongly correlated systems are, e.g., the rare-earth pnictides (R) with the general formula RX, where X=Bi, Sb, As, P. The unusual nature of their galvanomagnetic and thermodynamic properties has led to the formulation of new concepts for constructing the ground state of these compensated RX semimetals, among them the concepts of magnetopolaron liquids and crystals.[5,6] Many-body effects play a key role in generating these scenarios for electronic structures as well as the presence of long-range antiferromagnetic order.

In order to describe the magnetopolaron states of the valence band, we can use the ideas developed in the papers by Nagaev.[7] Here, in keeping with the known peculiarities of the band structure of rare-earth monopnictides, we will assume that the width of the filled valence band is small compared with the characteristic $s-f$-interaction energy. In these narrow-band antiferromagnets, it is well known that a magnetopolaron narrowing of the band takes place.[7] This phenomenon has been well studied for the collinear geometry.

In this paper we find the spectrum of magnetopolaron states of a strongly correlated antiferromagnet under conditions of large canting of the magnetic sublattices. The use of Hubbard operators[8–10] and diagram techniques for them[11–16] allow us to derive the required dispersion equation for the spectrum for arbitrary values of temperature, magnetic field, and spin. In the low-temperature regime we obtain an analytic expression for the energies of magnetopolaron states in the neighborhood of the spin-flip transition.

1. HAMILTONIAN OF A STRONGLY CORRELATED NARROW-BAND ANTIFERROMAGNET

Let us consider a strongly correlated narrow-band antiferromagnet with hole-type current carriers. We will describe this system within the framework of the $s-d(f)$-exchange model.[17] The physics of the narrow-band variant of this model has been described in detail in Ref. 7. Strong single-site correlations are conveniently taken into account by introducing an atomic representation[8–10] and the diagram technique for the Hubbard operators.[11–16]

Let us write the Hamiltonian of the model in the form

$$H=H_h+H_{sd}+H_m. \tag{1}$$

Here the first term describes the band current carriers. In order to describe the antiferromagnetic phase we introduce two sublattices F and G. Then within the Wannier representation, and taking into account the Hubbard repulsion on a single site, we have

$$H_h=\sum_{ff'\sigma}[t_{ff'}-\delta_{ff'}(2\mu_B H\sigma-\mu)]c^+_{f\sigma}c_{f'\sigma}$$
$$+\sum_{fg\sigma}t_{fg}(c^+_{f\sigma}d_{g\sigma}+\text{h.c.})+\sum_{gg'\sigma}[t_{gg'}-\delta_{gg'}$$
$$\times(2\mu_B H\sigma-\mu)]d^+_{g\sigma}d_{g'\sigma}$$
$$+\sum_f Un_{f\uparrow}n_{f\downarrow}+\sum_g Un_{g\uparrow}n_{g\downarrow}, \quad (2)$$

where the labels f,f', and g,g' enumerate sites on the F- and G-sublattices respectively, and the operators $c_{f\sigma}(c^+_{f\sigma})$ and $d_{g\sigma}(d^+_{g\sigma})$ describe the processes of annihilation (creation) of Wannier-representation holes in the F- and G-sublattices.

The second term of the Hamiltonian (1) describes the coupling between band carriers and localized spin moments via the $s-d(f)$-exchange interaction[17]

$$H_{sd}=-A\sum_f(\mathbf{S}_f\boldsymbol{\sigma}_f)-A\sum_g(\mathbf{S}_g\boldsymbol{\sigma}_g), \quad (3)$$

where A is the $s-d(f)$-exchange parameter, $\mathbf{S}_f$ is a vector operator for a localized spin on site f, and $\boldsymbol{\sigma}_f$ is a vector operator for the spin moment of a hole in the Wannier representation for the F sublattice. An analogous definition can be made for the G sublattice.

The last term in Eq. (1) describes the Heisenberg interaction in the subsystem of localized spins, and also its Zeeman energy.

When a magnetic field is applied to an isotropic antiferromagnet, its sublattices become canted.[18,19] In order to describe this effect it is convenient to change to local coordinates so that for each sublattice the equilibrium magnetization vector is oriented along a new axis Oz. We presented a detailed derivation of the Hamiltonian in local coordinates in Ref. 4, along with rules for transforming the Fermi and spin operators. Using these rules, it is not difficult to write down the Hamiltonian H'. In this case

$$H'_h=\sum_{ff'\sigma}t_{ff'}c^+_{f\sigma}c_{f'\sigma}+\sum_{gg'\sigma}t_{gg'}d^+_{g\sigma}d_{g'\sigma}$$
$$+\sum_{fg\sigma}t_{fg}(\cos\theta c^+_{f\sigma}d_{g\sigma}+2\sigma\sin\theta c^+_{f\sigma}d_{g\sigma}+\text{h.c.})$$
$$+\sum_{f\sigma}\{\mu_B H\sin\theta c^+_{f\bar{\sigma}}c_{f\sigma}-(2\mu_B H\cos\theta\sigma-\mu)$$
$$\times c^+_{f\sigma}c_{f\sigma}\}+\sum_f Un_{f\uparrow}n_{f\downarrow}-\sum_{g\sigma}\{\mu_B H\sin\theta d^+_{g\sigma}d_{g\sigma}$$
$$+2(\mu_B H\cos\theta\sigma-\mu)d^+_{g\sigma}d_{g\sigma}\}+\sum_g Un_{g\uparrow}n_{g\downarrow}. \quad (4)$$

The Hamiltonian for the $s-d(f)$-exchange interaction remains unchanged: $H'_{sd}=H_{sd}$. For the subsystem of localized spin moments the transformed operator is given by the expression

$$H'_m=-\frac{1}{2}\sum_{ff'}I_{ff'}(\mathbf{S}_f\mathbf{S}_{f'})-\frac{1}{2}\sum_{gg'}I_{gg'}(\mathbf{S}_g\mathbf{S}_{g'})$$
$$-g\mu_B H\left\{\sum_f S^z_f(\theta)+\sum_g S^z_g(\theta)\right\}$$
$$+\sum_{fg}K_{fg}\{\cos 2\theta(S^x_fS^x_g+S^z_fS^z_g)+S^y_fS^y_g$$
$$+\sin 2\theta(S^z_fS^x_g-S^x_fS^z_g)\}. \quad (5)$$

It is clear from Eq. (4) that the noncollinear phase is characterized not only by a θ-dependent effective overlap integral but also by an additional operator term corresponding formally to a hole hopping from site to site, accompanied by a change in the projection of the spin moment.

2. THE NARROW-BAND ANTIFERROMAGNET IN ITS NONCOLLINEAR PHASE IN THE ATOMIC REPRESENTATION

In studying narrow-band antiferromagnets it is assumed that the following inequality holds between the $s-d(f)$-exchange constant and the overlap integral: $|t_{fg}|\ll|A|$. Therefore, the $s-d(f)$ coupling between localized and collectivized subsystems must be taken into account exactly.[7,12] To this end, we separate out terms from the total Hamiltonian H' that contain only single site operators:

$$H_{\text{ion}}=\sum_f\{-A(\mathbf{S}_f\boldsymbol{\sigma}_f)-\bar{H}S^z_f-h\sigma^z_f-h_\perp\sigma^x_f+Un_{f\uparrow}n_{f\downarrow}\}$$
$$+\sum_g\{-A(\mathbf{S}_g\boldsymbol{\sigma}_g)-\bar{H}S^z_g-h\sigma^z_g+h_\perp\sigma^x_g+Un_{g\uparrow}n_{g\downarrow}\}, \quad (6)$$

where the effective field $\bar{H}$ includes the self-consistent field:

$$\bar{H}=g\mu_B H\cos\theta+I_0R-K_0\cos 2\theta R,\quad R=\frac{1}{N}\sum_f\langle S^z_f\rangle. \quad (7)$$

Here I_0 and K_0 are Fourier transforms of the exchange parameters for zero quasimomentum. The longitudinal and transverse components of the magnetic field acting on a hole are determined by the expressions

$$h=2\mu_B H\cos\theta,\quad h_\perp=-2\mu_B H\sin\theta. \quad (8)$$

In what follows we will assume that the Hubbard repulsion is so strong that we can neglect states of two holes on a single site. Since in reality the inequalities $|A|\gg\bar{H}$, $|A|\gg h$, $|h_\perp|$ hold, the Schroedinger problem of finding eigenstates of the single-site operator in the noncollinear phase can be solved by following a simple kind of perturbation theory.

As is well known,[17] the $s-d(f)$-exchange operator $-A(\mathbf{S}\boldsymbol{\sigma})$ has two eigenstates with energies $E_a=-AS/2$ when the total moment $J=S+1/2$ and $E_b=A(S+1)/2$ when $J=S-1/2$. For narrow-band magnets we can limit our discussion to only those single-site states that correspond to the smaller energy.[7] For $A<0$, the states of interest are $(n=1,2,\ldots,2S)$

$$|n\rangle = \sqrt{\frac{2S-n+1}{2S+1}}\,|S-n+1,\downarrow\rangle - \sqrt{\frac{n}{2S+1}}\,|S-n,\uparrow\rangle. \tag{9}$$

If we treat the remaining terms of the single-ion Hamiltonian by perturbation theory, it is not difficult to construct a basis of single-ion states $|\psi_n\rangle$. In this case the energy spectrum of the one-hole states can be written in the form

$$E_n = \varepsilon_1 + \varepsilon(n-1) + \frac{2n-2S-1}{(2S+1)^2}\left(\frac{v^2}{\varepsilon}\right), \quad n=1, 2, \ldots, 2S,$$

$$\varepsilon_1 = \frac{A(S+1)}{2} - \overline{H}\left(S - \frac{1}{2S+1}\right) + \frac{h}{2}\frac{2S-1}{2S+1},$$

$$\varepsilon = \frac{2S+2}{2S+1}\,\overline{H} - \frac{h}{2S+1}, \quad v = \mu_B H \sin\theta. \tag{10}$$

Knowing the solution to the single-ion problem, it is not difficult to write down a representation for the Fermi operators $c_{f\sigma}$ and $c_{g\sigma}$ in terms of the Hubbard operators X_f^{α}.[11–14]

$$c_{f\sigma} = \sum_{nM} \langle M|c_{f\sigma}|\psi_n\rangle X_f^{Mn} \equiv \sum_{\alpha} \gamma_\sigma(\alpha) X_f^{\alpha}. \tag{11}$$

Here the label *alpha* identifies the transition of an ion from state $|\psi_n\rangle$ to a state $|M\rangle$ corresponding to the ion without a hole with spin moment projection M. For the G sublattice the representation can be written in the form

$$c_{g\sigma} = \sum_{\alpha} \overline{\gamma}_\sigma(\alpha) X_g^{\alpha}. \tag{12}$$

In this description we have included the fact that the single-ion problem for the G sublattice differs from the same problem for the F sublattice only by a change in the sign of the angle θ. It is obvious that the parameters of the representation $\gamma_\sigma(\alpha)$ are in reality functions of the angle θ. For brevity we will use the following written forms: $\gamma_\sigma(\theta,\alpha) \equiv \gamma_\sigma(\alpha)$, $\overline{\gamma}_\sigma(\alpha) \equiv \gamma_\sigma(-\theta,\alpha)$.

Using Eqs. (11) and (12), we find the following form for the total Hamiltonian in the atomic representation:

$$H' = H'_{\rm ion} + H_{\rm int}, \tag{13}$$

where

$$H'_{\rm ion} = \sum_{fM} E_M X_f^{MM} + \sum_{gM} E_M X_g^{MM} + \sum_{fn} (E_n - \mu) X_f^{nn} + \sum_{gn} (E_n - \mu) X_g^{nn}. \tag{14}$$

The operator $H'_{\rm ion}$ differs from $H_{\rm ion}$ in Eq. (6). First of all, $H'_{\rm ion}$ is written in the atomic representation; secondly, in $H'_{\rm ion}$ we used a truncated basis corresponding to states of the lowest multiplet.

In Eq. (14) the first two terms take into account the single-ion states without holes with energies $E_M = -\overline{H}M$, $M = S, S-1, \ldots, -S$. The remaining terms in Eq. (14) correspond to inclusion of states with a single hole.

Let us write the interaction operator in a form that is convenient for applying the diagram technique for Hubbard operators:

$$H_{\rm int} = \sum_{AA'} \sum_{l\in A, l'\in A'} \sum_{\alpha\beta\sigma} V_\sigma^{\alpha\beta}(l,l') X_l^{-\alpha} X_{l'}^{\beta}. \tag{15}$$

Here, in the interest of abbreviating the description, we have denoted summation over the sublattices as sums over A and A', where the variables A and A' can take on two values: F and G. The matrix elements of the interaction operator are defined by the expressions

$$\begin{aligned}
V_\sigma^{\alpha\beta}(f,f') &= t_{f,f'}\gamma_\sigma(\alpha)\gamma_\sigma(\beta),\\
V_\sigma^{\alpha\beta}(g,g') &= t_{g,g'}\overline{\gamma}_\sigma(\alpha)\overline{\gamma}_\sigma(\beta),\\
V_\sigma^{\alpha\beta}(f,g) &= t_{f,g}[\cos\theta\gamma_\sigma(\alpha)\overline{\gamma}_\sigma(\beta) + 2\sigma\sin\theta\gamma_\sigma(\alpha)\overline{\gamma}_{\bar\sigma}(\beta)],\\
V_\sigma^{\alpha\beta}(g,f) &= t_{f,g}[\cos\theta\overline{\gamma}_\sigma(\alpha)\gamma_\sigma(\beta) + 2\sigma\sin\theta\overline{\gamma}_{\bar\sigma}(\alpha)\gamma_\sigma(\beta)].
\end{aligned} \tag{16}$$

3. GREEN'S FUNCTIONS AND DISPERSION EQUATION

In order to compute the spectrum of Fermi-type, we introduce into the discussion the Matsubara Green's function in its atomic representation:

$$G_{\alpha\beta}^{AA'}(l\tau,l'\tau') = -\langle T_\tau \widetilde{X}_l^{\alpha}(\tau)\widetilde{X}_{l'}^{-\beta}(\tau')\rangle, \tag{17}$$

where the lattice label $l(l')$ takes on a set of values corresponding to the $A(A')$ sublattice. The remaining notations are standard and are contained in Refs. 11 and 16. The following graphical equation can be written for the Fourier transforms $G_{\alpha\beta}AA'(\mathbf{k},\omega_n)$ in the simplest approximation:

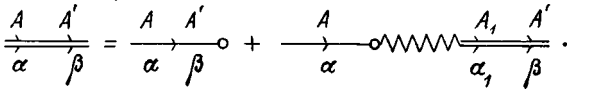

(18)

In this graphical equation, a thin line A/α corresponds to the intra-ion propagator

$$G_\alpha(\omega_n) = [i\omega_n + \alpha E]^{-1}, \quad \omega_n = (2n+1)\pi T, \tag{19}$$

in which the scalar product of the root vector α and the vector E is determined by the equation $\alpha E \equiv \alpha(M,n)E = E_M - E_n$. Because the sublattices are identical and the values of single-ion energy levels for them are the same, $G_\alpha(\omega_n)$ does not depend on the sublattice label. When the diagrams are written out in analytic form, the wavy lines correspond to the Fourier transform of the interaction matrix element (16) summed over values of the spin moment projection. The specific values that label the interaction matrix elements are determined by the labels of the Green's function lines that join with the wavy line. For example, in Eq. (18) for $A=F$ and $A_1=G$ the interaction lines represent the expression

$$\Gamma_{\mathbf{q}}^{\alpha\alpha_1} = \sum_\sigma \Gamma_{\mathbf{q}}[\cos\theta\gamma_\sigma(\alpha)\gamma_\sigma(\alpha_1) + 2\sigma\sin\theta\gamma_\sigma(\alpha)\overline{\gamma}_\sigma(\alpha_1)],$$

$$\Gamma_{\mathbf{q}}=\frac{1}{N}\sum_{g} t_{fg}\exp\{i\mathbf{q}(\mathbf{R}_f-\mathbf{R}_g)\}. \tag{20}$$

If, however, $A=F$, $A_1=F$, the wavy line corresponds to the following analytical description:

$$t_{\mathbf{q}}^{\alpha\alpha_1}=\sum_{\sigma} t_{\mathbf{q}}\gamma_{\sigma}(\alpha)\gamma_{\sigma}(\alpha_1),$$

$$t_{\mathbf{q}}=\frac{1}{N}\sum_{f'} t_{ff'}\exp\{i\mathbf{q}(\mathbf{R}_f-\mathbf{R}_{f'})\}. \tag{21}$$

The remaining notations are standard and are discussed in detail in Refs. 11 and 15.

From Eq. (18) there follows a system of equations in analytic form

$$G_{\alpha\beta}^{FF}(\mathbf{k},\omega_n)=\delta_{\alpha\beta}G_{\alpha}(\omega_n)+G_{\alpha}(\omega_n)b(\alpha)\times\{t_{\mathbf{k}}^{\alpha\alpha_1}G_{\alpha_1\beta}^{FF}(\mathbf{k},\omega_n)+\Gamma_{\mathbf{k}}^{\alpha\alpha_1}G_{\alpha_1\beta}^{GF}(\mathbf{k},\omega_n)\}, \tag{22}$$

$$G_{\alpha\beta}^{GF}(\mathbf{k},\omega_n)=G_{\alpha}(\omega_n)b(\alpha)\Bigg\{t_{\mathbf{k}}\sum_{\sigma}\overline{\gamma}_{\sigma}(\alpha)\overline{\gamma}_{\sigma}(\alpha_1)G_{\alpha_1\beta}^{GF}(\mathbf{k},\omega_n)+\Bigg[\Gamma_{\mathbf{k}}\cos\theta\sum_{\sigma\alpha_1}\overline{\gamma}_{\sigma}(\alpha)\gamma_{\sigma}(\alpha_1)+\Gamma_{\mathbf{k}}\sin\theta\sum_{\sigma\alpha_1}2\sigma\overline{\gamma}_{\sigma}(\alpha)\gamma_{\sigma}(\alpha_1)\Bigg]G_{\alpha_1\beta}^{FF}(\mathbf{k},\omega_n)\Bigg\}. \tag{23}$$

In solving this system of equations, it is very useful to note that the nature of the interaction matrix element leads to separability with respect to the labels of the root vectors α,α_1. This separability is quite evident from Eqs. (20) and (21). Using the methods for solving equations with separable kernels,[13,14] we find that the dispersion equation can be written in the form

$$\begin{aligned}0=&[(1-t_{\mathbf{k}}L_{\uparrow\uparrow})^2-\Gamma_{\mathbf{k}}^2M_{\uparrow\uparrow}^2][(1-t_{\mathbf{k}}L_{\downarrow\downarrow})^2-\Gamma_{\mathbf{k}}^2M_{\downarrow\downarrow}^2]\\&+\Gamma_{\mathbf{k}}^4M_{\uparrow\downarrow}^2M_{\downarrow\uparrow}^2+2(\Gamma_{\mathbf{k}}^2M_{\uparrow\downarrow}M_{\downarrow\uparrow}-t_{\mathbf{k}}^2L_{\uparrow\downarrow}^2)[(1-t_{\mathbf{k}}L_{\uparrow\uparrow})\\&\times(1-t_{\mathbf{k}}L_{\downarrow\downarrow})-\Gamma_{k}^2M_{\uparrow\uparrow}M_{\downarrow\downarrow}]+2t_{\mathbf{k}}\Gamma_{\mathbf{k}}^2L_{\uparrow\downarrow}\\&\times(M_{\uparrow\downarrow}-M_{\downarrow\uparrow})(M_{\uparrow\uparrow}-M_{\downarrow\downarrow})+t_{\mathbf{k}}^2L_{\uparrow\downarrow}^2[t_{\mathbf{k}}^2L_{\uparrow\downarrow}^2\\&-\Gamma_{\mathbf{k}}^2(M_{\uparrow\downarrow}^2+M_{\downarrow\uparrow}^2)],\end{aligned} \tag{24}$$

where

$$L_{\sigma\sigma_1}(\omega)=\sum_{\alpha}\overline{\gamma}_{\sigma}(\alpha)\overline{\gamma}_{\sigma_1}(\alpha)G_{\alpha}(\omega)b(\alpha),$$

$$M_{\sigma\sigma_1}(\omega)=L_{\sigma\sigma'}(\omega)\cos\theta+(2\sigma_1)L_{\sigma\sigma_1}^{-}(\omega)\sin\theta. \tag{25}$$

In studying the de Haas-van Alphen-effect it is the low-temperature regime that is of primary interest to us. This regime is defined mathematically by the inequality $T\ll T_N$. It is well known that occupation numbers for single-ion states are distributed according to atomic statistics. Therefore, in the temperature range of interest to us, only the numbers N_1 and N_S are interesting, while the others are exponentially small. This greatly decreases the number of intra-ion transitions that participate in forming the collective quasiparticle spectrum, and simplifies the form of the dispersion equation. In fact, when $T\ll T_N$ contributions come only from those transitions in which at least one of the low-lying states of the multiplets participates, with a hole or without one.

Another factor that allows us to simplify the structure of the dispersion equation is the existence of the small parameter (ν/ε). We will carry all calculations out to quadratic accuracy in this parameter. The need to do calculations to this level of accuracy is dictated by considerations involving effects that are $\sim\theta^2$ in the neighborhood of the transition from the canted to the collinear phase.

4. SPECTRUM OF HOLES IN A NEIGHBORHOOD OF THE SPIN-FLIP TRANSITION

After calculating the functions $L_{\sigma_1\sigma_2}$ and $M_{\sigma_1\sigma_2}$ to the specified accuracy, we obtain the dispersion equation in the following form:

$$(1-\Gamma_{\mathbf{k}}^2M_{\uparrow\uparrow}^2)(1-\Gamma_{\mathbf{k}}^2M_{\downarrow\downarrow}^2)+2\Gamma_{\mathbf{k}}^2M_{\uparrow\downarrow}M_{\downarrow\uparrow}\times(1-\Gamma_{\mathbf{k}}^2M_{\uparrow\uparrow}M_{\downarrow\downarrow})=0, \tag{26}$$

where we assume that analytic continuation has already been done. For simplicity we assume that the only nonzero matrix elements are those $t_{l'}$ which correspond to hopping of a charge carrier between nearest neighbors.

Solving Eq. (26), we find the branch of Fermi excitations of interest to us:

$$\begin{aligned}E(\mathbf{k})=&\frac{A(S+1)}{2}+\frac{\overline{H}}{2S+1}+\frac{h}{2}\frac{2S-1}{2S+1}-\frac{2S}{2S+1}|\Gamma_{\mathbf{k}}|\cos\theta\\&+N_1\Bigg\{\frac{2S-1}{(2S+1)^3}\left(\frac{v}{\varepsilon}\right)^2|\Gamma_{\mathbf{k}}|\\&+\frac{2(2S-1)}{(2S+1)^2}\left(\frac{v\sin\theta}{\varepsilon}\right)|\Gamma_{\mathbf{k}}|-\frac{2S-1}{(2S+1)^2}\left(\frac{v^2}{\varepsilon}\right)\\&-\frac{\sin^2\theta}{2S+1}|\Gamma_{\mathbf{k}}|\Bigg\}.\end{aligned} \tag{27}$$

It is clear that for $H=H_c$, when $\theta=0$ this spectrum becomes the polaron spectrum obtained previously by Nagaev.[7]

These expressions for the spectrum of magnetopolaron states of an antiferromagnet in the canted phase are fundamental for studying many kinetic and galvanomagnetic phenomena in conducting antiferromagnets in a magnetic field. This statement is especially true for the de Haas-van Alphen effect in these systems. Limitations of space have not allowed us to discuss studies of the influence of magnetopolaron states on magnetic moment oscillations in a quantizing magnetic field here. The corresponding results based on derivations in this work will be published in a separate article. We note here, however, that the expressions obtained will allow us to follow the temperature evolution of magnetopolaron states. This information is necessary, for example, when temperature behavior of magnetoresistance in conducting antiferromagnets is investigated.

This work was carried out with the financial support of the Science Fund from the Krasnoyarsk region (Grant No. 5F0158).

[1] M. Hunt, P. Meeson, P. A. Probst, P. Reinders, M. Springford, W. Assmus, and W. Sun, J. Phys.: Condens. Matter **2**, 6859 (1990).
[2] J. W. Rusul and P. Schlottmann, Physica B **163**, 689 (1990).
[3] R. Sollie and P. Schlottmann, Phys. Rev. B **41**, 8860 (1990).
[4] V. V. Val'kov and D. M. Dzebisashvili, Fiz. Tverd. Tela (St. Petersburg) **39**, 204 (1997) [Phys. Solid State **39**, 179 (1997)].
[5] T. Kasuya, T. Suzuki and Y. Haga, J. Phys. Soc. Jpn. **62**, 2549 (1993).
[6] T. Kasuya, J. Phys. Soc. Jpn. **64**, 1453 (1995).
[7] É. L. Nagaev, *The Physics of Magnetic Semiconductors* (Nauka, Moscow, 1979).
[8] J. Hubbard, Proc. Roy. Soc. A **285**, 545 (1964).
[9] L. A. Maksimov and K. A. Kikoin, Fiz. Met. Metalloved. **28**, 43 (1969).
[10] L. A. Maksimov and K. A. Kikoin, Zh. Éksp. Teor. Fiz. **58**, 2184 (1970) [Sov. Phys. JETP **31**, 1179 (1970)].
[11] R. O. Zaĭtsev, Zh. Éksp. Teor. Fiz. **70**, 1100 (1976) [Sov. Phys. JETP **43**, 574 (1976)].
[12] M. Sh. Erukhimov and S. G. Ovchinnikov, TMF **67**, 237 (1986) [in Russian].
[13] V. V. Val'kov and T. A. Val'kova, Fiz. Nizk. Temp. **11**, 951 (1985) [Sov. J. Low Temp. Phys. **11**, 524 (1985)].
[14] V. V. Val'kov, T. A. Val'kova, and S. G. Ovchinnikov, Zh. Éksp. Teor. Fiz. **88**, 550 (1985) [Sov. Phys. JETP **61**, 323 (1985)].
[15] Yu. A. Izyumov and Yu. N. Skryabin, *Statistical Mechanics of Magnetically Ordered Systems* (Nauka, Moscow, 1987) [in Russian].
[16] Yu. A. Izyumov, M. I. Katsnel'son, and Yu. N. Skryabin, *Magnetism of Collectivized Electrons* (Fiz. Mat. Lit., Moscow, 1994) [in Russian].
[17] S. V. Vonsovskiĭ, *Magnetism*, Vol. 1 and 2 [Wiley, New York, 1974; Nauka, Moscow, 1971].
[18] A. S. Borovich-Romanov, *Antiferromagnetism and Ferrites* (USSR Acad. Sci., Moscow, 1962) [in Russian].
[19] A. G. Gurevich, *Magnetic Resonance in Ferrites and Antiferromagnets* (Nauka, Moscow, 1973) [in Russian].

Translated by Frank J. Crowne

Magnetoresistance of the semiconducting spinelide $Cu_{0.625}Ga_{0.375}Cr_2Se_4$ having a low-temperature long-range magnetic order–spin glass transition

L. I. Koroleva and A. I. Abramovich

Moscow State University, 119899 Moscow, Russia
(Submitted September 15, 1997)
Fiz. Tverd. Tela (St. Petersburg) **40**, 315–317 (February 1998)

A study is reported of the dependence of magnetoresistance $\Delta\rho/\rho$ on the square of magnetization σ^2 of the semiconducting spinelide $Cu_{0.625}Ga_{0.375}Cr_2Se_4$, which exhibits a low-temperature transition from long-range magnetic order (LRMO) to the spin glass (SG) state in strong magnetic fields. It is shown that at the freezing temperature T_f the $\Delta\rho/\rho(\sigma^2)$ relations change their slope, and that below T_f this slope is about one half that for $T>T_f$. This finding, together with the earlier observation that the freezing temperature does not depend on the frequency of the ac magnetic field in which it was measured, suggests that the spin-glass phase consists of spins of individual Cr^{3+} ions, and that the SG-LRMO crossover is a phase transition. © *1998 American Institute of Physics.* [S1063-7834(98)03402-9]

The existence of a spin glass (SG) paramagnetism (PM) and SG-LRMO (long-range magnetic order) phase transition is presently a major problem in the physics of the spin-glass state. While the SG-PM transition was considered in many publications, the SG-LRMO transition is much less studied. It is well known that magnetoresistance (MR) in magnets is proportional to the square of magnetization σ, with the slope of the $\Delta\rho/\rho(\sigma^2)$ curves in the strong-field domain characterizing the intensity of the paraprocess. To reveal the nature of the SG state, it is of interest to compare these slopes in samples with the low-temperature LRMO-SG transition in different temperature regions, namely, in the region with LRMO and in the SG region. If these slopes are close in magnitude, then the SG phase is most likely a system of clusters, inside which the magnetic order is the same as in the LRMO phase. If, however, these slopes are essentially different, then the SG phase may differ substantially from the phase with LRMO. Several versions of the structure of the SG phase can be envisaged: (1) It consists of clusters with the same magnetic order as the LRMO phase, of other magnetic-moment carriers, for example, spins of individual ions, and of clusters with magnetic order other than that in the LRMO phase; (2) the SG phase is made up of clusters with another magnetic order than the LRMO phase; (3) the SG phase consists of clusters with magnetic order different from that of the LRMO phase, and of individual magnetic ions; and (4) the SG phase consists of individual magnetic ions. In the latter case one should expect the freezing temperature to be frequency independent.

We studied[1,2] earlier the magnetic and electrical properties of the solid-solution system $x\mathrm{CuCr_2Se_4}-(1-x)\times\mathrm{Cu_{0.5}Ga_{0.5}Cr_2Se_4}$. It was found that IR spectra of compositions with $0\leqslant x\leqslant 0.2$ contain seven fundamental absorption bands, which is in agreement with factor-group analysis of compounds with space group $F\bar{4}3m$, whereas IR spectra of the conventional spinel ($Fd3m$) have only four bands. This implies unambiguously 1:1 ordering in the tetragonal sublattice of these compositions. It thus appears more appropriate to call these compositions spinelides (or spinel-like). It was shown that the $0\leqslant x\leqslant 0.1$ compositions are nondegenerate semiconductors and possess properties characteristic of spin glasses. Their MR is isotropic, negative, and very large ($\sim$98% in a field of 40 kOe). Compositions with $0.1\leqslant x\leqslant 0.2$ exhibit a low-temperature LRMO-SG transition, which makes the semiconductor degenerate. It was found that the freezing temperature of these compositions, defined as the temperature at which the initial susceptibility measured in an ac magnetic field with frequencies in the range of 0.2 Hz to 8 kHz starts to drop, does not depend on the measurement frequency. Slightly below this temperature one observed a sharp minimum in negative isotropic MR down to $\sim$6% in absolute magnitude in a field of 40 kOe. For instance, for a $x=0.125$ composition $T_f=10.5$ K, while the minimum in MR was observed at $T=6.1$ K. This argues for the existence of an SG-LRMO phase transition at the freezing temperature T_f. Compositions with $x\geqslant 0.6$ are metallic ferromagnets. Thus we observed in the $x\mathrm{CuCr_2Se_4}-(1-x)\mathrm{Cu_{0.5}Ga_{0.5}Cr_2Se_4}$ solid-solution system a concentration-driven transition from the SG state to ferromagnetism through a mixed state (spin glass at low temperatures and long-range magnetic order at high temperatures), which was accompanied by a crossover from semiconducting

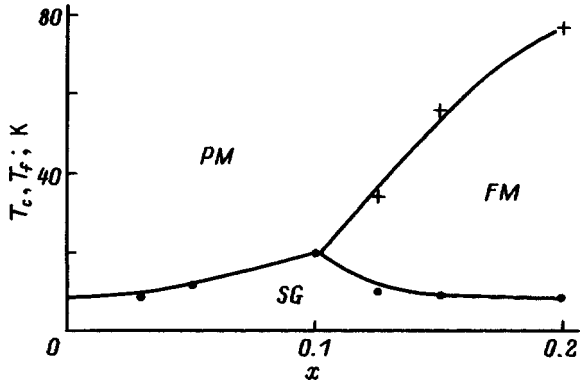

FIG. 1. Magnetic phase diagram of the $x\mathrm{CuCr_2Se_4}-(1-x)\mathrm{Cu_{0.5}Ga_{0.5}Cr_2Se_4}$ system. *PM*—paramagnetic phase, *FM*—ferromagnetic phase, SG—spin-glass phase.

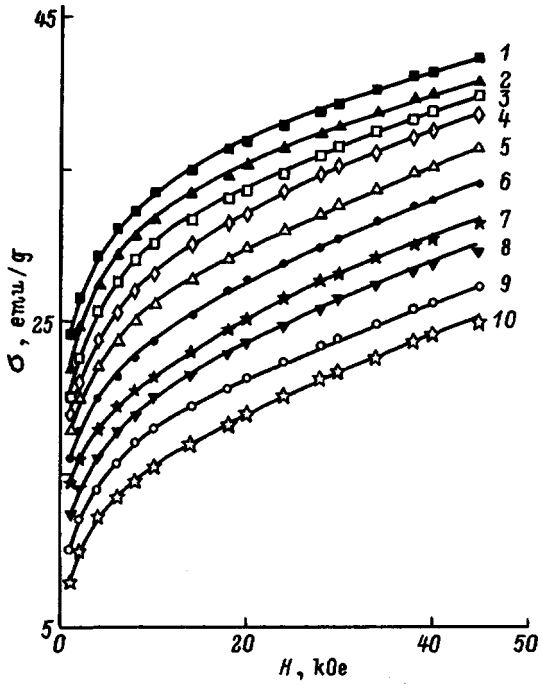

FIG. 2. Magnetization isotherms for different temperatures T(K): *1*—4.8, *2*—7.5, *3*—11, *4*—13.4, *5*—18, *6*—23.2, *7*—28, *8*—32.2, *9*—38.5, *10*—48.

to metallic conduction. Figure 1 presents a magnetic phase diagram for the system under study. Thus mixed-state compositions in this system are a convenient subject for verification of the above hypothesis.

In this work, we studied the dependence of MR on the square of magnetization, $\Delta\rho/\rho(\sigma^2)$, for the $Cu_{0.625}Ga_{0.375}Cr_2Se_4$ composition with a low-temperature LRMO-SG transition. Figure 2 shows magnetization isotherms for the given composition both above and below T_f. They are seen not to saturate up to 45 kOe. Presented in Fig. 3 are MR isotherms of the same composition obtained in fields $H \leqslant 45$ kOe in the same temperature region. We see that the $\Delta\rho/\rho(H)$ curves are far from saturation. We constructed $\Delta\rho/\rho(\sigma^2)$ plots in the strong-field domain, 30–45 kOe, for different temperatures near $T_f = 10.5$ K (Fig. 4). We see that the slope of these relations which are actually straight lines changes as one crosses the freezing temperature, namely, above T_f it is approximately twice that for $T < T_f$. This suggests that the intensity of the paraprocess increases above the freezing temperature, which is apparently caused by a significant rearrangement of the spin system at T_f. This provides an additional argument for the existence of an SG-LRMO phase transition at T_f. The independence of T_f of frequency, combined with the large difference in slope between the $\Delta\rho/\rho(\sigma^2)$ relations in the

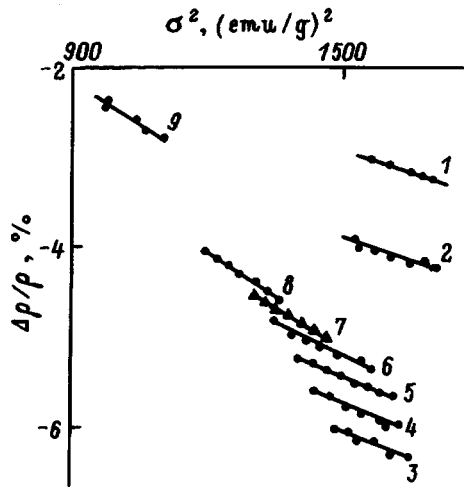

FIG. 4. Magnetoresistance vs squared magnetization plots for different temperatures around T_f. T(K): *1*—4.2, *2*—5.1, *3*—6.1, *4*—7.4, *5*—8.6, *6*—10.3, *7*—12.2, *8*—15, *9*—22.

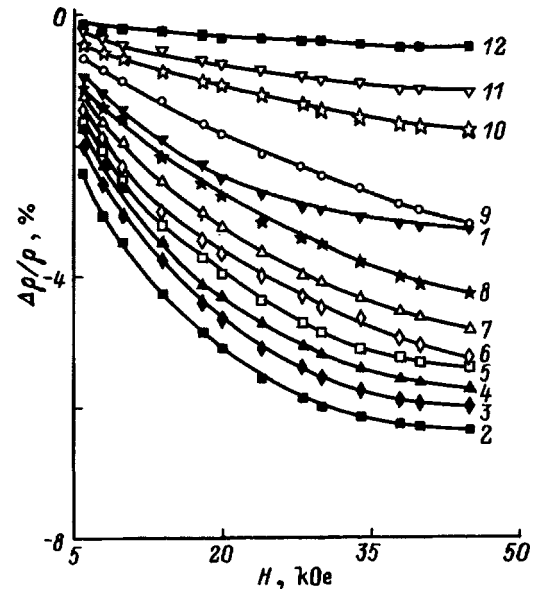

FIG. 3. Magnetoresistance isotherms for different temperatures T(K): *1*—4.2, *2*—6.1, *3*—7.4, *4*—8.6, *5*—10.3, *6*—12.2, *7*—15, *8*—17.7, *9*—22, *10*—26.7, *11*—31.5, *12*—41.

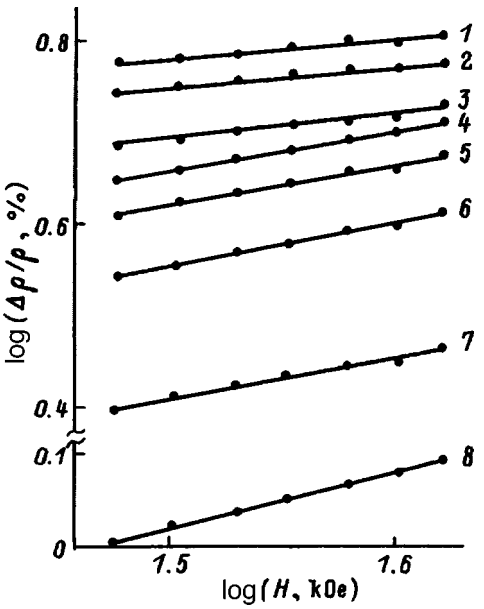

FIG. 5. $\log \Delta\rho/\rho$ vs $\log H$ plots for different temperatures T(K): *1*—6.1, *2*—7.4, *3*—10.3, *4*—12.2, *5*—15, *6*—17.7, *7*—22, *8*—31.5.

SG and LRMO phases, suggest that the structure of the SG phase corresponds to the fourth of the above versions, i.e., it consists of individual magnetic ions.

It was of interest also to study the dependence of the MR of this composition on magnetic field H. There is at present no theoretical description of the $\Delta\rho/\rho(H)$ relation for spin glasses and systems with a low-temperature transition from the SG to LRMO state. Based on general thermodynamic considerations and taking into account the properties of second-order phase transitions, it was shown[3,4] that for metallic ferromagnets at the Curie point $\Delta\rho/\rho \propto H^{2/3}$; for $T \gg T_c$, $\Delta\rho/\rho \propto H^2$; and for $T < T_c$, in the region of the paraprocess $\Delta\rho/\rho \propto H$. It was found that these relations hold for ferrites as well.[5] Figure 5 presents log-log plots of the $\Delta\rho/\rho(H)$ relation for strong magnetic fields in the temperature region 6.1–38.5 K. (For this composition, $T_c = 34$ K). We see that experimental points fit satisfactorily to straight lines. The slopes of these lines yielded the following relations: for $T \approx T_c$, $\Delta\rho/\rho \propto H^{0.6}$; for $T > T_c$, $\Delta\rho/\rho \propto H^{1.5}$; for $T_f < T < T_c$, $\Delta\rho/\rho \propto H^{0.4}$; and for $T < T_f$, $\Delta\rho/\rho \propto H^{0.2}$. A comparison of these relations with the ones presented above for ferromagnets and ferrites shows that MR depends weaker on the field everywhere, and, particularly, in the SG and LRMO regions. It was suggested[1] that in the composition under study SG regions are incorporated within an infinite ferromagnetic cluster. They occupy apparently a substantial volume in the sample, and this results in the $\Delta\rho/\rho(H)$ dependence which is weaker in all phases than it is in a pure ferromagnet.

Thus the increase in the intensity of the paraprocess observed by us to occur in the transition from the SG to LRMO phase, combined with earlier observations (the presence of a maximum in the temperature dependence of the absolute magnitude of MR around T_f, the change in the conduction activation energy at this temperature, and the independence of the freezing temperature itself of measurement frequency[1,2]), permit a conclusion that a thermodynamic phase transition takes place at T_f, and that the SG phase is made up of spins of individual ions.

Support of the Russian Fund for Fundamental Research (Grant 96-02-19684a) is gratefully acknowledged.

[1] L. I. Koroleva and A. I. Kuz'minykh, Zh. Éksp. Teor. Fiz. **84**, 1882 (1983) [Sov. Phys. JETP **57**, 1097 (1983)].
[2] L. I. Koroleva and A. I. Kuz'minykh, Fiz. Tverd. Tela (Leningrad) **26**, 56 (1984) [Sov. Phys. Solid State **26**, 31 (1984)].
[3] K. P. Belov, *Elastic, Thermal, and Electrical Phenomena in Ferromagnets* [in Russian] (Gostekhizdat, Moscow, 1957).
[4] K. P. Belov, *Magnetic Transitions* [Consultants Bureau, New York, 1961; Fizmatgiz, Moscow, 1959].
[5] S. Krupička, *Physik der Ferrite und der Verwandten Magnetischen Oxide* [Academia, Prag, 1973; Mir, Moscow, 1976].

Translated by G. Skrebtsov

Temperature anomalies in the relaxation of static photoelasticity in triglycine sulfate (TGS) crystals

B. G. Mytsyk and N. M. Dem'yanishin

Institute of Space Investigations, Ukrainian Academy of Sciences, 290601 L'vov, Ukraine
(Submitted May 28, 1997)
Fiz. Tverd. Tela (St. Petersburg) **40**, 318–320 (February 1998)

The relaxation of static photoelasticity in triglycine sulfate (TGS) crystals is investigated. The relaxing amplitudes are quite anisotropic, including changes in sign, and exhibit temperature anomalies. A mechanism is proposed for photoelastic relaxation and its temperature anomalies based on the piezocaloric effect. The corresponding calculations are presented.
 [S1063-7834(98)03502-3]

Static photoelasticity of ferroelectrics has been the subject of many papers (for example, Refs. 1–4), and the nature of related temperature anomalies has been studied as well.[5] Nevertheless, very little attention has been paid to the relaxation of photoelasticity, i.e., time-dependent changes in the crystal optical parameters (path difference, birefringence, and refractive index) induced by mechanical stresses that are fixed in magnitude. It is likely that the primary reason for the lack of work on photoelasticity relaxation is the complexity and precision the corresponding experimental methods require. In particular, we used the well-known polarization-optical method to study induced changes in the path difference[6] in this work; in order to do so we had to ensure the following experimental conditions: 1) stability of the intensity of our monochromatic light source to a level of $\leqslant 0.1\%$; 2) stabilization of sample temperature to an error of $\sim 0.01°$, which is ensured by temperature-stabilizing the path difference Δ_k to within $\sim 0.1\%$ of the induced Δ_k; and, 3) rigidity of the mechanical portion of the apparatus in order to exclude insignificant time-dependent translations and rotations of the loaded sample.

The relative amplitude of the relaxation is defined in this paper as follows:

$$\beta_{km} = (\delta\Delta_{km}^{\mathrm{rel}}/\delta\Delta_{km}) \cdot 100\%,$$

where $\delta\Delta_{km}^{\mathrm{rel}}$ is the absolute relaxation of the path difference, and $\delta\Delta_{km}$ is the path difference induced by a mechanical stress σ_m; the labels k, m take on values 1, 2, 3, and indicate the direction of propagation of the light and the effect of uniaxial compression along the corresponding axis of the optical indicatrices X_1, X_2, X_3 of the TGS crystals.

The relaxation is studied by determining the change in light intensity I with time on the linear portion of the function[6]

$$I_k = I_{\max} \sin^2(\pi\Delta_k/\lambda) \tag{1}$$

when a time-independent mechanical stress σ_m acts on the sample (here λ is the wavelength of light. Based on the measured relaxation-induced changes in light intensity $\delta I_{km}^{\mathrm{rel}}$, we calculate the quantity $\delta\Delta_{km}^{\mathrm{rel}}$ from Eq. (1). The induced path difference $\delta\Delta_{km}$ is determined from the well-known relation $\delta\Delta_{km} = -\pi_{km}^0 d_k \sigma_m/2$ using known piezooptical coefficients π_{km}^0 [7] and the effective value of σ_m. The quantities π_{km}^0 are also measured in the present paper by the method of half-wave stresses or the method of Senarmon. The sign of β_{km} is defined to be positive if the directions of change of the induced $\delta\Delta_{km}$ and relaxation-induced $\delta\Delta_{km}^{\mathrm{rel}}$ path differences coincide, and negative if $\delta\Delta_{km}^{\mathrm{rel}}$ decreases $\delta\Delta_{km}$.

Figure 1 shows an example of the relaxation dependence of the path difference $\beta_{km}(t)$ (where t is time). It is clear that the maximum relaxation amplitude, defined in the region of saturation of the functions $\beta_{km}(t)$, is significantly anisotropic both in magnitude and in sign. The quantities $\beta_{km}(t)$ do not depend on the magnitude of the applied mechanical stresses within the range of values $\sigma_m = (20-100)\times 10^5$ N/m^2 used in this paper.

Figure 2 shows the temperature dependence of the maximum relaxation amplitudes of the path differences β_{km}. The functions $\beta_{km}(T)$ increase significantly in absolute value as we approach the phase transition from the ferroelectric phase side, while the values of β_{km} far from the phase transition correspond to values extrapolated from the paraelectric phase. The most obvious mechanism for photoelastic relaxation is the change in induced path difference due to the piezocaloric effect, in which rapid application of σ_m leads to an adiabatic change in temperature by an amount δT^{rel} proportional to the value of σ_m. The temperature of the sample then becomes equal to the temperature of the external medium after a certain time τ (the relaxation time) due to heat exchange with the external medium. This relaxation-induced change in temperature causes a thermooptical change in the path difference and, accordingly, the relaxation of the light intensity I_k recorded in the experiment. This mechanism for photoelastic relaxation is confirmed by calculations based on the following expression:

$$\delta\Delta_{km}^{\mathrm{rel}} = \delta T_m^{\mathrm{rel}} d\Delta_k(T)/dT, \tag{2}$$

where the label m on $\delta T_m^{\mathrm{rel}}$ indicates the dependence of the piezocaloric effect on the direction of the uniaxial compression. The values of the temperature derivatives of the path difference $d\Delta_k(T)/dT$ are determined from data of Ref. 8, while the value of $\delta T_m^{\mathrm{rel}}(T)$ is given by the temperature dependences of the piezocaloric coefficients $dT_m^{\mathrm{rel}}/d\sigma_m$ given in Ref. 9:

$$\delta T_m^{\mathrm{rel}} = \sigma_m dT_m^{\mathrm{rel}}/d\sigma_m. \tag{3}$$

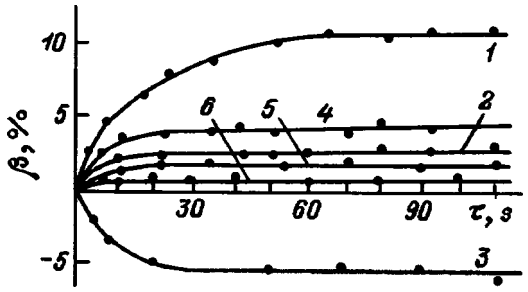

FIG. 1. Example of relaxation functions $\beta_{km}(t)$ for TGS crystals at $T=308$ K, $\lambda=0.63$ μm. *1*—β_{13}, *2*—β_{23}, *3*—β_{31}, *4*—β_{12}, *5*—β_{32}, *6*—β_{21}.

It is clear from Fig. 2 that within limits of error in processing graphical materials from Refs. 8 and 9 (5–10%) the experimental and computed functions $\beta_{km}(T)$ coincide.

Note that the quantities $\delta T_m^{\rm rel}$ can be determined from the coefficients of thermal expansion α_m of the sample as well:[10]

$$\delta T_m^{\rm rel} = -(T_0/C_p)\sigma_m\alpha_m, \tag{4}$$

where T_0 is the sample temperature in the external medium and C_p is the heat capacity per unit volume of crystal. In order to calculate $\delta T_m^{\rm rel}$, values of the heat capacity $C_m(T)$ of TGS crystals were taken from Ref. 11, taking into account the fact that $C_p=C_m(T)\rho$. The density $\rho=1690$ Kg/m^3 was taken from Ref. 12, and the thermal expansion coefficients $\alpha_m(T)$ along the crystallographic axes X_1, X_2, X_3, which coincide with the optical indicatrices of the TGS crystal, are determined by transforming the components of the second-rank tensor $\alpha_m(T)$ from the data of Ref. 13, where coefficients $\alpha_m(T)$ were given along axes X,Y,Z rotated through an angle of 18° around the axis $X_2\equiv b$ relative to the axes X_1 and X_3 of the optical indicatrices.

Differences between the functions $\delta T_m^{\rm rel}$ defined according to Eqs. (3) and (4) do not exceed 5%. However, in Fig. 2 we present the computed functions $\beta_{km}(T)$ starting from the function $\delta T_m^{\rm rel}$ defined in Eq. (4), because in contrast to Refs. 9 and 13, we clearly have indicated the system of coordinates in which the coefficients $\alpha_m(T)$ are determined.

Also noteworthy is the fact that the relative relaxation amplitudes β_{12} and β_{13} at temperature $T=293$ K change sign, which in accordance with Eq. (2) is due to a change in the sign of the piezocaloric effect at this temperature.[8] The function $\beta_{23}(T)$ changes sign at $T=303$ K, despite the fact that there is no change in the sign of $\delta T^{\rm rel}$ at this temperature. In this case, according to Eq. (2) the change in sign of $\beta_{23}(T)$ is caused by a change in the sign of the derivative $d\Delta_2(T)/dT$ at $T=303$ K. The latter fact is confirmed in this paper experimentally, because it is impossible to exactly determine the temperature where the derivative $d\Delta_2(T)/dT$ changes sign based on the temperature dependence of $\Delta_2(T)$ given in Ref. 8.

In conclusion, we note that we have also investigated photoelastic relaxation of TGS crystals with chromium-ion impurities (TGS+Cr^{3+}, 0.1% chromium in solution). At these chromium concentrations we observed no change within 10% in either the temperature dependence of the piezooptic coefficients or the functions $\beta_{km}(T)$ compared with the pure TGS crystals.[7]

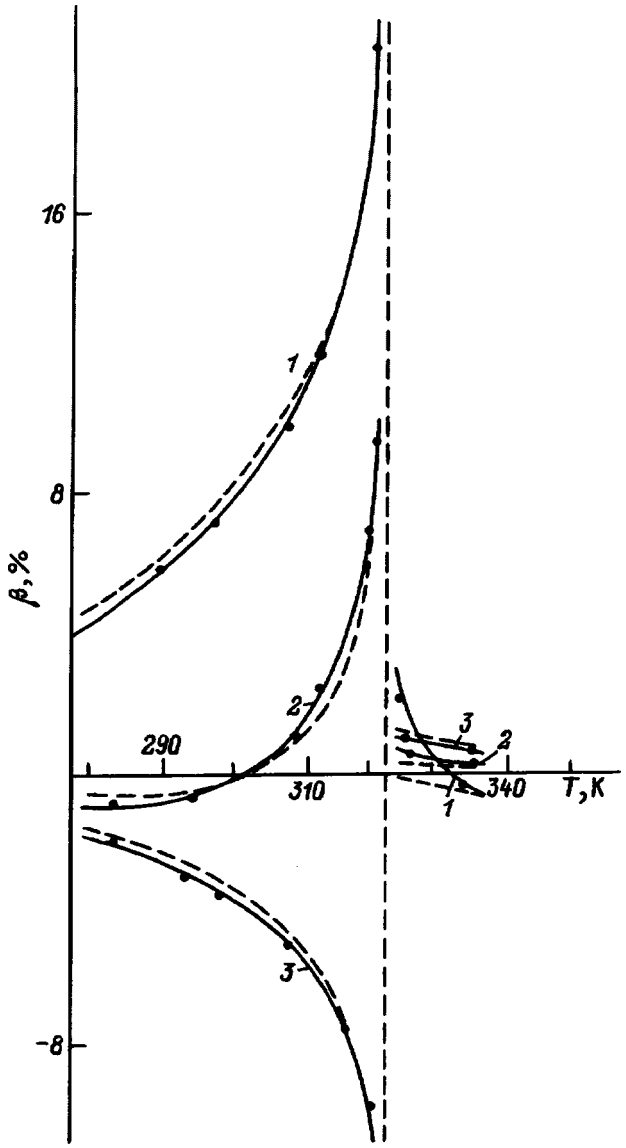

FIG. 2. Temperature dependence of the relaxation amplitude β_{km} for TGS crystals. *1*—β_{13}, *2*—β_{23}, *3*—β_{31}. The solid curves are experiment, the dashed lines are computed.

[1] B. G. Mytsyk, V. A. Romashko, and Ya. I. Shopa, Fiz. Tverd. Tela (St. Petersburg) **35**, 2272 (1993) [Phys. Solid State **35**, 1129 (1993)].
[2] B. G. Mytsyk, V. A. Romashko, and Ya. I. Seglin'sh, Fiz. Tverd. Tela (Leningrad) **33**, 2857 (1991) [Sov. Phys. Solid State **33**, 1614 (1991)].
[3] O. G. Vlokh, A. V. Kityk, and I. I. Polovinko, Ukr. Fiz. Zh. **31**(7), 1051 (1986).
[4] O. G. Vlokh, I. I. Polovinko, and S. A. Sveleba, Kristallografiya **35**, 780 (1990) [Sov. Phys. Crystallogr. **35**, 457 (1990)].
[5] S. S. Kotsur, B. G. Mytsyk, and V. A. Romashko, Kristallografiya **37**, 1517 (1992) [Sov. Phys. Crystallogr. **37**, 822 (1902)].
[6] A. S. Sonin and A. S. Vasilevskaya, *Electrooptic Crystals* (Nauka, Moscow, 1971).
[7] B. G. Mytsyk and N. A. Romanyuk, Ukr. Fiz. Zh. **28**, (4) 538 (1983) [in Russian].
[8] N. R. Ivanov, S. Ya. Benderskiĭ, and I. T. Tukhtasunov, Bull. USSR Acad. Sci. Ser. Phys. **39**(4), 798 (1975) [in Russian].

[9] K. Imai, J. Phys. Soc. Jpn. **38**, 836 (1975).
[10] Yu. I. Sirotin and M. P. Shaskol'skaya, *Principles of Crystallography* (Nauka, Moscow, 1979).
[11] B. A. Strukov, S. A. Taraskin, V. A. Koptsik, and V. M. Varikash, Kristallografiya **13**, 541 (1968) [Sov. Phys. Crystallogr. **13**, 447 (1968)].
[12] W. Pepinski, R. Okaya, and B. Yona, Bull. Am. Phys. Soc. Ser. II, **2**, 4, 220 (1957).
[13] J. Stankowski and W. Malinowski, Acta Phys. Pol. A **58**(6), 773 (1980).

Translated by Frank J. Crowne

Mechanisms of EPR line broadening in $Pb_5Ge_3O_{11}$ near a structural transition

V. A. Vazhenin, E. L. Rumyantsev, M. Yu. Artemov, and K. M. Starichenko

Scientific-Research Institute for Physics and Applied Mathematics, Ural State University, 620083 Ekaterinburg, Russia

(Submitted July 8, 1997)
Fiz. Tverd. Tela (St. Petersburg) **40**, 321–326 (February 1998)

The polar angular dependence of the anomalous linewidth of three EPR transitions in the Gd^{3+} trigonal center has been used to determine the broadening mechanism. It is shown that the dominant mechanism of Gd^{3+} EPR signal broadening in the vicinity of the ferroelectric transition is the critically growing spread of the b_{21} and c_{21} parameters accounting for the odd-order fields of remote charge-compensating defects. © *1998 American Institute of Physics.* [S1063-7834(98)03602-8]

1. Lead germanate (LG) $Pb_5Ge_3O_{11}$ undergoes a ferroelectric phase transition $P3(C_3^1)\leftrightarrow P\bar{6}(C_{3h}^1)$ at 450 K.[1] A distinctive feature of LG is the appearance in its ferroelectric phase of a natural optical activity, whose magnitude is linearly related to spontaneous polarization. The temperature dependence of the spontaneous polarization P_c, dielectric permittivity, optical activity and other parameters of LG exhibit additional anomalies,[2–8] suggesting the existence of other structural transformations.

An analysis of LG lattice vibrations[9,10] showed that one cannot obtain the ferroelectric structure without additional distortions by mere freezing of the IR-active mode responsible for spontaneous polarization. To describe the temperature behavior of LG, a sequence of structural transitions was proposed[9,10] [the group symmetry of the praphase is assumed to be $P\bar{6}2m(D_{3h}^3)$], in particular, with the order parameter transforming as an axial vector.

2. The room-temperature EPR spectrum of gadolinium-doped LG single crystals is characteristic of a trigonal (C_3) Gd^{3+} center, whose symmetry group becomes C_{3h} above the ferroelectric transition point. The presence in the spin Hamiltonian of parameters b_{43} and b_{63} (the latter is very small) related linearly (neglecting higher-order odd terms) to polarization P gives rise to EPR splitting, which is due to the existence of domains of two types and is maximum in a magnetic field B lying in the zx plane ($z\|C_3$, x is perpendicular to the growth face), with no splitting observed in the zy plane.[11,12]

For $\theta\neq 0°$, 90° (θ is the polar angle of B) all transitions of the trigonal center exhibit a broadening within a wide temperature region around the ferroelectric transition (Fig. 1).[13] For the linewidth ΔB_{pp} one takes the distance between the extrema of the first derivative of the absorption signal. The line-shape analysis is hindered by the presence of a large number of locally compensated triclinic Gd^{3+} centers, whose signals lie in the wings of the trigonal-center transitions.[14] One could establish only that near the phase transition the line shape is a superposition of a Gaussian and a Lorentzian, whereas far from T_c the central part of the line is a Lorentzian, with the wings falling off faster. Measurements of the temperature dependence of the EPR linewidth were performed on single-domain samples in order to avoid overlapping of signals from various domains near the ferroelectric transition.

In contrast to the trigonal Gd^{3+} center, the axial Mn^{2+} center observed in manganese-doped crystals and localized, similar to Gd^{3+}, in trigonal positions of LG, does not exhibit domain splitting ($b_{43}=0$),[15] as well as EPR line broadening in the vicinity of the structural transition.

Figure 2 shows polar angular dependences of the linewidth for three transitions of the trigonal Gd^{3+} centers measured in the zx plane at 453 K (i.e., in the paraphase). These dependences do not change their pattern within about 10° around the ferroelectric transition. Presented in Fig. 3 is the angular behavior of the anomalous part of the linewidth for two EPR transitions at 458 K, obtained by measuring the temperature dependence of the linewidth for several magnetic-field orientations and by subtracting from it the ''background'' width interpolated into the phase-transition region. We believe that the results displayed in Figs. 2 and 3 are in qualitative agreement (the relative positions of the linewidth extrema for various transitions), particularly if one takes into account the possibility of an angular dependence of the noncritical linewidth and a certain arbitrariness in estimating the background. In our opinion, the different and nontrivial angular behavior of the linewidth of the EPR transitions under study can be used in a search for the mechanism responsible for the anomalous linewidth in LG.

3. The broad temperature interval within which the Gd^{3+} centers exhibit anomalous EPR broadening, as well as the behavior of the line shape (the increasing contribution of the Gaussian near the transition) argue for a static mechanism of formation of the additional width, for instance, a spread in polarization because of defects in the crystal, which increases as one approaches the ferroelectric transition due to the increase of the polarizability and results in an ever increasing modulation of b_{43}.

An additional argument in support of this assumption comes from the absence of any broadening in Mn^{2+} EPR signals in the region of the structural transition, whose positions do not depend linearly on polarization. If this mechanism of broadening does operate, one should expect the angular dependences of the linewidth and of the domain splitting to behave similarly, since their angular course is

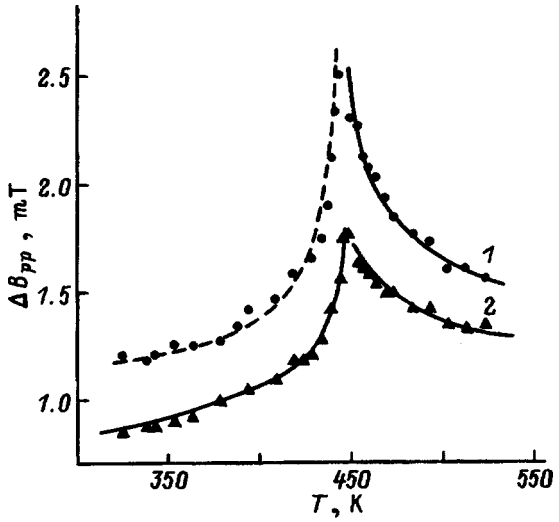

FIG. 1. Temperature dependence of EPR linewidth of Gd^{3+} trigonal center in the vicinity of the ferroelectric transition ($3\leftrightarrow4$ transition, levels numbered from bottom upward, $\theta=75°$, $\varphi=0°$). *1*—0.1% Gd_2O_3, *2*—0.01% Gd_2O_3.

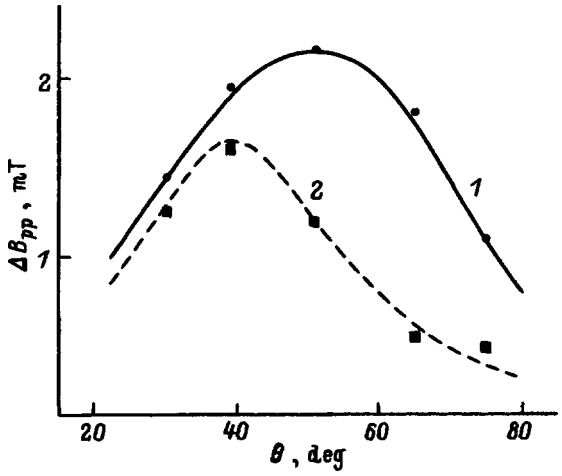

FIG. 3. Angular dependence of the anomalous part of linewidth in the *zx* plane. ($T=458$ K, 0.02% Gd_2O_3). *1*—$3\leftrightarrow4$ transition, *2*—$5\leftrightarrow6$ transition.

determined by $\frac{\partial B_{\rm res}}{\partial P}(\theta)\sim\frac{\partial B_{\rm res}}{\partial b_{43}}(\theta)$, and this is exactly what was observed[16,17] in a study of the $Fe^{3+}-O^{2-}$-vacancy axial center in $SrTiO_3$.

Figure 4 shows angular dependences of the domain splitting, both experimental and computed by diagonalization of the spin-Hamiltonian matrix, for the trigonal-center transitions treated in Fig. 2. No correlation between the angular dependence of linewidth and the domain splitting is seen. For instance, the domain splitting for the $5\leftrightarrow6$ transition passes through a maximum at $\theta\approx60°$, whereas the linewidth is the largest at $\theta=30\div40°$, although for the $3\leftrightarrow4$ transition the linewidth and domain splitting behave in a qualitatively similar way. It thus does not appear possible to attribute the angular dependence of EPR signal width near the ferroelectric transition to modulation of parameter b_{43}. The same conclusion can be drawn from the fact that the signal width in the *zy* plane, where spread in b_{43} should not produce any broadening, follows qualitatively the same angular behavior as that in the *zx* plane.

Figure 5 illustrates the behavior of the quantity $\delta(\theta)=\sqrt{\Delta B_{pp}^2(\theta,0°)-\Delta B_{pp}^2(\theta,90°)}$, where $\Delta B_{pp}(\theta,90°)$ and $\Delta B_{pp}(\theta,0°)$ are the angular dependences of linewidth measured in the *zy* and *zx* planes, respectively. The similar behavior of the curves and of the relations shown in Fig. 4 indicates the existence at $\theta=0°$ of a contribution to linewidth due to b_{43} modulation, although it is not dominant (see the vertical scales in Figs. 4 and 5). As for the dominant contribution to the anomalous linewidth, it is apparently axially symmetric.

Let us take into account the fact that the dependence of the spin-Hamiltonian parameters on polarization cannot be described only by the linear relation

$$b_{43}=cP, \tag{1}$$

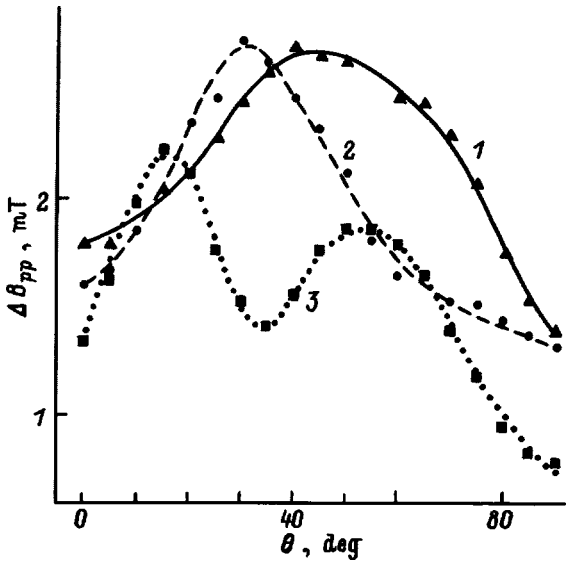

FIG. 2. Angular dependence of the linewidth in the *zx* plane ($T=453$ K, 0.1% Gd_2O_3). *1*—$3\leftrightarrow4$ transition, *2*—$5\leftrightarrow6$ transition, *3*—$4\leftrightarrow5$ transition.

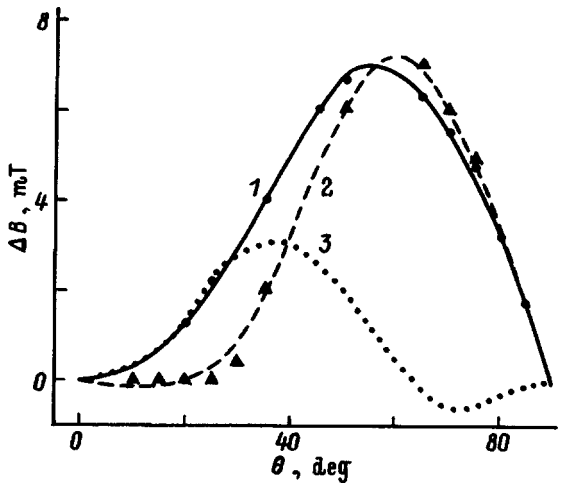

FIG. 4. Calculated (curves) and experimental (dots) angular dependences of domain splitting in the *zx* plane ($T=300$ K). *1*—$3\leftrightarrow4$ transition, *2*—$5\leftrightarrow6$ transition, *3*—$4\leftrightarrow5$ transition.

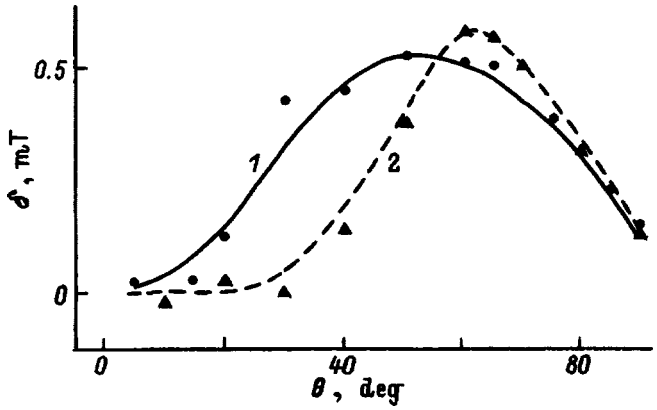

FIG. 5. Contribution to the EPR linewidth $\delta(\theta)$ in the zx plane due to modulation of $b_{43}(P)$. *1*—3↔4 transition, *2*—5↔6 transition.

where $c=42$ MHz$(\mu\text{C/cm}^2)^{-1}$.

A study[18] of the polar angular dependence of EPR signal shift in an external electric field $\mathbf{E}\|C_3$ in paraelectric phase showed that the observed effect can be described with a good accuracy by Eq. (1) and relations

$$b_{20}=b_{20}(T)+aP^2, \quad a=-2.6 \ \text{MHz}(\mu\text{C/cm}^2)^{-2}, \qquad (2)$$

$$b_{40}=b_{40}(T)+bP^2, \quad b=0.17 \ \text{MHz}(\mu\text{C/cm}^2)^{-2}, \qquad (3)$$

where P is induced polarization, and the coefficients a,b,c are estimated from the temperature dependence of the parameters of the spin Hamiltonian under the assumption that the paraphase relations $b_{20}(T)$ and $b_{40}(T)$ do not have singularities at the transition (at room temperature $P_c=4.8$ μC/cm^2, Ref. 2).

The square root of the second moment, which takes into account the variations in b_{20}, b_{40}, and b_{43} caused by the spread in spontaneous polarization [Eqs. (1)–(3)], differs very little in angular dependence from the domain splitting (Fig. 4), thus bringing us to the conclusion that the EPR line broadening near the structural transition cannot be attributed to the spread in the z component of polarization.

Taking into account the mosaic structure of the crystal is hardly promising because it would not result in an anomalous linewidth dependence on temperature.

The assumption of a spread in the transverse components of polarization (i.e. in the mean square of parameter b_{22}), whose contribution to linewidth becomes easier to estimate using measurements of the transverse electric-field effect[19]), leads to irrelevant polar dependences. Besides, as in the case of mosaic structure, one could hardly expect this contribution to increase in a ferroelectric transition.

4. In connection with the experimental observation of a weak dependence of linewidth near the structural transition on gadolinium concentration (Fig. 1), we considered the broadening of EPR transitions caused by the spin-spin interaction of paramagnetic centers via the soft-phonon field[20,21] of the kind[22]

$$R_{ij}(T,r_{ij},\theta_{ij})O^i_{43}O^j_{43}, \qquad (4)$$

$$Q_{ij}(T,r_{ij},\theta_{ij})O^i_{20}O^j_{20}, \qquad (5)$$

$$N_{ij}(T,r_{ij},\theta_{ij})O^i_{43}O^j_{20}, \qquad (6)$$

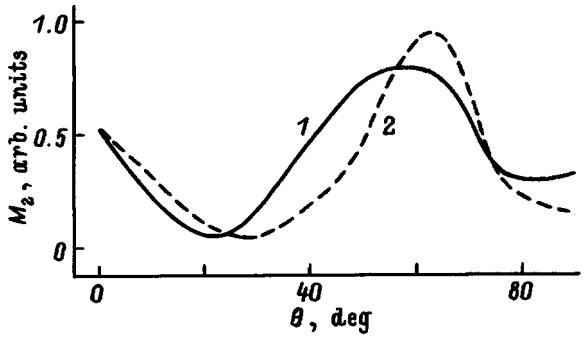

FIG. 6. Angular dependence of the second moment of the line caused by spin-spin interaction of type (4). *1*—3↔4 transition, *2*—5↔6 transition.

where $R_{ij}(T,r_{ij},\theta_{ij})$, $Q_{ij}(T,r_{ij},\theta_{ij})$, $N_{ij}(T,r_{ij},\theta_{ij})$ are interaction parameters depending on the ion spacing, the angle between the bond axis and C_3, and (anomalously) on temperature, and O^i_{nm} and O^j_{nm} are the Stevens operators for ions i and j.

The angular dependences of the second moment of the two EPR transitions appearing by mechanism (4) were obtained within Van Vleck theory, as well as estimated by numerical diagonalization of a 64-order matrix for a pair of interacting ions. The dependences were found to be close to one another and to the behavior of domain splitting (Figs. 4 and 6), while not correlating with the experimentally observed linewidth behavior (Fig. 2). The angular dependences of the second moment of the line resulting from mechanisms (5) and (6) were still farther from the observed pattern.

It was found to be possible to explain the angular dependence of the anomalous EPR linewidth of trigonal Gd^{3+} centers in LG by assuming the existence of fluctuating nondiagonal components of the g tensor.[23] Indeed, inclusion of terms $g_{xz}\beta H_x S_z$ and $g_{yz}\beta H_y S_z$ into the Hamiltonian (with $g_{zx}=g_{zy}=0$) results in a shift of the EPR signal, whose angular dependence (Fig. 7), in contrast to the above mechanisms, provides a qualitatively correct description of the linewidth behavior (Fig. 2). Symmetrization of the g tensor ($g_{zx}=g_{xz}$, $g_{zy}=g_{yz}$) changes substantially the angular dependences to make them totally unlike the observed patterns.

Nondiagonal components may appear in the g tensor due to spin-lattice interaction (in the C_{3h} group)

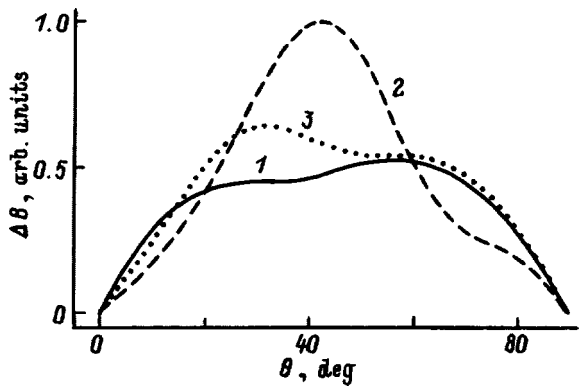

FIG. 7. EPR signal shift vs polar angle θ caused by inclusion of g_{yz} and g_{xz}. *1*—3↔4 transition, *2*—5↔6 transition, *3*—4↔5 transition.

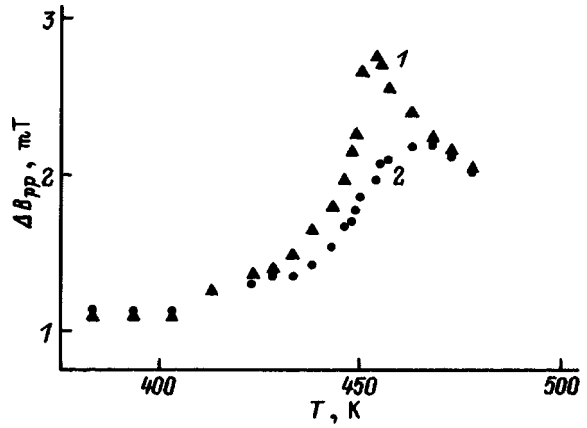

FIG. 8. Temperature dependence of linewidth for (1) $E=0$ and (2) $E=19$ kV/cm. $3\leftrightarrow4$ transition, low-field domain-doublet component, $\theta=63°$, $\varphi=0°$.

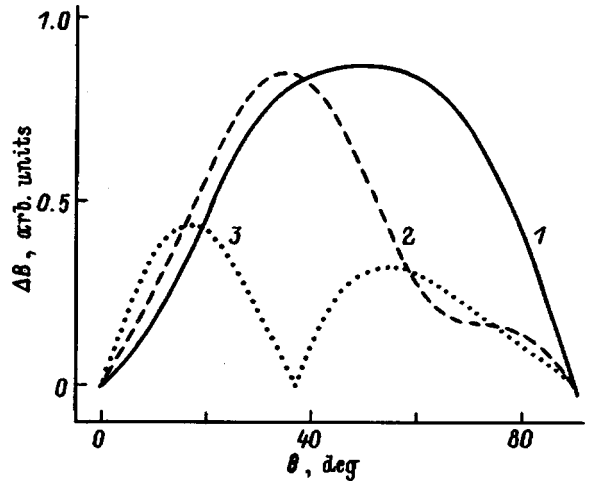

FIG. 9. Angular dependence of the modulus of EPR line shift in the zx plane as a result of inclusion of b_{21}. *1*—$3\leftrightarrow4$ transition, *2*—$5\leftrightarrow6$ transition, *3*—$4\leftrightarrow5$ transition.

$$g_{xz}=G_1e_{zx}+G_2e_{zy}, \quad g_{yz}=G_1e_{zy}-G_2e_{zx}, \tag{7}$$

where G_i are the components of a fourth-rank tensor, and e_{kl} are those of the strain tensor, or in the product of polar or axial vector components A_kA_l. Since, however, the g tensor in S state depends usually very weakly on crystalline environment, and the description of the observed relations is fairly conventional, this mechanism is hardly the one one would be looking for.

5. Studies of the effect of a strong electric field ($E\|C_3$) on Gd^{3+} EPR spectrum in the vicinity of the ferroelectric transition in LG revealed a noticeable field-induced signal narrowing, which was attributed to suppression of the multiphase state of the sample.[18] Figure 8 shows experimental temperature dependences of the linewidth obtained in a field of 19 kV/cm and with no field applied. The line shape with the field on approaches closer a Lorentzian. The small extent of the relations into the paraelectric phase is due to the low electric strength of the crystal at these temperatures, which results in a finite sample lifetime. After the electric breakdown and removal of the electrode, one sees in the sample triangular-based black needles directed along C_3.

The angular behavior of the anomalous linewidth in the presence of an external field is the same in the zx and zy planes and is similar to that shown in Fig. 2, which implies a closeness of the broadening mechanisms operating with and without a field. The line-broadening contribution associated with the multi-phase state and suppressed by an electric field can be explained as due to a high density of interfaces and domain walls near the structural transition, which give rise to arbitrary strain fields at paramagnetic centers. By analogy with Eq. (7) we can write relations

$$b_{21}=F_1e_{zx}+F_2e_{zy}, \quad c_{21}=F_1e_{zx}-F_2e_{zy}, \tag{8}$$

connecting the spin-Hamiltonian parameters b_{21} and c_{21} with components of the strain tensor e_{kl} and of the spin-lattice interaction tensor (in the C_3 group). While lowering of the Gd^{3+} symmetry will naturally generate other low-symmetry parameters of various ranks as well, the b_{21} and c_{21} parameters are remarkable in that their contribution to the angular dependence of the resonant positions of the transitions under study (Fig. 9) in the zx and zy planes, respectively, is in accord with the angular behavior of linewidth (Fig. 2), i.e. both are described by the $\partial B_{\rm res}/\partial b_{21}(\theta)$ relation. Thus the assumption of the existence and spread of parameters b_{21} and c_{21} or, according to Eq. (8), of nondiagonal components in the strain tensor, which appear in the vicinity of the structural transition, permits one to explain the contribution to the anomalous linewidth which vanishes in a strong electric field.

As mentioned in Sec. II, one observes in LG, besides the trigonal Gd^{3+} centers, a large number of triclinic centers, whose low symmetry is due to local compensation of the excess gadolinium charge by interstitial ions of chlorine, oxygen, and bromine present at distances of about and less than 1 nm. As the temperature is lowered, an ever larger number of lines become resolved in the wings of the trigonal-center signals because of the associated decrease in linewidth.[14] The compensating ions occupying positions with arbitrary polar and azimuthal angles generate both longitudinal and transverse odd-order fields at the paramagnetic ion, thus giving rise to Hamiltonian terms of the type $b_{21}O_{21}\sim p_zp_x$, $c_{21}\Omega_{21}\sim p_zp_y$ [p_i are local-polarization components, see Eqs. (7) and (8)], which produce transition shifts with the angular dependence shown in Fig. 9.

There are undoubtfully many Gd^{3+} ions which interact only weakly with more remote compensating ions and, therefore, give an experimentally unresolvable contribution to the intensity of the trigonal spectrum. Measurements of the temperature dependence of linewidth after a sample anneal in a chlorine ambient, which increases the concentration of interstitial chlorine ions, showed the anomalous linewidth to grow stronger than the background one.

As one approaches the ferroelectric transition, the p_z component induced by a charged point defect increases, so that one may expect $\langle p_z^2\rangle$ to follow the same temperature behavior as the mean square of polarization fluctuations[24]

$$\langle p_z^2\rangle=4kT\varepsilon/V, \tag{9}$$

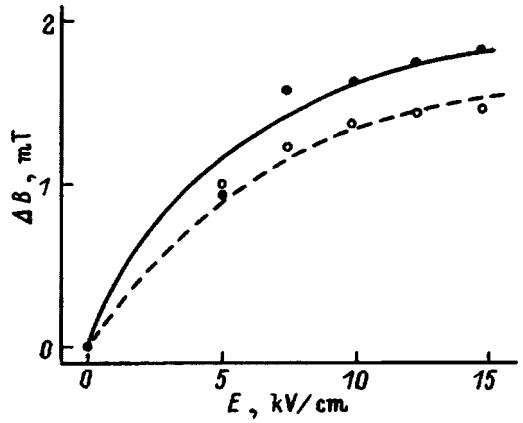

FIG. 10. Field dependence of the signal shift (dashed line) and of the signal narrowing (solid line) at $T=451$ K, $\theta=63°$, $\varphi=0°$ ($3\leftrightarrow4$ transition).

where ε is the dielectric permittivity, and V is the crystal volume. Assuming the longitudinal and transverse components of the defect-induced polarization to be unrelated, and no singularities in the behavior of $\langle p_x^2\rangle$ and $\langle p_y^2\rangle$, one can readily obtain the temperature dependence of linewidth. The dashed line in Fig. 1 shows the result of fitting the experimental data with a function

$$\Delta B=\left[(c_1T^2)^2+\frac{c_2T}{|T_c-T|}+c_3^2\right]^{1/2}, \tag{10}$$

where the radicand is a sum of second moments for the various mechanisms of EPR line broadening, namely, the first term is due to spin-lattice relaxation,[25] the second is the result of a spread in b_{21} and c_{21}, and the third accounts for the low-temperature linewidth. Despite the assumptions made here, relation (10) is seen to provide a fairly good fit to the experimental temperature behavior of linewidth. Thus the good description of the angular and temperature course of linewidth permits a conclusion that the main mechanism responsible for the anomalous EPR line broadening near the ferroelectric transition is coexistence of a spread in the longitudinal and transverse local-polarization components, which is generated by charged defects. In the vicinity of T_c, the parameters $\sqrt{\langle b_{21}^2\rangle}$ and $\sqrt{\langle c_{21}^2\rangle}$ of the spread in b_{21} and c_{21} are of the order of 10 MHz.

It should be pointed out that the contribution of this mechanism to linewidth in a strong electric field may also decrease because of the decrease in differential polarizability. In these conditions, the field dependence of the line narrowing should be close in character to saturation of induced polarization. In our opinion, the experimental data shown in Fig. 10 (the electric-field-induced shift of EPR signal is proportional to induced polarization[18]) support the latter statement.

One can now explain the absence of broadening in the lines belonging to Mn^{2+} paramagnetic centers near the ferroelectric transition. Since substitution of Mn^{2+} for Pb^{2+} does not involve a change in the charge state, one can hardly expect the appearance in its environment of a charged defect which could generate longitudinal and transverse components in the local polarization. The insensitivity of Mn^{2+} signals to the average magnitude and spread of P_z originates apparently from the smallness of its parameter c in Eq. (1), which is a component of the third-rank spin-lattice interaction tensor.

In the case of the Gd^{3+} triclinic centers in LG, interaction with the compensating ion creates its own EPR spectrum and determines the parameters of the ''average'' spin Hamiltonian. In these conditions, the probability for one more charged defect to be present in its vicinity is considerably smaller than that for nonlocally compensated centers. In connection with this, line broadening near the ferroelectric transition due to b_{21} and c_{21} fluctuations should be ineffective, and, as a result, the spread in b_{43} should be a dominant mechanism. Measurements probing the $5\leftrightarrow6$ transition of center II*a* (Gd^{3+} associated with an interstitial chlorine[14]) performed at $\theta=58°$ on an LG crystal annealed in a chlorine atmosphere showed that its linewidth also exhibits a maximum around the structural transition. Unfortunately, one did not succeed in measuring the angular dependence of linewidth near T_c and, hence, in establishing the dominant mechanism of broadening for the triclinic centers. The reason for this was the splitting (into six equivalent, but rotated centers) and broadening in arbitrary orientation of the EPR signal, which had low intensity and was located in the wing of the intense trigonal-center transition.

The authors express their gratitude to F. M. Musalimov for the samples of doped single crystals and to A. O. Sherstyankin for assistance in measurements.

[1] Y. Iwata, J. Phys. Soc. Jpn. **43**, 961 (1977).
[2] H. Iwasaki, S. Miyazawa, H. Koizumi, K. Sugii, and N. Niizeki, J. Appl. Phys. **43**, 4907 (1972).
[3] V. D. Salnikov, S. Yu. Stephanovich, V. V. Chechkin, M. V. Pentegova, Yu. Ya. Tomaspolskii, and Yu. N. Venevtsev, Ferroelectrics **8**, 491 (1974).
[4] M. Malinowski, A. Pietraszko, and M. Połomska, Phys. Status Solidi A **41**, K55 (1977).
[5] K. H. Germann, W. Mueller-Lierheim, H. H. Otto, and T. Suski, Phys. Status Solidi A **35**, K165 (1976).
[6] G. I. Rozenman and E. I. Boĭkova, Kristallografiya **23**, 644 (1978) [Sov. Phys. Crystallogr. **23**, 359 (1978)].
[7] E. L. Rumyantsev, V. A. Vazhenin, and M. S. Gol'dshtein, Fiz. Tverd. Tela (Leningrad) **21**, 2522 (1979) [Sov. Phys. Solid State **21**, 1457 (1979)].
[8] V. N. Gavrilov, A. G. Zakharyants, É. V. Zolotoyabko, E. M. Iolin, A. G. Maloyan, and A. V. Muromtsev, Fiz. Tverd. Tela (Leningrad) **25**, 10 (1983) [Sov. Phys. Solid State **25**, 4 (1983)].
[9] V. I. Cherepanov, E. L. Rumyantsev, A. N. Babushkin, and I. É. Pomeranets, Kristallografiya **25**, 595 (1980) [Sov. Phys. Crystallogr. **25**, 341 (1980)].
[10] A. N. Babushkin, *Author's Abstract of Dissertation* (Ural University, Sverdlovsk, 1986).
[11] Yu. A. Sherstkov, V. I. Cherepanov, V. A. Vazhenin, K. M. Zolotareva, and E. L. Rumyantsev, Izv. Akad. Nauk SSSR, Ser. Fiz **39**, 710 (1975).
[12] V. A. Vazhenin, Yu. A. Sherstkov, and K. M. Zolotareva, Fiz. Tverd. Tela (Leningrad) **17**, 2485 (1975) [Sov. Phys. Solid State **17**, 1655 (1975)].
[13] V. A. Vazhenin, E. L. Rumyantsev, and K. M. Starichenko, *Abstracts of the Tenth All-Union Conference on Ferroelectricity* (Minsk, 1982), Pt. 2, p. 158.
[14] V. A. Vazhenin, K. M. Starichenko, and A. V. Gur'ev, Fiz. Tverd. Tela (Leningrad) **30**, 1443 (1988) [Sov. Phys. Solid State **30**, 832 (1988)].
[15] V. A. Vazhenin, A. D. Gorlov, and A. P. Potapov, Fiz. Tverd. Tela (Leningrad) **28**, 2043 (1986) [Sov. Phys. Solid State **28**, 1142 (1986)].
[16] Th. von Waldkirch, K. A. Müller, and W. Berlinger, Phys. Rev. B **7**, 1052 (1973).
[17] G. F. Reiter, W. Berlinger, K. A. Müller, and P. Heller, Phys. Rev. B **21**, 1 (1980).

[18] V. A. Vazhenin, K. M. Starichenko, and M. Yu. Artemov, Fiz. Tverd. Tela (St. Petersburg) **39**, 1643 (1997) [Phys. Solid State **39**, 1466 (1997)].
[19] V. A. Vazhenin, L. I. Levin, and K. M. Starichenko, Fiz. Tverd. Tela (Leningrad) **23**, 2255 (1981) [Sov. Phys. Solid State **23**, 1320 (1981)].
[20] B. E. Vugmeĭster, M. D. Glinchuk, A. A. Karmazin, and I. V. Kondakova, Fiz. Tverd. Tela (Leningrad) **23**, 1380 (1981) [Sov. Phys. Solid State **23**, 806 (1981)].
[21] V. S. Vikhnin and Yu. B. Borkovskaya, Fiz. Tverd. Tela (Leningrad) **24**, 472 (1982) [Sov. Phys. Solid State **24**, 266 (1982)].
[22] V. A. Vazhenin, E. L. Rumyantsev, and K. M. Starichenko, *Abstracts of All-Union Conference on Magnetic Resonance* (Kazan, 1984), Pt. 3, p. 55.
[23] V. A. Vazhenin, K. M. Starichenko, and E. L. Rumyantsev, *Extended Abstracts of the XXVIIth Congress AMPERE* (Kazan, 1994), Vol. 2, p. 1048.
[24] V. M. Fridkin, *Photoferroelectrics* [Springer, Berlin, 1979; Nauka, Moscow, 1976].
[25] V. A. Vazhenin, K. M. Starichenko, and A. D. Gorlov, Fiz. Tverd. Tela (St. Petersburg) **35**, 2450 (1993) [Phys. Solid State **35**, 1214 (1993)].

Translated by G. Skrebtsov

X-ray structural and optical studies of $PbZrO_{0.598}Ti_{0.042}O_3$ single crystals in electric fields up to 4×10^7 V/m

A. V. Leiderman

Physics Department, University of Puerto Rico at Mayaguez, PR, 00680, USA

I. N. Leont'ev and V. Yu. Topolov

Rostov-on-Don State Technical University, 344090 Rostov-on-Don, Russia

O. E. Fesenko

Scientific Research Institute at Rostov-on-Don State Technical University, 344090 Rostov-on-Don, Russia

(Submitted June 17, 1997)
Fiz. Tverd. Tela (St. Petersburg) **40**, 327–329 (February 1998)

Field dependences of the rhombohedral unit cell parameter a and birefringence of crystals of lead titanate zirconate with 4.2 mol % additions of Ti are found to be linear in the range from zero to 400 kV/cm. The linear and bulk expansions of the crystal in a field of 400 kV/cm are close to 0.25 and 0.7% respectively. The coefficient of the longitudinal piezoeffect f_{33} computed based on data from F*x*-ray structural analysis exhibit a strong nonlinearity: it increases monotonically by a factor of 7–8 as the electric field increases from zero to 200 kV/cm, and reaches saturation at stronger fields. © *1998 American Institute of Physics.* [S1063-7834(98)03702-2]

Recent years have seen considerable progress in structural investigations of phase transitions induced by strong electrostatic fields.[1–5] In characterizing Refs. 1–5, it is worth noting that although these authors aimed to investigate radical structural changes that take place in fields of $E\sim2\times10^7$ V/m, they observed no changes in the structural parameters induced by the field in the range over which the crystalline phase under study is stable. Possible reasons for this could be insufficiently high values of the applied electric field, and also bending of the samples under the action of the field, which decreases the measurement accuracy.

In this paper, our goal is to investigate the field dependence of crystal lattice parameters. To do so, we have chosen as our object of investigation the rhombohedral compound lead titanate zirconate (PZT) in the composition $PbZr_{0.958}Ti_{0.042}O_3$, whose $R3c$ phase has a wide region of stability on the E-T plane.[6] The crystals were grown using the method described previously.[7]

The crystals chosen for this investigation were less than 25 μm thick. Vacuum sputtering was used to deposit a semitransparent graphite film on the developed face of the sample, which acted as one of the electrodes. In order to create the second electrode, the crystal was glued by a second developed face to glass coated with a conducting transparent layer of SnO_2 and a layer of glue a few microns thick. This latter procedure reduced random bending of the crystal during the measurements to a minimum.

The lattice parameters were measured with a DRON-2.0 diffractometer using the Cu $K\alpha_1$, $K\alpha_2$ emission lines. The positions of the diffraction peaks were refined by separate measurements with respect to 2θ and φ using the method described in Ref. 8. The optical path difference was determined using an Ehringauss compensator (Karl Zeiss Jena), and also tables of interference coloring.[9,10] The samples under study exhibit symmetric type of optical extinction within all intervals of electric field, which argues in favor of a rhombohedral type of distortion of the perovskite cell. The field dependence of birefringence in the plane perpendicular to the direction of the field **E** (the (001) plane of the perovskite unit cell) was given by the equation

$$|\Delta n| = 0.034 - 2.9\times10^{-10}E, \tag{1}$$

where the position of optical extinction was fixed (here E is the intensity of the field applied along the direction [001] expressed in V/m). For the case under study, the value of the birefringence expressed in terms of the principal refractive indices and the coefficient of the linear electrooptic effect are given in Ref. 11. The half-wave voltage calculated from Eq. (1) was around 1.9 kV. The values of the parameters of the rhombohedral lattice averaged over measurements of reflections from the (400) plane are shown in Fig. 1 as a function of the voltage of the DC electric field. The error in measuring these parameters was $\Delta a = 7\times10^{-14}$ m. The magnitude of the rhombohedral lattice angle remained constant over the entire range of fields and was $\alpha = 89.76\pm0.01°$.

In electric fields whose intensity does not exceed that of the coercive field, the quantity $(1/a)da/dE$ corresponds to the definition of the longitudinal inverse piezoelectric effect. However, in stronger fields polarization reversal occurs in the crystal, so that the sign of the effect does not change when the polarity of the electric field is reversed. In light of this statement, we can write

$$da/a = f\,dE, \tag{2}$$

where f is an effective piezomodulus and $dE = |d\mathbf{E}|$. Representations of longitudinal piezoelectric effects that appear when external fields are applied along directions of type

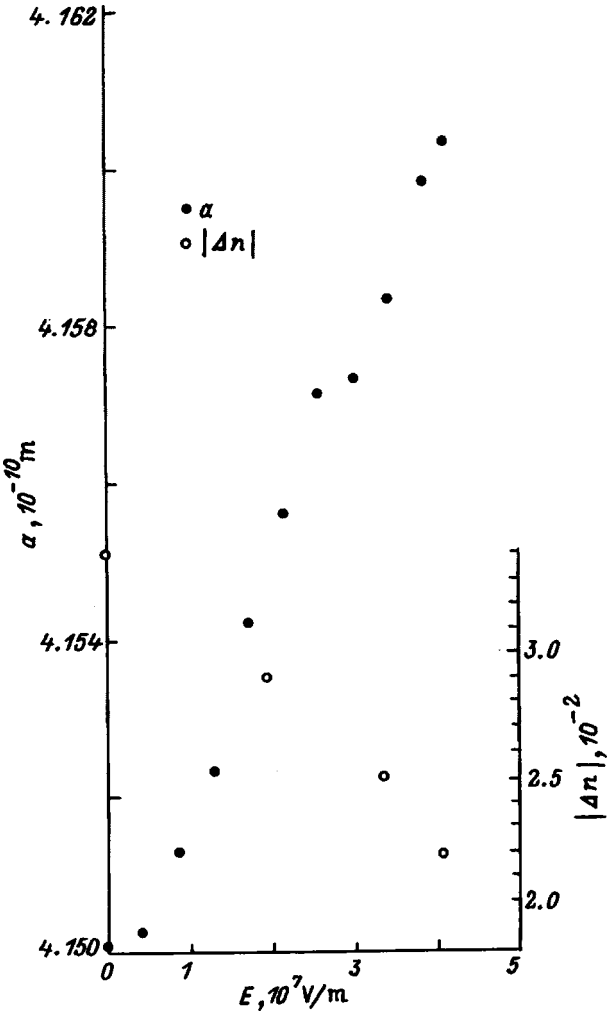

FIG. 1. Field dependences of the rhombohedral cell parameter a and birefringence $|\Delta n|$ measured in the (001) plane perpendicular to the direction of propagation of light in $PbZr_{0.958}Ti_{0.042}O_3$ single crystals.

{100}, which in particular do not coincide with orientations of the crystal polar axis,[12] suggest that the expression for the strain can be written in the form

$$\xi_l = f_{kl} E_k . \tag{3}$$

For symmetry class $3m$, the nonzero components of the longitudinal piezoeffect tensor expressed in two-label form in Eq. (3) can be written $f_{21} = -d_{22}$, $f_{22} = d_{22}$, $f_{31} = f_{32} = (d_{31} + d_{15})/3$, and $f_{33} = d_{33}$. Here d_{ij} are the piezoelectric moduli of a single-domain crystal defined along the principal crystallographic axes (axis OX_3 coincides with the axis 3 and is parallel to the spontaneous polarization vector $\mathbf{P}_s$, while OX_1 is perpendicular to the symmetry plane m). In describing the piezoeffect in PZT crystals we can assume with high accuracy that the electric field intensity vector $\mathbf{E}$ is directed almost parallel to an edge of the perovskite unit cell, and Eqs. (2) and (3) become

$$da/a = d_{33}(E)\,dE. \tag{4}$$

The dependence of the piezomodulus d_{33} on the intensity of the applied field E is shown in Fig. 2. Using Eq. (4), the quantity d_{33} can be determined from the relation

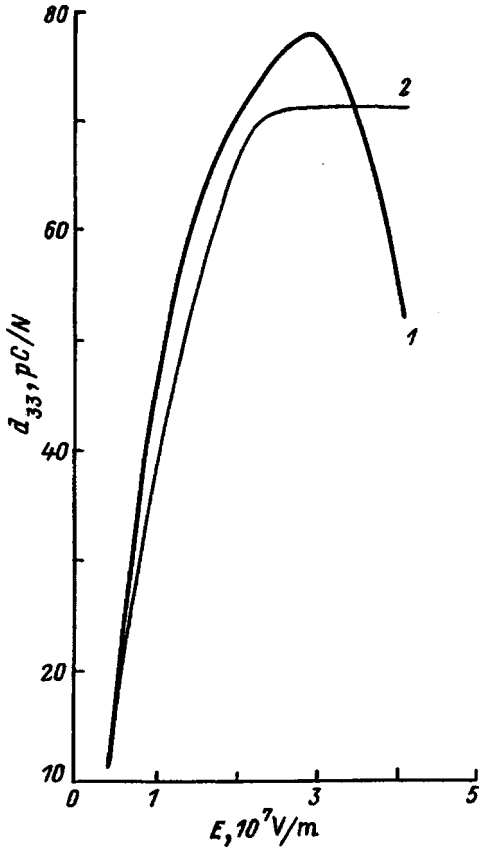

FIG. 2. Computed function $d_{33}(E)$ for a $PbZr_{0.958}Ti_{0.042}O_3$ single crystal determined from Eq. (5) (curve *1*) and Eq. (6) (curve *2*).

$$d_{33} = [1/a(E_n)][a(E_{n+1}) - a(E_n)]/(E_{n+1} - E_n), \quad n = 0,1,\ldots, \tag{5}$$

where the perovskite cell parameter a is determined for two rather close values of the field intensity such that $E_{n+1} - E_n < 10^6$ V/m (curve *1* in Fig. 2). For a comparison we also plot curve *2* (Fig. 2):

$$d_{33} = [1/a(0)][a(E) - a(0)]/E, \tag{6}$$

which corresponds to a hypothetical strain of the perovskite cell in a single crystal as the electric field increases from zero to its current value E. Both curves demonstrate the nonlinear behavior of $d_{33}(E)$ in strong electric fields and the possibility of reaching a limiting value (saturation) such that $d_{33} \lesssim 80$ pC/N. We mention that this piezomodulus coincides in order of magnitude with experimental values of d_{33} measured for perovskite single crystals in weak fields.[13] Because the piezoeffect is measured by recording changes in the interplanar spacings under the action of the field, and the coercive field of PZT single crystals in the $R3c$ phase[14] is roughly 30 times smaller than the field corresponding to saturation for the curves in Fig. 2, the nonlinear behavior we are describing of the piezomodulus $d_{33}(E)$ cannot be explained by domain orientation.

As far as we know, no data has been reported in the scientific literature on field dependences of unit cell parameters for field intensities higher than 5×10^6 V/m. Therefore, in this paper we can give only an elementary analysis of our

TABLE I. Computed values of the unit-cell parameter $a_{calc}(E)$ in the rhombohedral phase of the crystal $PbZr_{0.958}Ti_{0.042}O_3$, which satisfy the condition $f_{33}(E)=\text{const}$, and a comparison of them with the corresponding experimental values of $a(E)$

E, 10^7 V/m	$a_{calc}(E)$, 10^{-10} m	$a(E)-a_{calc}(E)$, 10^{-13} m
0	4.1500	0
0.426	4.1502	1.0
0.852	4.1504	1.9
1.28	4.1505	3.0
1.70	4.1507	3.8
2.13	4.1509	4.8
2.56	4.1511	5.9
2.98	4.1512	7.0
3.41	4.1514	8.0
3.83	4.1516	8.8
4.09	4.1517	9.7

results. There is only one type of dependence of the parameter $a(E)$ that leads to a piezomodulus f_{33} that is independent of the intensity of the applied field E. In fact, the condition $(1/a)da/dE=c_0=\text{const}$ can be integrated to obtain the dependence $a_{calc}(E)=a(0)\exp(c_0E)$. Consequently, only an exponential change in the absolute value of the unit cell parameter as a function of intensity of applied field will ensure that $f_{33}(E)=\text{const}$.

Values of the function $a_{calc}(E)$ calculated over a wide range of E are listed in Table I. For $a(0)$ we have taken the experimental value of the cell parameter at $E=0$; in agreement with experimental data, the constant c_0 is assumed to equal 10 pC/N. A comparison of $a_{calc}(E)$ with the experimental values of the parameters $a(E)$ shown in Fig. 1 indicates that the difference $a(E)-a_{calc}(E)>0$ and increases with increasing field intensity E (see Table I). The curve $a_{calc}(E)$ itself, which satisfies the condition $f_{33}(E)=\text{const}$, lies below the experimental curve shown in Fig. 1, while the quantity $a(E)-a_{calc}(E)$ exceeds (for $E\gtrsim 3\times 10^7$ V/m it even considerably exceeds) the measurement error for the interplanar spacing $\Delta a=7\times 10^{-14}$ m in our experiment.

Thus, the results given above imply the following: On the one hand, the linear relation between strain and electric field intensity in piezoelectric crystals can be violated in strong fields. On the other hand, the exponential dependence of $a_{calc}(E)$, which rigorously ensures this linear relation, is only a special type of functional dependence. Therefore, it is unlikely that the function $a_{calc}(E)$ can have broad application. This indicates that it is advisable to continue to investigate the function $a(E)$ for other similar piezoelectric crystals in strong fields.

One of the authors (A. V. Leiderman) is grateful to the National Aeronautics and Space Administration of the U.S.A. for support through Grants MAGW/4078 (Program NASA-IRA) and NCC8/37 (Program NASA-OMU).

[1] E. A. Wood, R. C. Miller, I. R. Remeika, Acta Crystallogr. **15**, 1273 (1962).
[2] G. E. Shatalova and E. G. Fesenko, Kristallografiya **21**, 1207 (1976) [Sov. Phys. Crystallogr. **21**, 698 (1976)].
[3] N. G. Leont'ev, R. V. Kolesova, O. E. Fesenko, and V. G. Smotrakov, Kristallografiya **29**, 398 (1984) [Sov. Phys. Crystallogr. **29**, 240 (1984)].
[4] V. A. Shuvaeva, M. Yu. Antipin, S. V. Lindeman, O. E. Fesenko, V. G. Smotrakov, and Yu. T. Struchkov, Ferroelectrics **141**, 307 (1993).
[5] V. A. Shuvaeva, M. Yu. Antipin, O. E. Fesenko, and V. G. Smotrakov, Kristallografiya **37**, 1033 (1992) [Sov. Phys. Crystallogr. **37**, 551 (1992)].
[6] N. G. Leont'ev, O. E. Fesenko, and V. G. Smotrakov, Fiz. Tverd. Tela (Leningrad) **25**, 1958 (1983) [Sov. Phys. Solid State **25**, 1144 (1983)].
[7] N. G. Leont'ev, V. G. Smotrakov, and O. E. Fesenko, Bull. Acad. Sci. USSR, Inorg. Mater. **18**, *3*, 449 (1982) [in Russian].
[8] J. Kobayashi, N. Yamada, and T. Nakamura, Phys. Rev. **11**, 410 (1963).
[9] A. Ehringhaus, Z. Kristallogr. A **102**, 85 (1939).
[10] A. V. Shubnikov, *Principles of Optical Crystallography*, p. 88 [Consultants Bureau, New York, 1960; USSR Acad. Sci. Press, Moscow, 1958].
[11] O. E. Fesenko and V. P. Dudkevich, Abstracts from the 2nd Republic Coll. on ''Modulation Spectroscopy of Semiconductors and Dielectrics,'' p. 202, Sukhumi (1975) [in Russian].
[12] Yu. I. Sirotin and M. P. Shaskol'skaya, *Principles of Crystallography* (Nauka, Moscow, 1979) [in Russian].
[13] I. S. Zheludev, Physics of Crystalline Dielectrics (Nauka, Moscow, 1968) [in Russian].
[14] O. E. Fesenko, I. G. Smotrakov, and N. G. Leont'ev, Bull. Acad. Sci. USSR, Ser. Phys. **47**, *4*, 643 (1983) [in Russian].

Translated by Frank J. Crowne

Mössbauer study of ^{119}Sn hyperfine interactions in the $KTi_{1-x}Sn_xOPO_4$ system

V. S. Rusakov

Moscow State University, 119899 Moscow, Russia

S. Yu. Stefanovich

Scientific Research Institute of Physics and Chemistry, 103064 Moscow, Russia

V. M. Cherepanov

Kurchatov Institute, 123182 Moscow, Russia

(Submitted June 23, 1997)
Fiz. Tverd. Tela (St. Petersburg) **40**, 330–336 (February 1998)

The first Mössbauer study of hyperfine interactions of ^{119}Sn nuclei in the complex ferroelectric oxides $KTi_{1-x}Sn_xOPO_4$ is reported. A one-to-one correspondence between the hyperfine interaction parameters and tin atom arrangement in *cis* and *trans* positions of the structure has been established. The electric-field gradient at ^{119}Sn nuclei is shown to be dominated by the contribution of valence electrons in the hybridized *p* and *d* orbitals. A linear correlation between the quadrupole displacement of the spectrum components and the average Sn–O distances has been revealed. The Mössbauer line shift data were used to estimate the number of valence *s* electrons of Sn^{4+} ions occupying the *cis* and *trans* positions throughout the *x* range covered. [S1063-7834(98)03802-7]

This work is a continuation of the nuclear gamma-resonance (NGR) investigation[1] of the potassium titanyl-phosphate family, $KTiOPO_4$ (KTP). While the earlier study[1] used ^{57}Fe nuclei to probe $KFeFPO_4$ (KFP), this work focuses attention on the state of ^{119}Sn nuclei in the $KTi_{1-x}Sn_xOPO_4$ system (KTSP).

The increasing interest in KTP and its analogs seen to emerge in recent years is due primarily to the ferroelectric, ionic-conduction, and nonlinear optical properties of these crystals, which promise considerable application potential.[2] The nature of the unique physical properties of KTP-type crystals still remains unclear. This relates, in particular, to the colossal difference in the magnitude of optical nonlinearity among crystals of this family,[3] specifically between its two outstanding representatives, KTP and KSP ($KSnOPO_4$), which are at the same time closely similar in structural[4] and dielectric[5,6] characteristics.

All KTP crystals studied thus far are ferroelectrics with high Curie temperatures.[5] The presence in some of them of iron, tin, or antimony permits one to use Mössbauer spectroscopy to probe fine features of chemical bonding in the octahedral anion groups centering on these atoms, which act as building blocks in the framework and dominate the nonlinear optical characteristics. The tetrahedral groups XO_4, where X=P, As, Si, or Ge, are more rigid than the octahedra, and they represent the second building block of the framework in KTP-type compounds. The skeletal crystal framework formed by the octahedra and tetrahedra is criss-crossed by channels filled by high-mobility alkali-metal or thallium cations or various hydrogen-containing groups.[3] It is these singly-charged particles in KTP-family crystals that play a dominant part in the phenomena of ferroelectricity and ionic conductivity.[7,8]

The complex structure of KTP crystals on the whole, and the specific features of the KFP structure discussed below do not permit one to extend the interpretation of ^{57}Fe spectra[1] to Mössbauer spectra of other representatives of this family. At the same time a common symmetry for all KTP ferroelectrics (rhombic, space group $Pna2_1$) and the presence of two structurally nonequivalent octahedra suggest the NGR spectra to be a superposition of two doublets differing both in the isomer and quadrupole shifts of the components. The latter is a consequence of substantially different states of the two neighboring Mössbauer atoms in the octahedron chain, which are responsible for the anion-cation-anion chemical bonding of two kinds, *cis* and *trans*, in this chain. In KFP, the octahedra are bonded through fluorine anions to form a chain, and in the case of KTP, KSP, and other, purely oxide compounds of the family, through the oxygen anions. The nearest-neighbor environment of iron atoms was shown to exert a dominant effect on ^{57}Fe Mössbauer spectra.[1] Changes in the nearest-neighbor environment of Mössbauer atoms cannot apparently be ignored for other compounds of this family as well.

It should be stressed that KFP and KSP crystals are very similar in their physical properties; indeed, they are ferroelectrics with close Curie temperatures (720 K for the first crystal[9] and 706 K for the second[6]), and are also close in their optical nonlinearity, which is substantially smaller than that of the KTP crystals. Therefore investigation of the KTSP system offers a possibility of identifying the colossal change in the optical nonlinearity of the solid solution observed to occur upon variation of the relative content of Ti^{4+} and Sn^{4+} ions with a comparatively small but important change in the nearest-neighbor oxygen environment of the latter.

The present work is a first Mössbauer study of ^{119}Sn hyperfine interactions in the ferroelectric complex oxides KTSP.

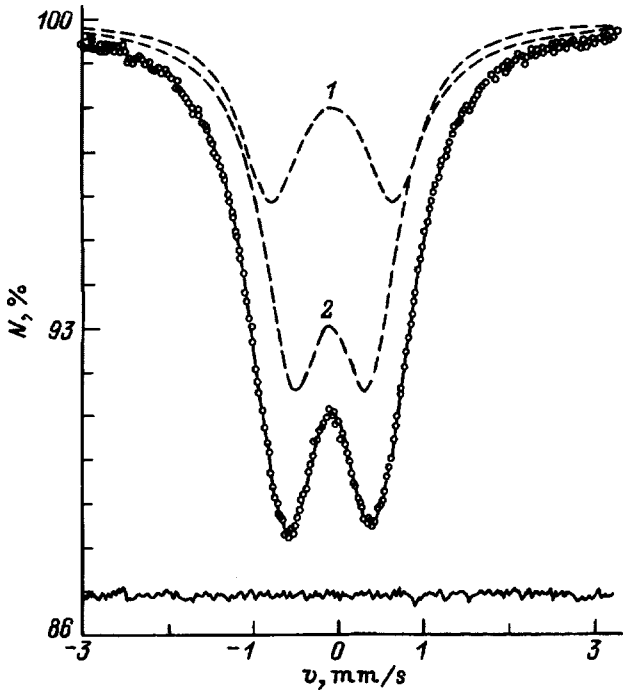

FIG. 1. ^{119}Sn Mössbauer spectrum of $KTi_{0.7}Sn_{0.3}OPO_4$ and its model assignment (curves *1* and *2*).

1. EXPERIMENT METHOD

Our experimental studies were performed on powder samples of the $KTi_{1-x}Sn_xOPO_4$ solid solutions ($0<x\leqslant 1$). The samples were prepared in high-temperature solid-phase chemical reactions.[1)] Polycrystalline samples for Mössbauer measurements were produced by grinding the synthesized material in an agate mortar, with its subsequent deposition in alcohol on an aluminum-foil substrate.

The Mössbauer measurements were made at room temperature in absorption geometry on an NGR spectrometer operating in the constant acceleration regime. The source was ^{119m}Sn in $BaSnO_3$ with activity of a few mCi. The spectrometer was calibrated against reference spectra of $BaSnO_3$, sodium nitroprusside, and α Fe. Model identification and reconstruction of the distribution functions of the hyperfine parameters in Mössbauer spectra, as well as calculation of the electric-field gradient (EFG) tensor were carried out using MSTools programs.[10]

2. RESULTS AND DISCUSSION

Mössbauer spectra of ^{119}Sn nuclei in the KTSP oxides were slightly asymmetric, broadened quadrupole doublets (Fig. 1). To reveal their fine structure, the resolution was improved using the DISTRI code[10,11] by reconstructing the distribution function $p(\delta)$ of the isomer shifts δ of the spectral components (Fig. 2). An analysis of the $p(\delta)$ functions showed the spectra to consist of two quadrupole doublets with close isomer shifts δ and essentially different quadrupole shifts ε, with components of one of them lying along the Doppler velocity axis between those of the other. Reconstruction of the distribution functions $p(\varepsilon)$ of quadrupole

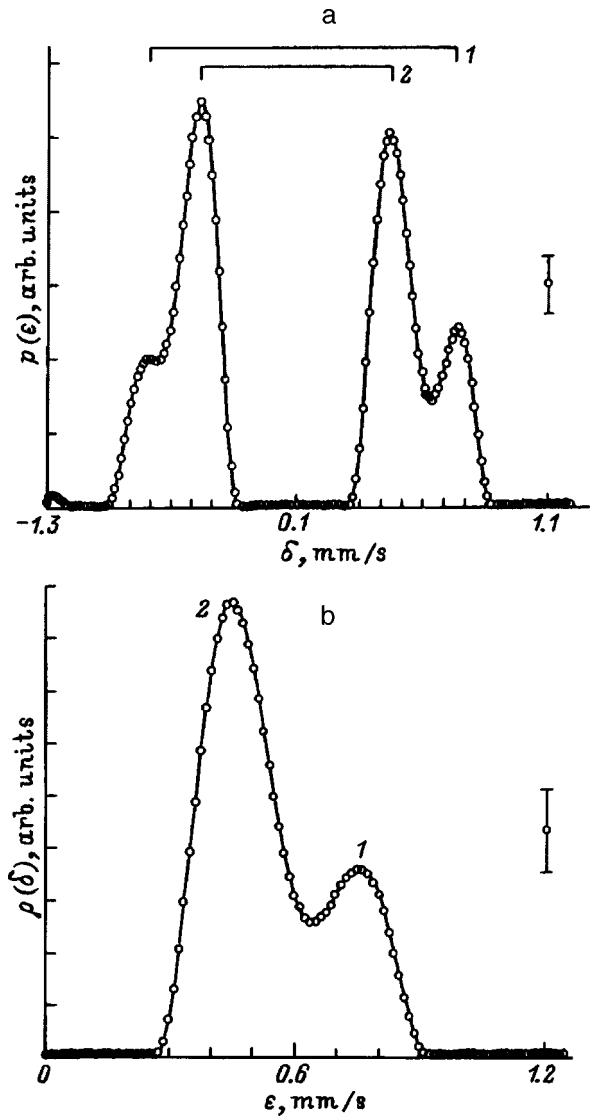

FIG. 2. Reconstruction of the distribution functions of (a) isomer shifts $p(\delta)$ and (b) quadrupole shifts $p(\varepsilon)$ for the components of ^{119}Sn Mössbauer spectrum in $KTi_{0.7}Sn_{0.3}OPO_4$.

shifts ε of the spectral components (Fig. 2) made under the assumption of two symmetric quadrupole doublets present confirmed the analysis of the $p(\delta)$ function.

In order to make a reliable estimate of the relative intensity of the components in each quadrupole doublet, control experiments were performed which were aimed at revealing the presence of crystal texture in the samples. Since the technique of sample preparation used in our case allows formation of a texture of cylindrical symmetry with the axis along the sample surface normal, we obtained spectra of samples whose normal made a characteristic angle $\vartheta\approx 54.7°$ with the γ-ray direction, at which texture must not be visible in the spectra.[12] Turning the samples by an angle ϑ did not change the component intensity ratio, thus indicating the absence of any texture.

In accordance with the results of the control experiments and with the analysis of the distribution functions $p(\delta)$ and $p(\varepsilon)$, all Mössbauer spectra were treated with the SPECTR code[10,13] under the assumption of the presence of two quad-

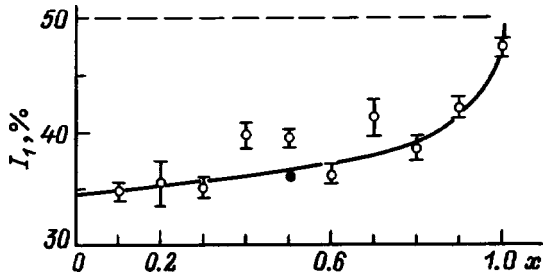

FIG. 3. Concentration dependence of the relative intensity I_1 of the partial spectrum of $KTi_{1-x}Sn_xOPO_4$ with a large quadrupole shift ε. The filled circle refers to the relative population of the *cis* positions by Sn atoms (Ref. 14).

rupole doublets having pairwise equal amplitudes and widths.

For illustration, Figs. 1 and 2 show the results of a model identification of the Mössbauer spectra of ^{119}Sn nuclei in $KTi_{0.7}Sn_{0.3}OPO_4$ and of a reconstruction of the distribution functions of the isomer shifts $p(\delta)$ and quadrupole shifts $p(\varepsilon)$ in the spectra. One readily sees the specific features of the spectrum and of the distribution functions described above.

The existence of two partial spectra corresponds to the presence in the oxides crystal structure under study of two crystallographically nonequivalent tin positions, *cis* and *trans*.[4,14] To identify the partial spectra, we shall use their relative intensities. Figure 3 presents the concentration dependence of the relative intensity I_1 of the quadrupole doublet (1) with a large quadrupole shift ε. We see that for small Sn concentrations the relative intensity $I_1 \sim 35\%$, and it increases continuously with concentration to reach $\sim 50\%$ at $x=1$, as this should be expected considering the equal multiplicity of the *cis* and *trans* positions in the structure.[4,14] For a sufficiently thin sample and equal Mössbauer effect probabilities for different positions, the relative intensity of a partial spectrum is equal to the relative occupation by Mössbauer atoms of the positions corresponding to this spectrum (see, e.g., Ref. 13). We shall use the results of Ref. 14, where combined application of x-ray and neutron diffraction methods permitted one to establish the relative population by Sn and Ti atoms of the *cis* and *trans* positions in the $KTi_{1/2}Sn_{1/2}OPO_4$ compound. The preferable distribution of Sn atoms was found[14] to be 64.1(5)% in *trans* positions (and, accordingly, 35.9(5)% in *cis* positions). A comparison of these data with the relative intensity I_1 (Fig. 3) of quadrupole doublet (1) leads one to a conclusion that the partial spectrum with the larger quadrupole shift ε and a smaller (for the given tin concentration) relative intensity I [partial spectrum (1)] belongs to *cis* Sn atoms, and the partial spectrum with the smaller quadrupole shift and larger relative intensity [partial spectrum (2)] is due to *trans* Sn atoms.

Figure 4 shows concentration dependences of the isomer shifts δ (measured relative to the ^{119}Sn Mössbauer line in $BaSnO_3$) and of the quadrupole shifts ε of the components in the partial spectra of *cis* and *trans* ^{119}Sn nuclei in KTSP oxides. We readily see that the isomer shift $\delta_{\rm cis}$ for the *cis* position is larger than the shift $\delta_{\rm trans}$ for the *trans* position throughout the range of tin concentrations x. As x increases,

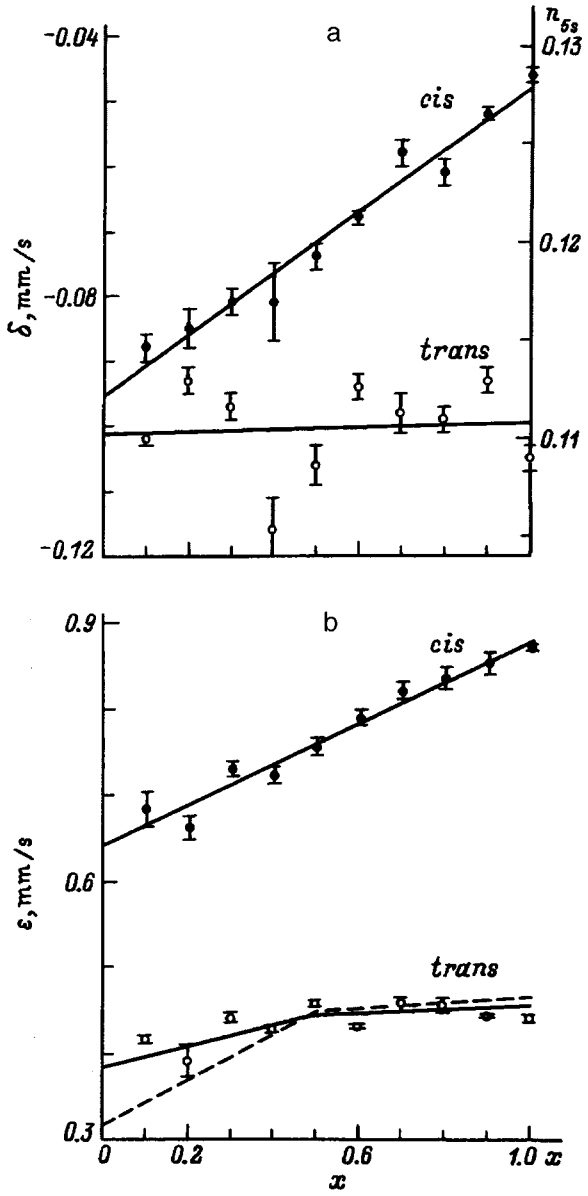

FIG. 4. Concentration dependences of (a) isomer shifts δ and (b) quadrupole shifts ε for the components of partial spectra of the *cis* and *trans* ^{119}Sn nuclei in $KTi_{1-x}Sn_xOPO_4$ structure.

$\delta_{\rm cis}$ increases noticeably, whereas $\delta_{\rm trans}$ remains practically constant and exhibits a large statistical scatter. The values of the shifts for both positions fit in a comparatively narrow interval, $(-0.12 - -0.04)$ mm/s, characteristic of quadrivalent tin ions (see, e.g., Ref. 15). Within this interval, a larger shift corresponds to a larger covalency of the Sn–O bond. This means that the Sn–O bond for *cis* positions is more covalent throughout the tin concentration range covered than that for the *trans* positions, and that the degree of its covalency grows with increasing tin concentration.

In accordance with the phenomenological description of the relation between the charge electron density $\rho(n_{5s}, n_{5p})$ at a ^{119}Sn nucleus and the electron configuration of the tin ion[16] one can write

$$\rho(n_{5s}, n_{5p}) = \rho(0,0) + \rho_s n_{5s} + S_s n_{5s} + S_{ss} n_{5s}^2 + 2S_{sp} n_{5s} n_{5p}, \quad (1)$$

where n_{5s} and n_{5p} are the numbers of valence electrons in the s and p states, respectively, ρ_s is the charge density due directly to one $5s$ electron, S_s is the effect of inner-shell screening by one $5s$ electron, and S_{ss} and S_{sp} are the results of screening of a $5s$ electron by one $5s$ and $5p$ electron, respectively. A comparison of calculated changes in the charge density at the ^{119}Sn nucleus[18] with experimental isomer shifts δ measured in ionic compounds of tin yielded[17] a calibration relation connecting shift δ relative to $BaSnO_3$ with the numbers of $5s$ and $5p$ valence electrons:

$$\delta(n_{5s},n_{5p}) = -0.433 + 3.01n_{5s} - 0.2n_{5s}^2 - 0.17n_{5s}n_{5p}. \quad (2)$$

We shall use this equation to estimate the population of the tin-ion valence shell. As seen from Eq. (2), in the case of the Sn^{4+} ion with weak covalent bonding, where the occupancy of the $5s$ and $5p$ orbitals is low, the Mössbauer line shift is dominated by the number of $5s$ electrons:

$$\delta(n_{5s},n_{5p}) \cong -0.433 + 3.01n_{5s}. \quad (3)$$

In this case one can estimate the number of $5s$ valence electrons, n_{5s}, to within $\sim 5\%$ directly from the Mössbauer line shift. It was found that the number of $5s$ valence electrons in the *trans* position is ~ 0.11 for any tin concentration, while in the *cis* position n_{5s} increases from ~ 0.112 to ~ 0.128 when Ti is totally replaced by Sn (Fig. 4).

The quadrupole shifts ε of components of the ^{119}Sn partial spectra for the *cis* and *trans* positions in the KTSP oxide system were found to be fairly large (0.4–0.9 mm/s) and essentially different. For the *cis* positions, the magnitude of ε is 1.5–2.0 times the quadrupole shift for the *trans* positions (Fig. 4).

Note that this result is the exact reverse of that obtained by us[1] for ^{57}Fe nuclei in $KFeFPO_4$, which is isostructural with the oxides under study. The quadrupole shift ε of the spectral components for the *trans* positions was found to be twice that for the *cis* positions. We showed[1] that this relative magnitude of quadrupole shifts for ^{57}Fe nuclei is connected with the mechanism of EFG formation at the nucleus, with the main contribution coming from localized matrix charges, and with the arrangement of F^{1-} and O^{2-} ions in the *cis* and *trans* positions around Fe^{3+} ions. In contrast to $KFeFPO_4$, in the KTSP oxides Sn^{4+} ions are the Mössbauer probes, and O^{2-} ions act in place of the F^- bonding ions.

The quadrupole shifts ε of components of the partial spectra due to *cis* and *trans* ^{119}Sn nuclei in the KTSP oxides, which are shown as functions of concentration in Fig. 4, have the same pattern as those of the isomer shifts δ. One observes a strong increase of ε (by ~ 0.23 mm/s) for the *cis* positions and a weak change (by ~ 0.05 mm/s) for the *trans* positions.

To discover the mechanism of nuclear quadrupole interaction with an inhomogeneous electric field, we calculated the EFG generated by localized matrix charges, and the hyperfine interaction parameters for the *cis* and *trans* ^{119}Sn in the KTSP oxides by means of the LATTICE code.[10]

It is known (see, e.g., Refs. 15 and 19) that in the case of ionic and covalent compounds the EFG tensor G can be presented as a sum of contributions of the charges external to the Mössbauer probe, $G_{\rm lat}$, and of valence electrons, $G_{\rm val}$, both involved, G_b, and not involved, G_{nb}, in ligand bonds. Taking into account the shielding and antishielding effects due to the inner closed electron shells, the G tensor can be written

$$G = (1-\gamma)G_{\rm lat} + (1-R)G_{\rm val} \equiv (1-\gamma)G_{\rm lat} + (1-R)G_{nb} + (1-R)G_b, \quad (4)$$

where R and γ are the Sternheimer shielding and antishielding factors.[15]

In the absence of magnetic hyperfine interaction, one can present the quadrupole shift ε of components of a ^{119}Sn spectrum in the form (see, e.g., Ref. 15):

$$\varepsilon = \frac{e^2qQ}{4}\left(1+\frac{\eta^2}{3}\right)^{1/2}, \quad (5)$$

where eQ is the quadrupole moment of the nucleus in excited state, $eq \equiv G_{zz}$ is the principal component of the EFG tensor G at the nucleus, and $\eta \equiv (G_{xx}-G_{yy})/G_{zz}$ is the asymmetry parameter of tensor G (here the axes x, y, and z form a right-handed coordinate frame, and $|G_{xx}|$, $|G_{yy}| \leqslant |G_{zz}|$).

We used x-ray diffraction data on atomic coordinates[4,14] and calculated for ^{119}Sn nuclei the contribution to tensor G due to lattice atoms, approximating them by point charges and accepting $\gamma = -10$ for the Sternheimer antishielding factor.[20] The calculations involved about 40000 atoms inside a sphere of radius ~ 40 Å. For the nuclear quadrupole moment we took $Q = -0.109$ barn (Ref. 21), and for the Mössbauer transition energy, $E_g = 23.871$ keV (Ref. 22). The calculations were performed for both formal atomic charges [$q(\mathrm{K}) = +1$, $q(\mathrm{Ti}) = +4$, $q(\mathrm{Sn}) = +4$, $q(\mathrm{P}) = +5$, $q(\mathrm{O}) = -2$] and effective charges [$q(\mathrm{K}) = +0.98$, $q(\mathrm{Ti}) = q(\mathrm{Sn}) = +2.9$, $q(\mathrm{P}) = +1.8$, $q(\mathrm{O}) = -1.136$]. The effective atomic charges in the KSP crystal were obtained[2)] by modeling the crystal structure of the compound by means of METAPOCS code.[23]

The calculated quadrupole interaction constant e^2qQ, asymmetry parameter η, and quadrupole shift ε for ^{119}Sn nuclei in KTSP oxides are presented in Table I. A comparison of Table I with Fig. 4 shows that the calculated quadrupole shifts are significantly smaller than those observed experimentally, particularly if one takes into account the effective charges localized at the atoms. This means that the EFG at *cis* and *trans* ^{119}Sn nuclei in the KTSP system is dominated by the contribution due to the valence electrons $G_{\rm val}$ [see Eq. (4)], and particularly, if we recall the electronic configuration of the Sn^{4+} ion, of the valence electrons involved in bonds with the ligands, G_b.

In connection with this, let us consider the correlation between the quadrupole shifts ε of spectral components for the *cis* and *trans* positions and the specific features of the mutual arrangement of tin and oxygen atoms in the structure of the oxides under study. KTSP oxides crystallize in orthorhombic space group $Pna2_1$ (C_{2v}^9).[4,14] The main structural elements are the phosphorus tetrahedra PO_4 and tin octahedra SnO_6 making up a mixed Sn,P framework. The structure contains wide helical channels localizing potassium atoms,

TABLE I. Quadrupole interaction constant e^2qQ, asymmetry parameter η, and quadrupole shift ε for *cis* and *trans* ^{119}Sn nuclei in KTSP calculated for the contribution of localized lattice charges.

		$KTiOPO_4$		$KTi_{0.5}Sn_{0.5}OPO_4$		$KSnOPO_4$	
Charges	Parameter	*cis*	*trans*	*cis*	*trans*	*cis*	*trans*
Formal	e^2qQ, mm/s	+0.687	+0.842	−0.655	−0.747	−0.632	+0.911
	η	−0.894	+0.374	+0.399	+0.536	+0.383	+0.531
	ε, mm/s	+0.193	+0.216	−0.168	+0.195	−0.162	+0.238
Effective	e^2qQ, mm/s	+0.280	+0.197	−0.200	+0.193	−0.196	+0.288
	η	−0.476	+0.368	+0.407	+0.691	+0.321	+0.606
	ε, mm/s	+0.073	+0.050	−0.051	+0.052	+0.050	+0.076

which are weakly bonded to the framework. The tin octahedra made up of a central tin atom surrounded by six oxygens are linked in chains –O–Sn–O–Sn–O– arranged along the [011] and $[0\bar{1}1]$ directions. Figure 5 displays a fragment of the chain of tin octahedra [the plane of the figure is perpendicular to the [110] crystallographic direction]. The SnO_6 chain octahedra share corners through the bonding oxygen atoms (O_{t1} and O_{t2}), which are located alternately on opposite sides (Sn *trans* positions) and on the same side (*cis* positions of Sn) of the central tin atom. Thus one half of the structurally independent tin atoms occupy the *cis*, and the other half, the *trans* positions of the structure.

Taking into account the possible spatial configuration of the *s*, *p*, and *d* tin orbitals in *cis* and *trans* positions of the structure, consider the concentration dependences of the average distances r_{Sn-O} from the Sn atom to the six oxygen atoms in the first coordination sphere, to the four oxygens lying in the planes of nearest-neighbor octahedra, and to the two oxygens located on opposite sides of the Sn atom (Fig. 6). A comparison of the dependences of quadrupole shifts ε and of the average distances r_{Sn-O} on tin concentration (Figs. 4 and 6) shows that the quadrupole shift for *trans* positions behaves with concentration similar to the average distance of the *trans* Sn to the bonding oxygen atoms O_{t1} and O_{t2} (Fig. 5), and that for *cis* positions, similar to the average distance of the *cis* Sn to the two oxygens O_5 and O_6 lying on opposite sides of the chain plane (Fig. 5). This permits a conclusion on the orientation of the strongest Sn-O bonds for the *cis* and *trans* Sn atoms. Namely, for the *trans* positions it is the $O_{t1}-Sn-O_{t2}$ bond in the –O–Sn–O–Sn–O– chain plane, and for the *cis* positions, the O_5–Sn–O_6 bond directed practically perpendicular to this plane.

As long as the relative change in distance from the Sn atom to the nearest O atoms induced by changes in tin concentration is relatively small (up to ~5%, see Fig. 6), one may expect that the population of Sn orbitals will, in the first approximation, vary linearly with distance. This will result,

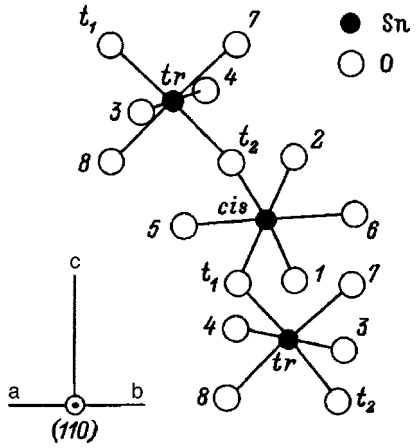

FIG. 5. Spatial arrangement of nearest-neighbor oxygen environment of tin in *cis* and *trans* positions of $KTi_{1-x}Sn_xOPO_4$.

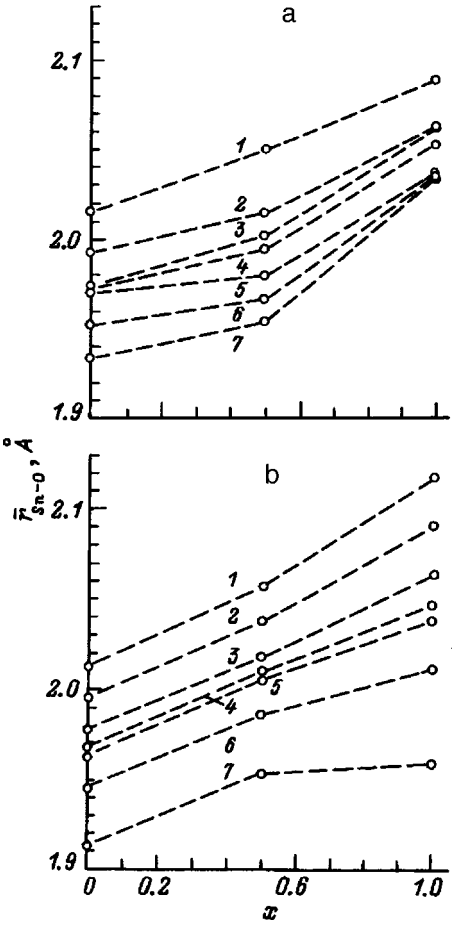

FIG. 6. Concentration dependences of the average distances r_{Sn-O} from the tin atom in (a) *cis* and (b) *trans* positions to the corresponding oxygens in the first coordination sphere in the $KTi_{1-x}Sn_xOPO_4$ system. (a) *1*—O_5, O_6; *2*—O_2, O_{t1}, O_5, O_6; *3*—O_1, O_5, O_6, O_{t2}; *4*—O_1, O_2, O_5, O_6, O_{t1}, O_{t2}; *5*—O_{t1}, O_2; *6*—O_1, O_2, O_{t1}, O_{t2}; *7*—O_{t2}, O_1. (b) *1*—O_3, O_4; *2*—O_3, O_4, O_7, O_8; *3*—O_7, O_8; *4*—O_3, O_4, O_7, O_8, O_{t1}, O_{t2}; *5*—O_3, O_4, O_{t1}, O_{t2}; *6*—O_7, O_8, O_{t1}, O_{t2}; *7*—O_{t1}, O_{t2}.

in its turn, in a change in the number of uncompensated electrons in the $5p$ and $4d$ orbitals, and a change in quadrupole shift ε linear with the corresponding distances $r_{\text{Sn-O}}$:

$$\varepsilon(x) = a + b r_{\text{Sn-O}}(x). \quad (6)$$

The most reliable correlation between the quadrupole shift ε for the *cis* positions and the average distance to the O_5 and O_6 pair in the nearest-neighbor environment (Figs. 4 and 6) yields the following values for the coefficients in Eq. (6): $a = -5.8(4)$ mm/s and $b = 3.2(2)$ mm/s· Å. Using these values and the dependence of the average distance $r_{\text{Sn-O}}$ from a *trans* Sn atom to the bonding oxygen atoms O_{t1} and O_{t2} (Fig. 6), one can obtain, in its turn, the concentration dependence of quadrupole shift $\varepsilon(x)$ for the *trans* positions (see dashed line in Fig. 4). As follows from Fig. 4, the calculations made under the assumption of a linear relation (6) between the quadrupole shift and the corresponding average distances $r_{\text{Sn-O}}$ agree well with the experimental values of $\varepsilon_{\text{trans}}(x)$. This implies that the EFG at *cis* and *trans* ^{119}Sn nuclei in the KTSP oxide structure is dominated by the contribution of the valence electrons involved in ligand bonds. Besides, the directions of the Sn-O bonds found for the *cis* and *trans* positions are the directions along which the change in distance between Sn and O atoms plays a dominant role in the population of the Sn $5p$ and $4d$ orbitals.

An attempt to establish a linear correlation between the shift $\delta(x)$ of the spectral components for the *cis* and *trans* positions and the change in Sn–O distance showed that a change in the population of the $5s$ orbital, essential for the shift with concentration x, does not involve a proportional change in population of the Sn $5p$ and $4d$ orbitals. In other words, the contribution of tin $5s$ electrons to the hybridized electronic states of SnO_6 octahedra depends differently on the relative population of oxygen octahedra by tin and titanium ions than those of the p and d electrons. This appears only natural, since s electrons of Ti^{4+} ions, in contrast to those of Sn^{4+}, are not involved in chemical bonding at all. To obtain a quantitative explanation for the isomer shift δ in the $KTi_{1-x}Sn_xOPO_4$ solid solution, one has to assume that the s electron states of tin are affected by K^+ and Ti^{4+} ions in the second coordination sphere.

Our results can be summarized as follows:

1. This is the first study of ^{119}Sn hyperfine interactions in the complex ferroelectric oxides $KTi_{1-x}Sn_xOPO_4$ by Mössbauer spectroscopy, and we have established a one-to-one correspondence between ^{119}Sn hyperfine interaction parameters and occupation by tin of the *cis* and *trans* positions in the structure.

2. It was shown that the EFG at ^{119}Sn nuclei is dominated by contribution of the valence electrons in the hybridized p and d orbitals.

3. The directions of the Sn–O bonds were found to be different, namely, for the *trans* positions the bond aligns with the line connecting oxygen ions in the $-O-Sn_{trans}-O-Sn_{cis}-O$-chain, and in the *cis* positions it is perpendicular to the plane containing these chains.

4. The quadrupole shift of the ^{119}Sn Mössbauer spectrum components was found to correlate linearly with the average Sn–O distances.

Support of the Russian Fund for Fundamental Research (Grant 96-02-17723a) is gratefully acknowledged.

[1)]The samples were synthesized by V. B. Kalinin.
[2)]The calculations were carried out by N. N. Eremin at Crystallography Chair, Department of Geology, Moscow State University.

[1] V. S. Rusakov, S. Yu. Stefanovich, and V. M. Cherepanov, Fiz. Tverd. Tela (St. Petersburg) **38**, 2851 (1996) [Phys. Solid State **38**, 1561 (1996)].
[2] M. E. Hagerman and K. R. Poeppelmeier, Chem. Mater. **7**, 602 (1995).
[3] G. D. Stucky, M. L. F. Phillips, and Th. E. Gier, Chem. Mater. **1**, 492 (1989).
[4] P. A. Thomas, A. M. Glazer, and B. E. Watts, Acta Crystallogr., Sect. B: Struct. Crystallogr. Cryst. Chem. **46**, 333 (1990).
[5] V. B. Kalinin and S. Yu. Stefanovich, *Solid-State Chemistry* [in Russian] (Itogi Nauki i Tekhniki, Ser. Khim. Tv. Tela, Vol. 8; VINITI, Moscow, 1992).
[6] S. Furusawa, H. Yanagisawa, and Y. Ishibashi, J. Phys. Soc. Jpn. **62**, 4152 (1993).
[7] S. Yu. Stefanovich, B. V. Mill, and A. V. Butashin, Ferroelectrics **144**, 237 (1993).
[8] S. Yu. Stefanovich, B. V. Mill, and E. I. Belokoneva, Ferroelectrics **185**, 63 (1996).
[9] S. Yu. Stefanovich, A. V. Mosunov, and V. B. Kalinin, Fiz. Tverd. Tela (St. Petersburg) **38**, 2845 (1996) [Phys. Solid State **38**, 1558 (1996)].
[10] V. S. Rusakov and N. I. Chistyakova, *LACAME92* (Buenos Aires, 1992), Abstract No. 7-3.
[11] L. K. Zhetbaev, K. K. Kadyrzhanov, T. É. Turkebaev, V. S. Rusakov, and M. Sh. Aĭmanov, *Phase Transformations in Metal-Metalloid Implanted Systems* (Gylym, Almaty, 1995).
[12] J. M. Greneche and F. Varret, J. Phys. C **15**, 5333 (1982).
[13] V. I. Nikolaev and V. S. Rusakov, *Mössbauer Studies of Ferrites* [in Russian] (MGU, Moscow, 1985).
[14] S. J. Crennell, J. J. Owen, A. K. Cheetham, J. A. Kaduk, and R. H. Jarman, Eur. J. Solid State Inorg. Chem. **28**, 397 (1991).
[15] V. S. Shpinel' *Gamma-Ray Resonance in Crystals* [in Russian] (Nauka, Moscow, 1969).
[16] J. K. Lees and P. A. Flinn, J. Chem. Phys. **48**, 882 (1968).
[17] O. A. Bayukov and A. F. Savitskiĭ, Kirenskiĭ Institute of Physics Preprint 568F, Krasnoyarsk, 1989.
[18] T. Okada, H. Sekizawa, and T. Yamadaya, J. Phys. (France) **40**, C2, 299 (1979).
[19] *Mössbauer Spectroscopy*, edited by D. P. E. Dickson and F. J. Berry (Cambridge Univ. Press, 1986).
[20] F. Borsa and R. G. Barnes, Phys. Rev. Lett. **12**, 281 (1964).
[21] H. Haas, M. Menninger, H. Andreasen, S. Damgaard, H. Grann, F. T. Pedersen, J. W. Petersen, and G. Weyer, Hyperfine Interact. **15/16**, 215 (1983).
[22] J. G. Stevens and V. E. Stevens, *Mössbauer Effect Data Index Covering the 1976 Literature* (Plenum Press, New York, 1978).
[23] S. C. Parker, C. R. A. Catlow, and A. N. Cormark, Acta Crystallogr. **40**, 200 (1984).

Translated by G. Skrebtsov

New long-lived memory effects in $LiNbO_3$ crystals

B. B. Ped'ko, É. V. Lebedev, and I. L. Kislova

Tver' State University, 170000 Tver', Russia

T. R. Volk

Institute of Crystallography, Russian Academy of Sciences, 117333 Moscow, Russia
(Submitted June 25, 1997)
Fiz. Tverd. Tela (St. Petersburg) **40**, 337–339 (February 1998)

This paper describes a new way of recording information by changing the potential contour at the surface of z-cut crystals of $LiNbO_3$. The effect of various kinds of external perturbations on the rate of decay of optical images written using this method is investigated, along with the possibility of writing information on crystals with transition-metal impurities. © *1998 American Institute of Physics.* [S1063-7834(98)03902-1]

It is well known that practical applications of lithium niobate crystals depend to a significant degree on optical uniformity, which characterizes the constancy of optical constants throughout the sample volume.[1] Optical nonuniformity, for example variations in the refractive index, can be caused both by structural nonuniformities and variations in the crystal composition[2] and can manifest itself in the form of locally reversible changes in double refraction when lithium niobate crystals are illuminated with laser beams.[3] The form and behavior of optical nonuniformities depends on a number of external factors: the presence of illumination in the crystal, thermal, electrical, or elastic fields, etc.[1] It is well known that the usefulness of the photorefractive effect for holographic writing of information[3] is based on the possibility of rewriting information, which is impossible when the refractive index modulation is due to structural nonuniformities in the crystal.

Using polarization-optics methods, we have investigated the optical uniformity of single crystals of lithium niobate, the kinetics of their behavior in the temperature range 20–200 °C, and the connection between these characteristics and domains and defect structures in the crystals revealed by various methods.[4,5] In the course of these studies, we used polar-cut crystals on which electrodes made of aquadag were placed, in the form of two parallel strips deposited on the surface and separated by a distance of 0.5–3 mm. We discovered the following phenomenon when we observed these crystals in polarized light: as a crystal was being heated to a temperature of the order 40–70 °C, an optical pattern was generated in the interelectrode gap in which the distribution of illumination was determined by the shape of the deposited electrodes. Our observation was made without an external electric field. After cooling the crystal and removing the electrodes, we saw an ''optical trace'' of the removed electrodes when we observed the crystal under crossed polaroids.

In order to study the details of this effect we deposited a conducting mask (a grid) with a regular structure and a lattice period of order 0.5 mm. To form the image we used $LiNbO_3$ crystals, both nominally pure and grown from a stoichiometric compound by the Czochralski method; contained these crystals metal impurities Mn, Zn, Fe, Cr, Ni, etc. in concentrations of less than 1 at. %. The films were cut perpendicular to the polar axis at inclinations of less than 30″, and were polished optically. A sample with a conducting grating deposited on the z-cut surface was heated to 150 °C and cooled down to room temperature, after which the mask was removed. Following this procedure, when observing the surface of the crystal in polarized light, we saw an optical image whose form corresponded to that of the conducting mask (see Figs. 1a and 1b).

We investigated the optimal temperature regimes for creating optical images. We established that the process of creating optical images in samples with deposited masks begins in the temperature range 40–70 °C. When a sample with a deposited conducting mask was heated above 80–100 °C, the contrast of the pattern observed was considerably lower, and upon heating the sample to 130–150 °C the pattern disappeared. The temperature interval 130–150 °C corresponded to thermal erasing of the effect, independent of the presence of the conducting mask. Note that this temperature interval corresponds to thermal erasure of holograms in lithium niobate,[1] and also to the disappearance of optical nonuniformities that are imaged in lithium niobate by polarization-optics methods.[4] When the crystal with a deposited conducting mask was cooled, the process was repeated in reverse order, but the resulting pattern obtained had a higher contrast. Images were formed both when observed in transmitted polarized light and in darkness.

After cooling to room temperature the mask was removed; in this case the optical images, whose shape corresponded to that of the conducting mask (see Figs. 1a and 1b), were maintained for a period of several months, after which loss of contrast took place. The optical images that formed were erased by heating the crystal to 150 °C without the conducting mask.

Our observation of this effect was hindered by ''old'' regions that were not subjected to the external perturbation, and the ''older'' the cut chosen to repeat the experiment was, the smaller was the contrast of the image obtained. After multiple annealings to a temperature of 200 °C, the creation of images took place in the usual order.

In our opinion, the heat-induced appearance of optical images that replicate the shape of a conducting mask deposited on the sample surface of z-cut lithium niobate crystals is

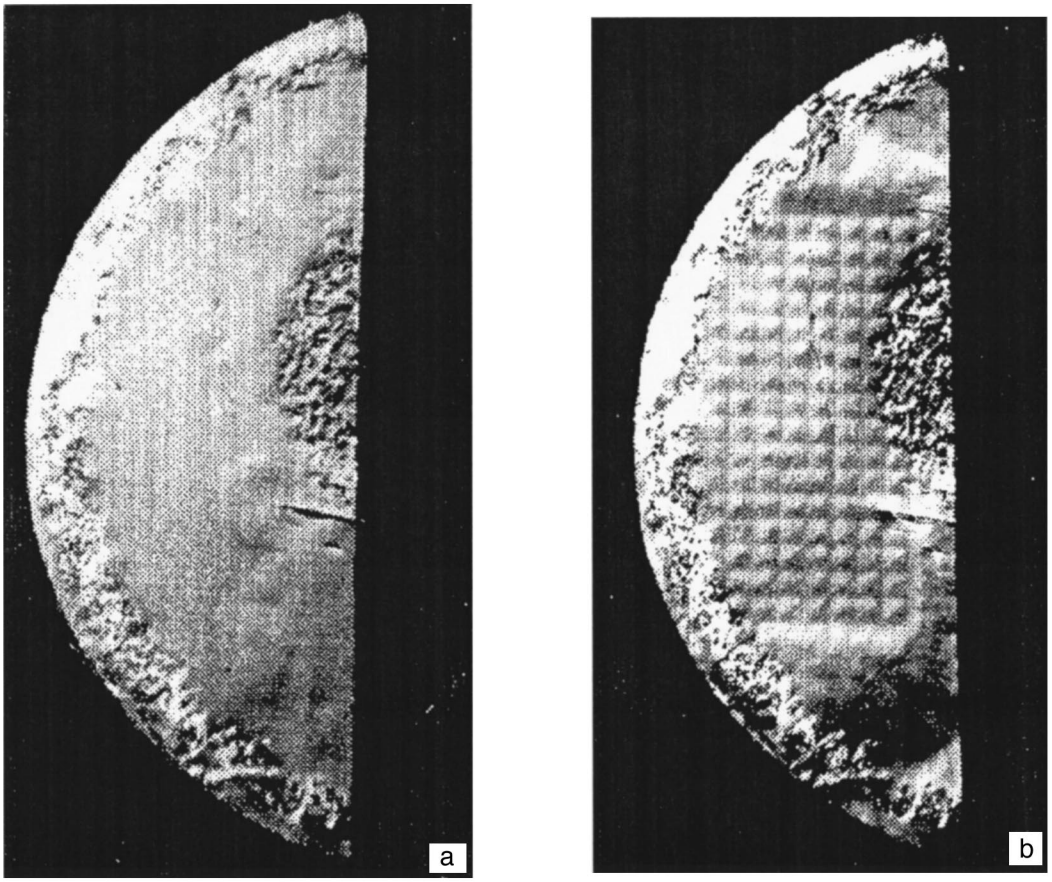

FIG. 1. Crystal of $LiNbO_3+0.1$ at %Mn (z-cut) observed in polarized light, the crystal diameter is ~ 1.5 cm, $T=20$ °C. a—before processing (the optical nonuniformity is made visible by polarization optics, b—the same crystal after processing.

connected with changes in the potential contour of the crystal surface while the latter is in contact with conducting and nonuniform distributions of screening charge. These pictures become visible because of the local electrooptic effect generated by components of the internal space-charge electric field perpendicular to the crystal polar axis. The temperature-dependent behavior is due to screening of these fields by nonequilibrium charges,[6] while the fixation of the optical images is due to trapping of these nonequilibrium carriers by deep traps. The correlation between the temperature dependence of the observed effects and well-known data on the temperature dependence of electrical conductivity of $LiNbO_3$ single crystals is evidence for the connection between the observed phenomena and effects arising from space-charge fields.

If this model is valid, it seemed advisable to study this effect in crystals with various impurities, since impurities determine the concentration and thermal activation energy of charge carriers, and also to study the influence of illumination by light with wavelengths corresponding to the appearance of the photorefractive phenomena on the optical images that form.

The images were obtained in pure lithium niobate crystals and crystals containing Mn and Fe impurities. They formed most clearly in crystals of $LiNbO_3+0.1$ at %Mn. In $LiNbO_3$ crystals without impurities, $LiNbO_3+0.1$ at %Fe, and $LiNbO_3+0.1$ at %Mn, the images that formed had a lower contrast. Characteristic differences in the process of forming optical images for crystals with various compositions were not identified to a first approximation.

It should also be noted that the observed generation of induced birefringence was bulklike in character, one consequence of which was observation of a thickness dependence for the process of creating the optical images. The best results were achieved for crystals with thicknesses up to 0.5 mm; further increases in sample thickness reduced the contrast of the images observed. Moreover, in crystals with sharply expressed optical nonuniformities, observation (or generation) of optical images was considerably hindered, since variations in the refractive index caused by structural nonuniformities and changes in crystal composition could significantly exceed the induced birefringence.

In order to investigate the effect of illumination on images obtained by thermal processing, we used a high-pressure DRS-250 mercury lamp. Samples with images created previously were placed in the observation mount and exposed to long-period optical illumination. In order to avoid heating the crystal by the light source and to eliminate the influence of temperature effects, the samples were cooled throughout the entire experiment. After the first 10 minutes of illumination, the contrast of the images decreased. Over the next two hours the character of the observed pattern was practically unchanged. However, long-period illumination (around three hours) led to recovery of the image contrast.

As we should expect, we were able to generate images similar to those described above by illuminating a z-cut crystal with a deposited opaque conducting or nonconducting mask. We carried out the corresponding experiments in which a crystal with a deposited mask was exposed to a long period of optical illumination. After the mask at the crystal surface was removed, there remained an optical image which was read by placing the sample between crossed polarizers and observing it in transillumination. Note that to a first approximation the process of generating images by illumination should occur in the same way both when conducting and nonconducting masks are used. The effect can be observed in $LiNbO_3$ crystals with Mn impurities. The physical model of this phenomenon corresponds to the model normally used to describe optical images formed by photorefraction, taking into account that the writing takes place on polar-cut crystals.

Thus, in this study we have obtained the following results:

1) We have observed a new memory effect in crystals of lithium niobate, which essentially consists of the following: a conducting mask is deposited on a polar cut $LiNbO_3$ single crystalthat repeats the information to be written; the crystal is then heated to 120–150 °C, and then cooled to room temperature, after which the mask is removed. As an optical image forms on the crystal surface that replicates the shape of the conducting mask. The optical image is read by placing the crystal between crossed polarizers and observing it in transmission.

2) The fact that the effect observed here manifests itself in the same way as the photorefractive effect allows us to propose a whole series of possible methods for writing information on polar-cut crystals of lithium niobate. The physical basis for these possibilities is the thermal fixation of changes created by some method or another in the potential contour of the crystal surface, and the nonuniform distribution of screening charge that arises as a result of this. In the context of this report, we feel it is necessary to point out qualitatively similar effects observed by the authors of Ref. 7 involving the appearance of optical images in $LiTaO_3$ crystals subjected to local mechanical perturbations.

The authors are grateful to the Russian Fund for Fundamental Research for support from Project 97-02-16600, whose subject is related to that of this paper.

[1] Yu. S. Kuz'minov, *Electrooptic and Nonlinear-Optic Lithium Niobate Crystals* (Nauka, Moscow, 1987) [in Russian].
[2] K. G. Belobaev, V. T. Gabrielyan, L. M. Kazaryan *et al.*, *Piezo- and Ferroelectric Materials and their Applications*, p. 29 (Materials Seminar, Moscow, 1972) [in Russian].
[3] M. Lines and A. Glass, *Principles and Applications of Ferroelectrics and Related Materials* (Clarendon Press, Oxford, 1977; [Mir, Moscow, 1981].
[4] E. I. Bratishchenko, B. B. Ped'ko, V. M. Rudyak, and V. P. Yarunichev, Bull. USSR Acad. Sci. Ser. Phys. **48**, *6*, 1213. (1984) [in Russian].
[5] B. B. Ped'ko, I. I. Sorokina, N. A. Hohonina, Book of Abs. 7th Int. Meeting on Ferroelectricity (Saarbrucken, Fed. Rep. Germany, 1989), p. 219.
[6] A. A. Blistanov, E. V. Makarevskaya, V. V. Geras'kin *et al.*, Fiz. Tverd. Tela (Leningrad) **20**, 2575 (1978) [Sov. Phys. Solid State **20**, 1489 (1978)].
[7] A. I. Otko, Yu. M. Poplavko, S. I. Chizhikov, and L. A. Shuvalov, Technical Digest for ''Photorefractive Materials, Effects and Devices,'' PRM-93 (Kiev, 1993), p. 310.

Translated by Frank J. Crowne

EPR and NMR line shapes in disordered ferroelectric crystals

M. D. Glinchuk and I. V. Kondakova

Institute of Materials Science Problems, Ukrainian Academy of Sciences, 252680 Kiev, Ukraine
(Submitted June 19, 1997; resubmitted August 14, 1997)
Fiz. Tverd. Tela (St. Petersburg) **40**, 340–347 (February 1998)

A theory is developed for the magnetic resonance line shape in disordered ferroelectric crystals. In a study of the random fields responsible for inhomogeneous line broadening, nonlinear and spatial correlation effects are taken into account. It is shown that homogeneous broadening depends on the temperature and on the magnitude and orientation of the external magnetic field, as well as on the nonlinearity parameters of the ferroelectric material. The resonance line shape is calculated as the envelope of homogeneously broadened Lorentzian spin packets. Analytic expressions for $I_2(\omega)$ and $I_3(\omega)$ are introduced to account for nonlinearity and correlation effects of second and third order, respectively. Calculations are done for centrally symmetric crystals, as well as for those without a center of symmetry. It is shown that homogeneous broadening is important near the line peak, while the wings are determined mainly by inhomogeneous broadening. Manifestations of the predicted effects in the spectrum lines of disordered ferroelectric crystals are discussed.
[S1063-7834(98)04002-7]

Because of their anomalous physical properties, disordered ferroelectric crystals, including the group of ferroelectric crystals with diffuse phase transitions, such as $PbMg_{1/3}Nb_{2/3}O_3$ (PMN), $PbSc_{1/2}Ta_{1/2}O_3$ (PST), and $Pb_{1-x}La_xZr_{1-y}Ti_yO_3$ (LPZT), the group of virtual ferroelectric crystals with off-center impurities, such as $K_{1-x}Li_xTaO_3$ (KLT) and $Pb_{1-x}Ge_xTe$, and the group of mixed systems in the KH_2PO_4 (KDP) family, such as $Rb_x(NH_4)_{1-x}H_2PO_4$ (RADP), have attracted the close attention of researchers. These anomalies are, to a substantial degree, related to the complexity of the phase diagrams in these systems which can include ferroelectric and antiferromagnetic phases and a dipole glass, as well as a mixed ferroelectric-glass phase. The variety in the phase diagrams of disordered ferroelectric crystals is caused mainly by the different sources for the random fields, by the form and magnitude of the fields they produce, and, especially, by their distribution functions.[1–4] As a result, the observed physical properties of systems of this type depend strongly on the characteristics of the random fields, so that the average macroscopic and local properties can differ substantially. The methods of radio frequency spectroscopy (EPR, NMR) have been particularly informative in connection with this latter point.[5,6] The random fields created by disordered substitution of cations (e.g., Mg and Nb in PMN and Sc and Ta in PST), by impurities and vacancies in the cation and anion sublattices, etc., cause inhomogeneous broadening of the resonance lines. Usually this broadening is greater than the contribution from homogeneous broadening, so that the distribution function of the random fields determines the line shapes in disordered ferroelectric crystals. Studies of the EPR and NMR line shapes can, therefore, yield valuable information on the features of the random field distributions when calculated and observed line shapes are compared. Up to now, the resonance line shapes have been calculated for mixed systems such as KDP assuming a gaussian distribution of the random electric fields and Ising-model dipole interaction constants based on the replica formalism employed for spin glasses.[7] A more general, rigorous computational technique that is free of assumptions regarding the shape of the random field distribution will be based on the use of statistical theory.[8,9] Calculations have mostly been made in the framework of a first order statistical theory which includes linear contributions from the random fields. It might be expected that for disordered ferroelectric crystals characterized by large random fields it would be necessary to include nonlinear and spatial correlation effects. We have recently developed a general formalism for calculating the distribution function of the random fields taking these effects into account in a statistical theory.[10]

In this paper, we use that formalism to calculate resonance line shapes and generalize it by including the contribution from homogeneous broadening. Theory and experiment are compared. It is shown that the calculated line shapes are in good agreement with the observed shapes in a number of disordered ferroelectric crystals.

1. THEORY OF THE RESONANCE LINE SHAPE

In the statistical theory the absorption intensity $I(\omega)$ is proportional to the number of source configurations for the random fields leading to a given frequency shift $\Delta\omega(r_1,\ldots,r_N)$ at the observation point,[8]

$$I_N(\omega)=\frac{1}{V^N}\int\ldots\int d^3r_1\ldots d^3r_N\,\delta[\omega-\Delta\omega(r_1,\ldots,r_N)]. \tag{1}$$

Here $V=\int d^3r$, N is the number of sources of the random field, which are assumed to be independent and isotropically distributed at the points $r_1,\ldots,r_N$, and the observation point coincides with the origin of the coordinate system. In general, the change in frequency of a resonance transition can include both linear and nonlinear contributions with respect to the local perturbation $\Delta\omega(r_i)$, specifically,

$$\Delta\omega(r_1,\ldots,r_N)=\omega_N+\alpha_2\omega_N^2+\alpha_3\omega_N^3+\cdots+\alpha_m\omega_N^m, \tag{2}$$

and

$$\omega_N = \sum_{i=1}^{N} \Delta\omega(r_i), \tag{3}$$

where the dimensions of the nonlinearity parameters α_m are given by the $(m-1)$-th power of the frequency. Note that the nonlinear terms in Eq. (2) include products of the type $(\Delta\omega(r_i))^k$ and the type $\Delta\omega(r_1)\Delta\omega(r_2)\ldots\Delta\omega(r_k)$, which account for the effect of spatial correlations.

On writing the δ function in Eq. (1) in the form of a Fourier integral and substituting Eqs. (2) and (3) in the integrand of the Fourier transform $I_m(\omega)$, after a number of transformations, we find[10]

$$I_m(\omega) = \sum_{k=1}^{m} \frac{I_1(\omega_k)}{|f'(\omega_k)|}, \tag{4}$$

and

$$f(\omega') = \omega - \omega' - \alpha_2\omega'^2 - \cdots - \alpha_m\omega'^m, \tag{5}$$

where the ω_k are the real roots of the equation

$$f(\omega')|_{\omega'=\omega_k} = 0. \tag{6}$$

Thus, the line shapes calculated in the m-th order statistical theory include nonlinear terms in the frequency shift up to the m-th order but are expressed in terms of $I_1(\omega)$, which is calculated in the first order statistical theory, which only includes terms linear in the frequency shift. The function $I_1(\omega)$ has been calculated for many of the most often encountered sources of random fields (point charges, electric dipoles, dilation centers) and it has been shown that it is usually linear and can be represented in a gaussian, Lorentz, or Holtsmark form.[8,9] As can be seen from Eqs. (4)–(6), the line shape $I_m(\omega)$ including nonlinear effects cannot be written simply as a sum of these forms, since the coefficients in $I_1(\omega)$ depend on ω. For example, Eqs. (4)–(6) imply that the calculated line shape including second order nonlinear effects, $I_2(\omega)$, is given by

$$I_2(\omega) = \frac{\theta(\mp\omega \pm \omega_c)}{|\sqrt{1+4\alpha_2\omega}|}\left[I_1\left(\frac{\sqrt{1+4\alpha_2\omega}-1}{2\alpha_2}\right) + I_1\left(-\frac{\sqrt{1+4\alpha_2\omega}+1}{2\alpha_2}\right)\right],$$

$$\theta(x) = \begin{cases} 1, & x>0, \\ 0, & x<0, \end{cases} \tag{7}$$

where the upper (lower) sign corresponds to positive (negative) values of α_2 and $\omega_c = -(1/4\alpha_2)$ is the critical frequency at which $I_2(\omega)$ diverges. $I_2(\omega)=0$ for $\omega<\omega_c$ $(\alpha_2>0)$ or for $\omega>\omega_c(\alpha_2<0)$. Thus, $I_2(\omega)$ is an asymmetric function of the frequency. The critical frequencies at which the line intensity increases without bound have also been obtained taking third order nonlinear terms into account for $\alpha_3<0$.[10] In the case of $\alpha_3>0$, on the other hand, the line shape was symmetric with respect to the resonance frequency which we chose to coincide with the origin for ω. The divergences mentioned above vanish when any (even a small) contribution owing to homogeneous broadening is taken into account by replacing ω by $\omega \pm (i/\tau)$. This substitution corresponds to having inhomogeneous broadening of the line in the form of the envelope of Lorentzian spin packets with a half-width, half-maximum of I/τ. Note that this procedure is simpler than that customarily employed, where an inhomogeneously broadened line with both homogeneous and homogeneous contributions is represented in the form

$$I_m(\omega) = \int_{-\infty}^{\infty} J(\omega,\omega') f_m(\omega') d\omega', \tag{8}$$

where

$$J(\omega,\omega') = \frac{\tau}{\pi(1+(\omega-\omega')^2\tau^2)}. \tag{9}$$

Here $f_m(\omega')$ is the distribution function of the random fields and $I(\omega,\omega')$ is a Lorentzian spin packet. It is clear that when $J(\omega,\omega')=\delta(\omega-\omega')$, $I_m(\omega)=f_m(\omega)$. Later it will be shown that Eqs. (8) and (9) give the same result as replacing ω by $\omega\pm(i/\tau)$ in Eq. (4). In the case where the homogeneous broadening is small compared to the inhomogeneous broadening, the line shape near $\omega\simeq\omega_c$ is determined mainly by the mechanisms for homogeneous line broadening (e.g., reorientational motion, dipole interaction of identical spins), while the line shape is mainly determined by inhomogeneous broadening in the region $\omega>\omega_c$. We emphasize that this separation of the contributions from homogeneous and inhomogeneous broadening is a characteristic feature which occurs when nonlinear effects control the inhomogeneous broadening of resonance lines. These are especially important in disordered ferroelectric crystals and, as shown below, become larger as the degree of disorder and the dielectric constant increase, so that the line shape should depend on temperature. Since the temperature dependence of the inhomogeneous broadening of resonance lines in disordered ferroelectric crystals originates in the nonlinearity parameters, let us discuss this question in more detail.

2. RESONANCE FREQUENCY SHIFT AND THE NONLINEARITY PARAMETERS

1) In disordered ferroelectric crystals, random electric fields govern the properties and form of the phase diagram. In the following we shall regard these fields as the main cause of the frequency shift owing to the electric field effect in radio frequency spectroscopy.

The frequency shift owing to electric field effects can be linear or nonlinear with respect to the electric field.[9] Linear effects are possible only at paramagnetic centers whose local symmetry does not contain a center of symmetry, while nonlinear effects always occur. Note that the local symmetry depends both on the structure of the paramagnetic center and on the lattice symmetry. For example, in non-centrally symmetric structures, the local symmetry does not contain a center of symmetry, while in cubic lattices this is true only for off-center ions or complex centers of the impurity-vacancy type, etc.

The magnitude of the electric field effects depends[9] on the magnitude of the spin and, in an approximation that is linear in E, the spin-hamiltonian H_E has the form

$$\hat{H}_E = \sum E_i S_j (T_{ijk} H_k + F_{ijk} I_k) + R_{ijk} E_i \{\hat{S}_j \hat{S}_k\}, \qquad (10)$$

where S_i, I_j, E_i, and H_k are, respectively, the components of the electron and nuclear spins and of the electric and magnetic fields. The third term in Eq. (10) equals zero for $S = 1/2$. The frequency shifts of the resonance transition which are linear and nonlinear in the electric field can be obtained by expanding the matrix elements of the spin-hamiltonian (10) in terms of wave functions of the electric field-independent spin-hamiltonian $\hat{H}_0$ in, respectively, the first and higher orders of perturbation theory. In addition, the frequency shifts that are nonlinear in E can be obtained in first order perturbation theory by including the terms of the spin-hamiltonian that a nonlinear in E.[11] It should be emphasized that the electric field effect can not only lead to a frequency shift, but also to line splitting, for example, in crystals with a T_d symmetry. In lattices of this type, there are two nonequivalent positions with respect to inversion for which all the parameters are the same, while the field E differs in sign, and this leads to the splitting of the lines in an external field that has been observed in a number of crystals.[9] In ferroelectric crystals, this kind of splitting has been observed, for example, in the EPR spectrum of Tl^{2+} owing to spontaneous polarization in the paraferroelectric transition in RbH_2PO_4, as well as in the disordered ferroelectric crystal RADP.[12]

2) The nonlinear parameters for ferroelectric crystals are usually obtained by studying the effect of an external electric field on the lattice polarization P and are described using an expression for the free energy $\Phi(P)$. As an illustration, let us consider the case of the polarization P induced by a field $E \| z$ ($E_z \equiv E$, $P_z \equiv P$) in centrally symmetric lattices:

$$\Phi(P,E) = \Phi_0 + \frac{1}{2} aP^2 + \frac{1}{4} bP^4 + \frac{1}{6} cP^6 + \cdots - PE. \qquad (11)$$

The polarization, as usual, is determined from the condition $d\Phi/dP = 0$, i.e.,

$$aP + bP^3 + cP^5 + \cdots = E. \qquad (12)$$

In the linear case ($b = c = \cdots = 0$, $P \equiv P_l$, $E \equiv E_l$),

$$P_l = \xi E_l, \quad \alpha = \xi^{-1}, \qquad (13)$$

where ξ is the dc dielectric permittivity of the system. Substituting P_i in Eq. (12), we find

$$E = E_l + b\xi^3 E_l^3 + c\xi^5 E_l^5 + \cdots . \qquad (14)$$

Comparing Eq. (14) with Eq. (2), where ω_N is the frequency shift in the linear approximation with respect to the field, we find

$$\alpha_m = \frac{\alpha_m^0 \xi^m}{A^{m-1}}. \qquad (15)$$

Here $\alpha_3^0 \equiv b$, $\alpha_5^0 \equiv c$, etc., depend on the type of material and usually are temperature independent, while $\xi^m(T)$ determines the temperature dependence of the nonlinearity parameters α_m. The constant $A = |d\omega/dE|$ is determined by the matrix elements of the hamiltonian H_E for the electric field effect (see Eq. (10), for example) and can depend on the magnitude of the magnetic field and its orientation relative to the crystal lattice. In ordinary ferroelectric crystals $\xi \sim 1/(T - T_c)$ (T_c is the phase transition temperature), so that the α_m should increase rapidly near T_c. In disordered ferroelectric crystals, ξ depends both on the temperature T and on the degree of disorder in the system. Thus, for example, it has been shown[13] that in the ferroelectric crystal PST, which has a diffuse phase transition and can be obtained with any degree of disorder, the ratio of the maximum values of ξ ($f = 0.1$ kHz) for two samples with substantially different degrees of ordering is 1.5 and that ξ' decreases as the degree of ordering increases while the maximum becomes sharper. An analysis of the measured temperature dependences of the third order nonlinearity coefficients of PST samples with different degrees of ordering showed[13] that the nonlinearity parameters of samples with a higher degree of disordering are much higher than in the more ordered samples, and Eq. (13) fits the experiment fairly well for $T \leqslant T_m$ (T_m is the temperature at which $\xi(T)$ has a maximum), while for $T > T_m$ we can only speak of a qualitative agreement which improves with increasing ordering of the sample. The latter appears to be related to the fact that Eqs. (11)–(15), which were derived for illustrating the temperature dependence of the nonlinearity parameters, are strictly valid for ordered ferroelectric crystals. For disordered ferroelectric crystals, a comparison with experiment[13] shows that Eq. (15) provides a qualitatively correct temperature variation in the nonlinearity parameters.

3. RESONANCE LINE SHAPES IN NONCENTRIC CRYSTALS

1) In these systems the frequency shift caused by random fields includes both even and odd powers of the nonlinear contributions. Since the magnitude of these contributions usually decreases as the degree of nonlinearity increases, we shall restrict ourselves to the largest (quadratic) contribution, i.e., we shall retain the first two terms in the frequency shift (2). In this case, the shape of the inhomogeneously broadened lines is determined by Eq. (7), where it is necessary to replace ω by $\omega(i/\tau)$, where $1/\tau$ is the half width of the spin packet. For the following calculations we choose a gaussian form for $I_1(\omega)$:

$$I_1(\omega) = \frac{1}{\sqrt{2\pi}\Delta} \exp(-\omega^2/2\Delta^2). \qquad (16)$$

Then the real part of Eq. (7) for the resonance line shapes can be rewritten in the form

$$I_2(\omega)=\frac{(1/2)+(1/\pi)\operatorname{arctg}\tau(\omega-\omega_c)}{\Delta\sqrt{2\pi}(\varphi(\omega))^{1/2}}$$
$$\times\left\{\exp\left[\frac{f_1(\omega)-2(1+2\alpha_2\omega)}{8\alpha_2^2\Delta^2}\right]\right.$$
$$\times\cos\frac{(4\alpha_2/\tau)-f_2(\omega)}{8\alpha_2^2\Delta^2}$$
$$+\exp\left[\frac{\sim f_1(\omega)-2(1+2\alpha_2\omega)}{8\alpha_2^2\Delta^2}\right]$$
$$\left.\times\cos\frac{(4\alpha_2/\tau)+f_2(\omega)}{8\alpha_2^2\Delta^2}\right\},$$
$$\varphi(\omega)=\sqrt{(1+4\alpha_2\omega)^2+(4\alpha_2/\tau)^2},$$
$$f_{1,2}(\omega)=\sqrt{2}\sqrt{\varphi(\omega)\pm(1+4\alpha_2\omega)}. \qquad (17)$$

Equation (17) clearly transforms to Eq. (7) as $1/\tau\to 0$. In the limit of a large nonlinear contribution (dimensionless nonlinearity parameter $\alpha_2\Delta>1$), the exponents in Eq. (17) approach unity, so that Eq. (17) also implies that for $\omega>\omega_c$, $I_2(\omega)\to 1/\sqrt{1+4\alpha_2\omega}$. Lineshapes constructed in accordance with Eq. (17) for different values of the nonlinearity parameter α_2 and of $1/\tau$ are shown in Fig. 1. Clearly, the line shapes differ substantially from the gaussian shape corresponding to the linear approximation. The most important point is that the line shape is asymmetric even for small nonlinearity parameters and its asymmetry increases rapidly with increasing $\alpha_2\Delta$, approaching the limit $I_2(\omega)=1/\sqrt{1+4\alpha_2\omega}$ for $\omega>\omega_c$. Near the critical frequency ($\omega\simeq\omega_c\pm 1/\tau$) the line shape is entirely determined by the homogeneous broadening contribution. This is true both for large (Fig. 1a) and intermediate (Fig. 1b) values of the nonlinearity parameter, when the line shape consists of not one, but two peaks with different intensities, one of which is related to the denominator and the other, to the exponents in Eq. (17). It is also clear from Figs. 1a and b that the shape of the right hand wing is determined by inhomogeneous broadening, while the left hand wing results from homogeneous broadening. In the case of large nonlinearity parameters, the line shape is given by a curve with a sharp peak at $\omega=\omega_c$ (Fig. 1a) whose intensity increases, while its half width decreases as the homogeneous contribution becomes smaller. For smaller nonlinearity parameters, the line has two peaks which merge into one as $1/\tau$ increases (Fig. 1b).

Figure 2 shows the expected transformation of the line shape with temperature on approaching the phase transition temperature. The nonlinearity parameter was estimated using Eq. (14) and it was assumed that $1/\tau$ increases exponentially with rising temperature. For concreteness we have used the values of $\xi(T)$ and $1/\tau(T)$ for $KTa_{1-x}Nb_xO_3$ ($x=0.157$).[14]

2) We now consider ferroelectric crystals in the KDP family with a T_d symmetry in the paraelectric phase. As indicated in paragraph 1 of Section 2, in systems of this type there are two inversion-nonequivalent positions and this leads to splitting of the resonance lines in a field E owing to the polarization of the lattice in the ferroelectric phase. The positions of the first and second lines are usually determined

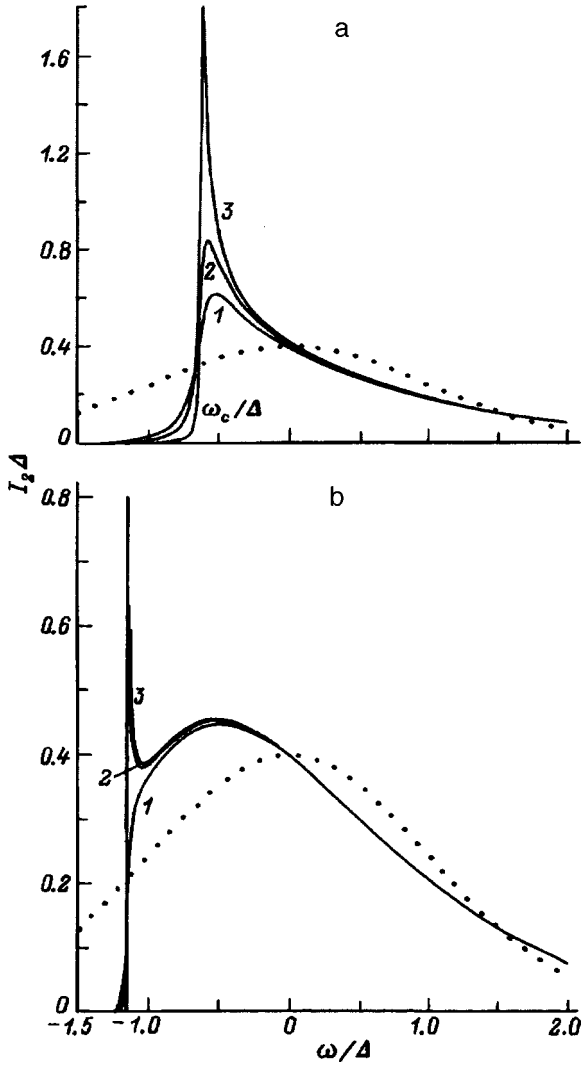

FIG. 1. Inhomogeneously broadened line shapes calculated using Eq. (17). The dotted curve is a gaussian shape corresponding to the linear approximation without homogeneous broadening. $\alpha_2\Delta=0.4$ (a) and 0.22 (b). $(\tau\Delta)^{-1}$: (a) 0.1 (*1*), 0.05 (*2*), 0.01 (*3*); (b) 0.3 (*1*), 0.016 (*2*), 0.01 (*3*).

by first order perturbation theory, where the spin-hamiltonian (10) for $+E$ and $-E$, respectively, serves as the perturbation. In this approximation the center of gravity of these lines is $\omega=0$, so that one line lies in the region $\omega>0$ and the other in the region $\omega<0$. The shapes of the two lines are given by Eqs. (7) and (17), respectively, for $\omega>0$ and $\omega<0$. Note that the origin of the frequency ω axis is taken to be the resonance frequency ω_0, i.e., $\omega\equiv\omega'-\omega_0$, so that including terms nonlinear in E leads to a renormalization of ω_0 for the even terms in E or to an additional shift of the lines for the odd.

Figure 3 shows the shape of the spectra that can be observed in the disordered KDP ferroelectric family. Profiles were calculated for several values of the nonlinearity parameter and of the homogeneous width. The overlap of the tails of the lines clearly enhances $I_2(\omega)$ near $\omega\simeq 0$, while the line shapes are essentially unchanged near the maxima (cf. Figs. 1 and 3a). This behavior should be typical of all ordinary ferroelectric crystals, since the lattice polarization that causes the line splitting is always much greater than the fluctuations

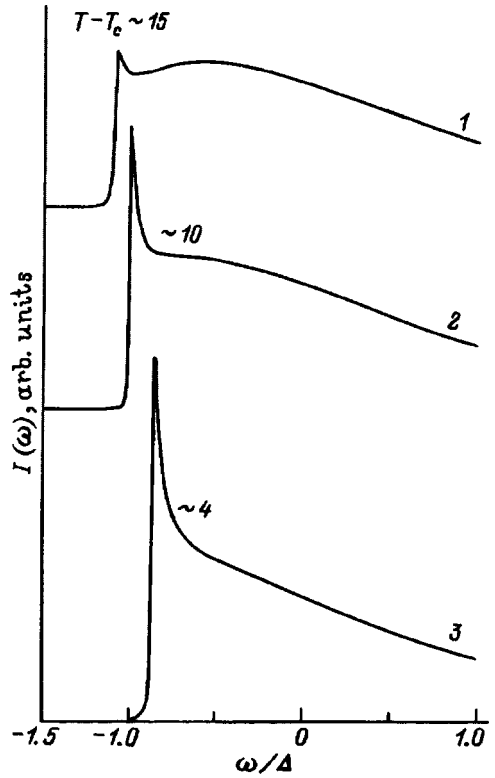

FIG. 2. Calculated transformed shapes of spectrum lines near the transition temperature. $\alpha_2\Delta$ and $(\tau\Delta)^{-1}$: 0.22 and 0.014 (*1*), 0.25 and 0.011 (*2*), 0.3 and 0.008 (*3*).

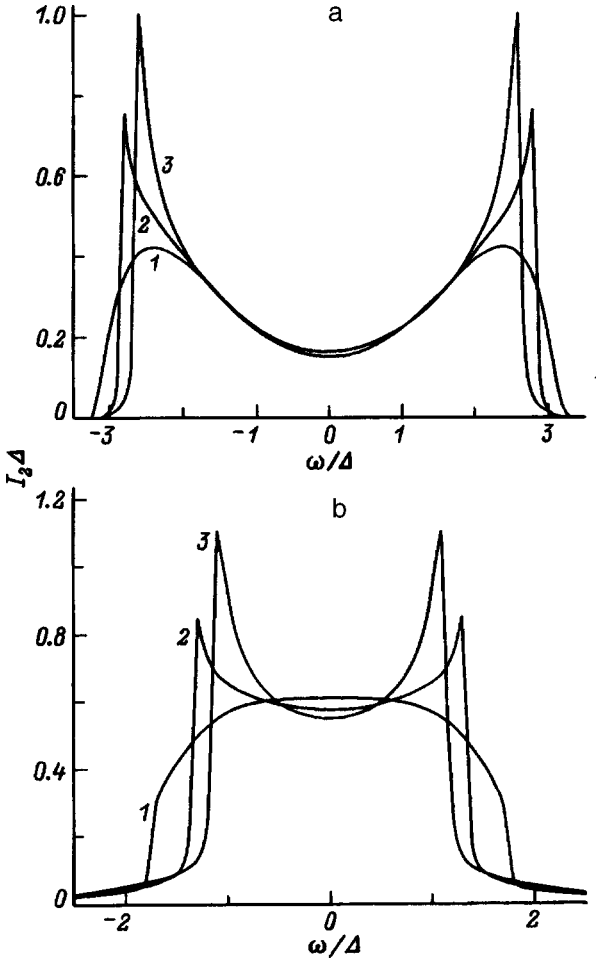

FIG. 3. Spectra consisting of two lines in crystals with T_d symmetry. $\alpha_2\Delta$ and $(\tau\Delta)^{-1}$: 0.22 and 0.02 (*1*), 0.3 and 0.027 (*2*), 0.4 and 0.035 (*3*). The distance between the lines is 4Δ (a) and Δ (b).

in the internal fields responsible for inhomogeneous broadening. In the case of the dipole glasses, however, the fluctuations can be of the same order as the average field. This leads to greater overlap of the lines and to a more complicated spectrum (Fig. 3), right up to the disappearance of the peaks near $\omega=\pm(\omega_0'+\omega_c)$ and the appearance of a single broad line with a peak at $\omega=0$ as the homogeneous contribution increases. Since the nonlinearity parameter increases with rising temperature for $T<T_c$ and decreases for $T>T_c$, the line shapes will be substantially different in these temperature intervals. When $1/\tau$ is determined by jumps between equivalent positions, this analysis generalizes the theory of resonance lines in the motional broadening regime to the case of intrinsically nonlinear contributions to inhomogeneous broadening. Note that under the conditions of motional narrowing usually observed at high temperatures, nonlinear effects will be small, so that the changes in the spectrum with temperature will have the customary form.[15]

4. RESONANCE LINE SHAPES IN CENTROSYMMETRIC SYSTEMS

In these systems the line shapes are given by Eqs. (4)–(6), with only the odd-power nonlinearity parameters retained, i.e., $\alpha_{2k+1}\neq 0$, $\alpha_{2k}=0$ $(k=1,2,...)$. Actually, in this case, when the frequency shifts are caused by the random electric fields from sources located at the points $r_1,\ldots,r_n$, the α component of the random field including the linear and nonlinear contributions can be written in the form

$$E_\alpha(r_1,\cdots,r_N)=\varepsilon_{\alpha N}+\beta_2\varepsilon_{\alpha N}^2+\cdots+\beta_3\varepsilon_{\alpha N}^3,$$

$$\varepsilon_{\alpha N}=\sum_{i=1}^{N}\varepsilon_\alpha(r_i). \tag{18}$$

Since the left and right hand sides should vary the same way under inversion $(\varepsilon_{\alpha N}\to-\varepsilon_{\alpha N},\ E_\omega\to-E_\alpha)$, we conclude that $\beta_2=\beta_4=\cdots=\beta_{2k}=0$. Given that $\alpha_m=\beta_m/A^{m-1}$, we conclude that only the odd-power nonlinearity parameters are nonzero in centrally symmetric systems.

It appears that $I_3(\omega)$ depends significantly on the sign of the nonlinearity parameter α_3. Equation (15) implies that $\alpha_3>0$ and $\alpha_3<0$ correspond to ferroelectric crystals with second and first order phase transitions, respectively. Let us examine the case $\alpha_3>0$.

(2) For $\alpha_3>0$ Eq. (6) has a single real root. Including the contribution of homogeneous broadening in Eq. (4) for the case of a gaussian line shape in the linear approximation (16), we find

$$I_3(E)=\mathrm{Re}\,\frac{1}{\Delta\sqrt{2\pi}|1+3zx_0^2|}\exp\left(-\frac{x_0^2}{2}\right), \tag{19}$$

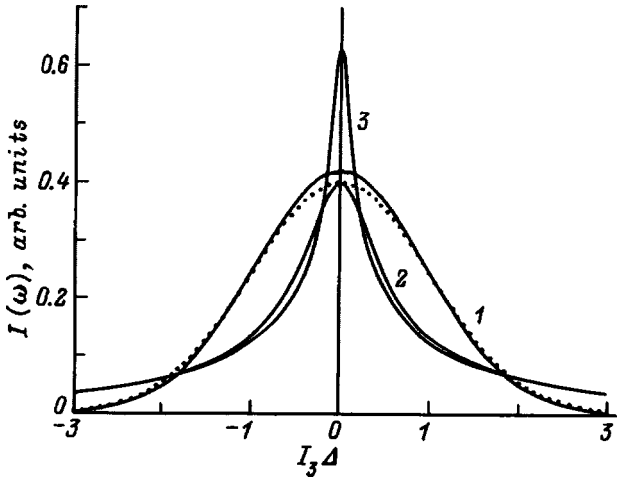

FIG. 4. Inhomogeneously broadened line profile including third-order nonlinear effects [see Eqs. (19) and (20)]. $\alpha_3\Delta^2$ and $(\tau\Delta)^{-1}$: 0 and 0.3 (*1*), 1 and 0 (*2*), 1 and 0.3 (*3*).

$$x_0 = 2^{-1/3} z^{-1/2} \left[\left(z^{1/2} x + \sqrt{\frac{4}{27} + x^2 z} \right)^{1/3} + \left(z^{1/2} x - \sqrt{\frac{4}{27} + x^2 z} \right)^{1/3} \right]. \quad (20)$$

Here $z \equiv \alpha_3 \Delta^2$ is a dimensionless nonlinearity parameter, $x \equiv \omega/\Delta$ is a dimensionless frequency, and $y = 1/(\tau\Delta)$ is a dimensionless half width of the spin packet which determines the homogeneous broadening contribution.

Figure 4 shows an inhomogeneously broadened line profile constructed on the basis of Eqs. (19) and (20). It is clear that, as opposed to $I_2(\omega)$, a function of the form $I_3(\omega)$ is strictly symmetric with respect to the resonance frequency, at which it has a maximum. Nonlinear effects in the inhomogeneous broadening narrow the line and enhance its wings (cf. curves *1* and *2* of Fig. 4). It is also clear from Fig. 4 that homogeneous broadening changes the line shape mainly near the resonance frequency, leaving the wings of the profile essentially unchanged as their behavior is controlled by inhomogeneous broadening. Note that when the inhomogeneous broadening is caused only by the linear terms in the random fields, i.e., is determined only by the line *I* of Fig. 4, introducing homogeneous broadening of the same magnitude as in curve 3 $(1/(\tau\Delta) = 0.3)$ causes only a negligible increase in the height of the peak, a slight narrowing of the line, and a small enhancement in the wings (cf. profile *I* and the dotted curve). Thus, it is nonlinear inhomogeneous broadening effects which enhance the influence of the homogeneous broadening mechanisms which turned out to be especially important near the resonance frequency. Since the magnitude of the nonlinearity parameter varies with temperature as $\alpha_3 \sim \xi^3(T)$ (see paragraph 2 of Section 2), the line should become narrower as the temperature is reduced for $T > T_c$ and wider for $T < T_c$.

5. DISCUSSION OF RESULTS

The above theory for the inhomogeneously broadened magnetic resonance line shape in disordered ferroelectric crystals can be used for describing other spectrum lines, specifically in optical, Mössbauer, dielectric, and other spectra. Given that the mechanisms responsible for inhomogeneous line broadening are extremely diverse and can be significant, not only in disordered, but also ordinary ferromagnetic and ferroelectric crystals, where the nonlinear contributions become much greater near the transition temperature T_c,[15] the theory of inhomogeneously broadened spectrum lines developed in this paper applies to a broad class of solids. For example, the transformation of the line shape on approaching the phase transition temperature in $KTa_{1-x}Nb_xO_3$ ($x = 0.157$) shown in Fig. 2 is close to that observed recently in the spectrum of first-order Raman scattering by the TO_2 optical phonon in this material.[14] We emphasize that immediately adjacent to T_c, the observed line shape for $\omega > \omega_c$ is well described by the theoretically predicted expression $I_2(\omega) \sim 1/\sqrt{1 + 4\alpha\omega}$. Note that a second, less intense maximum which occurs away from the transition temperature at $\omega \simeq 220\ \mathrm{cm}^{-1}$ has been mistakenly interpreted[14] as an additional peak caused by acoustic phonons.

The observed variation with increasing temperature in the EPR spectrum of Tl^{2+} in $Rb_{0.3}(NH_4)_{0.7}H_2PO_4$ (RADP-70)[12] is qualitatively consistent with the curve shown in Fig. 3b, which is illustrative, since the nonlinearity and homogeneous broadening parameters in it were chosen quite arbitrarily. In addition, calculations were made assuming that the homogeneous width is caused by the motion of this spin or its surroundings with a single time $(1/\tau)$. In a spin or dipole glass state there is usually a spectrum of relaxation times characterized by a distribution function. Including such a function $f(\tau)$ in a calculation of the line shape by taking an average of the type $\int I_2(\omega,\tau) f(\tau) d\tau$ could lead to a change in the distribution function and, apparently, the peaks near $\omega \simeq \omega_c$ in Figs. 1–3 would become less pronounced. On the other hand, calculating $f(\tau)$ is a rather complicated task and the form of $f(\tau)$ is determined essentially by the distribution of random electric fields in the system,[3] so that some sort of self-consistent procedure is needed in order to find the line shape. In the theory with one time τ it is possible to assume that this time corresponds to the most probable time, which is greater than the half width $\Delta\tau$ of the distribution.[16]

The proposed theory, in which the dynamics is determined by a single time τ also gives a qualitatively correct description of the observed temperature variation in the NMR line shape of deuterium in RADP-44.[7] The observed NMR and EPR line shapes have been described[7,12] in terms of a distribution function of the local polarization of disordered ferroelectric materials which corresponds to a dipole glass model phase for an Ising model assuming a gaussian distribution for the random interaction and for the random fields. The form of this distribution function in the motional broadening regime is close to that shown in Figs. 3a and 3b. Our results, however, are not limited to the assumptions listed above, but include nonlinearity effects and are, therefore, more general. The NMR lines of nuclei with a large quadrupole moment can be broadened inhomogeneously in disordered ferroelectric crystals owing to fluctuations in the gradients of the electric fields. In particular, the observed[17]

NMR line shapes of ^{93}Nb and PMN have been fitted by numerical Monte-Carlo calculations in which the electric field gradients owing to the disorder in the ion substitution were calculated for a Gaussian distribution of the Nb substitutions relative to the lattice site in an ideal PMN structure. NMR spectra of ^{87}Rb broadened by a quadrupole interaction have been fitted[18] using both a Monte-Carlo calculation and another approach in which the distribution of the electric field gradient was coupled to the distribution of the local lattice polarization. It is possible that the observed[5,17] NMR line shape of ^{93}Nb in PMN is close to that in Fig. 4 because of this coupling. In our approach, the shape of lines broadened by a quadrupole interaction can, in general, be calculated using Eqs. (4)–(6) since the mechanisms responsible for the frequency shift in Eqs. (2) and (3) can be arbitrary. Difficulties may arise only in the case of $\pm 1/2 \rightarrow \mp 1/2$ transitions, for which the frequency shift begins with terms that are quadratic in the field gradients and, therefore, does not contain the linear contributions which essentially determine the form of Eq. (4). A preliminary examination shows that magnetic resonance line shapes can also be calculated by this method in the case where there are no linear terms in Eq. (2). In conclusion, we note that an experimental manifestation of the nonlinear effects in magnetic resonance spectral line shapes predicted here should be sought at temperatures corresponding to the maximum dielectric constant, as well as at the particular orientations of the external magnetic field in the crystals implied by Eq. (15). A study of the features of the magnetic resonance spectra in disordered ferroelectric crystals such as PST and PLZT with different values of nonlinearity parameters would be of special interest. An examination of the magnetic resonances in systems of this type would yield valuable information on the nature of the mechanisms responsible for the features of the phase diagram and the properties of disordered ferroelectric crystals.

[1] M. D. Glinchuk and V. A. Stephanovich, J. Phys.: Condens. Matter **6**, 6317 (1994).
[2] M. D. Glinchuk and V. A. Stefanovich, Fiz. Tverd. Tela **37**, 139 (1995) [Phys. Solid State **37**, 75 (1995)].
[3] M. D. Glinchuk and V. A. Sephanovich, Ferroelectrics **169**, 281 (1995).
[4] M. D. Glinchuk and R. Farhi, J. Phys.: Condens. Matter **8**, 6985 (1996).
[5] R. Blinc, D. C. Ailion, B. Gunther, and S. Zumer, Phys. Rev. Lett. **57**, 2826 (1986).
[6] V. V. Laguta, M. D. Glinchuk, I. P. Bykov, A. N. Titov, and E. M. Andreev, Fiz. Tverd. Tela **32**, 3132 (1990) [Sov. Phys. Solid State **32**, 1818 (1990)].
[7] R. Blinc, J. Doninchek, R. Pirc, B. Tadic, B. Zalar, R. Kind, and O. Liechti, Phys. Rev. Lett. **63**, 2248 (1989).
[8] A. U. Stoneham, Rev. Mod. Phys. **41**, 82 (1969).
[9] M. D. Glinchuk, V. G. Grachev, M. F. Deĭgen, A. B. Roĭtsin, and L. A. Suslin, *Electrical Effects in Radio Frequency Spectroscopy* [in Russian], Nauka, Moscow (1981).
[10] M. D. Glinchuk, I. V. Kondakova, and D. V. Anchishkin, *Proceedings of the 28th Congress Ampere*, Canterbury (1996).
[11] I. B. Aleksandrov, *The Theory of Magnetic Relaxation* [in Russian], Nauka, Moscow (1974).
[12] R. Kind, R. Blinc, J. Dolinchek, N. Korner, B. Zalar, P. Cevc, N. S. Dalal, and J. Toulouse, Phys. Rev. B **43**, 2511 (1991).
[13] M. Bogs, H. Beige, P. Pitzius, and H. Schmitt, Ferroelectrics **126**, 127 (1992).
[14] B. E. Vugmeister, P. di Antonio, and J. Toulouse, Phys. Rev. Lett. **75**, 1646 (1995).
[15] A. Abragam, *The Principles of Nuclear Magnetism*, Oxford (1961).
[16] U. T. Hochli, R. Knorr, and A. Lidl, Adv. Phys. **39**, 405 (1990).
[17] M. D. Glinchuk, J. P. Bykov, and V. V. Laguta, Ferroelectrics **143**, 39 (1993).
[18] N. Korner and R. Kind, Phys. Rev. B **49**, 5918 (1994).

Translated by D. H. McNeill

Determining the Debye temperature and Grüneisen constant of solid hydrogen at high pressures

Yu. V. Petrov

L. D. Landau Institute of Theoretical Physics, Russian Academy of Sciences, 142432 Chernogolovka, Moscow Region, Russia

(Submitted June 26, 1997)
Fiz. Tverd. Tela (St. Petersburg) **40**, 348–349 (February 1998)

A method is proposed for determining the Debye temperature and Grüneisen parameter from data on the equation of state of solid hydrogen and deuterium at low ($T=5$ K) and room ($T=300$ K) temperatures.
[S1063-7834(98)04102-1]

Solid hydrogen has never ceased to be an object of intense study, both in the low-pressure region (where it is one example of quantum crystals) and at high pressures, where phase transitions in it cause interest, in particular the insulator-metal transition.[1–15] In determining the equation of state of hydrogen, the highest accuracy is provided by static compression experiments in diamond anvils. By now,[11] errors in measurements are sufficiently small that we can distinguish the equation of state of the two isotopes (hydrogen and deuterium) and how they change at temperature differences near room temperature. There is even greater expectation for accuracy of planned experiments using intense synchrotron radiation to determine the sample volume. This makes it possible to directly determine such important characteristics of solids, and in particular hydrogen, as the Debye temperature and Grüneisen parameter.

In the Mie-Grüneisen approximation, the pressure of hydrogen can be written in the form

$$P(v,T)=P_s(v)+P_0(v)+P_a(v)+P_t(v,T). \tag{1}$$

Here T, ν, and P are the temperature, specific volume, and pressure, P_s is the static pressure, P_0 and P_a are pressures of zero point oscillations caused respectively by optical and acoustic branches, and P_t is the thermal part of the pressure arising from acoustic phonons. P_a and P_t are determined by the expressions

$$P_a=-\frac{9}{8}k_{\mathrm{B}}\frac{d\Theta_D}{dv}, \tag{2}$$

$$P_t=-3k_{\mathrm{B}}\frac{T}{\Theta_D}D\left(\frac{\Theta_D}{T}\right)\frac{d\Theta_D}{dv}, \tag{3}$$

where k_{B} is Boltzmann's constant, Θ_D is the Debye temperature, and

$$D(x)=\frac{3}{x^3}\int_0^x\frac{t^3dt}{e^t-1} \tag{4}$$

is the Debye function. Using labels h and d to refer to hydrogen and deuterium respectively, let us write four Eqs. (1) for these two isotopes with the same specific volume and two values of the temperature T_1 and T_2. Then by eliminating from these equations the common static pressure and taking into account the connection between Debye temperatures of hydrogen and deuterium:

$$\xi=\Theta_D^d/\Theta_D^h=1/\sqrt{2}, \tag{5}$$

we obtain an algebraic equation that determines Θ_D^h (it is convenient to introduce the dimensionless quantity $\tau=\Theta_D^h/T_2$ in place of Θ_D^h):

$$F(\tau)\equiv\frac{D(\tau)-\frac{T_1}{T_2}D\left(\tau\frac{T_2}{T_1}\right)}{D(\xi\tau)-\frac{T_1}{T_2}D\left(\epsilon\tau\frac{T_2}{T_1}\right)}-\frac{P^h(v,T_2)-P^h(v,T_1)}{P^d(v,T_2)-P^d(v,T_1)}=0. \tag{6}$$

For each specific volume v, which is a parameter (in this case, T_1, T_2, P^h and P^d are also parameters), the algebraic Eq. (6) with respect to the single unknown τ can be solved numerically, for example, Newton, as $\tau=\lim_{n\to\infty}\tau^{(n)}$, according to using the recursive Newtonian procedure: $\tau^{(n+1)}=\tau^{(n)}-F(\tau^{(n)})/F'(\tau^{(n)})$ $(n=1,2,\dots)$. The derivative of the function $F(\tau)$ required for this with respect to τ is

$$\begin{aligned}F'(\tau)=\frac{3}{\tau^3}\left[f(\tau)-\left(\frac{T_1}{T_2}\right)^3 f\left(\tau\frac{T_2}{T_1}\right)\right]\left[D(\xi\tau)-\frac{T_1}{T_2}D\right.\\ \left.\times\left(\xi\tau\frac{T_2}{T_1}\right)\right]-\frac{1}{\xi^3}\left[f(\xi\tau)-\left(\frac{T_1}{T_2}\right)^3 f\left(\xi\tau\frac{T_2}{T_1}\right)\right]\\ \times\left[D(\tau)-\frac{T_1}{T_2}D\left(\tau\frac{T_2}{T_1}\right)\right]\Bigg/\\ \left[D(\xi\tau)-\frac{T_1}{T_2}D\left(\xi\tau\frac{T_2}{T_1}\right)\right]^2,\end{aligned} \tag{7}$$

where $f(x)=x^3/(e^x-1)$.

In this case, the Grüneisen parameter for the value v that is the same for both isotopes can be found from the equation

$$\gamma=-\frac{(P^h(v,T_2)-P^h(v,T_1))v}{3k_{\mathrm{B}}T_2\left[D(\tau)-\frac{T_1}{T_2}D\left(\tau\frac{T_2}{T_1}\right)\right]}. \tag{8}$$

TABLE I. Debye temperature Θ_D and Grüneisen parameter γ of hydrogen, obtained by solving Eq. (6) according to the experimental data of Ref. 11.

v, cm^3/mol	τ	Θ_D, K	γ
8	2.543	763	0.863
7	2.871	861	0.828
6	3.780	1134	0.856

As an example of the use of this procedure we will recover the values of the Debye temperature and Grüneisen parameter from data given in Ref. 11 on the equation of state of hydrogen and deuterium at low ($T=5$ K) and room ($T=300$ K) temperatures. The results of the calculation are shown in Table I.

We note that if a value $\tau_0=\Theta_D^h/T_2$ is found from Eq. (6) for some value of the specific volume v_0, then by integrating with respect to specific volume the difference between pressures of only a single isotope (hydrogen) $\delta P^h(v)=P^h(v,T_2)-P^h(v,T_1)$, we obtain the equation

$$W(\tau)\equiv D(\tau)-D(\tau_0)-3\ln\frac{1-e^{-\tau}}{1-e^{-\tau_0}}-\frac{T_1}{T_2}\left[D\left(\tau\frac{T_2}{T_1}\right)-D\left(\tau_0\frac{T_2}{T_1}\right)-3\ln\frac{1-e^{-\tau T_2/T_1}}{1-e^{-\tau_0 T_2/T_1}}\right]-\frac{1}{k_B T_2}\int_{v_0}^{v}\delta P^h(v)dv=0, \quad (9)$$

which also determines τ, and thus Θ_D^h as a function of the specific volume v. The derivative of the function $W(\tau)$ required for its numerical solution by Newton's method has the form

$$W'(\tau)=-\frac{3}{\tau}\left[D(\tau)-\frac{T_1}{T_2}D\left(\tau\frac{T_2}{T_1}\right)\right]. \quad (10)$$

In conclusion, we note that the same procedure can be applied to determine the Debye temperature and Grüneisen parameter of a crystal of another light element (helium), starting from measurements of the equation of state of ^{4}He and ^{3}He crystals. Despite the fact that the mass difference for this system is relatively smaller than that for hydrogen isotopes, solid helium has the advantage in that it is better described by the Grüneisen equation over a wide range of specific volumes due to its atomic character. In it, in particular, there does not appear a phase transition caused by rotating a molecule out of its orientational order, as happens in solid hydrogen crystals.

This work was carried out with the financial support of Grant RFFI-95-02-04535*a* and INTAS-94-1105.

[1] D. E. Rumaker, L. Kumar, and F. E. Harris, Phys. Rev. Lett. **34**, 812 (1975).
[2] C. Friedli and N. W. Ashcroft, Phys. Rev. B **16**, 662 (1977).
[3] J. van Straaten, R. J. Wijngaarden, and I. F. Silvera, Phys. Rev. Lett. **48**, 97 (1982).
[4] W. J. Nellis, M. Ross, A. C. Mitchell, M. van Thiel, D. A. Young, F. H. Ree, and R. J. Trainor, Phys. Rev. A **27**, 608 (1983).
[5] B. I. Min, H. I. F. Jansen, and A. J. Freeman, Phys. Rev. B **33**, 6383 (1986).
[6] D. M. Ceperley and B. J. Alder, Phys. Rev. B **36**, 2092 (1987).
[7] J. van Straaten and I. F. Silvera, Phys. Rev. B **37**, 1989 (1988).
[8] R. J. Hemley and H. K. Mao, Phys. Rev. Lett. **61**, 857 (1988).
[9] T. W. Barbee III, A. Garcia, M. L. Cohen, and J. L. Martins, Phys. Rev. Lett. **62**, 1150 (1989).
[10] H. E. Lorenzana, I. F. Silvera, and K. A. Goettel, Phys. Rev. Lett. **64**, 1939 (1990).
[11] R. J. Hemley, H. K. Mao, L. W. Finger, A. P. Jephcoat, R. M. Hazen, and C. S. Zha, Phys. Rev. B **42**, 6458 (1990).
[12] H. K. Mao, R. J. Hemley, and M. Hanfland, Phys. Rev. Lett. **65**, 484 (1990).
[13] R. J. Hemley, H. K. Mao, and J. F. Shu, Phys. Rev. Lett. **65**, 2670 (1990).
[14] E. Kaxiras, J. Brouthon, and R. J. Hemley, Phys. Rev. Lett. **67**, 1138 (1991).
[15] H. K. Mao and R. J. Hemley, Rev. Mod. Phys. **66**, 671 (1994).

Translated by Frank J. Crowne

Lattice dynamics of ionic crystals in a model of ''breathing'' and polarizable ions

N. G. Zamkova and V. I. Zinenko

L. V. Kirenskii Institute of Physics, Siberian Branch of the Russian Academy of Sciences, 660036 Krasnoyarsk, Russia

(Submitted June 4, 1977; resubmitted August 18, 1997)
Fiz. Tverd. Tela (St. Petersburg) **40**, 350–354 (February 1998)

An expression is written down for the dynamic matrix of ionic crystals in terms of a microscopic, parameterless model of ''breathing'' and polarizable ions. Results from a calculation of the complete spectrum of the lattice vibrations of ionic crystals having an NaCl structure are presented as an illustration. © *1998 American Institute of Physics.* [S1063-7834(98)04202-6]

Recently Ivanov and Maksimov have presented[1,2] microscopic justifications for a model of ionic crystals consisting of individual ions whose interaction also determines all the static and dynamic properties. This picture of ionic crystals is described rather completely by a simplified version of the functional density method proposed by Gordon and Kim.[3] The later work[1,2] generalizes the Gordon–Kim model so as to include the multipole polarizabilities of the ions. These must be included when calculating the electronic polarizability of the ions in the crystal, the dielectric permittivity, and the spectrum of the crystal lattice vibrations. The polarizability and deformability of the ions have been taken into account previously through a phenomenological model[4–6] and an adequate description of the lattice dynamics of ionic crystals was obtained by including these effects. This approach, however, could only be used to calculate the lattice vibration frequencies of ionic crystals with a simple structure, since a large number of unknown parameters are involved. In Ivanov and Maksimov's method[1,2] there are no fit parameters and this method can be used for calculating the lattice vibrations of ionic crystals with a complicated crystalline structure. In it[1,2] the lattice vibration frequencies are calculated by the frozen phonon method, which greatly limits the possible applications, since the whole frequency spectrum of the lattice vibrations cannot be calculated by the frozen phonon method.

In this paper the approach employed in Refs. 1 and 2 is used to derive expressions for the dynamic matrix and high-frequency dielectric constant and to calculate the complete phonon spectrum of the lattice vibrations of alkali halide crystals and alkaline earth oxides with an NaCl structure.

1. DYNAMIC MATRIX

An ionic crystal is treated as consisting of spherically symmetric overlapping ions and the total electron density can be written in the form

$$\rho(r)=\sum_i \rho_l(\mathbf{r}_i-\mathbf{R}_i). \tag{1}$$

The total energy of the crystal is given by[1,2]

$$\begin{aligned}E=&\frac{1}{2}\sum_{ij}\frac{Z_i^{\rm ion}Z_j^{\rm ion}}{|\mathbf{R}_i-\mathbf{R}_j|}+\sum_i E_i^{\rm self}(V_l)\\&+\frac{1}{2}\sum_{ij}\Phi_{ij}(V_i,V_j,|\mathbf{R}_i-\mathbf{R}_j|)+\sum_i\frac{\mathbf{P}_i^2}{\alpha_i(V_i)}\\&+\frac{1}{2}\sum_{ij}\mathbf{P}_iQ_{ij}(|\mathbf{R}_i-\mathbf{R}_j|)\mathbf{P}_j\\&+\frac{1}{2}\sum_{ij}\mathbf{P}_i\Gamma_{ij}(V_i,V_j,|\mathbf{R}_i-\mathbf{R}_j|)\mathbf{P}_j-\sum_{ij}\mathbf{P}_i\mathbf{S}_j(i)\\&-\sum_i\mathbf{P}_i\mathbf{E}_i,\end{aligned} \tag{2}$$

where the first term describes the Coulomb interaction of the nuclei and the second is the intrinsic energy of an ion, which depends on the potential V_i created by the crystalline environment. The pairwise interaction energy Φ_{ij} is defined as[2,7]

$$\begin{aligned}\Phi_{ij}=&E[\rho_i(\mathbf{r}_i-\mathbf{R}_i)+\rho_j(\mathbf{r}_i-\mathbf{R}_j)]-E[\rho_i(\mathbf{r}_i-\mathbf{R}_i)]\\&-E[\rho_j(\mathbf{r}_j-\mathbf{R}_j)].\end{aligned} \tag{3}$$

In Eq. (1) $\mathbf{R}_i=\mathbf{R}_i^0-\mathbf{u}_i$, $\mathbf{u}_i$ is the displacement of an ion from its equilibrium position, P_i and α_i are the dipole moment and polarizability of the i-th ion, respectively, and E_i is the electric field at the i-th ion owing to the displacement of the atoms from their equilibrium position, i.e.,

$$\mathbf{E}_i=-\sum_j Q_{ij}Z_j^{\rm ion}\mathbf{u}_l. \tag{4}$$

The matrices Q_{ij} and Γ_{ij} describe the long and short range parts, respectively, of the dipole-dipole interaction, $\mathbf{S}_j(i)=\Sigma_k m_{jk}\mathbf{u}_k$, and the matrix m_{jk} describes the deformability of an ion. Expanding the first three terms in Eq. (1) in terms of the small displacements $\mathbf{u}_i$, eliminating $\mathbf{P}_i$ from the minimum energy condition, and transforming to normal coordinates, we obtain an expression for the dynamic matrix,

$$D_{\alpha k,\beta k'}(\mathbf{q})=(D^{\rm pib}_{\alpha k,\beta k'}(\mathbf{q})+D^{\rm pol}_{\alpha k,\beta k'}(\mathbf{q}))(m_k m_{k'})^{-1/2},$$

$$D^{\rm pib}_{\alpha k,\beta k'}(\mathbf{q})=\frac{1}{2}Z_kQ_{\alpha k,\beta k'}(\mathbf{q})Z_{k'}$$

TABLE I. Cell parameters, dielectric constants, limiting phonon frequencies, and dynamic charges.

Crystal	α, Å		ε_∞		ω_{T0}, cm^{-1}		ω_{L0}, cm^{-1}		Z_{eff}	
	Exp.	Theor.	Exp.	Theor.	Exp.	Theor.	Exp.	Theor.	Exp.	Theor.
LiF	4.03	4.02	1.9	1.71	308	343	636	536	1.0	0.70
NaF	4.63	4.66	1.7	1.54	239	229	413	338	1.02	0.72
KF	5.34	5.24	1.5	1.69	191	127	323	269	1.01	0.95
RbF	5.60	5.61	1.9	1.84	154	156	286	277	1.25	1.16
LiCl	5.14	4.5	2.7	3.36	191	364	398	557	1.15	1.27
NaCl	5.64	5.4	2.3	2.30	164	161	265	239	1.13	0.9
KCl	6.29	5.92	2.1	2.25	143	102	212	180	1.11	0.99
RbCl	6.60	6.24		2.32	124	112	172	169	1.13	1.08
LiBr	5.50	5.03	3.2	3.25	159	319	323	466	1.18	1.25
NaBr	6.00	5.82	2.6	2.38	133	139	207	193	1.14	0.88
KBr	6.60	6.24	2.4	2.36	120	111	166	154	1.11	0.94
RbBr	6.88	6.56		2.38		82		115		0.96
LiI	6.00	5.32		3.91		326		506		1.72
NaI	6.48	6.14	2.9	2.70	120	169	170	216	1.07	1.06
KI	7.06	6.59	2.7	2.58	101	109	138	150	1.14	1.10
RbI	7.34	6.88	2.6	2.58	74	76	101	102	1.13	1.01
MgO	4.21	4.21	3.0	2.83	400	476	750	617	1.15	0.98
CaO	4.81	4.79	3.4	2.95	300	350	574	516	1.26	1.28
SrO	5.16	5.10	3.3	3.09	240	330	495	474	1.40	1.41
BaO	5.54	5.50	3.3	3.32	150	222	430	418	1.45	1.75

$$
\begin{aligned}
&+\sum_{\mathbf{n}j}\ \frac{\partial}{\partial V_k}\,\Phi\begin{pmatrix}0 & \mathbf{n}\\ k & j\end{pmatrix} Q_{\alpha k,\beta k'}(\mathbf{q})Z_{k'}\\
&+\frac{\partial E_k^{\mathrm{self}}}{\partial V_k}\,Q_{\alpha k,\beta k'}(\mathbf{q})Z_{k'}\\
&-\frac{1}{2}\left\{\sum_j\ p^j_{\alpha k}(\mathbf{q})\ \frac{\partial V_j}{\partial R_\beta}+\sum_j\ p^{*j}_{\beta k'}(\mathbf{q})\ \frac{\partial V_j}{\partial R_\alpha}\right.\\
&+d_{\alpha k}\ \frac{\partial V_k}{\partial R_\beta}+d_{\beta k'}\ \frac{\partial V_k}{\partial R_\alpha}+\sum_j\ i_j\ \frac{\partial V_j\partial V_j}{\partial R_\alpha\partial R_\beta}\\
&\left.+\sum_{\mathbf{n}}\left[\frac{\partial^2}{\partial R_\alpha\partial R_\beta}\,\Phi\begin{pmatrix}\mathbf{n} & 0\\ k & k'\end{pmatrix}\right]\exp(-i\mathbf{qn})\right\}\\
&\times\exp(-i\mathbf{q}(\mathbf{r}_k-\mathbf{r}_{k'})),
\end{aligned}
\tag{5}
$$

$$
\begin{aligned}
D^{\mathrm{pol}}_{\alpha k,\beta k'}(\mathbf{q})=&-\frac{1}{2}\sum_{\gamma i,\gamma' i'}\ [Z_kQ^*_{\gamma i,\gamma k}(\mathbf{q})\\
&\times R_{\gamma' i',\beta k'}(\mathbf{q})Q_{\gamma' i',\beta k'}(\mathbf{q})Z_{k'}\\
&+T^*_{\gamma i,\alpha k}(\mathbf{q})R_{\gamma i,\gamma' i'}(\mathbf{q})Q_{\gamma' i',\beta k'}(\mathbf{q})Z_{k'}\\
&+Z_kQ^*_{\gamma i,\alpha k}(\mathbf{q})R_{\gamma i,\gamma' i'}(\mathbf{q})T_{\gamma',i',\beta k'}(\mathbf{q})\\
&+T^*_{\gamma i,\alpha k}(\mathbf{q})R_{\gamma l,\gamma' l'}(\mathbf{q})T_{\gamma' i',\beta k'}(\mathbf{q})],
\end{aligned}
\tag{6}
$$

where

$$
p^j_{\alpha k}(\mathbf{q})=\sum_{\mathbf{n}}\left[\frac{\partial^2}{\partial V_k\partial R_\alpha}\,\Phi\begin{pmatrix}\mathbf{n} & 0\\ k & k'\end{pmatrix}\right]\exp(-i\mathbf{qn}),
$$

$$
d_{\alpha k}=-\sum_{\mathbf{n}j}\left[\frac{\partial^2}{\partial V_k\partial R_\alpha}\,\Phi\begin{pmatrix}0 & \mathbf{n}\\ k & j\end{pmatrix}\right],
$$

$$
g_{k,k'}(\mathbf{q})=\sum_n\left[\frac{\partial^2}{\partial V_k\partial V_{k'}}\,\Phi\begin{pmatrix}\mathbf{n} & 0\\ k & k'\end{pmatrix}\right]\exp(-i\mathbf{qn}),
$$

$$
i_k=-\sum_{\mathbf{n}j}\left[\frac{\partial^2}{\partial V_k^2}\,\Phi\begin{pmatrix}0 & \mathbf{n}\\ k & j\end{pmatrix}\right]+\frac{\partial^2E_k^{\mathrm{self}}}{\partial V_k^2},
$$

$$
\hat{R}=(\hat{\Gamma}+\hat{Q}+\hat{\alpha})^{\sim 1},\quad(\hat{\alpha})_{\gamma i,\gamma' i'}=\delta_{\gamma\gamma'}\delta_{ii'}\alpha_i,
$$

TABLE II. Electronic polarizabilities of oxygen, halogens, and metals in compounds with an NaCl structure.

Crystal	α_M, Å^3	α_x, Å^3	Crystal	α_M, Å^3	α_x, Å^3
LiF	0.02	0.71	Kl	0.71	5.09
NaF	0.12	0.79	RbI	1.29	5.24
KF	0.73	0.86	LiBr	0.02	3.21
RbF	1.36	0.89	NaRb	0.12	3.58
LiCl	0.02	2.35	KBr	0.71	3.76
NaCl	0.12	2.69	RbBr	1.3	3.88
KCl	0.71	2.89	MgO	0.06	1.6
KbCl	1.32	2.99	CaO	0.38	2.03
LiI	0.02	4.38	SrO	0.75	2.28
NaI	0.12	4.84	BaO	1.3	2.63

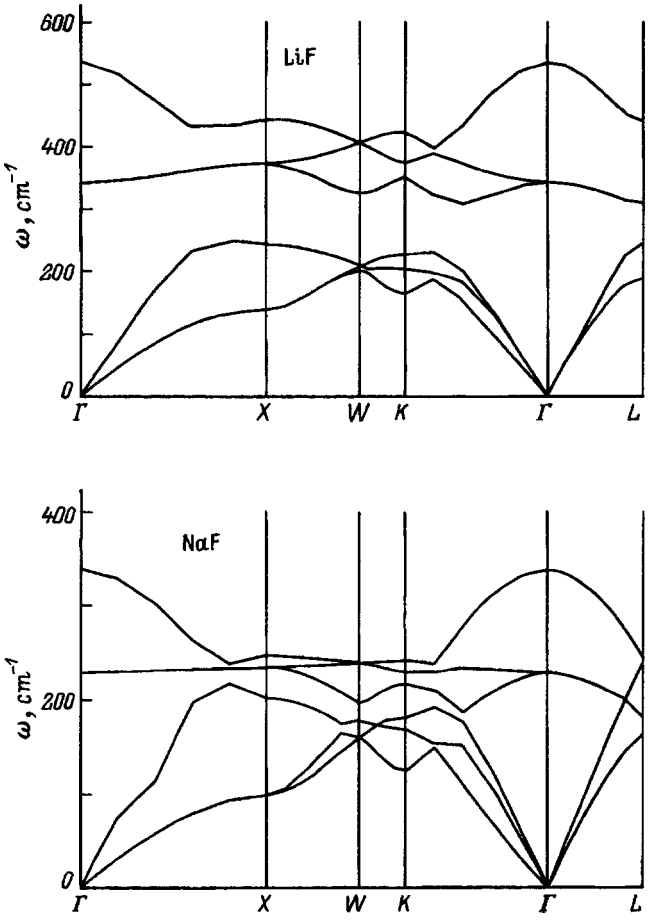

FIG. 1. Phonon dispersion in MF (calculated).

$$T_{\alpha k,\beta k'}(\mathbf{q}) = \Bigg\{ \sum_{\mathbf{n}j} \left[\frac{\partial}{\partial V_k} S_\alpha \begin{pmatrix} 0 & \mathbf{n} \\ k & j \end{pmatrix} \right] \frac{\partial V_k}{\partial R_\beta} \exp(i\mathbf{qn}) + \sum_{\mathbf{n}j} \left[\frac{\partial}{\partial V_j} S_\alpha \begin{pmatrix} \mathbf{n} & 0 \\ k & j \end{pmatrix} \right] \frac{\partial V_j}{\partial R_\beta} + \sum_{\mathbf{n}} \left[\frac{\partial}{\partial R_\beta} S_\alpha \begin{pmatrix} \mathbf{n} & 0 \\ k & k' \end{pmatrix} \right] \exp(-i\mathbf{qn}) \Bigg\} \times \exp(-i\mathbf{q}(\mathbf{r}_k - \mathbf{r}_{k'}))$$

An expression for the dynamic matrix D^{pib} in the ''breathing'' ion model has been obtained in Ref. 7.

2. LATTICE DYNAMICS OF CRYSTALS WITH AN NACL STRUCTURE

We shall use this expression for the dynamic matrix to calculate the lattice dynamics of alkali halide crystals and alkaline earth oxides with an NaCl structure. The calculated equilibrium values of the unit cell parameters, limiting vibration frequencies, high-frequency dielectric constant, and dynamic Born charges, as well as experimental data for comparison, are listed in Table I. The calculated polarizabilities of the metals, oxygen, and halogens are given in Table II. Dispersion curves together with available experimental data for the symmetric directions of the Brillouin zone are shown in Figs. 1–5. As can be seen from Table I and the figures, the agreement between the calculated and experimental values and dependences is quite satisfactory, except for LiCl and LiBr crystals, for which the calculated transverse optical mode frequencies are 2 times the experimental values.

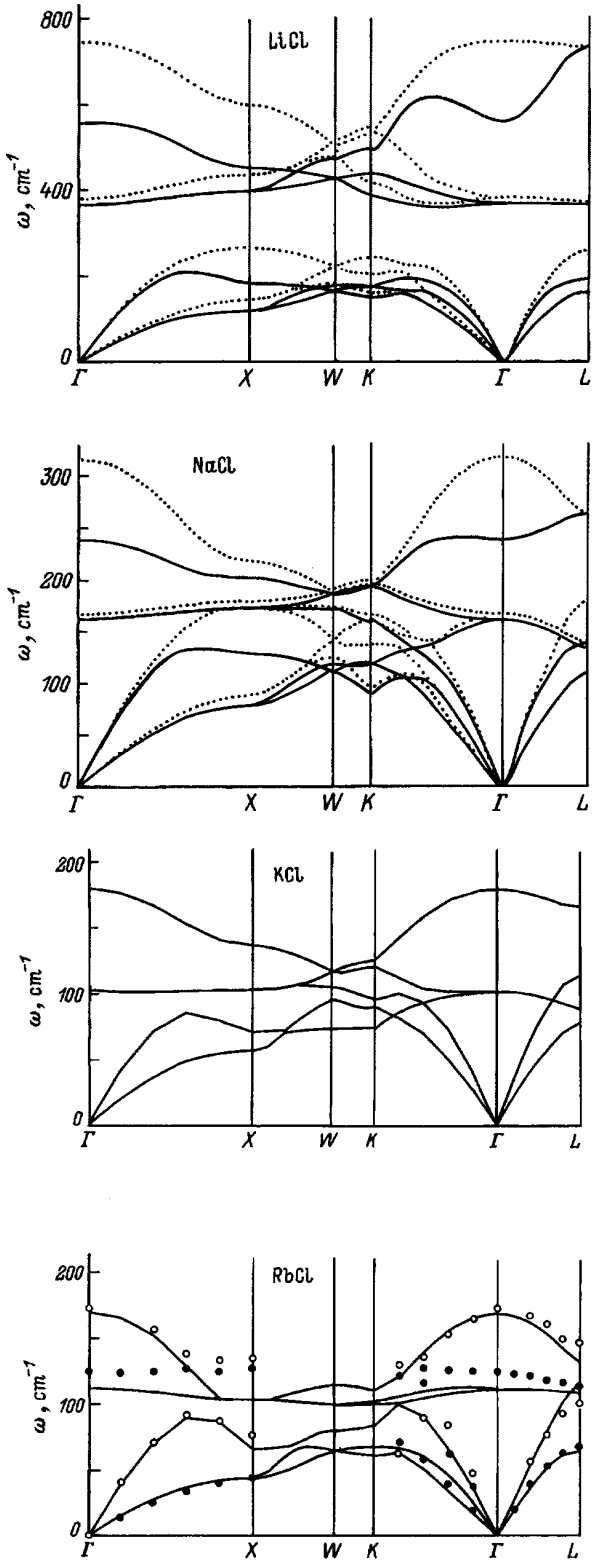

FIG. 2. Phonon dispersion in MCI. The smooth curves are calculated. For comparison, the results of a ''breathing''-ion-model calculation neglecting the ion polarizability are shown as dotted curves. The hollow and solid circles are the experimental dependences for the longitudinal and transverse branches, respectively.[13]

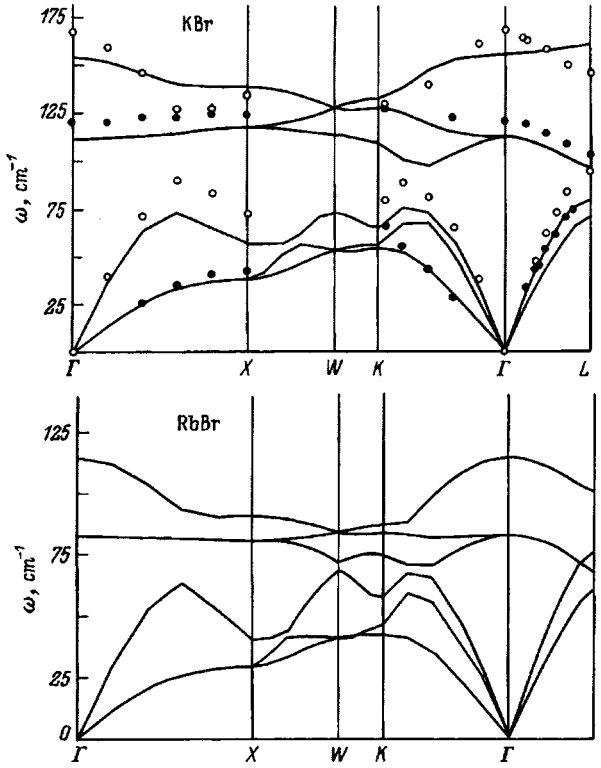

FIG. 3. Phonon dispersion in MBr. The smooth curves are calculated. The hollow and solid circles are the experimental dependences for the longitudinal and transverse branches, respectively.[14]

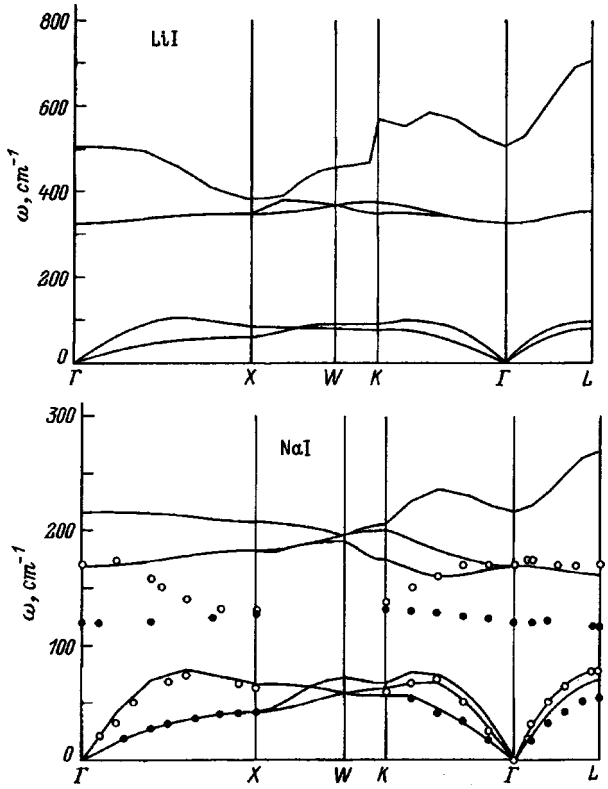

FIG. 4. Phonon dispersion in MI. The smooth curves are calculated. The hollow and solid circles are the experimental dependences for the longitudinal and transverse branches, respectively.[14]

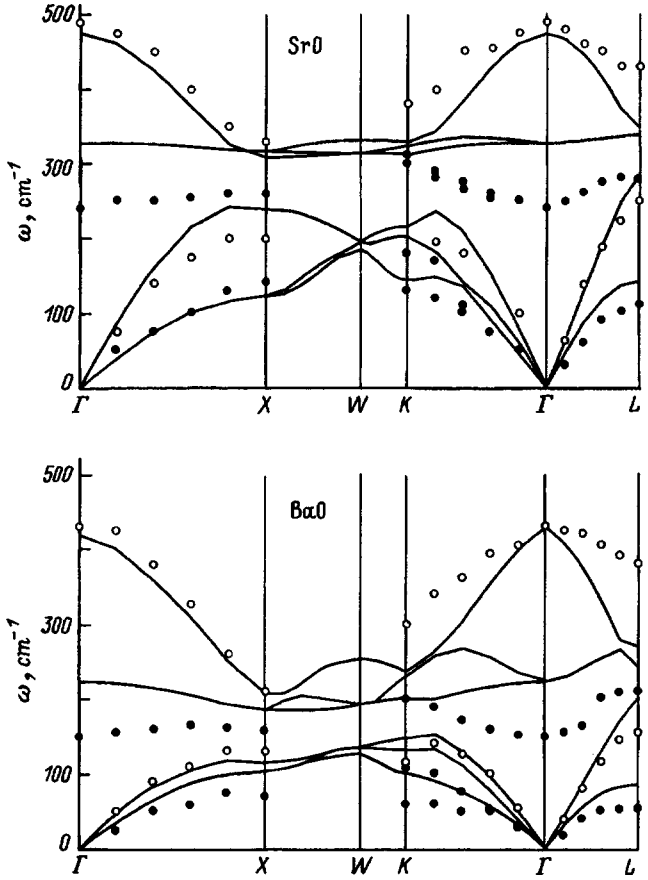

FIG. 5. Phonon dispersion in MO. The smooth curves are calculated. The hollow and solid circles are the experimental dependences for the longitudinal and transverse branches, respectively.[9–12]

Thus, the calculations made here show that a rather simple microscopic model of ionic crystals including the monopole and dipole polarizability of the ions can be used successfully to calculate the static and dynamic properties. The advantage of this method is that the time to compute the complete phonon spectrum is several orders of magnitude shorter than for the other known methods of calculating the crystal lattice vibrational frequencies based on first principles and this offers the possibility of calculating the lattice dynamics of compounds having a complicated crystalline structure.

We thank O. V. Ivanov and E. G. Maksimov for providing the programs for calculating the total ion energy and polarizability.

This work was supported by the Russian Fund for Fundamental Research (Project 97-02-16277).

[1] O. V. Ivanov and E. G. Maksimov, Phys. Rev. Lett. **69**, 268 (1992).
[2] O. V. Ivanov and E. G. Maksimov, Zh. Eksp. Teor. Fiz. **108**, 1841 (1995) [JETP **81**, 1008 (1995)].
[3] R. G. Gordon and Y. S. Kim, Chem. Phys. **56**, 3122 (1972).
[4] B. G. Dick and A. W. Overhauser, Phys. Rev. **112**, 90 (1958).
[5] J. R. Hardy, Philos. Mag. **7**, 73, 315 (1962).
[6] V. Schroder, Solid State Commun. **4**, 347 (1966).
[7] R. E. Cohen, I. L. Boyer, and M. J. Mehl, Phys. Rev. B **35**, 5749 (1992).
[8] C. Kittel, Introduction to Solid State Physics, Wiley, N.Y. (1976).
[9] M. J. L. Sangster, G. Peckman, and D. H. Saunderson, J. Phys. C **3**, 1026 (1970).

[10] D. H. Saunderson and G. Peckman, J. Phys. C **4**, 2009 (1971).
[11] S. A. Chang, C. W. Tompson, E. Gurmen, and L. D. Muhlestein, J. Phys. Chem. Solids **36**, 769 (1975).
[12] K. N. Rieder, B. A. Weinstein, M. Cordona, and H. Bilz, Phys. Rev. B **8**, 4780 (1973).
[13] G. Raunio and S. Rolandson, J. Phys. C **3**, 1013 (1970).
[14] A. D. B. Woods, B. N. Brockhouse, and R. A. Cowley, Phys. Rev. **131**, 1025 (1963).

Translated by D. H. McNeill

Characteristic behavior of the specific heat of exsolving ^{3}He–^{4}He solid solutions

T. N. Antsygina, V. A. Slyusarev, and K. A. Chishko

Physicotechnical Institute of Low Temperatures, Ukrainian Academy of Sciences, 310164 Khar'kov, Ukraine
(Submitted April 14, 1997; resubmitted August 8, 1997)
Fiz. Tverd. Tela (St. Petersburg) **40**, 355–361 (February 1998)

A theory that includes a substantial contribution of the correlation effects to the specific heat of exsolving ^{3}He–^{4}He solid solutions is constructed on a lattice-gas model. This theory makes it possible to construct a unified description of the temperature variation of the specific heat of these systems for a wide range of values of the ^{4}He impurity density n_0. It is shown that, to obtain quantitative agreement of the proposed theory with published experimental data, the effective coordination number z for the impurity in the solution must be treated as an adjustable parameter. For concentrated solutions ($5\%<n_0<50\%$) the optimal value $z\simeq 250$ is independent of density, while for dilute solutions ($n_0<5\%$) it decreases with n_0. Specifically, $z=5$ for $n_0=0.28\%$ and $z=3$ for $n_0=0.11\%$. This suggests that a second phase can precipitate in the form of low-dimensional fractal structures during the exsolution of dilute solutions. © *1998 American Institute of Physics.* [S1063-7834(98)03501-1]

It is well known[1] that solid solutions of helium isotopes with any concentration of the components segregate if they are cooled below the segregation temperature T_s, whose value depends on both the composition of the mixture and the external pressure. Exsolution is a first-order transition leading to the formation of a two-phase heterostructure in the crystal. In the case of the exsolution of dilute solutions each phase consists of virtually pure ^{3}He or ^{4}He.[1] For the case of exsolution in concentrated solutions, phases have the same property provided the temperature of the system is sufficiently low. The presence of structural transformations in a solid solution strongly affects its thermodynamic properties. Specifically, the specific heat of a crystal in the two-phase region contains a contribution (large compared with the specific heat of a homogeneous lattice) due to the additional degrees of freedom of the heterophase system. In a homogeneous solution, however, the impurity contribution to the specific heat is very small, so that, in the case of a transition into the single-phase region, the total specific heat drops abruptly to values which are virtually equal to the specific heat of the lattice. Behavior of this kind was first observed experimentally in Refs. 2 and 3, where the temperature dependences of the specific heat of solid solutions of ^{4}He in a ^{3}He matrix, with ^{4}He concentrations n_0 in the interval $1.1\times 10^{-3}<n_0<0.5$, were measured, and confirmed by later investigations[4–6] performed under different experimental conditions. Nonetheless, the experimental data[2,3] are more helpful in the development of a theory of the specific heat of exsolving solid mixtures of helium isotopes, since such data consist of results obtained under identical experimental conditions for solutions having a wide range of ^{4}He concentrations.

In Ref. 3 it was shown that the behavior of the systems of interest to us in the two-phase region, at temperatures $T\leqslant T_s$, can be described satisfactorily in the self-consistent-field approximation (SCF). The interpretation of their thermal properties for the case of a transition to a homogeneous solution (at temperature $T>T_s$) is a more complicated problem, since in this region the impurity specific heat is small and determined exclusively by fluctuation effects. In Ref. 7 the dependences of the specific heat of a solution on the temperature and ^{4}He concentration at $T>T_s$ were obtained under the assumption that the impurity density fluctuations are Gaussian. It was assumed that the rigidity of the Gaussian mode is proportional to $T-T_s$, while in reality, as follows from microscopic analysis,[8] it should be proportional to $T-T_c$ (T_c is the critical temperature of the mixture). Attention to this important circumstance was also drawn in Ref. 9, but the corresponding theoretical analysis is not available in the literature.

Thus, it is obvious that the problem of developing adequate models for describing the specific heat of exsolving ^{4}He–^{3}He solid solutions above the separation temperature remains open. Our objective in the present paper is to construct a theory of the specific heat of such systems with arbitrary concentration of the components in the entire temperature range, including near T_s.

1. FORMULATION OF THE PROBLEM

We shall assume that the Hamiltonian of the system under study can be represented by a lattice-gas model[10]

$$H=\varepsilon_0\sum_{\mathbf{f}} n_{\mathbf{f}}-\frac{1}{2}\sum_{\mathbf{ff'}} V_{\mathbf{ff'}}n_{\mathbf{f}}n_{\mathbf{f'}}. \tag{1}$$

Here $n_{\mathbf{f}}$ are the occupation numbers of ^{4}He impuritons occupying a site $\mathbf{f}$, ε_0 is the impuriton energy, and $V_{\mathbf{ff'}}=V(|\mathbf{f}-\mathbf{f'}|)$ is the interaction energy of impuritons located at the sites $\mathbf{f}$ and $\mathbf{f'}$. Since the segregation curve of the solid solutions ^{4}He–^{3}He in the concentration–temperature coordinates n-T is virtually symmetric with respect to the point $n=0.5$,[11] we shall employ a Hamiltonian that is explicitly invariant with respect to the substitution $n_{\mathbf{f}}\to 1-n_{\mathbf{f}}$

$$H=\frac{1}{2}\sum_{\mathbf{ff'}} V_{\mathbf{ff'}}n_{\mathbf{f}}(1-n_{\mathbf{f'}}),\quad \frac{1}{2}\sum_{\mathbf{f'}} V_{\mathbf{ff'}}=\varepsilon_0. \tag{2}$$

For further calculations, it is convenient to introduce the variable $\sigma_{\mathbf{f}}=1-2n_{\mathbf{f}}$, after which, to within an nonessential constant, the equations (2) transform to

$$H=-\frac{1}{2}\sum_{\mathbf{ff}'} J_{\mathbf{ff}'}\sigma_{\mathbf{f}}\sigma_{\mathbf{f}'}, \quad J_{\mathbf{ff}'}=\frac{1}{4}V_{\mathbf{ff}'}. \tag{3}$$

The self-consistent field (SCF) approximation provides a very simple method for describing qualitatively correctly the behavior of the impurity specific heat. It is formally exact in the limit of an infinite impuriton interaction length under the condition $\Sigma_{\mathbf{f}}\, J_{\mathbf{ff}'}=\text{const}$. In specific calculations, a model is often used in which the interaction of an atom, occupying a site **f**, with all other impurities is assumed to be constant (equal to J) right up to a definite coordination sphere containing z neighbors. The interaction is assumed to vanish outside this sphere.[8] Thus, the number of neighbors z with which an impurity atom interacts effectively is a characteristic of the interaction length. The SCF approximation corresponds to the limit $z\to\infty$ with $Jz\to\text{const}$. We also note that this approximation gives the correct asymptotic behavior of the thermodynamic functions in the low-temperature limit, irrespective of the value of the coordination number.

In the SCF approximation the expression for the specific heat (here and below all extensive thermodynamic functions are calculated per lattice site) have the form

$$C^{\text{mf}}=Jz\sigma\frac{d\sigma}{dT}, \tag{4}$$

where $\sigma=1-2n$ is an order parameter related with the ^{4}He density n in the separating phases. The order parameter as a function of temperature must be found from the equation[10]

$$\sigma=\tanh\frac{Jz\sigma}{T} \tag{5}$$

until the order parameter reaches, as the temperature increases, the limiting value $\sigma_0=1-2n_0$ corresponding to a homogeneous solution with average density n_0. The temperature at which σ becomes equal to σ_0 is the separation temperature T_s

$$T_s^{-1}=\frac{1}{2Jz\sigma_0}\ln\frac{1+\sigma_0}{1-\sigma_0}.$$

In the case of transition to the single-phase region at $T>T_s$, the order parameter is temperature-independent and remains equal to σ_0. Then, in the SCF approximation the quantity $d\sigma/dT$ appearing in Eq. (4) satisfies

$$\frac{d\sigma}{dT}=\begin{cases}-(\sigma/T)[\lambda/(1-\lambda)], & T<T_s,\\ 0, & T>T_s,\end{cases} \tag{6}$$

where

$$\lambda=\frac{Jz}{T}(1-\sigma^2). \tag{7}$$

The SCF approximation completely ignores the existence of fluctuations in the system, so that for $T>T_s$ the impurity contribution to the specific heat identically equals zero. Thus, despite the fact that the variation of the specific heat in the two-phase region can be explained satisfactorily in the SCF model,[1,2] it is inapplicable in the region of a homogeneous solution ($T>T_s$). Allowance for correlations in the system under study could be made by using, first, different variants of cluster approximations (for example, the quasichemical approximation[10] or the Kikuchi method[11]) and, second, different variants of the random-phase approximation.[8] Further, exact methods based on virial expansions are applicable at low concentrations.[10] Finally, in the specific case when the impurity concentration equals 50% extrapolation of the high- and low-temperature expansions of the specific heat to temperatures near the critical temperature can be used.[12,13]

2. DETERMINATION OF THE SPECIFIC HEAT BY EXTRAPOLATION OF SERIES

We begin our discussion of the applicability of different approximations for describing the specific heat $C(T)$ with an analysis of the last possibility listed in the preceding section. At concentration $n_0=0.5$ the separation temperature $T_s=T_c$. Low-temperature (in powers of $u=\exp(-4J/T)$) and high-temperature (in powers of $\nu=\tanh(J/T)$) expansions of the specific heat are presented in Ref. 14 for a system described by the Hamiltonian (3) in the nearest-neighbor interaction approximation for three types of cubic lattices (sc, fcc, and bcc). As is well known,[1] a solid solution of helium isotopes with equal concentrations of the components has a bcc lattice. The low-temperature series[14] for this case is irregularly sign-alternating and its coefficients differ sharply in absolute magnitude. The direct application of this series for the interpretation of the experimentally observed specific heat of the mixture ^{3}He–^{4}He[2] is ineffective, since its region of applicability is limited to extremely low temperatures. Moreover, the specific heat calculated using this series becomes negative, even at $T\simeq 0.3T_c$. This behavior is due to the fact that the convergence radius of this series is determined by nonphysical singularities in the complex u-plane which are located closer to the origin of coordinates than the physical singularity.[15,16]

Following Ref. 15, this difficulty can be circumvented by re-expanding the series, as proposed in Ref. 14, in terms of the variable y related with u by the relation

$$u=\left(\frac{y}{1-y}\right)^2.$$

The result is a new representation for the low-temperature ($T<T_c$) specific heat $C^{LT}(T)$ in the form of a sign-constant expansion

$$G^{LT}(T)=16\left(\frac{J}{T}\right)^2 y^8\sum_{n=0}^{26} b_n y^n. \tag{8}$$

The coefficients in this series are given in the Appendix. For this series the singularity closest to the origin lies on the positive real semiaxis and corresponds to the true physical singularity.

The expansion of the specific heat $C^{HT}(T)$ for a bcc lattice at high temperatures ($T>T_c$) is sign-constant and depends only on the variable $w=\nu^2$ (Ref. 14)

$$C^{HT}=\left(\frac{J}{T}\right)^2\sum_{n=0}^{4} d_n w^n, \tag{9}$$

where the coefficients d_n are: $d_0=4$, $d_1=140$, $d_2=4056$, $d_3=129360$, and $d_4=4381848$. As shown in Ref. 13, the high-temperature expansions converge in the entire temperature range $T>T_c$ and the ratio d_n/d_{n-1} of coefficients rapidly approaches the asymptotic value $w_c^{-1}[1+(\alpha-1)/n]$ ($\alpha\simeq 1/8$ is the critical exponent for the specific heat, $w_c\simeq\tanh^2(J/T_c)$).

To describe the specific heat in the entire temperature range, the low- and high-temperature branches of the specific heat must be extrapolated to temperatures near the critical temperature with allowance for the critical behavior of the function $C(T)$ as $T\to T_c$.

It is known[17] that near T_c the specific heat diverges as $A_{\pm}|1-T/T_c|^{-1/8}$ (where the coefficients $A_{\pm}$ refer to temperatures above and below T_c, respectively). These coefficients are related with one another by the approximate relation[18]

$$\frac{A_+}{A_-}=4\left(\frac{\beta}{\gamma}\right)^2\left[\frac{\gamma(1-2\beta)}{2\beta(\gamma-1)}\right]^{\gamma+2\beta}, \tag{10}$$

where $\beta=5/16$ and $\gamma=5/4$ are critical exponents.[13] We now supplement the high-temperature series (9) by a term of the form

$$\delta C^{HT}=B_+\left[\left|1-\frac{w}{w_c}\right|^{-1/8}-\sum_{n=0}^{3} a_n\left(\frac{w}{w_c}\right)^n\right], \tag{11}$$

where a_n are the coefficients in the Taylor series expansion of the first term in square brackets in Eq. (11)

$$a_n=\frac{\Gamma(n+1/8)}{\Gamma(n+1)\Gamma(1/8)}, \tag{12}$$

($\Gamma(x)$ is the Euler gamma function). Thus, the expansion (11) in powers of w/w_c starts with a term proportional to $(w/w_c)^4$. Next, we choose the coefficient B_+ so that the term of the expansion of δC^{HT} that is proportional to $(w/w_c)^4$ is identical to the last term of the starting exact high-temperature expansion (9). Then

$$B_+=\frac{73308}{425}(16w_c)^4.$$

As a result, for $T>T_c$ the specific heat is described by the sum of the terms C^{HT} and δC^{HT}, in one of which a term proportional to the fourth power of w has been dropped so as to avoid taking this term into account twice.

Similarly, a term δC^{LT} of the form

$$\delta C^{LT}=B_-\left[\left|1-\frac{y}{y_{c'}}\right|^{-1/8}-\sum_{n=0}^{34} a_n\left(\frac{y}{y_c}\right)^n\right], \tag{13}$$

where the coefficients a_n are once again determined by the relation (12) and $2y_c=1-\tanh(J/T_c)$, must be added to the low-temperature expansion. Despite the fact that the low-temperature expansion re-expanded in terms of y is sign-constant and its coefficients exhibit a more regular behavior than those of the starting series, the coefficients nonetheless converge nonuniformly to the asymptote

$$y_c^{-1}=\lim_{n\to\infty}\frac{b_n}{b_{n-1}}$$

in the sense that the difference $y_c^{-1}-b_n/b_{n-1}$ changes sign irregularly with increasing n. In this connection the coefficient B_- in Eq. (13) cannot be determined by analogy to B_+. Here it is necessary to use the relation between B_+ and B_- that can be obtained from Eq. (10), if the first terms in Eqs. (11) and (13), respectively, are re-expanded in the powers of $1-(T/T_c)$. The result is

$$\frac{B_+}{B_-}=\frac{A_+}{A_-}\left[2\left(\frac{1}{\sqrt{w_c}}-1\right)\right]^{-1/8}.$$

To compare the present theory with the experimental data, terms taking account of, respectively, the lattice contribution to the specific heat $C_{\rm ph}=(12\pi^4/5)(T/\Theta_D)^3$ (where Θ_D is the Debye temperature) and the contribution $C_{\rm ex}$ due to the exchange interaction of ^{3}He atoms must be added to the expressions obtained above. The latter contribution can be represented in the form[11]

$$C_{\rm ex}=3(1-n)^2\left(\frac{I}{T}\right)^2\left[1-\frac{I}{T}+\frac{7}{4}\left(\frac{I}{T}\right)^2\right],$$

where I is the exchange integral. We shall always take these corrections into account when we compare with the experimental data all the expressions for the specific heat that are presented in the present paper. It should be noted that because these corrections are small we neglected the pressure dependence of I in our calculations, taking for it the maximum value corresponding to a molar volume of 24.2 cm^3/mole. According to different published data,[11] the experimentally determined value of I under these conditions is 0.88–1.22 mK. We shall employ the average numerical value $I\simeq 1$ mK. Moreover, we neglect the temperature dependence of Θ_D, since the associated corrections are small in the temperature interval where the effects of interest to us occur.

The results of a comparing of the extrapolation formulas derived above for the specific heat with the experimental data of Ref. 2 as well as SCF calculations for solutions with $n_0=0.5$ are presented in Fig. 1. The quantity J was determined from the real experimental value $T_c=0.38$K,[2,9] so that $J=-0.25T_c\ \ln(0.5327)\simeq 0.15$ K,[14] for the expressions (9)–(13) while for the SCF approximation $J=T_c/z$. At high temperatures, the theory agrees only qualitatively with experiment. Ways to improve the theory will be discussed below. As one can see from Fig. 1, the low-temperature branch of the specific heat in the SCF approximation (4) agrees somewhat better with experiment than does the extrapolation of the power series. In our opinion, the discrepancy between theory and experiment is due to the following. Although, in principle, power series formally give exact solutions in the corresponding temperature intervals, the interaction of only nearest neighbors is taken into account in the derivation of the series expansions.[14] This suggests unequivocally that the nearest-neighbor approximation is insufficient for describing

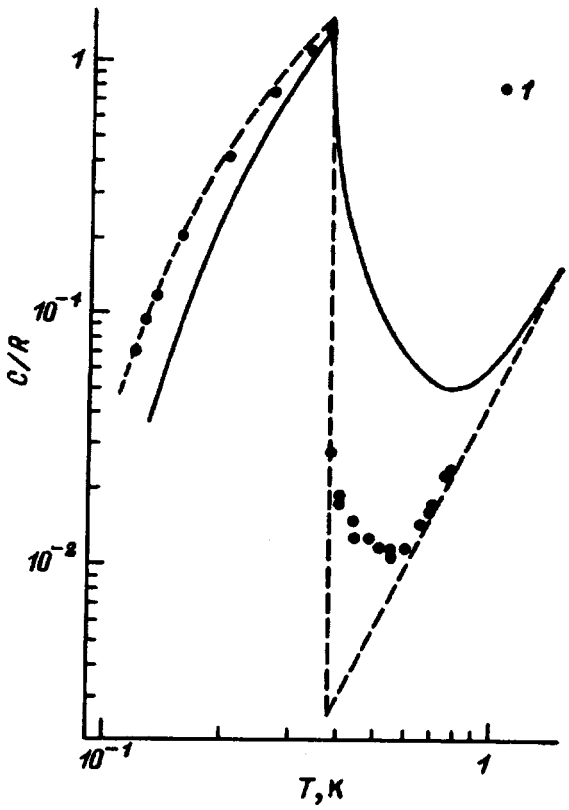

FIG. 1. Temperature dependence of the specific heat of a 50% ^{3}He–^{4}He mixture. Solid curve—theory, obtained by extrapolating power series. Dashed line—SCF approximation. *1*—Experimental data from Ref. 2. Here and in the following figures the specific heat is normalized to the universal gas constant R.

our system, and we are apparently dealing with a situation where the contribution of the distant coordination spheres must be taken into account.

3. CORRELATION CORRECTIONS TO THE SCF APPROXIMATION

A natural method for obtaining the correlation corrections to the SCF for lattices with large coordination numbers z is to expand the thermodynamic functions in powers of $1/z$. The first term of this expansion corresponds to the so-called random-phase approximation (RPA).[8] The correction to the average energy of the system in this approximation equals

$$\Delta E^{\mathrm{RPA}}=-\frac{1}{2NT}\sum_{q}\frac{J^2(\mathbf{q})(1-\sigma^2)^2}{1-J(\mathbf{q})(1-\sigma^2)/T}. \tag{14}$$

Here $J(\mathbf{q})$ is the Fourier transform of the function $J_{\mathbf{ff}'}$, N is the total number of sites in the system, and the order parameter σ satisfies Eq. (5). We call attention to the fact that the impurity interaction length is of the order of $z^{1/3}$. For this reason, the terms with $0<q<q_0$, where $q_0\sim z^{-1/3}$, make the main contribution to the sum in Eq. (14). To estimate this sum we approximate the potential $J(\mathbf{q})$ by the expression[8]

$$J(\mathbf{q})=\begin{cases} Jz(1-q^2/q_0^2), & q<q_0,\\ 0, & q>q_0. \end{cases} \tag{15}$$

Switching in Eq. (14) from summation to integration, we find

$$\Delta E^{\mathrm{RPA}}=\frac{Tq_0^3v_0}{12\pi^2}\left\{1-\frac{3}{\lambda}\left(1-\sqrt{\frac{1-\lambda}{\lambda}}\times\arctan^{-1}\sqrt{\frac{\lambda}{1-\lambda}}\right)+\frac{2}{5}\lambda\right\}, \tag{16}$$

where λ is determined by the relation (7) and ν_0 is the cell volume.

In a model where the interaction is constant (and equal to J) right up to the coordination sphere containing z neighbors, the first correction with respect to the parameter J/T to the specific heat equals[19]

$$\Delta E=-\frac{J^2z}{2T}(1-\sigma^2)^2=-\frac{\lambda^2T}{2z}. \tag{17}$$

On the other hand, the first term in the expansion in Eq. (16) in powers of the reciprocal of the temperature must be the same as in Eq. (17). This makes it possible to find a relation between the cutoff parameter q_0 and the effective coordination number. The result is

$$q_0^3v_0=\frac{105\pi^2}{4z}. \tag{18}$$

The corresponding correction to the specific heat has the form

$$\Delta C^{\mathrm{RPA}}=\frac{\Delta E^{\mathrm{RPA}}}{T}+\frac{1}{1-\lambda}\left[\left(\frac{3}{2}-\lambda\right)\frac{\Delta E^{\mathrm{RPA}}}{T}+\frac{7}{4z}\lambda^2\right]\times\left(1+2\frac{Jz\sigma}{\lambda}\frac{d\sigma}{dT}\right). \tag{19}$$

Here $d\sigma/dT$ is once again given by Eq. (6).

Comparing the obtained result with the experimental data[2] for ^{4}He concentrations $n_0=0.5$, 0.21, and 0.5 showed that to achieve good agreement between theory and experiment the coordination number z in the above-obtained formulas must be treated as an adjustable parameter, whose value turns out to be unexpectedly large. Thus, for all concentrations listed above $z=250$. This means that the nearest-neighbor approximation does not give an adequate description of the observed specific heat in the concentration range studied and the impurity interaction extends at least over several (four to five) coordination spheres. The fact that the optimal (from the standpoint of agreement with experiment) values found here for the parameter z are comparatively large must signify, on the one hand, that the above-calculated fluctuation corrections are small (proportional to $1/z$) and, on the other, that the conditions of applicability of the SCF approximation are satisfied (formally corresponding to the limit $z\to\infty$). In reality, however, above the exsolution temperature, $T>T_s$, in the homogeneous solution region the excess specific heat in the SCF approximation equals identically zero and the lattice specific heat of the matrix near T_s is still very small. For this reason, the fluctuations make the main contribution to the specific heat of the solid solution at $T\sim T_s$.

We note, however, that in the case of low concentrations the correction (16) presented above is negligibly small even compared with the lattice contribution. This is evidently so

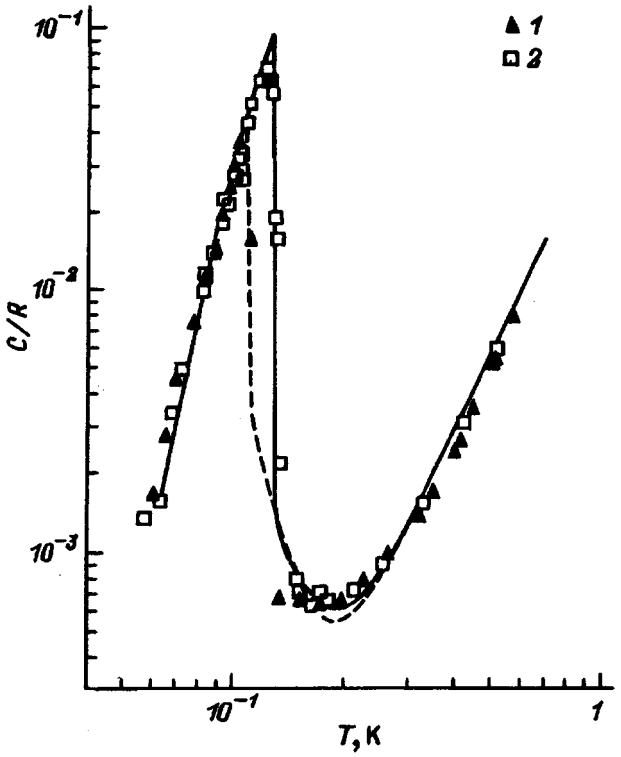

FIG. 2. Temperature dependence of the specific heat of dilute ^{3}He–^{4}He solid solutions. Experimental data:[2] *1*—0.11% ^{4}He, *2*—0.28% ^{4}He. Curves are results of the theoretical calculations in this work.

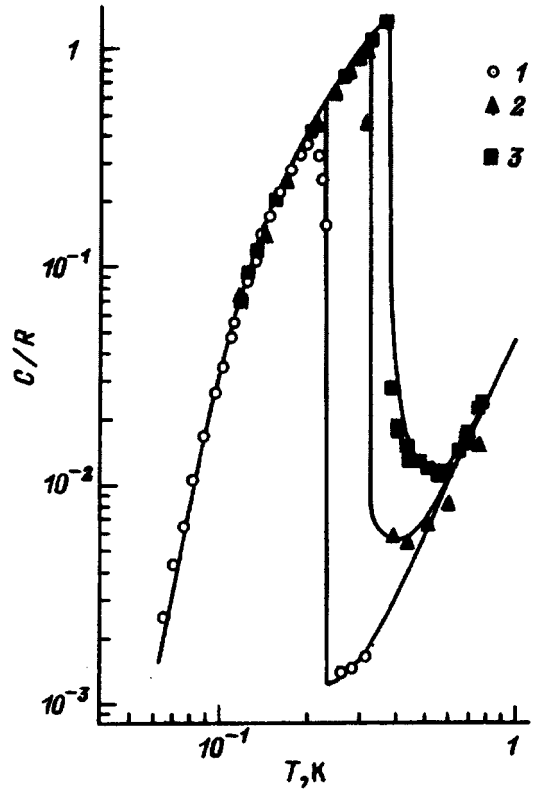

FIG. 3. Temperature dependence of the specific heat of concentrated ^{3}He–^{4}He solid solutions. Experimental data:[2] *1*—5% ^{4}He, *2*—21% ^{4}He, *3*—50% ^{4}He. Curves are results of the theoretical calculations in this work.

because the RPA describes the interaction due to substantially collective effects, provided that the interaction within each pair of sites is determined in the first nonvanishing order of perturbation theory.

For low concentrations, an approach based on expansion of the thermodynamic functions using Mayer groups[10] is more effective. The corresponding correction to the energy in the approximation of the second virial coefficient ΔE_2 depends only on the coordination number and is independent of lattice type. In our case

$$\Delta E_2 = -\frac{Jz}{8}(1-\sigma^2)^2[\exp(4J/T)-1]. \tag{20}$$

Let us combine both approximations (16) and (20) so as to obtain a unified description for both low and high concentrations. A diagrammatic analysis of the Ising model[8] shows that the correction (17) is taken into account in both the relation (16) and (20). For this reason, it must be subtracted from the sums (16) and (20). The resulting total correction to the specific heat is

$$\Delta C = \Delta C^{\mathrm{RPA}} - \frac{4J}{T}\left[\frac{\Delta E_2}{T} + \frac{Tz\sigma}{\lambda}\frac{d\sigma}{dT}\left(\frac{\Delta E_2}{T} + \frac{\lambda^2}{2z}\right)\right]. \tag{21}$$

Figures 2 and 3 display theoretical curves and experimental data for all ^{4}He concentrations presented in Ref. 2. The proposed theory contains two adjustable parameters: T_c and z. The first one is taken directly from experiment (for our system $T_c = 0.38$ K), and the coordination number z must be set equal to 250 for all high concentrations ($n_0 = 50$, 21, and 5%) and $z = 5$ ($n_0 = 0.28\%$) and $z = 3$ ($n_0 = 0.11\%$), respectively, for low concentrations. The quantity J was assumed to be equal to $J = T_c/z$ for all concentrations on the basis of the fact that at $T < T_c$ the specific heat lies on the same curve for all solutions.

4. DISCUSSION

Our analysis shows unequivocally that the existing experimental results can be interpreted only under the assumption that the impurity interaction is long-range. We took account of this long-range interaction indirectly by introducing an effective coordination number. Thus, in all approximations discussed above the coordination number z must be treated as an adjustable parameter. The entire concentration interval $n_0 \leqslant 50\%$ separates naturally into two parts. At high concentrations (5% and higher) z is virtually independent of n_0 and good agreement with experiment is obtained with $z \simeq 250$. For each of the low concentrations ($n_0 = 0.28$ and 0.11%), however, the values of z are different: $z = 5$ and 3, respectively. We note that this choice is unique, i.e. agreement with experiment cannot be obtained for any values of z different from those indicated above. Indeed, the leading term in the low-temperature asymptotic expansion of the specific heat depends only on the combination Jz. At the same time, in the single-phase region, where the impurity density is fixed, $C(T)$ is determined by two independent parameters: J and z. This last circumstance makes it possible to determine uniquely the value of the coordination number.

We underscore that the virial approximation is certainly applicable at low concentrations. Moreover, the first virial correction does not depend on the specific type of lattice, but in the lattice-gas model (Ising model) unique agreement with experiment obtains only for $z=3$ or $z=5$, which does not correspond to any regular spatial structure. This suggests that, at low concentrations, exsolution in the solution occurs with formation of a new phase in the form of fractal structures of the Cayley tree type. This is not surprising, since the impurity interaction at large distances r decreases as $1/r^3$ and is strongly anisotropic (it is attractive for some directions and repulsive for others). The magnitude and sign of the interaction depends strongly on the crystallographic direction in which the radius vector connecting the interacting impurities lies.[20–22] For this reason, at low concentrations, when the average impurity separation is much greater than the interatomic separation, a new phase grows in the form of a tree, the degree of whose vertex is determined by both the concentration and the number of crystallographic directions along which there is attraction.

At high concentrations, when the impurity separation is comparable to interatomic distances, the elastic fields of the impurities overlap and the effective interaction between the impurities becomes substantially isotropic, but remains long-range. In this case, the nuclei of the new phase grow in the form of compact formations. Thus, the large difference in the values of the effective coordination number with high and low ^{4}He concentrations is in our opinion due to the specific nature of the impurity interaction in bcc ^{3}He lattices.

We note that the character of the impurity interaction at large distances is very similar to the dipole-dipole interaction (electrostatic and magnetic) in the sense that it depends on distance as r^{-3} and the angular dependence is such that it vanishes after averaging over directions. It is known[23] that very complex structures with a nontrivial distribution of orientations of the dipole moments at the lattice sites can appear in systems with an interaction of this type. This circumstance can serve as an additional argument in support of our conjecture that fractal structures consisting of ^{4}He impurities form in dilute ^{4}He–^{3}He solutions.

Of course, it could be assumed that, for $z=3$, regularly packed planar structures consisting of ^{4}He atoms appear when the solution segregates. This assumption would be obvious only if the ^{3}He matrix possessed the specific anisotropy that is characteristic of, for example, layered crystals. Since the bcc lattice of ^{3}He does not possess such properties, it is very unlikely that planar nuclei of a new phase exist in it. Impurity precipitation at grain boundaries can serve as another possibility for the formation of planar precipitates. Verifying this conjecture, however, falls outside the scope of our model of a solid solution (it assumes, specifically, that an additional adjustable parameter is introduced into the problem—the impurity–boundary interaction energy).

We also call attention to the fact that, in the opposite limiting case of very dilute solutions of ^{3}He in a ^{4}He matrix,[6] the behavior of the specific heat can be explained under the by assuming that there exist quasi-one-dimensional nuclei of a new phase that form, for example, at dislocations in the crystal.[24] It seems to us that this model cannot be directly applied to describe the thermodynamics of ^{3}He crystals with a small quantity of ^{4}He impurities. The reason is that the ^{3}He lattice is substantially more ''quantum,'' so that dislocation mobility is high in it and, therefore, there is a high probability that dislocations will leave the crystal during growth of the sample.

In conclusion, we note that the further investigation of the problem should involve a systematic microscopic description of the impurity interactions, taking into account the discrete nature of the crystal lattice. Unfortunately, we do not know of any works where measurements of the specific heat of solutions were performed in the intermediate concentration range $0.3<n_0<5\%$. Such results would make it possible to draw more definite conclusions about the change in the mechanism of nucleation as a function of the composition of the solid solution.

We wish to thank Professor D. O. Edwards (Ohio State University, USA) for discussions which led to the publication of this paper and also V. N. Grigor'ev and É. Ya. Rudavskiĭ for valuable remarks and for their interest in this work.

5. APPENDIX

The coeffiicients in the expansion in Eq. (8) are as follows:

$$b_0=4;\quad b_1=32;\quad b_2=144;\quad b_3=480;\quad b_4=1320,$$

$$b_5=3168;\quad b_6=6913;\quad b_7=14414;\quad b_8=30813,$$

$$b_9=72048;\quad b_{10}=184620;\quad b_{11}=488376,$$

$$b_{12}=1252648;\quad b_{13}=3006272;\quad b_{14}=6674186,$$

$$b_{15}=13811996;\quad b_{16}=27447686;\quad b_{17}=55431280,$$

$$b_{18}=121396999;\quad b_{19}=293835094;$$

$$b_{20}=749271795,$$

$$b_{21}=1884259692;\quad b_{22}=4474431975,$$

$$b_{23}=9864530634;\quad b_{24}=20287650355,$$

$$b_{25}=40058936096;\quad b_{26}=80443615062.$$

[1] B. N. Esel'son, V. N. Grigor'ev, V. G. Ivanov, É. Ya. Rudavskiĭ, D. G. Sanikidze, and I. A. Serbin, *Solutions of Quantum Liquids* ^{3}He–^{4}He [in Russian], 1973.
[2] D. O. Edwards, A. S. McWilliams, and J. G. Daunt, Phys. Lett. **1**, 218 (1961).
[3] D. O. Edwards, A. S. McWilliams, and J. G. Daunt, Phys. Rev. Lett. **9**, 195 (1962).
[4] P. M. Tedrow and D. M. Lee, Phys. Rev. **181**, 399 (1969).
[5] G. O. Zimmermann, Proc. LT-9. Columbus **1**, 244 (1964).
[6] R. Schrenk, O. Friz, Y. Fujii, E. Siskakis, and F. Pobell, J. Low Temp. Phys. **84**, 155 (1991).
[7] P. Kumar and M. Bernier, J. Low Temp. Phys. **79**, 1 (1990).
[8] R. Brout, *Phase Transitions* [Benjamin, New York, 1965; Moscow, 1967].
[9] D. O. Edwards and M. S. Pettersen, J. Low Temp. Phys. **87**, 473 (1992).
[10] T. Hill, *Statistical Mechanics* [McGraw-Hill, New York, 1956; Moscow, 1960].
[11] S. Triki, V. Krik, and E. Adams in *Quantum Crystals* [in Russian], Moscow, 1975.
[12] V. G. Vaks, V. I. Zinenko, and V. E. Shneĭder, Usp. Fiz. Nauk **141**, 629 (1983) [Sov. Phys. Usp. **26**, 1059 (1983)].
[13] H. E. Stanley, *Introduction to Phase Transitions and Critical Phenomena*

[Oxford University Press, New York, 1987; Moscow, 1973].
[14] G. A. Baker, Phys. Rev. **124**, 768 (1961).
[15] A. J. Guttman, C. J. Thompson, and B. W. Ninham, J. Phys. C **3**, 1641 (1970).
[16] C. Domd and A. J. Guttman, J. Phys. C **3**, 1652 (1970).
[17] C. Domb, Adv. Phys. **19**, 339 (1970).
[18] A. Z. Patashinskiĭ and V. L. Pokrovskiĭ, *Fluctuation Theory of Phase Transitions* [Pergamon Press, New York, 1979 (1st edition); Moscow, 1982].
[19] R. Kubo, *Statistical Mechanics* [North-Holland, Amsterdam, 1965; Moscow, 1967].
[20] J. R. Hardy and R. Bullough, Philos. Mag. **15**, 237 (1967).
[21] R. Bullough and J. R. Hardy, Philos. Mag. **17**, 833 (1968).
[22] V. A. Slyusarev, M. A. Strzhemechnyĭ, and I. A. Burakhovich, Fiz. Nizk. Temp. **4**, 698 (1978) [Sov. J. Low Temp. Phys. **4**, 333 (1978)].
[23] P. I. Belobrov, R. S. Gekht, and V. A. Ignatchenko, Zh. Éksp. Teor. Fiz. **84**, 1097 (1983) [Sov. Phys. JETP **57**, 636 (1983)].
[24] T. N. Antsygina, V. A. Slyusarev, and K. A. Chishko, Fiz. Nizk. Temp. **21**, 583 (1995) [Low Temp. Phys. **21**, 453 (1995)].

Translated by M. E. Alferieff

Propagation of quasi-two dimensional exciton polaritons in a quantum well waveguide

V. A. Kosobukin

A. F. Ioffe Physicotechnical Institute, Russian Academy of Sciences, 194021 St. Petersburg, Russia
(Submitted July 17, 1997)
Fiz. Tverd. Tela (St. Petersburg) **40**, 362–365 (February 1998)

The propagation of exciton polaritons in an optical waveguide with a quantum well is studied. Spatial dispersion of the excitons causes the wave vector of the exciton polaritons to split between waveguide and exciton modes at resonance. The magnitude of this splitting is determined by the radiative decay parameter of excitons with corresponding polarization in the quantum well. The group velocity of the waveguide exciton polaritons in the resonance region can be three or four orders of magnitude lower than the speed of light in vacuum.
 [S1063-7834(98)04402-5]

Energy transport of optical excitation by exciton polaritons plays an important role in understanding the mechanisms for the interaction of light with excitons.[1] In particular, the multimode character of energy transport by polaritons caused by the spatial dispersion of excitons in bulk crystals has been established.[2–4] There is special interest in analogous effects which occur in solid-state waveguide structures, where coupled exciton and electromagnetic waves are quasi-two dimensional.

A time-of-flight experiment for observing waveguide exciton polaritons has been performed[5] in which a delay time of ~ 5 ps was found for pulses propagating along a waveguide with a quantum well of length 250 μm. Models of semiconductor structures with an isolated quantum well which lies inside the waveguide[6] or itself serves as a waveguide[7] have been proposed for the theoretical description of waveguide exciton polaritons. In this paper we examine the first type of model. This model has been used[6] to simulate numerically the propagation of a TE-mode in an experimental waveguide structure.[5] It was found[6] that the group velocity of the waveguide exciton polariton was no more than an order of magnitude lower than the speed of light in vacuum. The existence of certain contradictions between Refs. 5 and 6 and of major discrepancies between the results of Ref. 6 and their analogs for bulk exciton polaritons[2–4] suggest that the dispersion and, especially, the propagation characteristics of waveguide exciton polaritons are issues that have not been fully resolved.

The purpose of this paper is to investigate a simple model which provides a reliable estimate of the propagation characteristics of waveguide exciton polaritons. The dispersion relation for waveguide exciton polaritons, including the spatial dispersion of quasi-two dimensional excitons, and the corresponding group velocities are discussed for TM-modes, which have not been analyzed theoretically before.

1. MODEL AND DISPERSION RELATION

As a model for a symmetric optical waveguide, we consider a layer of semiconductor ($|z|<L/2$) with a quantum well inside it ($|z|<a/2$). The waveguide thickness $L\sim c/\omega$ and the quantum well width $a\sim a_B$ (ω and c are the frequency and speed of the light, a_B is the Bohr radius of the exciton) obey the inequality $a\ll L$ and correspond to a low-dimensional spatial limit along the z axis for both the exciton and the electromagnetic modes. The background dielectric constant is ε_b for $|z|<L/2$ and ε_b' for $|z|>L/2$ ($\varepsilon_b'<\varepsilon_b$), and an optical waveguide mode can propagate in this structure when there is no quantum well. The interaction of this mode with the polarization field of a quasi-two dimensional exciton of the quantum well can lead to the formation of a waveguide exciton polariton near the exciton resonance frequency.

Outside the quantum well the electric field of a monochromatic TM wave is given by

$$\mathbf{E}(\mathbf{r},\omega)=\exp(i\varkappa x)[\mathbf{e}_x+\mathbf{e}_z(i\varkappa/k_z^2)d/dz]E_x(z,\varkappa,\omega). \quad (1)$$

Here $\varkappa$ is the magnitude of the wave vector in the interface plane, k_z takes values $q=\sqrt{\varepsilon_b k_0^2-\varkappa^2}$ for $|z|<L/2$ and $q'=\sqrt{\varepsilon_b' k_0^2-\varkappa^2}$ for $|z|>L/2$, $k_0=\omega/c$, and e_α is the unit vector along the α-th cartesian axis. The normal waveguide modes are enumerated by integers m that are related to the z component of the wave vector by $q_m\approx\pi m/L$, and the m-th waveguide mode at frequency ω exists if $L>m\pi c/\omega\sqrt{\varepsilon_b}$. In the absence of a quantum well, we denote the TM mode of type (1) by $\mathbf{E}_0$, where the parity of the given TM mode is determined by the component $H_y^0\sim dE_x^0/dz$ in the expression for the magnetic field, $\mathrm{H}_0=\mathrm{e}_y(-i\varepsilon_b k_0^2/l_z^2)(dE_x^0/dz)$. For the odd ($m=1,3,5,...$) TM-modes we have $E_x^0(z)=C\cos(qz)$ and $H_y^0\sim\sin(qz)$, while for the even ($m=2,4,...$) we have $E_x^0(z)=C\sin(qz)$ and $H_y^0\sim\cos(qz)$.

When the nonlocal contribution of the quasi-two dimensional exciton to the polarization,[8–10] which is assumed anisotropic here, is taken into account, we can write the electric field in a semiconductor layer that includes a quantum well in the form

$$E_\alpha(z)=E_\alpha^0(z)-\frac{2k_0\sqrt{\varepsilon_b}}{I_c^2}\sum_\beta\int dz' D_{\alpha\beta}^0(z,z')\Psi(z')$$
$$\times\frac{2M\Gamma_\beta^0/\hbar}{\varkappa^2\sim(\varkappa_{ex}^0)^2}\int dz''\Psi(z'')E_\beta^0(z''). \quad (2)$$

Here the $D^0_{\alpha\beta}(z-z')$ are Fourier components of the form (1) of the electrodynamic tensor Green function for a homogeneous (without a quantum well) semiconductor, $I_c=\int dz\Psi(z)\cos(qz)$, and

$$\varkappa^{\alpha}_{cx}(\omega)=\sqrt{(2M/\hbar)(\omega-\omega_a+i\Gamma)}. \tag{3}$$

Equations (2) and (3) correspond to the condition $|\omega-\omega_\alpha| \ll \omega_\alpha$, where ω_α is the resonance frequency of the quasi-two dimensional exciton, $\Psi(z)$ is the envelope of its wave function, M is the translational mass, Γ^0_α is the radiative decay constant, and Γ is the dissipative damping constant. Equation (2) shows that, because the functions $\Psi(z)=\Psi(-z)$ are even, in the ground state the exciton interacts with the α-th component of the field of the waveguide mode, for which $E^0_\alpha(z)=E^0_\alpha(-z)$ inside the quantum well. As a consequence, the odd and even TM modes form waveguide exciton polaritons with the x and z components of the polarization, respectively.

In order to calculate the waveguide exciton polariton field for $|z|<L/2$, in Eq. (2) we substitute the components of the Green function,

$$D^0_{xx}=\frac{q^2}{\varepsilon_b k_0^2}\,\frac{\sin q|z-z'|}{2q},$$

$$D^0_{xz}=D^0_{zx}=\frac{i\varkappa q}{\varepsilon_b k_0^2}\,\frac{\cos q(z-z')}{2q}\,\mathrm{sign}(z-z'),$$

$$D^0_{zz}=\frac{\varkappa^2}{\varepsilon_b k_0^2}\,\frac{\sin q|z-z'|}{2q}+\frac{\delta(z-z')}{\varepsilon_b k_0^2}. \tag{4}$$

Using Maxwell boundary conditions, we then match the functions (2) at the interface boundaries $z=\pm L/2$ with a field of the form (1) for $|z|>L/2$ in which $E_x(z)=C'\exp(iq'|z|)$. This yields dispersion relations for the waveguide exciton polariton,

$$F_\alpha(\varkappa,\omega)=\left\{\frac{\hbar}{2M}\,\varkappa^2+\omega_a-\omega-i\Gamma\right\}f_a(\varkappa,\omega)-\Gamma_a=0, \tag{5}$$

which are different for the different Cartesian components α. Here

$$f_x=\frac{i\beta'\,\mathrm{ctg}(qL/2)+\beta}{i\beta'-\beta\,\mathrm{ctg}(qL/2)},\quad f_z=\frac{\beta-i\beta'\,\mathrm{tg}(qL/2)}{\beta\,\mathrm{tg}(qL/2)+i\beta'}, \tag{6}$$

$\beta=\varepsilon_b/q$, and $\beta'=\varepsilon_b'/q'$. In solving Eq. (5) we use an analytic continuation of the radiative decay parameters $\Gamma_x=\Gamma^0_x(qc/\omega_x\sqrt{\varepsilon_b})$ and $\Gamma_z=\Gamma^0_z(\varkappa^2c/q\omega_z\sqrt{\varepsilon_b})$ with constants Γ^0_α that depend on the polarization direction of the quasi-two dimensional exciton states. The parameters Γ_α for the exciton of a quantum well are given explicitly elsewhere.[10] For $\Gamma_\alpha=0$ (i.e., no interaction between the exciton and light), Eqs. (5) determine the dispersion relations $\varkappa^\alpha_{\mathrm{ex}}(\omega)$ and $\varkappa^\alpha_{\mathrm{wg}}(\omega)$ for the uncoupled exciton and waveguide modes, respectively, where $\varkappa^\alpha_{wg}(\omega)$ is the solution of the equation $f_\alpha(\varkappa,\omega)=0$. In the absence of spatial dispersion ($M\to\infty$), Eq. (5) transforms to $f_\alpha(\varkappa,\omega)=\Gamma_\alpha/(\omega_\alpha-\omega-i\Gamma)$.

The type of boundary conditions which determine the form of the functions $f_\alpha(\varkappa,\omega)$ does not have a critical effect on the theoretical characteristics of waveguide exciton polariton propagation. Thus, in the following, we shall examine TM mode waveguide exciton polaritons using the simplified equations

$$f_x(\varkappa,\omega)=\cot(qL/2),\quad f_z(\varkappa,\omega)=-\tan(qL/2), \tag{7}$$

which correspond to the tangential component's, $E_x(z)$, going to zero at the waveguide walls $z=\pm L/2$ and is obtained from Eq. (6) in the limit $|\varepsilon_b'/\varepsilon_b|\to\infty$. We might expect that Eqs. (5) with the substitution (7) would be suitable for a waveguide bounded by a precious metal (e.g., $\varepsilon_b'\approx-30+0.4i$ for silver at a photon energy $\hbar\omega=1.6$ eV[11] in the region of the exciton resonances of GaAs[12]).

For clarity, near $\varkappa=\varkappa^\alpha_{wg}(\omega)$ we approximate the functions (7) of $\varkappa^2$, by $f_\alpha=A_\alpha\{\varkappa^2-[\varkappa^\alpha_{wg}(\omega)]^2\}$ with constants $A_\alpha>0$. Then the solution of the equation obtained from Eq. (5) has the form

$$(\varkappa^a_{1,2})^2=\frac{(\varkappa^a_{cx})^2+(\varkappa^a_{wg})^2}{2} \pm\sqrt{\frac{[(\varkappa^a_{xz})^2-(\varkappa^a_{wg})^2]^2}{4}+(\Delta\varkappa^a)^4}, \tag{8}$$

where the quantity $(\Delta\varkappa^\alpha)^4=(2M/\hbar)(\Gamma_\alpha/A_\alpha)>0$ calculated for $\varkappa=\varkappa^\alpha_{wg}$ has the significance of a photon-exciton interaction constant. Equation (8) implies that near the resonance frequency determined by the condition $\varkappa^\alpha_{ex}(\omega)=\varkappa^\alpha_{wg}(\omega)$, the wave vector splits into components $\varkappa^\alpha_1(\omega)$ and $\varkappa^\alpha_2(\omega)$ corresponding to the upper and lower dispersion branches of the waveguide exciton polariton. This resonance splitting, whose magnitude is determined by the quantity $(\varkappa^\alpha_1)^2-(\varkappa^\alpha_2)^2=2(\Delta\varkappa^\alpha)^2$, is a consequence of including the spatial dispersion of the exciton ($M\neq0$), and its existence means that at the given frequency two waveguide exciton polariton modes should propagate and interfere with one another.

Figures 1a and 2a show the waveguide exciton polariton dispersion branches calculated from Eqs. (5) and (7) with typical parameters for quasi-two dimensional excitons in GaAs/AlGaAs quantum wells. Figure 1 corresponds to the odd $m=1$ waveguide mode interacting with the x component of the polarization of an $e1-hh1$ heavy hole exciton and Fig. 2, to the even $m=2$ mode interacting with the z component of the polarization of an $e1-lh1$ light hole exciton. It is clear from Fig. 1a that the upper waveguide exciton polariton dispersion branches $\varkappa_1(\omega)$ found from Eq. (5) or Eq. (8) approach the curve $\varkappa^\alpha_{ex}(\omega)$ from below or above, respectively, for $(\omega-\omega_x/\Gamma^0_x\gg1$. However, these details of the asymptotic behavior of $\varkappa_1(\omega)$ are only of theoretical interest here, since in GaAs they should be strongly affected by the analogous polariton resonance which is coupled to the $e1-lh1$ light hole exciton and lies several tens of units higher in frequency on the scale of Fig. 1a.[12] Figure 2a illustrates the anticrossing of the dispersion curves, which is uniquely possible for the z component of the exciton polarization, since $\Gamma^0_z=0$ for the $e1-lh1$ exciton.

2. GROUP VELOCITY

The group velocity $v=\partial\omega/\partial x$ of the waveguide mode is

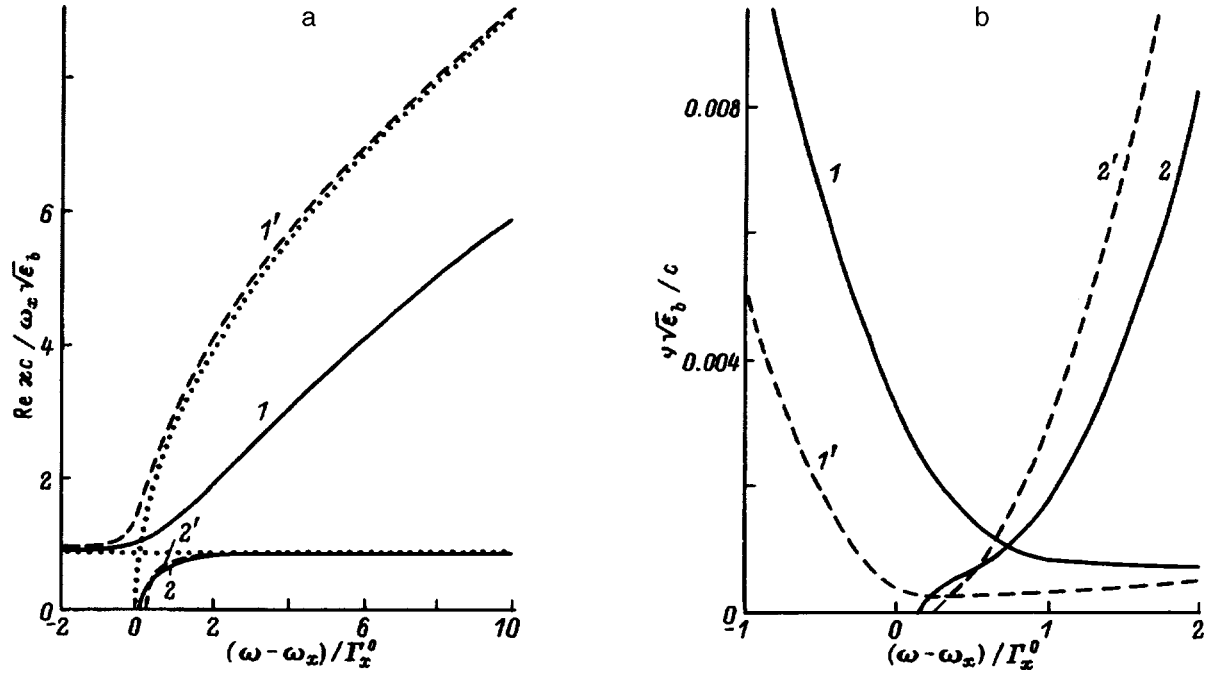

FIG. 1. The dimensionless wave numbers Re $\varkappa c/(\omega_x\sqrt{\varepsilon_b})$ (a) and group velocities $\nu\sqrt{\varepsilon_b}/c$ (b) as functions of the frequency detuning $(\omega-\omega_x)/\Gamma_x^0$ for odd $m=1$ mode *TM* mode exciton polaritons in a waveguide with $\varepsilon_b=12.6$, $|\varepsilon_b'|\gg\varepsilon_b$, and $L\omega_x\sqrt{\varepsilon_b}/c=6$ ($L=1.3$ μm). The smooth (*1*, *2*) and dashed (*1′*,*2′*) curves were obtained from the dispersion relations (5) and (8), respectively, for the upper $\varkappa_1$ (*1*, *1′*) and lower $\varkappa_2$ (*2*, *2′* branches of the waveguide exciton polariton and the dashed curve shows the functions $\varkappa_{\rm ex}^{\alpha}(\omega)$ and $\varkappa_{\rm wg}^{\alpha}(\omega)$ for the noninteracting modes. The parameters $\beta_x=10^{-4}$, $\Gamma_x^0/\omega_x=4\times10^{-4}$, and $\hbar\Gamma_x^0\approx0.6$ meV, corresponding to a quasi-two-dimensional $e1-hh1$ exciton in an $a=50$ Å wide GaAs quantum well, have been used. Dissipative losses are neglected for both the exciton ($\Gamma=0$) and waveguide (Im $\varepsilon_0=0$) modes.

a fundamental characteristic of the transport of optical excitation energy by it in a wave packet. For a waveguide exciton polariton, the group velocity can be calculated as follows:

$$v_{1,2}=-\frac{(\partial F/\partial\varkappa)_{1,2}}{(\partial F/\partial\omega)_{1,2}},\quad \text{or}\quad v_{1,2}=\frac{1}{(\partial\varkappa_{1,2}/\partial\omega)},\tag{9}$$

where the solutions $\varkappa=\varkappa_{1,2}(\omega)$ of Eqs. (5) or (8), respec-

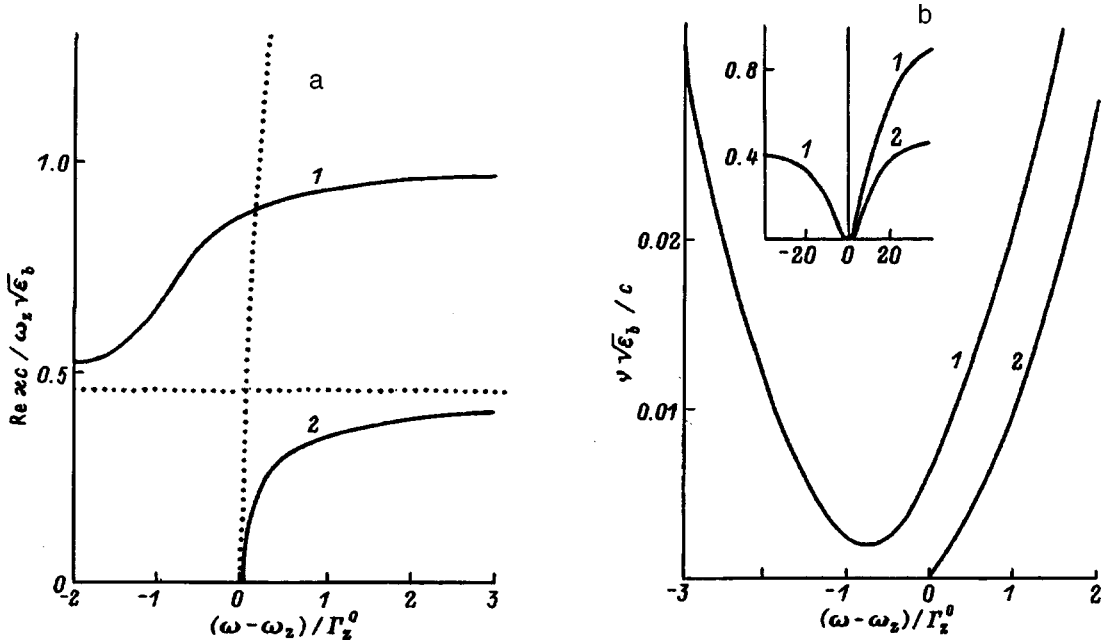

FIG. 2. The dimensionless wave numbers Re $\varkappa c/(\omega_z\sqrt{\varepsilon_b})$ (a) and group velocities $\nu\sqrt{\varepsilon_b}/c$ (b) as functions of the frequency detuning $(\omega-\omega_c)/\Gamma_z^0$ for even $m=2$ mode *TM*-mode exciton polaritons in a waveguide with $L\omega_z\sqrt{\varepsilon_b}/c=7$ ($L=1.5$ μm). The dotted curve shows the functions $\varkappa_{\rm ex}^{\alpha}(\omega)$ and $\varkappa_{\rm wg}^{\alpha}(\omega)$ for the noninteracting modes. The parameters $\beta_z=2.6\times10^{-4}$, $\Gamma_z^0/\omega_z=6.2\times10^{-4}$, and $\hbar\Gamma_z^0\approx1$ meV, corresponding to a quasi-two-dimensional $e1-lh1$ exciton in an $a=50$ Å wide GaAs quantum well, have been used. The notation for the curves and other computational parameters are as in Fig. 1. The inset shows the same curves on a reduced scale.

tively, are used. Here and in the following, we shall omit the polarization index α. For the $m=1$ ($\alpha=x$) mode, for example, the first of Eqs. (9) gives

$$\frac{v}{c/\sqrt{\varepsilon_b}}=\beta\,\frac{\varkappa c}{\omega_0\sqrt{\varepsilon_b}}\,\frac{1+S}{1+\beta S}, \tag{10}$$

where

$$\beta=\varepsilon_b\hbar g q_0/(Mc^2), \tag{11}$$

ω_0 is the exciton resonance frequency of the quantum well (ω_x in this case), and $S(\varkappa,\omega)=\{\varkappa^2-\varkappa_{ex}^2(\omega)\}\{1+q(\varkappa,\omega)L/\sin[q(\varkappa,\omega)L]\}/q^2(\varkappa,\omega)$. In order to obtain $\nu_{1,2}(\omega)$ from Eq. (10), it is necessary to replace $\varkappa$ by $\varkappa_{1,2}(\omega)$ in the range of frequencies where the latter are real. After the substitution (8), the second of Eqs. (9) yields

$$\frac{v_{1,2}}{c/\sqrt{\varepsilon_b}}=2\beta\,\frac{c\varkappa_{1,2}}{\omega_0\sqrt{\varepsilon_b}} \tag{12}$$

at the frequency ω corresponding to $\varkappa_{\rm ex}(\omega)=\varkappa_{\rm wg}(\omega)=\sqrt{\varepsilon_b\varkappa_0^2-(\pi/L)^2}$, where the quantities $\varkappa_{1,2}=\sqrt{\varkappa_{wg}^2\pm(\Delta x)^2}$ are also real. Similar relations are easily obtained for the y and z components of the exciton polarization.

In the resonance region, $\varkappa_{1,2}\sim\varkappa_{\rm ex}\approx\varkappa_{\rm wg}\sim\sqrt{\varepsilon_b}\omega_0/c$ in Eqs. (10) and (12) and the small parameter (11) determines the reduction in the group velocity of the waveguide exciton polariton in a way similar to the case of bulk exciton polaritons.[2–4] For heavy and light hole excitons in bulk GaAs and the corresponding quantum wells, the parameter (11) is of order $\approx 10^{-4}$. Thus, the group velocity may be reduced by three-four orders of magnitude compared to the speed of light in the region where the waveguide exciton polariton exists, while the exact values of ν_1 and ν_2 may be affected by the details of the waveguide exciton polariton dispersion relation.

This conclusion is confirmed by the numerical calculations of the waveguide exciton polariton group velocities ν_1 and ν_2 shown in Figs. 1b and 2b. The curves in Fig. 1b show that in the region of the exciton-polariton anticrossing, the group velocity ν_1 for the modes in the upper waveguide exciton polariton branch decreases sharply with frequency, while ν_2 for the lower-branch waveguide exciton polariton modes increases. It also follows from Fig. 1b that the simplified solution based on Eqs. (8) and (12) gives much greater reduction in the waveguide exciton polariton group velocity. Figure 2b illustrates another situation, in which, because of the peculiarities of the photon-exciton interaction, the modes in the upper dispersion branch are faster at any frequency, while the minimum velocity of these modes turns out to be comparable to the results shown in Fig. 1. Thus, the curves of Fig. 2b can scarcely be interpreted using Eq. (8). Assuming as an estimate that the two monochromatic waveguide exciton polariton modes at a given frequency propagate independently of one another, we can approximately ascribe the propagation velocity of the electromagnetic energy to the faster of these modes. Then, as Figs. 1b and 2b imply, this transport velocity must have a minimum near the frequency of the photon-exciton resonance at which the reduction in the velocity will be related to the parameter (11).

We have found, therefore, that the features of the resonance splitting of the waveguide exciton polariton wave vector depend strongly on both the polarization direction of the exciton component and the symmetry (parity) of the waveguide mode. In the neighborhood of an isolated resonance state of the quasi-two-dimensional exciton, the waveguide exciton polariton group velocity or the transport velocity for the optical excitation energy is characterized by the same small parameter as for bulk exciton polaritons. The calculated waveguide exciton polariton group velocities in the resonance region are three-four orders of magnitude lower than the speed of light in vacuum (Figs. 1b and 2b). This is close to the estimates of the group velocity for bulk exciton polaritons,[2–4] but differs substantially from Ref. 6 for the *TE*-polarized waveguide exciton polariton mode. In this regard, we note that all the above conclusions regarding the x component of the waveguide exciton polariton *TM* mode are qualitatively valid for the waveguide exciton polariton *TE* mode. It might be expected that these conclusions would retain their validity even in more precise models which, as must be done, take into account the interference of two monochromatic waveguide exciton polariton modes or of the waveguide exciton polariton wave packets considered above.

The author thanks R. P. Seisyan for his interest in this work and for fruitful discussions, as well as A. V. Sel'kin and F. Lavallard for useful comments.

[1] V. M. Agranovich and V. L. Ginzburg, Crystal Optics with Spatial Dispersion and the Theory of Excitons [in Russian], Moscow (1978), 432 pp.
[2] R. G. Ulbrich and G. W. Fehrenbach, Phys. Rev. Lett. **43**, 963 (1979).
[3] T. Itoh, P. Lavallard, J. Reydellet, and C. Benoit a la Guillaume, Solid State Commun. **37**, 925 (1981).
[4] A. Puri and J. L. Birman, Phys. Rev. Lett. **47**, 173 (1981).
[5] K. Ogawa, T. Katsuyama, and H. Nakamura, Phys. Rev. Lett. **64**, 796 (1990).
[6] K. Oimatsu, T. Iida, H. Nishimura, K. Ogawa, and T. Katsuyama, J. Lumin. **48–49**, 713 (1991).
[7] S. Jorda, Phys. Rev. B **50**, 2283 (1994).
[8] L. C. Andreani and F. Bassani, Phys. Rev. B **41**, 7536 (1990).
[9] E. L. Ivchenko, Fiz. Tverd. Tela **33**, 2388 (1991) [Sov. Phys. Solid State **33**, 1344 (1991)].
[10] V. A. Kosobukin and M. M. Moisceva, Fiz. Tverd. Tela **37**, 3694 (1995) [Phys. Solid State **37**, 2036 (1995)].
[11] P. B. Johnson and R. W. Christy, Phys. Rev. B **6**, 4370 (1972).
[12] E. L. Ivchenko, V. P. Kochereshko, P. S. Kop'ev, V. A. Kosobukin, I. N. Uraltsev, and D. R. Yakovlev, Solid State Commun. **70**, 529 (1989).

Translated by D. H. McNeill

Two-particle correlations in 1D-lattice systems with δ-interactions

A. N. Kocharyan and A. S. Saakyan

State Engineering University of Armenia, 375009 Erevan, Armenia
(Submitted May 20, 1997)
Fiz. Tverd. Tela (St. Petersburg) **40**, 366–370 (February 1998)

The problem of two interacting particles in finite closed and open chains is solved by the Lifshitz method. The ''density-density'' correlation function, the dependence of the ''surface'' energy on the two-particle interaction energy and number of links in the chain, and the two-particle distribution on the chain are found and the nature of the ground state is clarified.
 [S1063-7834(98)04502-X]

1. Correlations between particles are known to determine the physical properties of many systems. The simplest models in which particle interactions are rigorously taken into account are the 1D Bose-gas[1] and Hubbard models[2] which are solved exactly by the Bethe-Ansatz method.[3,4] In the case of a finite number of particles, it is incorrect to make the transition to the thermodynamic limit; hence the problem must be solved for a finite chain. The two-particle problem on a finite low-temperature lattice is of current interest from the standpoint of clarifying the mechanisms for high-temperature superconductivity,[5] as well as clarifying the nature of the magnetic ordering in highly-correlated systems with hole exchange[6] (a generalization of the Nagaoka theorem). This explains the heightened interest in the two-particle problem on a finite low-dimensional lattice. A variational technique has been used[7,8] to study the ground state of two electrons on a closed chain and an expression has been obtained for the ground-state energy that is asymptotic in the number of links, N. An attempt has been made[8] to solve this problem numerically on a 2D lattice. This problem has been solved for asymptotically large N.[9] An exact expression has been obtained[10] for the density-density correlation function for two spinless fermions on a closed chain and the ground-state energy of the system has been determined. Thus, at the present time there is an entire series of separate results obtained by different, mainly approximate, methods. All these results can be combined in a single approach, which makes it possible to find an exact solution for the problem, such as the Lifshitz method.[11] In this paper we solve the problem of two particles (identical and nonidentical) and, in some cases, compare our results with the earlier work.[7–10]

2. The hamiltonian of a system of interacting bosons on a lattice has the form

$$H=\sum J(n_1-n_2)a^+_{n_1}a_{n_2}+U\sum \delta_{n_1n_2}a^+_{n_1}a^+_{n_2}a_{n_2}a_{n_1}, \tag{1}$$

where $n_{1,2}$ are the discrete vectors of the lattice, and a^+_n and a_n are the Bose creation and annihilation operators. In the case of the Hubbard model, in the Fermi creation and annihilation operators it is necessary to add a spin subscript, while the interaction operator has the form

$$H_{\rm int}=\frac{1}{2}\,U\sum \delta_{n_1n_2}\delta_{\sigma_1,-\sigma_2}a^+_{n_1\sigma_1}a_{n_1\sigma_1}a^+_{n_2\sigma_2}a_{n_2\sigma_2}. \tag{2}$$

When $U=+\infty$ two particles cannot simultaneously be at a single lattice site.

The two-particle wave function is taken to have the form

$$|2\rangle=\sum_{n_1n_2}\psi(n_1n_2)a^+_{n_1}a^+_{n_2}|0\rangle, \tag{3}$$

where $\psi(n_1n_2)$ is the ''first-quantized'' wave function and $|0\rangle$ is the vacuum ket vector corresponding to an empty lattice. Acting with operator (1) on the state (3), we arrive at the Schrödinger equation

$$\sum_{n'} J(n_1-n')\psi(n',n_2)+\sum_{n'} J(n_2-n')\psi(n',n_1) + U\delta_{n_1n_2}\psi(n_1,n_2)=E\psi(n_1,n_2). \tag{4}$$

We seek a solution of Eq. (4) in the form

$$\psi(n_1,n_2)=\frac{1}{N^d}\exp[i(Q/2)(n_1+n_2)] \times\sum_k \exp(ik(n_1-n_2))\psi(k,Q), \tag{5}$$

where $\psi(k,Q)$ is the two-particle wave function in the momentum representation, d is the dimensionality of the problem, Q is the quasimomentum of the center of mass, and k is the bare quasimomentum of the relative motion. Substituting Eq. (5) in Eq. (4), we obtain

$$\psi(n_1,n_2)=-\frac{U_\tau}{N_d}\exp(i(Q/2)(n_1+n_2)) \times\sum_k \frac{\exp(ik(n_1-n_2))}{\varepsilon(k+Q/2)+\varepsilon(k-Q/2)-E}, \tag{6}$$

where

$$\tau=\psi_{\rm rel}(n_1-n_2)|_{n_1=n_2}$$

is the wave function for the relative motion at zero and

$$\varepsilon(k)=\frac{1}{N^d}\sum_n J(n)e^{ikn}$$

is the dispersion relation of the particles. We shall work in the nearest neighbor approximation below. Then, in the case $d=1$, we have $\varepsilon(k)=-2t\cos k$, where $2t$ is the width of the energy band. We assume that the lattice constant is unity.

In order to find the constant τ it is necessary to write the general solution of Eq. (4), augmenting Eq. (6) with the plane wave

$$\psi(n_1,n_2)=\exp(i(Q/2)(n_1+n_2))\left[\exp(ik_0(n_1-n_2))-\frac{U_\tau}{N^d}\sum_k \frac{\exp(ik(n_1-n_2))}{\varepsilon(k+Q/2)+\varepsilon(k-Q/2)-E}\right]. \tag{7}$$

Examining this expression for $n_1=n_2$, we obtain the following self-consistency condition:

$$\tau^{-1}=1+\frac{U}{N^d}\sum_k \frac{1}{\varepsilon(k+Q/2)+\varepsilon(k-Q/2)-E}. \tag{8}$$

The energy spectrum of the system E is the solution of the equation

$$\frac{1}{N^d}\sum_k \frac{1}{\varepsilon(k+Q/2)+\varepsilon(k-Q/2)-E}=-\frac{1}{U} \tag{9}$$

and is determined by the poles of the mutual particle scattering amplitude, i.e., from the condition $\tau^{-1}=Q$.

Let us examine the solution of the problem of two bosons on a one dimensional lattice. We choose a parametrization of the energy E of the form

$$E=-4t\,\cos(Q/2)\cos\,p. \tag{10}$$

Substituting Eq. (10) in Eq. (6) and proceeding to the integration,[11] we obtain two solutions corresponding to converging and diverging waves:

$$\psi_\pm(x,y)=\frac{\mp i\,\eta}{\sin\,p\,\cos(Q/2)\pm in}\,e^{i(\pm px+(Q/2)y)},$$

$$\eta=\frac{U}{4t},\quad x=n_1-n_2,\quad y=n_1+n_2. \tag{11}$$

The eigenvalues of the parity operator are linear combinations of $\psi_\pm(x,y)$,

$$\psi(x,y)=e^{i(Q/2)y}[\cos(kx+\delta)\,\theta(-x)+\cos(kx-\delta)\,\theta(x)],$$

$$\delta=\arctan\frac{\eta}{\sin\,p\,\cos(Q/2)}. \tag{12}$$

These solutions satisfy the boundary condition

$$\lim_{x\to 0}\lim_{U\to\infty}\psi(x,y)=0. \tag{13}$$

The solutions corresponding to the reflected and transmitted waves have the form

$$\psi(x,y)=e^{i(Q/2)y}\begin{cases} e^{-ipx}-\dfrac{i\,\eta e^{ipx}}{\sin\,p\,\cos(Q/2)+i\,\eta}, & x<0,\\ \dfrac{\sin\,\rho\,\cos(Q/2)e^{ipx}}{\sin\,p\,\cos(Q/2)+i\,\eta}, & x>0.\end{cases} \tag{14}$$

this yields the transmission and reflection coefficients

$$R=\frac{i\,\eta}{\sin\,p\,\cos(Q/2)+i\,\eta},$$

$$S=\frac{\sin\,p\,\cos(Q/2)}{\sin\,p\,\cos(Q/2)+i\,\eta}. \tag{15}$$

On passing from the coefficients R and S to the scattering phase,[12] we again arrive at the eigenstates (12).

3. In the case of a closed chain, we must impose the following boundary conditions on the wave function (6) or (12):

$$\psi_A(n_1+N,n_2)=\psi_B(n_1,n_2),$$

$$\psi_B(n_1,n_2+N)=\psi_A(n_1,n_2), \tag{16}$$

where $\psi_{A,B}(n_1,n_2)$ are the wave functions in the regions $n_1<n_2$ and $n_1>n_2$, respectively. In order to find the eigenvalues of the problem from the Lifshitz equation (9), first of all we have to determine the spectrum of the seed values of k starting with the boundary conditions (16). Thus, we assume that translation by N does not change the state with respect to the motion of two particles. Then,

$$k=\frac{2\pi m}{N},\quad m=0,\,1,\,2,\,\ldots,\,N-1$$

and the Lifshitz equation takes the form

$$I(p)=\frac{1}{N}\sum_{n=0}^{N-1}\frac{1}{\cos(2\pi n/N)-\cos\,p}=\frac{\cos(Q/2)}{\eta}. \tag{17}$$

To find the sum, we multiply both sides of Eq. (17) by $\sin\,p$ and integrate with respect to p,

$$\int I(p)\sin\,p\,dp=N\,\ln 2+\ln\prod_{m=0}^{N-1}\sin\left(\frac{\pi m}{N}+\frac{p}{2}\right)\times\prod_{m=0}^{N-1}\sin\left(\frac{\pi m}{N}-\frac{p}{2}\right), \tag{18}$$

then we use the fact that[13]

$$\prod_{m=0}^{N-1}\sin\left(\frac{\pi m}{N}\pm\frac{p}{2}\right)=\pm 2^{1-N}\sin\frac{N_p}{2}.$$

Finally, we obtain

$$\frac{\cot(Np/2)}{\sin\,p}=\frac{\cos(Q/2)}{\eta}. \tag{19}$$

We introduce the simplest solutions of Eq. (19):

a. $U=0,\quad p=2\pi m/N,$

b. $U=+\infty,\quad p=(2\pi/N)(n+(1/2)),$

i.e., in the ground state $p=\pi/N$,

c. $\eta\gg 1,\quad p=(2\pi n/N)+(\pi/N)-(4\pi/N^2),$

d. $\eta\ll 1,\quad p=\sqrt{\eta/N}.$

Thus, the ground state energy, in particular for $U=+\infty$, is

$$E_0 = -4t\,\cos\frac{\pi}{N}, \tag{20}$$

or, in the asymptotic approximation in N^{-1}, we have

$$E_0 = -4t\left(1-\frac{\pi^2}{2N^2}\right). \tag{20a}$$

The result (20) was first obtained in Ref. 9 for spinless fermions and a result similar to (20a), in Ref. 6 (see Section 1 of this paper).

In the case of attraction ($U<\infty$), the solution of the Lifshitz equation corresponding to the ground state has the form

$$E_0 = -4t\sqrt{1+\eta^2}+O(e^{-pN/2}), \tag{21}$$

which corresponds to a bound state of the particles, and the wave function is

$$\psi(x) = \sqrt{\frac{2}{R}}\exp\left(-\frac{|x|}{R}\right). \tag{22}$$

where $R = 1/\sinh^{-1}\eta$ is the ''radius'' of the bound state.

For a repulsive interaction the probability density of the particle distribution in the chain in the ground state for $U=+\infty$ is given by the expression

$$P(x) = \sin^2\frac{\pi x}{N}, \tag{23}$$

which implies that after a single scattering event the particles separate to a maximum distance equal to the chain length (the dynamic ground state).

From Eqs. (6) and (19) it is easy to obtain the ground state energy and the wave function of a ''diatomic molecule'', a system consisting of two particles on a two-point lattice,

$$E_0 = \begin{cases} -\frac{1}{2}\,(\sqrt{U^2+(8t)^2}-U), & U>0, \\ -\frac{1}{2}\,(\sqrt{U^2+(8t)^2}+|U|), & U<0, \end{cases} \tag{24a}$$

and

$$\Psi(n_1,n_2) = \begin{cases} \dfrac{\delta_{n_1n_2}\cos p}{\sqrt{1+\cos^2 p}}+\dfrac{1-\delta_{n_1n_2}}{\sqrt{1+\cos^2 p}}, & U>0, \\ \dfrac{\delta_{n_1n_2}\cosh p}{\sqrt{1+\cosh^2 p}}+\dfrac{1-\delta_{n_1n_2}}{\sqrt{1+\mathrm{ch}^2 p}}, & U<0, \end{cases} \tag{24b}$$

where

$$\cos p = -\frac{\eta}{2}+\sqrt{\frac{\eta^2}{4}+1}, \quad U>0,$$

$$\cosh p = \frac{|\eta|}{2}+\sqrt{\frac{\eta^2}{4}+1}, \quad U<0.$$

The pairwise correlation function has the form

$$G(n_1,n_2) = (a^+_{n_1}a_{n_1}a^+_{n_2}a_{n_2}). \tag{25}$$

The averaging in Eq. (25) should be taken over the two-particle states (3). Substituting Eq. (3) in Eq. (25) and using Eq. (12), we obtain

$$G(n_1,n_2) = \frac{2}{N}\,\delta_{n_1n_2}+\frac{4}{N^2}\cos^2\{p(n_1-n_2)+[\theta(n_1-n_2) - \theta(n_2-n_1)]\delta(p)\}. \tag{26}$$

In particular, for $U\to+\infty$, we have

$$G(n_1,n_2) = \frac{2}{N}\,\delta_{n_1n_2}+\frac{4}{N^2}\sin^2 p(n_1-n_2). \tag{27}$$

Equation (27) was first derived in Ref. 10 for 1D spinless fermions.

4. Let us consider the two-boson problem on an open lattice. We write the parameters Q and p in the form

$$2Q_{ij} = \varepsilon_i p_1+\varepsilon_j p_2, \quad 2p_{ij} = \varepsilon_i p_1-\varepsilon_j p_2, \quad \varepsilon_i = 1,-1. \tag{28}$$

This allows us to include all the waves incident on and reflected from the chain boundary. The seed spectrum can be found from the condition that the wave function goes to zero when the particles are separated by a distance equal to the chain length, $\psi(0,N)=\psi(N,0)=0$. Applying these boundary conditions to Eq. (6), we obtain

$$kN = \pi(n+1/2), \quad n=1,\ldots,N,$$

so that the Lifshitz equation becomes

$$\frac{1}{N}\sum_{k=1}^{N}\frac{1}{\cos[\pi(2n+1)/2N]-\cos p_{ij}} = \frac{\cos(Q_{ij}/2)}{\eta}$$

and, after summing, takes the form

$$\tan Np_{ij} = -\frac{1}{\eta}\sin p_{ij}\cos(Q_{ij}/2), \tag{28a}$$

or, using the definition of the parameters p_{ij} and Q_{ij},

$$\tan N_p = -\frac{1}{\eta}\sin p\,\cos(Q/2),$$

$$\tan\frac{NQ}{2} = -\frac{1}{\eta}\cos p\,\sin(Q/2). \tag{29}$$

We introduce the simplest solutions of the system of Eqs. (29):

a. $\eta=0$, $p_1=p_2=2\pi m/N$,

in the ground state $n=m=1$,

$$E_0 = -4t\,\cos(\pi/N),$$

b. $\eta=+\infty$, $p_1=\pi(n+1)/N$, $p_2=\pi m/N$,

in the ground state

$$n=m=1, \quad E_0 = -2t(\cos(\pi/N)+\cos(2\pi/N)),$$

c. $n\gg 1$,

$$E_0 = -2t\left[\cos\left(\frac{2\pi}{N}-\frac{2\pi}{\eta N^2}\right)+\cos\left(\frac{\pi}{N}-\frac{\pi}{\eta N^2}\right)\right],$$

and

d. $\eta \ll 1$, $E_0 = -4t\cos\left(\frac{\pi}{N}+\frac{2\eta}{\pi}\right)\cos\sqrt{\frac{\eta}{N}}$.

The wave function can be obtained, as in Section 2, from Eqs. (6) using Eqs. (28) and (29),

$$\psi(n_1,n_2)=\begin{cases}(-1)^{l_1}\sin p_1 n_1 \sin p_2(n_2-N)+(-1)^{l_2} \\ \quad \sin p_2 n_1 \sin p_1(n_2-N), \quad n_1<n_2, \\ (-1)^{l_2}\sin p_2 n_2 \sin p_1(n_1-N)+(-1)^{l_1} \\ \quad \sin p_1 n_2 \sin p_2(n_1-N), \quad n_1>n_2,\end{cases} \tag{30}$$

where $l_{1,2}$ are the single-particle quantum numbers on an open chain. The main difference from the problem of a closed chain is that here the quasimomenta of the center of mass and of the relative motion appear in a resonant form: because of reflection processes at the ends of the chain, they ''periodically'' exchange roles. In the case of attraction, $U>0$, the ground state energy is

$$E_0 = -4t\sqrt{\eta^2+\cos^2\frac{\pi}{2N}}. \tag{31}$$

Evidently, the energy of a two-particle system on an open chain is higher than on a closed one. Let us define the surface energy as

$$\Delta E = E_{\text{open}} E_{\text{closed}}. \tag{32}$$

Thus, for $U=+\infty$, we have

$$\Delta E = \frac{3\pi^2}{N^2}t, \quad N\gg 1, \tag{33}$$

and for $U<0$,

$$\Delta E = \frac{2\pi^2}{|U|N^2}t^2, \quad |U|/t\gg 1, \quad N\gg 1.$$

5. We now examine the problem of two electrons on a finite chain. We write the two-particle wave function in the form

$$|2\rangle = \sum_{\substack{n_1 n_2 \\ \sigma_1\sigma_2}} \psi(n_1\sigma_1,n_2\sigma_2)a^+_{n_1\sigma_1}a^+_{n_2\sigma_2}|0\rangle. \tag{34}$$

Applying the Hubbard hamiltonian to the state (34), we arrive at the Schrödinger equation

$$\begin{aligned}&\sum_{n'\sigma'} J(n_1-n')\psi(n'\sigma',n_2\sigma_2)+\sum_{n'\sigma'} \\ &\quad \times J(n_2-n')\psi(n'\sigma',n_1\sigma_1)+U\delta_{n_1n_2}\delta_{\sigma_1,-\sigma_2} \\ &\quad \times \sum_{nm\sigma\sigma'}[\delta_{nn_1}\delta_{mn_2}\delta_{\sigma_1,\sigma}\delta_{\sigma_2,\sigma'} \\ &\quad -\delta_{nn_2}\delta_{mn_1}\delta_{\sigma_1,\sigma'}\delta_{\sigma_2,\sigma}]\psi(n_1\sigma_1,n_2\sigma_2) \\ &= E\psi(n_1\sigma_1,n_2\sigma_2).\end{aligned} \tag{35}$$

The expression in the square brackets is the matrix element of the operator $\hat{I}-\hat{P}_{12}$ where $\hat{I}$ is the unit operator and $\hat{P}_{12}$ is the permutation operator. We seek, therefore, a solution to this equation in the form

$$\begin{aligned}\psi(n_1\sigma_1,n_2\sigma_2) &= (I-\hat{P}_{12})\chi_{\alpha\beta}\frac{1}{N^d}\sum_{kQ}\exp(i(Q/2) \\ &\quad \times(n_1+n_2))\times\psi_{\sigma_1\sigma_2}(kQ)e^{ik(n_1-n_2)},\end{aligned} \tag{36}$$

where $\chi_{\alpha\beta}$ is the singlet spin wave function. Then

$$\begin{aligned}&\left[\varepsilon\left(k+\frac{Q}{2}\right)+\varepsilon\left(k-\frac{Q}{2}\right)-E\right]\psi_{\sigma_1\sigma_2}(k,Q) \\ &\quad = -U(\tau_{\sigma_1\sigma_2}-\tau_{\sigma_2\sigma_1}),\end{aligned} \tag{37}$$

where

$$\tau_{\sigma_1\sigma_2} = \psi(n_1\sigma_1,n_2\sigma_2)|_{n_1=n_2}.$$

Using the self consistency condition (see Section 2), we obtain the following expression for τ:

$$\tau_{\sigma_1\sigma_2(\sigma_2\sigma_1)} = \pm\left(1\pm\frac{U}{N^d}\sum_k \frac{1}{\varepsilon\left(k+\frac{Q}{2}\right)+\varepsilon\left(k-\frac{Q}{2}\right)-E}\right) \tag{38}$$

and then, using Eqs. (36)–(38), we finally obtain the following for the coordinate part of the singlet wave function:

$$\begin{aligned}\psi(n_1n_2) &= -\frac{U}{N^d}\exp i(Q/2)(n_1+n_2) \\ &\quad \times\left[\left(1+(U/N^d)\sum_k \frac{1}{z(kQ)-E}\right)^{-1}\right. \\ &\quad \times\sum_k \frac{\exp(ik(n_1-n_2))}{Z(kQ)-E} \\ &\quad +\left(1-(U/N^d)\sum_k \frac{1}{Z(kQ)-E}\right)^{-1} \\ &\quad \left.\times\sum_k \frac{\exp(-ik(n_1-n_2))}{z(kQ)-E}\right], \\ Z(kQ) &= \varepsilon\left(k+\frac{Q}{2}\right)+\varepsilon\left(k-\frac{Q}{2}\right),\end{aligned} \tag{39}$$

while the energy spectrum is determined from Eq. (9). As can easily be shown, in the 1D case Eq. (39) is the same as the Bose two-particle wave function (12). The 1D wave functions (12) and (30) both have the feature that they go identically to zero for $p_1=p_2$, i.e., they obey the Pauli principle, and the system becomes ''fermiized'' with an arbitrarily small interaction, but it should be noted that this result cannot be obtained using perturbation theory. Clearly, the pairwise correlation function for the singlet electrons is determined by Eqs. (26) and (27).

Thus, 1D systems of two spinless bosons, two singlet electrons, and, for $U=+\infty$, two spinless fermions, are equivalent, i.e., they have the same wave functions, energy spectra, and pairwise correlation functions.

6. In a similar fashion we can obtain an exact solution for two particles with different band widths $t_1 \neq t_2$. Here we give the Lifshitz equation which determines the energy spectrum of this system on a closed chain,

$$\frac{1}{\sin(p+\varphi_0)}\left[\cot\frac{Np}{2}+\cot\ N\left(\frac{p}{2}+\varphi_0\right)\right]=\frac{2t}{U},$$

$$t=\sqrt{t_1^2+t_2^2+2t_1t_2\ \cos\ Q},\quad \tan\ \varphi_0=\frac{t_1-t_2}{t_1+t_2}\tan\frac{Q}{2}. \tag{40}$$

The problem of two particles on a chain can, therefore, be solved exactly using the Lifshitz approach. Another approach, in the spirit of the Bethe Ansatz, also leads to the stated goal and the Yang equations coincide with the corresponding Lifshitz equations, i.e., both approaches to the 1D problem are equivalent.

We thank A. F. Andreev for discussing this article and for helpful advice.

[1] T. D. Lee and C. N. Yang, Phys. Rev. **113**, 1406 (1959).
[2] Y. Hubbard, Proc. Roy. Soc. A **276**, 238 (1963).
[3] C. N. Yang, Phys. Rev. Lett. **19**, 1312 (1967).
[4] E. H. Lieb and F. Y. Wu, Phys. Rev. Lett. **64**, 1445 (1968).
[5] Y. G. Bednorz and K. A. Muller, Z. Phys. **64**, 189 (1986).
[6] L. Chen and Ch. Mei, Phys. Rev. B **39**, 9006 (1989).
[7] Ch. Mei and L. Chen, Z. Phys. B **72**, 429 (1988).
[8] A. N. Kocharian, G. B. Reich, and A. S. Saakian, Physica B **206–207**, 332 (1995).
[9] M. Caspers, Z. Phys. B **74**, 718 (1990).
[10] I. M. Lifshitz, Zh. Eksp. Teor. Fiz. **18**, 293 (1948).
[11] L. D. Landau and E. M. Lifshitz, Quantum Mechanics [in Russian], Nauka, Moscow (1974).
[12] H. Lipkin, Quantum Mechanics, North Holland, Amsterdam (1973).
[13] I. G. Gradshtein and I. M. Ryzhik, Table of Integrals, Series, and Products, Academic Press, N.Y. (1980).

Translated by D. H. McNeill

Initial stages in the Sm-Si(111) interface formation

T. V. Krachino, M. V. Kuz'min, M. V. Loginov, and M. A. Mittsev

A. F. Ioffe Physicotechnical Institute, Russian Academy of Sciences, 194021 St. Petersburg, Russia
(Submitted May 26, 1997)
Fiz. Tverd. Tela (St. Petersburg) **40**, 371–378 (February 1998)

The initial stages in the formation of the Sm-Si(111) interface have been studied by thermal desorption, atomic beam modulation, and low-energy-electron-diffraction spectroscopy. The structure of adsorbed films and samarium silicide films, as well as the Sm atom desorption kinetics have been investigated within a broad range of surface coverages and temperatures. The activation energy of desorption from the thermally most stable 3×2 submonolayer structure, as well as the binding energy of a single samarium atom with the substrate, have been measured. The temperature of the onset of silicide decomposition and the activation energy of this process have been determined. It is shown that the Sm-Si(111) interface forms by a mechanism close to that of Stransky-Krastanov. © *1998 American Institute of Physics.* [S1063-7834(98)04602-4]

Thin silicide films formed in deposition of rare-earth metals (REM) on a silicon surface exhibit a number of specific physicochemical properties (for instance, a high thermal stability and metallic conduction), which make them promising for use in micro- and nanoelectronics.[1–3] This attracts considerable interest to the processes occurring in different stages of REM silicide formation from both a scientific and practiced standpoint.

Attention to REM-silicon and, in particular, to samarium-silicon film structures has been focused until recently on the electronic properties of the silicides, which form on the substrate surface coming in contact with the adsorbate material.[4,5] One still does not know, however, the mechanisms of formation of the interfaces of this type, as well as the part played by the adsorbed phase in this process. Our investigation of the adsorption and desorption kinetics of atoms of Eu (Ref. 6) and Yb (Refs. 7 and 8) and of the kinetics of formation and thermal decomposition of their silicides on the Si(111) surface provided answers to some of these questions. The present work deals with the Sm-Si(111) system.

1. EXPERIMENTAL METHOD

The experiments were carried out in an ultrahigh-vacuum chamber with a base pressure less than 1×10^{-10} Torr described elsewhere.[6,8] The substrates were phosphorus-doped *n*-silicon samples cut parallel to the (111) plane and having resistivity of 1–10 $\Omega\cdot$cm. They were thin ribbons $40\times2\times0.3$ mm in size prepared by the method of Ref. 9. Heating was done by passing dc current through the sample. The cleanness and structure of the surface were monitored by Auger electron spectroscopy (AES) and LEEDS. The diffraction patterns were studied at room temperature.

The adsorbate (Sm) was deposited onto the substrate surface from an evaporator.[6] During the deposition the pressure in the chamber was not worse than 1×10^{-9} Torr. The flux intensity from the evaporator ν_0 was calibrated against known thermal desorption spectra of the Sm-W(100) system.[10] The samarium surface concentration $N_{ML}=7.84\times10^{14}$ cm^{-2} at which there is one deposited atom per one substrate atom in the Si(111)1×1 structure was assumed to correspond to monolayer coverage ($\theta=1$).

This work reports results obtained by thermal desorption spectroscopy (TDS), atomic beam-modulation (ABM), and LEEDS. TD spectra were recorded in the ν-I_s coordinates, where ν is the Sm atom desorption flux measured with a mass-spectrometer,[6] and I_s is the current through the sample. The heating current was increased linearly with time, $I_s(t)=I_0+\beta t$ ($I_0,\beta=$const). The substrate temperature T was determined with an optical pyrometer. The second method, ABM, was described in detail earlier.[6,8]

Experimental data obtained by the first two techniques were analyzed under the assumption that the flux intensity ν obeys a kinetic equation of the type

$$\nu=CN^n\exp(-E_d/kT), \tag{1}$$

where C is a prefactor, N is the adsorbate atom concentration, n is the order of desorption, and E_d is the desorption activation energy. The latter quantity was derived from the slope of the straight line drawn in log $\nu=f(1/T)$ coordinates (the Arrhenius plot), and the prefactor C, from the known values of ν, N^n, E_d, and T using Eq. (1). For more details, see Refs. 6 and 8.

2. EXPERIMENTAL RESULTS

As already mentioned, adsorption of REM atoms on a silicon surface can give rise to the formation of silicides. Heating the substrate may result in evaporation from its surface either of the silicide molecules or of the products of their complete or partial decomposition. Preliminary experiments performed within broad temperature and coverage ranges revealed that heating desorbs only free Sm atoms, with the silicides being completely decomposed. It was also established that surface migration of adsorbate atoms to the back side of the substrate, which could introduce serious error into our measurements[6] is either absent altogether or small enough to be neglected.

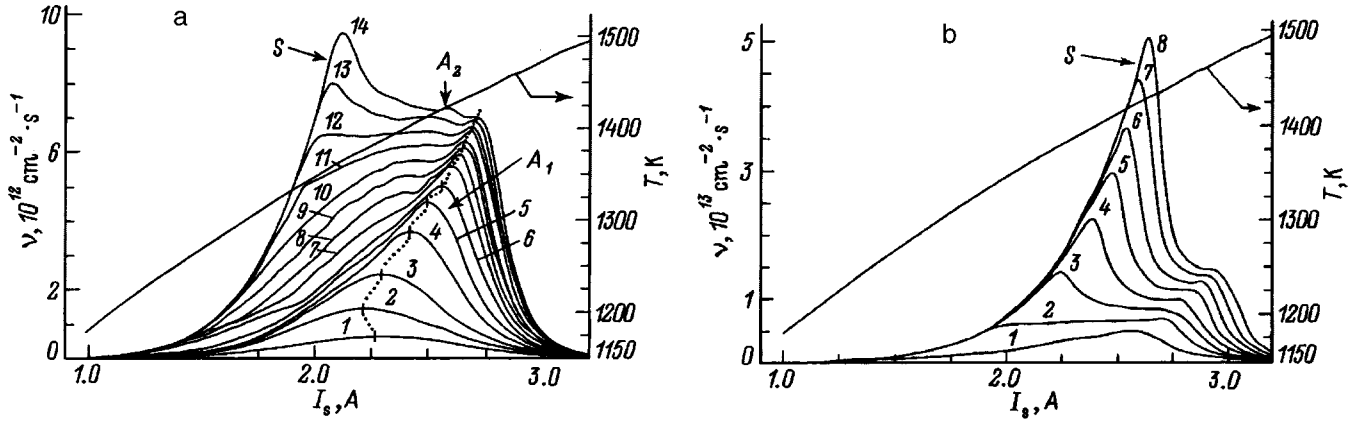

FIG. 1. TD spectra obtained at different initial coverages θ. Heating rate $\beta = 0.03$ A/s. Dashed line *a* shows the shift of the top of peak A_1. Also shown is the $T = f(I_s)$ relation. θ: (a) *1*—0.04, *2*—0.07, *3*—0.11, *4*—0.14, *5*—0.18, *6*—0.21, *7*—0.25, *8*—0.29, *9*—0.32, *10*—0.36, *11*—0.39, *12*—0.43, *13*—0.46, and *14*—0.5; (b) *1*—0.21, *2*—0.43, *3*—0.64, *4*—0.86, *5*—1.07, *6*—1.29, *7*—1.50, and *8*—1.71.

A. Thermal desorption spectroscopy

Prior to starting a systematic investigation, we carried out control experiments to learn the effect of prehistory of the Sm-Si(111) adsorption system on the shape of TD spectra. It was found that the spectra do not depend on whether the adsorbed layer was heated before their measurement or not. The structure of the spectra did not change either when the sample heating rate β was varied. This implies that the rates of the surface processes substrate heating exceeded rates.

Figure 1a shows TD spectra obtained for different coverages of the Si(111) surface by Sm atoms. Within the $\theta \leqslant 0.17$ coverage interval, only one peak, A_1, is present in the spectra. The position of its maximum on the temperature scale varies nonmonotonically with increasing density of the adsorbed layer. At the lowest coverages, this maximum moves toward lower temperatures (see the dashed line and spectra 1 and 2). Above $\theta = 0.06-0.07$, the peak begins to shift in the opposite direction (spectra 3–6). While the rate of desorption in the low-temperature domain does depend on adsorbate concentration, this dependence is weak.

With further deposition of Sm atoms onto the substrate the structure of the spectra becomes more complex and exhibits two new peaks, A_2 and S, lying at temperatures lower than that of A_1. No more maxima appear with further evaporation of the adsorbate (our measurements extended to 17 monolayers). In contrast to TD spectra obtained by us earlier[7,8] for the Yb-Si(111) system, all three peaks resolve very poorly, thus making their analysis difficult.

As seen from Fig. 1a, the third peak, S, becomes clearly pronounced in the coverage interval $\theta = 0.35-0.40$. Figure 1b illustrates its growth in the region of large coverages. Inspection of the two plots reveals a number of characteristic features.

First, starting with practically the very earliest stage of formation, one observes zero-order desorption ($n = 0$) in the low-temperature part of peak S. This permitted us to determine by means of Eq. (1) the activation energy E_d of desorption from the given adsorption state. Figure 3 (curve *10*) illustrates the plot of log flux ν vs reciprocal temperature, $1/T$, used in these calculations. The desorption activation energy was found to be $E_d(S) = 4.1$ eV.

Second, the monotonic intensity increase of peak S without appearance of any additional maxima in the TD spectra suggests that Sm evaporates from an infinitely growing film with constant desorption parameters. Such a film can consist either only of Sm atoms (metal) or from atoms of samarium and silicon (silicide). The second possibility is argued for by the fact that the rate of evaporation of Sm from a metal film, estimated from its vapor pressure at $T = 1220$ K, should exceed by more than eight orders of magnitude the flux ν observed experimentally, and the value $E_d(S) = 4.1$ eV exceeds by two eV the sublimation energy of metallic Sm [2.14 eV (Ref. 11)]. These two considerations suggest that the S peak in the TD spectra is due to evaporation of adsorbate atoms from the silicide layer.

B. Atomic beam-modulation method

Figure 2 presents isothermal dependences of the desorption flux ν on coverage θ obtained in the course of adsorbate deposition onto the sample surface. The temperatures at

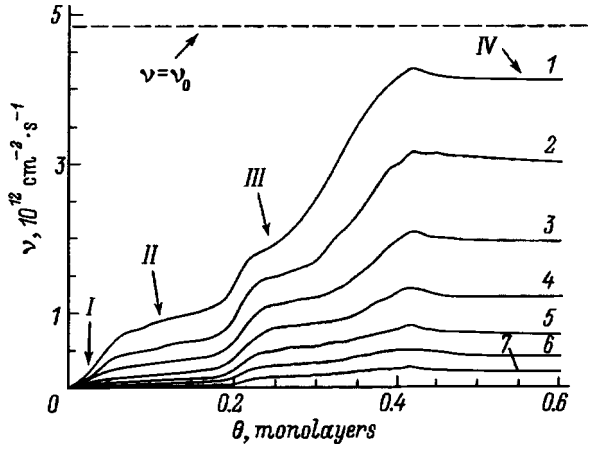

FIG. 2. Isothermal $\nu = f(\theta)$ relations obtained with samarium deposited on the substrate at T(K): *1*—1315, *2*—1300, *3*—1285, *4*—1270, *5*—1255, *6*—1235, *7*—1215. Incident flux $\nu_0 = 4.83\times 10^{12}$ cm^{-2} s^{-1}.

which the isotherms were measured were determined by the thermal properties of the adsorption system and were above the temperature of the $7\times7\leftrightarrow1\times1$ phase transition of the clean Si(111) surface [$T_c=1100$ K (Ref. 12)]. A special experiment showed that the material deposited onto the substrate surface does not dissolve in the bulk of silicon throughout the temperature range $T=1215-1315$ K studied.

One can discriminate four characteristic parts in each isotherm. Section I is observed in the earliest stage ($\theta\leqslant0.03-0.04$) of metal deposition onto the substrate. It is characterized by a close-to-linear dependence of the desorption rate on atom concentration in the adlayer. The slope of the linear portion decreases with decreasing temperature, since the lifetime of adsorbed atoms increases. As the samarium concentration increases, new parts appear in the curves: II ($0.08\leqslant\theta\leqslant0.18$) and III ($0.23\leqslant\theta\leqslant0.34$), where the growth of flux ν slows down substantially. The extent of these regions grows with decreasing temperature. As one transfers from region I to region II, the order of desorption changes from $n=1$ to a value close to $n=1/2$.

As the coverage reaches $\theta=0.42$, a maximum appears in the curves. Further increase of θ results in flux ν reaching saturation (Part IV), with the level being independent of the adsorbate concentration (zero adsorption order). No equilibrium is reached between the incident, ν_0, and desorbing, ν, fluxes at any coverage (i.e., we have always $\nu<\nu_0$). This implies unlimited growth of the Sm silicide film. The reasons why we associate region IV with the growth of the silicide rather than metallic samarium film have been pointed out in Subsection A.

The isothermal curves presented in Fig. 2 permit one to follow the concentration dependence of the desorption activation energy of Sm atoms. The calculation of E_d was made under the assumption that desorption takes place from adsorption states of one type and is described by Eq. (1). The families of curves $\nu=f(\theta)_{T=\text{const}}$ similar to the ones displayed in Fig. 2 were converted to $\log\nu=f(1/T)|_{\theta=\text{const}}$ for a number of values of θ. Some of these plots representing straight lines are shown in Fig. 3 (curves 1–9). Their slope was used to derive the value of E_d for the corresponding coverage. The results of several series of such measurements are displayed in Fig. 4.

A characteristic feature of this relationship is the nonmonotonic variation of E_d in the earliest stage of the interface formation. For $\theta<0.17$, its value first rises sharply from $E_d=3.2$ eV to reach a maximum of 4.95 eV at $\theta=0.07-0.08$, after which it decreases to 4.5 eV. The lack of data in the coverage interval $0.2\leqslant\theta\leqslant0.35$ is due to a nonlinearity of the $\log\nu=f(1/T)|_{\theta=\text{const}}$ plots in this region. The reasons for this will be discussed later.

Finally, after a silicide film has grown on the surface, the desorption activation energy from this layer becomes 4.1 eV. The dashed line shows the value of $E_d(S)$ which was derived from a TD analysis of peak S.

C. Low-energy-electron diffraction

If a samarium adlayer deposited on silicon at room temperature was not heated, the (7×7) reflections from the clean Si(111) surface gradually disappeared, to reveal, already at coverages $\theta=0.1-0.2$, a (1×1) pattern with a higher background.

Heating the substrate produced significant changes in the adlayer structure. In the first place, annealing at $T=750-800$ K resulted in film ordering, which was evidenced by the appearance of additional reflexes. Second, heated films exhibited a successive sequence of diffraction patterns replacing one another with increasing Sm concentration on the surface. It could be obtained in two different ways. In the first of them, the adsorbate deposited on the sample at room temperature was heated for three minutes at $T=900$ K. In the second, the adsorbate was evaporated directly on a substrate maintained at $T=900$ K. Both methods produced the same results presented in Table I, which specifies the coverage intervals within which the corresponding diffraction patterns were observed. Our diffraction measure-

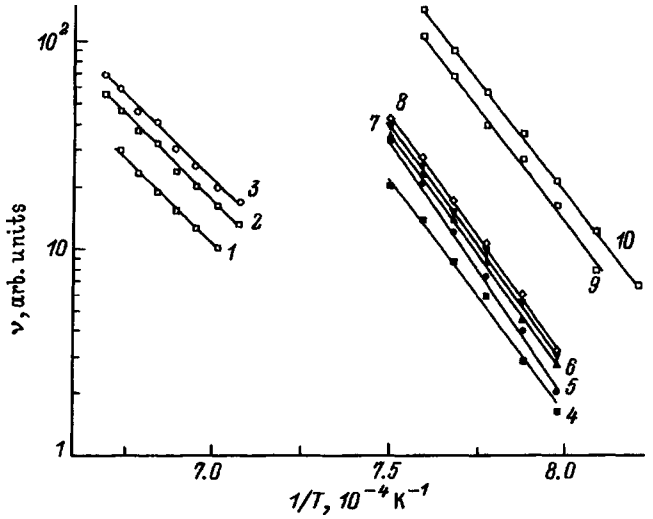

FIG. 3. Arrhenius plots obtained by ABM for different coverages θ: *1*—0.007, *2*—0.015, *3*—0.018, *4*—0.05, *5*—0.08, *6*—0.11, *7*—0.14, *8*—0.17, *9*—16. Curve 10 was obtained by TDS on the low-temperature side of peak S.

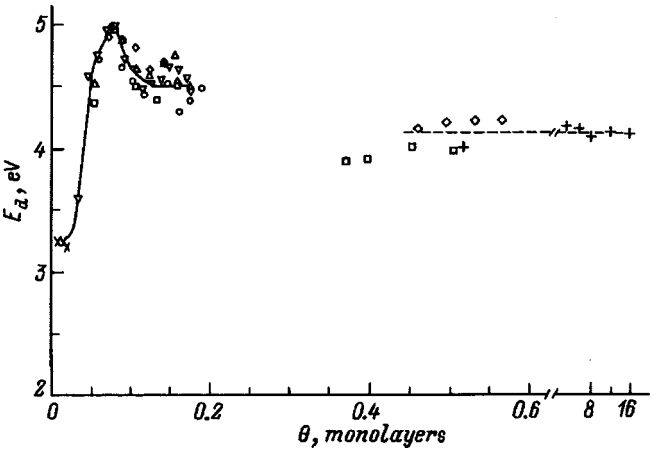

FIG. 4. $E_d=f(\theta)$ relation. The various symbols correspond to different series of ABM measurements. Dashed line shows the silicide decomposition activation energy obtained by TDS.

TABLE I. Diffraction patterns and corresponding coverages $\theta_1 \leqslant \theta \leqslant \theta_2$ for Sm-Si(111) structures obtained at $T=900$ K.

θ_1	θ_2	Diffraction pattern
0	0.06	(7×7)
0.07	0.09	$(7\times7)+(3\times1)$
0.12	0.29	(3×1)
0.33		$(3\times1)+(5\times1)$
0.36	0.39	(5×1)
0.42		$(5\times1)+(7\times1)$
0.46		(7×1)
0.49		$(7\times1)+(\sqrt{3}\times\sqrt{3})R30°$
0.52	10	$(\sqrt{3}\times\sqrt{3})R30°$

ments are in good agreement with the data of other researchers.[13,14]

In order to compare LEEDS data with TDS and ABM measurements performed at temperatures above 900 K, we carried out additional diffraction studies of adlayers deposited on the substrate at 1300 K. The observed diffraction patterns and the corresponding coverage intervals are given in Table II.

Upon inspection of the two Tables we see that, for coverages $\theta \leqslant 0.4$, both sequences of the diffraction patterns coincide. Differences appear at higher adsorbate concentrations. Namely, in the case of interfaces formed at $T=900$ K (Table I) we observed (7×1) and $(\sqrt{3}\times\sqrt{3})R30°$ patterns which were not seen from interfaces formed at $T=1300$ K.

The diffraction patterns obtained after the substrate heating at $T=800$ K were compared with scanning tunneling microscopy (STM) data for the Sm-Si(111) system.[13] It was found that the (3×1), (5×1), and (7×1) patterns can be identified with STM images obtained from the 3×2, 5×1, and 7×1 structures (we shall in what follows drop the parentheses in the STM notation and leave them in the diffraction patterns).

3. DISCUSSION OF RESULTS

TDS and ABM (Subsections II.A and II.B, respectively) showed that the appearance of the Sm-Si(111) interface can be separated into an adsorption and a silicide formation stage. In the first stage, samarium atoms reside on the surface in adsorbed state. The growth of this film leads eventually to the second stage, namely, silicide formation, where the rupture of interatomic valence bonds in the substrate makes it possible for Sm and Si atoms to combine in a chemical compound.

TABLE II. Diffraction patterns and corresponding coverages $\theta_1 \leqslant \theta \leqslant \theta_2$ for Sm-Si(111) structures obtained at $T=1300$ K.

θ_1	θ_2	Diffraction pattern
0	0.06	(7×7)
0.07	0.10	$(7\times7)+(3\times1)$
0.12	0.31	(3×1)
0.33		$(3\times1)+(5\times1)$
0.35	>15	(5×1)

A. Adsorption stage

For low adsorbate concentrations corresponding to initial region I in the $\nu=f(\theta)|_{T=\text{const}}$ relations plotted in Fig. 2, the samarium atom flux from the surface grows nearly linearly with increasing number of samarium atoms in the adlayer and is described by first-order $(n=1)$ desorption equation (1). This reflects formation of a two-dimensional gas of single adsorbate atoms on the surface. To estimate the kinetic parameters of the desorption, we chose the lowest possible values of θ, at which lateral interactions may be neglected. The activation energy of desorption, $E_d=3.2$ eV, obtained for $\theta=0.007$ is thus the binding energy of a single Sm atom with the substrate, and the prefactor $C\approx1\times10^{11}$ s^{-1} is typical of desorption of atoms from the 2D gas state.[15]

Growth of the adsorbed film results in a qualitative change in the pattern of the $\nu=f(\theta)_{T=\text{const}}$ relations. This change occurs in the coverage interval $\theta=0.04-0.07$ and becomes manifest in the appearance of region II in the isotherms. The rate of increase of the desorption flux $\Delta\nu/\Delta\theta$ within this region is substantially smaller than that in the preceding one. The transition from the first to second region indicates a change in state of the adsorbed film. TDS senses this change also. The motion of the top of peak A_1 in TD spectra (Fig. 1a) reverses direction exactly at the adsorbate concentrations at which region II appears in the isotherms. On reaching $\theta=0.06-0.07$, this peak begins to shift toward higher temperatures.

The two above observations suggest that the desorption activation energy for samarium atoms in new adsorption states is higher than that for atoms of a two-dimensional gas. This is clearly seen from Fig. 4 showing that an increase of adlayer thickness only by a few hundredths of a monolayer brings about a strong increase of E_d, which becomes as high as 4.95 eV for $\theta=0.07-0.08$. This value is considerably in excess (by 1.75 eV) of the binding energy to the surface of a samarium atom in the 2D gas.

LEEDS measurements lead one to a conclusion that the filling of new adsorption states characterized by substantially higher values of E_d is a consequence of a structural rearrangement in the adlayer. This is evidenced by the appearance at $\theta=0.07$ of reflections belonging to a new diffraction pattern, (3×1). This pattern persists without any change within a broad adsorbate concentration range, and its reflexes grow in intensity as one moves toward larger θ, thus implying that the geometric structure of the growing adsorbed film remains unchanged. As for the (7×7) reflections from the clean surface, they die out gradually as the adlayer fills up the substrate surface, to vanish altogether at $\theta=0.12$.

The above results obtained independently by means of three methods suggest that, similar to the Yb-Si(111) case studied by us earlier,[8] structural rearrangement in the adlayer in the Sm-Si(111) system proceeds from the 2D-gas state to 2D islands, after which the growth follows a domain pattern. The evolution of the two-dimensional structure occurring at the interface is accompanied by a change in desorption order n as one transfers from region I to region II in the isotherms (Fig. 2). Deviations from the first-order characteristic of desorption from a two-dimensional gas are seen in the coverage

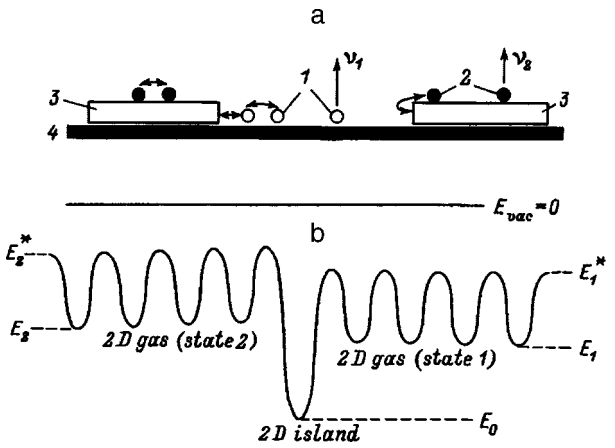

FIG. 5. Scheme illustrating the model of desorption processes in the 2D-islands–adsorbed-gas system.

interval $\theta \approx 0.03-0.04$, which signals nucleation of an island phase at the given adsorbate concentration. In contrast to the system Yb-Si(111), however, where formation of 2D domains from atoms of the adsorbing substance results in the onset of zeroth-order deposition, in the Sm-Si(111) system n becomes close to 1/2.

The desorption kinetics are determined both by the adlayer structure and by the conditions in which particles evaporate into vacuum. Two limiting cases of desorption kinetics from the system containing a mixture of 2D islands with a 2D gas were considered.[15,16] In the first case, the desorption is zero order $(n=0)$, and in the second, $n=1/2$. Figure 5a shows schematically an adlayer consisting of two phases, namely, 2D islands and an adsorbed gas, whose atoms can reside either on the substrate (state 1) or on an island (state 2). The corresponding energy diagram in Fig. 5b illustrates adsorption centers with a high binding energy E_0 (particles in an island) and centers with lower binding energies, E_1 and E_2, for adsorbed-gas atoms. Desorption from the island phase, where most of the adsorbate is concentrated, takes place in such a system in two stages. In the first stage the particle transfers to one of the 2D-gas states, from which it can subsequently leave the surface.

Here a very essential simplifying assumption was made, namely, that the 2D-gas atoms residing in the two different adsorption states have the same desorption parameters, i.e. $E_1=E_2$ and $E_1^*=E_2^*=E^*$.[15,16] If within this approximation it is assumed that the mean diffusion path X_s of gas particles exceeds by far the average distance between islands, $\rho^{-1/2}$ (where ρ is their density), then the desorption kinetics will be zero order. In this case the measured desorption activation energy is E_0. In the other limiting case, $X_s < \rho^{-1/2}$, the desorption order is one half, with the activation energy decreasing by E^*.

In actual fact, however, the desorption parameters of the 2D gas from states 1 and 2 may differ considerably, since the substrate and the island have essentially different surfaces. Obviously enough, the desorption flux will in this case be a sum of two terms, ν_1 and ν_2. The first of them is determined by the surface properties of the substrate, and the second, by those of the domain. If (i) the desorption through state 1 is zero order, and that through state 2 occurs by the $n=1/2$ order, and (ii) the gas atom concentration is negligible compared to the total adsorbate concentration N, then the flux can be written

$$\nu=\nu_1+\nu_2=(1-\alpha)C_0\exp(-E_0/kT)+\alpha C_2 N^{1/2} \times \exp[-(E_0-E_2^*)/kT], \quad (2)$$

where C_0 and C_2 are the preexponential factors, and α is the relative area of the surface occupied by the island phase. For $\alpha \ll 1$ the second term, which describes desorption through state 2, may be neglected. In this case the desorption is zero order, and the measured energy of its activation is equal to the energy required to remove an atom from a domain into vacuum, E_0. Conversely, when the surface is filled completely by islands, the first term becomes negligible, and the desorption order becomes close to $n=1/2$. In this case the desorption activation energy is $E_d=E_0-E_2^*$ (Fig. 5).

The above approach offers a qualitative interpretation for the course of the concentration dependence $E_d=f(\theta)$. The maximum energy $E_d=4.95$ eV obtained in the early stage of island formation (i.e. when their total area is small) approaches most closely the energy E_0 required to remove an atom from a domain. As the substrate surface becomes filled more and more by the island phase (as follows from TDS and ABM measurements, this process is completed at $\theta=0.17$), the activation energy of desorption drops to 4.5 eV. This yields $E_2^*=0.45$ eV.

LEEDS data (Tables I and II) reveal a (3×1) diffraction pattern for the adsorbate concentration corresponding to completion of the island phase formation. The STM image corresponding to this diffraction pattern was shown[13] to have 3×2 structure. The maximum filling for this surface superlattice is also $\theta=0.17$. One can therefore conjecture that at coverages up to $\theta=0.17$ the island-layer domains have 3×2 structure at high temperatures as well.

An analysis of STM images and of photoelectron spectra provided a basis for an atomic model of the Sm-Si(111)3×2 structure.[13] In this model, bridge-type adsorption centers were chosen as preferable sites for Sm adsorption on the Si(111) 1×1 surface. The Sm atoms adsorbing at these centers and having a valence of $2+$ become bound to two silicon atoms and form rows with Sm atoms spaced by $2a$ and a row-to-row separation of $3a$, where $a=3.84$ Å is the Si(111) 1×1 lattice parameter. The other four silicon atoms (Si*), which are contained in the 3×2 unit cell and are not bound to samarium atoms, have one dangling bond each. The atomic model of the Sm-Si(111) 3×2 structure is shown in Fig. 6a.

The data obtained in this work permit a suggestion that Si* atoms play a decisive role in the increase of the desorption activation energy E_d when 3×2 domains form from the two-dimensional gas. If we assume that the energy required to remove a samarium atom from such a domain into vacuum is 4.95 eV, then incorporation into this domain should increase E_d by 1.75 eV. The distance between nearest-neighbor samarium atoms in an island is, however, too large (about 8 Å) for direct lateral interaction to contribute noticeably to this value. The energy E_d may increase

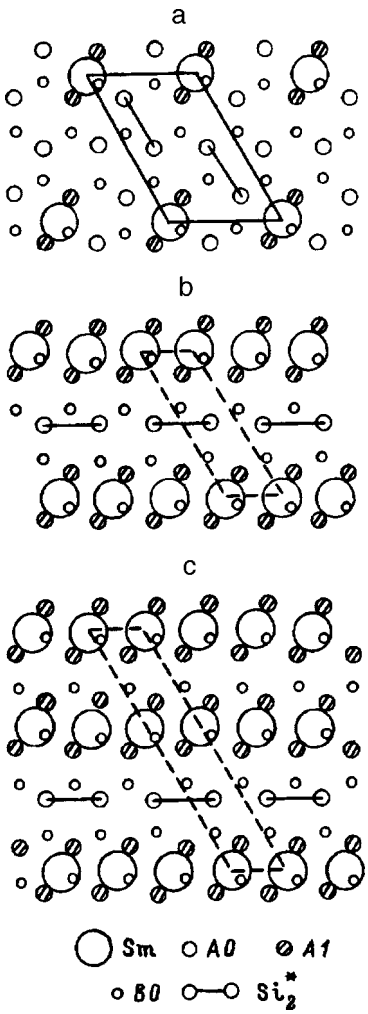

FIG. 6. Atomic models of unit cells of the Sm-Si(111) submonolayer structures; a—3×2, b—3×1, c—5×1. $A0$ and $A1$—Si atoms in the first substrate layer, not bound to Sm and bound to one Sm atom, respectively. $B0$—Si atoms in the second substrate layer, Si_2^*—two Si atoms making up a dimer.

through formation of Si*-Si* dimer pairs on the substrate surface. One of the versions of this process is shown in Fig. 6a. Charge redistribution between Si* atoms and the corresponding enhancement of their interaction should bring about a decrease of the energy of the system and an increase of E_d.

The assumption of the dimer formation is in accord with a study by photoelectron spectroscopy.[13] It was found[13] that the 3×2 structure does not have dangling bonds (i.e. the surface has a semiconducting character).

Our results permit an evaluation of the binding energy of the Si*-Si* dimer. Formation of the 3×2 domain increases the bond strength by 1.75 eV. In the unit cell of such a domain, there are two silicon dimers per one samarium atom. Hence the energy required to break each of them should be 0.85 eV. Evaluation of this quantity for the Yb-Si(111)3×2 structure yielded 0.75 eV.[8]

In this case the activation energy of the desorption process equals $E_d=E_0-E_2^*$ (Fig. 5). The energy E_d within the coverage interval $0.2<\theta<0.35$ was not evaluated, since the Arrhenius plots at these adsorbate concentrations are nonlinear. This may be due to the fact that desorption occurs simultaneously from several adsorption states, and its rate is determined by the sum of the rates of these states. As for the presence in the isotherms (Fig. 2) of region III similar to region II, it argues for the domain character of growth of the adsorbed film. Turning now to the structure of this film, it is believed[13] that after the 3×2 domain layer has been filled, a thicker film with 5×1 structure begins to grow. The latter was studied by STM. The data obtained provided a basis for development of an atomic model, by which Sm atoms, similar to the 3×2 structure, occupy bridge-type adsorption centers on the Si(111) 1×1 surface. They combine to form linear chains with period a, spaced alternately by $2a$ and $3a$. This model is shown in Fig. 6c.

Our LEEDS data suggest that the (5×1) diffraction pattern corresponding to the 5×1 structure appears only after $\theta=0.33$ has been reached. At lower concentrations, the 3×1 pattern is observed. The maximum coverage at which it is seen is $\theta=0.33$. This number of adsorbed atoms corresponds to complete filling of the 3×1 structure. Although this structure was not observed by STM,[13] we believe that the 3×1 adlayer forms within the coverage interval $0.17<\theta<0.33$, with 5×1 layers growing above $\theta=0.33$. Thus for $\theta>0.17$ domains of different types coexist on the surface. The nonlinearity of the Arrhenius plots reflects the fact that samarium atoms desorb from different adsorption states corresponding to domains with different structure.

Our introduction of a new structure, 3×1, in an attempt to explain the experimental data appears logical if we take into account that it is an intermediate step in the evolution of an adlayer from 3×2 to 5×1 structure. Figure 6b proposes an atomic model for the lattice of such a layer. By this model, Sm atoms occupying bridge-type adsorption centers make up rows separated by $3a$, similar to the 3×2 structure. As in the 5×1 structure, the distance between the neighboring atoms in the row is a.

The growth of 3×1 and 5×1 domains is apparently also accompanied by a rearrangement of the substrate surface and formation of Si*-Si* dimers. The desorption activation energy E_d from the three above structures (3×2, 3×1, and 5×1) depends on the concentration of these dimers.

B. Silicide formation

As seen from Fig. 1a and 1b, the film consisting of atoms of the adsorbate and substrate materials, samarium silicide, starts to form at high temperatures at coverages $\theta\leqslant0.4$. The Sm desorption kinetics from such a layer is zero order already at low coverages, less than one monolayer, and a maximum appears in the isotherms (Fig. 2) around a coverage $\theta=0.42$. Both these observations argue for the island pattern of growth. The feature in the form of a maximum is due to the existence of an activation barrier against the growth of a silicide film and can be explained in terms of the theory of heterogeneous nucleation.[17,18] According to this theory, thin-film growth on a substrate passes through a stage of formation of a nucleus of critical size, which possesses the largest free energy. In these conditions, the adsorbate desorp-

tion rate from the surface is maximum. The desorption rate decreases after the nucleus has grown beyond the critical size.

Our results permit a conclusion on the dimension of the silicide islands. The unlimited growth of the TD peak S (Fig. 1) without the appearance of any new features, as well as the existence of region IV in the isotherms (Fig. 2) with no additional maxima present, give us grounds to believe that the crystallites forming at the interface are three-dimensional.

Our data provide also an answer to the question of why a silicide and not a metallic phase grows on an adsorbed monatomic samarium film. The explanation lies in that formation of a layer consisting of atoms of the adsorbate and substrate materials is energetically preferable to growth of a metallic film; indeed, the value $E_d = 4.1$ eV for samarium silicide, which is actually the activation energy of silicide decomposition, is nearly twice that of sublimation of pure samarium, which is 2.14 eV (Ref. 11). Moreover, the decomposition energy of the silicide forming on a monatomic adsorbed film with domain structure 5×1 is so high as to make formation of the silicide phase energetically favored even before the completion of the intermediate adsorbed layer. The higher thermal stability of Sm silicide films with a decomposition temperature $T \cong 1200$ K compared to the silicides of Eu and Yb (Refs. 6 and 8, respectively) is due to the higher chemical activity of samarium atoms.

As for the film structure of such a silicide, LEEDS data show it to depend on substrate temperature. If the adsorbate material was deposited at $T = 900$ K, a $(\sqrt{3}\times\sqrt{3})R30°$ diffraction pattern was observed throughout the coverage range from 0.5 to 10 monolayers. The $\sqrt{3}$ reflections are apparently due to formation on the substrate surface of samarium disilicide with stoichiometric composition $SmSi_{2-x}$, where $x \approx 0.3$.[14] As already mentioned (Table II), at higher temperatures of about $T = 1300$ K the 5×1 diffraction pattern was observed in place of $(\sqrt{3}\times\sqrt{3})R30°$. It may be argued that at this temperature the surface of silicide islands is covered by a 5×1 samarium-atom layer, with the stoichiometric composition of the silicide itself being Sm_2Si_5. This surface phase is characterized by a higher percentage content of silicon atoms compared to the disilicide $SmSi_{1.7}$. This may be explained by the higher mobility of silicon atoms in an adsorbed film at higher temperatures.

A special experiment showed the structural rearrangement in the samarium silicide layer to have thermally activated. Heating the sample with a $\theta = 1$ samarium film at $T = 1100$ K revealed a transition from the $(\sqrt{3}\times\sqrt{3})R30°$ diffraction pattern to (7×1). If this layer was heated at $T = 1140$ K, the (5×1) diffraction pattern appeared. As follows from TDS measurements (Fig. 1a and 1b), at these temperatures adsorbate desorption may be neglected.

In conclusion, it should be pointed out that the Sm-Si(111) interface forms by a mechanism close to that of Stransky-Krastanov.[19] The difference lies in that the 3D islands growing on a monatomic Sm film consist of atoms not only of the adsorbate but of the substrate as well. The intermediate layer grows also by the island pattern. The structure of its domains (3×2, 3×1, 5×1, and 7×1) is determined by the adsorbate concentration and the formation temperature. The silicide phase starts to form even before the completion of the intermediate adlayer. The structure and stoichiometric composition of a silicide film depend on the substrate temperature at which it grew. All structural rearrangements in the system under study exhibit thermally irreversible character.

Financial support of the Russian Fund for Fundamental Research (Grant 96-02-16898) is gratefully acknowledged.

[1] K. N. Tu, R. D. Thompson, and B. Y. Tsaur, Appl. Phys. Lett. **38**, 626 (1981).
[2] R. D. Thompson and K. N. Tu, Thin Solid Films **93**, 265 (1982).
[3] N. Norde, J. deSousa Pires, F. d'Heurle, F. Pesavento, S. Petterson, and P. A. Tove, Appl. Phys. Lett. **38**, 865 (1981).
[4] G. Rossi, Surf. Sci. Rep. **7**, 1 (1987).
[5] F. P. Netzer, J. Phys.: Condens. Matter **7**, 991 (1995).
[6] M. V. Kuz'min, M. V. Loginov, M. A. Mittsev, and T. V. Krachino, Fiz. Tverd. Tela (St. Petersburg) **37**, 1030 (1995) [Phys. Solid State **37**, 559 (1995)].
[7] M. V. Kuz'min, M. V. Loginov, and M. A. Mittsev, Pis'ma Zh. Tekh. Fiz. **21**, No. 19, 73 (1995) [Pis'ma Zh. Tekh. Fiz. **21**, 803 (1995)].
[8] T. V. Krachino, M. V. Kuz'min, M. V. Loginov, and M. A. Mittsev, Fiz. Tverd. Tela (St. Petersburg) **39**, 256 (1997) [Phys. Solid State **39**, 224 (1997)].
[9] A. Ishizaka and Y. Shiraki, J. Electrochem. Soc. **133**, 666 (1986).
[10] M. V. Loginov, M. A. Mittsev, and V. A. Pleshkov, Fiz. Tverd. Tela (Leningrad) **34**, 3125 (1992) [Phys. Solid State **34**, 1672 (1992)].
[11] E. M. Savitskiĭ and V. F. Terekhova, *Metallography of Rare-Earth Metals* [in Russian] (Nauka, Moscow, 1975).
[12] W. Mönch, *Semiconductor Surfaces and Interfaces* (Springer-Verlag Series in Surface Science, Berlin, 1993, Vol. 22).
[13] C. Wigren, J. N. Andersen, R. Nyholm, M. Göthelid, M. Hammar, C. Törnevik, and U. O. Karlsson, Phys. Rev. B **48**, 11014 (1993).
[14] C. Wigren, J. N. Andersen, R. Nyholm, and U. O. Karlsson, Surf. Sci. **293**, 254 (1993).
[15] R. Kern, G. Le Lay, and J. J. Metois, in Current Topics in Materials Science, Vol. 3, edited by E. Kaldis, North-Holland (1979), p. 131.
[16] G. Le Lay, M. Manneville, and R. Kern, Surf. Sci. **65**, 261 (1977).
[17] J. P. Hirth and G. M. Pound, *Condensation and Evaporation. Nucleation and Growth Kinetics* (*Progress in Material Sciences*), edited by B. Chalmers [Pergamon, Oxford, 1963; Metallurgiya, Moscow, 1966].
[18] J. P. Hirth and K. L. Moazed, *Nucleation Processes in Thin Film Formation* (*Physics of Thin Films. Advances in Research and Development*), edited by G. Hass and R. E. Thun, Academic Press, 1967; Vol. IV) Moscow, 1970.
[19] E. Bauer and H. Poppa, Thin Solid Films **12**, 167 (1972).

Translated by G. Skrebtsov

Unusual behavior of thermal conductivity of a crystalline-NaCl–opal nanocomposite

L. I. Arutyunyan, V. N. Bogomolov, N. F. Kartenko, D. A. Kurdyukov, L. S. Parfen'eva, I. A. Smirnov, and N. V. Sharenkova

A. F. Ioffe Physicotechnical Institute, Russian Academy of Sciences, 194021 St. Petersburg, Russia

A. Jezowski, J. Mucha, and H. Misiorek

Institute for Low-Temperature and Structural Research, Polish Academy of Sciences, 50-950 Wrocław, Poland

(Submitted September 2, 1997)
Fiz. Tverd. Tela (St. Petersburg) **40**, 379–380 (February 1998)

An opal-based nanocomposite has been prepared with NaCl incorporated in its pores. The nanocomposite was produced by impregnating the opal with a NaCl solution at room temperature. Thermal conductivity of the nanocomposite has been measured in the temperature range 4.2–300 K. The effective heat conductivity of the nanocomposite was found to be equal to that of pure opal. The observed phenomenon can be explained by assuming that NaCl resides in opal pores in the form of noncontacting needles, thus precluding heat propagation through it.
 [S1063-7834(98)04702-9]

A number of our studies dealt with the thermal conductivity of nanocomposites based on synthetic opal.[1–4] The corresponding publications discussed in detail the opal structure and the specific features of formation of opal-based nanocomposites.

An investigation[5] of the surface oscillations of NaCl introduced from a water solution into porous glass with pore diameter of ~70 Å showed NaCl to reside in the pores in the form of needles which do not contact each other.

The temperature hysteresis observed in thermal conductivity measurements of opal-2[1)] was attributed by us to the presence in some of the closed opal pores of supercooled water crystallizing in ice needles, which are not in contact with each other and, thus, do not transmit heat flux.

The objective of this work was twofold: to prepare a NaCl-opal nanocomposite by impregnating opal samples with a saturated NaCl solution at room temperature, i.e., to try to produce a composite by a technology similar to the one employed in Ref. 5, and to measure its thermal conductivity within a broad temperature range.

NaCl was introduced into opal-1 by the above technique, after which the samples were dried at 100 °C. The pore fill-

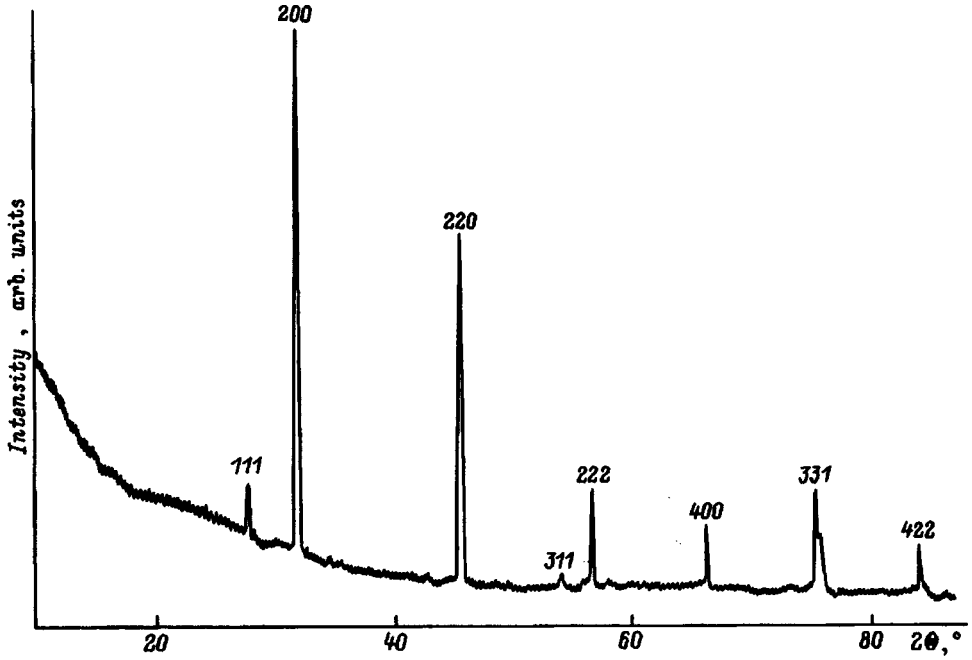

FIG. 1. Diffractometer curve for the nanocomposite representing opal-1 in which 45% of the volume of first-order pores is filled by NaCl.

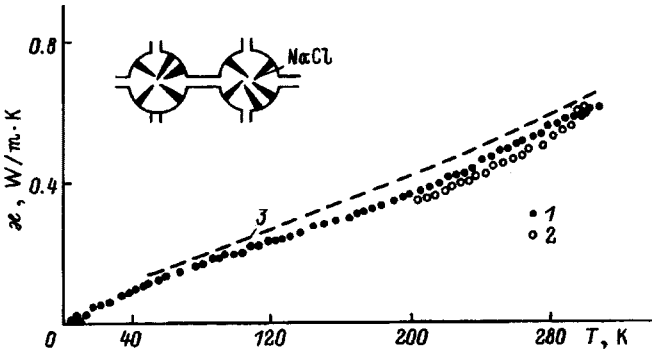

FIG. 2. Thermal conductivity of (*1*,*2*) the nanocomposite representing opal-1 in which 45% of the volume of first-order pores is filled by NaCl, and (*3*) opal-1 (Refs. 1 and 2). The numbers 1 and 2 refer to the nanocomposite measurements performed in heating and cooling runs, respectively. Shown in the top left corner is the proposed arrangement of NaCl crystals in first-order opal pores. Pore diameter ~800 Å (Refs. 1–3).

ing, determined by the solubility of the substance in water, was found to be 45% of the volume of the first-order pores.[2)]

The conductivity measurements were performed in a vacuum of $\sim 10^{-5}$ mm Hg in an arrangement described in detail elsewhere.[6]

Figure 1 displays a diffractometer curve for the nanocomposite representing opal-1 in which 45% of the volume of first-order pores was filled by NaCl. Similar curves supporting the amorphous state of opal-1 were obtained by us earlier.[1–4]

X-ray diffraction analysis of opal-1 and of the nanocomposite was performed on a DRON-2 diffractometer (Cu $K\alpha$ radiation, Ni filter) within the angular range $2\theta = 4 - 100°$. The diffraction patterns indicate the presence in the sample of a well-developed NaCl phase and the absence of any traces of opal crystallization. The cell constant of NaCl in the opal was found to be 5.641 Å (reference tables give 5.6402 Å for the unit cell parameter of bulk NaCl).

Figure 2 shows the experimental thermal conductivity data of the nanocomposite and of opal-1 (the latter were taken from Refs. 1–3).

We readily see that the heat conductivity of the opal-1 matrix and of the nanocomposite practically coincide throughout the temperature range covered by the measurements.

We may thus conclude that NaCl resides in opal pores (the largest diameter of first-order pores in opal is[1–4] ~800 Å) in the form of noncontacting needles and, therefore, there was no heat flux through NaCl.

Support of the Russian Fund for Fundamental Research (Grant 96-03-32458a) is gratefully acknowledged.

[1)]We are following here the terminology accepted earlier.[1–4]
[2)]The volume of the first-order pores constituted 26% of the total theoretical opal porosity (59%).[1–3]

[1] V. N. Bogomolov, L. S. Parfen'eva, A. V. Prokof'ev, I. A. Smirnov, S. M. Samoĭlovich, A. Jezowski, J. Mucha, and H. Misiorek, Fiz. Tverd. Tela (St. Petersburg) **37**, 3411 (1995) [Phys. Solid State **37**, 1874 (1995)].
[2] V. N. Bogomolov, D. A. Kurdyukov, L. S. Parfen'eva, A. V. Prokof'ev, S. M. Samoĭlovich, I. A. Smirnov, A. Jezowski, J. Mucha, and H. Misiorek, Fiz. Tverd. Tela (St. Petersburg) **39**, 392 (1997) [Phys. Solid State **39**, 341 (1997)].
[3] L. I. Arutyunyan, V. N. Bogomolov, N. F. Kartenko, D. A. Kurdyukov, V. V. Popov, A. V. Prokof'ev, I. A. Smirnov, and N. V. Sharenkova, Fiz. Tverd. Tela (St. Petersburg) **39**, 586 (1997) [Phys. Solid State **39**, 510 (1997)].
[4] V. N. Bogomolov, N. F. Kartenko, L. S. Parfen'eva, A. V. Prokof'ev, I. A. Smirnov, H. Misiorek, J. Mucha, and A. Jezowski, Fiz. Tverd. Tela (St. Petersburg) **40**, (1998) (in press).
[5] M. I. Abaev, V. N. Bogomolov, V. V. Bryksin, and N. A. Klushin, Fiz. Tverd. Tela (Leningrad) **13**, 1578 (1971) [Sov. Phys. Solid State **13**, 1323 (1971)].
[6] A. Jezowski, J. Mucha, and G. Pome, J. Phys. D **20**, 739 (1987).

Translated by G. Skrebtsov